europhysics
conference
abstracts

16 th European Conference on

Controlled Fusion and Plasma Physics

Venice, March 13-17, 1989

Editors: S.Segre, H. Knoepfel, E. Sindoni

Contributed Papers
Part I

VOLUME
13B
Part I

blished by: European Physical Society
ies Editor: Prof. K. Bethge, Frankfurt/M.
naging Editor: G. Thomas, Geneva

XVI FUSION VENEZIA 1989

S. Giorgio Maggiore Island

16th European Conference on

Controlled Fusion and Plasma Physics

Venice, March 13-17, 1989

Editors: S. Segre, H. Knoepfel, E. Sindoni

Contributed Papers

Part I

EUROPHYSICS CONFERENCE ABSTRACTS is published by the
European Physical Society,

PREFACE

The 16th European Conference on Controlled Fusion and Plasma Physics was held in Venice, Italy, from 13th to 17th March 1989 by the Plasma Physics Division of the European Physical Society (EPS).

The Conference has been organized under the sponsorship of the Italian National Research Council (CNR), the Italian Commission for Nuclear and Alternative Energy Sources (ENEA) and the International School of Plasma Physics "Piero Caldirola" (ISPP).

The programme, format and schedule of the Conference were determined by the International Programme Committee which was appointed by the Plasma Physics Division of the EPS.

The programme included 17 invited lectures, 23 orally presented contributed papers and more than 450 contributed papers presented in poster sessions.

This 4-volume publication contains all accepted contributed papers received in due time by the Organizers. It is published in the Europhysics Conference Abstracts Series. The 4-page extended abstracts were reproduced photographically using the camera-ready manuscripts submitted by the authors. The invited papers will be published in a special issue of the journal "Plasma Physics and Controlled Fusion" and sent free of charge to each registered participant.

The organizers would like to acknowledge the skillful and dedicated support given by Maria Polidoro of the ENEA Fusion Department at Frascati to the editing of these four volumes.

The Editors

INTERNATIONAL PROGRAMME COMMITTEE

S. Segre (Chairman), University of Rome II, Rome, Italy
K. Appert, CRPP, Lausanne, Switzerland
H.A.B. Bodin, Culham Laboratory, Abingdon, United Kingdom
F. De Marco, ENEA, Frascati, Italy
E. Fabre, Ecole Polytechnique, Palaiseau Cedex, France
M. Fontanesi, CNR, Milan, Italy
V.E. Golant, Joffe Physics Institute, Leningrad, USSR
J. Jacquinot, JET, Abingdon, United Kingdom
G.M. Mc Cracken, JET, Abingdon, United Kingdom
J. Nührenberg, MPI, Garching, F.R.G.
J. Tachon, CEN, Cadarache, France
F. Wagner, MPI, Garching, F.R.G.
R.R. Weynants, ERM, Brussels, Belgium

ORGANIZING COMMITTEE

M. Fontanesi (Chairman), CNR, Milan
H. Knoepfel, Associazione Euratom-ENEA, Frascati
M. Lontano, CNR, Milan
G. Malesani, CNR, Padua
E. Sindoni, University of Milan, Milan
M. Polidoro, ENEA, Frascati

CONTENTS

PAPER IDENTIFICATION

Each paper is identified with a 6 character code. The code u v wx yz has the following structure:

u - type of contribution; u = O, P for oral and poster contributed paper

v - the day of event; v = 1,2,3, ...9 for Monday morning, Monday afternoon, Tuesday morning, ... to Friday morning

wx - the topic and subtopic of the contribution

yz - progressive number within session and topic

Example

P4 F6 11

P	4	F6	11
↓	↓	↓	↓
Paper type	Half-day number of event	Topic and Subtopic	Progressive number
↓	↓	↓	↓
Poster	Tuesday afternoon	Plasma heating and current drive Current drive and profile control	Poster number 11

TITLE LIST OF CONTRIBUTED PAPERS

A. TOKAMAKS

A1. Experiments

A3. Theory

B. STELLARATORS

C. ALTERNATIVE MAGNETIC CONFINEMENT SCHEMES

C1. Reverse field pinch

C2. Other alternative magnetic confinements schemes

D. INERTIAL CONFINEMENT

F2. Electron cyclotron resonance heating (ECRH)

F3. Lower hybrid heating (LHH)

F4. Alfvén and other RF-methods

G. GENERAL PLASMA THEORY

H. DIAGNOSTICS

I. BASIC COLLISIONLESS PLASMA PHYSICS

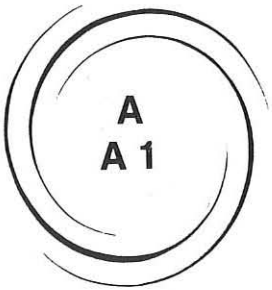

TOKAMAKS
EXPERIMENTS

ENHANCED PERFORMANCE OF HIGH CURRENT DISCHARGES IN JET PRODUCED BY ICRF HEATING DURING THE CURRENT RISE.

M.Bureš, V.Bhatnagar, G.Cottrell, S.Corti, J.P.Christiansen, L.-G.Eriksson*, T.Hellsten, J.Jacquinot, P.Lallia, P.Lomas, J.O'Rourke, A.Taroni, F.Tibone, and D.F.H.Start.

JET Joint Undertaking, Abingdon, Oxon, OX14 3EA, UK.
*Chalmers University of Technology, Gothenburg, Sweden.

Abstract. The performance of high current discharges can be increased by applying central ICRF heating before or shortly after the onset of sawtooth activity in the plasma current rise phase. Sawtooth-free periods have been obtained resulting in the enhanced discharge performance. High $T_e(0) = 9$ - 10.5 keV with peaked profiles $T_e(0)/\langle T_e \rangle = 3$ - 4 were obtained giving values of $n_e(0)T_e(0)$ up to 6 10^{20} (keV m^{-3}). Improvements in $T_i(0)$ and neutron production are observed. A 60% enhancement in D-D reaction rate from 2nd harmonic deuterium ($2\omega_{CD}$) heating appears to be present. In all current rise(CR) discharges radiation amounts to 25-50% of total power.

Introduction. ICRF heating experiments at 5 and 6 MA during the current rise were carried out in the D(H) heating scheme at 48 MHz. The RF antennae were phased as dipoles with maximum power emitted at $k_{\parallel} = 7$ m^{-1}. During the 5 MA discharges the RF power was applied at the level of $I_p = 3.7$ to 3.9 MA and ramped up during 0.5 sec to reach the full value at $I_p = 4$ to 4.2 MA. During the 6 MA discharges the corresponding current levels were 4.45 and 4.75 MA. The CR heating data are compared to the flat-top(FT) heating data performed for each plasma current during the same day and therefore with the same conditions of the tokamak. Typical FT target density and Z_{eff} were $\langle n \rangle = 2.3$ - 3 10^{19} m^{-3}, $Z_{eff} = 1.6$ - 2.5 for 5 MA discharges and $\langle n \rangle = 2$ 10^{19} m^{-3}, $Z_{eff} \approx 4$ for 6 MA.

Current penetration and sawtooth behaviour. During the 5 MA discharges the sawtooth activity starts when the plasma current reaches the value 4.6 - 4.7 MA. The application of RF heating delays the onset of sawteeth, the delay increasing with RF power. Fig.1 compares the evolution of the central electron temperature during RF heating to that of the ohmic discharge. A measure of current penetration is shown by polarimetric measurement of the central safety factor q(0). The first sawtooth crash occurs when q(0) is close to unity. While in the ohmic phase the reduction in $T_e(0)$ is $\approx$ 200eV, it reaches 3 to 3.5 keV in the case of RF heating. It implies that q is $\approx$ 1 over a substantial part of the plasma core. This is supported by the T_e profile measurements shown in Fig.2a. The inversion radius of the first crash is roughly 40 cm compared to 15 cm in the ohmic case. During the FT heating the corresponding value is $\approx$ 60 cm. In 6 MA discharges the sawtooth activity starts when the plasma current reaches 4 MA, clearly much earlier than during 5 MA

discharges. The difference may be due to higher resistivity from a higher Z_{eff}. By application of RF power the sawtoothfree period was obtained following the normal sawtooth activity. Thus, as demonstrated by 6 MA results, the dominant physical mechanism responsible for the delay of sawteeth is similar to that of the Monster sawtooth stabilisation. As indicated by polarimetric measurements, the delay of **current penetration also contributes.**

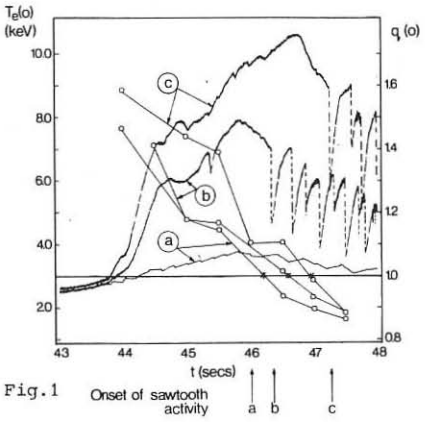

Fig.1

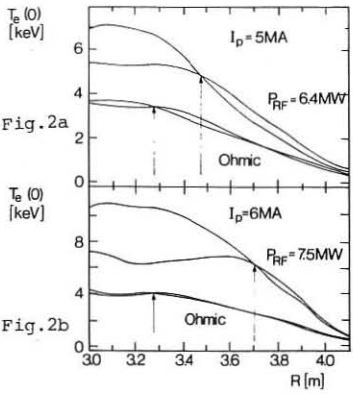

Fig.2a

Fig.2b

Fig.1 **Central electron temperature and q(0)** time evolution in a)ohmic, b)$P_{RF} = 4.3$ MW and c)$P_{RF} = 11$ MW discharges.
Fig.2a,b Electron temperature profiles associated with the first sawtooth colapses(just before and after) in ohmic and RF heated discharges in CR. The arrows indicate the inversion radii.

Enhanced performance during CR heating. The main observed improvements over heating during the current flat-top can be summarised: 1) factor 1.4 (5MA discharges) and 1.8 - 2 (6 MA discharges) increase in α, where α is defined by $\Delta T_e(0) = \alpha P_{RF}/n_e(0)$; 2) 10-20% increase in $T_i(0)$ in both 5 and 6 MA discharges; 3) 10-20% increase in $\Delta W/\Delta P_{TOT}$; 4) factor 2 increase in D-D reaction rate for 5 MA discharges. The relatively high gain in $T_e(0)$ during 6 MA discharges (shown in Fig.3) is explained by the low $T_e(0)$ values obtained in the FT phase. Such low values are consequence of a large plasma volume within the $q = 1$ surface affected by losses associated with sawtooth instability (Fig.2b). The rate of increase of $T_i(0)$ with $P_{RF}/n_e(0)$ is roughly the same in all cases of FT and CR heating, but the absolute values are systematically higher in the current rise. Presently it is not clear if the $\Delta W/\Delta P_{TOT}$ is conserved at higher powers than those achieved, i.e., above $P_\Omega + P_{RF} = 15$ MW. In Fig.4 the value of $n_e(0)T_e(0)$ is plotted for two 5 MA discharges during current FT and CR, with $P_{RF} = 11$ MW. A value of $6\ 10^{20}$ (keV m^{-3}) has been reached during both CR and more recently with combined RF heating and pellet

injection into a 3 MA discharge{1,2}. The electron temperature peaking ratio $T_e(0)/<T_e>$ reaches values 3.5 - 4.2 during 5 MA CR compared to 3 in 6 MA CR. Density peaking ratios in CR and FT are similar $n_e(0)/<n_e> = 1.4$ - 1.6. The D-D reaction rate data is shown in Fig.5. As explained below, a significant contribution to the neutron enhancement results from the creation of high energy deuterium tail. The reason why the 6 MA discharges did not produce a comparable improvement is the relatively high Z_{eff}.

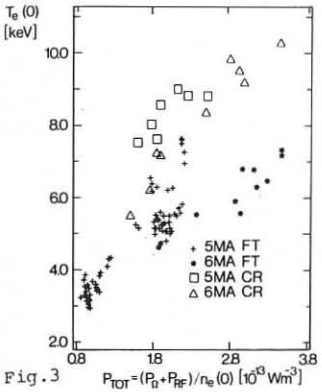

Fig.3

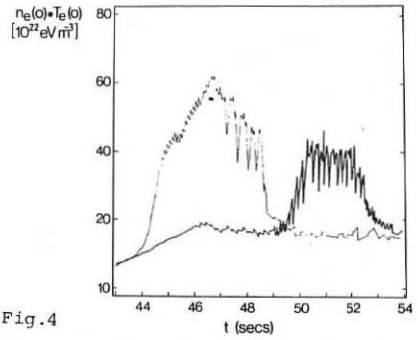

Fig.4

Fig.3 Central electron temperature versus total power per particle.
Fig.4 $n_e(0)T_e(0)$ during CR and FT 5 MA discharges, $P_{RF} = 11$ MW.

$2\omega_{CD}$ heating. The neutral particle spectra measurements indicate that the fast hydrogen and deuterium tails are formed after the application of RF power. During the 5 MA CR discharge with 11 MW of RF power the hydrogen spectrum develops a tail with a "temperature" $\approx$ 45 keV. A substantial fraction of particles is in the high energy range. Similarly deuterium spectra indicate a tail formation with a "temperature" $\approx$ 30 - 35 keV. In this case the majority of particles is in the bulk of the distribution fuction. The neutral particle analyser measures the energy of hydrogen neutrals up to 65 keV and deuterium up to 45 keV. Thus the information is of qualitative nature and the true tail temperature is certainly much higher. The correlation between the fluxes of high energy neutrals and neutrons also suggests that $2\omega_{CD}$ heating is present. The low energy channels do not exhibit such a correlation. To estimate the importance of the $2\omega_{CD}$ heating for the neutron yield, a self-consistent full wave RF power deposition calculation{3} in conjuction with Fokker-Planck calculations of the hydrogen and deuterium distribution functions were carried out. The complete spectrum of the dipole antenna was used. Fig.6 shows the results from the calculations which are compared with the measured neutron yield. The open circles represent the simulation of the thermal part of the yield. An agreement with

the measured values can be obtained if we assume Z_{eff} 30% higher than the measured one(2.6 instead of 2). The 60% contribution from the fast deuterons is also indicated. The power deposition calculation does not include electron Landau and TTMP damping. Estimates suggest that 10 - 20% of the power can be directly damped by electrons. This will slightly decrease the calculated enhancement, bringing it even closer to the measured value.

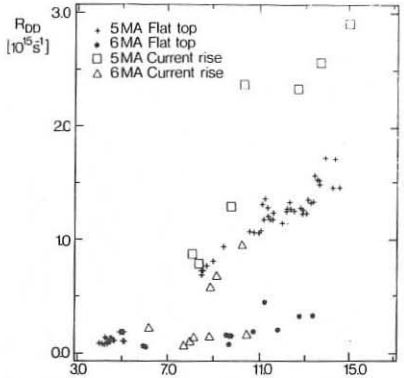

Fig.5

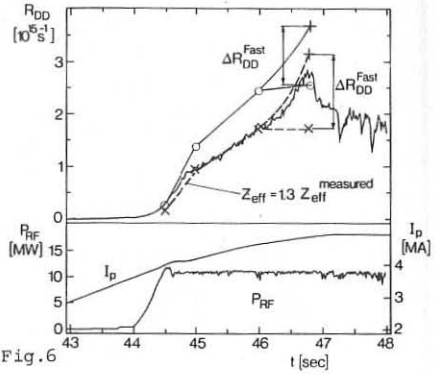

Fig.6

Fig.5 Neutron yield as a function of power input.
Fig.6 Time evolution of measured and calculated neutron yield. ΔR_{DD} represents the contribution from the $2\omega_{CD}$ heating. Plasma current and RF power are also shown.

Conclusions. Elimination of sawtooth activity by application of high power ICRF heating during the plasma current rise phase of 5 and 6 MA discharges results in an enhanced performance in terms of all major plasma parameters. In particular high value of $n_e(0)T_e(0) = 6\ 10^{20}$ (keV m^{-3}) has been reached together with enhanced neutron yield by $2\omega_{CD}$ heating. The peaking $T_e(0)/<T_e>$ reaches the value 4.2 which is a factor 2 higher than in the flat-top phase. The density peaking $n_e(0)/<n_e> = 1.5$ remains unchanged. Current rise heating appears to be one of the candidates for T(D) operation{4} in JET, eventually combined with pellet injection. It also provides an interesting target for NBI heating. The possibility of extending this mode of operation for longer period will be a subject of future experiments.

References.

1. G.Hammet et al., this conference.
2. V.Bhatnagar et al., this conference.
3. L.-G.Erikson et al., to be published in Nuclear Fusion.
4. J.Jacquinot et al., Plasma Phys. and Contr. Fus., Vol.30, no.11, p.1467.

ANALYSIS OF ICRH INDUCED ENERGETIC MINORITY PARTICLES AND THEIR EFFECT ON CONFINEMENT AND SAWTEETH.

R.R. Weynants*, M. Gaigneaux, J-M. Beuken, T. Delvigne, P. Descamps, F. Durodié, M. Jadoul, R. Koch, D. Lebeau, A.M. Messiaen*, X.M. Shen, P.E. Vandenplas, D. Van Eester, R. Van Nieuwenhove, G. Van Oost, G. Van Wassenhove

Laboratoire de Physique des Plasmas - Laboratorium voor Plasmafysica
Association "Euratom-Etat belge" - Associatie "Euratom-Belgische Staat"
Ecole Royale Militaire - B 1040 Brussels - Koninklijke Militaire School

Abstract : An analysis is presented of the energetic minority particles created by ICRH in TEXTOR in the minority (H-D) scenario and of their repercussion on various plasma properties.

Introduction: Heating at the fundamental hydrogen frequency in a deuterium plasma containing hydrogen as a minority results in the creation of a perpendicular, energetic hydrogen population [1]. As the distribution of this component is non-Maxwellian with an excess at high energies, it is usually referred to as a tail.

In this paper we compare the experimental data on tail energy obtained on TEXTOR [2] with a theoretical model based on [1], using as input the experimental (and theoretically confirmed) power splitting between the heating mechanisms (mode conversion *vs* minority heating) and the experimentally determined power densities. The results can be understood in the context of a confinement scheme in which the tail incremental confinement is roughly twice better than that of the thermal components and where the thermal confinement itself is not altered by the presence of the energetic particles. The tail particles might also be responsible for an observed stretching of the sawtooth period.

Tail characteristics: The energy E_H contained in the tail is found from the measured differences between the diamagnetic energy E_{dia}, the energy derived from the MHD equilibrium E_{equi} and the kinetic energy (summing over electrons and deuterons) E_{kin} following the well-known relations

$$E_H = \alpha\,(E_{dia} - E_{kin}) = \beta\,(E_{equi} - E_{kin}),$$

with $\alpha = \beta = 1$ for an isotropic tail or $\alpha = 2/3$ and $\beta = 4/3$ for an anisotropic one with an energetic perpendicular component. Figure 1 shows for a number of discharges the variation of $E_{dia} - E_{kin}$ versus $E_{equi} - E_{kin}$. Notwithstanding the large errorbars on the individual energy measurements, the data clearly favours $\beta/\alpha = 2$, thus confirming the tail's anisotropy. The values of E_H henceforth used are then equated to $1/3(E_{dia} + 2E_{equi} - 3E_{kin})$.

The dominant scaling parameters of E_H are the ICRH power P_{RF} and the electron line density $\bar{n}_e$, the best fit being obtained in the combination $P_{RF}^2/\bar{n}_e$. For our usual operational conditions (I_p = 340 kA, $P_{RF,max}$ = 2.6 MW, $\bar{n}_{e,min} = 2.2\ 10^{13}\ cm^{-3}$) up to 60 % of the energy increase induced by the RF has been found in the tail component, corresponding then to an mean equivalent hydrogen temperature of 16 keV (n_H/n_e =0.08).

---

* Research Director at NFSR, Belgium

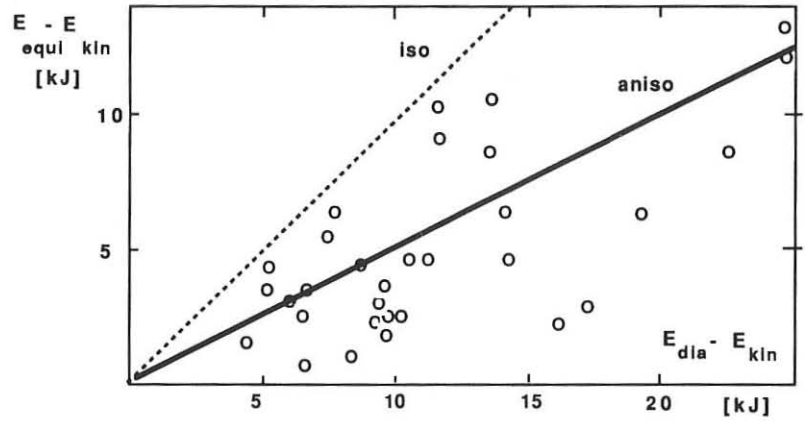

Fig. 1 Data showing anisotropy of tail particles.

Tail simulation: The prime loss channel for the minority particles is their slowing-down on the electrons and deuterons. Hence, one expects E_H to change like

$$E_H = P_{min}\,\tau_s\,, \qquad (1)$$

where P_{min} is that part of P_{RF} that is absorbed by minority heating, and $\tau_s = \tau_{se}\,\tau_{si}/(\tau_{se}+\tau_{si})$ is the effective energy slowing-down time. Under such conditions where P_{min} practically coincides with P_{RF} and $\tau_{se} \ll \tau_{si}$, Eq. (1) reduces to $E_H \sim P_{RF}\,T_e^{1.5}/n_e$, thus rendering the aforementioned scaling plausible. As these two prerequisites are never totally fulfilled in TEXTOR, a more rigorous modelling is required to obtain P_{min} and τ_s.

The relative splitting between minority damping and mode conversion damping is obtained from a 1-D full wave code [3]. The calculations are performed using the average k_z of the antenna spectrum. The tail characteristics and the partition of the collisional transfer between electrons and ions are found from [1] using the experimental power densities

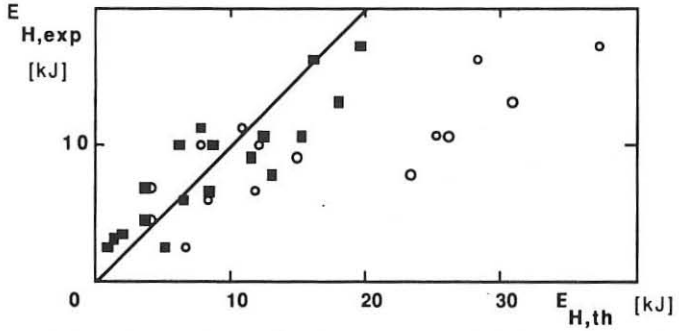

Fig. 2 Comparison between theoretical and experimental tail energies.The closed symbols take the minority confinement into account.

obtained by power modulation [4] and other techniques [2]. Figure 2 (open symbols) shows a comparison between the tail energy so obtained and the corresponding experimental data.

Clearly, a divergence develops at long slowing-down times. It is conjectured that this might be related to the own, finite confinement of the minority particles, characterized by the incremental time τ_{min}. Equation [1] should then be replaced by $E_H = P_{min}\,\tau_s'$, with $\tau_s = \tau_s\,\tau_{min}/(\tau_s+\tau_{min})$. Confronting the experimental data with this revised expression yields (Fig. 2, closed symbols) good agreement for $\tau_{min} = 25 \pm 5$ ms.

Confinement of thermal particles: The above results suggest a transfer of power according to the scheme shown in Fig. 3 (the channel of direct ion heating by harmonic deuteron resonance accounting for less than 5 %). The power corresponding to E_{min}/τ_{min} will not contribute to the heating of the thermal components and the proper quality factor for describing the latter's confinement should be

$$\tau_{inc} = \Delta E_{kin}/(P_{inc} - E_H/\tau_{min}). \qquad (2)$$

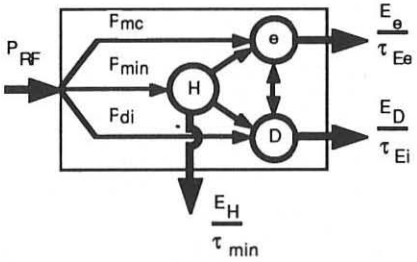

Fig.3 Power transfer scheme.

Fig.4 shows as a function of τ_{min} the τ_{inc} values that result as the averages over a large series of discharges ($0.8 < P_{inc}$ [MW]< 2.3; $1.8 < \bar{n}_e$ [10^{13} cm-3]< 4.4 ; $0.04 < n_H/n_e < 0.08$). This incremental confinement time can be compared with the published TEXTOR scaling, obtained with high field side (HFS) ICRH launching [5] having quite comparable power deposition profiles [2]. For the prevailing machine conditions this scaling predicts $\tau_{inc} = 11.9 \pm 2.4$ ms (horizontal line in Fig. 4) : a reduction of about 10 % of τ_{inc} might be deduced for $\tau_{min} = 25$ ms.

Conversely, the arguments leading to Fig. 4 can be viewed as an alternative τ_{min} evaluation, yielding $\tau_{min} = 19$ ms. It should be remarked that under the old HFS conditions about 20 % of the power went to the minority particles (vs 80 % now), while τ_{inc} was derived from diamagnetism (hence possibly being somewhat overestimated). It appears then that one could conclude that, within the experimental error bars, the confinement of the thermal particles is almost not affected by the tail's presence and that the latter has a global confinement which is about twice better than that of the thermal particles.

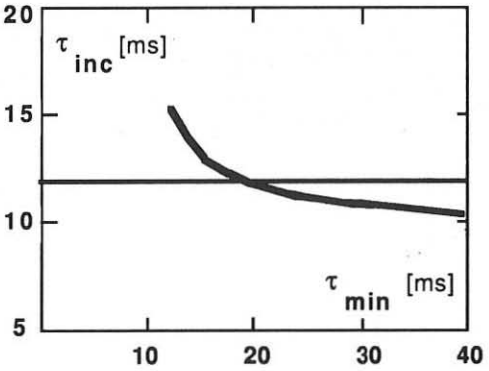

Fig.4 τ_{inc} as a function of τ_{min} following Eq. 2.

Sawtooth Behaviour: Going from HFS to LFS ICRH led to interesting changes in the sawtooth behaviour. In OH plasmas the electron temperature modulation equals 1.1 to 1.15 and the period increases with density to saturate around 20 ms under strong gas puffing.

With LFS operation, the modulation can increase up to 1.4 and the period can be stretched at a maximum rate of about 8 ms/MW at constant density. This contrasts with the HFS operation where the only systematically observed dependence was on density. The reasons for these differences are not clear. It should be noted that no fundamental change has occurred in the power deposited centrally into the electrons nor in the central electron temperature reached [2]: the mere increase of T_e does not suffice to explain the stretching. As one of the important modification related to the switch from HFS to LFS heating is the predominance acquired by the minority tail, a candidate for the period enhancement might be this tail occurrence. Fig. 5 shows that such a connection might indeed exist, the highest stretching rates being obtained when the energy in the tail is highest. This matter is the subject of further investigations.

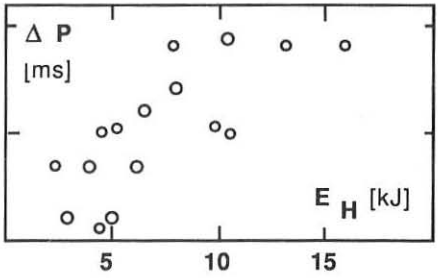

Fig. 5 Increase of sawtooth period with tail energy ($n_H / n_e = 0.08$)

References:

[1] T.H. STIX, Nuclear Fusion 15 (1975) 737

[2] R.R. Weynants, J.M. Beuken, L. De Keyzer, et al., 12th int. Conf. on Plasma Phys. and Controll. Nucl. Fusion Res., IAEA, Nice,1988, paper IAEA-CN-50/E-2-1.

[3] D. Van Eester, Proc. of Joint Varenna-Lausanne Int. Workshop on Theory of Fusion Plasmas, Chexbres, Oct. 1988.

[4] D.Lebeau, A.M. Messiaen, R.R. Weynants, this conference.

[5] R.R. Weynants, M. Jadoul, A.M. Messiaen, Proc.14th Europ. Conf. on Controll. Fusion and Plasma Phys.,Madrid 1987, ECA. Vol. 11d, part 1,p. 197.

IMPROVED CONFINEMENT IN L-MODE JET PLASMAS

T T C Jones, B Balet, V Bhatnagar, D Boyd[1], M Bures, D J Campbell, J P Christiansen, J G Cordey, W F Core, S Corti, A E Costley, G A Cottrell, A Edwards, J Ehrenberg, J Jacquinot, P Lallia, P J Lomas, C Lowry, M Malacarne, D G Muir, M F Nave, P Nielsen, C Sack, G Sadler, D F H Start, A Taroni, P R Thomas, K Thomsen

JET Joint Undertaking, Abingdon, Oxon, OX14 3EA, UK
[1]University of Maryland, College Park, MD20742, USA

1. Introduction

The JET confinement data show considerable variations of stored plasma energy W (thermal + fast ions) at fixed input power P, plasma current I, toroidal field B and plasma configuration C. The data on confinement properties, e.g. the confinement time τ_E or its incremental value τ_E(inc), derived from variations of P at fixed I, B, C thus exhibit scatter which makes the scaling of τ_E with P, I, B, C difficult to establish. The effects from sawteeth, from variations in the power deposition profiles and from plasma edge physics on confinement do not depend on P, I, B, C in any simple way which would permit a deduced scaling law to be identified with a single (or more) physics loss mechanism(s). In this paper we examine the response of confinement to variations in plasma configuration at fixed I and B (3 MA and 3 T). Results from global and local transport analysis are discussed in sections 2 and 3; section 4 describes the role of fast ions produced by ICRF and NBI heating. High confinement in the L-mode regime at increased plasma currents up to 6 MA is also studied, in particular the effects from sawteeth on stored energy W. Such effects increase with current and presently only predictive transport studies (section 5) can estimate what may be achieved at high current without sawteeth effects. The predictive studies also assess the benefits which may arise from an increase of the neutral beam energy at high plasma currents (section 6). The conclusions are based on an extensive study of data from JET pulses with up to 14 MW of ICRH, 21 MW of NBI and 6 MW of ohmic power. None of the pulses included in the study show the sudden reduction of D_α emission characteristic of the L to H mode transition of confinement.

2. JET plasma configurations

At fixed current (3 MA) and field (3 T) JET has been operated with several plasma configurations which are labelled as follows: LIM, a plasma attached to one or both of the belt limiters; IWL, a plasma attached to the inner vessel wall; DN, an up-down symmetric plasma with a separatrix inside the vessel. Up to 21 MW of NBI power has been applied to all configurations while only the DN and LIM configurations have had more than 10 MW of ICRH either alone or combined with NBI. Fig.1 presents a subset of the JET confinement data at 3 MA; the subset includes data from power scans in which the ICRH power does not exceed 50% of the total input power.

Each data point in Fig.1 corresponds to the value of confinement time τ_E and power P measured at the maximum of W (inferred from the diamagnetic loop diagnostic). When $W = W_{max}$, dW/dt is small such that the data in Fig.1 should represent steady state values. The various symbols refer to the different configurations described above. The solid line shows the variation of τ_{EG} with P derived from the Goldston scaling law [1]. In general the highest τ_E values occur in the DN configuration in which sawteeth are suppressed by ICRH; such high values are comparable with those obtained in JET H-mode plasmas [2].

3. Local transport calculations

Those JET pulses which exhibit L-mode high confinement, are studied by predictive transport calculations. The calculations employ electron and ion heat fluxes represented either by the Rebut-Lallia model [3] or a modified model appropriate to H-mode confinement [4]. The profiles of electron and ion heating rates from NBI and ICRH are calculated by the PENCIL and QFLUX codes; the profile of radiated power is obtained by Abel inversion of bolometer data. In order to match the predicted to the measured temperature profile, when $\tau_E > \tau_{EG}$, it is necessary to employ the H-mode model for the heat flux.

4. Fast ion energy

High values of τ_E are reached usually in the DN configuration if the initial (target) density is low (of order $10^{19}/m^3$). Application of ICRH to such a target establishes a population of high perpendicular energy ($\sim$ 1 Mev) minority H ions which heat the electrons to temperatures in excess of 10 keV. This population exists for several confinement times in the centre of the plasma (where the ICRF resonance position is located); the absence of sawtooth crashes maintains this population. A second population of fast D ions is generated by neutral beam injection. While the energy content of the anisotropic H minority ions can be estimated from two magnetic energy measurements, that of the nearly isotropic NBI generated D ions can not. In order to evaluate the total fast ion energy content full transport calculations with the TRANSP interpretation code have been performed for a few high τ_E pulses. The calculations confirm that the thermal energy content $W_{th} = W - W_{fast}$ is still above the value W_G obtained from the Goldston scaling law [1]. Fig.2 shows values of W_{kin} vs P. W_{kin} is the plasma thermal energy content derived from kinetic measurements of ion and electron temperature and electron density. Fig.2 also confirms that the 3 MA DN data shows an improvement in confinement over the Goldston scaling.

5. Sawteeth effects at 3, 5, 6 MA

Fig.3 shows variations of W with P for selected 3, 5 and 6 MA pulses. It can be seen that doubling I from 3 to 6 MA does not double W as suggested in earlier scalings [5]. The stored energy W at 5 and 6 MA is affected more strongly by sawteeth than at 3 MA. The inversion radius increases with current I since the field is fixed at $\sim$ 3 T. A sawtooth collapse reduces the thermal energy content inside the inversion radius and

it also reduces the fast ion energy [6]. The reduced performance due to sawteeth can be modelled by predictive transport calculations. The sawtooth effects are taken into account by enhancing the heat transport coefficient in the sawtooth region to a Bohm-like value. The heat fluxes are otherwise given by the Rebut-Lallia model [3]. Fig.4 demonstrates how the time evolution of total stored energy W for a 6 MA JET discharge would improve if sawteeth were stabilised. The increase in W that would arise at 5, 6 and 7 MA is likely to restore the dependence of W (or τ_E) upon I previously reported [5]; presently such an improvement remains however a conjecture.

6. Beam deposition profiles and the effect of radiated power

The efficiency of NBI heating as defined in [7] reduces with increasing plasma density n, due to poorer beam penetration. The efficiency at a fixed beam energy of 80 keV is lower at 6 MA than at 3 MA due to the increased density associated with high plasma current. Calculations show that increasing the D° beam energy to 140 keV would be sufficient to yield a peaked deposition profile in a 6 MA plasma provided the density can be controlled during injection. However, local transport calculations at 6 MA indicate that a more peaked power deposition profile will be beneficial only if the deleterious effects of sawteeth can be eliminated. The importance of power radiated from the plasma core has also been examined for high current discharges; local transport calculations indicate that it does not contribute more than $\sim$ 10% to the confinement degradation.

7. Conclusions

The DN configuration at 3 MA is found to exhibit confinement properties better than those predicted by the scaling law proposed in [1]. The favourable current dependence implied in the Goldston scaling is however not established by the present data from JET high current discharges. The departure from the scaling law is attributed to sawteeth effects; elimination of sawteeth at high current should yield high confinement as demonstrated by the predictive calculations.

References

[1] R J Goldston, Plasma Physics and Controlled Fusion 126 p87 (1984).
[2] M Keilhacker, IAEA-CN-50/A-III-2, Nice (1988).
[3] P-H Rebut et al, IAEA-CN-50/D-4-1, Nice (1988).
[4] P-H Rebut et al, Proc XV EPS Conf. on Controlled Fusion and Plasma Physics, Vol I p247, Dubrovnik (1988).
[5] J G Cordey et al, IAEA-CN-47/A-II-3, Kyoto (1986)
[6] V Bhatnagar et al, this Conference.
[7] J D Callen et al, Nucl. Fusion 27 p 1857 (1987).

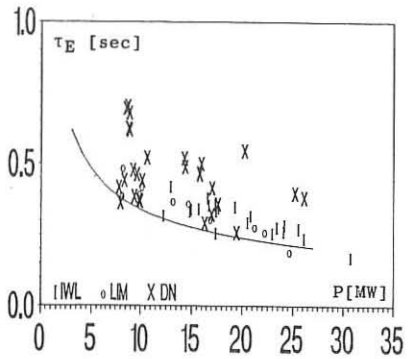

Fig.1 Confinement time τ_E vs P at various 3 MA configurations. Solid line represents Goldston scaling [1].

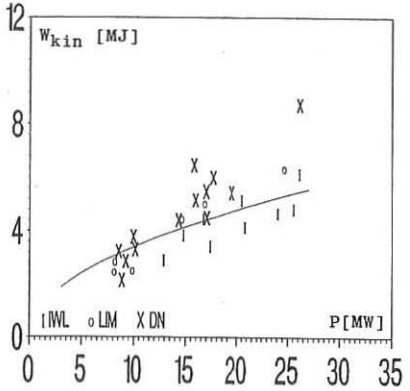

Fig.2 W_{kin} vs P at various 3 MA configurations. Solid line as in Fig.1.

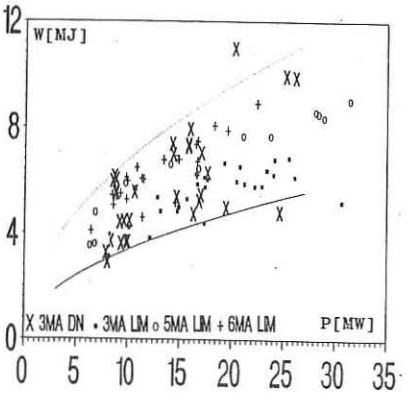

Fig.3 Total energy W vs P for selected 3, 5 and 6 MA pulses. Solid line represents Goldston scaling [1] at I = 3 MA, broken line at I = 6 MA.

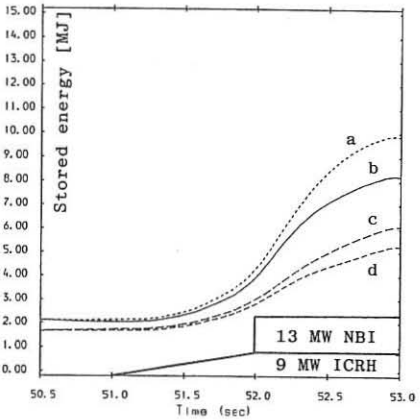

Fig.4 Calculated stored energies vs time from predictive simulations based on Rebut-Lallia transport model [3] in a 6 MA pulse: a, total stored energy without sawteeth; b, as a with sawteeth effects; c, electron stored energy without sawteeth; d, as c with sawteeth effects.

DETERMINATION OF DEUTERIUM CONCENTRATIONS IN JET PLASMAS FROM FUSION REACTION RATE MEASUREMENTS

O N Jarvis, J M Adams[1], B Balet, S Conroy[2], J G Cordey, T Elevant[3], P D Morgan, G Sadler, N Watkins[1] and P van Belle

JET Joint Undertaking, Abingdon, Oxon, OX14 3EA, UK
[1] Harwell Laboratory, UKAEA, Oxon, OX11 ORA, UK
[2] Imperial College of Science and Technology, London, SW7 2BZ, UK
[3] Royal Institute of Technology, Stockholm, Sweden

ABSTRACT

The concentration of deuterium in the central regions of JET plasmas, expressed as a fraction of the electron concentration (n_d/n_e), has been determined using four different methods involving neutron detection. These measurements are found to be consistent and agree within experimental errors with values deduced from Z_{eff} measurements using visible bremsstrahlung radiation.

1. INTRODUCTION

Fusion reaction rates are determined by the velocity distributions and densities of the interacting ions. In the case of plasmas in thermal equilibrium, the velocity distributions are Maxwellian and are determined by the ion temperature which, in JET, is routinely measured using a variety of techniques. For the other cases of current interest, involving neutral deuterium beam injection and the study of the tritons emitted from d-d fusion reactions, the source velocity distributions are known and the slowing down distributions are determined by classical Coulomb collisions. Thus, measurements of the t-d and d-d fusion reaction rates determine the effective deuterium density. Since the fusion reaction rates are strongly peaked at the centre of the plasma, the density measured will be essentially the central density.

2. DIAGNOSTIC TECHNIQUES

The nuclear measurements can be divided into four classes: studies of ohmic and ICRF heating, Neutral Beam Heating, Neutral Beam Injection transient analysis and examination of triton burnup. These various neutron techniques have to be applied with some circumspection with regard to plasma operating conditions. For example, high power ICRF heating tuned to hydrogen may give rise to energetic deuterons through second harmonic acceleration; the presence of these high energy deuterons is not taken into account in the analysis, as yet.

i) **Ohmic and ICRF Heating** - For this case, the plasma is assumed to be in thermal equilibrium with the fusion-reaction-rate radial profiles being described in terms of the magnetic flux surfaces. The central ion temperature is obtained from several diagnostics including Neutron

Spectrometry [1], Ni x-ray crystal spectrometry [2] and Neutral Particle Analysis [3]. According to availability, a suitable average of these measurements is taken. The 2.5 MeV neutron emission profiles are routinely recorded with the 19 channel profile monitor [4]. A computer code (ORION) is used to reproduce the experimental line-integrated count-rates by adjusting a parametrized neutron source profile to the data using a maximum likelihood technique, assuming a given deuterium density. This density is then iterated until the central temperature reproduces the independently measured value. In this way, $n_d(o)/n_e(o)$ is derived.

ii) **Neutral Beam Heating** - The 2.5 MeV neutron energy spectra from the central region of the JET plasma are measured using a double-interaction Time-of-Flight neutron spectrometer [5]. The neutron energy spectra contain two components, the contribution from thermal (plasma-plasma) reactions and that from beam-plasma reactions. The thermal contribution is well-known to be Gaussian with width proportional to $T_i^{\frac{1}{2}}$. The beam-plasma contribution is more complicated with a shape which depends on geometry and beam injection energy; it is calculated using the kinematics code FPS [6]. With the shapes of the two contributions known, it is a relatively straightforward matter to adjust their relative proportions so as to obtain a good fit to the measured spectrum [7]. In this manner we obtain the thermal to total neutron production ratio. At this point, we have sufficient information to be able to invoke the code ORION and to deduce the central density ratio as was done for Ohmic discharges. It should be noted that this derivation is but an approximation because (inter alia) the magnetic flux surfaces are not precise contours of neutron emission in the case of strong neutral beam heating (beam trapping effects).

iii) **Neutral Injection Transient Analysis** - This technique exploits the fact that the slope of the neutron emission rate at beam switch-on (which is abrupt) is almost entirely due to beam-plasma interactions and is principally dependent on the beam power, energy and deuterium concentration n_d/n_e, and only weakly dependent on the electron temperature. The time-dependent transport code TRANSP [8] is used to enforce agreement between measurement and prediction at switch-on time by adjusting the n_d/n_e value. This provides a normalization factor for the Z_{eff} value obtained from measurements of the visible bremsstrahlung. The adjusted Z_{eff} is found to have the correct time evolution to provide excellent agreement between calculated and measured neutron yields for all later times in the discharge. Only selected discharges have been studied with TRANSP so far.

iv) **Triton Burnup** - The 14 MeV neutron emission from JET plasma is measured by a combination of techniques; an activation technique provides the absolute magnitude of the emission whilst a silicon diode technique provides the time evolution [9,10]. In the present application it is assumed that the triton burnup is described perfectly by the standard formulae and any deviations are ascribed to a correction factor to be applied to Z_{eff}.

v) **Z_{eff} from Visible Bremsstrahlung** - The results from the neutron measurements have been compared with the n_d/n_e ratios derived from visible

bremsstrahlung measurements of Z_{eff} for a variety of plasma conditions. The bremsstrahlung determination involves electron density and temperature profile information and a knowledge of the plasma geometry. A horizontal chord through the plasma is used for the standard measurement of Z_{eff}. A 15 chord array is also used to provide a Z_{eff} profile [11]. An n_d/n_e ratio can be derived from $Z_{eff}(o)$ on the assumption that the major impurities are carbon and oxygen in the ratio 3:1. However, helium is occasionally employed for operational reasons but the helium content is not measured. Furthermore, the hydrogen content is uncertain. Thus the visible bremsstrahlung measurement really provides the ratio of the sum of hydrogen, deuterium and helium densities to the electron density and consequently may overestimate the n_d/n_e ratio. The neutron measurements provide n_d/n_e ratios to an accuracy of about 20%. The Z_{eff} measurement has an absolute accuracy of ± 25% but this implies decreasing accuracy for n_d/n_e as Z_{eff} rises.

3. CONCLUSION

The various measurements of Z_{eff} and n_d/n_e are presented in Table I for a list of representative discharges from the operation of JET in 1988. The time intervals under investigation were those corresponding to the maximum neutron emission intensities. It is important to note that H-mode discharges are unusual in having hollow Z_{eff} profiles. Flat profiles were assumed for the H-mode neutron values quoted within parentheses, in Table I; these correspond to neutron-weighted rather than central values of n_d/n_e. The following conclusions can be drawn:

(i) The neutron measurements agree within their respective errors.
(ii) The visible bremsstrahlung estimate of n_d/n_e is in broad agreement with the neutron assessment. A comparison is provided in figure 2.
(iii) The deuterium concentration is found to vary over the range 0.3 to 1.0, depending on discharge conditions.

REFERENCES

[1] O N Jarvis et al, Rev Sci Instr 57 (1986) 1717.
[2] R Bartiromo et al, "The JET High Resolution Bent Crystal Spectrometer", JET-P(88)11.
[3] R Bartiromo et al, Rev Sci Instr 58 (1987) 788.
[4] J M Adams et al, this conference.
[5] T Elevant et al, Bull Am Phys Soc 32 (1987) 1870.
[6] P V Belle and G Sadler, in Basic and Advanced Diagnostic Techniques for Fusion Plasmas (Proc Course and Workshop, Varenna 1986), Vol III, Rep EUR 10797 EN, CEC (1987) 767.
[7] M J Loughlin, PhD Thesis, Harwell Laboratory Report HL/1382.
[8] R J Goldston et al, J Comput Phys 43 (1981) 61.
[9] S Conroy et al, "Time-Resolved Measurements of Triton Burn-Up in JET Plasmas", JET-P(88)16.
[10] S Conroy et al, this conference.
[11] P D Morgan, 15th European Conference on Controlled Fusion and Plasma Heating, 1988. Europhys. Conf. Abstracts, Vol 12B, Part 1, p139.

TABLE I

Discharge		Vis. Bremm.			Neutron (n_d/n_e)			
Class	Number	$\bar{Z}_{eff}$	$Z_{eff}(o)$	n_h/n_e	Spectra	Tritons	TRANSP	Average
6 and 7MA Ohmic	17793	3.7	4.6	0.35	0.3	0.4		0.35
	17796	3.9	4.9	0.3	0.3	0.35		0.3
He prefill	17797	3.7	4.6	0.35	0.3	0.4		0.35
High T_i	17836	4.2	4.8	0.3	0.4	0.25		0.3
$P_{RF}>10MW$	17838	4.7	5.4	0.2	0.35	0.25		0.3
High Power 5MA	16370	2.6	3.3	0.6	0.4	0.4		0.4
	16382	3.5	4.0	0.45	0.35	0.3		0.3
High T_i	16041	3.0	3.5	0.55	0.35	0.4	0.5	0.45
	16066	4.5	5.2	0.25	≤0.5	-	0.3	0.3
H-Mode 3MA	15894	2.1	1.9	0.8	0.65	(0.55)	0.55	0.6
	16259	1.9	2.1	0.8	0.8	(0.55)	(0.35)	0.8
	16268	2.7	2.4	0.75	0.7	(0.45)	(0.35)	0.7
	17933	3.2	2.8	0.7	0.5			0.5
Pellets 3MA	16211	1.4	1.7	0.85	0.85			0.85
	16228	1.4	1.7	0.85	1.0			1.0
	16235	1.6	1.9	0.8	0.65			0.65
	17279	1.9	2.3	0.8	0.7			0.7

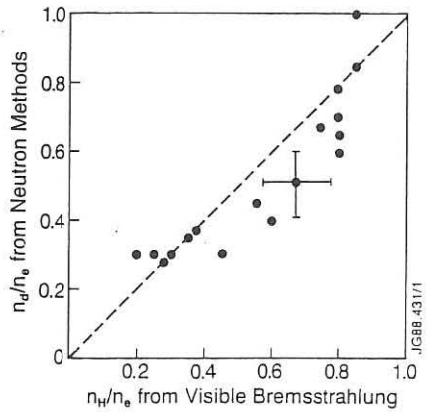

Fig. 1: Comparison of deuterium concentration from neutron measurements with estimates from Bremsstrahlung measurements.

RUNAWAY ELECTRONS DYNAMICS AND CONFINEMENT IN TORE-SUPRA

M. CHATELIER , A. GERAUD , P. JOYER , G. MARTIN & J.M. RAX

Association EURATOM-CEA sur la fusion / CEN CADARACHE
13108 SAINT-PAUL-LEZ-DURANCE CEDEX / FRANCE

- * - * - * - * - * - * - * -

I) Introduction :

Ohmic discharges in TORE-SUPRA are sufficiently long (≈ 6 s) for runaway electrons (R.E.) to reach a steady energy state : their energy limit is determined by the balance between parallel electric field acceleration (20 MeV/V.s in TORE-SUPRA) and radiation losses due to the curvature of the trajectories . When R.E. energy is supposed to be only parallel , this provides estimate of order of 70 MeV (value usually called "synchrotron limit") reached in less than 2 seconds . Experimental observations on TORE-SUPRA of photoneutron emission together with residual induced radioactivity in the first wall components tend to prove that the actual value is much lower than 70 MeV (i.e. 15-35 MeV) .

Earlier observations in ORMAK [1] , PLT [2] and TFR [3] already showed R.E. energy a slightly less than expected from standard loop voltage acceleration calculations . Explanations given for this lack of energy (as skin-effect lowering the electric field during the ramp-up phase or balance beetween continuous creation and losses) seems not to hold on TORE-SUPRA and therefore another mechanism must be considered to explain the R.E. energy limitation .

II) Experimental observations :

Ohmic discharges obtained with helium gas in TORE-SUPRA [4] exhibit a small amount of R.E. identified on both hard X-ray monitors and neutron detectors . The time behaviour of a typical photoneutron signal is shown on figure 1 together with plasma current . Analysis of many shots shows that :

→ R.E. are likely produced at the start-up phase of the discharge , when the break-down voltage reached values as high as 25 volts , for the two following reasons : (i) when M.H.D. activity in the current ramp-up phase is strong , all R.E. are lost and no further production is observed afterwards ; (ii) the photoneutron signal starts ≈ 30 ms after the plasma current which indicates an extreme early creation in addition to a high accelerating voltage during this period of time to reach the photonuclear reaction threshold (8 MeV) so rapidly (electric field must be at least 70% of the loop voltage) .

→ The photoneutron signal increases during the rising phase of the plasma current and sharp spikes (< 1ms) are observed during it , corresponding to

extra R.E. losses when the edge safety factor q_A is integer . This feature will not be discussed in this paper .

→ At the current plateau , the photoneutron signal exhibits an exponential decay with a e-folding time of order of 1 second . Assuming that R.E. have reached a steady energy state , this time can be interpreted in terms of a confinement time of the R.E. population .

→ On short discharges (as that shown on figure 1) , there remain a sufficiert number of R.E. during the decay phase of the plasma current so that a positive slope can be easily observed on the photoneutron signal for the lowest values of current . This enhanced losses interpreted as classical drift orbit losses suggest a R.E. energy of 10-20 MeV (for residual R.E. lost during this phase) . Taken in account the negative loop-voltage during the current decay phase , this suggest that R.E. energy was between 20 and 35 MeV durirg the plateau phase .

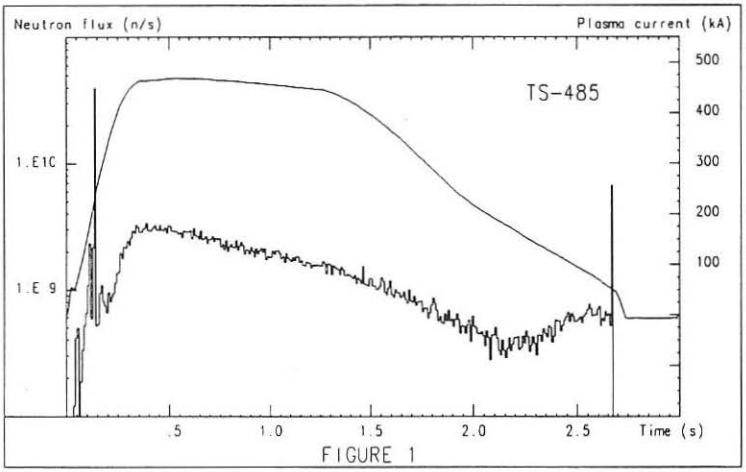

FIGURE 1

A residual activation spot was identified on the stainless steel wall located in the bremsstrahlung beam behind the outboard carbon limiter . The ratio between radioisotopes corresponding to high threshold ($Cr^{50}(\gamma,np)V^{48}$: T = 21.6 MeV) to nuclei with lower ones ($Mn^{55}(\gamma,n)Mn^{54}$: T = 10.2 MeV) allows a rough estimate of the R.E. energy which is found to be 25±10 MeV . Note that $C^{12}(\gamma,n\alpha)Be^{7}$ reactions have been also identified in the carbon limiter , proving the existence of electrons at energies larger than 27 MeV .

III) Discussion :

The different observations which have been made on TORE-SUPRA :

→ a creation of R.E. only at the very beginning of the discharge ,
→ an efficient acceleration in the ramp-up phase ,
→ a relatively low mean energy (15-35 MeV) of those R.E. in comparison to classical synchrotron limit , suggests that a slowing down mechanism takes place counteracting the acceleration experienced by R.E. in the parallel electric field . It must be much more efficient than the synchrotron radiation process which becomes predominant only when R.E. energy is close to the limit (70 MeV) .

An explanation for such a slowing down could be residual pitch angle scattering processes :

The radiation losses of a highly relativistic electron on a curved trajectory is given by : $d\gamma/dt = K \gamma^4/R^2$ where $K = 5.632\ 10^{-7}\ m^2/s$, γ is the energy on mass ratio of the electron and R the curvature radius of the trajectory . In the classical limit calculation , R is taken equal to the field line curvature , i.e. roughly the large radius of the tokamak . But , with a small perpendicular velocity , the actual curvature of the trajectory can be strongly reduced , due to the small value of the larmor radius λ (on TORE-SUPRA , $\lambda \approx \gamma$ when expressed in mm) . The increase in radiation power is $(1+R^2\sin^2\theta/\lambda^2)$ where R is the curvature of the field line (i.e. ≈2.5 m) and θ the pitch-angle . Because of the large value of the R/λ ratio , an 8° pitch-angle is enough to reduce the radiation limit from 70 MeV to 25 MeV .

The question is then raised of the origin for such a process , and a quantitative analysis has been carried out to compare different candidates for pitch-angle scattering : magnetic fluctuation ($\delta B \approx 10^{-3}$ B) and electric fluctuation ($\delta E \approx 1$ V/mm) effects have been calculated to be many orders of magnitude under the residual coulomb collisions . The corresponding diffusion coefficient is $D_c = 8\pi c(Z+1)nr^2 \ln\Lambda/\gamma^2 \approx 3.35\ 10^{20}\ n/\gamma^2$ (rd^2/s) , where n is the electron density (m^{-3}) . The mean pitch-angle reached by R.E. at equilibrium between diffusion and electric field (which reduces it) is around $60°/\gamma$, a value much lower than the 8° needed .

The R.E. energy is shown on figure 2 as a function of time for different assumptions illustrating the cases discussed before :

(1) Pure acceleration by the electric field (the experimental loop-voltage signal from shot 485 has been used , as shown on the bottom curve) .
(2) With addition of synchrotron radiation , at zero pitch-angle .
(3) The same as (2) , but with a 30% reduction in loop-voltage (to evaluate the role of a skin-effect) : increase in energy is delayed but final values are not very different .
(4) With full loop-voltage , and synchrotron radiation increase due to the mean pitch-angle obtained with coulomb scattering (i.e. ≈ $60°/\gamma$) .
(5) Full loop-voltage and synchrotron radiation obtained with a permanent pitch-angle around 7° . This last value as been adjusted to insure a final energy of 15 MeV , coherent with experimental value (see § II) . Note that this value cannot be obtained in any other cases ((1) to (4)) .

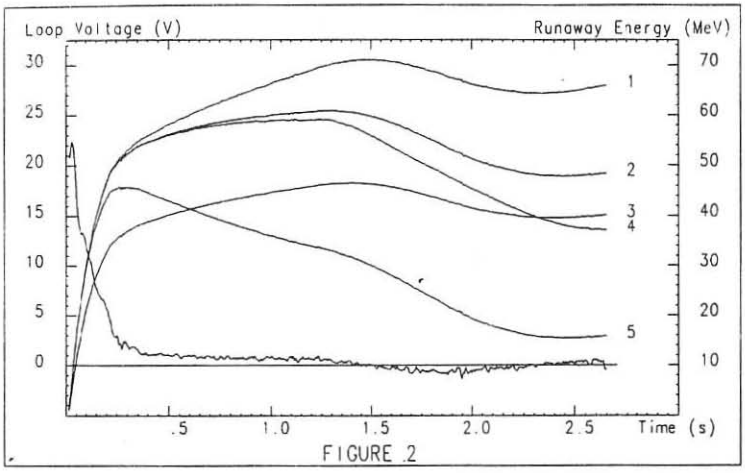

FIGURE 2

IV) Conclusion :

Two different observations have shown an important lack of energy for runaway electrons confined in TORE-SUPRA . This has been assumed due to a small pitch-angle scattering (a few degrees) , and many candidates for this have been compared : the strongest known one , collisions , seems not to be enough by an order of magnitude .

Density and magnetic scans on TORE-SUPRA will be needed to discriminate between enhanced collisional scattering processes ($D_c \alpha n$) and purely magnetic phenomena .

- * - * - * - * -

[1] H. KNOEPFEL & S.J. ZWEBEN - Phys. Rew. Lett. 35(1975)1340
[2] J.D. STRACHAN et al. - Nucl. Fusion 17(1977)140
[3] Equipe TFR - 8th Eur. Conference on Plasma Physic and Controlled Fusion - PRAGUE (1977)
[4] Equipe TORE-SUPRA - IAEA Conference on plasma physic and Nuclear Fusion - NICE (1988)

DENSITY LIMIT IN ASDEX DISCHARGES WITH PEAKED DENSITY PROFILES

A. Stäbler, H. Niedermeyer, R. Loch, V. Mertens, E. R. Müller, F. X. Söldner,
F. Wagner and the ASDEX-, NI- and Pellet-Teams

Max-Planck-Institut für Plasmaphysik, EURATOM Association, D-8046 Garching, FRG

1. INTRODUCTION

Results concerning the density limit in OH and NI-heated ASDEX discharges with the usually observed broad density profiles have been reported earlier /1,2/: In ohmic discharges with high q_a (q-cylindrical is used throughout this paper) the Murakami parameter ($\overline{n}_e R/B_t$) is a good scaling parameter. At the high densities edge cooling is observed causing the plasma to shrink until an m=2-instability terminates the discharge. When approaching q_a=2 the density limit is no longer proportional to I_p; a minimum exists in $\overline{n}_{e,max}(q_a)$ at $q_a \approx 2.15$. With NI-heating the density limit increases less than proportional to the heating power; the behaviour during the pre-disruptive phase is rather similar to the one of OH discharges.

There are specific operating regimes on ASDEX leading to discharges with strongly peaked density profiles: the improved ohmic confinement regime /3/, counter neutral injection /4/, and multipellet injection /5/. These regimes are characterized by enhanced energy and particle confinement. The operational limit in density for these discharges is, therefore, of great interest having furthermore in mind that high central densities are favourable in achieving high fusion yields. In addition, further insight into the mechanisms of the density limit observed in tokamaks may be obtained by comparing plasmas with rather different density profiles at their maximum attainable densities.

2. CO AND COUNTER NEUTRAL INJECTION INTO GAS FUELLED DISCHARGES

A series of experiments to compare the density limits of co- and ctr-NI heated plasmas have been performed on the same day ($H^0 \rightarrow D^+$, P_{NI}=1.3 MW, B_t=1.86 T, I_p=320-460 kA). By feedback controlled gas puffing the density was steeply ramped up to values slightly below the density limit followed by a slow rise until the plasma disrupted. In all co- and some of the ctr-heated discharges the slow rise required a slowly increasing gas puff rate. For the remaining ctr-heated discharges (preferably those at higher I_p) the gas puff rate continuously dropped to zero during the slow density rise. These discharges show all the signs of an improved confinement with ctr-NI which usually is triggered by a reduction in gas puffing /6/: ß increases considerably, the density profile continuously peaks ($Q_n = n_e(o)/\langle n_e \rangle$ rises from 1.15 to above 1.8), the central SX radiation increases with initially large sawtooth amplitudes; in the later phase sawteeth completely disappear which leads to a further steep rise of the SX signal. In contrast, those discharges requiring an increasing gas puffing show normal L-mode behaviour up to the disruptive limit with the density profiles staying broad ($Q_n \leq 1.15$).

The maximum line averaged densities obtained prior to the disruption are shown in a Hugill diagram in Fig. 1a (□: peaked ctr-NI, O: broad ctr-NI, ●: co-NI). The $\overline{n}_e$-values obtained with peaked profiles exceed the ones with broad profiles (either co- or ctr-NI) by up to about 20%. They do not show the minimum in $\overline{n}_{e,max}(q_a)$ at $q_a \approx 2.15$.

The plasma behaviour close to the disruption is quite different for the two types of discharges. The density limit shots with broad n_e-profiles are characterized by the development of a cold dense divertor plasma as shown by a decreasing C III radiation from the divertor and increasing H_α light measured close to the divertor plate. This is not observed for the discharges with peaked profiles. As already indicated by the SX signal the bolometrically measured radiation profiles develop quite differently. With

co-NI the central radiation stays at a low level for the whole of the discharge, in contrast to the peaked ctr-NI case (Fig. 2) where the central radiation steeply increases, as soon as the sawteeth disappear, to values above 1 W/cm^3 exceeding the local power input of about 0.6 W/cm^3. This rise is due to central accumulation of heavy impurities /6/. Consistently, in this final phase a hollow T_e-profile develops. The discharges with peaked density profiles, therefore, are terminated by a thermal collapse in the plasma centre, not by edge cooling. This is supported also by electron temperature measurements (laser scattering) close to the plasma edge: $T_e(r=0.88 \cdot a)$ drops during the last few 10 ms for broad profiles and stays roughly constant for the peaked profiles.

The density development close to the plasma edge is also different for the two types of discharges: for broad profiles $n_e(r=0.88 \cdot a)$, measured by laser scattering, slowly rises in parallel to $\overline{n}_e$ whereas with peaked profiles it remains constant or even slightly decreases during the density peaking, in all cases staying below the corresponding broad profile values. Data taken just before the plasmas disrupts are shown in Fig. 1b, again in a Hugill-type presentation. The edge densities of those discharges terminated by a normal density disruption are higher by roughly 20% compared to the discharges terminated by a central thermal collapse. Fig. 1c shows the results for the maximum $n_e(o)$ values and clearly demonstrates the advantage of peaked profiles in attaining high central density values: $n_e(o)$ is enhanced by 35-65% for the peaked ctr-NI plasmas compared to the corresponding co-NI plasmas. The increase in volume-averaged density, however, is rather small; it amounts to about 5% for the low q_a-values.

The same type of behaviour was observed during another series of experiments (D^0-> D^+-plasma, 1.97 T, 420 kA) with only 300 kW (< P_{OH}) of ctr-injected beam power. By tailoring the gas puff program it was possible to switch between discharges showing the development of peaked n_e-profiles (Q_n≈1.9) or staying broad (Q_n≈1.3) up to the density limit. The results of the various density values obtained are also shown in Figs. 1a, 1b and 1c (+: peaked n_e, x: broad n_e). Peaked density profiles lead to an improvement in $\overline{n}_e$ of about 25% and in $n_e(o)$ of more than 40%, whereas the edge densities (at r=0.88·a) do not exceed those of the broad density profiles.

3. THE IMPROVED OHMIC CONFINEMENT REGIME

In the improved ohmic confinement regime (IOC), recently discovered on ASDEX /3/, the linear increase of confinement time with $\overline{n}_e$ is maintained up to the highest densities. It gradually develops upon reduction of the external gas puffing. Steady state discharges with sawteeth have been run at densities close to the density limit of the saturated ohmic confinement regime. By slightly increasing the gas feed under IOC conditions (at I_p=380 kA, B_t=2.2 T) $\overline{n}_e$ non-linearly increases to values above the ones obtained in a normal density limit (DL) discharge two shots later. These non-stationary IOC discharges show exactly the same type of behaviour as the peaked ctr-NI ones: the density profile further peaks to Q_n=2.1 whereas the normal density limit shot stays at Q_n≈1.4, the SX level rises, sawteeth are finally lost, and the behaviour of T_e at r=0.88·a as well as of the divertor signals prior to the disruption is as described above for the peaked ctr-NI discharges indicating that the discharges are terminated again by a central thermal collapse and not by edge cooling.

The values of $\overline{n}_e$, $n_e(r=0.88 \cdot a)$, and $n_e(o)$ for the IOC and the corresponding density limit shots prior to the disruptions are included in Figs. 1a, b, and c (Δ: IOC, ▲: DL). The situation is equivalent to peaked ctr-NI and co-NI shots, respectively: $\overline{n}_e$ in the IOC regime increases by up to 15%, $n_e(o)$ by up to 60%, and $n_e(r=0.88 \cdot a)$ is lower by about 20% compared to the corresponding DL shot under saturated conditions.

There exists one discharge showing all the signs of IOC behaviour but a slightly smaller increase in profile peaking (Q_n≈1.95) where the density at r=0.88·a reaches the value of the normal density limit shot. In this case T_e at the edge and all the divertor signals behave as they do in a normal density limit shot indicating that the discharge is terminated by edge cooling. This observation supports the picture that peaked n_e-profiles may be operated at higher $\overline{n}_e$-values than broad n_e-profiles as long as the density close to the edge does not exceed the one of the corresponding broad profile discharges.

4. PELLET INJECTION

Injection of pellets into a tokamak plasma is another way of obtaining improved confinement correlated with the development of peaked n_e-profiles, not only on ASDEX /5/ but also in other experiments (see references in /5/). A successful density build-up could only be obtained by providing a substantial gas flow onto the plasma boundary (e.g. by external gas puffing) leading to densities well above the normal gas puff density limit, as reported earlier /7/. In the context of this paper it is of interest how the results fit into those given for IOC and peaked ctr-NI discharges.

Compared are pairs of OH and co-NI (1.3 and 2.5 MW) shots (I_p=350-380 kA, B_t=2.2 T) running into the density limit either with gas puff only or with multipellet injection assisted by gas puffing. Corresponding shots are from the same experimental campaign. All discharges with gas puff only remain broad (Q_n=1.2-1.45) whereas in the pellet fuelled shots the density strongly peaks (Q_n≈2.7, 2.0 and 1.7; decreasing for increasing heating power). Contrary to the peaked ctr-NI and IOC discharges described above, however, the pellet discharges discussed here keep sawtoothing up to the maximum $\overline{n}_e$. They do not show any signs of significant impurity accumulation and their radiation profiles remain hollow. They, therefore, do not suffer a central thermal collapse.

The densities obtained are shown in Fig. 1a, b, and c. The strong enhancement in the Murakami parameter as well as in $n_e(o)$ for pellet fuelled discharges is obvious. Concerning the edge densities (r=0.88·a) there may be a tendency of a slight increase for the pellet discharges compared to their corresponding gas puff discharges but this increase is small compared to the overall gain in $\overline{n}_e$ and $n_e(o)$ and probably disappears when comparing values closer to the separatrix /5/. For these discharges the volume averaged density increases significantly as well.

5. SUMMARY AND CONCLUSIONS

Peaked density profiles in ASDEX obtained by three different operating scenarios have been shown to allow higher Murakami parameters and a significant increase in central density compared to corresponding discharges with broad density profiles. The measured densities close to the plasma edge (at r=0.88·a) for peaked profiles, however, are either slightly below (for some ctr-NI and IOC shots) or very similar to the ones with broad profiles. The maximum edge density obtained is depending on heating power (see Fig. 1b) but increases less than proportional with power as observed for the density limit. The termination of those discharges with a lower edge density was shown to be due to a central thermal collapse contrary to the effects of edge cooling in the other cases where substantial gas puffing is required to obtain the high densities. These results suggest that the local density close to or at the plasma edge and the rather high edge losses seen at high edge densities are the determining factors in the density limit observed in tokamaks. Discharges with peaked densities which, in ASDEX, are also correlated with an improved energy and particle confinement are, therefore, very attractive for fusion application.

REFERENCES

/1/ H. Niedermeyer et al., Proc. 12th Europ. Conf. on Contr. Fus. and Plasma Phys. (Budapest 1985), Vol. I, p. 159

/2/ H. Niedermeyer, F. Wagner et al., Proc. 11th Intern. Conf. on Plasma Phys. and Contr. Nucl. Fus. Research (Kyoto 1986), IAEA, Vienna, Vol. I (1987), p. 125

/3/ F. X. Söldner et al., Phys. Rev. Lett. 61 (1988) 1105

/4/ O. Gehre et al., Phys. Rev. Lett. 60 (1988) 1502

/5/ M. Kaufmann et al., Nucl. Fus. 28 (1988) 827

6/ G. Fussmann et al., Proc. 12th Intern. Conf. on Plasma Phys. and Contr. Nucl. Fus. Research (Nice 1988), IAEA, Vienna, to be published

/7/ O. Gruber et al., Plasma Phys. and Contr. Fus. 30 (1988) 1611

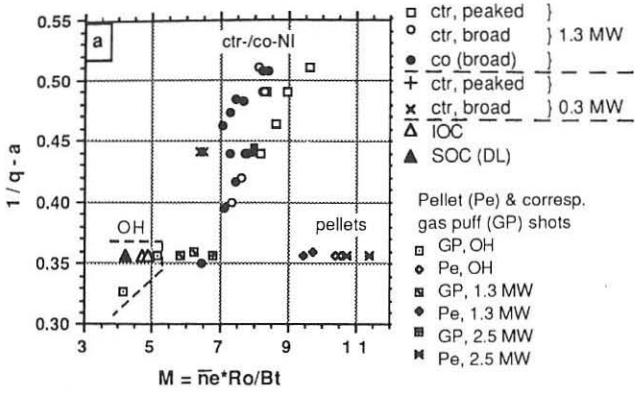

Fig. 1

Densities prior to the disruption for peaked and broad density profiles, presented in a Hugill-diagram:

a. line-averaged $\overline{ne}$
b. ne at r=0.88xa
c. central density

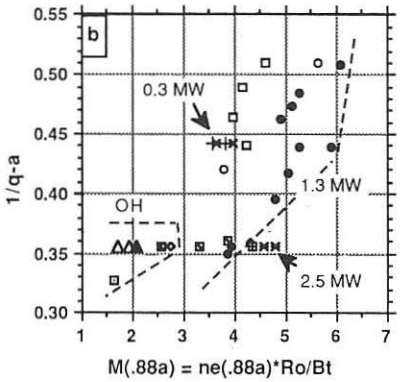

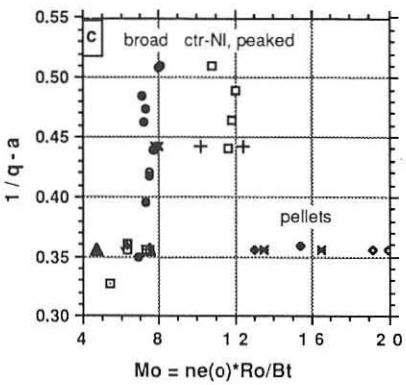

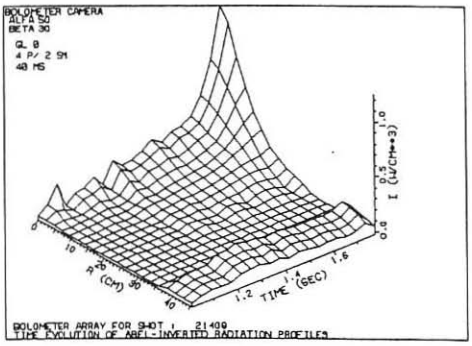

Fig. 2

Time evolution of Abel-inverted radiation profiles for ctr-NI (1.3 MW) with peaked density profiles (Ip=440 kA, Bt=1.86T), indicating the strong increase of central radiation towards the end of the discharge

INVESTIGATION OF LOW-FREQUENCY FLUCTUATIONS IN THE EDGE PLASMA OF ASDEX

A.Rudyj, Roger D.Bengtson[1], A.Carlson, L.Giannone, M.Krämer[2], H.Niedermeyer, Ch.P.Ritz[1], N.Tsois[3] and the ASDEX-Team

Max-Planck-Institut für Plasmaphysik, EURATOM Association, D–8046 Garching, Federal Republic of Germany

[1] University of Texas, Austin, USA;
[2] Ruhr-Universität Bochum, FRG; [3] NRS Demokritos, Attiki, Greece

Introduction

Density fluctuations in the edge plasma of tokamaks in the frequency range up to a few 100 kHz have been reported for many years. A review of the earlier papers can be found in ref 1. The fluctuations are easily observed with Langmuir probes and are also visible in the H_α emission at locations with sufficient neutral gas density. High speed cine films taken on ASDEX[2] show fluctuating stripes aligned approximately parallel to the magnetic field. It has been shown that these fluctuations, which are electrostatic, cause a major part if not all of the particle transport at the plasma edge[3]. The mechanism driving these instabilities is however not yet clear.

Langmuir probe measurements and optical observations were performed on ASDEX and a comparison was made with magnetic fluctuation measurements in order to further clarify the mechanism responsible for the edge turbulence.

Radial profiles

Fig. 1 shows radial profiles of characteristic parameters in the boundary layer on the midplane outside the separatrix. They were evaluated from a radial scan of a quadruple Langmuir probe with two pins working in the ion saturation mode and two pins measuring the floating potential. All pins were located at the same radius and were arranged at the corners of a square of 2×2 mm^2. The signals were digitized with a sampling frequency of 1 MHz during an interval of 20 ms and analyzed numerically. T_e-values were taken from probe measurements with voltage sweep performed in other similar discharges. The ohmic discharges were run in deuterium at $n_e = 4.5 \cdot 10^{19}$ m^{-3}, $B_t(0) = 1.86$ Tesla and $I_p = 460$ kA resulting in $q_{cyl} = 1.96$. Assuming cross-field transport due to the E×B-drift induced by the fluctuating electric field and fluctuating density one calculates the particle flux density

$$\Gamma = \langle \tilde{n} \cdot \tilde{v} \rangle = \left\langle \tilde{n} \cdot \tilde{E} \times B / B^2 \right\rangle$$

We approximate the radial component of this expression by

$$\Gamma = \int \frac{1}{4\pi B} |P_{n\Phi}| \cdot \sin\alpha \cdot k(\omega)\, d\omega$$

where $P_{n\Phi}$ is the cross-power spectral density between density and potential fluctuations, α is the phase difference between density and potential fluctuations and k is the average wave number. All terms are functions of the frequency ω. Because the turbulence is strong, we have a spectrum of k-values for each value of ω which might extend from positive to negative wave numbers. In agreement with common practice k_r is determined from the the phase difference between the potential fluctuations measured with two different pins. This approximation may break down if the k-spectrum becomes very broad or has even two maxima at k-values with opposite sign

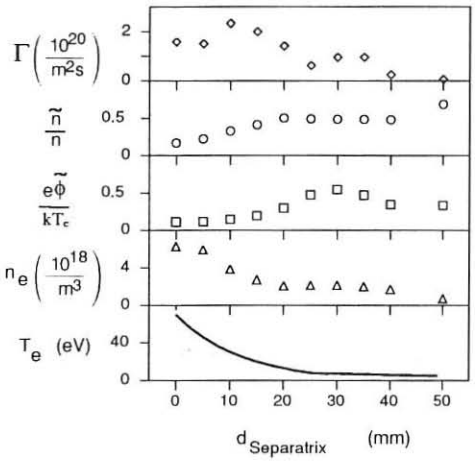

Fig.1. Radial profile of plasma parameters and fluctuation amplitudes. Top: particle flux calculated from fluctuation amplitudes.

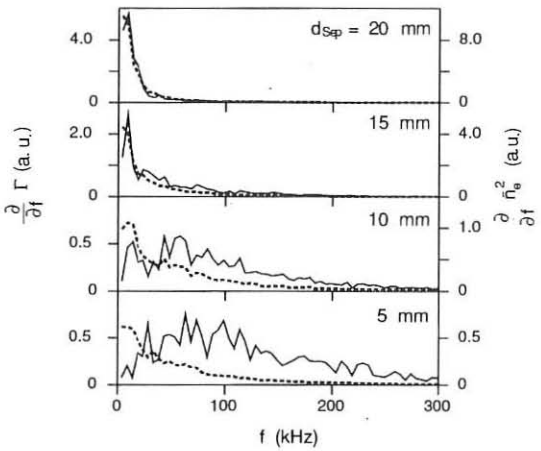

Fig. 2. Power spectra of the density fluctuations (dashed) and spectral contribution to the particle flux at various distances from separatrix.

(standing waves). The particle flux determined by this method is plotted at the top of Fig. 1. Its maximum agrees roughly with the value which is estimated assuming uniformity over the surface and a particle confinement time equal to half of the energy confinement time. The non-monotonic decay with distance from the separatrix is unexpected. It might be explained by problems with the approximation explained above or with a slight toroidal asymmetry of the configuration causing magnetic islands.

The power spectrum of the density fluctuations and the integrand in the formula for the particle flux are shown in Fig. 2 for different distances from the separatrix. For a distance of 2 cm or larger (not shown here) the spectra are restricted to frequencies below about 20 kHz and the different frequencies contribute to the transport corresponding to the fluctuation amplitude. Closer to the separatrix the fluctuation spectrum extends to higher frequencies, but the maximum remains at low frequencies. The maximum contribution to the transport in this zone comes from higher frequencies. Very low frequencies do not contribute substantially to the transport despite their high amplitude. It is not yet clear whether this change indicates the existence of two different modes or is merely caused by the strong variation of the plasma parameters and of the magnetic shear in the vicinity of the separatrix.

Close to the separatrix one observes an abrupt change of the sign of k, i.e. of the average propagation velocity of the fluctuations. Further outside the fluctuations propagate in the diamag-

netic ion drift direction. With increasing distance from the separatrix the propagation velocity decreases. The observations are consistent with the assumption that the propagation corresponds essentially to a plasma rotation due to the radial electric field. A propagation with the electron diamagnetic drift velocity relative to the moving plasma may be superimposed[4].

Correlation parallel and perpendicular to the magnetic field

Langmuir probes and optical observations were used to determine the correlation of the fluctuations in the directions parallel and perpendicular to the magnetic field. Optical observations were performed in the vicinity of a gas puffing valve to get sufficient H_α-light. Optical fibres connected to photomultipliers were imaged on the surface of the discharge. This method averages over the edge plasma in radial direction but permits qualitative measurements in a very flexible way.

Good correlation has been found along the magnetic field between the midplane and the divertor over a distance of about 12 m. Two probes each with two tips operating in the ion saturation mode were positioned on the same flux surface, one on the midplane and one in the upper divertor chamber. The toroidal field was varied in tiny steps until correlation between both probes was found. Field calculations with the Gourdon-code were used to determine the starting conditions. Fig.3 shows the results. The column on the left shows coherence spectra between two different signals (dashed, left scale), and the phase difference. The column on the right displays the equivalent cross-correlation functions. The first row shows coherence γ, phase angle α and cross–correlation function φ between the two tips in the divertor. Below the same functions between the two tips on the midplane are shown. In both cases the tips are positioned with a small distance perpendicular to the toroidal field. For this reason the phase shift is not zero, but increases with

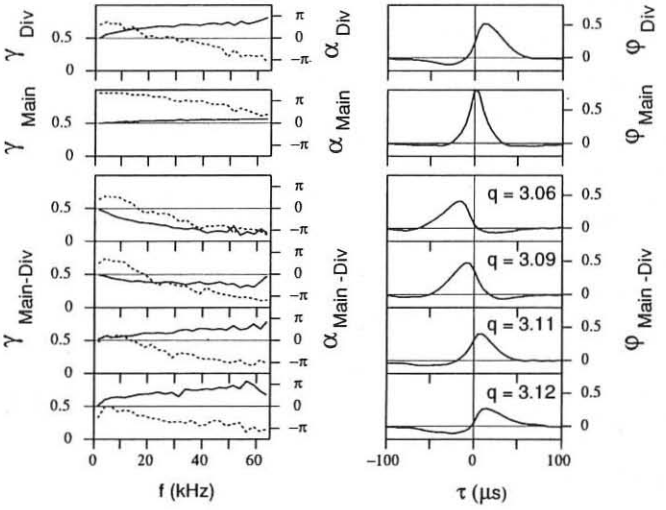

Fig. 3 Coherence γ (left column, left scale, dashed), phase angle α (left column, right scale, solid) and cross-correlation φ between probe signals.

the frequency, and the coherence decreases. The four rows at the bottom show correlations between one divertor tip and one tip on the midplane at different values of q_{cyl} indicated at the right. Maximum coherence and no phase shift (no delay) are observed between $q_{cyl} = 3.09$ and 3.11. Within the accuracy of the measurement of currents the same field line passes through both probes under these conditions. A very small angle of propagation, as expected for drift waves, cannot be excluded because of the limited accuracy of the q-measurement. The phase plots in Fig. 3 indicate however that the fluctuations propagate exactly in the same direction, as we would not observe a simultaneous change of the sign of the phase for all frequencies at the same q-value. This appears to be extremely unlikely if the line of constant phase would not coincide with the field line.

The picture of good correlation along the field lines is confirmed by the observation that the profiles of $\tilde{n}/n$ are similar in the divertor and on the midplane.

The four rows at the bottom of Fig. 3 look very similar to measurements performed in the same poloidal plane with different probes or optical channels. While the fluctuations are extremely well correlated along the magnetic field lines the peak value of the cross-correlation function decreases to less than half of the maximum over a poloidal distance of 1.5 cm.

Parameter studies

Systematic parameter studies have been performed with the optical method only. The evaluations are still on the way. Up to now the following facts can be stated.

— The poloidal propagation velocity determined from the delay of the correlation maximum over a fixed distance d varies with $d^{-0.5}$.

— The poloidal propagation velocity scales like $I_p/(n_e \cdot B_t^{2.5})$.

— The edge frequency of the power spectrum decreases strongly with increasing toroidal field.

— The fluctuations are detected only on the low field side of the torus during double null discharges. During single null discharges the fluctuations are also observed on the high field side. We conclude that the origin of the fluctuations is on the low field side. In single null discharges they can propagate along the magnetic field to the high field side.

Discussion

A comparison with magnetic fluctuation measurements indicates, that close to the separatrix the magnetic fluctuations originate from the same mechanism as the electrostatic fluctuations described above. The transport estimated from the magnetic fluctuations[5] is by far smaller than that induced by electric field fluctuations. One should therefore concentrate on electrostatic modes to explain the transport in the plasma edge. In the past it has not been sufficiently taken into account that the field lines outside the separatrix or the limiter edge are not closed. This fact might suppress drift modes and permit MHD instabilities of the flute type because line tying is not perfect. With probes one observes a sheath potential at the target plates which increases the sheath resistivity substantially so that the pressure gradient can drive instabilities in the region of unfavourable curvature. All the observations described above agree with the assumption of flute modes. More work is however necessary to confirm this picture.

References

1 P. C. Liewer, Nucl. Fusion 25, 543 (1985)
2 H. Niedermeyer, IPP Annual Report 1981, p. 10
3 W. L .Rowan, C. C. Klepper, Ch. P. Ritz et al, Nucl. Fusion 27, 1105 (1987)
4 Ch. P. Ritz, R. D. Bengtson, S. J. Levinson, and E. J. Powers, Physics Fluids 27, 2956 (1984)
5 A. B. Rechester and M. N .Rosenbluth, Phys. Rev. Letters 40, 38 (1978)

NON-THERMAL ELECTRON CYCLOTRON EMISSION FROM TFTR SUPERSHOT PLASMAS*

G. Taylor, C.W. Barnes**, B.J. Braams, A. Cavallo, P.C. Efthimion, C.F.F. Karney, S. Tamor***, M.C. Zarnstorff and S. Zweben.

Princeton Plasma Physics Laboratory, Princeton University, Princeton, N.J. 08543, USA

Introduction

The Ohmic targets of Supershot [1] plasmas in the Tokamak Fusion Test Reactor (TFTR) are often characterized by the presence of non-thermal electron cyclotron emission (ECE) from a runaway or slideaway electron population. However, in the 100-150 msec after the start of neutral beam injection (NBI) this non-thermal ECE decays away as the electron density rises and the loop voltage drops. After this usual slideaway-induced, non-thermal ECE is quenched a new non-thermal feature develops at frequencies just below both the optically thick, thermal emission of the ECE fundamental ordinary mode, and the second harmonic extraordinary mode. This paper presents an analysis of the ECE data which indicates a possible source of this non-thermal emission feature. In addition, correlation of the peak intensity of the non-thermal feature with various plasma parameters for 130 TFTR discharges from 1988 provides some clues toward identifying possible physical conditions which give rise to the feature.

Behavior of the Non-Thermal Feature

ECE from TFTR is measured on the horizontal midplane by a Michelson interferometer [2], a grating polychromator [3], and a scanning heterodyne radiometer system [4]. The Michelson interferometer and the grating polychromator share a view of the plasma in the extraordinary mode which includes a focusing reflective carbon target which provides >80% reflectivity into the same polarization and <15% mixing into the orthogonal polarization. The heterodyne radiometer views the plasma in the ordinary mode at a position which is toroidally almost diametrically opposite the other two instruments.

The behavior of the non-thermal feature is illustrated in Figs.1 and 2 for a typical TFTR Supershot [1] plasma (Shot#36640). This discharge had a minor radius of 0.79 m, a major radius of 2.45 m, a plasma current of 1.6 MA and a toroidal field of 4.75 T. 28 MW of NBI (having a similar power parallel and counter parallel to the plasma current) with an average energy of 105 keV was injected from 3.5 to 4.5 seconds. During injection the electron and ion temperatures reached 8.5 and 25 keV, respectively. At about 4 seconds an increased carbon influx from the limiter resulted in a significant degradation of the plasma performance. Figure 1 shows the ECE spectrum at 3.9 seconds measured at the fundamental ordinary mode by the scanning heterodyne radiometer (shaded line) and at the second harmonic extraordinary mode by the Michelson interferometer (solid line). Both instruments were independently and absolutely calibrated, it is interesting to note that the non-thermal feature measured by both instruments is similar in magnitude and shape. The peak of the non-thermal feature at the second harmonic occurs at slightly less than twice the frequency of the peak at the fundamental, since the optical depth at the second harmonic is higher for a given plasma condition than at the fundamental. Figure 2 shows the time evolution of the peak of the non-thermal features at the fundamental and second harmonic, which for this plasma are at 98 and 190 GHz, respectively. When the NBI is turned on at 3.5 seconds there is still some non-thermal ECE which has the broad frequency spread associated with slideaway or runaway induced ECE. This emission is quenched in the first 100-150 msec of NBI as the electron density increases to 7×10^{13} cm^{-3} and

the loop voltage falls to 0.1 V. The non-thermal feature described earlier appears at about 300 msec after the start of injection at a time when β_p is increasing and approaching unity. When β_p saturates the intensity of the non-thermal feature also stops growing and when the carbon influx from the limiter occurs at 4.2 seconds, resulting in a drop in β_p, the feature disappears.

We do not see the non-thermal feature below the third harmonic, since on TFTR the plasma aspect ratio is normally such that there is a significant overlap between the second and third ECE harmonics and during supershots the second and third harmonic, extraordinary mode both become optically thick. Since the non-thermal feature is seen below the fundamental and the second harmonic and not above the fundamental it is consistent with relativistically down-shifted cyclotron emission. Further, correlation of the time dependence of the intensity of the peak of the non-thermal feature with MHD (eg. small sawteeth) in the plasma indicates that the emission is coming from a region midway between the magnetic axis and the plasma edge.

Modeling the Non-Thermal ECE Feature

A time-independent, transport code which solves the three-dimensional radiation transport equations in a toroidally symmetric, two-dimensional geometry [5] is used to generate ECE spectra of the radiation collected on the horizontal midplane. In particular, the code was used to simulate the Michelson spectrum obtained between 160 and 520 GHz in shot #36640 at 3.9 seconds (this frequency range spans the second, third and fourth ECE harmonics). The effect of non-thermal electrons is simulated by allowing the addition of a velocity-shifted Maxwellian. The electron temperature profile input to the code comes from the ECE radiometer system. Near the edge of the electron temperature profile, where the plasma is optically thin the temperature is extrapolated to zero at the limiter. The electron temperature data are mapped to major radius including the effects of the plasma diamagnetism and poloidal field. The electron density profile is obtained by Abel inverting data from a ten channel far-infrared interferometer [6]. In the model the plasma poloidal cross-section is divided into ten radial zones, each zone is circular and centered about a Shafranov-shifted axis. The acceptance angle of the detector in the code is choosen to be 2^o, similar to the Michelson interferometer optics. The model does not include finite density refractive effects, such as the upper hybrid resonance; however the maximum plasma frequency is typically <70GHz in supershot plasmas and the upper hybrid resonance <160GHz, somewhat below the non-thermal feature at 190 GHz in shot #36640.

The model was initially used to generate the spectrum without assuming a non-thermal electron population. Although the model predicted (within approximately 10-15%) the intensity of the second, third and fourth harmonics it did not predict the non-thermal feature below the second harmonic. The electron distribution in the model was modified to include a "bump-on-tail" non-thermal component 30 cm from the magnetic axis. The velocity shift, energy spread and number density of this non-thermal component were adjusted for a best fit to the measured spectrum. Figure 3 shows a comparison of the measured spectrum (shaded line) with one model prediction (solid line) which gave a relatively good fit to the measured data. This example was generated by including a bump-on-tail component which has a mean energy of 60 keV, an energy spread corresponding to a 20 keV Maxwellian and a density of 10^{12} cm^{-3}, 30 cm from the magnetic axis. The observed feature appears to be consistent with a 40-80 keV energetic tail with a density of $0.5\text{-}2 \times 10^{12}$ cm^{-3}. X-ray spectra from a pulse-height analyzer which views the plasma vertically at a major radius of 297 cm have been inspected up to 50keV. Initial analysis does not confirm a non-Maxwellian electron distribution at the

anticipated levels, although interpretation is complicated by high energy background counts from DD neutrons and secondary gamma rays [7].

Database Results for 1988 Plasmas

A database of 130 TFTR 1988 plasmas was created which included plasmas with currents between 0.8 and 1.6 MA, NBI powers up to 30 MW, and toroidal fields between 4 and 5.2T. The plasmas had major radii between 2.44 and 2.52 m and minor radii between 0.79 and 0.86 m. The peak equivalent radiation temperature of the non-thermal feature for these plasmas varied from 0.8 to 6.4 keV. For plasmas with the same current and toroidal field the intensity of the non-thermal feature was found to increase as approximately β_p squared. In addition to global dependences, the database was used to investigate the dependence of the intensity of the feature on the electron temperature and density profile shape. A significant correlation was found between the intensity of the non-thermal feature and the slope of the electron pressure profile in the region 2.9-3.0 m, shown in Fig.4. This is the region of steepest pressure gradient in these plasmas and also the region identified as the possible source of emission from correlation of MHD activity with the time dependence of the non-thermal feature.

Conclusions

In conclusion, the non-thermal feature is consistent with relativistically down-shifted ECE from an energetic electron population with energies in the range 40-80 keV situated in a region midway between the magnetic axis and the plasma edge where the electron pressure gradient is steepest. It should also be noted that this is a region of the plasma profile which is strongly fuelled by the neutral beams. The computer code indicated tail densities of approximately $0.5\text{-}2\times10^{12}$ cm^{-3} would be required in this region to generate the observed feature intensity, this is about 1-4% of the local electron density and would support all the plasma current if directed toroidally in one direction. Since the collision time for 40-80 keV electrons is only 5 msec this energetic population must be created and sustained by a new mechanism; the electric field in the plasma is over an order of magnitude too small to generate this energetic population by a "conventional" runaway process. This mechanism could be associated with an instability driven by the pressure gradient or by the fast ions which result from the beam fuelling. Molvig *et al.* [8] have proposed that if the anomalous electron heat loss seen in tokamaks is due to resonant magnetic fluctuations a non-thermal electron distribution could be created away from the magnetic axis as a result of "leakage" of energetic electrons from the Maxwellian tail of the hot core plasma. The expected enhancement of the Maxwellian tail due to this mechanism at 60 keV is approximately 5-10, the enhancement deduced from our model is approximately 20-80.

References

[1] J.D. Strachan *et al.*, Phys. Rev. Lett., **58** (1987)1004.
[2] F.J. Stauffer *et al.*, Rev. Sci. Instrum., **59** (1988) 2139.
[3] A. Cavallo *et al.*, Rev. Sci. Instrum., **59** (1988) 889.
[4] G. Taylor *et al.*, Rev. Sci Instrum., **55** (1984) 1739.
[5] The computer code used here is SNECTR which was authored by S. Tamor.
[6] D.K. Mansfield *et al.*, Applied Optics, **26** (1987) 4469.
[7] K. Hill, Private Communication (1988).
[8] K. Molvig *et al.*, Phys. Rev. Lett., **41** (1977) 1240.

*Work supported by DoE contract #DE-AC02-76-CHO-3073.

**Los Alamos National Laboartory, Los Alamos, New Mexico 87545, USA.
***Present address 2165 Via Don Benito, La Jolla, California 92037, USA.

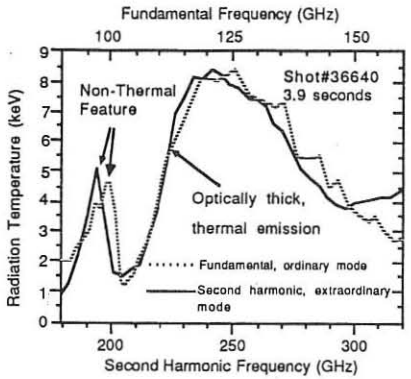

Fig.1.Comparison of fundamental, ordinary mode data and second harmonic, extraordinary mode data shows a similar feature during neutral beam injection.

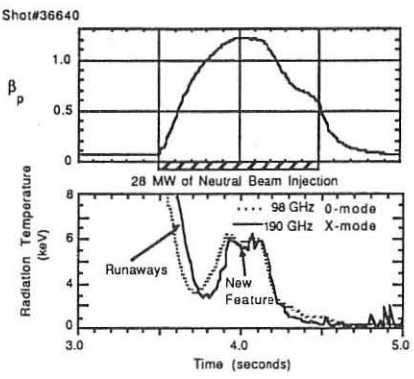

Fig. 2. Plot of the evolution of the peak of the non-thermal feature at fundamental, ordinary mode and second harmonic extraordinary mode. The feature develops as β_p rises and decays when β_p falls.

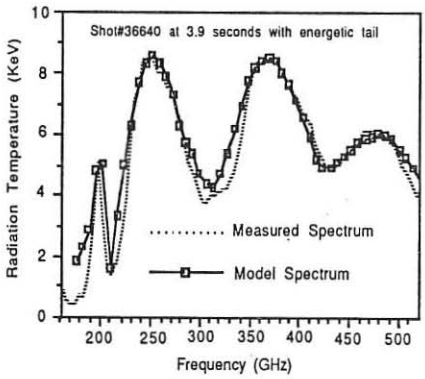

Fig.3 A model spectrum which fits the measured data was generated by including a bump-on-tail component with a mean energy of 60 keV, an energy spread corresponding to a 20 keV Maxwellian and a density of 10^{12} cm^{-3}, approximately 30 cm from the magnetic axis.

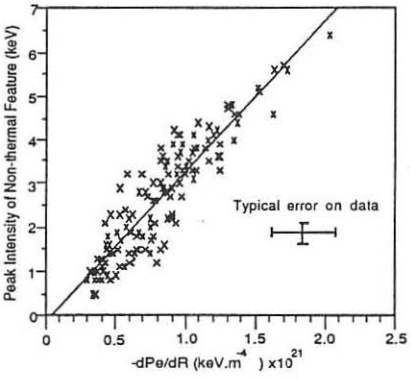

Fig.4 Plot of the peak intensity of the non-thermal ECE feature versus the slope of the electron pressure at a major radius of 2.9-3.0 m for 130 TFTR plasmas with plasma currents between 0.8 and 1.6 MA and beam powers up to 30 MW. The line represents the best linear fit to the data.

TRANSPORT ANALYSIS OF TFTR SUPERSHOTS.

M.C. Zarnstorff, R.J. Goldston, M.G. Bell, M. Bitter, C. Bush, R.J. Fonck, B. Grek, K. Hill, B. Howell, K. Jaehnig, D. Johnson, D. Mansfield, D. McCune, H. Park, A. Ramsey, J. Schivell, and G. Taylor.

Plasma Physics Laboratory, Princeton University, Princeton NJ 08543 USA.

The radial energy transport in neutral-beam heated TFTR plasmas has been analyzed in order to understand the enhanced confinement "supershot" regime [1] relative to plasmas having L-mode confinement. Supershots are obtained using near-balanced co- and counter-tangential neutral-beam injection, and a highly conditioned limiter, having a hydrogenic recycling coefficient ~ 0.5, and plasma current I_P ranging from 0.7 - 1.9 MA. The global confinement time τ_E^M, as determined by magnetic measurements, is up to three times greater than that predicted by Goldston L-mode scaling [2] and is roughly independent of I_P and P_{inj} [3]. This regime is interesting because of its strongly peaked density profiles ($n_e(0)/ < n_e >$ up to 3, where $< n_e >$ is the volume-average density) which results from the primary particle source being in the plasma core (from beam fueling) rather than at the plasma edge. Plasmas with L-mode confinement were previously obtained [4] on TFTR with gas-loaded limiters, which produced a large recycling neutral influx thus keeping the edge density high and the edge temperature low. To obtain this situation without deconditioning the limiter, we have injected deuterium neutral beams into helium target plasmas of various densities. L-mode confinement has also been obtained in deuterium plasmas with $P_{inj} = 30$ MW after the broadening of the density profile associated with a transient increase in the carbon limiter-recycling light. All plasmas discussed here have balanced co- and counter-tangential injection.

The particle and energy transport in these plasmas have been analyzed [5] by the 1-D steady-state transport analysis code SNAP and the $1\frac{1}{2}$-D time-dependent code TRANSP [6] using the experimentally measured temperature and density profiles. $T_e(r,t)$ is measured by ECE spectroscopy and Thomson scattering, $T_i(r,t)$ is measured by charge-exchange recombination spectroscopy, $n_e(r,t)$ by a ten-channel infrared interferometer array and Thomson scattering. The ion depletion is calculated using tangential visible-bremsstrahlung measurements for Z_{eff} and x-ray spectroscopic measurements of metallic concentrations. Edge hydrogenic-neutral influx is inferred [7] from the measurements of an array of absolutely calibrated H_α detectors. The beam-ion slowing down distribution is simulated as a separate species not subject to anomalous transport, consistent with experimental observations at low power [8]. The beam ions are treated as joining the background thermal ion species when their energy falls below $\frac{3}{2}T_i$. Electron-ion energy exchange is assumed to be classical.

For $r < a/3$ the energy transport in supershots is dominated by convection (both for ions and electrons). In this region, it is found that $Q_i/\Gamma_i T_i$ is as low as $\sim \frac{3}{2}$ and $Q_e/\Gamma_e T_e$ is as low as 2 - 2.5, where Q_i (Q_e) is the total ion (electron) heat flux and Γ_i (Γ_e) is the ion (electron) particle flux [9]. Thus, use of the usual convective heat flux of $\frac{5}{2}\Gamma_i T_i$ would require a non-physical negative χ_i in the central region. For this paper, the electron and ion thermal diffusivities χ_e and χ_i are defined by $Q_e = n_e\chi_e\nabla T_e + \frac{3}{2}\Gamma_e T_e$ and $Q_i = n_i\chi_i\nabla T_i + \frac{3}{2}\Gamma_i T_i$, where n_i is the total thermal ion density.

The analyzed thermal transport coefficients for a high power supershot and a comparable L-mode plasma (obtained using helium) are shown in Fig. 1. Both plasmas have I_P = 1.4 MA, B_T = 4.8 T, and P_{inj} = 22 MW. The supershot has $\bar{n}_e = 3.9\times10^{19}$ m^{-3}, $n_e(0) = 8.2\times10^{19}$ m^{-3}, $T_e(0)$ = 8.2 keV, $T_i(0)$ = 27 keV, Z_{eff} = 2.4, thermal energy confinement time of 0.12 sec, and τ_E^M = 0.18 sec. The L-mode plasma has $\bar{n}_e$ = 4.4 × 10^{19} m^{-3}, $n_e(0)$ = 6.2 × 10^{19} m^{-3}, Z_{eff} = 2, $T_e(0) \sim T_i(0) \sim$ 4 keV, thermal energy confinement time of 0.040 sec, and τ_E^M = 0.061 sec. The L-mode predicted [2] global confinement time for these plasmas is 0.056 sec. The error-bars on χ_e and χ_i in the figure represent the standard deviation of the calculation when the experimentally measured quantities are randomly varied within their individual ranges of systematic and statistical uncertainty. It is evident, in Fig. 1, that the L-mode plasma has substantially higher χ_i and modestly higher χ_e than for the supershot. In both cases, the ion thermal diffusivity is found to be much larger [10] than predicted by neoclassical theory [11], by as much as a factor of 40 in the outer region of the plasma. The neoclassical enhancement to the thermal diffusivity due to the presence of unthermalized beam ions [12] is calculated to be very small, due to the balanced injection.

The variation from supershot to L-mode confinement is continuous, and is strongly correlated with the peakedness of the density profile $n_e(0)/ < n_e >$, see Fig. 2. The variation of χ_e and χ_i at the half radius with density profile peakedness is shown in Fig. 3, for the same plasmas. χ_i drops strongly, and χ_e weakly, with the peaking of the density profile. Similar trends are also found correlating decreasing χ_i (and χ_e) with decreasing local density-gradient scale length, decreasing $\eta_e \equiv \partial_r \log T_e/\partial_r \log n_e$, decreasing ν_{*i} or ν_{*e}, and increasing T_i/T_e or β_P.

Figure 4 shows the calculated variation of the heating-profile effectiveness parameter defined by Callen and co-workers [13] with density profile peakedness. While the measured τ_E increases by a factor of three in going from a broad to a peaked density profile, the heating-profile effectiveness increases by only 27%. Thus, changes in the calculated deposition profile only account for a small portion of the increase in confinement time, with the bulk of the increase being due to the changes in thermal transport.

The total-ion density (including non-thermal ions and assuming Z_{eff} is radially uniform) gradient scale length $L_{n_i}^{tot}$ and the thermal-ion temperature gradient scale length L_{T_i} separately vary by roughly a factor of 4 in this data set, but are seen to be correlated, Fig. 5. In contrast, L_{T_e} is varies by less than a factor of 2 for these plasmas, and is uncorrelated with L_{n_e}. The measured values of $\eta_i^{tot} \equiv L_{n_i}^{tot}/L_{T_i}$ lie within 2±1. While this is a wider range for η_i than might be expected from marginal stability of ion-temperature-gradient turbulence, the correlation of L_{T_i} with $L_{n_i}^{tot}$ near the predicted critical $\eta_i \sim 1.5$ suggests that they may be responsible for the observed variation in χ_i and χ_e.

In summary, the thermal energy transport has been analyzed for deuterium neutral-beam heated plasmas in TFTR. The ion thermal diffusivity is found to be much larger than neoclassical predictions, and increases strongly in going from the supershot regime to plasmas having L-mode confinement. The change in energy confinement time between L-mode and supershots is seen to be due almost entirely to changes in thermal transport, not due to changes in heating profile. χ_i, and to a lesser extent χ_e, changes systematically as the density profile shape changes in such a way that the value of η_i^{tot} remains $\sim$ 2, suggesting ion-temperature-gradient

turbulence as the transport mechanism.

We are grateful for discussions with J.D. Callen, P. Diamond, and D. Meade. This work was supported by USDOE contract DE-AC02-76-CHO-3073.

[1] STRACHAN, J. D. et al., Phys. Rev. Lett. **58** (1987) 1004.
[2] GOLDSTON, R. J., Plasma Phys. **26** (1984) 87, The values of L-mode confinement used here do not include any correction for ion mass.
[3] BELL, M. G. et al., *Proc. 12th Int. Conf. on Pl. Phys. and Contr. Fus. Res.*, Nice, 1988, A-I-2.
[4] BELL, M. G. et al., Plasma Phys. **28** (1986) 1329.
[5] ZARNSTORFF, M. C. et al., *Proc. 12th Int. Conf. on Pl. Phys. and Contr. Fus. Res.*, Nice, 1988, A-III-3.
[6] HAWRYLUK, R. J., in *Physics of Plasmas Close to Thermonuclear Conditions*, edited by COPPI, B. et al., volume 1, page 19, Brussels, 1980, CEC.
[7] HEIFETZ, D. H. et al., J. Vac. Sci. Technol. A **6** (1988) 2564.
[8] RADEZTSKY, R. H. et al., in *Proc. 15th European Conf. on Contr. Fus. and Pl. Heating*, volume 1, EPS, 1988.
[9] ZARNSTORFF, M. C. et al., in *Proc. 15th European Conf. on Contr. Fus. and Pl. Heating*, volume 1, EPS, 1988, The difference between the convective limits quoted here and in this reference is due to inclusion of beam energy diffusion, beam-beam charge-exchange, and a previous error in the SNAP analysis of experimental T_i profiles at high β_P.
[10] FONCK, R. J. et al., in *Proc. 15th European Conf. on Contr. Fus. and Pl. Heating*, volume 1, EPS, 1988.
[11] CHANG, C. S. and HINTON, F. L., Phys. Fluids **29** (1986) 3314.
[12] KIM, Y. B., CALLEN, J. D., and HAMNEN, H., in *Proc. 14th European Conf on Contr. Fus. and Pl. Heating*, volume 3, EPS, 1987.
[13] CALLEN, J. D. et al., Nucl. Fusion **27** (1987) 1857.

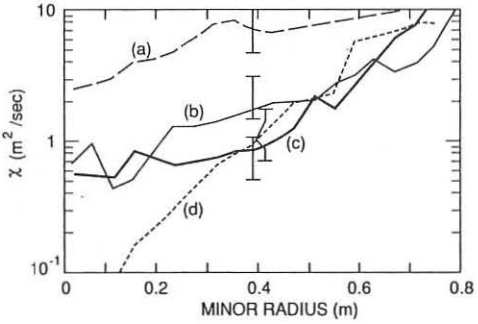

Fig. 1. Radial profile of experimental χ_i and χ_e for the supershot and L-mode plasmas: (a) L-mode χ_i, (b) L-mode χ_e, (c) supershot χ_e, (d) supershot χ_i.

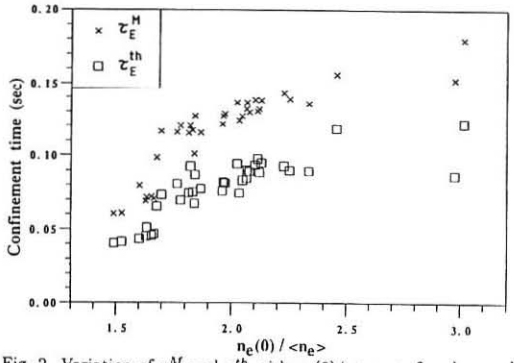

Fig. 2. Variation of τ_E^M and τ_E^{th} with $n_e(0)/ < n_e >$ for plasmas having confinement ranging from L-mode to 3× L-mode, I_P: 1.0 to 1.8 MA, and P_{inj}:12 to 30 MW.

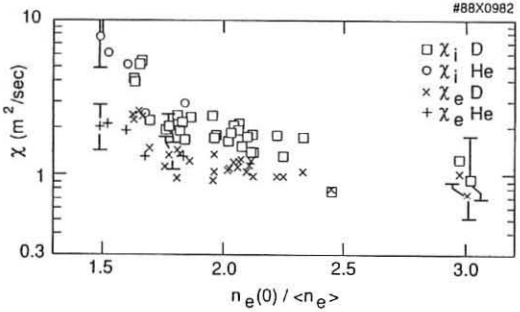

Fig. 3. Variation of χ_i and χ_e at $r = a/2$ with $n_e(0)/ < n_e >$.

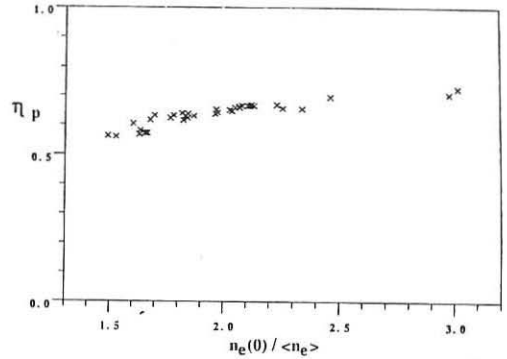

Fig. 4. Variation of heating-profile effectiveness [13] η_P with $n_e(0)/ < n_e >$.

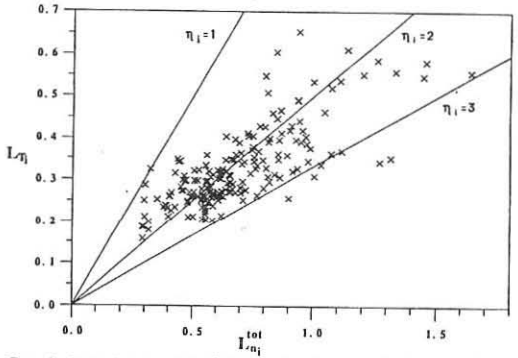

Fig. 5. Correlation of L_{T_i} with $L^{tot}_{n_i}$ for $a/4 < r < a/2$ showing their clustering within $\eta_i \approx 2 \pm 1$. The points with small values of L_{T_i} and $L^{tot}_{n_i}$ are from supershots, while those with large values are from L-mode plasmas.

ESCAPING 1 MEV TRITONS IN TFTR

S.J. Zweben, J.D. Strachan, R. Boivin, C.W. Barnes*, A. Cavallo,
E.D. Fredrickson, K. McGuire, H.E. Mynick, R.B. White

Princeton Plasma Physics Laboratory, Princeton, N.J. 08543
*Los Alamos National Laboratory, Los Alamos, N.M. 87595

Introduction:

1 MeV tritons created by D-D reactions can simulate the "single-particle" behavior expected with 3.5 MeV D-T alphas, since the gyroradii and slowing-down of these two particles are similar. This paper describes measurements of the flux of escaping 1 MeV tritons from the TFTR plasma during high power D^0-> D neutral beam injection, and shows that in most cases the observed triton loss is consistent with the classical (single-particle) first-orbit loss model. In this model tritons are lost if their first orbit intersects the wall due to their large banana width, while almost all tritons confined on their first orbit should stay confined until thermalized.

The triton detectors are ZnS(Ag) scintillator screens housed in light-tight boxes located just outside the plasma boundary at the bottom of the TFTR vessel. They are particle "pinhole" cameras which can resolve the triton flux vs. pitch angle (to $\pm 5^0$), energy (to ±50%), and time (to <20μsec). The 2-D images of triton flux onto these scintillators are optically coupled to either an intensified TV camera or to photomultiplier tubes for fast time resolution. The soft x-ray background in an earlier prototype [1] has been eliminated.

Although there are presently 8 such detectors in TFTR, this paper discusses results from only the detector located just below the vessel center (R=259 cm, r=102 cm). Note that the "1 MeV triton" signal discussed below also has about a 30% contribution from 3 MeV protons; however, since these two particles have identical gyroradii they should behave alike.

Experimental Results:

(a) MHD-Quiescent Plasmas

The pitch angle dependence of the escaping 1 MeV triton flux during a discharge without strong MHD activity is shown in Fig. 1. In this case the plasma current was a relatively low 1.0 MA, the neutral beam injection (NBI) power was 12 MW, and the peak neutron source rate was 7×10^{15} n/sec (shot #34801). The data were taken from a series of TV camera frames averaged over about 0.5 sec during the steady state of NBI in this shot.

The location of the peak of the measured flux at $60^0 \pm 5^0$ (with respect to the plasma current direction) agrees well with the location of the calculated peak corresponding to the "fattest banana orbit" at 63^0, although the width of the measured distribution is larger than expected. Note that the detector has an angular resolution of at least $\pm 5^0$ and an alignment uncertainty of $\pm 2^0$ which

are not taken into account in the model curve, and that the experimental flux was normalized to the model curve at 63^{o}. These results are consistent with the previous result with a prototype detector [1], and are the first pitch-angle resolved measurements of escaping tritons in a tokamak.

The shape of this pitch angle distribution remains approximately constant as a function of triton source strength and plasma current (to within about 5^{o}), as expected from the first-orbit loss model. Further agreement with this model was seen in the plasma current dependence of the escaping triton flux per neutron, which decreased by a factor of 20 between 0.8 and 2.0 MA[2]. The measured triton energy of 1 MeV (±50%)[1] was also consistent with this picture, since the energy loss expected during the first orbit is negligible.

The time dependence of the escaping triton flux for MHD-quiescent discharges is similar to the time dependence of the neutron flux (triton source rate), as shown in Fig. 2. In this case the plasma current was a relatively high 1.6 MA, the NBI power was 25 MW, the peak neutron rate was 2.5×10^{16} n/sec (shot #37915), and the triton signal was normalized to the neutron signal at 4.5 sec. This escaping triton signal came from a single photomultiplier channel viewing 1 MeV tritons at a pitch angle $60^{o} \pm 5^{o}$, i.e. near the peak of the 2D image of triton flux at the scintillator. Similar time-dependent behavior is obtained over 0.8-1.6 MA up to 30 MW NBI when large MHD is absent.

This result also agrees with the first-orbit loss model, since the first orbit takes <100μsec. Small variations of the triton/neutron rate, such as at 3.8-4.0 sec in Fig. 2, are probably due to source or current profile variations. Note the absence of triton loss 0.2-0.5 sec after NBI when the confined triton population is still high (since the triton thermalization time is about 1 sec).

(b) MHD Effects

When large MHD is present the triton loss at high current can increase a factor of 3-5 over the "no-MHD" loss level, as shown in Fig. 3. This discharge is similar to that in Fig. 2 (1.6 MA, 30 MW NBI, neutron rate 3.7×10^{16} n/sec, #37913), but with large coherent magnetic fluctuations coincident with the periods of increased triton loss (the normalization is the same as for Fig.2). This is the first direct observation of MHD-induced triton loss in a tokamak, although similar behavior was seen previously as reduced triton burnup correlated with large levels of MHD in PDX[3].

This extra triton loss occurs in phase with the mode over a wide range in frequency 2-2000 Hz, e.g. when the mode slows down and "locks" with respect to the vacuum vessel. When the MHD level is roughly $\tilde{B}_p/B_p = 0.5\%$ at the wall, at high current (1.4-1.6 MA) the instantaneous triton loss per neutron can be up to 5-10 times the no-MHD level, while at low current (1 MA) the MHD-induced loss is always less then the classical loss.

Extra triton loss is also observed at sawtooth crashes during NBI[2]. These losses occur in single "bursts" of 0.1-10 msec duration over a current range 0.8-1.6 MA, but not all sawtooth crashes produce such a burst. The time-integrated loss due to these bursts was negligible, since there were typically only a few crashes per shot. This phenomenon appears similar to bursts of 15 MeV protons ejected with sawtooth crashes in JET[4].

The pitch angle dependence of escaping triton flux for the shots of Figs. 2 and 3 (and for sawtooth crash cases #37082-3), all at 1.6 MA, is shown in Fig. 4. The pitch angle distribution during coherent MHD has a shape similar to that without MHD, while at sawtooth crashes the loss is peaked at unusually low pitch angles, i.e. 50^{o}. This data comes from an array of 8 photomultiplier channels viewing the scintillator at a triton energy of 1 MeV with a pitch angle resolution of about $\pm 5^{o}$. Some corresponding 1 MeV triton orbit trajectories at 1.6 MA are shown in Fig. 5, including the "fattest banana" orbit at about 60^{o}.

Discussion:

In normal MHD-quiescent discharges the relative dependence of escaping triton flux on pitch angle, energy, time, and plasma current is consistent with the expected classical first-orbit loss. At first this seems to exclude the possible effects of TF ripple or small-scale turbulence on triton confinement[5].

However, calculations of TF ripple effects on "trapped" tritons in TFTR have shown that at low current (1.0 MA) the TF ripple effects should be negligible since most trapped tritons are lost on their first orbit. At high current (1.6 MA) the TF ripple should increase the total triton loss by about x2, but at high current the ripple loss should be localized just below the outer equatorial plane, so that the effects at the present detector should also be negligible.

An upper limit to the possible turbulent radial diffusion of "passing" confined tritons can be set by the observed time dependence of the escaping triton flux at the detector after NBI (see Fig. 2). The ratio of the diffusive flux Γ(diff) across the passing-trapped boundary to the expected prompt loss flux Γ(prompt) is roughly $\Gamma(\text{diff})/\Gamma(\text{prompt}) = D\tau/L\Delta$, where D is the presumed triton radial diffusion coefficient, τ is the triton slowing-down time, L is the radial triton density gradient, and Δ is the radial range seen by this detector over a sightline which includes the "fattest banana" orbit at $\approx 60^{o}$. The apparent <u>absence</u> of non-prompt loss 0.2-0.5 msec after NBI, i.e. Γ(diff, after NBI)/Γ(prompt, during NBI)<0.1, suggests a upper limit of roughly D<100 cm^2/sec after NBI. This appears to be consistent with the expected reduction in turbulence-induced triton diffusion by a factor of 50-300 (with respect to thermal ion diffusion) due to orbit-averaging effects[5].

Possible causes of the observed MHD-induced losses are (a) distortion of the triton source or plasma current profiles by MHD, (b) deconfinement of previously passing tritons due to $\tilde{B}$ near the banana tip, (c) stochastic diffusion of previously confined trapped tritons, or (d) radial diffusion of passing tritons. The relative magnitudes of these effects are under investigation.

[1] S.J. Zweben, Princeton Plasma Physics Laboratory Report PPPL 2582 (1989)
[2] J.D. Strachan, S.J. Zweben, et. al. IAEA Nice Paper CN-50/A-IV-5 (1988)
[3] W.W. Heidbrink, R.E. Chrien, and J.D. Strachan, NF 23 (1983) 917
[4] G. Martin, N.O. Jarvis, et. al., Physica Scripta T16 (1987) 171
[5] R.B. White and H.E. Mynick, Princeton Plasma Lab Report PPPL 2563 (1988)

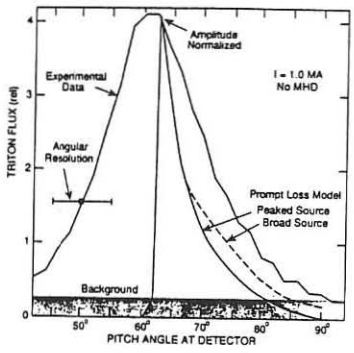

Fig. 1 TRITON FLUX VS. PITCH ANGLE (NO MHD)

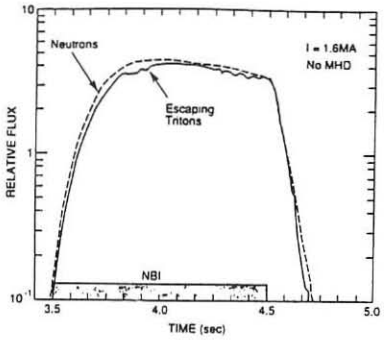

Fig. 2 TRITON FLUX VS. TIME (NO MHD)

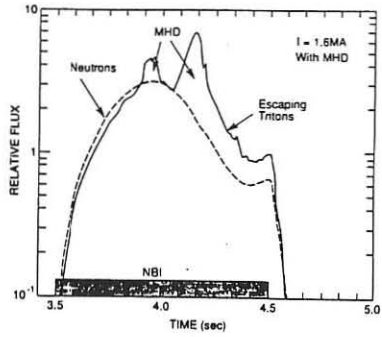

Fig. 3 TRITON FLUX VS. TIME (WITH MHD)

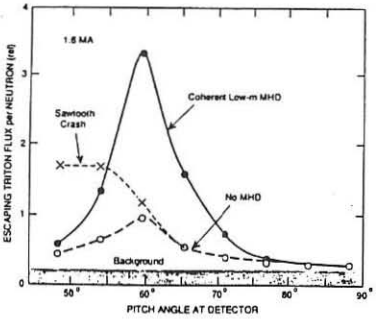

Fig. 4 TRITON FLUX VS. PITCH ANGLE (WITH MHD)

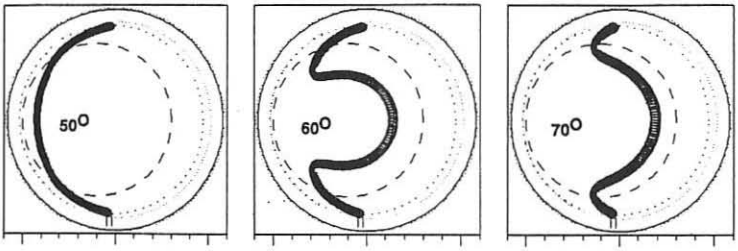

Fig. 5 TRITON ORBITS VS. PITCH ANGLE

LANGMUIRE PROBE MEASUREMENTS ON LIBTOR TOKAMAK

A.M.ALABYAD, N.M.BHEIH, S.A.SEGHAYER, V.G.ZHUKOVSKY

LIBTOR GROUP

I. INTRODUCTION. In the previous work/1/ the influence of screening effect of a limiter scrape-off layer /SOL/ on plasma parameters was investigated and the optimum width of SOL was determined. The aim of the given work is to investigate and compare the boundary plasma parameters in two regimes of Libtor Tokamak: with stationary limiter /D/ and with SOL.

II. EXPERIMENTAL CONDITIONS. The stationary limiter of the Libtor installation is the aperture diaphragm of the radius $r=a_1=10$cm, chamber wall radius $a_0=11.5$cm, large radius of plasma R=53cm. Parameters of discharge with a stationary limiter D : $B_T=1.9$T, $I_p=36$kA, $q(a_1)=5$. SOL is created by introduction the moving molybdenum limiter /L/, radius $a_2=7$cm, into plasma. Plasma parameters in the SOL regime undergo insignificant changes: $B_T=2.6$T, $I_p=30$kA, $q(a_2)=4$. The distributions of plasma density $n_e(\Delta r)$, electron temperature $T_e(\Delta r)$ and density fluctuations $\Delta n_e(\Delta r)$ have been measured by means of a single Langmuire probe, where $\Delta r=a_0-r$ which is the distance from the chamber wall. The accuracy of measurements is approximately ±10%.

III. EXPERIMENTAL RESULTS AND DISCUSSION. In Fig.1 the curves 1,2 and 3,4 show the distributions of $n_e(\Delta r)$ and $T_e(\Delta r)$ in the regimes D and SOL, accordingly. Behaviour of $n_e(\Delta r)$ and $T_e(\Delta r)$ is described by the exponential laws of decay from plasma boundary both in the SOL region (a_1-a_2) and near the wall region (a_0-a_1). The knees of distributions coincide with radial positions of D and L. The characteristic e-folding length of radial density profiles for the D and SOL-regimes are: near the wall $-\Delta_1=0.8$cm and $\Delta'_1=0.43$cm, and in SOL $-\Delta_s=1.2$cm.

The diffusion coefficients $D_\perp$ in regions SOL and near the wall can be calculated by the formula /2/:

$$D_\perp = \Delta^2 V_s / L_{//},$$

where $V_s = 0.5 V_{Ti}$ - ion sound velocity, V_{Ti} - ion thermal velocity, $L_{\parallel}$ - an effective length of the magnetic line of force. Near the wall $L_{\parallel} = 2\pi R$, in the SOL region $L_{\parallel} = 2\pi R q(a_2)$. The calculations of $D_\perp$ for T_e in points a_1, a_2 give: $D_{\perp 1} = 9.3\ 10^3\ cm^2 s^{-1}$, $D'_{\perp 1} = 1.3\ 10^3\ cm^2 s^{-1}$ and $D_{\perp S} = 4.4\ 10^3\ cm^2 s^{-1}$. Thus, in the SOL-regime diffusion coefficient in the SOL region $D_{\perp S}$ is two times smaller than $D_{\perp 1}$ in the D-regime. Near the wall diffusion coefficient in the SOL-regime $D'_{\perp 1}$ is seven times smaller than $D_{\perp 1}$ in the D-regime. The evaluations show that these values of $D_\perp$ are close to the Bohm difusion coefficients D_B. For Bohm diffusion coefficients the relation of Δ_S/Δ'_1 must be /2/:

$$\frac{\Delta_S}{\Delta'_1} = \left(\frac{q_1 D_{BS}}{D'_{B1}} \sqrt{\frac{T_e(a_1)}{T_e(a_2)}} \right)^{1/2} \simeq 2.6$$

The experimental result $\Delta_S/\Delta'_1 \simeq 2.8$ is another proof of the fact that diffusion coefficients in the boundary plasma region of Libtor Tokamak are the Bohm diffusion coefficients.

The gross particle confinement time in D-regime $\tau_{p1} = a_1^2/2D_{\perp 1} = 5.4$ms and practically it does not change in the SOL-regime on the boundary of the main plasma ($\tau_{pS} = 5.6$ms). From the measurement of distributions $n_e(\Delta r)$ and $T_e(\Delta r)$ we can calculate the fluxes on chamber walls Γ_w and stationary limiter Γ_D. The flux through the surface of radius r is equal to /2/, $\Gamma_w = 4\pi r \cdot n_e(r)\Delta \cdot V_S(r)$. In the D-regime for r=11cm $\Gamma_w = 6\ 10^{19}\ s^{-1}$. The particle flux on the stationary limiter is

$$\Gamma_D = n_e(a_1) e^{(a_1/\Delta_1)} \int_{a_1}^{a_2} e^{-(z/\Delta_1)} V_S(z) 2\pi z\, dz \simeq 2.5 10^{20}\ s^{-1}$$

The total particle flux $\Gamma = \Gamma_w + \Gamma_D = 3.1\ 10^{20}\ s^{-1}$. This value determines the gross particle confinement time by the equation $\tau_p = N_e/\Gamma$, where $N_e = \int n_e d^3 r$ is the total amount of electrons in plasma. According to /1/, $N_e = 1.5\ 10^{21}$ particles and $\tau_p \simeq 4.7$ms which is close to the measured value of τ_{p1}. In work /3/ τ_{pT} was calculated on the basis of plasma turbulence model when plasma is brought into contact with an obstacle. However, the evaluations show that τ_{pT} is more than ten times less than τ_p. From this we can conclude that the turbulence mechanism does not define τ_p for Libtor parameters.

Plasma density fluctuations have been determined from the amplitude of oscillations of the ion saturation current on the probe. In Fig.2 the curves 1,3 show the behaviour of $\Delta n_e(\Delta r)$ in D and SOL-regimes, accordingly. The amplitude of fluctuations increases with Δr and the magnitudes of fluctuations on the boundary of the main plasma are $\Delta n_e \simeq 10^{11}\ cm^{-3}$ in both regimes. The curves 2 and 4 on Fig.2 show the behaviour of the relative

levels of fluctuations $\Delta n_e/n_e$ in D and SOL-regimes, accordingly. Near the wall we have sharp decrease of $\Delta n_e/n_e$ in both regimes. Line extrapolations to the wall give $(\Delta n_e/n_e)_w \cong 30\text{-}40\%$. This value and the sharp decrease of $\Delta n_e/n_e$ near the wall are in agreement with the results /4/. In the nearest vicinity to the material obstacles we can see some features of $\Delta n_e/n_e$ behaviour. The density fluctuations are increased in plasma near the edge of obstacles (D or L). Such behaviour is observed in all the cases with material obstacles. The raise in the fluctuation level may be the result of turbulence development near the obstacles /3/ but it does not lead to the decrease of τ_p.

IV. CONCLUSION. Results of measurements of the boundary plasma parameters in SOL (scrape-off layer) regime and comparison them with the stationary limiter regime D are obtained from Libtor Tokamak:

- the diffusion coefficients in the boundary region are the Bohm's coefficients;
- near the wall in the SOL-regime the diffusion coefficient is seven times less and in the SOL region - two times less than the diffusion coefficient near the wall in the D-regime;
- the gross particle confinement time $\tau_{p\perp} = 5.4$ms and it does not change in the SOL-regime;
- the relative level of plasma density fluctuations sharply decreases near the wall , slowly decreases in the SOL region and is characterized by some increase in the nearest vicinity to the edge of material obstacles - diaphragm and limiter.

REFERENCES:

1. A.M.Alabyad et al. 12-th Int. Conf. on Plasma Phys. Nice. I A E A - CN - 50 / A - 7 - 13 (1988).

2. K.Uehara, Y.Gomay, T.Yamamoto et al. Plasma Phys. 21 (1979) 89.

3. P.Staib. J. of Nucl. Materials, 111 - 112 (1982) 109.

4. Ch.P.Ritz, R.D.Bengtson, S.J.Levinson et al. Phys. Fluids 27 (1984) 2956.

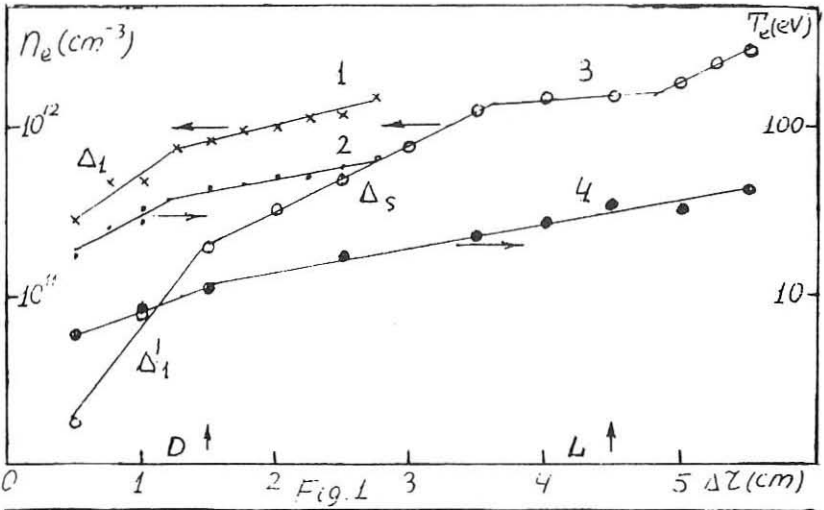
$n_e (cm^{-3})$
$T_e (eV)$
10^{12}
10^{11}
100
10
1
2
3
4
Δ_1
Δ_s
Δ'_1
D
L
0
1
2
3
4
5 Δz (cm)

Fig. 1

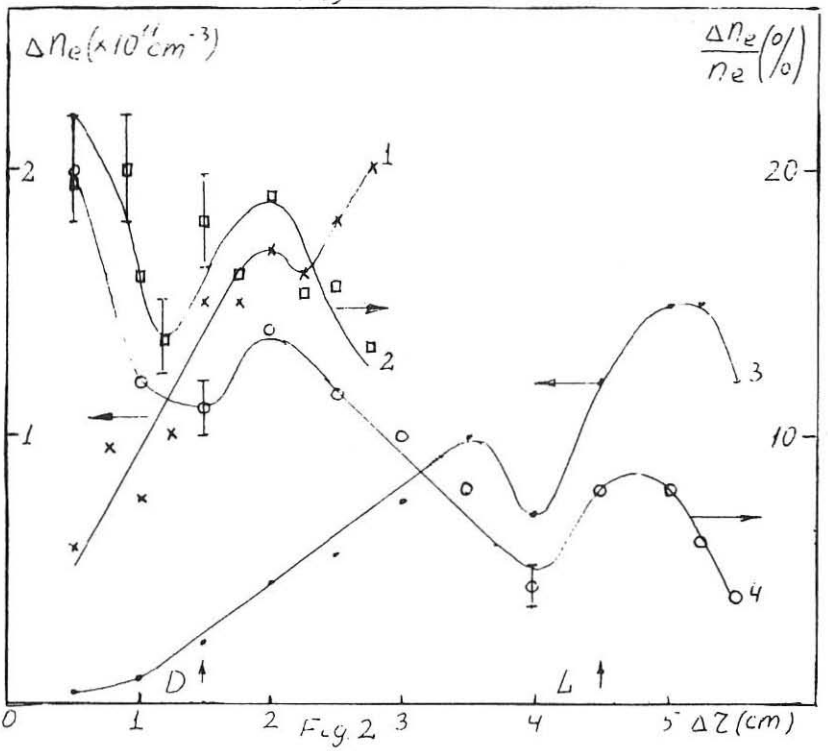
$\Delta n_e (\times 10^{11} cm^{-3})$
$\frac{\Delta n_e}{n_e} (\%)$
2
1
20
10
1
2
3
4
D
L
0
1
2
3
4
5 Δz (cm)

Fig. 2

ELECTRON TEMPERATURE PROFILES IN DISCHARGES WITH PELLET INJECTION AND IN OTHER MODE DISCHARGES

M. Kaufmann, W. Sandmann, M. Bessenrodt-Weberpals, K. Büchl, O. Gruber, O. Kardaun, K. Lackner, R. Lang, V. Mertens, H. Murmann, J. Neuhauser, F. Söldner

IPP Garching, EURATOM-Association, D-8046 Garching, Fed. Rep. of Germany

1. Introduction. Pellet injection in ASDEX can result in a plasma regime with substantially improved plasma performance. This regime is characterised by strongly peaked electron density profiles, while the electron temperature profile shows little change. The energy confinement is significantly enhanced [1]. At least part of the reduced transport can be attributed to an improved ion energy confinement [2, 3]. When the density peaks during ohmic discharges, the ion transport becomes neoclassical over a large part of the plasma cross-section. It is interesting to note that this holds for deuterium as well as for hydrogen discharges. As in discharges without pellets, however, one still observes the global energy confinement to be worse for hydrogen than for deuterium. An enhanced electron transport compensates the better ion confinement which leads to a nearly unchanged temperature profile compared to the deuterium discharge. Another observation seems to support the picture of a very "stiff" electron temperature profile: after pellet injection the relative electron temperature profile recovers within a few milliseconds, although the pellet mass is very inhomogeneously deposited around half the plasma radius.

Earlier investigations on ASDEX [4] found already the high insensitivity of the relative electron temperature profile, especially in the outer part. An independent recent analysis of ohmic discharges [5] confirmed this result. The investigation reported here broadens the experimental basis by a larger number of discharges with different confinement modes, includes an analysis of the absolute value of the temperature, and discusses the energy confinement time.

The electron temperature profile was statistically investigated by applying the SAS-code [6]. About 5000 data points of 70 discharges measured by the ASDEX YAG-system [7] covered the following parameter range:

$5 \cdot 10^{18}\ m^{-3}$	$\leq n_{35}$	$\leq 6 \cdot 10^{19}\ m^{-3}$
$2 \cdot 10^{19}\ m^{-3}$	$\leq n_o$	$\leq 2.3 \cdot 10^{20}\ m^{-3}$
$0.2\ MW$	$\leq P$	$\leq 3.5\ MW$
1	$\leq Z_{eff}$	≤ 2.7
$0.24\ MA$	$\leq I_p$	$\leq 0.47\ MA$
$1.7\ T$	$\leq B_t$	$\leq 2.6\ T.$

(n_{35}: density at r=35 cm, n_o: central density, P: power flowing through the boundary determined as heating minus radiation power, I_p: plasma current, B_t: toroidal field). The analysis included pellet and non-pellet discharges in different modes of confinement (OH-SOC, -IOC, L-mode) and with different heating methods (OH, NI-co, -counter, ICRH). The working gas was deuterium or hydrogen. All discharges were carried out in divertor configuration (old and new design) with a plasma radius of a=40 cm. The data set excludes H-mode data and does not cover the low density range ($\bar{n} \lesssim 2 \cdot 10^{19}\ m^{-3}$).

2. The boundary temperature. If the electron temperature profile is "stiff" in its relative shape, the absolute overall temperature is proportional to the boundary temperature. Precisely speaking it is the temperature at that location in the boundary where "stiffness" stops. For practical reasons the boundary temperature was taken at r=35 cm, which means 5 cm inward from the separatrix. At this location reliable electron temperatures can be obtained from the YAG system. Meanwhile, the system has been improved and temperature at locations, closer to the separatrix will be analysed in the future.

The electron temperature T_{35} at r=35 cm shows significant variations with the density n_{35} at the same location, the heating power P_{tot}, the toroidal current I_p and the toroidal magnetic field B_t. The boundary temperature increases weakly from hydrogen to deuterium. The influence of pellet injection is small. On average T_{35} is about 10 % smaller immediately after injection while 10 ms after injection and later no significant difference can be found. This holds even for the extended periods of improved confinement after injection. No significant dependence on the confinement mode, the heating scenario or Z_{eff} was observed.

In summary, the boundary temperature can be described by

$$T_{35} = 600 \cdot n_{35}^{-0.4} \cdot P^{0.2} \cdot I_p^{1.4} \cdot B_t^{-0.4} \cdot A^{0.2} \quad [eV, 10^{20} m^{-3}, MW, MA, T] \quad \text{A : atomic weight}$$

For simplicity, we used ordinary least squares after a logarithmic transformation. The uncertainty of the exponents is typically $\pm$ 0.1 and the rootmean squared error (rmse) of the fit is 17 %. In the investigated data set, T_{35} ranges from 140 eV to 330 eV where the lower limit seems to correspond to the density limit. It should be noted that the I_p and B_t-dependencies can not be expressed as a pure q_a-dependence.

3. The relative temperature profile. The relative electron temperature profile was analysed in terms of the two ratios T_{20}/T_{35} and T_0/T_{20} (T_0: central temperature, T_{20}: temperature at $r = a/2 = 20$ cm). The reference value at r=20 cm was chosen as a radius value always outside the q=1-radius.

The analysis revealed the following dependencies:

$$T_{20}/T_{35} = 3 \cdot \left(\frac{n_{20}}{n_{35}}\right)^{-0.2} \cdot A^{0.2} \qquad T_0/T_{20} = 0.19 \cdot I_p^{-1.2} \cdot B_t^{1.2} \cdot \left(\frac{n_o}{n_{20}}\right)^{-0.2}$$

The uncertainty in the exponents is again $\pm$ 0.1 and the rmse is 17 % and 10 % respectively. The relative temperature gradient in the outer part is invariant to a high degree. It decreases somewhat at a higher density gradient and gets somewhat larger if one switches from hydrogen to deuterium. If we take deuterium, and the average

n_{20}/n_{35}-value the ratio T_{20}/T_{35} corresponds to a critical temperature decay length of $L_T \equiv T_{20}/\partial T/\partial r = 0.23$ m ($L_T = 0.25$ m was found in [4]).

In the inner part, a strong dependence on q_a is found: $T_0/T_{20} \propto q_a^{1.2}$ which can be attributed to the shrinking of the q=1-radius. Besides this effect, no other strong influence on the temperature profile was observed.

4. Consequences for the energy confinement scaling. If we fix I_p and B_t and neglect the small other causes for a change, we can assume $T(r)$ to be self-similar. Together with the assumption $T_e \approx T_i$ we can rewrite the energy confinement τ_E:

$$\tau_E = \frac{E}{P} = c\frac{\int r dr n_e T_e}{P} = c\frac{T_e(a)\int r dr n_e(r)\Theta(r)}{P}$$

canonical profile of the relative temperature: $\Theta(r) \equiv T(r)/T(a)$,

with: $\langle n\rangle_T \equiv \int r dr n(r)\Theta(r)/\int r dr \Theta(r)$,

we get: $\tau_E \propto T_e(a)\cdot\langle n\rangle_T \cdot P^{-1}$,

with the scaling-law (see above): $T_e(a) \approx T_{35} \propto n_{35}^{-0.4}\cdot P^{0.2}\cdot A^{0.2}$,

one gets finally: $\tau_E \propto \langle n\rangle_T \cdot n_{35}^{-0.4}\cdot P^{-0.8}\cdot A^{0.2}$.

If we allow I_p and B_t to change we have to include two effects:

1. The temperature averaged density has to include the different $\Theta(r)$ profiles for different q;
2. The I_p and B_t influence of T_{35} has to be taken into account.

Hence we get: $\tau_E \propto \langle n\rangle_T \cdot n_{35}^{-0.4}\cdot P^{-0.8}\cdot A^{0.2}\cdot I_p^{1.4}\cdot B_t^{0.4}$.

A direct regression analysis of τ_E ($T_i = 0.9\ T_e$) with these parameters yields

$$\tau_E \propto \langle n\rangle_T^{0.5}\cdot n_{35}^{-0.2}\cdot P^{-0.7}\cdot A^{0.2}\cdot I_p^{0.7}\cdot B_t^{-0.1}.$$

The τ_E-values for all the investigated conditions are relatively well described by this scaling law with a rmse of 14 % (see figure). Phases of discharges with pellet injection, IOC periods, and L-mode periods do not show a significant deviation from the fit to the complete data set. The improvement of energy confinement in pellet and IOC discharges enters the τ_E expression via the increased $\langle n\rangle_T/n_{35}$-value, that means through the density peaking.

In assessing the differences between these two expressions for τ_E it has to be noted that n_{35} and $\langle n\rangle_T$ are of course highly correlated in our data base, and that the shape factor represented by the ratio $\langle n\rangle_T/n_{35}$ will itself depend on I_p/B_t in a form leading to a partial cancellation of the discrepancies. The very unfavourable power dependence of τ_E is at least partly a consequence of the assumption $T_i = 0.9\ T_e$, which will systematically tend to underestimate the increase in energy content with heating power.

References.

[1] M. Kaufmann et al., Nucl. Fusion **28** (1988) 827.

[2] O. Gruber et al., Plasma Physics and Contr. Fusion, to be published.

[3] M. Kaufmann et al., Proc. 12th Int. Conf. on Plasma Phys. and Contr. Nucl. Fusion Res., Nice, 1988.

[4] H. Murmann et al., Proc. 13th Europ. Conf. on Contr. Fusion and Plasma Heating, Schliersee 1986, **I**, 216.

[5] P.J. McCarthy, private communication, to be published.

[6] SAS, User's Guide: Statistics, SAS Institute Inc., Cary, North Carolina (1985).

[7] H. Röhr et al., IPP-Report III/121B, 1987.

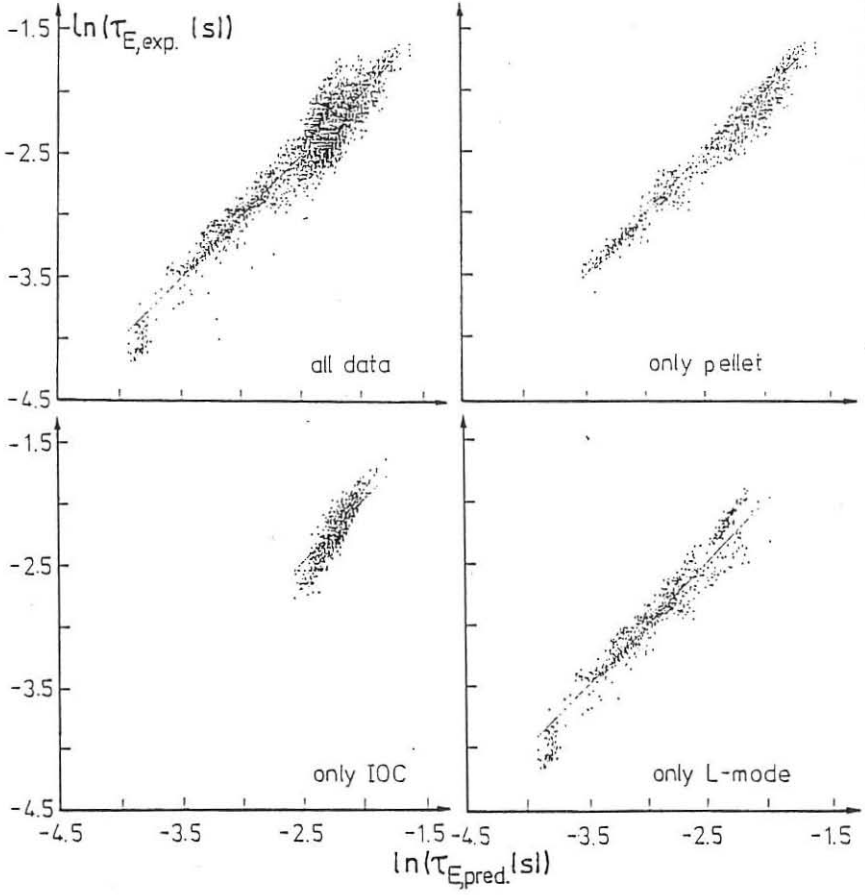

RADIAL PROFILE OF ELECTRON DENSITY FLUCTUATIONS IN THE TJ-1 TOKAMAK FROM MICROWAVE REFLECTOMETRY MEASUREMENTS*

J.M. Sentíes , E.G. Bustamante, M.A.G. Calderón
Departamento de Física Aplicada, Univ. Cantabria
39005 Santander, ESPAÑA
E. Anabitarte, A.P. Navarro, P. Rípodas, J. Sánchez
Asociacion EURATOM/CIEMAT
28040 Madrid, ESPAÑA

INTRODUCTION

Experimental determination of electron density fluctuations in plasmas plays an important role in tokamak, where investigation of the effects from turbulence on energy and particle confinements is a field with increasing attention [1], and in stellarator where the behavior of these fluctuations can be used as indication of the access to the second stability regime [2]. Microwave reflectometry [3] , based in the change of phase that appears in a wave propagating in the plasma when a cutoff layer is reached and the wave is reflected, can be used to measure these density fluctuations by keeping fixed the incident wave frequency and relating the fluctuations in the obtained signals with the density fluctuations at the reflection layer. The main potential of this technique comes from the fact that with a relatively simple experimental system it is possible to deduce the radial profile of electron density fluctuations in the plasma just by changing the frequency of the incident wave because for each frequency there is a different position for the cutoff layer. Having a wide range of frequencies in the oscillator, it would be possible to cover the full plasma radius.

In this paper a microwave reflectometer has been used to determine the radial profile of density fluctuations in the TJ-1 tokamak, (R_0 = 30 cm, a = 10 cm, B_t = 1 T) for discharge with and without dominant MHD activity in the plasma in order to check the validity of this technique and the effect from this kind of instability in the electron density. A numerical simulation code for the behavior of the reflectometer phase has been developed in order to interpret the obtained signals in these experiments.

SIGNAL SIMULATION

The effect of density fluctuations on wave propagation and reflection in the plasma has been simulated with the approximations of geometrical optics for these processes. A parabolic electron density profile is assumed with monochromatic perturbations given by:

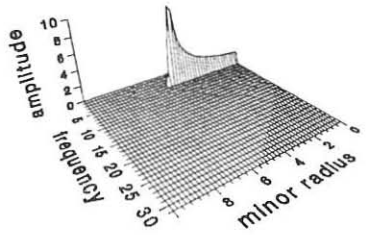

Fig. 1 $\Phi(t)$ spectrum for X- mode

$$\tilde{n}_e(r,t) = \Delta_0 \, e^{-\left(\frac{r - r_s}{\lambda}\right)^2} \sin\omega t$$

where r_s is the radial location of the perturbation and Δ_0 its amplitude. The radial extension of the perturbation is determined by :

$$\lambda = r_s - \sqrt{1 - n_e(r_s) + \Delta_0}$$

All the previous magnitudes are relative quantities. The time variation of the phase for the launched wave is calculated using [3] :

$$\Phi(t) = \frac{4\pi F_0}{c} \int_a^{x_c(t)} N(t)\,dx - \frac{\pi}{2}$$

where F_0 is the incident wave frequency, x_c the radial position where the reflection takes place and N(t) the wave propagation index in the plasma.

Once the phase time evolution is known, its spectrum can be calculated using FFT and compare with the corresponding to the density perturbation. Fig. 1 shows this spectrum for a X mode propagating in a plasma with a 2% density perturbation located at half the plasma radius. Similar result is obtained for the O mode. A dominant component, at the frequency of the incident wave, appears. Its radial distribution peaks at the position of the perturbation layer but there is also component further inside the plasma. This phenomena is due to the effect from the perturbation on waves propagating along the region with the density perturbation, because its frequency is higher that the required

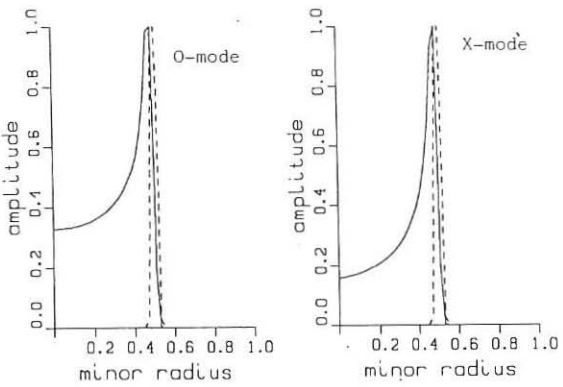

Fig. 2 Radial profiles for phase amplitude (solid line) and density perturbation (dashed line).

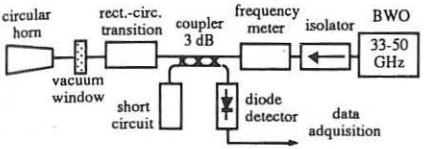

Fig. 3 Experimental set-up

value to have reflection at the perturbation layer. Fig. 2 presents this radial dependence of the amplitude at the dominant frequency for the cases of O and X mode. The ratio between the phase due to reflection and to-propagation increases when going from the ordinary to the extraordinary mode and, in both cases, is big enough, to allow the determination of the position and radial extension of the density perturbation.

EXPERIMENTAL SETUP

The experimental setup used for this measurements is shown at figure 3. It is basically a reflectometer working in the Q band, 33 - 50 GHz [4]. The circular horn is located at the equatorial midplane inside the vacuum chamber of the TJ-1 tokamak Measurements were made during the plateau of the discharge, keeping the frequency fixed at the BWO, and radial scans were made in a shot-to-shot basis by changing the frequency in the available range. X mode was used in all the experiments due to higher sensitivity and radial resolution of this mode.

RESULTS

Two different kind of discharges were analyzed in the TJ-1 tokamak, in the first one a big MHD activity was produced by increasing gas puffing. Reflectometer signals were recorded for 0.5 ms during this burst of activity and, using reproducible shots, frequency at the reflectometer was changed to cover the full operational range available at the time of the experiment: 33 to 40 GHz. This enables to scan only one third of the plasma radius for the density conditions, value and profile, during the TJ-1 discharges. In the second type of discharge the gas puffing was reduced to avoid the MHD activity and reflectometer data were recorded at the same times than in the previous series. Simultaneously, signal from Mirnov coils were recorded to correlate its dominant frequencies with those appearing in the reflectometer signals. Figure 4 presents the results obtained from the analysis of these measurements for the cases with and without MHD activity, where the integral of fluctuation spectra is taken as a measure of the turbulence level. From these results it seems that turbulence dominates at the edge for the case without big MHD activity and, when this is present, it peaks at one position close to the q=3 resonant surface. Nevertheless with the available range of frequency it is not possible to cover the full plasma and deduce if this level at the resonant surface is bigger than the produced by the turbulence at the edge. In an

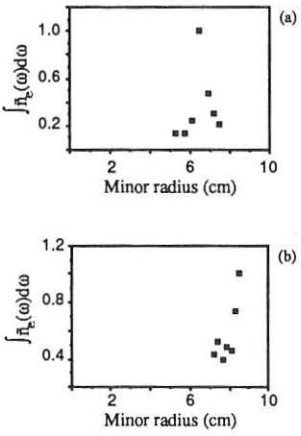

Fig. 4 Radial profile of fluctua tion amplitude (a) with MHD (b) without MHD.

attempt to clarify the role of MHD in density fluctuations, radial profile of signal phase spectrum amplitude at the MHD dominant frequency is plotted at figure 5. This profile is very similar to the corresponding to the total one plotted at figure 4a, and it can be taken as an additional indication of the contribution from MHD to density fluctuations in the plasma.

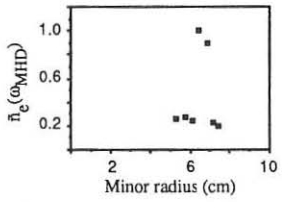

Fig.5 Fluctuation radial profile at MHD dominat frequency.

CONCLUSIONS

Results at TJ-1 tokamak prove that radial profile of density fluctuations can be determined by microwave reflectometry. They also seem to prove that MHD instabilities produce density fluctuations that peak at the resonant surface position. Nevertheless it was not possible to compare these MHD generated fluctuations with those due edge turbulence because the short range of frequency available at the reflectometer at the time of the experiments.

* This work was partially supported by the C.I.C.Y.T., Spain.

REFERENCES

[1] P. Liewer, Nucl. Fusion **25,** 543, (1985).
[2] B.A. Carreras et al., Nucl. Fusion **28**, 1613, (1988)
[3] A. Cavallo and R. Cano, Report EUR-CEA 1137, (1982).
[4] E. Anabitarte et al., J. Phys. D: Appl. Phys. **21**, 1384, (1988).

A SEARCH FOR NONAMBIPOLAR PARTICLE TRANSPORT IN THE TJ-I TOKAMAK

B. Zurro and TJ - I Group
Asociación **EURATOM/CIEMAT.** E - 28040 Madrid. Spain

The aim of this work is to explore whether nonambipolar particle transport can be revealed by means of a perturbative experiment carried out in the TJ-I tokamak. When a short pulse of impurities are injected into a hot plasma by using the laser ablation technique, an enhancement is simultaneously produced in both electron density and impurity concentration. If both perturbations can relax independently driven by their own transport mechanisms, we would have a direct method to measure the impurity and electron particle transport. Even if they relax separately no significant differences are a priori expected between both confinement times. We have compared, using available data in ohmically and additionally heated tokamak discharges, τ_p (global particle confinement time) measured by the H_α method and τ_I (impurity confinement time) measured by the laser blow-off technique; their ratio τ_I/τ_p ranges between 0.5 and 2.3. Part of this difference could be ascribed to uncertainties of the first method and to the fact that the laser ablation technique measure a central confinement value whereas the first one measures a global confinement time and it is well known that the central confinement time is higher than the global one (1), (2). It is generally accepted that nonambipolar processes like charge exchange and magnetic fluctuations play some role on particle transport, but its influence has not been observed by using standard techniques, only some hints on it there has been provided by internal potential measurements using a heavy ion beam probe (3).

In this paper we have study the decay time of the perturbation, for different electron densities, of the total radiation and line average density, produced by injecting a short pulse of impurities in the the TJ-I tokamak by the laser blow-off technique.

Iron was injected into ohmically heated discharges in the TJ-I tokamak (major radius 30 cm, minor radius 10 cm), operated for this experiment at a toroidal field of 1 T and a plasma current of around 40 kA. Hydrogen is puffed in the discharge, with a piezoelectric valve, started at a base pressure of $2x10^{-4}$ torr. Impurity injection takes place once the plasma current reaches its plateau value. The time behaviour of the injected iron in the hot plasma core has been monitored with a pyroelectric detector and a vacuum ultraviolet monochromator provided with a channeltron, both collimated along the central chord. The electron density enhancement is monitored by means of a 2 mm interferometer measuring the line averaged density along a central vertical chord.

The halo of electrons due to impurity ionization has been tracked by using a full impurity transport code (4). The injection experiment was simulated by producing an enhancement in the impurity concentration lasting 0.4 ms, which is the time width of the injected beam as measured by the injection monitor focused at the plasma edge and placed at the injection port. This monitor measures the enhancement in the 3581 Å Fe line as consequence of the interaction between the injected beam and the plasma edge.

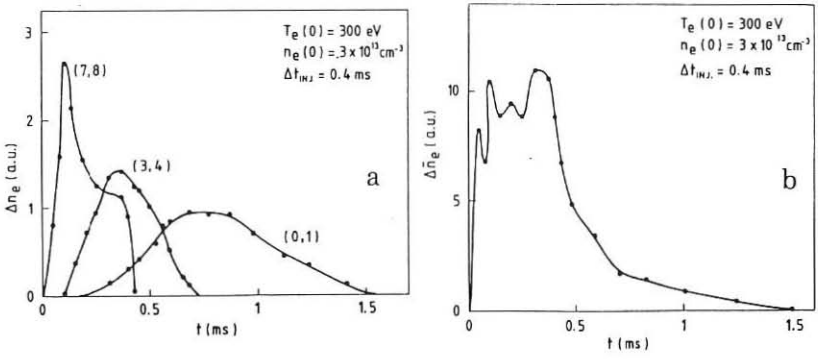

Fig. 1. Calculated temporal evolution of electron deposition due to impurity ionization: a) In three different shells with limiting radius (r_1,r_2); b) The whole plasma.

The electrons are released by the impurities, for typical plasma conditions in TJ-I, as a pulse with the same width as the impurity beam and with a tail decaying with a time constant comprised between 0.17 - 0.25 ms. In Fig. 1 we depict the calculated temporal evolution of electron density enhancement (ignoring electron transport), for three different shells and the total line averaged enhancement as determined by the former code. These results allow to consider the electron halo narrow enough and its later evolution, as measured by the interferometer, as being due to their transport in the plasma core and not to a continuous releasing of electrons.

We have studied the decay time of electron density and impurity perturbation as a function of the target plasma density. For this purpose laser blow-off impurity injection was performed in discharges with different puffing levels, the density was quantified with a H_α monitor coupled to the same toroidal sector as the piezoelectric valve. The decay constant of both perturbations are plotted, see Fig. 2, versus the H_α signal. The line averaged electron density range displays in the former figure span from 0.5 to 1.5×10^{13} cm^{-3}. The confinement time decreases as the plasma density increases although not so dramatically as in previous published scans, which were performed with cleaner discharges covering a broader range of densities (5). The electron density perturbation generally tends to decay slightly slower, by a factor ranging from 1 to 1.3, than the impurity decay. Due to the small difference in the decay times we can not conclude whether this small difference is due to similar transport or to the fact that both perturbation can not evolve independently. However, since the electron density enhancement is echoed in the line radiation of some impurities, like the resonant line of OVI, we claim it is an indication of the detachment of the electron from the parent ion and a point supporting the independent evolution of both perturbations. An additional influx of oxygen has been ruled out as a potential cause of this enhancement. We are trying to look for discharges in which this difference be more significant what would be a stronger support of the decoupling of both componenets. If we use heavy ion beam data (3) as a guide for the present experiment, we should try to cover a broader range of densities and measure the density decay with spatial resolution to distinguish the plasma core from the edge behaviour, but until now there has not been possible in the TJ-I tokamak.

In conclusion, the ion and electron density perturbation time evolution have been studied in the TJ-I tokamak in a limited range of densities by injecting iron by the laser blow-off technique, no significant distinct transport is observed for those two type of particles at least for the standard discharges reported in this work.

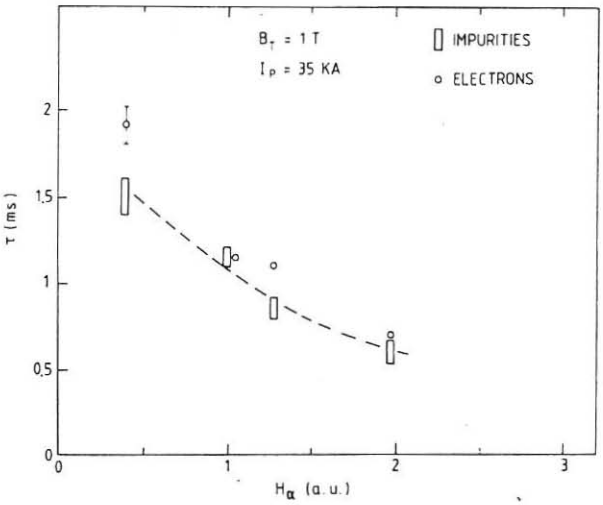

Fig. 2. Plot of the impurity and electron density decay times as a function of density, measured by the laser ablation technique.

REFERENCES

(1) G. Vlases, K. Büchl and D. Campbell Proc. 11th Europ. Conf. Controll. Fusion Plasma Phys. 127 (1983).

(2) T. Yamauchi, M. Nagami and S. Sengoku Jpn. J. Appl. Phys. **9**, 1737 (1980).

(3) V. I. Bugarya et al. Nuclear Fusion **25**, 1707 (1986)

(4) K. Behringer Report JET - R (08) (1988).

(5) B. Zurro, C. Pardo and F. Mompeán Plasma Phys. Controll. Fusion **30**, 1767 (1988).

INVESTIGATION OF THE ENERGY TRANSPORT MECHANISM IN THE TCA TOKAMAK BY STUDYING THE PLASMA DYNAMICAL RESPONSE

Th. Dudok de Wit, B.P. Duval, B. Joye, J.B. Lister, J.-M. Moret

Centre de Recherches en Physique des Plasma, Association Euratom-Confédération Suisse
Ecole Polytechnique Fédérale de Lausanne
21, Av. des Bains, CH-1007 Lausanne, Switzerland

The energy transport mechanisms that govern the electron temperature behaviour of a tokamak remain very badly understood and up to now no proper model has been proposed that can explain experimental observations such as profile consistency or the influence of the density profile. One approach to this problem, extensively used on TCA, is to study the dynamical response of the plasma due to externally imposed modifications of parameters which have an influence on the plasma energy content. The temporal evolution of the electron temperature will closely depend on the type and the characteristics of the implied mechanisms. Thus a detailed measurement of the dynamical response would reveal experimentally the dominant properties that would have to be taken into account in the elaboration of a model of the transport processes.

Most of the results presented here were obtained by analysing the electron temperature response inferred from soft X-ray emissivity during modification of the plasma density due to either gas puffing, laser impurity ablation or Alfvén wave heating on TCA ($a = 0.18$ m, $R = 0.61$ m, $B_\phi = 1.52$ T), using the techniques described in [1].

Dynamical response of the electron temperature - Average plasma density has long been identified as an important parameter in the parametrisation of the global energy confinement time. And more recently the density profile has also shown a considerable effect [2]. The dynamical response of the electron temperature on TCA was first measured by sinusoidally modulating the gas valve between 30 and 300 Hz. Profiles of the relative amplitude and of the phase of the soft-X-ray response exhibit two distinct regions. The inner volume of the discharge displays the lowest gains and phases; outside a well-defined radius both the gain and the delay increase. Care was taken to ensure that the phase profile was continuous from low to high modulation frequency and that there were no unobserved 360° phase jumps. It has also been checked that throughout the discharge the relative density modulation is much smaller than the relative soft-X-ray modulation, guarantying that the observed effect is the consequence of an electron temperature variation. A plasma current scan between 55 kA and 125 kA clearly demonstrated that the surface separating the two regions is linked to the sawtooth inversion radius : results for 125 kA and 85 kA are plotted in Fig. 1. At the highest modulation frequencies used, the phase profile inside $q=1$ becomes slightly convex. Therefore, the outermost part of the inner region possesses the lowest phase, unambiguously indicating the presence here of an effective energy source. Surprisingly, the observed reaction of the electron temperature is not due to edge cooling by an influx of cold gas and another interpretation is required which will be discussed later.

Beside the dominant role played by the current profile via the $q=1$ radius in determining the electron temperature behaviour, it should be emphasised that the temporal evolution of the

soft-X-ray emissivity can be exactly reproduced with several different perturbations : modification of the density by gas puffing, density increase following a short rf power pulse or reaction to injection of aluminium by laser ablation. In all these cases, the analysis of the temperature response leads to a transfert function in excellent agreement with the measured frequency response with harmonic modulation of the gas valve. Again we conclude that systematicly the sudden temperature decrease in the outermost observed region is not caused by radiation or cooling by new particles.

Variation of the current profile - Density modulation experiments are accompanied by a modulation of the Shafranov parameter $\Lambda = \beta_p + li/2 - 1$ measured via the vertical equilibrium field. Unfortunately, a diamagnetic measurement often used to determine the internal inductance, suffers from a vessel frequency cut-off and had to be discarded. Nevertheless, it is possible to have an idea of the current profile variation: Fig. 2 shows the complex amplitude of the modulated component of different parameters during a gas valve modulation at 100 Hz. The Shafranov parameter has been corrected for the vessel time constant. The density was chosen as the phase reference so that its amplitude is real. Also plotted is the modulation of the central soft-X-ray diode which is colinear with the central electron temperature amplitude. Due to the peakedness of the pressure profile, the β_p modulation must be close to a linear combination of both the density and the central electron temperature modulations with positive real coefficients. Thus the variation of the Shafranov parameter can only be explained if it is accompanied by a modification of the internal inductance and, therefore, of the current profile.

Influence on the sawtooth parameters - As the electron temperature response profile is essentially determined by the position of the q=1 surface, the sawtooth activity must have a considerable influence on its dynamic response. One should note that it is easy to achieve a variation of the base flux whose time derivative approaches or equals the sawtooth slope as seen in Fig. 4. Nevertheless, even under these circumstances, it has never been possible to observe zero or negative sawtooth slope in the plasma center. We see that most of the electron temperature variations are due to modifications in the sawtooth activity characteristics. The latter, namely the amplitude of the ramp, which is equal to the product of the slope and the period, and the amplitude of the crash, have been plotted on Fig. 3. In both cases the electron temperature response results from a net difference between the two quantities. More precisely, the same figure shows that the ramp amplitude variation is the consequence of a sawtooth period modification at constant slope which would not have been the case if the sawtooth signal were simply superposed on the base signal. The crash amplitude is found to be reduced during the central temperature rise and to greatly increase during the temperature drops. The opposite behaviour is observed outside the inversion radius where the small crashes lead to a reduction of the average electron temperature which can explain a 180^o phase shift in the phase profile.

Discussion - We shall now discuss the implications of the previous results on the modelling of the transport processes and their relation with other observations. To explain the observed dynamic response of the electron temperature, we require an apparent thermal energy source localised near the q=1 surface and an abrupt increase of the phase just outside this surface. This energy source may be due to magnetic to thermal energy exchange arising from the observed variation of the current distribution, and the large phase jumps could be attributed to a thermal insulation barrier associated with the q=1 surface also observed during pellet injection in TFR [3]. These two features may be more conveniently produced by a variation of the thermal electron conductivity localised around the q=1 surface. This increase results in a local decrease of the outward heat flux, leading to an energy accumulation just inside and a lack of energy outside this region, thus producing an apparent energy source and

a 180^{o} phase shift. Such a variation of the thermal energy diffusion coefficient during a transient was also used to simulate the evolution of the energy content at a ECH power step on TFR [4]. In an alternate model, the presence of an insulation layer in the q=1 region is supported by the lack of significativ central sawtooth slope variation even during very transient regimes, as if the plasma center were fully insulated from the outside. Here, an evolution of the time averaged central temperature is possible only if the elapsed time between crashes or their amplitude vary. When the crashes are small, there is an accumulation of thermal energy inside the q=1 surface but also a lack of energy outside the mixing radius to sustain the heat losses, producing a decrease of the peripheric temperature. It still remains unclear whether the determining parameter is the crash amplitude or the point at which the crash ends, two situations that would arise from quite different mechanisms.

The close link of these observations with the so-called profile resiliency has already been mentioned and is quite reasonable if one considers the role of the current profile in determining either the stationary temperature profile and its dynamical response profile. In addition, the systematic study of the electron temperature dynamic response has clearly established that the thermal insulation at the q=1 surface and the sawtooth activity characteristics are the most important elements in explaining the electron temperature behaviour and the energy transport in the plasma. This demonstates the power of such techniques in the investigation of the transport in a tokamak plasma.

This work was in part supported by the Fonds National Suisse de la Recherche Scientifique.

References

[1] J.-M. Moret, Thesis No 758, Ecole Polytechnique Fédérale de Lausanne, and Lausanne Research Paper LRP 358/88, October 1988.

[2] O. Gruber et al., Plasma Phys. and Contr. Fusion **30** (1988) 1611.

[3] TFR Group, 14th Europ. Conf. on Contr. Fusion and Plasma Physics, Madrid, Spain, 1987, Part I, Vol. 11D, p. 29.

[4] H.P.L. de Esch et al., Conf. on Contr. Fusion and Plasma Physics, Madrid, Spain, 1987, Part III, Vol. 11D, p. 876.

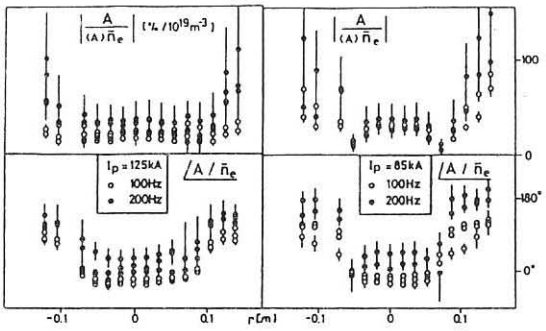

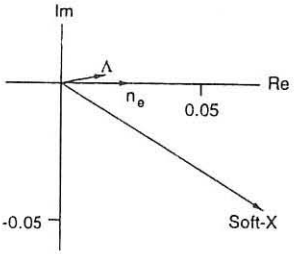

↑ **Fig. 1** Relative gain and phase profiles of the Soft X-ray response during gas valve modulation.

← **Fig. 2** Vector representation of the complex amplitude of the Shafranov parameter Λ during gas valve modulation.

↓ **Fig. 3** Raw Soft X-ray traces in and outside the inversion radius, during : a) RF power modulation, b) aluminium injection by laser ablation. The two upper graphs also show the sawtooth slope (–) and crash (--) amplitude. The lower graph gives the sawtooth frequency (--) and the time derivative of the slope at the center of the plasma (–).

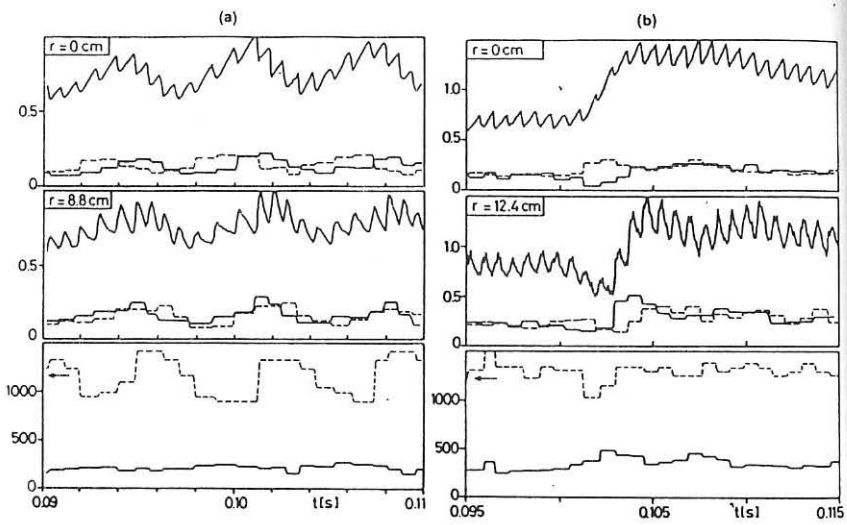

RADIAL PROFILES OF NEUTRON EMISSION FROM OHMIC DISCHARGES IN JET

J M Adams[1], A Cheetham, S Conroy[2], G Gorini[3], N Gottardi, T Iguchi[4], O N Jarvis, G Sadler, P Smeulders, N Watkins[1] and P van Belle

JET Joint Undertaking, Abingdon, Oxon, OX14 3EA, UK
[1] Harwell Laboratory, UKAEA, Oxon, OX11 ORA, UK
[2] Imperial College of Science and Technology, London, SW7 2BZ, UK
[3] Scuola Normale Superiore, Pisa, Italy
[4] University of Tokyo, Tokyo 113, Japan

ABSTRACT

Neutron emission profiles from several ohmically heated discharges have been studied using a variety of analytical techniques to extract the ion temperature profiles which are found to agree well, both in shape and magnitude, with the electron temperature profiles as measured by the LIDAR Thomson scattering diagnostic.

INSTRUMENTAL DETAILS

The neutron emission profile measurement diagnostic at JET [1] has been in routine operation for the past 18 months. It measures the spatial neutron emission, as a function of time, in a poloidal section through the JET plasma. The instrument comprises a total of 19 lines-of-sight, with 10 horizontal channels measuring the vertical profile and 9 vertical channels measuring the horizontal profile. The associated 19 NE213 liquid organic scintillator detectors, suitably shielded against the high magnetic fields around JET, are housed in 2 'heavy' concrete fan-shaped multi-collimator arrays, (or cameras), at a distance 5.5-5.8 m from the centre of the vacuum vessel. The detector lines-of-sight are shown schematically in figure 1. An indication of the spatial resolution of the instrument can be given by considering the individual channel separations at the centre of the plasma; for the vertical profile this is 22 cm, and for the horizontal profile 18 cm.

Pulse shape discrimination techniques are employed to distinguish between neutron and γ-ray events in the liquid scintillators. In order to reduce the backscattered neutron contribution from the vessel walls, a lower neutron energy bias of 2 MeV is employed. Based on the FURNACE calculations of Verschuur [2], this results in the backscattered neutron contribution being $\sim$ 3% of the direct neutron yield in the central channels of the horizontal camera. A strong ^{252}Cf source placed at the collimator entrance has been used to show that the "cross-talk" between adjacent channels is negligible.

The neutron emission data recorded in the individual channel line integrals were all corrected for the backscattered neutron contribution, live time, absolute neutron detection efficiency, neutron attenuation and

collimator scattering, and the known collimator solid angles.

Considerable effort has been expended in validating the overall performance of the instrument, including independent measurements of the absolute response of the individual detectors. No instrumental defects were discovered and it is now considered that the experimental data are essentially correct for the D-D plasma 2.45 MeV neutron emission from ohmic discharges. The total neutron yields from the time-dependent neutron yield and neutron profile monitor diagnostics agree to within ± 20%, which is within the absolute errors of these instruments. Summation of the measurements over several weeks of operation has been compared with the integrated profiles obtained with small solid state track detectors located in the collimators; good agreement between the profile shapes was obtained, affording a test of the diagnostic for high power additionally heated discharges.

As a first application of the instrument, a series of ohmic discharges, with plasma currents between 3 and 6 MA, have been analysed using several techniques. The objective of this exercise was to compare the ion temperature profile as derived from the neutron emission data with the electron temperature profiles provided by the ECE and LIDAR diagnostics. For these discharges, the neutron data were integrated over several seconds in order to obtain good statistics and were normalised, in absolute terms, to the time dependent total neutron yield monitor diagnostic.

ANALYSIS OF RADIAL PROFILE DATA

Four analytical techniques have been applied to these discharges with the objective of determining the optimum technique for the particular circumstances under study. One technique is a forward calculation which relies on flux surface symmetry and assumes a given neutron emission radial dependence with parameters optimised by straightforward least squares fitting of predictions to experimental data. The other three are inversion techniques: (i) Cormack tomography [3] which makes no assumptions about the plasma geometry, (ii) Generalised Abel inversion [4] which assumes flux surface symmetry, and (iii) Constrained Tomography [3] using near-elliptic contours described by a 4-term polynomial expansion. The results obtained using these codes were in agreement in all the essential quantities.

(a) **Forward Calculations** - An example of a fit using this approach is given in figure 1, showing the deviation between the fit and measurement. Typically, the deviation from a particular channel is ± 20% which is greater than the expected channel to channel uncertainty of ± 10%. An axial ion temperature of $\sim$ 2 keV is obtained for a range of different source profiles which fit the data equally well.

(b) **Cormack Tomography** - This method fits the data perfectly because of the large number of coefficients used, but is very sensitive to experimental uncertainties. For this reason the other techniques are preferred for the present instrument which has rather few lines-of-sight.

(c) Generalised Abel Inversion and Constrained Tomography - Figures 2 and 3, respectively, show the reconstructed neutron emission and deduced ion temperature profiles for a typical ohmic discharge, obtained using both techniques; the results from the forward calculations are also shown.

These independent analyses lead to a number of interesting observations: (1) within the uncertainties, the neutron emission is indeed constrained to the magnetic flux surfaces, (2) the neutron emission centroid is displaced $\sim$ 5 cm outwards from the magnetic centre (the accuracy with which the latter is known is $\pm$ 7 cm), (3) the deduced neutron emission profiles are well determined in regions of strong gradient, but are subject to large uncertainties in the centre (as would be expected for line-of-sight integrated data), (4) the deduced ion temperature profiles are more precisely determined, with an absolute uncertainty of up to $\pm$ 20% (mainly due to the n_d/n_e uncertainty as obtained from Z_{eff} determinations), and (5) the constrained tomography gives ellipicities in good agreement with the magnetic flux surfaces at large radii.

More generally the central ion temperature obtained from these neutron measurements is typically 5 to 10% lower than those obtained by the large crystal X-ray spectrometer [5], but still within the experimental errors. As shown in figure 3, the ion temperature profiles fall close to the electron temperature profiles as measured by the LIDAR [6] diagnostic, at least out to 3.7 m, after which the neutron emission data becomes too weak to be usable. On the other hand, the ECE [7] temperature profile seems to be 40% higher, and rather broader. For these ohmic discharges, the ion-electron equipartition time is much shorter than the energy confinement time so the temperature difference between electrons and ions would be expected to be small.

REFERENCES

[1] J M Adams, O N Jarvis, J Källne et al, Controlled Fusion and Plasma Heating, (Proc 14th Europ Conf Madrid, 1987), Vol 11D, Part III, European Physical Society (1987) 1224.

[2] K A Verschuur, "Furnace Calculations for JET Neutron Diagnostics", ECN Report 146 (1983), and private communication.

[3] R S Granetz and P Smeulders, Nuclear Fusion 28 (1988) 457.

[4] N Gottardi, H Krause and K F Mast, Controlled Fusion and Plasma Heating (Proc 12th Europ Conf, Budapest, 1985), Vol 9F, Part I, European Physical Society (1985) 30.

[5] R Bartiromo et al, "The JET High Resolution Bent Crystal Spectrometer", JET-P(88)11.

[6] H Salzmann et al, Nuclear Fusion 27 (1987) 1925.

[7] D V Bartlett et al, Electron Cyclotron Emission and Electron Cyclotron Resonance Heating, (Proc. 6th Joint Workshop, Oxford, 1987), CLM-ECR(1987)137.

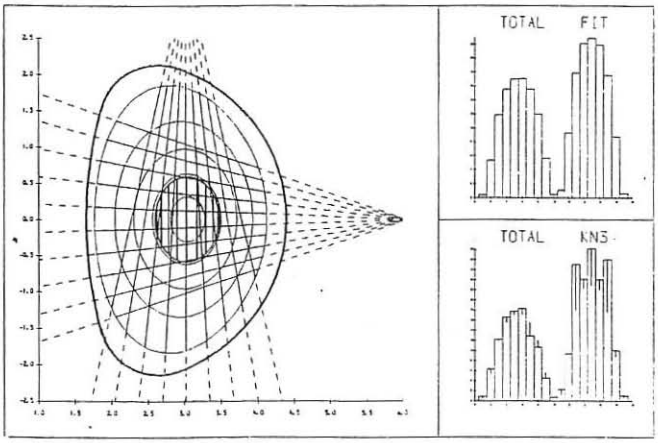

Fig.1. Showing the magnetic flux surfaces in the JET tokamak for discharge number 15149 and the 19 lines-of-sight of the profile monitor. The half-width of the neutron emission profile is indicated by the shading. The figures to the right show the predicted best-fit signals in the 19 channels (upper) and the measured signals (lower), where the mismatch is indicated by the vertical bars.

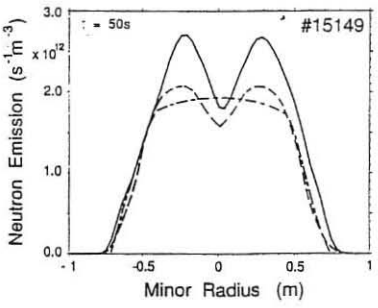

Fig.2. Neutron emission profiles deduced from Generalized Abel Inversion (solid curve), constrained tomography (dashed) and the forward calculation (dot-dashed).

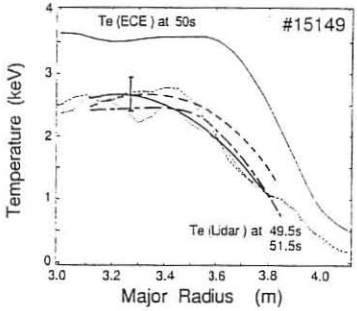

Fig.3. Comparing the three ion temperature profiles deduced from the neutron emission profiles of fig.2 with the electron temperature profiles provided by LIDAR and ECE diagnostics.

Triton burnup in JET

S Conroy[1], J P Argyle[2], P Batistoni[3], E Clipsham, G B Huxtable[2]
O N Jarvis, M Pillon[3], S Podda[3], M Rapisarda[3], G Sadler, P van Belle

JET Joint Undertaking, Abingdon, Oxfordshire OX14 3EA, UK
[1]Imperial College of Science, Technology and Medicine, London, SW7 2BZ, UK
[2]Harwell Laboratory, UKAEA, Oxfordshire OX11 0RA, UK
[3]ENEA, CRE Frascati,Italy

Abstract

Triton burnup measurements have been made at JET using time-integrated copper activation and time-resolved silicon detector techniques. The results confirm the classical nature of both the confinement and the slowing down of the 1 MeV tritons in a plasma.

Introduction

D-D fusion reactions produce approximately equal quantities of 2.5 MeV neutrons and 1.0 MeV tritons. The 1.0 MeV tritons slow down over a period of order 0.5 second and whilst doing so may undergo a D-T fusion reaction, emitting a 14 MeV neutron. Measurements of both 2.5 MeV and 14 MeV neutrons have been made at JET and are used here to analyse the confinement and thermalisation properties of fast tritons.

Neutron detection

The 2.5 MeV neutron emission is measured with a fission chamber system (1) which is calibrated by direct (ie not activation) techniques to an accuracy of better than $\pm 10\%$. The time-integrated 14 MeV neutron flux at a point just outside the vacuum vessel is measured through the induced activation of copper foils (2). Neutron transport codes are used to relate the flux to the total yield, with an estimated error of $\pm 15\%$ (3). These codes are also used to relate the induced activation of Indium foils to the 2.5 MeV neutron yields and good agreement is found with the fission chamber results, giving confidence in the accuracy of the codes. Time-resolved 14 MeV neutron emission rates are measured using (n,p) and (n,α) reactions in a 450mm^3 silicon diode positioned outside the vacuum vessel. The charged reaction products slow down in the diode generating an output pulse-height spectrum proportional to the energy deposited. By counting only pulses corresponding to an energy of greater than 6 MeV deposited in the diode, a signal proportional to the 14 MeV neutron emission rate is obtained. Finally, cross calibration with the activation system provides an

absolute measurement (±20% accuracy).

Previously, one of the main experimental limitations with the silicon diode was the appearance of a breakthrough signal at very high count rates, believed to be due to pile-up of individual signals due to neutrons and gamma-rays (4). In the present apparatus, this effect has been reduced by increasing the maximum count-rate capability of the diode electronics and removing the diode from the immediate vicinity of the plasma, thereby increasing the maximum 2.5 MeV rate at which the diode operates reliably by approximately a factor of 10. This limit now corresponds to a total neutron emission strength of 10^{16} n/s.

Data analysis

Analysis of the data is performed by comparison with a simple time-dependent classical model of the 14 MeV neutron emission rate (4). The model uses 10 nested flux surfaces to model the plasma. Each surface has its own triton source rate, electron temperature, electron density and deuterium density which are taken from other diagnostics. Tritons are slowed down on each surface and the 14 MeV neutron emission calculated for each time point, taking into account the temporal variations in the background plasma parameters. When run for stationary (time-independent) problems, the code provides results which are almost indistinguishable from those obtained with the more sophisticated full orbit codes HECTOR and SOCRATE (5,6) , demonstrating that the departures of the fast ions from their birth flux surfaces are insignificant for the JET plasmas of interest. The model does not include triton diffusion or sawtooth effects, although these are not thought to be large effects for most of the plasmas studied here.

Results

Fig 1 shows a typical neutral beam heated discharge. The delay in the 14 MeV neutron emission relative to the 2.5 MeV neutron emission agrees well with the model. In order to optimise the fit over a wide range of shots, the energy loss rate has been enhanced by 15% in the model, which is smaller than the estimated error of ±20-25%. This factor is reduced if the ECE temperature data is normalised to the LIDAR electron temperature data, as previously reported (2), however the ECE data are preferred for the time-dependent calculation as they are available with good time resolution. From this we deduce that the triton slowing down process in JET is classical, within experimental errors.

Fig 2 shows the comparison of the time-integrated silicon diode data with the model (including the 15% enhanced energy loss) over a wide range of plasma discharges with $I_p > 3$ MA and $Z_{EFF} < 3$. The agreement is good apart from a systematic overestimate by the model of 40%. This is thought to be due in part to errors in the derivation of the deuterium density from Z_{EFF} measurements; the same conclusion is obtained from fusion reaction product measurements in general (7). If the absolute 14 MeV neutron emission rates and the model are assumed to be correct then triton burnup may be used to determine the

deuterium density with an accuracy of approximately 20% by dividing the experimentally observed 14 MeV neutron emission rate by the calculated 14 MeV neutron emission rate for a pure deuterium plasma. The technique is of use mainly when $Z_{EFF} > 4$ as the errors on the Z_{EFF} measurement cause errors of $> 50\%$ in the n_D/n_e ratio deduced from it. The results of this technique are reported elsewhere at this conference (7).

The confinement of fast tritons during major MHD events has also been investigated. At a normal sawtooth crash, no evidence of triton losses has been found, implying these losses to be $< 10\%$. The large crash associated with many pellet shots usually causes no significant losses of tritons. For monster sawteeth just one case has been found where the 14 MeV neutron emission fell abruptly at the crash (fig. 3). For this 3MA combined heating discharge the 2.5 MeV neutron profile monitor (8) shows unusually large inverted sawteeth in the outer regions of the plasma after the crash, indicative of the transport of high energy deuterium ions from the centre of the plasma. A similar movement of tritons could give rise to the observed drop in the 14 MeV neutron emission rate, either due to the loss of tritons from the plasma or by relocation of tritons to regions of lower deuterium dilution.

Conclusions

The combination of the absolutely calibrated activation system and the time-resolved silicon diode provides an accurate measurement of the time-resolved 14 MeV neutron emission rates at JET. The slowing down and burnup of the tritons agrees with a simple classical code, within errors. The confinement of tritons appears very good at JET for plasmas with $I_p > 3$ MA.

Acknowledgement

S Conroy would like to thank the SERC for their financial assistance.

References

1. O N Jarvis et al, 'Further calibrations of the time-resolved neutron yield monitor', JET IR(85)06
2. P Batistoni et al, Proc. 15th European Conference on Controlled Fusion and Plasma Physics, Dubrovnik 1988, vol 12B part I (1988) 135 et loc cit
3. M Pillon et al, 'Calibration of neutron yield activation measurements at JET using MCNP and FURNACE neutron transport codes ', JET P(88)10
4. S Conroy et al, 'Time-resolved measurements of triton burnup in JET plasmas', JET P(88)16
5. M Kovanen et al, 'HECTOR: a code for the study of high energy charged particles in axisymmetric tokamak plasmas', JET R(88)01
6. G Gorini et al, 'Calculation of the classical triton burnup in JET deuterium plasmas', JET P(87)35
7. O N Jarvis et al, these proceedings
8. J M Adams et al, these proceedings

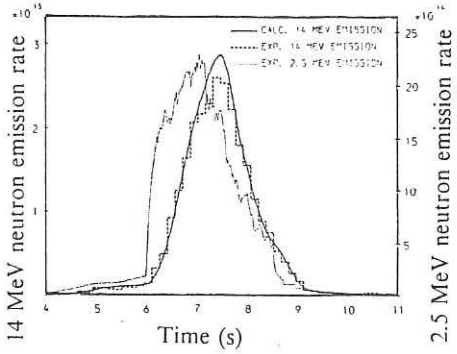

Figure 1. Comparison of calculated 14 MeV neutron emission rates with the experimentally observed rates. The calculation has been normalised to the experimental neutron yield to show the temporal agreement.

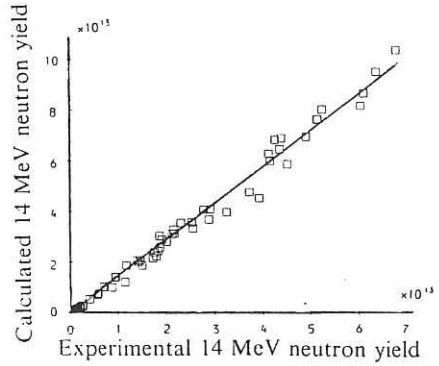

Figure 2. Comparison of experimental and calculated 14 MeV neutron yields for a variety of shots. The straight line is the best fit passing through the origin and has a gradient of 1.4. This discrepancy is thought to be due to an overestimation of the n_D/n_e ratio derived from Z_{EFF} measurements.

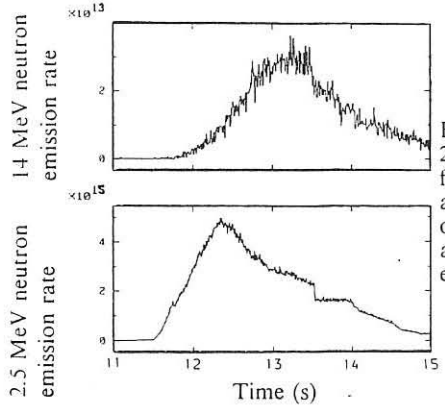

Figure 3. Comparison of experimental 2.5 and 14 MeV neutron emission rates for a disharge with a monster sawtooth at 3.5 seconds. This is the only observation of a sawtooth causing an abrupt drop in the 14 MeV neutron emission rate.

NON–THERMAL DT YIELD WITH (D)T ICRH HEATING IN JET

G.A.Cottrell, V.P.Bhatnagar, M.Bures, L.G.Eriksson+, T.Hellsten,
J.Jacquinot and D.F.H.Start.
JET Joint Undertaking, Abingdon, Oxon., OX14 3EA, United Kingdom.
+Chalmers University, Sweden.

Abstract. We present projections of the (D)T fusion yield expected during fundamental ICRH heating of D in JET plasmas. To obtain high Q, one needs to use a relatively high plasma density ($n_{e_0} > 5\times10^{19}$ m^{-3}) and dipole antenna ($k_{\parallel} \approx 7m^{-1}$) to reduce mode conversion. For high minority concentration ($n_D/n_e \approx$ 10%–30%), we have used ray–tracing and global wave ICRH codes to estimate cyclotron damping on deuterium (≈80%) and the rf power coupled directly to electrons (≈17%) via TTMP and Landau damping. With launched rf power P_{rf}=12MW deposited ≈0.3m off–axis, we predict fusion powers P_{fus} up to ≈ 8MW for a range of JET plasmas with achieved plasma pressure $n_{e_0}T_{e_0} = 6\times10^{20}$keV m^{-3} and Z_{eff}=2. Projecting to P_c=20MW, P_{fus} increases to 17MW with Z_{eff}=2.

Introduction. In a two–ion component plasma, the fast wave can be damped on a minority ion species at its fundamental cyclotron resonance causing the minority ion distribution function to develop a non–Maxwellian velocity distribution with a high energy tail. The tail will also enhance the fusion reaction rate with the background ion species [1]. Earlier JET experiments [2,3] in the (^3He)D minority scheme have produced <1MJ of fast ^3He ions in the plasma (with particle energies up to a few MeV) and a ^3He–D reaction rate R<2×10^{16} s^{-1} (≈ 60kW of fusion power). Measured fast ion energy content and fusion reactivity in these experiments have been modelled in detail [3,4] using Fokker–Planck and global wave codes. Good agreement between experiment and theory was found, consistent with i) classical slowing down of fast ions and ii) correct prediction of the cyclotron damping on the ^3He. The possibility of using the deuterium cyclotron resonance (D)T scheme has been considered [5] for the JET active phase. This paper discusses its optimisation.

Modelling. We have used experimental data to predict the (D)T performance. Measured temperature and density profiles for three types of ICRH heated discharge [6] were studied and used as the basis for predictions. These were: ***a)*** 3MA peaked profile (pellet) cases [7,8], ***b)*** 5MA current–rise heating cases [9] and ***c)*** 3MA 'monster' sawtooth cases. For the pellet cases the plasma profiles, taken from laser scattering (LIDAR) data, were peaked and were parameterised by: $y(x) = y_a + (y_0 - y_a).(1-x^2)^\gamma$ where $x = r/a$. For electron temperature profiles y_a/y_0 =0.1 and γ=2 and for electron density profiles y_a/y_0 =0.2 and γ=4. To obtain high projected Q values, it was found necessary to use higher ($n_D/n_e \approx$ 10%–30%) minority concentrations than have been

used in previous JET experiments. In the absence of experimental data in these conditions, we have estimated wave damping in simulated (D)T plasmas using both global wave and ray–tracing codes. The result of a ray–tracing calculation [10] of the full $k_{\|}$ spectrum of the toroidal dipole antenna is shown in Fig.1. Of the launched rf power, 80% was damped in a single pass on the D minority, 17% was deposited on the electrons via TTMP and Landau damping and 3% was unabsorbed.

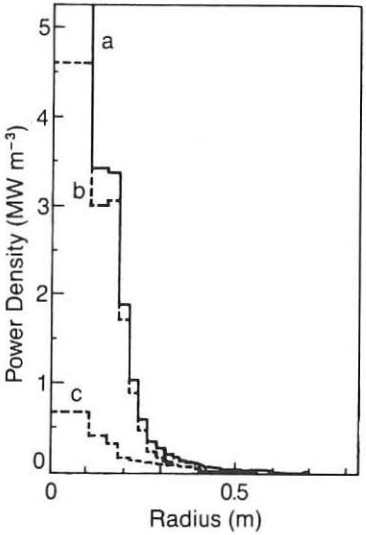

Figure 1 Calculated ICRH deposition profiles of: a) total, b) deuterium and c) electron power densities for the case of central heating (f=25MHz, $B_{\varphi}(0)$=3.55T) in simulated (D)T plasma based on experimental conditions of peaked–profile (pellet) discharge (case a, see text) but with assumed values n_D/n_e = 30% and P_c=20MW.

To estimate the fusion yield we used a gaussian radial power deposition profile and the Stix solution ($k_{\perp}$=0) for the tail [3]. Inclusion of finite ion Larmor radius effects and, in particular, the E_- component of the rf electric field in the Fokker–Planck calculations results in a more energetic tail which tends to reduce the fusion yield compared with the Stix model. For high D minority concentration (n_D/n_e <30%), $|E_-|/|E_+| \approx 12$, and the reduction is typically 20%. The Stix model was applied (Fig.2) to data for case *a*) assuming, for simplicity, $T_i = T_e$ and Z_{eff}=1. To project the model to higher rf power heating cases it was necessary to predict the plasma temperatures expected for the new conditions. In doing this (Fig.4), we have extrapolated measured empirical temperature scaling laws based on existing JET results. Each of the datasets for cases *a*)–*c*) could be well described by the offset–linear relation: $T_{j0}(\mathrm{keV}) = \alpha_j + \beta_j [P_t(\mathrm{MW})/n_{e0}(10^{19}\mathrm{m}^{-3})]$ where j = electrons or ions and P_t the input power. In making these extrapolations, we have assumed no degradation in heating efficiency (*i.e* the coefficients β_j are independent of power). The coefficients are, for case *a*) α_e=0.8, β_e=4.1, α_i=1.1, β_i=3.6; case *b*) α_e=0.8, β_e=4.1, α_i=1.1, β_i=2.6; and case *c*) α_e=0.7, β_e=2.7, α_i=2.3, β_i=1.2. The higher power cases (Fig.4) show optimal Q values at central densities typically $n_{e0} \approx 1 \times 10^{20}\mathrm{m}^{-3}$.

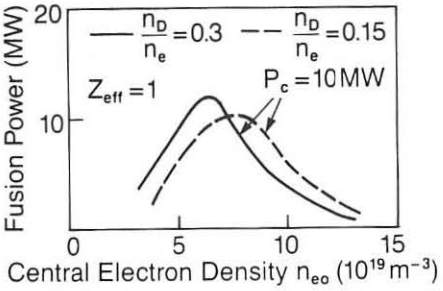

Figure 2 Stix code results for the ICRH driven DT fusion power with fixed $n_{e_0}T_{e_0}$= 6×10^{20} *keV* m^{-3} *and coupled rf power* P_c = *10MW. Off–axis* (r_{oa}= *0.3m) rf heating was modelled with gaussian deposition width* r_d =*0.2m.*

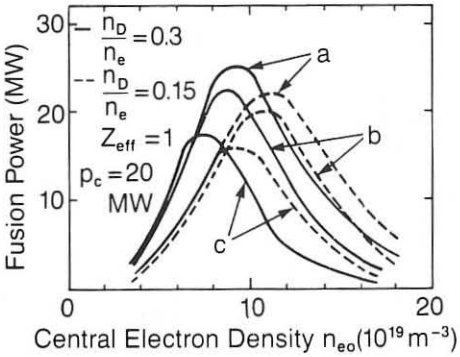

Figure 3 Stix code results for three projected cases: a) peaked profiles (pellet injection), b) current–rise heating and c)'monster' sawtooth cases. Off–axis (r_{oa}=*0.3m) rf heating was modelled with gaussian deposition width* r_d =*0.2m.*

Sensitivity analysis and impurity dilution effects. To illustrate the sensitivity of the ICRH–driven fusion yield with resonance location, we examine a test case A with parameters: n_D/n_e = 0.3, P_c=10MW, n_{e_0}=$6\times10^{19}$$m^{-3}$, T_{e_0}=T_{i_0}=10keV, rf deposition gaussian width r_d =0.2m and off–axis heating distance r_{oa} =0.3m (corresponding to the distance between the cyclotron resonance and the magnetic axis). Variations with respect to r_{oa} and Z_{eff} are shown in Fig.4. A maximum in the fusion yield occurs at $r_{oa}\approx$ 0.3m where the maximum deuterium tail temperature [3] $T_{tail}\approx$ 140keV. If the ICRH power is deposited too centrally, the minority ions are driven to energies beyond the maximum in the DT cross–section. Conversely, if the ICRH power is deposited too far off–axis, the tail energy is too low and the tail is generated in a low temperature region of the plasma where the collision time is smaller. We have neglected any variations in the heating efficiency with r_{oa}. In the scan with respect to variations in Z_{eff}, carbon impurities were assumed. In the peaked profile case *a*), the volume average Z_{eff} falls to $\approx$1 immediately following pellet injection but then rises to approximately 3 1s later; impurities are known to accumulate on the axis after pellet injection. For the current–rise heating case *b*), $Z_{eff}\approx$2, and, in the 'monster' sawtooth case *c*), Z_{eff} values range between 4.0–2.5. Fig.4 shows that the fusion power has degradation factors, *f*,

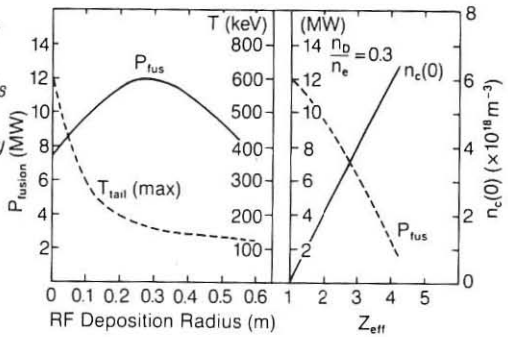

Figure 4 Sensitivity analysis (case A) of the variation of a) DT fusion power and minority tail temperature with rf power off–axis displacement and, b) DT fusion power and carbon impurity density with Z_{eff}

equal to a) 50%, b) 75% and c) 20%–66% respectively of the values calculated for Z_{eff}=1. The lower limit corresponds to the upper limit of Z_{eff}. In case b), analysis of the central neutron emissivity (from the neutron profile monitor) and T_{i_0} (from neutron spectroscopy and doppler broadening of Ni impurity lines) gave a central concentration ratio n_D/n_e=90% ± 10%. If the dilution is identical when P_C=20MW, the optimum fusion powers (for n_D/n_e=30%) are: a) P_{fus} ≈13MW (Q_{rf} ≈50%), b) P_{fus} ≈17MW (Q_{rf} ≈67%) and c) P_{fus} ≈(4–12)MW (Q_{rf} ≈14%–46%). Extrapolation of the experimental scaling: $Z_{eff} \propto 1/n_e$ to the optimum density ($n_{e_0} \approx 1\times10^{20}$ m^{-3}) of Fig.3 then gives degradation factors, *f*, of a) 81%, b) 96% and c) 67%–92% respectively. We note that both the peaked–profile (pellet) and the current–rise heating cases were not in steady–state conditions. Detailed analyses of these discharge types can be found in references [8] and [9] respectively.

Conclusion. A study of ICRF–driven DT fusion reactivity of projected JET plasmas shows the possibility of reaching Q_{rf} ($\equiv P_{fus}/P_{rf}$) ≈ 70% provided impurity dilution can be kept to a reasonable level. Particularly encouraging is the DT projection based on the 5MA current–rise heating case (at density $n_{e_0} = 6\times 10^{19}$m^{-3}) where values $n_{e_0}T_{e_0} = 6\times10^{20}$ keV m^{-3} and Z_{eff} ≈2.0 have been obtained simultaneously.

References

[1] Stix, T.H. Nuc.Fusion, **15**, 737. (1975)
[2] Cottrell, G.A., et al., Bull.Amer.Phys.Soc. **33**, 2032 (1988)
[3] Boyd, D.A., et al. Nuc.Fusion(1989) to be published.
[4] Eriksson, L.G., et al. Nuc.Fusion Lett. (1989) to be published.
[5] JET Team, Plas.Phys. and Contr.Fus. **30**, 1467 (1988)
[6] Jacquinot, J., et al. Bull.Amer.Phys.Soc. **33**, 2031 (1988)
[7] Bhatnagar, V.P. et al. this conference
[8] Hammett, G. et al. this conference
[9] Bures, M. et al. this conference
[10] Bhatnagar, V.P., et al. Nuc Fusion **24**, 955 (1984)

CORRELATION REFLECTOMETRY

P Cripwell*, A E Costley and A E Hubbard#

JET Joint Undertaking,Abingdon,Oxon,OX14 3EA,U.K.
* Imperial College of Science,Technology and Medicine, University of London,U.K.
# Centre Canadien de Fusion Magnetique, Varennes, Quebec,Canada

Introduction

The diagnosis of density microturbulence is important in the experimental investigation of energy transport in tokamak plasmas. Scattering of coherent electromagnetic radiation (microwaves and laser light) is used to determine the power spectrum of the fluctuations at discrete values of the wavenumber k./1/ However, scattering techniques do not usually distinguish between radially and poloidally propagating waves and they do not determine the coherence length of the waves.

In this paper, we present a new technique based on microwave reflectometry for diagnosing density microturbulence./2/ We believe that the technique will provide, within certain limits, the dispersion relation and coherence length of the waves charachterising the turbulence. Since the technique involves the correlation of signals from two or more reflectometers, we have termed it *correlation reflectometry*. We have constructed a preliminary correlation reflectometer and we present the first results of measurements on JET.

Principle

Two independent reflectometers operating with radiation of slightly different frequencies, f_1 and f_2 ,are arranged to probe the plasma along the same line of sight. The reflectometers probe density layers at R_1 and R_2 separated by a small amount Δx.

Turbulent fluctuations in the electron density give rise to rapid changes in the optical path length of the plasma arms of both reflectometers and therefore to changes in the phase of the reflected radiation. These phase changes are caused by (a) variations in the refractive index in the propagation region and (b) movement of the reflecting layer. Calculations, relevant to tokamak plasmas, have shown that (b) dominates (a) by a large factor (typically several orders of magnitude. /3/

The flucuations can be represented as a broadband spectrum of electrostatic waves. Each wave has a frequency ω, wavenumber k, and a finite coherence length l_c which can be defined as the length of the coherent wavetrain to the e^{-1} amplitude points. The magnitude of the fluctuating phase measured by the reflectometer operating at f_1 will therefore be:

$$\Delta\phi_1(t) = \mu \frac{4\pi f_1}{c} \sum_m \Delta L_{m1} \sin(\omega t + \delta_{m1})$$

where ΔL_{m1} is the amplitude of movement of the layer at R_1 caused by the wave m and δ_{m1} is the phase of the wave. $\mu^* = (1/2\Delta L)\int_{2\Delta L}\mu(R)\,dR$ is the average refractive index over ΔL and is a constant for different values of ΔL. A similar expression exists for $\Delta\phi_2$ by replacing the subscript 1 with 2.

The relative power at each frequency ω is given by the autopower spectrum denoted $G_1(\omega)$ while the power that is common to both signals is given by the crosspower spectrum $G_{1,2}(\omega)$. The full expressions for $G_1(\omega)$ and $G_{1,2}(\omega)$ are given in standard texts on spectral analysis /4/. $G_{1,2}(\omega)$ may be expressed as a complex number:

$$G_{1,2} = C_{1,2} + i.Q_{1,2}$$

where $C_{1,2}$ is the in-phase power that is common to both signals while $Q_{1,2}$ is the $\pi/2$ out of phase common power. At any given frequency the phase difference between signals common to both sets of data is given by:

$$\Theta_{1,2}(\omega) = \tan^{-1}(Q_{1,2}(\omega) / C_{1,2}(\omega))$$

The phase difference between the signals common to both sets of data is due to the propagation of the wave between R_1 and R_2 and so :

$$\Theta_{1,2}(\omega) = k(\omega).\Delta x$$

Hence, from a measurement of $\Theta_{1,2}(\omega)$ and a knowledge of Δx, we can determine k at a range of frequencies, i.e. we can determine the *dispersion relation* for the waves describing the density fluctuations. Strictly, we measure the dispersion relation of the component of k along the line of sight of the reflectometer.

In the above we have implicitly assumed that $\Delta x << l_c$, however, this may not always be the case. In fact, if f_2 is changed so as to increase Δx, then the power common to both signals will decrease as Δx becomes greater than $l_c(\omega)$. This effect may be quantified using the coherence function $\gamma^2_{1,2}$ which is a measure of the power common to both signals normalised to the total power in both signals:

$$\gamma^2_{1,2}(\omega) = \frac{|G_{1,2}(\omega)|^2}{|G_1(\omega)|\ |G_2(\omega)|}.$$

$|G_{1,2}|$ is the magnitude of the crosspower spectrum. The correlation length $l_c(\omega)$ is found by analysing the variation of $\gamma^2_{1,2}(\omega)$ with increasing Δx.

Limitations

Several effects can limit the information that can be obtained by this technique. First, the reflection does not in practice take place at a single plane but occurs over a layer of finite thickness, ΔR. This is a consequence of the fact that the refractive index goes to zero over a finite distance. It means that the technique can only be used to examine waves with $l_c \gtrsim \Delta R$.

Second, because the sets of data are finite, there will be a lower limit to the coherence which is significant. Such a limit is a statistical factor and it may be calculated

accordingly. The other limits of reflectometry, for example limits of accessibility due to electron cyclotron absorption, will also apply /2/.

Preliminary Implementation

A correlation reflectometer has been constructed on JET to examine the feasibility of the technique. The reflectometer operates in the extraordinary mode and probes the plasma along a major radius in the midplane. In the experiment, the frequency of one beam was fixed at 49 GHz whilst the frequency of the second was varied in steps from 51 - 57 GHz. Signals at the two frequencies were separated using a purpose built diplexer which ensures an isolation of > 20 dB, between the channels. The fluctuating signals were detected with Schottky diode detectors and digitised with a video bandwidth of 20kHz.

A limited amount of data has been obtained on ohmic and additionally heated plasmas. Figures 1 through 4 show the crosspower spectrum, the coherence, the crossphase spectrum, and the derived dispersion curve obtained on an ohmic pulse with B_t = 2.1 T and I_p = 3 MA. For these data f_1 = 49 GHz, f_2 = 51.3 GHz, $\Delta R \cong 2$ cm, $\Delta x \cong 2$ cm and the reflectometers probe the region r/a = 0.8 where n_e = 1.5 10^{19} m^{-3} and T_e = 1.2 keV. Clear evidence for correlation is seen and we note from figure 4 that the wave phase velocity is $\cong 5.10^5$ $m.s^{-1}$. When f_2 was changed to 53 GHz the correlation was significantly less, indicating that over most of the frequency range examined the correlation length for the radially going waves is in the range $2 < l_c < 4$ cm.

Conclusions

A new diagnostic technique for probing density microturbulence using microwave reflectometry appears feasible. The technique should provide the dispersion relation of radially propagating waves and, within certain limits, give an estimation of the wave correlation length. Preliminary measurements on JET under one specific ohmic plasma condition gives a wave phase velocity of 5.10^5 $m.s^{-1}$ and a correlation length in the range $2 < l_c < 4$ cm.

Acknowlegements

The authors would like to thank Drs D Bartlett and T Hughes for useful discussions and one of the authors (P.C.) would like to thank the S.E.R.C for their financial assistance.

References

1. Liewer P. Nucl Fusion **25**, 5, 543
2. Costley. A.E. Proc Course and Workshop, Basic and Advanced Diagnostic Techniques for Fusion Plasmas, EUR 10797, Vol 2 379 - 396, Varenna, 1986
3. Simonet F. These de Doctorat D'Etat, Universite de Nancy 1 : Etude de la Reflectometrie Hyperfrequence, 1985
4. Bendat and Piersol - Random Data: Analysis and Measurement Techniques, Wiley

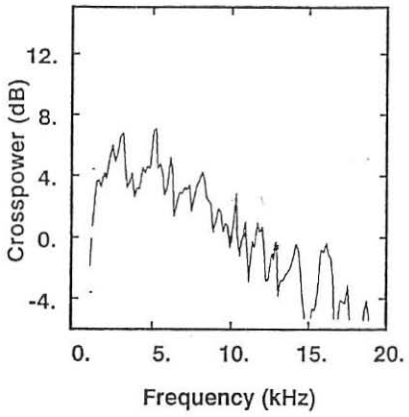

Fig 1: The crosspower spectrum of two signals when the reflectometers were tuned with their reflection layers approx 2cm apart

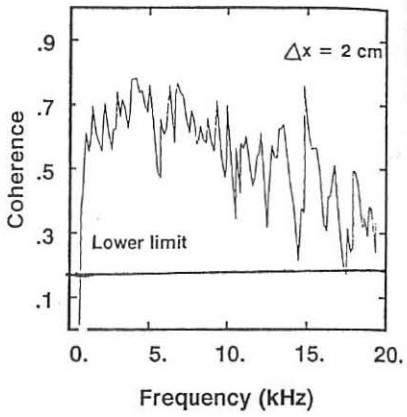

Fig 2: The derived coherence function corresponding to the the crosspower in fig 1.

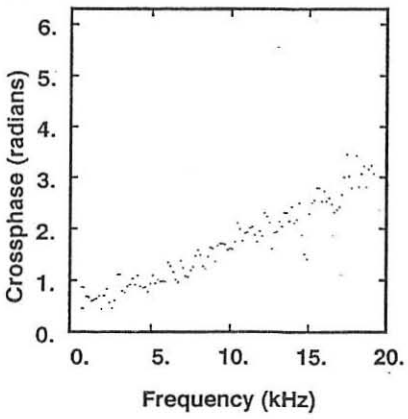

Fig 3: The crossphase spectrum

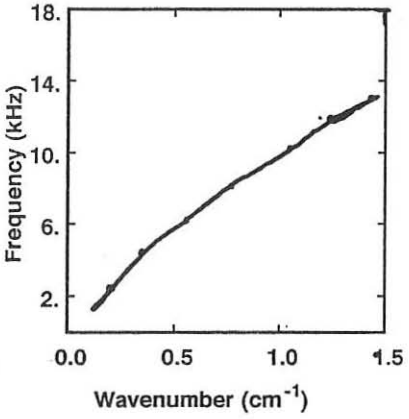

Fig4: The derived dispersion relation.

TRANSPORT STUDIES DURING SAWTEETH AND H-MODES ON JET USING LASER ABLATION.

N Hawkes[a], Z Wang, R Barnsley, K Behringer[b], S Cohen[c], B Denne, A Edwards, R Giannella, R Gill, G Magyar, D Pasini, N Peacock[a], U Schumacher[b], C Vieider[d] and D Zasche[b]

JET Joint Undertaking, Abingdon, Oxon, OX14 3EA, UK
[a] *UKAEA Culham Lab., Abingdon, Oxon, OX14 3DB,* UK
[b] *Max-Planck-Institut fur Plasmaphysik, D-8046, Garching,* FRG
[c] *Plasma Physics Laboratory, Princeton Univ., Princeton, NJ 08544,* USA
[d] *Uppsala Institute of Technology,* SWEDEN

A system for the controlled injection of trace impurities by laser ablation has recently been commissioned on JET. Small amounts of metallic impurities have been injected in order to study transport phenomena. In all cases the amounts, corresponding to an injected quantity of a few 10^{18} atoms (an impurity concentration of 0.01% of n_e), were sufficiently small to avoid perturbing any plasma parameter apart from the radiation (ΔP_{rad} < 0.5 MW). We report here on measurements of impurity confinement time (τ_{imp}) and observations of impurity transport effects using this technique.

A suite of spectrometers viewing fixed lines of sight was used to gather information on the time behaviour of a range of ionisation stages. In addition measurements of the soft X-ray emission were obtained with good spatial and temporal resolution from two X-ray cameras.

Sawteeth observations - The soft X-ray cameras show inverted sawteeth during the rise phase of radiation from injected impurities. Figure 1 shows the time development of the central chord soft X-ray signal and central electron temperature (T_e) illustrating the inversion of the first sawtooth after impurity injection.

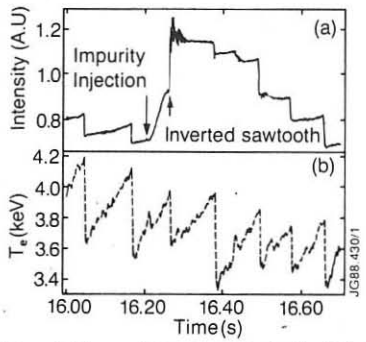

Figure 1. Time evolution of central chord soft X-ray signal (a) and electron temperature (b) during a discharge with Mo injection.

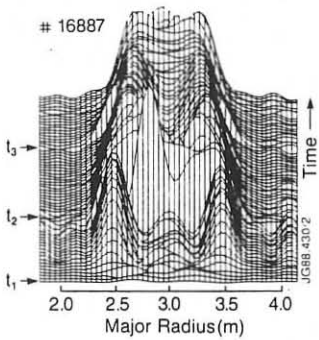

Figure 2. Time evolution of the injected impurity X-ray emission distribution along the horizontal central chord: t_1, impurity injection, t_2, t_3 sawtooth crashes (Shot 16887).

Clearly the increase in radiation due to the influx of impurities into the central region of the plasma at the time of the sawtooth crash overcompensates the drop in T_e. In most cases the inverted sawtooth is accompanied by a large amplitude $m = 1$ oscillation. This oscillation usually disappears within less than half a sawtooth period. During this time the amplitude of the oscillation decays gradually. Their frequency also decreases, from 500 Hz immediately after the sawtooth crash to 400 Hz as the oscillation disappears. A clear understanding of these oscillations is still lacking.

Tomographic reconstruction of the plasma emissivity reveals that impurity transport within the central region (inside the $q = 1$ surface) is profoundly different from that in the rest of the plasma. Figure 2 shows a sequence of radial emission profiles from the same discharge for times after the ablation. Background radiation, present before ablation, has been subtracted out. Immediately after ablation the radiation profile builds up at mid radius, with no growth in radiation from the centre. This central region, inside $q = 1$, only fills in when a sawtooth crash occurs, time t_2 in the figure. The filling is incomplete even after the first crash, it taking typically two to three sawtooth cycles for the intially hollow profile to become peaked on axis. The radiation profiles indicate that rather than a transport barrier at $q = 1$, impurity transport inside the $q = 1$ region is reduced, there being only a slow evolution of the radiation profile in this zone between sawtooth crashes. During the decay phase the reverse situation applies in that impurities linger in the central region, again only crossing $q = 1$ at the time of the sawtooth crash.

Scaling studies - Scaling studies were performed in ohmic L-mode shots of the decay time of XUV radiation intensity from high ionization stages (ionisation energies typically > 1 KeV) of the injected metals. Such radiation is emitted from the outer 1/3rd of the plasma radius. At this radius the decay time of the intensity is representative of the global impurity containment time (τ_{imp}). The decay curves of the intensity were corrected for variations in T_e and n_e with the application of an empirical correction formula derived from modelling calculations performed with an impurity transport code. The corrected decay curves were then fitted by an exponential to give the decay time and the resulting times stored in a database. The X-ray observations indicate that diffusion of impurities inside $q = 1$ is much lower than in the outer regions but since transport is effectivly enhanced during the sawtooth crash and the decay times span many sawtooth cycles the times we measure are governed by the transport in the region outside $q = 1$.

No dependence of τ_{imp} with charge of the ablated ions was detected, thus simplifying the further analysis of the data. An apparent scaling of τ_{imp} with density was observed in the data (figure 3) with the form $.09(n_e/10^{19})^{.4}\sqrt{q_L}$. However with the parameter range explored it is not yet possible to rule out other dependencies. τ_{imp} and the energy confinement time, τ_E, were found to be uncorrelated. In particular no reduction in τ_{imp} with auxilliary heating was detected (up to $P_{tot} < 15$ MW) although the number of heated shots studied was limited. During H-mode, however, the impurity confinement time became much longer than under any other operating condition, exceeding τ_E.

Transport in H-mode - Our dataset includes two observations of impurity transport during H-mode which we have modelled using an impurity transport code. In a 4MA

shot, 18627, cobalt was injected into the discharge at 12s, 0.5s after the start of the H-mode. Figure 4 shows the time traces of the injected Co as well as the time traces of the intrinsic impurities nickel and oxygen.

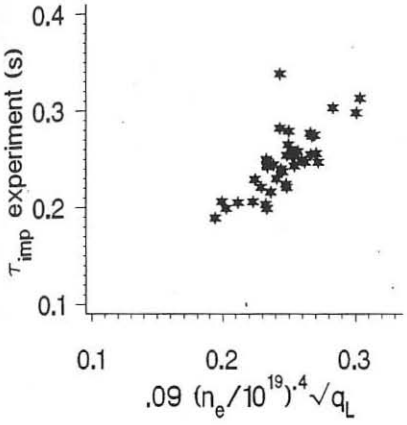

Figure 3. Scaling of t_{imp} with volume average electron density and safety factor.

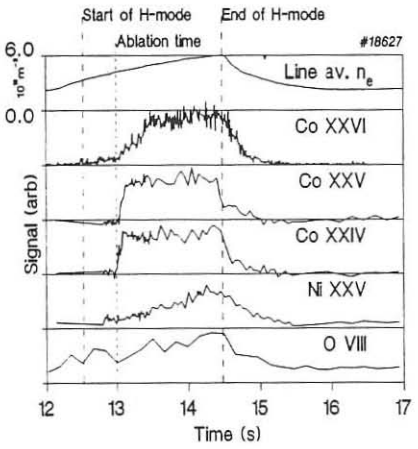

Figure 4. Time development of injected Co and intrinsic Ni and O during an H-mode (Shot 18627).

The emission from the lower ionisation stages of Co rises rapidly (within 0.1s) to a steady value which persists up to the end of the H-mode. The lower stages of C and O show little effect of the H-mode whereas OVIII and CVI (ionisation energies 870 and 490 eV) behave like the nickel lines /1/ (ionisation energies > 2000 eV) and ramp up during the H-mode. The bulk plasma therefore behaves as an almost ideal 'integrator' of impurities. Adjustment of the raw signal intensities to take account of the changing n_e and T_e modifies the near rectangular Co XXIV and Co XXV time traces, giving them a slow decay with time, leading to the plasma being described better as a slightly 'leaky' integrator with confinement time of 4s ($> > \tau_E$).

A transport model describing the behaviour of intrinsic impurities during H-mode had previously been proposed /2/. This model accounted for the time development of radiation from iron injected near the H-mode transition of a 3MA shot (17068) (giving an impurity decay time of 0.8s - nearly equal to τ_E). To account for the data in figure 4, however, it is necessary to include a stronger inwards convection (V) at the very edge of the plasma. The profiles of diffusion (D) and V adopted for the modelling are shown in figure 5 and the resulting time evolution of Co, Ni and O radiation in figure 6 which well describe the experimental observations. The lower ionisation stages of oxygen lie in the scrape off (or in the region of inwards convection) and hence do not see the impurity build up of the bulk plasma.

The neoclassical transport description of Hirshman and Sigmar /3/ as evaluated by Fussmann /4/ is implemented in the transport code allowing comparisons to be made with our coefficients. The crucial feature in our model is the ratio of V/D (~ 50 m^{-1}) at the plasma edge. Whilst the $\nabla n_i/n_i$ terms of the drift (arising out of the steep edge

density gradients) are of approximately the correct shape the $\nabla T_i/T_i$ screening terms are hard to estimate from the T_i profiles. The neoclassical ratio V/D is plausibly comparable with our model ratio. The D profile is not a sensitive parameter in the model and the profile selected is greater than the neoclassical diffusion by a factor varying between 3 in the centre and 50 at the edge. The choice of a lower D value leads to a slower penetration by impurities of the core plasma and thus gives a slower rate of rise of emission from (particularly) Co XXVI. The effect of sawteeth has not been included, however, in this model and will act to mitigate this slower rise.

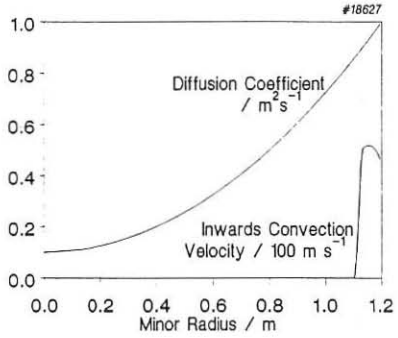

Figure 5. Transport parameters used in modelling.

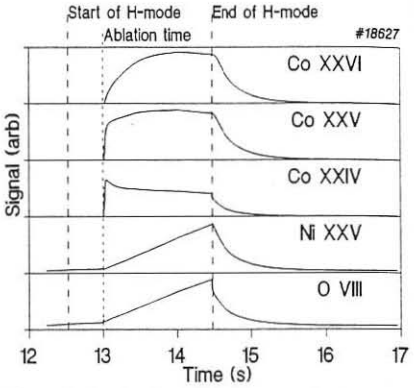

Figure 6. Results of modelling. A correction for density variation has been applied.

Conclusions - Laser ablation of test impurities into JET plasmas has demonstrated a significant reduction of transport within the $q = 1$ surface as well as the expected increase in transport during a sawtooth crash. Studies of the variation of τ_{imp} with plasma parameters have yielded a scaling model but it cannot yet be regarded as complete.

Studies of H-mode plasmas extend observations of intrinsic impurity behaviour and confirm the significance of the edge (within 0.2m of the separatrix) with respect to the retention of impurities. Whilst not adequately described by neoclassical transport there are enough similarities to encourage further investigation in this direction. The particular effects of the neutral beam driven momentum source and the non circularity of the minor cross-section are not included in the neoclassical description adopted here.

References

/1/ Giannella R. *et al.* this conference.
/2/ Behringer K *et al.* EPS Dubrovnik in Europhys. Conf. Abs. **12B** I p338.
/3/ Hirshman S.P. and Sigmar D.J. Nucl. Fus **21** (1981) 1079
/4/ Fussmann G. *et al.* J. Nucl. Mater. in print (1988) (8th PSI, Jülich 1988)

CONSEQUENCES OF TRAPPED BEAM IONS ON THE ANALYSIS OF NEUTRON EMISSION DATA

M J Loughlin, J M Adams*, N Hawkes*, M Hone, O N Jarvis, B Laundy, G Sadler, D B Syme*, N Watkins* and P van Belle

JET Joint Undertaking, Abingdon, Oxon, OX14 3EA, UK
* Harwell Laboratory, Didcot, Oxon, OX11 ORA, UK

ABSTRACT

Neutron energy spectra have been measured during D° neutral beam heating of deuterium plasmas. The thermonuclear to beam-plasma neutron production ratios are deduced. For a non-radial spectrometer line-of-sight, the trapped beam-ion fraction must be considered.

INTRODUCTION

The neutron spectrum from a pure thermonuclear plasma is a gaussian whose width is determined by Doppler broadening which arises from the thermal motion of the ions. For a deuterium plasma, the full width at half maximum (fwhm) of the neutron energy distribution can be related to the ion temperature T_i according to the equation fwhm = $c\sqrt{T_i}$, (T_i and fwhm in keV) [1]. The parameter c is weakly dependent on T_i and is approximately equal to 82.5. This equation is only valid during pure ohmic or low power RF heating when the ion energy distribution is Maxwellian. This is clearly not the case during neutral beam injection (NBI). Under these circumstances the neutron spectrum is very broad ($\sim$ 400 keV) and distinctly non-gaussian. The detailed shape of the neutron spectrum depends primarily on the neutral-beam energy and the injection angle, the angle of the neutron emission and, as will be seen later, the proportion of beam ions in trapped orbits. At JET, neutron spectra are measured along two lines-of-sight using two high resolution neutron spectrometers. The first spectrometer, a ^{3}He ionisation chamber, is positioned in the roof laboratory, directly above the torus, with a line-of-sight perpendicular to the magnetic field [2]. The second, a nominally identical detector, is positioned in the torus hall, inside a massive hydrogenous shield, with a well collimated line-of-sight in the vessel mid-plane and at approximately 60 degrees to the magnetic field. These spectrometers have been used to measure the neutron spectra produced during NBI.

NEUTRON SPECTRA DURING NBI

Calculations of neutron spectra have been made for the lines-of-sight used at JET using the code FSPEC [1]. These show that there are four distinct spectra which need to be considered (figure 1); (i) the thermonuclear spectrum which is a gaussian centred at 2.45 MeV with width of the order of 100-200 keV, (ii) the beam-plasma spectrum emitted in a direction perpendicular to the magnetic field, also centred at about 2.45

MeV but considerably broader and showing a 'double humped' shape, (iii) the beam-plasma spectrum produced by beam ions in passing orbits which move towards the spectrometer, this is similar to that emitted perpendicularly but shifted up in energy, and (iv) the spectrum which arises from the trapped beam ions which oscillate towards and away from the detector. This spectrum is noticeably broader and is peaked at 2.45 MeV.

The spectrometer in the roof laboratory is insensitive to the motion of the beam ions in the toroidal direction, and is therefore insensitive to the trapped particles. The observed neutron spectrum is the sum of the thermonuclear spectrum and the beam-plasma spectrum. The spectrometer in the torus hall, however, is sensitive to the direction of the toroidal motion of the beam ions and therefore to the presence of neutrons produced from trapped ions.

MEASUREMENTS

Both spectrometers have been operated at JET since November 1986. A series of spectra are accumulated for each JET discharge during 'time slices' of 1.0 second and adjustable pre-collimators are used to ensure that the count-rates in the detectors are optimized for good statistics whilst avoiding pile up distortion.

The response of a ^{3}He chamber is complex because there are a number of reactions in the detector which can lead to pulse production. It is only the full energy peak, produced by the ^{3}He(n,p)T reaction, which is useful in determining the incident neutron spectrum. In order to maximise the number of 'useful' counts, a great deal of attention has been paid to the shielding for the spectrometers. The position in the roof laboratory is ideal; the detector was simply placed over a penetration in the 2 m thick floor, which provides an excellent neutron shield. To operate a spectrometer in the torus hall required the construction of a massive enclosure with 60 to 100 cm of lithiated paraffin wax walls to shield the detector from the thermal neutrons to which it is very sensitive. The spectrometer itself is further shielded by lead to reduce the number of counts due to gamma-rays. The total weight of the shield is approximately 17 tonnes.

ANALYSIS AND RESULTS

A survey of NBI heated discharges during the 1988 campaign has been made. Those shots in which the detector count-rate was in excess of 5 kHz or with too few counts (< 500 counts) were eliminated.

We consider first the simpler case of the spectrum emitted normally to the magnetic field, ie. towards the roof laboratory. The measured pulse height spectrum is a convolution of the incident neutron spectrum and the detector response function (the noise introduced by the processing electronics is negligible, as indicated by the width of a pulser). The incident neutron spectrum consists of the sum of the thermonuclear spectrum and the beam-plasma spectrum. The ion temperature is obtained from either the large crystal X-ray spectrometer [3]or from the active charge-exchange diagnostic [4]. The ratio of the neutron emission from these two processes

was determined by summing the two spectra, folding with the detector response function and comparing the result with the data. By adjusting the area of each spectrum, the fit of the resultant spectrum to the measured data was optimised using the method of least squares; then the thermonuclear (plasma-plasma) fraction was determined.

The thermonuclear fraction was determined in the same way using the data obtained with the torus hall spectrometer. However, in this case the beam-plasma spectrum due to trapped ions must also be considered. If the spectrum due to trapped ions is not taken into account, good fits are not possible and large systematic errors in the value obtained for the plasma-plasma fraction are introduced (figs. 2 and 3). With the trapped ions taken into account, the values of the plasma-plasma fraction obtained with each spectrometer are consistent, to within the estimated errors (figure 3).

The presence of trapped beam particles has implications for other neutron diagnostics. Since the orbits of trapped particles are predominantly on the outboard side of the plasma, their presence indicates that the 'centre of gravity' of the neutron emission has a tendency to become displaced outwardly from the toroidal magnetic axis. This deduction is supported by the measurements obtained from the neutron emission profile monitor [5]. Figure 4 shows the neutron emission profiles for discharges 18618 and 18620, the latter having a higher electron density. The neutron spectrometer indicated that the trapped fraction for these was 12% and 71% respectively. Figure 4 shows the neutron emission profile as viewed from a vertical direction. The increased asymmetry of the emission in 18620 relative to 18618 is clear. This provides an indication that the neutron emissivity from deuterium beam-heated plasma is not constant around the magnetic flux surfaces. Therefore the interpretation of neutron emission data becomes considerably more complex.

REFERENCES

[1] P van Belle and G Sadler, in Basic and Advanced Diagnostic Techniques for Fusion Plasmas, (Proc Course and Workshop, Varenna 1986), Vol III, Rep EUR 10797 EN, CEC (1987) 767, Varenna 1986.
[2] O N Jarvis et al, Rev Sci Instr, 57 (1986) 1717.
[3] R Bartiromo et al, "The JET High Resolution Bent Crystal Spectrometer", JET-P(88)11
[4] M G Von Hellerman et al, "Charge Exchange Recombination Spectroscopy on JET", JET-P(86)45.
[5] J M Adams et al, this conference

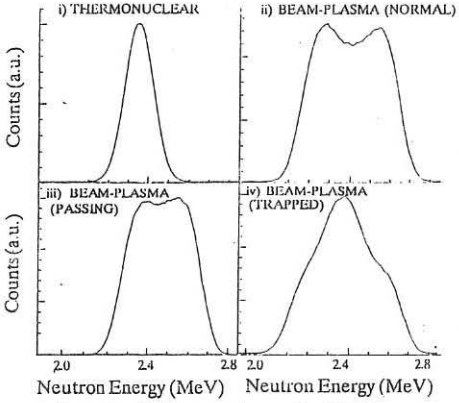

Figure 1: Neutron spectra produced during NBI

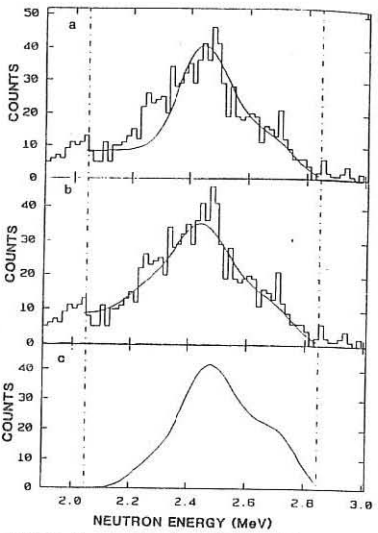

Figure 2: a) Experimental data (histogram) and fit (curve) assuming no trapped fraction.
b) Experimental data and fit, trapped fraction included.
c) Incident neutron spectrum which gave fit (b).

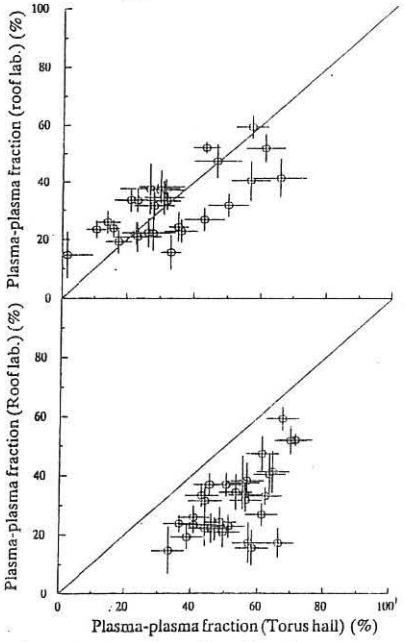

Figure 3: Comparison of results of determination of plasma-plasma fraction from the two spectrometers with (upper) and without (lower) trapped fraction.

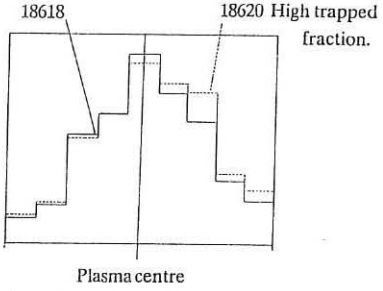

Figure 4: Radial neutron emission profiles for two discharges 18618 - trapped fraction 12%. 18620 - trapped fraction 71%. The latter discharge shows greater neutron emission on the outboard side of the plasma.

THE HOT ION MODE OF SMALL BORE PLASMAS IN JET

C.G.Lowry , D.A.Boyd[1], C.D.Challis, J.P.Christiansen, J.G.Cordey, G.A.Cottrell, A.W.Edwards, T.T.C.Jones, P.P.Lallia, P.Nielsen, G.Sadler, G.Schmidt[2], D.F.H.Start, D.Stork, P.R.Thomas, B.Tubbing

JET Joint Undertaking, Abingdon, Oxon. OX11 3EA, England
1 University of Maryland, College Park, MD20742, USA.
2 Princeton Plasma Physics Laboratory, New Jersey, USA.

ABSTRACT

Ion temperatures in excess of 20 keV and high D-D neutron rates have been achieved in JET. by the injection of 80 keV neutral beams into low density, low volume plasmas. Two small bore configurations were tried, one limited on the inner wall and the other on the belt limiters (low field side). Both configurations had plasma current of 3 MA and toroidal field of 3.4T at the vessel axis. The small plasma minor radius aids the beam penetration while the low density increases the power per particle and beam slowing down time. The inner wall configuration has several advantages; it can have a smaller volume because of the lower major radius and higher toroidal field, the neutral beams are closer to tangential, and the inner wall is known to pump deuterium effectively. The limiter configuration, however, allows the use of combined RF and NBI heating systems and could benefit from geometrical scaling of confinement.

OPERATING PROCEDURE

Extensive helium conditioning of the limiting surfaces was required to obtain the low density target plasma. During these conditioning discharges the ability of the wall to pump was monitored by the decay rate of neutron production after a small deuterium puff. In subsequent deuterium discharges the increase in the target density was slow, but the pumping ability of the wall deteriorated after only a few pulses, and disruptions caused instant de-conditioning. For the inner wall pulses the plasma was initially full bore and limited on the belt limiter it was then pushed to the inner wall over a period of 1.5 to 2 seconds. The reverse procedure was used to produce the small bore limiter plasmas.

NEUTRAL BEAM HEATING AND FUELING

The objectives of operating such small bore plasmas was to increase the peak neutron production rate by entering the hot-ion mode and to achieve axially peaked beam deposition. The achievement of 23 keV ion temperature is consistent with the high ratio of NBI power to the total number of plasma electrons. With an electron temperature of only 9 keV these plasmas can clearly be regarded as being in the hot-ion mode. Both inner wall and limiter pulses had axially peaked beam deposition, figure 1, in the inner wall case this lead to strong peaking of the density within the half radius, figure 2. However, in the limiter case wall pumping was insufficient to maintain the low edge density. Between 400 ms and 800 ms into the beam pulse the carbon influx from the limiting surface was observed to increase dramatically for a period of a few hundred milliseconds, which had the effect of creating a density pedestal. Even at the higher density the beam source was strongly peaked, and when switched off the rapid edge pumping of the inner wall pulses produced almost triangular density profiles.

Figure 1

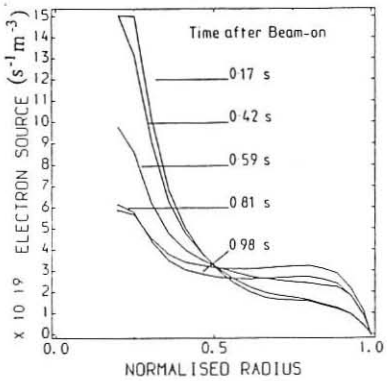

Figure 2

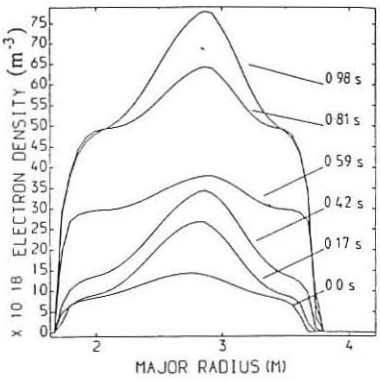

Figure 3

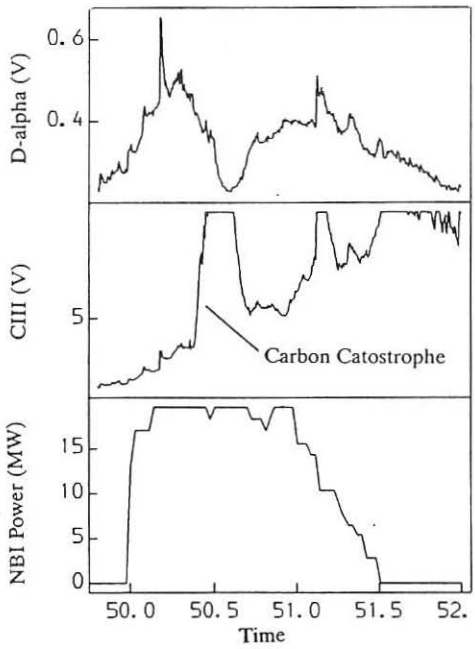

Figure 1 shows the electron source due to the neutral beam injection as a function of the normalised minor radius at 200 ms intervals.

Figure 2 shows the electron density profile as a function of the major radius, for the same times as figure 1.

Figure 3 shows the CIII and H-alpha emission during the heating phase of an inner wall plasma. The 'carbon catostrophe' is seen to last for only 200 ms and is accompanied by a reduction in the H-alpha emission.

The carbon event or 'catastrophe' has not only been observed in such small bore configurations but has become a characteristic of high power heating in JET. After the start of the beam pulse the CIII emission from the limiting surface begins to increase in proportion to the D-alpha emission, followed by a burst of CIII emission which saturates the detector for some 200 ms and returns to a level which can be extrapolated from before the burst, see figure 3. Up to three such bursts have been seen in one pulse, the first seem to be accompanied by a decrease in D-alpha emission although subsequent bursts show no such correlation. The delay of the first burst after beam-on decreases with increasing beam power, this favours a surface temperature dependant mechanism. However, the return to a similar level of emission suggests some form of bifurcation.

CONFINEMENT

These small bore plasmas provide two opportunites to examine confinement scaling. First we have the largest variation in major radius possible for JET, and secondly the inner wall plasmas are close in geometry to the TFTR configuration. Figure 4 summarises the results of both comparisons. The limiter pulses show confinement similar to that for the inner wall indicating no major radius dependance of confinement. If compared to the Goldston confinement scaling an enhancement of 1.7 is observed for the inner wall plasmas, but the enhancement is less for the limiter discharges. Using TRANSP[1] to analyse one discharge of each of these configurations it can be seen that fast ions account for 25 % of the stored energy in the inner wall case, and 15 % on the limiter. The fast ions therefore account for half of the measured enhancement. Also shown in figure 4 are some of the first TFTR 'supershots'[2], with co-injection, for these pulses the stored energy has been multiplied by a factor of 3 to allow for the different plasma current. With such an adjustment the results from the two machines are in good agreement.

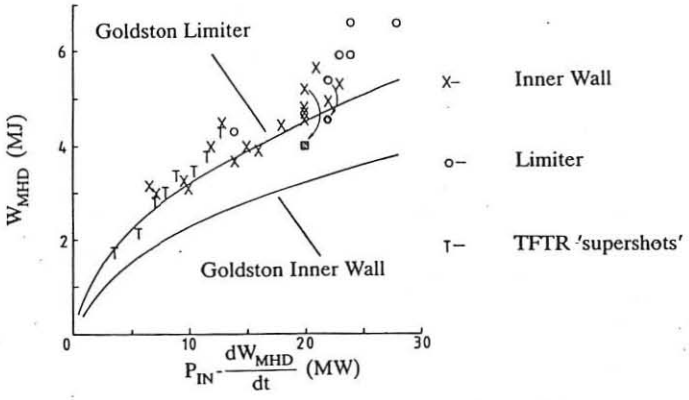

Figure 4 This shows the stored energy, W_{MHD}, versus the total input power taken when $\frac{dW_{MHD}}{dt} = 0$, for the inner wall and limiter configurations, and for some TFTR 'supershots'. The two shaded points show the stored thermal energy as calculated by TRANSP. For comparison the Goldston scaling is shown for the two JET configurations.

NEUTRON PRODUCTION

The maximum neutron rate is observed to depend only on the NBI power and the pumping ability of the wall. TRANSP runs show that for both small bore configurations 60% of the peak neutron production is from beam-beam reactions with only 4 % from thermal reactions. The beam-thermal reaction rate is similar to that for beam-beam but peaks a few hundred milliseconds later, by which time the beam-beam contribution is significantly less. Large bore double null x-point plasmas show the beam-thermal reactions to dominate the peak neutron rate. It is thus surprising that the peak total rate is a similar function of the NBI power in both configurations, Figure 5. Methods which were tried in order to deviate from the curve included the use of RF heating and pellet injection. RF heating in monopole has been used in double null x-point plasmas and showed an enhancement in neutron rate of typically 30 %. However, in the small bore limiter plasmas no such enhancement was observed. A 10 % improvement was achieved by injecting 2.7 mm pellets into the plasma just before the expected peak in the neutron rate. Although the onset of the carbon catastrophe was delayed in some cases, the 10 % improvement seemed to be due to a reduced ratio between carbon and deuterium release prior to the event. Pellets injected before beam-on reduced the maximum neutron rate due to an associated increase in the target density.

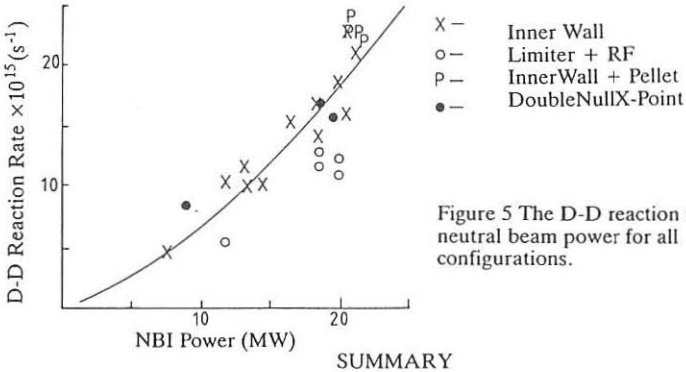

Figure 5 The D-D reaction rate versus neutral beam power for all configurations.

SUMMARY

Small bore plasmas on JET have shown strongly peaked density profiles and confinement 1.7 times the Goldston scaling. The enhanced confinement is partially accounted for by the fast ion content of the plasma and is in line with observations under similar conditions on TFTR. The neutron production in these plasmas lie on a similar curve as a function of NBI power as for other JET configurations, with a small improvement possible by injecting pellets during the beam pulse. Attempts to purify the target plasma using pellets failed due to the associated density increase, a situation which can be resolved only by reducing the carbon level in the plasma.

REFERENCES

1. R.J.Goldston et al, J. Comput. Phys. **43** 61 (1981).
2. R.J.Hawryluk et al, in Plasma Physics and Controlled Nuclear Fusion Research 1986 (Proc. 11th Int. Conf. Kyoto, 1986), Vol. 1, 51.

SUMMARY OF ENERGY AND PARTICLE CONFINEMENT IN PELLET-FUELLED, AUXILIARY-HEATED DISCHARGES ON JET*

S.L. Milora[1], D.V. Bartlett, L.R. Baylor[1], K. Behringer, D.J. Campbell, L. Charlton[1], A. Cheetham, J.G. Cordey, S. Corti, M. Gadeberg, R. Galvão, A. Gondhalekar, N.A. Gottardi, R. Granetz[3], G. Hammett[2], M. von Hellermann, K. Hirsch, J.T. Hogan[1], W.A. Houlberg[1], O.N. Jarvis, T.C. Jennigan[1], P. Kupschus, G.S. Lee[1], P. Morgan, C.K. Phillips[2], J. O'Rourke, G. Sadler, G.L. Schmidt[2], J. Snipes, D. Stubberfield, A. Taroni, B. Tubbing, H. Weisen

JET Joint Undertaking, Abingdon, Oxon. OX14 3EA, U.K.
[1]Oak Ridge National Laboratory, Oak Ridge, Tennessee, U.S.A.
[2]Princeton Plasma Physics Laboratory, Princeton, New Jersey, U.S.A.
[3]Massachusetts Institute of Technology, Cambridge, Massachusetts, U.S.A.

INTRODUCTION

A transient improvement in plasma performance and central confinement has been observed in auxiliary heated JET limiter plasmas associated with a peaking of the plasma density profile and strong centralized heating[1,2]. Suitable target plasmas for ICRF and NBI heating experiments are created by deuterium pellet injection with a multi pellet injector system developed jointly by ORNL and JET[3]. Two types of discharge conditions have been observed. In the first (type A), the density profiles decay gradually during the first 1.3s of the heating pulse while maintaining an elevated density core plasma inside $r/a < 0.6$ superimposed on a flat density pedestal as shown in Figs. 1b and 2a. During this phase the central electron and ion temperatures increase rapidly (up to 12 keV and 10 keV respectively in the best discharges). This results in an increase in the central plasma pressure by approximately a factor of three ($\beta(0) \approx 5\%$) above gas fuelled discharges and gives rise to sharply increased pressure gradients in the plasma core. As shown in Fig. 1, an abrupt collapse of the central electron and ion temperatures terminates the enhanced phase at 1.3 s and leads eventually to a 20% decrease in plasma stored energy. While these discharges are predicted to be stable to kink modes, they approach the first stability boundary for ballooning modes in the region of steepest pressure gradient[2,4]. The pressure and q profiles inferred from transport analysis are also close to those for which 'infernal' (intermediate-n) mode instability is predicted. This phenomenon, which does not occur in all cases, relaxes the discharge parameters to the less peaked standard profile shapes. Under conditions for which the temperature collapse does not occur (type B), the core plasma parameters also improve initially; but, in the latter phase of the decay of the density perturbation, the central ion temperature is observed to decrease while the electron temperature remains elevated. Ion thermal diffusivities inferred in this phase are comparable to those predicted by η_i mode turbulence theory[5].

*This work has been performed under a collaboration agreement between the JET Joint Undertaking and the U.S. Department of Energy.

PARTICLE TRANSPORT

Particle transport in pellet fuelled discharges has been evaluated by interpretative and predictive 1-1/2 D radial transport codes (PTRANS[6] and WHIST[7] respectively) using density measurements from the 6-channel interferometer and H_α detectors to infer the edge particle source strength. Particle diffusivity in the core of the plasma is found to depend on the profile shape. Particle balance calculations for peaked density profiles ($n_e(0)/\langle ne \rangle > 2$) give $D \approx 0.08$ m²/s while for non pellet-fuelled plasmas with $n_e(0)/\langle ne \rangle \approx 1.5$, D is in the range of 0.2 - 0.3 m²/s. The time evolution of the electron density profile for the shot shown in Fig. 1 was modelled with the PTRANS code using a neoclassical pinch velocity and a time dependent diffusion coefficient which is uniform inside the central plasma core and increases abruptly at the radius where the density pedestal forms as shown in Fig. 2b. The shape of D is found to be similar in both ohmic discharges and rf heated discharges up to the point where the temperature collapse takes place. Afterward, the density profile broadens and the central value of D increases abruptly to the value found in the density pedestal region. A similar diffusion model used in the predictive WHIST code ($D^{an} = 0.08$ m²/s in the core, rising sharply to 0.2 m²/s at $r/a = 0.4$, and then increasing as r^2 to 0.4 m²/s at the edge) gives good agreement with the density profile evolution and central density decay rate (Fig. 1b).

ENERGY CONFINEMENT AND TRANSPORT

The global energy confinement times evaluated during stationary conditions ($dW/dt \approx 0$) are compared in Fig. 3 with Goldston scaling[8]. The best discharges show an improvement relative to L-mode scaling of up to 50%. For type A cases, the open symbols indicate the confinement time measured after the enhanced phase. A single fluid transport analysis indicates that the 20-30% improvement in global confinement observed in the enhanced phase is due to a local improvement in confinement inside $r < 0.5$ m which is associated with a factor of 2-3 reduction in thermal diffusivities[9].

Time dependent details of energy transport in type A cases have also been analyzed with WHIST[7] and the interpretative transport analysis code TRANSP[10]. In both analyses, a constant H minority species concentration was assumed. For concentrations in the range of 1-2.5% the resulting ion and electron heating rates are approximately equal as is observed experimentally. The WHIST results are shown in Fig. 1 for a heat transport model in which the anomalous electron heat diffusivity is assumed not to vary in time and is taken to be proportional to the particle diffusivity as determined from the above analysis (ie. $\chi_e^{an} = 13\ D^{an}/4$) and for the anomalous ion contribution given by $\chi_i^{an} = \chi_e^{an}$. This model, which was chosen because of the similarity in the measured ion and electron temperature profiles, adequately reproduces the plasma response ($T_e(r)$, $T_e(0)$ and $T_i(0)$) in the ohmic phase and during the first 1 s of auxiliary heating. The improvement in global energy confinement at the start of rf heating (Fig. 1e) is a consequence of the assumption that the transport is constant in time (ie. no degradation relative to the ohmic levels) and that the heating profile becomes more peaked compared to the broader ohmic profile[11]. Experimentally the global confinement time follows this increase initially but eventually decreases to 60% of the WHIST value. This discrepancy is partly due to an increase in total radiated power (which affects the power balance only in the plasma edge) observed experimentally but not predicted by WHIST which assumes a

constant impurity concentration. The TRANSP analysis of this discharge also indicates that the core plasma confinement is not strongly degraded in the first 1s of heating; but, subsequent to that, χ_i in particular increases up to the time of the temperature collapse where an abrupt increase in both χ_i and χ_e takes place[10].

The TRANSP code has also been used to study type B discharges in which the ion temperature gradually decreases in the latter phase of the density decay as shown in Fig. 4. The ion and electron thermal diffusivities shown in Fig. 4 were inferred for a model that assumes $\chi_i = \alpha(t)\chi_e$. The TRANSP results indicate an increase in χ_i during the phase in which $T_i(0)$ decreases. While χ_i on axis is approximately equal to the neoclassical (Chang-Hinton) level during this period, the values at the half radius and beyond are more than an order of magnitude larger. However, within r = 0.6m, χ_i calculated by TRANSP and the predicted values from the theory of η_i mode turbulence extended to account for the weak density gradient seen in the discharge[5] are in reasonable agreement. Immediately after pellet injection and during the early enhanced phase, $\eta_e = d\,\ell n\, T_e / d\,\ell n\, n_e = \eta_i \leq 2$ within r/a = 0.5 because of the steep internal density gradients. As the density decreases and the plasma reheats, η increases beyond the threshold value for instability and this could be responsible for a decrease in confinement within the core plasma. Outside r/a = 2/3 where the density profiles are relatively flat even after pellet injection, η_i mode turbulence alone cannot explain the anomalous ion transport.

CONCLUSIONS

Several predictive and interpretive transport codes have been used to study the transient enhanced confinement regime observed on JET when a core plasma densified by pellet injection is heated by high power ICRF heating. Particle and heat transport coefficients within the region where the density gradient is pronounced ($r \leq 0.5$ m) are reduced by factors of 2-3 relative to standard rf heated limiter discharges. The enhanced confinement appears to be correlated with density profile peaking and can be terminated abruptly by an expulsion of energy from the core caused by steep pressure gradients[4], or more gradually by an increase in transport coefficients which may be associated with η_i mode turbulence.

REFERENCES

[1] P. Kupschus et al., Proc. 15th Eur. Conf. on Contr. Fus. and Plasma Heating, Dubrovnik, 1988, Vol.1, p.143. S.L. Milora et al., ibid, p.147.
[2] G.L. Schmidt et al., Proc. 12th Int. Conf. Plasma Phys. and Contr. Nucl. Fusion Res. (Nice, 1988) IAEA-CN-50A-IV-1.
[3] S.L. Milora et al., in Proc. 12th Symp. on Fusion Eng. (Monterey 1987), IEEE Vol.2, p.784 (1987). P. Kupschus et al., ibid, p. 781.
[4] R. Galvão et al., this conference.
[5] G.S. Lee and P.H. Diamond, Phys. Fluids 29, 3291 (1986) and G.S. Lee in preparation.
[6] L.R. Baylor et al., presented at the IAEA Technical Committee Meeting on Pellet Injection and Toroidal Confinement, Gut Ising, FRG, Oct. 1988.
[7] W.A. Houlberg et al., ibid.
[8] R.J. Goldston, Plasma Phys. Controlled Fusion 26, p.87 (1984).
[9] A. Taroni et al., Proc. 12th Int. Conf. Plasma Phys. and Contr. Nucl. Fusion Res. (Nice, 1988) IAEA-CN-50A-7-1.

[10] G Hammett et al., this conference.
[11] J.D. Callen et al., Nucl. Fusion 27, p.1857-75 (1987).

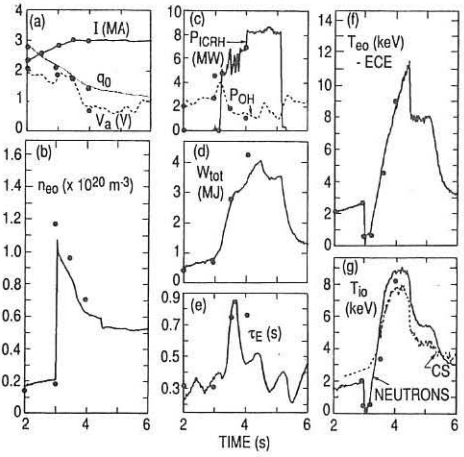

Fig.1 Summary for shot 16211 and comparison with WHIST code results(·)

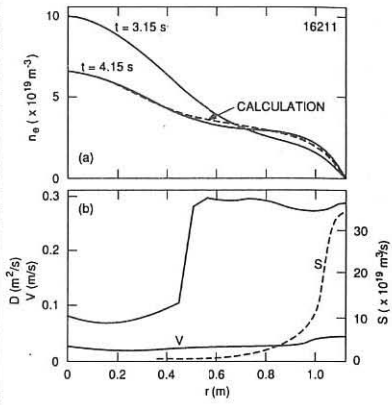

Fig.2 Comparison of measured and calculated n_e profile evolution for shot 16211.

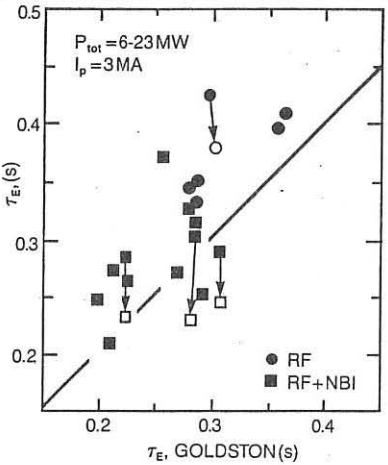

Fig.3 Comparison of global τ_E with Goldston scaling for pellet fuelled auxiliary heated plasmas.

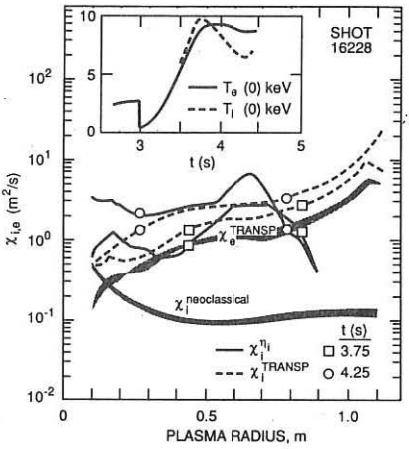

Fig.4 Thermal diffusivity profiles obtained from TRANSP compared with predictions from η_i mode theory. Heating power = 11 MW.

STUDIES OF VISIBLE IMPURITY RADIATION FROM JET PLASMAS DURING HEATING AND FUELLING EXPERIMENTS

P D Morgan, A Boileau[1], M J Forrest[2], M von Hellermann, L Horton[3], W Mandl, M F Stamp, H P Summers, H Weisen and A Zinoviev[4]

JET Joint Undertaking, Abingdon, Oxon OX14 3EA, UK / [1] Tokamak de Varennes, Varennes, CANADA / [2] UKAEA Culham Laboratory , Abingdon, Oxon OX14 3DB, UK / [3] ORNL ,Oak Ridge, Tennessee 37830, USA / [4] Joffe Inst., Leningrad, USSR

1. INTRODUCTION

At JET extensive use is made of visible spectroscopy in the study of plasma impurities, [1]. Measurements of absolute line intensities from such species as O II, C III and D I are used to deduce the influxes of light impurities as well as deuterium at the plasma periphery. The absolute continuum emission at 523.5nm, measured using a 15-telescope poloidal array, is used to determine $Z_{eff}(r)$ and its temporal evolution. Charge-exchange recombination spectroscopy (CXRS) has proved to be a powerful technique during NBI to measure, amongst other parameters, the density of C and O at up to 15 separate points on the plasma minor radius.

The combination of these diagnostic techniques permits the global impurity behaviour in the plasma to be followed. In this paper, results are reported pertaining to studies of plasmas heated by NBI and ICRF, and fuelled by the injection of D_2 pellets.

2. APPARATUS AND ANALYSIS

The apparatus is described in detail elsewhere, [2,3,4]. Using a spectrometer equipped with an OMA, line emissions at the plasma edge from the light impurity and fuel species are measured absolutely. For a given atom or ion the measured intensity I can be used to deduce the influx Γ of that species, since $\Gamma = 4\pi IS/XB$,where S is the ionisation rate, X is the excitation rate and B is the branching ratio, [2].

Each channel in the poloidal array measures the line integral of the continuum emissivity, or the brightness, along a chord through the plasma. Using the technique of Abel inversion the brightnesses are transformed into the radial profile of emissivity, $\varepsilon(r)$. Knowledge of $n_e(r)$ and $T_e(r)$ permits the radial profile of Z_{eff} to be determined, [3], since $\varepsilon(r) \propto Z_{eff}(r).n_e^2(r).g_{ff}(r)/T_e^{1/2}(r)$ - g_{ff} being the free-free Gaunt factor.

The CX spectra are recorded using 3 spectrometers equipped with OMAs. The path through the plasma of the octant 8 neutral beam is observed using a fan of 15 sight-lines. These are almost horizontal and intersect the beam at various radial positions, [4]. The intensities of the C^{5+} and O^{7+} lines recorded are proportional to the neutral beam density and to the density of the appropriate fully-stripped ion, permitting the densities of these impurities to be derived. A novel diagnostic method is being developed at

JET, based on the analysis of Balmer-Alpha light emitted by fast injected D atoms colliding with deuterons and fully-stripped impurity ions, [5]. Local values of Z_{eff} can be derived from the measured intensity ratio of the spectrum representing the 80 keV neutrals and that of the thermal CX D_α feature. The latter directly gives the deuteron density.

3. RESULTS AND DISCUSSION

(a) H-Mode Discharges In the case of discharges limited by a single-null magnetic separatrix, following NBI and the establishment of an H mode, throughout its life there is a steady increase in $\bar{Z}_{eff}$. In Fig 1, a selection of radial profiles of Z_{eff} are shown at various times during the X-point and H-mode phases of a discharge. The maximum value of $Z_{eff}(r)$ does not occur on axis, rather it is situated at $R \simeq 3.6$ m ($r \simeq a/2$) which is approximately the location of the q=1 surface. As time evolves the profile becomes more hollow and $\bar{Z}_{eff}$ increases from ~ 2.2 at 8.9s to ~ 3.1 at 14.3s. At 15s, following an H to L transition, the profile of $Z_{eff}(r)$ is no longer hollow but has a rather flat form.

From a spectroscopic survey it is seen that the dominant impurity is C with O being the next most important. The metallic impurities make a negligible contribution to Z_{eff}. Fig 2 shows a time sequence of C radial density profiles, derived from CXRS. The carbon density increases throughout the H mode and exhibits a rather flat radial dependence, with a tendency to peak at around 3.7m. Following the H to L transition, the $n_c(r)$ profile is rearranged to give a steady decrease in C density from the centre to the edge, with a substantial reduction in total carbon content.

The increase in the fuel and impurity densities during the life of the H mode can be understood in terms of an improved particle confinement - by a factor ranging from 3 to 5, [3]. This is confirmed by measurements of the C influx at the plasma periphery. At the onset of the H mode the influx deduced from the intensity of C III drops by a factor of 2. Thereafter, the influx increases by ~ 30 % during the life of the H mode, in which time $\bar{n}_e$ has increased by over a factor of 3. At the end of the H-mode phase, on transition to the L mode there is an abrupt increase in the C influx by more than 100 % - as the barrier to good particle and thermal transport suddenly collapses and $\bar{n}_e$ and n_c drop by almost a factor of 2.

(b) Discharges Fuelled By Pellet Injection Pellet injection has a dramatic effect on the temporal evolution of $Z_{eff}(r)$. Where substantial density is deposited on axis , values of $Z_{eff}(0)$ close to 1 can be transiently achieved, through dilution of the core impurities by D ions from the pellet. However, on a time scale of 2 to 3s, which is several particle containment times, recycling establishes a higher $\bar{Z}_{eff}$, consistent with edge fuelling.

On the application of additional heating to plasmas with highly-peaked electron density profiles, impurity accumulation has been observed in the plasma centre. Because of the higher charge of the impurity ions, their density profiles are more strongly peaked on axis than that of the plasma deuterons. In Fig 3 a time sequence of $Z_{eff}(r)$ profiles is presented for a discharge into which a 4 mm D_2 pellet was injected at 3s, during the current-ramp phase. Subsequently, a combination of ICRF and NBI was applied beginning at 3.25 and 3.65s, respectively.

Prior to pellet injection the profile of $Z_{eff}(r)$ is almost flat,

exhibiting a slight drop towards the plasma edge. The average value $\bar{Z}_{eff}$ is $\simeq$ 2.4. The whole profile has been substantially depressed 0.1s after injection, with $Z_{eff}(0) \leq 1.4$ and $\bar{Z}_{eff} \simeq 1.6$. The profile is hollow on axis, with $Z_{eff}(r)$ rising towards the plasma edge. At 3.9s, following the application of ICRF and NBI, the profile has changed dramatically to exhibit a plateau extending from ~ 3.6m to the plasma edge and a peak rising to a maximum at the plasma centre. At this time $\bar{Z}_{eff}$ has risen to ~ 2.4. Finally at 4.2s, shortly before the peaked density profile flattens due to a sawtooth crash, the profile of $Z_{eff}(r)$ is even more pronounced in its division into a central peak and an outer plateau. The average value $\bar{Z}_{eff}$ has risen to ~ 2.7 with $Z_{eff}(0)/Z_{eff}(a/2) \simeq 2$.

In Fig 4 the radial C density profiles measured by CXRS are presented. At 3.7s, shortly after the application of NBI, the C density is ~ 1.2×10^{18} m^{-3} on axis, and roughly half this value for $r \geq a/2$. As time progresses, the density both on axis and over the outer half of the minor radius increases steadily, until at ~ 4.2s $n_c(0)$ is about 2.2×10^{18} m^{-3} with an edge density around half this value. The general form of the $n_c(r)$ profiles is in good agreement with that of the $Z_{eff}(r)$ profiles, showing a relatively-narrow peaked central density and a pedestal for $r \geq a/2$. However, at 4.8s, after the sawtooth crash the profile of $n_c(r)$ is essentially flat, the carbon density having redistributed itself.

4. SUMMARY

The global impurity behaviour in JET has been studied using visible spectroscopy. From absolute measurements of line and continuum emission, repectively, the influxes of light impurities at the plasma edge and the profile of $Z_{eff}(r)$ have been derived. Also, CXRS permits the radial density profiles of C and O to be measured during NBI.

In the case of X-point plasmas, at the onset of an H mode following NBI, the influxes of the hydrogenic and light impurity species are seen to decrease sharply, corresponding to an improved particle confinement. Throughout the life of the H mode, $\bar{Z}_{eff}$ increases steadily. The $Z_{eff}(r)$ profile becomes hollow on axis and peaks at around half the minor radius. CXRS measurements show a steady increase in the C density during the H mode with the profile tending to peak at $r \simeq a/2$.

The injection of a D_2 pellet into the plasma produces a highly-peaked profile of $n_e(r)$ and an abrupt reduction of $Z_{eff}(0)$, provided deep penetration is achieved. On the application of NBI and ICRF, from CXRS the density of C is seen to increase substantially on axis and to exhibit significant peaking. This indication of an accumulation of light impurities at the plasma centre is supported by the peaked profile of $Z_{eff}(r)$, with $Z_{eff}(0)/Z_{eff}(a/2) \simeq 2$.

5. REFERENCES

[1] K H Behringer et al., Proc. 13th Symposium on Phys. Ionised Gases, Sibenik, p.241, (1987).
[2] M F Stamp et al., this conference, (1989).
[3] P D Morgan and J J O'Rourke, Proc. 14th Europ. Conf. on Controlled Fusion and Plasma Physics, 11D, (pt.3), p.1240, (1987).
[4] M von Hellermann et al., this conference, (1989).
[5] A Boileau et al., Research Note, J. Phys. B, to be published, (1989).

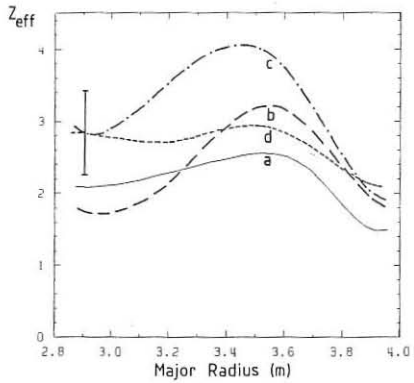

FIG. 1: $Z_{eff}(r)$ profiles for pulse #18663. (a) t=8.9s, during X-point phase. (b) t=12.3s, (c) t=14.3s; during H-mode phase. H mode starts at 11.6s. (d) t=15s, 0.6s after H to L transition. P_{NBI}=7.5 MW.

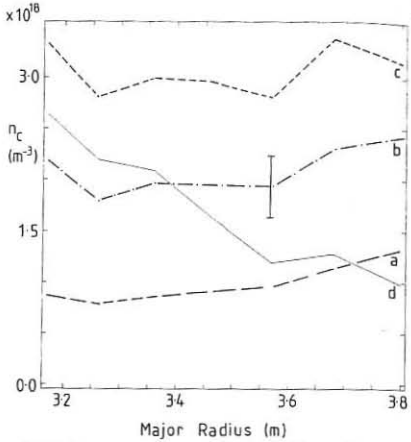

FIG. 2: Radial profiles of carbon density for pulse #18663. (a) t= 12.3s, (b) t=13.2s, (c) t=14.1s; during H-mode phase. (d) t=14.8s, 0.4s after H to L transition. I_p=3.1 MA.

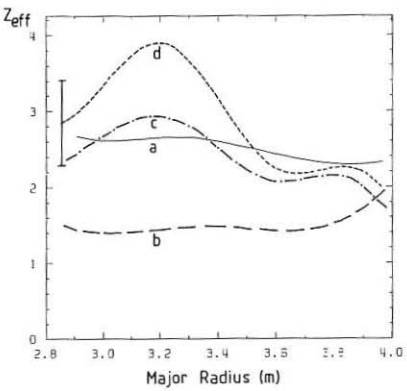

FIG. 3: $Z_{eff}(r)$ profiles for pulse #17279. (a) t=2.8s, OH phase. (b) t=3.1s, 0.1s after pellet injected. (c) t=3.9s, (d) t=4.2s; during NBI and ICRH. P_{NBI}=2.8 MW. P_{ICRH}=7.3 MW.

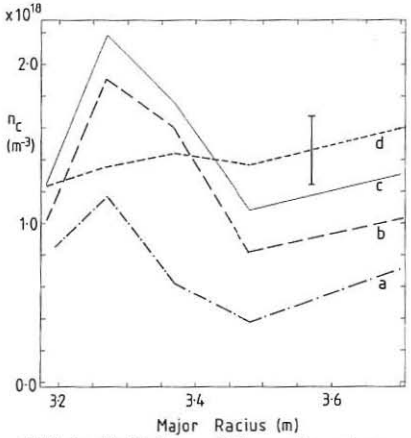

FIG. 4: Radial profiles of carbon density for pulse #17279. (a) t= 3.7s, (b) t=3.9s, (c) t=4.2s; during NBI and ICRH. (d) t=4.8s, 0.4s after collapse of peaked $n_e(r)$ profile. I_p=3.1 MA.

MEASUREMENTS OF THE ELECTRON PARTICLE DIFFUSION COEFFICIENT WITH THE JET MULTICHANNEL REFLECTOMETER

A C C Sips+, A E Costley, J C M de Haas+ and R Prentice

JET Joint Undertaking, Abingdon, Oxon, OX14 3EA, UK
+ FOM "Rijnhuizen", The Netherlands

INTRODUCTION

Experimental determinations of the cross-field particle diffusion coefficient (D_p) are important in studies of transport in tokamak plasmas [1,2]. D_p has been determined from measurements of density perturbations following a sawtooth collapse [2,3], oscillating gas puff [4], and injected high velocity pellets [2]. In each case the density changes have been measured using multichord interferometry and D_p is obtained with an accuracy of typically 20%.

At JET, D_p has been determined by using microwave reflectometry to measure changes in the density profile following a sawtooth collapse. Reflectometry provides relatively localized information on the electron density and so offers the promise of providing accurate measurements of the radial dependence of D_p. Initially, a single channel reflectometer was used to measure an outward propagating density pulse following a sawtooth collapse [5]. More recently, a multichannel reflectometer [6] has been used to study a dominant inward propagating pulse following the collapse of a monster sawtooth [7]. The inward going pulse is thought to be generated by the faster heat pulse reaching the plasma limiter in advance of the density pulse. These studies demonstrate that, in general, simultaneous inward and outward propagating pulses have to be taken into account in determinations of D_p using the sawtooth collapse.

In this paper, we present our most recent measurements of D_p. The experimental data are compared with the prediction of a comprehensive numerical transport model which includes both outward going and inward going density pulses.

THE MULTICHANNEL REFLECTOMETER

The reflectometer at JET has 12 probing frequencies in the range 18-80 GHz. It operates in the ordinary mode and so probes electron densities in the range $0.4 - 8.0 \times 10^{19}$ m^{-3}. It can be operated either with the source frequencies fixed, or swept over a narrow range. In the former mode it provides the magnitude and direction of rapid movements of the density layers. The sensitivity of the system is such that movements of 1.0 mm of the 0.4×10^{19} m^{-3} density layer, and 0.2 mm of the 8.0×10^{19} m^{-3} density layer, can be clearly resolved. In the narrow band swept mode, the positions of the different density layers are determined.

The data presented in this paper are obtained with the seven channels which probe the density layers $0.4 - 4.0 \times 10^{19}$ m^{-3}. The reflectometer is operated in the fixed frequency mode. The data are recorded with a bandwidth of 700 Hz, at a sampling rate of 1-2 kHz and 8-4 seconds of a JET discharge are monitored.

DENSITY PULSES FOLLOWING A SAWTOOTH COLLAPSE

For the discharges investigated, typically five of the probed density layers lie outside the mixing radius, figure 1. Following a sawtooth collapse, the phase change measured on these channels rises and falls, figure 2. The time interval between the sawtooth collapse and the peak of the phase change is termed the delay time. This time is observed to decrease with increasing radius, figure 3, demonstrating the existence of an inward propagating density pulse. This pulse originates at the plasma edge 10-40 ms after the sawtooth collapse.

NUMERICAL MODEL

Our model is a 1-D numerical transport model in which diffusive and convective terms are included. The model is outlined in figure 4.

First an equilibrium electron density profile is established assuming a radially dependent particle diffusion coefficient of the form $D_p(r) = D_0(1 + \alpha r^2/a^2)$ and an anomalous pinch velocity $v_p(r) = CD_p(r)\ r/a^2$. The coefficient C is adjusted, keeping the total number of particles constant, until the predicted central density is the same as that measured by the JET multichord interferometer.

Next the sawtooth oscillations, and the consequential density pulses, are simulated. The outward propagating pulse is simulated by collapsing the density profile inside the mixing radius, while the inward propagating pulse is simulated by changing the edge recycling coefficient (R) during the sawtooth period (figure 5). The recycling coefficient is temporarily raised above 1 by an amount A_r. This gives the influx of particles from the edge and increases the total number of particles in the plasma. After time τ_r, R is decreased to a value below 1 to restore the total number of particles to the initial value (at the crash). The particle diffusion time is comparable with the sawtooth period at JET and so it is necessary to simulate a sequence of density pulses.

The computed phase changes on each channel are compared with the measured phase changes. D_0, A_r, τ_r and α are adjusted to give the best fit to the measurements. A typical fit is shown in figure 2.

RESULTS

Thus far we have analysed sawteeth measured on seven different plasma pulses. In all cases the pulses had a current of 5 MA, toroidal field of 3.1 T, and were limited on the belt limiters. The plasmas were heated with ICRH in the range 0 to 7 MW. A total of sixteen sawteeth (an average of two per discharge) have been compared with the model predictions. The best fit to all the measurements is obtained with $\alpha = 2$ but α values in the range 1-4 cannot be excluded. Typically we find D_0 equal to 0.16 ± 0.02 m^2/s and the best fitted value for all the data lies in the range 0.16 ± 0.04 m^2/s. D_0 is independent of the amount of ICRH coupled into the plasma.

Further, we have examined the relationship between A_r and the drop in the electron temperature at the crash $\Delta T_e(o)$ (as measured by ECE). We observe that A_r is proportional to $\Delta T_e(o)$, figure 6. This supports the suggestion that the inward propagating density pulse is due to the increased energy flow to the limiters resulting from the heat pulse associated with the sawtooth collapse. We have also observed that the predicted maximum increase in the total number of particles in the plasma

during the sawtooth period agrees well with that calculated from independent D_α measurements.

CONCLUSIONS

A radially dependent electron particle diffusion coefficient is derived by modelling the changes in the electron density profile after a sawtooth collapse as measured with a multichannel reflectometer at different radial positions outside the mixing radius. An important feature of the numerical model is that it contains outward and inward propagating density pulses. The inward propagating pulse is simulated by changing the edge recycling coefficient during the sawtooth period. Comparing the data from the reflectometer with the model predictions for several plasma shots, the value for D_p is found to be $(0.16 \pm 0.04)\ (1 + \alpha\ r^2/a^2)$ m^2/s with $\alpha = 2$. This agrees with values obtained by other methods at JET [2]. The value for χ_e for these plasma conditions lies typically in the range of 3-5 m^2/s at $r/a = 0.8$ [8]. This confirms the large value for χ_e/D_p found in recent transport studies at JET [2].

REFERENCES

[1] J Callen et al, Nuclear Fusion 27 (1987) p1857.
[2] A Cheetham et al, 12th International Conference on Plasma Physics and Controlled Nuclear Fusion Research, Nice, October 1988, IAEA-CN-50/I-2-2.
[3] S K Kim et al, 15th European Conference on Controlled Fusion and Plasma Heating, Dubrovnik, May 1988. Vol 12B, Part I, p187.
[4] O Gehre et al, 15th European Conference on Controlled Fusion and Plasma Heating, Dubrovnik, May 1988. Vol 12B, Part I, p7.
[5] A E Hubbard et al, 13th European Conference on Controlled Fusion and Plasma Heating. Schliersee, April 1986. Vol 10C, Part I, p232.
[6] R Prentice et al, 15th European Conference on Controlled Fusion and Plasma Heating, Dubrovnik, May 1988. Vol 12B, Part III, p1115.
[7] R Prentice et al, 30th Annual Meeting of APS, Hollywood, November 1988, Poster paper.
[8] J C M de Haas et al, this conference.

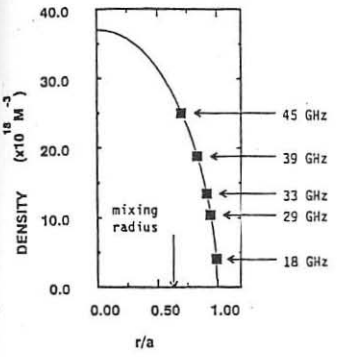

Figure 1: Example of an electron density profile with the position of the reflectometer channels outside the mixing radius (squares).

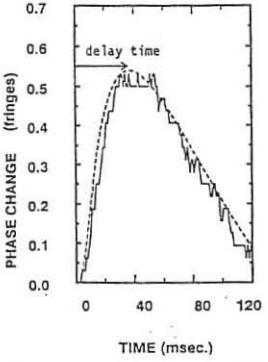

Figure 2: Signal on reflectometer channel (F=39 GHz, r/a=0.83) during sawtooth period (solid line) and best fit model prediction (dashed line).

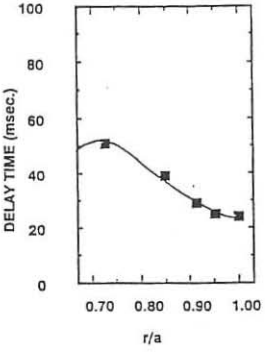

Figure 3: The observed delay time at different radial positions (squares) compared with model prediction (best fit, solid line).

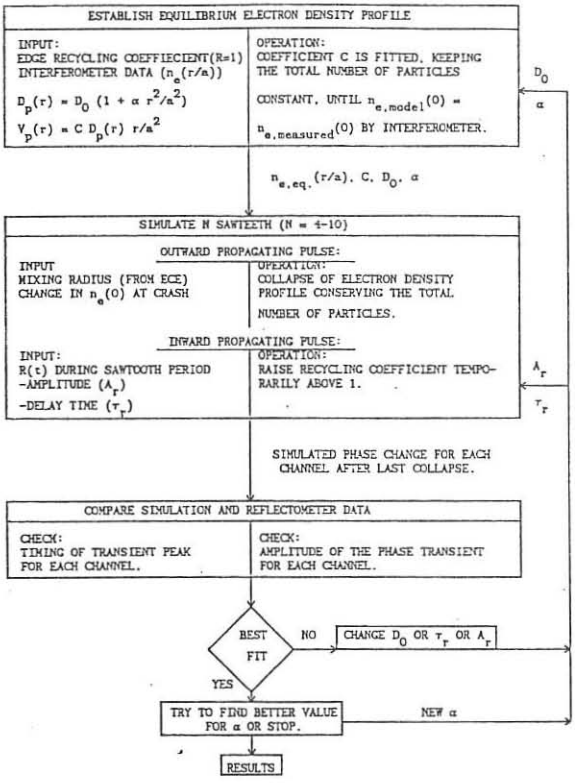

Figure 4: Description of numerical model used to simulate the observed density pulses after a sawtooth collapse.

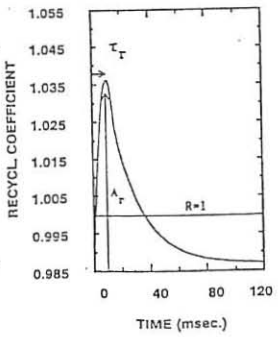

Figure 5: Time dependent recycling coeffient used by the model to simulate the inward propagating density pulse.

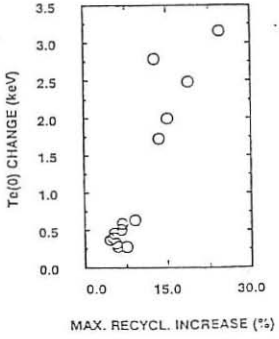

Figures 6: Comparison of simulated maximum increase in the edge recycling (A_r) and the change in central electron temperature at the sawtooth crash.

OPERATION AT HIGH PLASMA CURRENT IN JET

A. Tanga, M. Bures, M. Garribba, B.J. Green, J. How, J. Jacquinot, J. Last, P. Lomas, C.G. Lowry, M. Malacarne, P. Mantica[+], P.L. Mondino, P. Noll, P.H. Rebut, A. Santagiustina, F.C. Schueller[++], J. Snipes, P.R. Thomas, B. Tubbing.

JET Joint Undertaking, Abingdon, Oxfordshire, OX14 3EA, U.K.
[+]Istituto di Fisica del Plasma, Associazione Euratom-ENEA-CNR
Via Bassini 15, 20133 Milano, Italy
[++]FOM Institut voor Plasmafysica, 3430 BE Nieuwegein, The Netherlands

The achievement of high plasma currents

A plasma current of 7MA has been obtained in JET with limiter configuration, 5.3MA has been obtained with single null magnetic separatrix, and 3.5MA has been obtained with double null.

The volt-second available has been increased and more fully utilized by: 1) Differential current control of the primary windings, thus increasing by 50% the maximum current in the midplane coil; 2) The reduction of stray field at plasma breakdown by adding two coils at primary top/bottom.

Current ramp at costant toroidal field are limited by instability at rational values of q_ψ, which can lead to quasi-stationary modes and subsequent disruption. This limits the rate of rise of plasma current to typically 0.25MA/s at 6MA when q_ψ=3. Despite the low loop voltage (0.5V on axis) this scenario is expensive in v-s. At constant q_ψ, higher current ramp rates are possible, e.g. 0.75MA/s up to 7MA at q_ψ=2.5. In such a case the sawtooth is present throughout the current rise and the loop voltage on axis is typically 1 Volt. The saving of resistive volt-s with this scenario permitted a flat-top of 2s at 7MA. The ohmic discharges can be made free from disruptions. However, with additional heating power above 20MW at 5 or 6MA the ineraction with the limiter is strongly enhanced. This can lead to significant modulation of the total radiated power, carbon influxes, MARFE like phenomena and disruptions.

Magnetic separatrix configuration can be formed in JET at high plasma currents using the combined fields from the primary leakage, shaping coils and, in the case of single null, from the radial field produced by unbalanced currents in the main vertical field coils. At 5MA the separatrix clears the limiters and the inner wall by 8cm or more and the single X-point is 10cm in front of the dump plates. When such a configuration is formed, the plasma density pumps out very strongly, up to 10^{22} particles/s.

Vessel conditioning and plasma desity control

During routine operation with water cooled graphite limiters He glow cleaning is performed overnight. He conditioning causes depletion of graphite surfaces from Hydrogenic species, thus good density control is achieved also in limiter discharges together with reduction of oxygen impurities. Plasma discharges following deuterium glow cleaning with room temperature limiters are characterized by strong desorption of deuterium trapped on the cold limiters during conditioning.

High plasma current radial disruptions cause overheating of limiter/inner wall graphite. Recovery of high current plasma discharges requires reconditioning of graphite surfaces by He glow cleaning followed by tokamak pulses with high breakdown voltages and high toroidal field and with the use of the inert He as filling gas.

+Ohmic He conditioning pulses have effects similar to He glow cleaning. In general 5-10 He discharges with flat-top of 20s are sufficient to reduce the relative deuteron concentration to below .01.

Rapid plasma density decay, required to avoid disruptions during the termination phase of additional heating and of plasma current, is achieved either by moving the plasma in contact with the inner wall or vessel top/bottom tiles.

High current plasma disruptions.

Disruptions at high plasma current cause stong mechanical forces and severe deconditioning effects of the vacuum vessel.

The disruptive limit of the operational space both in high density and low q follows the same scaling as at lower currents[1,2]. The tendency toward a more rapid decay of plasma current leads to values of the time derivative of plasma current in excess of 10^9 A/s. However the maximum rate of current decay during a disruption, shown in fig. 1 for all JET radial disruptions, shows that the max. value of time slope can be between 5 and 10 ms, independent of the value of plasma current.

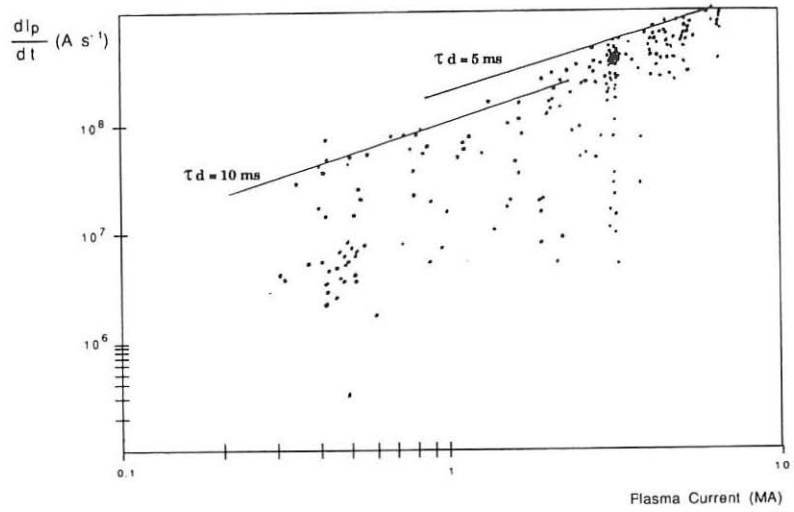

Fig. 1 Maximum value of Plasma Current Decay Rate during radial disruptions vs. Plasma Current.

Time dependent equilibrium calculations, by PROTEUS code[3], of the plasma current decay phase is shown in fig 2 for a 5MA limiter radial disruption at the density limit. It is possible to see that during most of the plasma current decay the plasma radial position changes very slowly. The current in the vertical field coils is only partially under feedback control, the plas

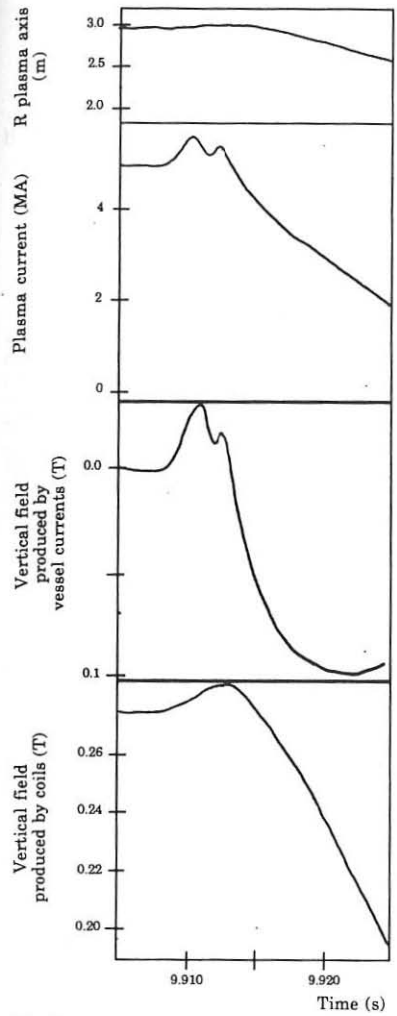

Fig. 2

Equilibrium parameters of the plasma current decay phase of # 16364, computed by PROTEUS code

ma column radial position is kept with the contribution of the vertical field generated by the induced vessel currents, as shown in fig. 2. Loss of stabilization of the vertical position, leading to plasma disruption, can occurr, in single null configuration at plasma current above 4MA, at the transition from H-mode to L-mode, due to rapid vertical plasma movement.

The H to L mode transition is always characterized by a big spike in the magnetic coil signals, which is often preceded by a precursor mode lasting 1ms. The precursor is coherent, f=6-8kHz, high m (5-10), n=1 mode rotating opposite to the Neutral Beam. The spike itself always shows a dominant poloidal number m=1, with inversion of phase near the equatorial plane, as shown in fig. 3. There is a fast vertical movement of the plasma column when the transition occurs. Also toroidally , the n=0 component due to displacement is of the same order of the n=1 component driven by the destabilising mode, as shown in fig. 4.

Conclusions

Enhancement of the JET poloidal system has made possible the achievment of higher plasma current discharges.

The ohmic discharges can be made disruption-safe by careful control of plasma current ramp-up and termination scenarios. Vessel conditioning and density control techniques contribute to reduce the occurrence of disruptions in discharges with additional heating (above 20MW).

Loss of control of vertical position can occurr in high current single null discharges at the transition from H-mode toL-mode.

References:
(I) J.Wesson et al. "Disruption in JET"; submitted for publication in Nuclear Fusion.
(2) P. Lomas et al. in Proc. of I5th Conference on Controlled Fusion and Plasma Heating, Dubrovnik, May I6-20 I988.
A. Tanga ,P.R. Thomas et al. "Start-up of the Ohmic Phase in JET" in "Tokamak Start-up" Plenum Press I986, New York.
(3) R.Albanese, J. Blum,O. De Barbieri-Workshop on "Feedback Systems for Shape Control of non-circular Tokamaks" ,Lausanne, Sw., July I987.

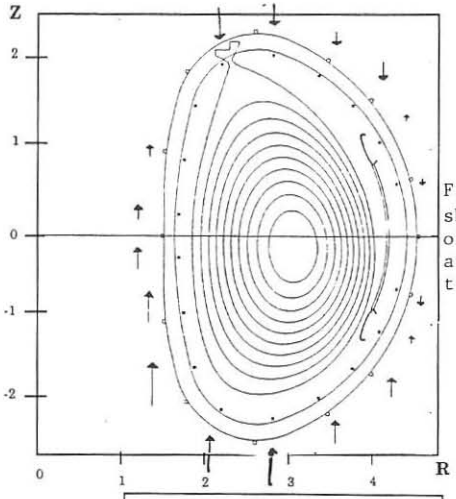

SHOT	18660
T-SLICE	53.449
IP	= 3.126
BETA	= 0.434
LI	= 0.892
DPSI	= 0.830

Flux contours during H-mode.The arrows show the relative amplitude and sign of the splike observed by the poloidal array of I8 pick-up coils at the transition.

Fig. 3

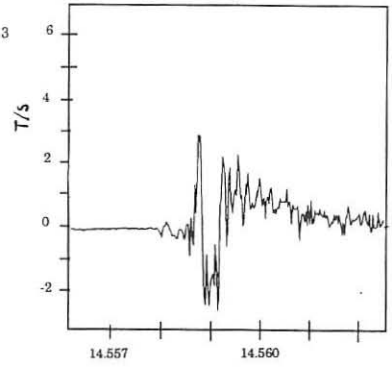

Fig. 4a

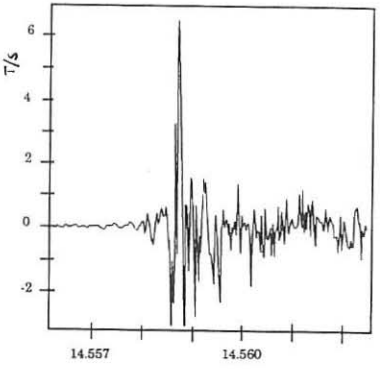

Fig. 4b

Comparison of n=0 and n=I components of the magnetic spike,#I8660

ION TEMPERATURE PROFILES IN JET

M von Hellermann, A. Boileau [+], L. Horton [*], W. Mandl, H. P. Summers, H. Weisen

JET Joint Undertaking , Abingdon, Oxon OX14 3EA, UK
[+] IREQ, Tokamak de Varennes, Canada, [*] ORNL , Oak Ridge, USA

Introduction: Radially and temporally resolved ion temperature profiles in auxiliary-heated and pellet-fuelled JET plasmas are obtained routinely from the observation of charge exchange line spectra of fully stripped carbon and oxygen. In addition the Doppler width of the x-ray emission spectrum of highly ionized nickel provides a measurement of the on-axis ion temperature. Analysis of the CX deuterium Balmer alpha spectrum shows that the deuteron temperatures are in close agreement to simultaneously measured carbon and oxygen temperatures. First results of this novel technique are reported in [1].

Results and Discussions : In this paper we describe characteristic features of ion temperature profiles for different JET operation modes such as low-density high-temperature plasmas, high-density pellet-fuelled plasmas, and high-density high-confinement H-mode plasmas.

The JET charge-exchange diagnostic employs one vertical line of sight and a horizontal multichord array (Fig. 1), which intersects the heating neutral beams at 15 points along the minor radius. The spatial resolution defined by the intersection of the pencil like viewing lines and neutral beam is +/- 2cm , that is less than 1% of the major tokamak radius. The collected light is transferred by optical fibres to a set of 3 remote spectrometers and is recorded by multi channel detector arrays. The time evolution of ion temperature profiles can be monitored with a temporal resolution varying typically between 12 to 100 msec.

The development of the ion temperature profile was investigated in the extreme cases of high-ion-temperature, but low-density plasmas (T_i= 23 keV, T_e=10keV, n_D= 1.5 $10^{19} m^{-3}$) and in high-density, but moderate temperature , pellet-fuelled discharges ($T_e = T_i$ = 11 keV, n_D = 4 10^{19} m^{-3}). In the first case, an input of 19 Mwatts of NB heating power has led to very peaked profiles of ion temperature , toroidal plasma rotation and ion pressure , accompanied by a simultanenous increase in the neutron reaction rate . Fig. 2a and 2b show the radial profiles of ion temperature and ion pressure . The deuteron density in this example has been derived from electron and CX carbon densities [2] . The collapse of ion temperature and neutron rate coincides with a sharp increase in density , both of electrons and impurities, approximately 0.6 sec after the onset of neutral beam heating and fuelling. Fig. 3 shows the temporal development of central ion temperature, electron and carbon density and neutron reaction rate .

In pellet-fuelled ICRH-heated plasmas, comparable high peaking factors are observed with almost identical radial profiles of ion and electron

temperatures (Fig.4). Only 2 neutral beams with a power of 1.3 MWatt each were switched on in this example, to provide a minimum of neutral particle density required for the operation of the CX diagnostic.

Rather broad ion temperature profiles are observed during high confinement modes in the magnetic limiter configuration. Figs.5 and 6 show the evolution of ion temperature during a long neutral beam pulse, displaying an extended H-mode phase, followed by a brief L-mode and then a second H-mode phase. Minute details of the transition L to H and H to L can be recorded by the very intense outer channels of the CX diagnostic which enable an integration time as short as 12 msec (Fig.7). The transition from L- to H-mode and vice versa is typically accompanied by a distinctive change in temperature and density near the plasma boundary. The signals in Fig.7 (H_α-plasma-boundary and T_i at 3.82m) start with a back-transition from H- to L-mode , illustrated by a sudden drop of ion temperature from 1.4 keV down to 0.7 keV. The change occurs in a time scale of 10 msec. The second H-mode following an L-mode period of approximately 300 msec displays an increase in ion temperature to an almost constant level of approx. 1.1 keV. The end of the H-mode is associated with a drop to 0.6 keV 1.2 sec later.

Summary: The results presented in this paper have shown some extreme cases of ion temperature profiles illustrating the different operation modes of the JET tokamak. In the three examples of low-density high temperature, high-density moderate temperature and high-density high-confinement plasmas comparable values of a maximum fusion product $n_d T_i \tau_E$ in the order of 10^{20} keV m^{-3} sec are achieved.

References: [1] A.Boileau et al. " Observations of Motional Stark Features in the Balmer Alpha Spectrum of Deuterium in the JET Plasma", submitted to J.Phys.B, [2] P.D.Morgan et al., this conference, [3] G.Schmidt et al., IAEA-CN-50/A-IV-1, Nice, Oct. 88

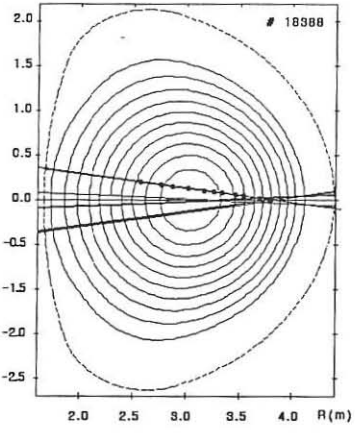

Fig.1 Poloidal view of the JET heating neutral beams and intersection points with the CX multichord array (octant 8) .

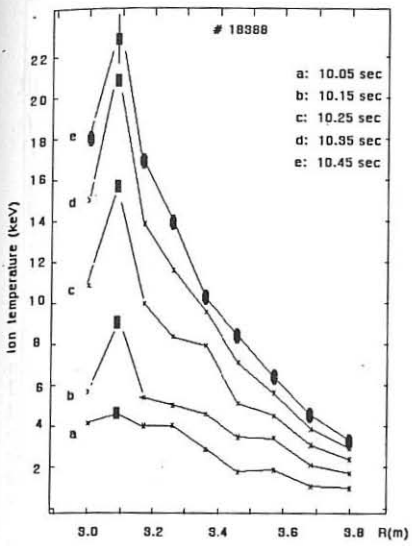

Fig.2a

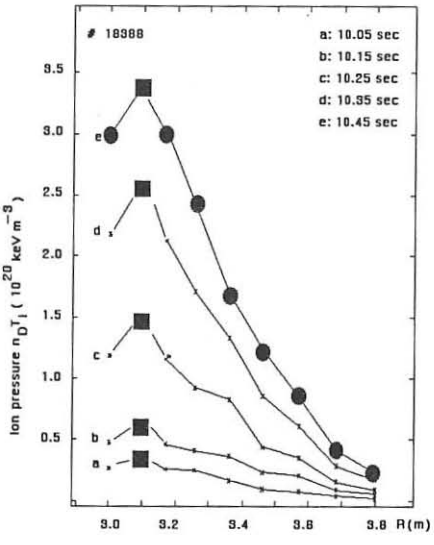

Fig.2b

Radial profiles of ion temperature and ion pressure. JET pulse 18388

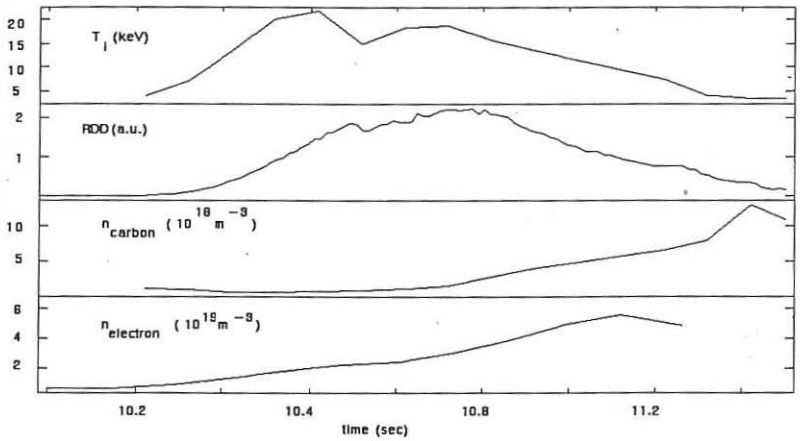

Fig.3

Survey of T_i, n_e, n_C, RDD in a hot-ion-mode plasma

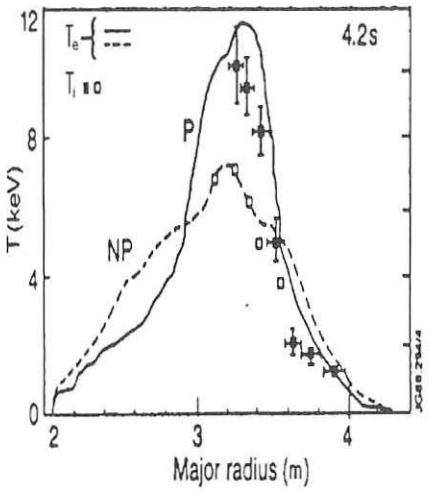

Fig.4 Profiles of electron and ion temperature in comparable pellet (P) and non-pellet (NP) plasmas , cf. [3]

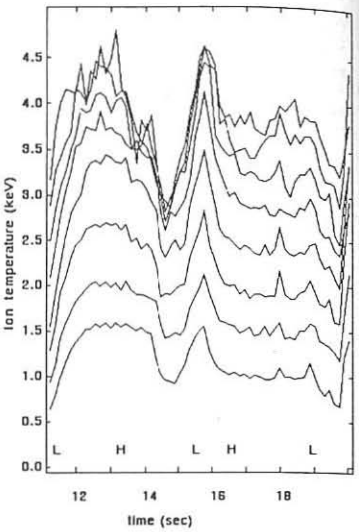

Fig.5 Ion temperature traces at 8 radial chords during a long NB pulse, with several transitions from L- to H-mode

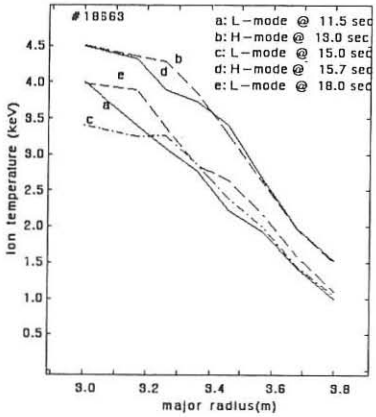

Fig.6 Radial ion temperature profiles in L- and H-mode phases of the same pulse

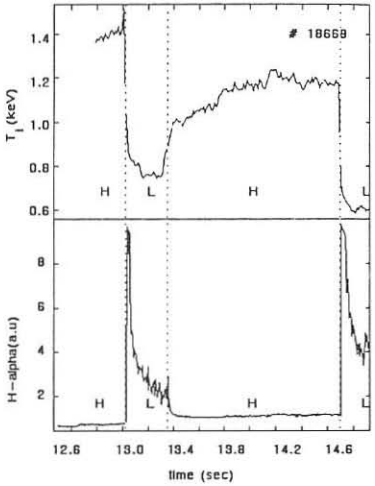

Fig.7 H-alpha, plasma boundary and Ti at R=3.82m, showing details at high sampling rate

HIGH DECAY INDEX PLASMAS IN DIII-D

J.B. Lister, J.-M. Moret, E.A. Lazarus*, A.G. Kellman+, T.S. Taylor+, J.R. Ferron+

Centre de Recherches en Physique des Plasmas
Association Euratom - Confédération Suisse
Ecole Polytechnique Fédérale de Lausanne
21, Av. des Bains, 1007 Lausanne, Switzerland

* Oak Ridge National Laboratory, P.O. Box Y, Oak Ridge, Tennesse 37831, U.S.A.
+ GA Technologies Inc. P.O. Box 81608, San Diego, California 92138, U.S.A.

The production of highly elongated plasmas requires large values of the vertical field decay index ($n=-R/B_z\, dB_z/dR$), which in turn render the plasma more and more difficult to maintain up to a critical decay index at which the plasma is ideally positionally unstable. In the DIII-D tokamak plasmas with n up to -0.96 were obtained with little trouble. This experimental limit was much lower than the predicted critical decay index. This paper describes the experiments carried out in order to study the vertical position problem in DIII-D, and the technique which was applied to stabilise high decay indices, up to ~-1.3, close to the predicted limit. This work prepares the way for the high plasma elongation which would be obtained with such a high decay index if the safety factor were also lower.

An approach to this problem has recently been evolved for improving the DIII-D tokamak vertical position feedback control [1]. The starting point for the model of the vertical stability dynamics is a rigid massless plasma which experiences a vertical force approximated as $F_V \sim I_p \times B_r(\text{axis})$. The vacuum vessel provides a restoring force via the radial field resulting from the image currents induced in it. The vessel currents are usefully decomposed into orthogonal modes, of which the first antisymmetric mode dominates, in the sense that both its coupling to the vertical movement and its decay time are largest. Active coils were added to the model in terms of their mutual inductance to the vessel current modes and their radial field at the plasma axis. Such a simple system as this leads to a low order dynamical system model, 2nd order when only one active pair of poloidal field control coils is considered.

Out of this very simple formulation, came the concept of hybrid vertical control. It was realised that no one active coil placement or control algorithm can usefully stabilise the vertical position. However, the hybrid system, in which the main, slower, radial field was provided by an outboard coil and a faster but weaker radial field was provided by inboard coils, seemed extremely promising, allowing the control of plasmas up to decay indices close to the ideal MHD positional stability limit with considerably reduced power requirements.

Experiments to study the stabilisation of high decay index plasmas were carried out on the DIII-D tokamak, R_0, a= 1.67, 0.67 m, B_ϕ = 2T, I_p = 1MA. The poloidal field system is extremely flexible, with 18 independantly controllable coils. The equilibrium field is programmed using all the coils, and the vertical position control is superimposed onto selected coils. The vertical position is detected using a combination of flux-loop signals and radial field coils.

The vertical feedback control was performed using two proportional plus derivative (PD) controllers (Gz+sGv) controlling either the F7 coils or the F7 and F2 coils

independently. A minimum number of active coils was used in order to reduce the imposed complexity of the control dynamics.

As a first step towards an understanding of the dynamical system which we must improve, we performed a set of perturbation injection experiments with a square-wave modulation (5Hz) introduced into the reference signal of the control loop. The vertical excursion was of the order 1-2 cm, ≈ 1% of the plasma height. We inspect the system response for three characteristic discharges. Figure 1a) shows a typical discharge. The response is damped, with a rise time of around 20msec. The controller in this case had a large value of $G_V \approx -10^{-2}$ and a large value of $G_Z = -2$. Figure 1b) shows an oscillating but damped response, still stable therefore, with much less velocity gain. Finally, Fig. 1c), we obtain an oscillatory but unstable discharge, with similar gains, but at a slightly larger decay index. The positive pole in the third case remains small, around $Re(s_1) \sim 10 sec^{-1}$, being vertically unstable in the closed loop control sense rather than the ideal MHD sense. In these three cases, there is no evidence of any difference between the response of the magnetic and soft X-ray measurements of the vertical position.

A system identification tool [2] was developed for dynamical studies on TCA. The modelling was carried out on the data of Fig. 1a), averaging 3 square-wave cycles to increase the signal-to-noise ratio. The results in Fig. 2 show the measured response, dashed curve, and the modelled response, solid curve, to the square wave stimulus also shown. The model agreement improves as the determinant order increases to second order, after which the character is barely modified by the presence of more degrees of freedom. This saturation is seen in the correlation coefficient which increases up to a second order denominator. The pronounced characteristic knee when the model order exceeds the identified system order is frequently used as a criterion to choose the optimum model structure. Since the experimentally observed behaviour of the vertical position control loop is that of a low order system, we should be able to model it with a low order model such as the three determining equations which were derived in [1]. The control strategy should be developed within the framework of this simple model.

A series of discharges was run to check the controller action. When both proportional and derivative controller gains are varied, the behaviour of the square wave response was in qualitative agreement with the model.

As the vertical field decay index is increased, the results of [1] predicted an increase in the more dangerous root of the transfer function, and subsequent loss of control at a certain decay index. Above the coil critical decay index, n_a, there is no stabilised solution without derivative gain, and above the vacuum vessel decay index, n_c, there is no stabilised solution at all. Prior to this systematic study, the loss of vertical control had always occurred in DIII-D at a decay index of $n_a = -0.95$, well below the value of $n_c = -1.35$ which was calculated for the discharges studied, but close to the coil critical decay index. Figure 3 shows the square-wave response as the decay index is ramped from $n \approx 0.8$ to $n \approx -1.1$, with the controller gains set at $-G_Z = 0.20$, $-G_V = 1.0$. The response at the start of the ramp shows very little overshoot, being roughly critically damped ($t \approx 1.3$ sec.). As the decay index increases negatively, the response starts to overshoot ($t \approx 1.5$ sec.) and by $t \approx 1.7$ sec. the response is oscillatory. The oscillatory nature increases, corresponding to a more inertial system until at $t = 2.1$ sec the oscillation becomes unstable and a disruption ensues. In this one discharge we have seen the characteristic behaviour predicted in [1], namely that of a low order system whose stability boundaries are moving as the decay index varies.

Since the G_Z, G_V settings determine the closed-loop poles, we expect the operational range to vary with the gains. Figure 4 shows three discharges (crosses) which were obtained

by increasing G_V. In each case we measure the maximum value of the decay index achieved just before the disruption, and plot this value against the velocity gain used. The decay index achieved increased significantly following the addition of a significant derivative gain, from - 0.96 to - 1.16. Between G_V = - 3 and G_V = - 10 little improvement was found, as predicted. The value of n = - 1.16 was the limiting value calculated for vertical control by the F7 coils, and is well below the critical decay index of the vacuum vessel for these discharges ($n_c \sim 1.35$).

The hybrid control was tested on the same series of discharges for comparison, and the results are illustrated in Fig. 4. Adding only derivative feedback to the F2 coils (G_{VF}), a value of n = - 1.18 was achieved at low G_V = - 0.1. This already exceeded the F7 coil optimum, n = - 1.16. Increasing G_V to - 10, the velocity feedback on the F2 coils still produced a significant increase in the decay index, up to 97 % of the calculated maximum, shown by the asterisks and rectangle.

These data show that the predictions of a simple vertical control model can lead to significant improvements in the achieved decay index, by providing a simple clear picture of the controlled system. Such an improvement was in addition obtained with a small amount of experimental data, contrary to the habitual trial and error optimisation.

The aim of the control optimisation was to achieve the higher plasma elongations which result from the higher decay indices. This series of discharges was run in abnormally dirty, high q, i.e. high l_i, conditions. When l_i is large, $\approx$ 1.4, the decay index necessary to achieve high elongation, K > 2.5, exceeds the vessel critical decay index. However, the elongation achieved with hybrid control, up to K = 2.38, exceeded previous attempts.

Acknowledgement - Two of the authors (E.A. Lazarus and J.B. Lister) would like to thank Ron Stambaugh, Tony Taylor and the DIII-D physics staff for their hospitality during their detachment at General Atomics. The work described was partly funded by the Fonds National Suisse de la Recherche Scientifique.

REFERENCES

[1] LAZARUS, E.A., LISTER, J.B, NIELSON, G.H., to be published
[2] MORET, J.M., Thesis No. 758, EPFL, Switzerland. Lausanne Research Paper LRP 258/88.

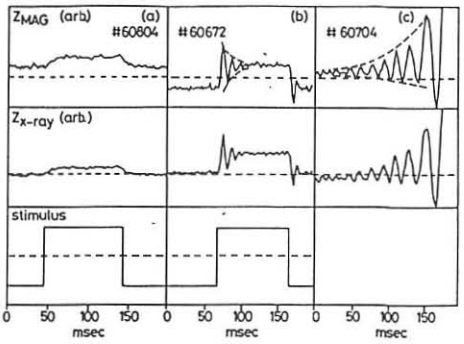

Fig. 1: Square-Wave Responses
a) overdamped **b**) underdamped
c) unstable oscillatory

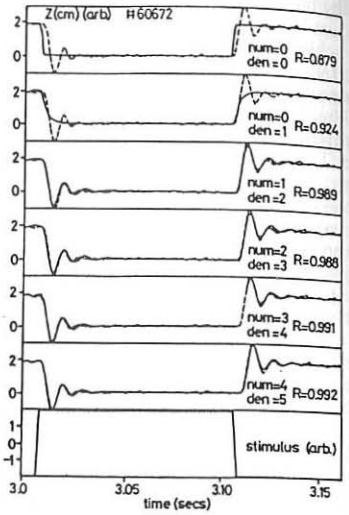

Fig. 2: Low-order dynamic modelling

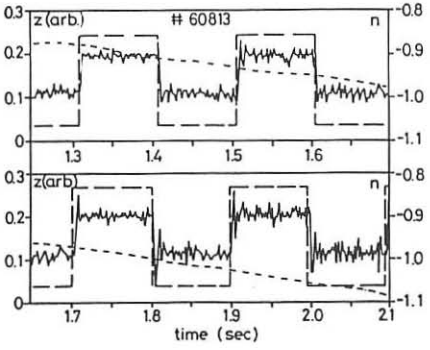

Fig. 3: Varying response during n-ramp

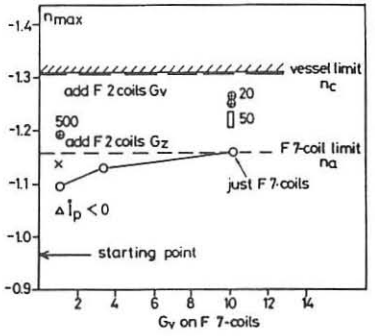

Fig. 4: Improvements with hybrid control

CONFINEMENT SCALING STUDIES IN DIII–D

D.P. Schissel, N. Brooks, K.H. Burrell, J.C. DeBoo, R.J. Groebner, G.L. Jackson, A.G. Kellman, L. Lao, M. Matsumoto,* T.H. Osborne, R.D. Stambaugh, S. Wolfe,† and the DIII–D Research Team

General Atomics, San Diego, California, USA
*Japan Atomic Energy Research Institute, JAPAN
†Massachusetts Institute of Technology, USA

Understanding and increasing the energy confinement time ($\tau_E \equiv W/P$) remains a primary goal of fusion research. This objective is being pursued on DIII–D via investigations of τ_E in limiter and single– and double–null divertor discharges with Ohmic heating[1] and neutral beam heating.[2,3,4] This paper examines the dependence of τ_E on ion mass, plasma current (I_p), neutral beam power (P_b), toroidal field (B_T), and safety factor (q). The data presented is for neutral beam injection in the direction of the plasma current, although τ_E is the same for both co– and counter–injection.[5]

Confinement is best in pure deuterium H–mode discharges with a confinement quality of 120 ms/MA that is independent of power for 3 to 6.4 MW of NBI at 1.0 MA. H–mode τ_E in pure hydrogen plasmas is about a factor of 2 smaller than measured deuterium τ_E values, while discharges operated in a mixture of hydrogen and deuterium are in between the two extremes. Confinement in pure helium H–mode plasmas is similar to those obtained in pure hydrogen. Unlike the deuterium H–mode, H–mode τ_E in hydrogen, helium, and mixed H/D plasmas decreases with increasing power. This decrease in H–mode τ_E with increasing power is accompanied by an increase in the ELM frequency. The change in ELM behavior during changes in neutral beam power makes it difficult to determine whether the intrinsic confinement properties of the plasma are changing or simply that the ELMs are becoming more prevalent and therefore adversely affecting the confinement. The total power dependence and lack of isotope dependence of L–mode confinement is well described by Kaye–Goldston scaling.[6] The dependence of τ_E with power is illustrated in Fig. 1.

In a mixed H/D H–mode plasma, τ_E increases with I_p at constant P_T for $q_{95} > 3$ (Fig. 2). Confinement quality is 85 ms/MA at 5.6 MW for full field operation (2.1 T). In the regime where $q_{95} > 3$, incremental confinement ($\tau_E^{inc} \equiv \Delta W/\Delta P$) also increases with I_p at a rate of 40 ms/MA. Transport analysis of these discharges indicate that as I_p is raised both χ_e and χ_i decrease. In deuterium and H/D mixture H–mode plasmas, τ_E is independent of B_T for $q_{95} > 3$. For $q_{95} < 3$, τ_E is independent of I_p and instead is proportional to B_T. The degradation in τ_E/I_p is not related to reaching a saturated Ohmic level of confinement as expressed by Shimomura, *et al.*,[7] despite the similarity in the B_T dependence. For $q_{95} < 3$, the measured τ_E decreases with P_b, while Ref. 7 predicts a saturation at the same value of τ_E that is independent of P_b.

Confinement times that have exceeded saturated Ohmic confinement have been observed in high current NBI H–modes and high current, low B_T Ohmic H–modes. With 4 MW of NBI, mixed H/D H–mode τ_E at 2.0 MA can exceed saturated Ohmic confinement by 30% to 40%. As the auxiliary power is increased to near 10 MW, τ_E reduces only to the Ohmic value. These results are illustrated in Fig. 3. These data dispute the contention that τ_E with auxiliary heating cannot exceed Ohmic τ_E (e.g. Shimomura scaling[7]). The Ohmic H–mode requires low q and low B_T operation and is always triggered by a sawtooth. The Ohmic H–mode is a transient event (~175 ms) that is ELM–free and terminated by increasing edge radiation from low Z impurities. Time dependent confinement analysis prior to significant impurity accumulation is performed utilizing magnetic measurements. This analysis indicates that τ_E in the Ohmic H–mode exceeds the saturated Ohmic τ_E by about a factor of two (Fig. 4). The solid line in Fig. 4 is the prediction from Neo–Alcator scaling.[8] Unlike other regimes of improved confinement (pellet,[9] IOC,[10] counter–injection[11]) that require peaked density profiles, the density profiles in the Ohmic and neutral beam heated H–mode are broad.

The H–mode has also been obtained in discharges which are defined by a material limiter on the inside wall (centerpost graphite tiles). This limiter H–mode[12] exhibits the standard divertor H–mode features of a decrease in edge recycling, an increase in density, and an increase in τ_E. These hydrogen/deuterium mixture plasmas have only been attempted at low q where their τ_E is 50% greater than similar L–mode plasmas (Fig. 5). The τ_E obtained with the limiter H–mode is near the Ohmic value and is similar to previous low q, high β single null H–mode divertor discharges. The best values of τ_E are obtained with either longer He glow between discharges or overnight baking and He Taylor discharge cleaning. Limiter H–mode density profiles are broader than in their limiter L–mode counterpart. Greater values of β should be possible with the the limiter H–mode as compared to the single null H–mode due to the greater elongation and triangularity attainable.

Comparison of Doublet III (a = 0.41 m, R = 1.45 m) and DIII–D (a = 0.65 m, R = 1.69 m) L–mode limiter data indicates that $\tau_E/I_p\sqrt{\kappa}$ is the same for both tokamaks (35 ms/MA at 6 MW). This result implies that either τ_E has no dependence on a and R individually or that their dependencies are offsetting, for example as described by Kaye–Goldston scaling.[6] The Kaye–Goldston scaling of $\tau_E \propto R^{1.65}a^{-0.49}$ implies a ratio of DIII–D to Doublet III τ_E of 1.0. A collaboration with JET is planned in the near future to do size scaling experiments on H–mode discharges.

This work was supported by the U.S. Department of Energy under Contract No. DE-AC03-84ER51044.

REFERENCES

1. Osborne, T.H., *et al.*, GA–A19362 (1988), to be submitted to Nuclear Fusion.
2. Burrell, K.H., *et al.*, Phys. Rev. Lett. **59** (1987) 1432.
3. Schissel, D.P., *et al.*, to be published in Nuclear Fusion **29** (1989).
4. Burrell, K.H., *et al.*, GA–A19443 (1988), to be published in Plasma Physics and Controlled Nuclear Fusion Research 1989 (Proc. 12th Int. Conf. Nice, 1988).
5. Schissel, D.P., *et al.*, GA–A19503 (1988), submitted to Phys. Fluids B.

6. Kaye, S.M., *et al.*, Nuclear Fusion **25** (1985) 65.
7. Shimomura, Y., *et al.*, JAERI M 87–080 (1987).
8. Parker, R.R., *et al.*, Nuclear Fusion **25** (1985) 1127.
9. Greenwald, M., *et al.*, Phys. Rev. Lett. **53** (1984) 352.
10. Söldner, F.X., *et al.*, Phys. Rev. Lett. **61** (1988) 1105.
11. Gehre, O., *et al.*, Phys. Rev. Lett. **60** (1988) 1502.
12. Jackson, G.L., *et al.*, Bull. Am. Phys. Soc. **33** 4T20 (1988) 1963.

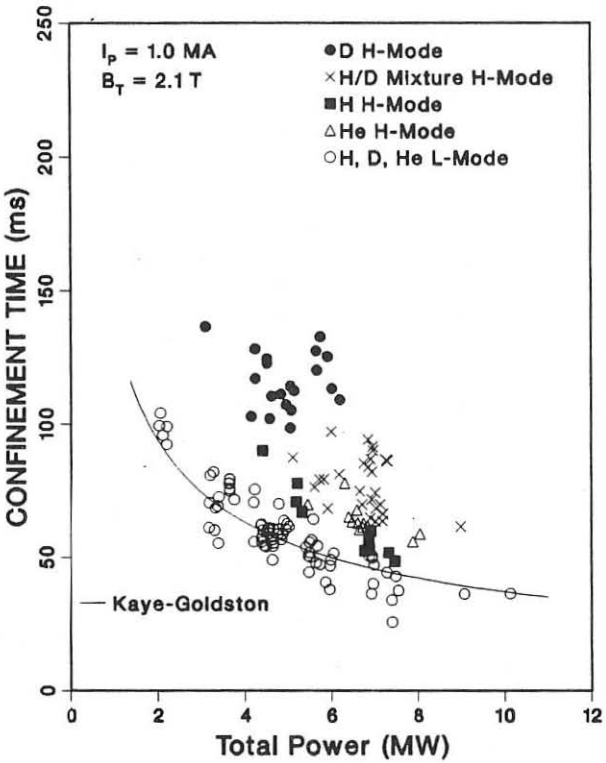

Fig. 1. Single null divertor H–mode and L–mode τ_E versus total input power for different ion species. The prediction of Kaye–Goldston L–mode scaling is shown for comparison with the L–mode data.

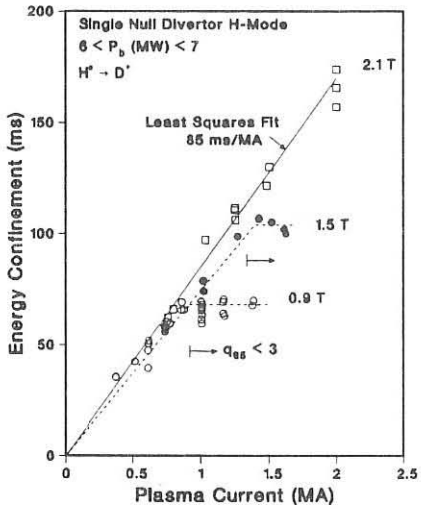

Fig. 2. H–mode energy confinement versus plasma current.

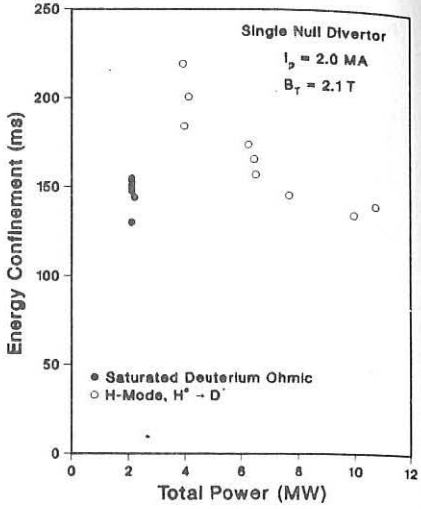

Fig. 3. Ohmic and H–mode energy confinement time versus total power.

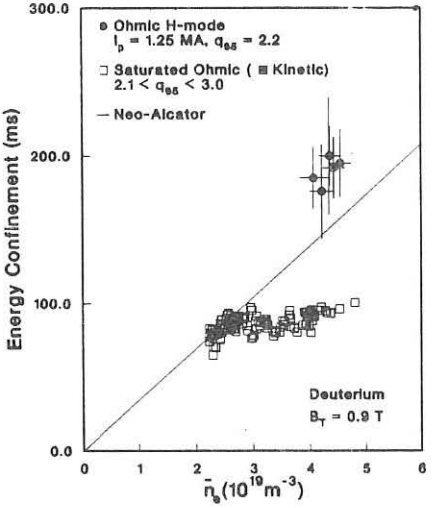

Fig. 4. Normal Ohmic and H–mode Ohmic energy confinement time vs. density deduced from magnetic measurements.

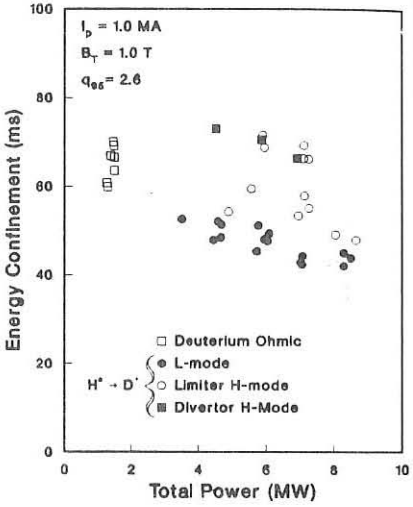

Fig. 5. Ohmic, L–mode, and H–mode energy confinement time versus power. The limiter data has the separatrix at least 3 cm behind the limiting surface.

ANALYSIS OF TOROIDAL ROTATION DATA FOR THE DIII–D TOKAMAK

H. St. John, U. Stroth,* K.H. Burrell, R. Groebner, J. DeBoo, and P. Gohil

General Atomics, San Diego, California 92138-5608, U.S.A.
*Max Planck Institut für Plasmaphysik, Garching, Federal Republic of Germany

INTRODUCTION

Both poloidal and toroidal rotation are observed during routine neutral beam heating operation of the DIII–D tokamak. Poloidal rotation results and the empirical techniques used to measure toroidal and poloidal rotation speeds are described by Groebner et al.[1] Here we concentrate on the analysis of recent measurements of toroidal rotation made during diverted, H–mode operation of the DIII–D tokamak during co– and counter–neutral beam injection of hydrogen into deuterium plasmas. Similar studies have been previously reported for Doublet III,[2] ASDEX,[3] TFTR,[4] JET,[5] and other tokamaks.

Our results are based on numerical inversions using the transport code ONETWO,[6] modified to account for the radial diffusion of toroidal angular momentum. In its simplest, time-independent form, the momentum equation is

$$\nabla \cdot \left(\vec{\Gamma}^{\nu}_{w} + \sum_{i} \vec{\Gamma}^{c}_{w,i} \right) = T \quad , \tag{1}$$

where $\vec{\Gamma}^{\nu}_{w}$ and $\vec{\Gamma}^{c}_{w,i}$ are the viscous and convective fluxes. The torque T is similar to the prescription given by Goldston,[7] neglecting field ripple and radial diffusion of fast ions, but accounting for the neutral charge exchange drag term using neutral speeds determined from the model developed by Burrell.[8] Inclusion of the above equation in the ONETWO transport prescription induces a coupling to the electron and ion energy equations which is not significant for the results presented here.

RESULTS

Unlike ASDEX[9] we have not observed significant density peaking during counter injection in DIII–D.[10] However rotation speed profiles do show peaking, with central rotation speeds two to three times as high as similar co-injection discharges, as is obvious from examination of Fig. 1. The increased central rotation speed during counter injection is generally accompanied by reduced rotation speeds over the transport region of the plasma, enhancing the velocity shear (and hence viscous heating) while reducing the stored angular momentum to values closer to co injection discharges. The very low (less than 0.2×10^7 cm/sec) central rotation speeds observed for some of the co-injected high beta discharges is probably associated with MHD activity although low m/n modes were not observed.

Examination of Figs. 2 and 3 reveals that the energy and angular momentum confinement times for co and counter injection are approximately equal with similar dependencies on plasma current and beam heating power. The discharges shown in Fig. 2 have $q_{95} > 3.2$ with the momentum and energy confinement times scaling as previously reported for the energy confinement time during co-injection.[11] Although it cannot be supported statistically, the figure suggests that angular momentum confinement may be better for counter-injection at high currents. We do not have the experimental data necessary to resolve this conjecture at the present time but it would be consistent with scalings reported for ASDEX,[9] where an increase in both energy and momentum confinement times is observed.

The behavior of the angular momentum and energy confinement times as a function of absorbed neutral beam power (P_a) for a range of densities, toroidal fields, and plasma currents is given in Fig. 3. There is some evidence that the energy and momentum confinement for these deuterium H–mode plasmas decreases as P_a increases at low toroidal fields [Fig. 3(a)]. This dependency appears to be largely lost at higher toroidal fields [Fig. 3(a,b,c)], with the momentum confinement time closely tracking the energy confinement time. If there is a difference in scaling for counter-injection, we are unable to resolve it due to the limited data available.

The plasma viscosity for four different discharges is shown in Fig. 4. Agreement between the average thermal energy and momentum diffusivities to the degree shown is considered very good, given the inherent uncertainty in these profiles. We have not plotted the diffusivities out to the plasma edge ($\rho = 1.0$) since complicated edge effects, not accounted for in our analysis, are expected to be dominant there.

The Mattor-Diamond[12] theory of ion temperature gradient driven turbulence predicts that ion thermal and momentum diffusivities are equal when η_i modes are active. Our results show consistency with this theory when the observed η_i is approximately equal to 1.5, as in Fig. 4(a). The remaining cases shown in Fig. 4 fall well outside this range due to the flat density profiles observed during H–mode. In all of the cases investigated we found that the enhancement of the turbulence by the sheared toroidal velocity profile, as predicted in Ref. 12, is an insignificant contribution to the total thermal and momentum diffusivities, even in the high shear counter-injection cases.

CONCLUSION

We obtained angular momentum confinement times in a range from ~30 to ~120 msec, comparable to energy confinement times and following the same scaling laws. For counter-injection, where peaked rotation profiles with central rotation speeds as high as $\sim 1.3 \times 10^7$ cm/sec have been observed, the angular momentum confinement time is close to the values for co-injection at the same absorbed power. The angular momentum diffusivity is found to be in good agreement with the average of the ion plus electron thermal diffusivities.

Evaluation of η_i indicates that ion temperature gradient-driven turbulence is expected to be active, perhaps explaining the equality of thermal and momentum diffusivities. However, most cases investigated to date have η_i values significantly larger than the critical value ($\eta_i^c \approx 1.5$ or $\frac{L_{T_i}}{R} \approx 0.2$) so that direct comparison with experimental data was not possible using our time independent analysis technique. Further investigations using time dependent threshold models developed by Dominguez and Waltz[13] will be made in the future.

This work was supported by U.S. Department of Energy Contract No. DE-AC03-89ER51114.

REFERENCES

1. Groebner, R.J., Gohil, P., Burrell, K.H., Osborne, T.H., Seraydarian, R.P., St. John, H., this conference.
2. Burrell, K.H., *et al.*, Nuclear Fusion **28**, 1988 (3).
3. Roberts, D.E., *et al.*, 15th European Conference on Controlled Fusion and Plasma Heating, Dubrovnik, May 16, 1988, p. 15.
4. Scott, S.D., *et al.*, ibid, p. 103.
5. Hawkes, N.I., *et al.*, ibid, P. 1061.
6. Pfeiffer, W.W., *et al.*, General Atomics Report GA–A16178, December 1980.
7. Goldston, R.J., Proceedings of Course and Workshop: Basic Physical Processes of Toroidal Plasmas (Varenna, 1985) p. 165.
8. Burrell, K.H., J. Comp. Phys. **27** (19768) P. 88.
9. Fussmann, G., *et al.*, Twelfth International Conference on Plasma Physics and Controlled Nuclear Fusion Research, IAEA, Nice, France, October 1988, IAEA-CN-50/A-3-1.
10. Schissel, D.P., *et al.*, General Atomics Report GA–A19503, December 1988.
11. Schissel, D.P., *et al.*, General Atomics Report GA–A19243, February 1988.
12. Mattor, N., Diamond, D.H., Phys. Fluids **31**, (1988) p. 1180.
13. Dominguez, R., and Waltz, R., General Atomics Report GA–A19342, November 1988.

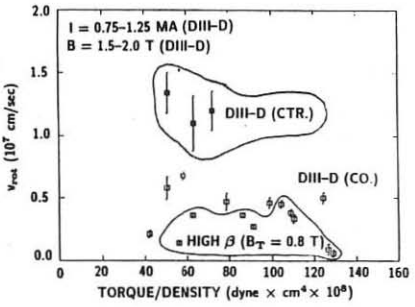

Fig. 1. Central rotation versus torque per ion/m^3

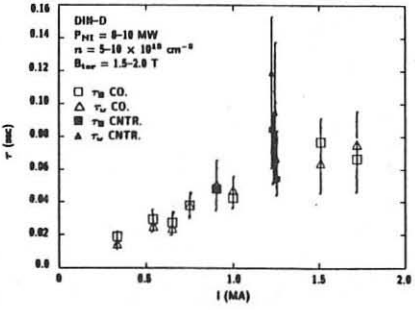

Fig. 2. Energy and momentum confinement time versus plasma current

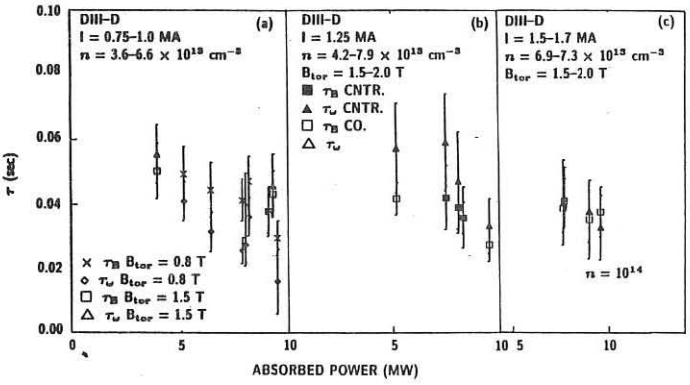

Fig. 3. Energy and momentum confinement time versus absorbed power

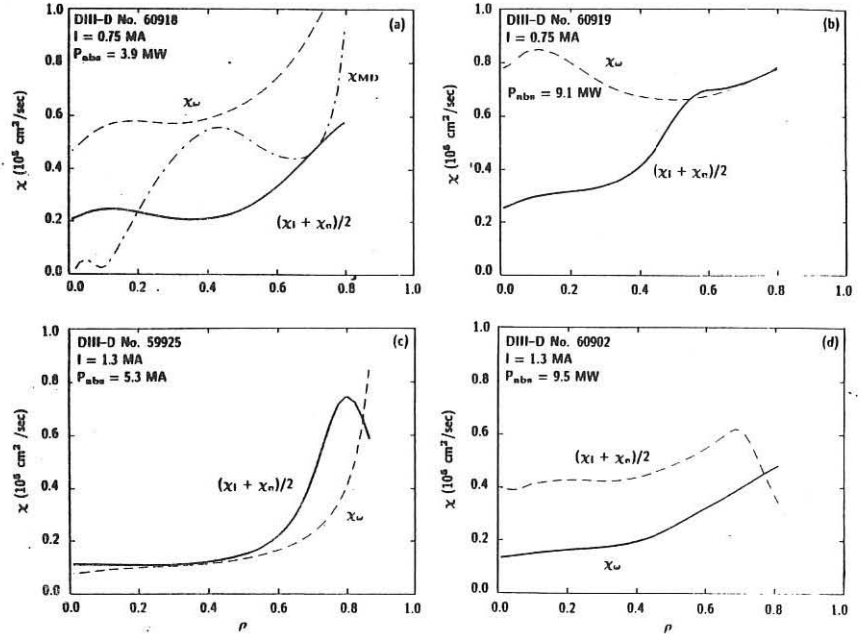

Fig. 4. Comparison of thermal and momentum diffusivities.

RESULTS FROM THE DIII-D MILLIMETER-WAVE REFLECTOMETER

T. Lehecka, E.J. Doyle, R. Philipona, N.C. Luhmann, Jr., W.A. Peebles
C.L. Hsieh,* T.N. Carlstrom,* R.P. Seraydarian,* and the DIII-D Group*

Institute of Plasma & Fusion Research, Univ. of California, Los Angeles, CA, USA
*General Atomics, San Diego, California, USA

INTRODUCTION

The limited viewing access and asymmetric D-shaped plasmas on DIII-D make millimeter-wave reflectometry an attractive diagnostic for density profile and fluctuation measurements. For a reflectometer the Abel inversion of the phase information is performed *along* the line of sight, so only a single viewing chord, and no symmetry assumption, is required for density profile measurements. The quantity required for the profile determination is a measure of the propagation delay (phase or time) to the cutoff layer and back, either continuously or at several points on the density profile. [1,2,3,4]

In its final form the reflectometer system for DIII-D will be composed of two independent reflectometers; a seven channel narrowband reflectometer for density profile and fluctuation measurements, primarily in the plasma edge region, and a broadband reflectometer for full density profile measurements.[5] Laboratory testing of the broadband system is nearly complete, and we are aiming for installation on DIII-D in early 1989. In this paper we will restrict our attention to some of the results which have been obtained with the narrowband reflectometer.

DESCRIPTION OF THE SYSTEM

The multichannel reflectometer has been operational on DIII-D since mid 1988. The operating frequencies are 15, 24, 32, 40, and 50 GHz, corresponding to cutoff densities of 0.2, 0.7, 1.3, 2.0, 3.1 $\times$ 10^{13} cm^{-3} for the O-mode propagation which is utilized. Channels at 60 and 75 GHz will be added in the near future. The reflectometer views radially across the midplane of DIII-D.

This multichannel system has two modes of operation: Frequency Modulated (FM) which monitors the *position* of the reflecting layer, and fixed frequency where *fluctuations and movements* of the cutoff layer are monitored. Modulated operation is basically an FM radar measurement of the propagation delay time to the reflecting layer. A block diagram of a single channel is shown in Fig. 1. A novel feature of this system is that the Gunn oscillator is modulated by a combination of three triangle waves, to reduce the step error associated with a short range FM radar.[6] The radiation propagates to the tokamak through approximately 5 m of fundamental waveguide. Homodyne detection is employed with the local oscillator generated by leakage in the directional coupler and spurious reflections in the microwave circuit. A single horn antenna is used for both transmission and reception. Before propagation into DIII-D the 15, 24, 32, and 40 GHz radiation are combined into a single waveguide, as will be the 50, 60, and 75 GHz radiation. This multiplexing is accomplished in suspended stripline filter circuits, which also separate the individual frequencies after reception. The IF signal produced in the single ended mixer is amplified by 40 dB. The IF frequency from signals in the plasma is

in the 2–4 MHz range. The high pass filter has a 2 MHz 3 dB point, effectively reducing stray signals from spurious reflections. The frequency of the IF signal, proportional to the propagation delay time, is measured by the discriminator which functions as a frequency to voltage converter. The discriminator output is low pass filtered at 500 Hz, with the resulting output voltage proportional to delay time. Fixed frequency operation is achieved by simply removing the modulation on the Gunn oscillator, and replacing the high pass filter/discriminator/low pass filter combination with an antialiasing low pass filter.

REFLECTOMETER RESULTS

An example of FM operation is shown in Fig. 2, with the y–axis voltage inversely proportional to the propagation delay time (or optical path length) to the reflecting layer. Plots of the line averaged density measured by the CO_2 interferometer, and the H_α emission from the divertor region are shown for comparison during this H–mode discharge. For a better understanding of these signals let us look at the 32 GHz channel ($1.3 \times 10^{13} cm^{-3}$). Before the discharge the radiation is reflected from the inside wall of the vessel, corresponding to a voltage of approximately zero. At t=0 the plasma is initiated, the group index of refraction inside the vessel begins to increase, but the radiation is still reflected from the inside wall. This increases the propagation delay, thus the IF frequency increases. Normally, in the discriminator's linear operating range, voltage increases with decreasing frequency. As the delay increases over the inside wall value however, this appears as an *increasing* voltage because the discriminator is no longer operating in its linear range and the frequency to voltage characteristics of the discriminator are not monotonic. It should be noted that this ambiguity is not a problem when the radiation is reflected from the plasma, as the delay time is always less than that from the inside wall.

At t=270 ms the plasma reaches the cutoff density for this frequency at some point in the plasma, and the radiation is reflected. This is indicated by the sharp drop in the voltage, and the discriminator is now operating in its linear range. As the plasma continues to develop, this cutoff layer moves toward the outside of the vessel, as shown by the increasing voltage, reaching its flattop value at t~1000 ms. At t=1300 ms an L to H–mode transition occurs, but this density layer moves only a small amount. Response to the giant ELMs during the H–mode phase is also observed. If we assume a constant index of refraction, an increase in voltage represents an outward movement, with a voltage decrease indicating an inward movement. Each of the 5 channels shows a slightly different response to the L–H transition and the ELMs. At the L–H transition, an increase in the edge density gradient is indicated, as expected from Thomson scattering measurements.[7] The effect of the ELMs on the edge density gradient is currently being analyzed. Inconsistencies between an absolute system calibration performed with a mirror inside the vacuum vessel during a vent and the measurements from the plasma have, to date, precluded an accurate determination of the density profile via Abel inversion techniques. However, the basic features of the profile modifications are able to be clearly observed.

This multichannel system can also be operated in a fixed frequency mode to investigate either low frequency MHD fluctuations or higher frequency microturbulence. The system bandwidth is limited to 400 kHz by the digital sampling rate (800 kHz). High frequency microturbulence exhibits interesting behavior during L and H–mode operation. Figure 3 shows the frequency spectra of these fluctuations on the 40 GHz channel during L–mode, quiescent H–mode, and ELM phases of a single discharge. During the quiescent H–mode the high frequency fluctuations are significantly reduced from those during L–mode and ELM phases. This feature is most pronounced on the 32 and

40 GHz channels, is only slightly less noticeable at 24 GHz, and insignificant at 15 GHz where the spectra are quite narrow during both L and H–mode phases. Depending on the discharge conditions the high frequency fluctuations on the 50 GHz layer may or may not be reduced. These differences in behavior between the channels show the variations of the density fluctuations in several regions of the plasma. The 15 GHz channel is located well outside the separatrix, the 24, 32, and 40 GHz layers span from just outside to just inside the separatrix, and the 50 GHz layer is slightly further into the plasma. This is shown on the Thomson scattering density profile in Fig. 4. Note that the Thomson measurement is made along a vertical chord, with the transformation from vertical to radial dimensions given roughly by $\Delta z = 2\Delta r$. In the edge region with steep density gradients the cutoff layers for these channels are located only a few centimeters apart, but the fluctuation spectra are noticeably different. These data also demonstrate a major advantage of the reflectometer for fluctuation measurements, excellent spatial resolution.

CONCLUSION

A five channel reflectometer system has been installed on DIII–D, and has provided unique information regarding the electron density profiles and fluctuations. Significant changes in both the profile and fluctuations associated with ELMs and the L to H–mode transition have been observed. Simultaneous operation of the broadband reflectometer, to be installed in the near future, for profile measurements and the multichannel system for fluctuation studies should prove useful for issues such as MHD mode localization, determination of magnetic island widths, and the spatial distribution of density fluctuations associated with drift waves and other microturbulence. Additionally, it should be noted that a collective far infrared scattering system was recently installed on DIII–D. The fluctuation wavenumber resolution of the scattering system, combined with the spatial resolution of the reflectometer will provide an improved capability for density fluctuation measurements on DIII–D.

Work was supported by U.S. DOE Contract No. DE-AC03-84ER51044 through General Atomics P.O. No. SC076524.

REFERENCES

1. Simonet, F., Rev. Sci. Instrum. **56**, 664, (1985).
2. Bottolier–Curtet, H. and G. Ichtchenko, Rev. Sci. Instrum. **58**, 539, (1987).
3. Anibitarte, E., *et al.*, J. Phys. D, 1384, (1988).
4. Prentice, R., *et al.*, These proceedings.
5. Lehecka, T., *et al.*, Rev. Sci. Instrum. **59**, 1620, (1988).
6. Katano, T., Electr. and Comm. in Japan **57–B**, 90, (1974).
7. Gohil, P., *et al.*, Phys. Rev. Lett., **61**, 1603, (1988).

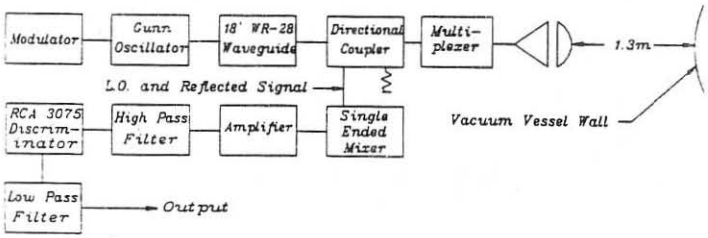

Fig. 1. Narrowband reflectometer block diagram.

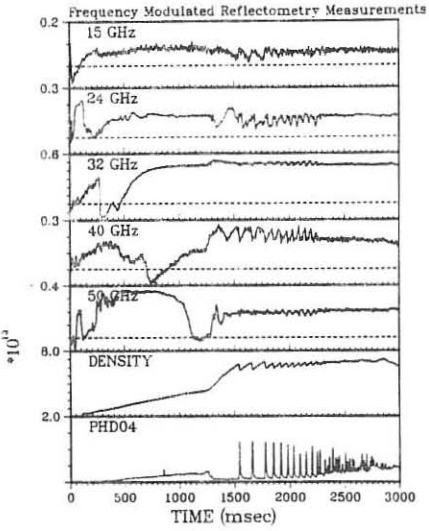

Fig. 2. Narrowband reflectometry data.

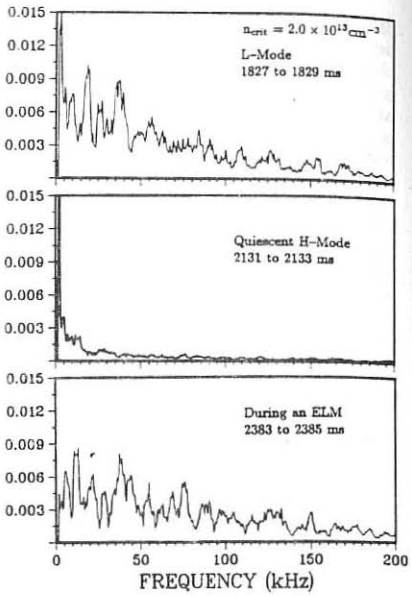

Fig. 3. Fixed frequency reflectometer density fluctuation spectra.

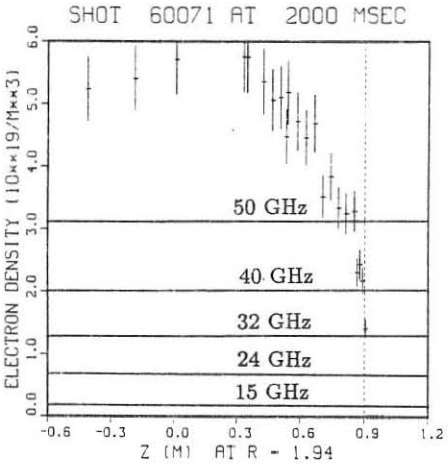

Fig. 4. Thomson scattering density profile.

ICRF POWER-DEPOSITION PROFILES AND HEATING IN MONSTER SAWTOOTH AND PEAKED-DENSITY PROFILE DISCHARGES IN JET

V.P. Bhatnagar, A.Taroni, J.J. Ellis, J. Jacquinot, D.F.H. Start

JET Joint Undertaking, Abingdon, Oxfordshire, England OX14 3EA

1. INTRODUCTION : The ion-cyclotron resonance heating (ICRH) of JET tokamak has demonstrated, among other results, (a) that the plasma can undergo a transition to a new regime, the so called 'monster sawtooth' [1] in which the plasma enjoys long quiescent periods where there is little coherent MHD activity and the sawtooth instability is suppressed for durations of up to 3 s and, (b) that the pellet-produced peaked-density profiles can be reheated [2],[3] and sustained for up to 1.2 s resulting in high values of central electron and ion temperatures simultaneously and leading to an increased nuclear reactivity of the plasma. In this paper, we compare experimental results of electron and ion-heating in discharges that feature monster sawtooth with those in pellet-produced peaked-density profile discharges which were heated with ICRF.

Also we carry out a comprehensive analysis of ICRF-heated peaked-density profile discharges by a transport code to simulate the evolution of JET discharges and to provide an insight into the improved heating and confinement found in these discharges. In this analysis, the ICRF power-deposition profile in the minority-heating scenario is computed by the ray-tracing code BRAYCO [4] that self-consistently takes the finite antenna geometry, its radiation spectrum and the hot-plasma damping into account. The power delivered to ions and electrons is calculated based on Stix model.[5]

2. RESULTS :

(a) Monster Sawtooth: The ICRF minority heating generally produces 'giant' sawteeth where $T_{e0}(max)/T_{e0}(min) \cong 2$ compared to 1.1-1.2 in the ohmic phase and the sawtooth period is also increased by a factor of 2-3. The strong electron heating is related to the fact that during ICRH, a long minority-ion tail is produced which relaxes on the electrons and heats them predominantly. When the ICRF power is centrally deposited and exceeds a certain threshold (minimum $\cong$ 3 MW), monster sawteeth are produced generally when $q_{cyl} \cong 3.3$ and the stabilisation is beleived to be due to the presence of fast ions. [6] During the stable period, density and stored energy rise slowly but T_e saturates and the T_e-profile peaks which would lead to higher reactivity.

For limiter ICRH discharges, in Fig. 1 and 2, We plot T_{e0} and T_{i0} as a function of P_{TOT}/n_{e0} for a range of plasma currents I_p = 2-6 MA, where 0 refers to the central values. The data for 2-3 MA is mostly of monster sawtooth whereas for 5-6 MA, it refers to the usual giant sawteeth. For a given central confinement-volume, the data in Fig. 1 and 2 can be directly related to central electron and ion kinetic-energy confinement times respectively. A clear off-set linear behaviour is seen in the T_{e0}-plot whereas the T_{i0}-plot tend to saturate. This behaviour is a general characteristic of the ICRF minority-heating and will be compared to the particularly interesting case of peaked-density profile heating (see below). We note

that within the scatter of the data there is little difference in the central incremental confinement time for 2-6 MA which has been independently verified by a local analysis. [7]

(b) Peaked-Density Profile Heating : We present results of peaked-density profiles that are produced by pellet fuelling in the current ramp-up phase and are followed by ICRH in JET limiter discharges. In Fig. 3, we present time traces of RF-power launched, DD-reaction rate, T_{e0}, T_{i0}, and $<n_e>$ of a 3 MA shot in which a 4 mm pellet penetrates deep inside the plasma and produces $n_{e0} = 1 \times 10^{20}$ m^{-3} which slowly decays but the peaked-profile is maintained for 1.2 s (see Fig. 13 of Ref. 2). Due to cooling by the pellet, T_{e0} initially drops but the immediate application of ICRH heats electrons steadily. Initially the T_e-profile is flat but becomes more and more peaked as time evolves. Note that T_{i0}-rise initially steepens but T_{i0} then saturates. There is a crash at which time the peaked profile disappears and R_{DD}, T_{e0}, T_{i0} all drop though P_{RF} is still maintained. RF power delivered to electrons ($P_{e\infty}$) and ions ($P_{i\infty}$) and their profiles calculated by ray-tracing[4] for a peaked-profile discharge are shown in Fig. 4, where the symbol ∞ refers to the steady-state when the minority tail has been fully formed. Note that, due to higher density, a significant fraction of the minority power goes to background ions. Such a calculation made at a few time slices of this shot is plotted in Fig. 3. The steady-state calculation overestimates P_e and P_i. For electrons, the steady-state is reached in about a Spitzer time [5] τ_s and for ions it is even quicker. Generally, the error is largest at the start of the RF pulse but, decreases as time progresses. However, in the present case, τ_s = 30 ms at t = 43.2 s and increases to 0.6 s at t = 44.2 s. Relative to charateristic time of the variation $\cong$ 0.35 s, the error in P_i is small but, P_e is moderately overestimated. Note that initially a larger fraction of power is delivered to ions which is consistent with the rapid rise of T_{i0} which then saturates. The steady rise of T_e is related to the continuously increasing P_e. In these calculations peaking of T_e, T_i and n_e-profiles is appropriately taken into account. For central heating there is little difference in the (H)-minority power-deposition profile, but, the redistribution of power among electrons and deuterons depends sensitively on the local plasma parameters.

In Fig. 1 and 2, we compare the electron and ion heating of peaked-density profile dicharges heated with ICRF with the heating of broad-density profiles obtained both in monster and non-monster sawtooth dischrges. We note that T_{e0} is improved by about 35% but, the most important gain is obtained in the ion temperature which is increased by a factor of 2 and allows high T_{e0} and T_{i0} simultaneously which is not achieved otherwise. Also on a similar comparison (not presented), the neutron production rate is found to be higher by a factor of 4. The comparison shown in Fig. 1 and 2 demonstrates that the central confinement has improved significantly. But, there is only a small improvement when $<T_e>$ is compared at a fixed $P_{TOT}/<n_e>$. By another analysis, we find that with peaked-density profile heating, the global electron kinetic-energy confinement is about 20% better.

(c) Transport-Code Simulations : We use the Rebut-Lallia model [9] in our 1½-D transport code that solves the electron and ion energy-balance equations and the poloidal-field diffusion equation with neo-classical resistivity. The density profiles, the radiated-power profiles and Z_{eff} are taken from the JET experimental data base. The deposition profiles of the RF-power imparted to electrons and ions are computed by ray-tracing[4]. This permits the evaluation of χ_e and χ_i seperately and supplements the analysis presented in Ref. (10). The time evolution of T_e and T_i for several shots has been simulated but, for illustration here, results of T_e and T_i-profiles at two time-points before and after the 'crash' when the peaked profiles are lost (see Fig. 3) are presented. The temperature profiles after the crash are similar to the standard monster-like discharges and are simulated in the usual way[10] giving good agreement with experimental profiles as shown in Fig. 5(a). However, to reproduce the temperature profiles in the 'good confinement-phase' (before the crash) where the density profile is peaked in the central region ($\rho/a < 0.5$), the values of the

electron and ion heat-conductivities are required to be reduced by a factor of 2 and 4.5 respectively in the inner-half radius. With such a prescription the characteristic profiles of improved confinement are well reproduced as shown in Fig. 5 (b). We note that though the values of χ_e and χ_i were reduced from the normal monster-like values based on the ray-tracing calculations of power deposition, these values, however, remain 'anomalous' in the region $0.2 < \rho/a < 0.8$. The coefficients can be calculated with confidence in this region as most of input power is deposited here whereas the radiation takes place outside this region.

3. CONCLUSIONS : In the ICRF heating of peaked-density profile in JET limiter discharges, we find typically that T_{i0} is higher roughly by a factor of 2 and T_{e0} roughly by 35 % at a fixed P_{TOT}/n_{e0} when compared to non-peaked profile cases. Also, on a similar comparison, the neutron production rate is found to be higher roughly by a factor of 4. The central confinement improves significantly whereas there is about 20% improvement in global electron kinetic-energy confinement. For central heating, the power-deposition profile changes little with the peaking factor but ion heating is improved in the pellet case due to a higher collisionality between the background ions and the energetic minority. Full ray-tracing calculations of power transferred to electrons and ions are consistent with the rate of rise of T_{e0} and T_{i0} in peaked-profile cases. The transport-code simulation of these discharges reveals that there is a reduction of both χ_e and χ_i in the central region of the plasma in the ICRF heated peaked-profile discharges. However, identification of the physical mechanism(s) that play a role in this improvement must await further evaluation.

ACKNOWLEDGEMENT : We wish to thank our colleagues in the JET team, especially the RF plant team, joint JET-USDOE pellet group, the tokamak operation team and those operating the diagnostics used in the experiments reported in this paper.

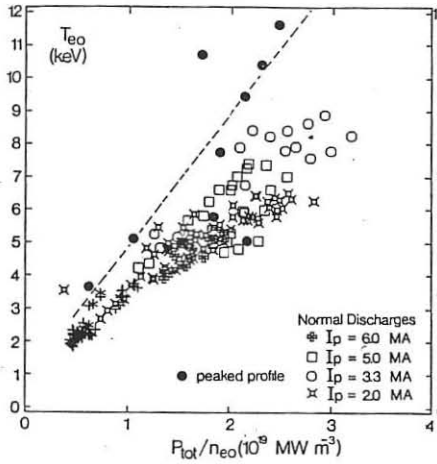

FIG. 1. A plot of T_{e0} vs P_{tot}/n_{e0} for peaked profile and normal discharges. Macroscopic data analysis does not reveal any insight as to why two peaked-profile shots performed poorly.

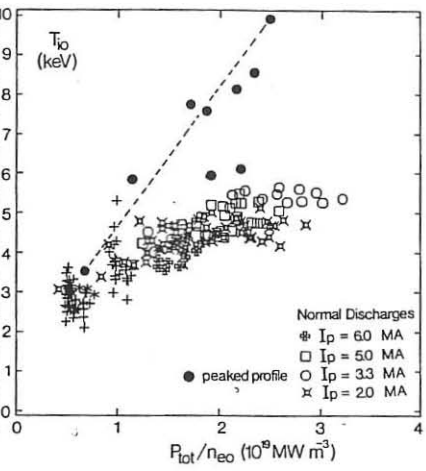

FIG. 2. A plot of T_{i0} vs P_{tot}/n_{e0} for peaked profile and normal discharges. See remark in Fig. 1.

REFERENCES :
(1) D.J. CAMPBELL et al, Phys. Rev. Letters, 60, (1988) 2148.
(2) J. JACQUINOT et al, Plasma Phys Contr. Fusion, 30 (1988) 1467.
(3) G. SCHMIDT et al, IAEA Conf., Nice, France, (1988) CN-50/A-4-1.
(4) V.P. BHATNAGAR et al, Nuclear Fusion, 24, (1984) 955.
(5) T.H. STIX, Nuclear Fusion, 15, (1975) 737.
(6) F. PEGORARO et al, IAEA Conf., Nice, France, (1988) CN-50/D-4-6.
(7) J.P. CHRSITIANSEN et al, Bull. American Phys Society 33 (1988) 2030
(8) V.P. BHATNAGAR et al, JET Joint Undertaking, (1988) JET-P(88)51.
(9) P-H. REBUT et al, IAEA Conf., Nice, France, (1988) CN-50/D-4-1.
(10) A. TARONI et al, IAEA Conf., Nice, France, (1988) CN-50/A-7-1.

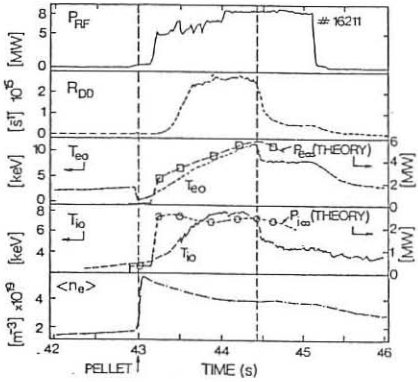

FIG. 3. Time traces of P_{RF}, R_{DD}, T_{e0}, T_{i0} and $< n_{e0} >$. Theory refers to ray-tracing.

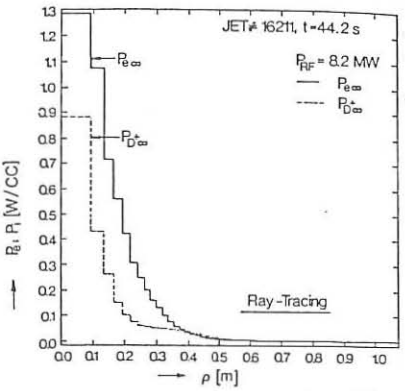

FIG. 4. Steady-state power-deposition profile of elctrons and ions.

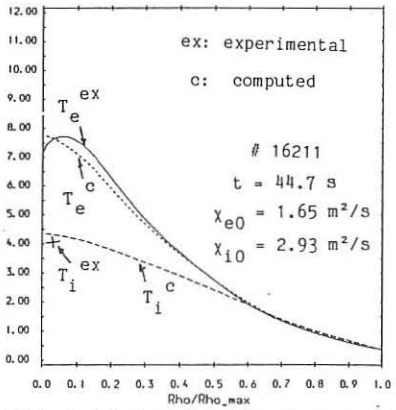

FIG. 5 (a) Experimental and computed temperature profiles after crash.

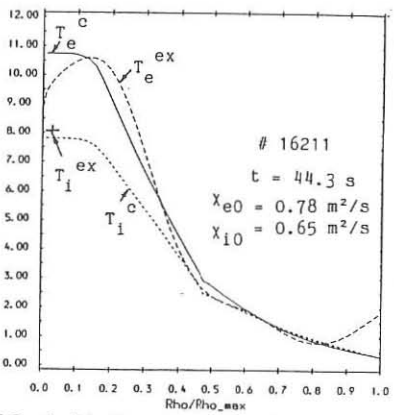

FIG. 5 (b) Experimental and computed temperature profiles before crash.

TRANSPORT ANALYSIS OF PELLET-ENHANCED ICRH PLASMAS IN JET

G. W. Hammett, P.L Colestock, R.S. Granetz, P. Kupschus[a], D.C. McCune, C.K. Phillips, G.L. Schmidt, D.N. Smithe, and members of the JET/USDOE Pellet Collaboration[1].

Princeton Plasma Physics Laboratory, P.O. Box 451, Princeton NJ 08543 USA
[a]JET Joint Undertaking, Abingdon, Oxon OX143EA, U.K.

INTRODUCTION: Performance of JET ICRH heated discharges has been significantly enhanced by using pellet fueling to produce a peaked density target for ICRH[1, 2]. The central T_i is observed to increase by up to 80%, central T_e by up to 40%, and the neutron rate by up to 400%, over their no-pellet values (which are already in the enhanced "monster-sawtooth" regime). In this paper we describe the transport analysis of these discharges using the TRANSP code. These results indicate that the thermal diffusivities χ_i and χ_e are reduced by a factor of ~ 2 near the plasma center where the pellets have increased the density gradient.

This paper focuses on JET discharge 16211 which is documented more fully in a companion paper[2]. Fig. 1 summarizes its time history. The pellet is injected at t=3.00 s and is followed by 6–9 MW of hydrogen minority ICRH heating until t=5.1 s. In the middle of the enhanced phase, at t=3.7 s, the temperatures are strongly rising; T_i reaches a maximum at t=4.1 s while T_e maximizes at t=4.35 s. At t=4.45 s, an MHD event (perhaps a double-tearing mode) flattens the density profile to the shape typical of no-pellet discharges. By t=4.75 s, during the 'normal' monster-sawtooth phase, plasma parameters return to their no-pellet values.

ICRH MODELLING: The TRANSP transport analysis code uses detailed profile measurements together with a model of the heating physics to infer χ_i and χ_e. Two packages have recently been added to TRANSP to model ICRH heating. The one used in this paper is a 3-D poloidal mode expansion code[3] which solves a contracted second-order equation for the fast wave (including fundamental and second harmonic ion damping, electron damping, and mode conversion), coupled to a bounce-averaged Fokker-Planck code[4] which calculates the minority ion distribution function $f(E, \mu, r, t)$. The poloidal mode-expansion code assumes a circular vacuum vessel for the boundary conditions, but is able to treat an arbitrarily shaped plasma within this vacuum vessel. While this was an adequate model for the tokamaks for which this code was originally developed (PLT and TFTR), it has limitations when dealing with JET's elongated plasma and vacuum vessel. With a limited number of poloidal modes (7), this code tends to focus too much of the RF power to the center of the vacuum vessel. This can be compensated somewhat by offsetting the vacuum vessel center from the plasma center. Too much shift, however, introduces large vacuum regions which give the shooting method numerical difficulties. Upgrades to allow a non-circular vacuum vessel and to generally improve the numerical stability are currently being studied. Nevertheless, when the minority concentration is low ($< 4\%$) it is possible to make a reasonable compromise on the boundary conditions which produce wave focussing consistent with ray-tracing results. The code calculates power profiles which are slightly more peaked during the enhanced phase than during the normal phase, perhaps because of the density peaking. 50% of the ICRH power is absorbed inside of r=25 cm during the enhanced phase, expanding to r=30 cm during the normal phase. 75% of the power

[1]Pellet team members are listed as authors of Ref. 2

is absorbed inside of r=42 cm during the enhanced phase, expanding to r=52 cm during the normal phase. (r is defined as an area-equivalent radius, i.e., $r = \sqrt{ab}$ for an elliptically shaped flux surface with height $2b$ and width $2a$.)

The hydrogen minority concentration plays an important role in determining the ICRH power flow to the thermal ions and electrons. Unfortunately n_h/n_e is difficult to measure accurately. It is typically in the range of 5-10% in an ohmic plasma, but is diluted by the pellet which increases the central n_e by a factor of 5 and the volume averaged n_e by a factor of 2. The strong ion heating which is observed when the ICRH is turned on is difficult to explain unless more than 50% of the ICRH power eventually flows to the thermal ions. This constrains the minority concentration either to be low enough so that a significant amount of second harmonic deuterium heating occurs, or to be high enough so that most of the minority ions do not exceed the critical energy and therefore collide primarily with the thermal ions.

Shown in Fig. 1 is the X-ray crystal spectrometer measurement of T_i compared with TRANSP's prediction of this diagnostic. (TRANSP includes a model for profile effects on this diagnostic which can be important when T_e exceeds 8.2 keV, the excitation energy of the line. In this shot where T_e reached 10.8 keV and the x-ray crystal measurement reached 7.8 keV, TRANSP's corrected central T_i was 9.8 keV.) A constant hydrogen concentration n_h/n_e of 1% was assumed, which puts 40–50% of the power into the ions (as much as 30% of the power is directly absorbed by the thermal ions via second harmonic damping). The calculation was done assuming $\chi_i(r,t) = \mathrm{Max}(\alpha(t)\chi_e(r,t), \chi_{i,neo}(r,t))$, with α adjusted to match the X-ray crystal T_i measurement. The ion heating is so strong that even when χ_i was reduced to its minimum neoclassical value (which can be significant near the axis), TRANSP is unable to match the measurement until t=3.9 s. An ad hoc ICRH model was also tried in which 75% of the power was decreed to go to the ions, and 25% to the electrons, with a Gaussian power profile with σ = 20 cm. In this case TRANSP was able to match the measured T_i as early as t=3.5 s.

Of course it is preferable to use a full measurement of $T_i(r)$ in order to infer the full $\chi_i(r)$ profile, rather than using a model to fit the central T_i. JET has measured $T_i(r)$ profiles using charge-exchange recombination spectroscopy in other pellet-enhanced shots, and TRANSP is currently being upgraded to simultaneously handle ICRH and beam heating in order to analyze these shots. (These shots include ^{3}He minority heating discharges which may also help resolve other ambiguities since they do not have any direct second harmonic ion heating and there is a measure of the ^{3}He concentration from the initial ^{3}He gas puff.) Nevertheless, the $\chi_i \propto \chi_e$ assumption produces T_i profiles which are similar in shape to the T_e profile, qualitatively consistent with charge-exchange recombination spectroscopy from these other shots.

TRANSPORT RESULTS: Fig. 6 shows that most of the improvement in the electron temperature occurs inside r=40 cm. Fig. 5 shows that the strongest density gradients are close to this core region. (These density profiles are based on a 6-channel interferometer system which has a $\delta R \approx 30$ cm spacing near the plasma center.)

Figs. 7 and 8 show the heat diffusivities inferred from the data by TRANSP using the standard ICRH model with n_h/n_e = 1%. Again, the improvement in the transport is primarily in the core of the plasma ($r < 45$ cm). The central χ's are reduced by a factor of ~ 2 during the enhanced phase, consistent with one-fluid transport analysis of similar discharges[5]. The

results in the middle region (50 cm $< r <$ 100 cm) are more ambiguous (where χ_e is actually worse at t=3.7 s, and χ_i is slightly worse at t=4.35 s when T_i has already begun to roll over). But the pellet has done little to change the density gradient in this region, and so no change in behaviour would be expected on the basis of η_i models.

Fig. 2 focuses our attention on the time-behaviour of the χ's at r = 35 cm, showing their correlation with the density gradient (Fig. 4). χ_i rises towards the end of enhanced phase as $\nabla \log n_i$ is dropping. When $\nabla \log n_i$ drops a factor of 2 at the crash, χ_i rises by a factor of 2. There is also some correlation with η_e (used here as a surrogate for the less-well known η_i). It is puzzling that η_e is so much larger than simple estimates of the critial η, although in a heated no-pellet discharge it would be even larger[1]. In this TRANSP calculation with 1% hydrogen, the ICRH model could not put enough power into the ions to explain the rapid ion heating observed, thus TRANSP reduced χ_i to its minimum neoclassical value for $t <$ 4.0 s. Fig. 3 shows the result of a calculation with the ad hoc ICRH model where 75% of the ICRH power goes to the ions with a gaussian width σ = 20 cm. Although the absolute values of the χ's are now different, the qualitative improvement of χ with ∇n remains the same. Alternatively, the improvement in the transport may be due to a reduction in the shear, which is also strongly affected by the pellet. TRANSP predicts that the q profile not only flattens in the region r< 50 cm, but may eventually become non-monotonic[1, 6]. The sudden crash at t=4.45 s may be the resulting double-tearing mode. It may be some other MHD mode, but it is not an m=1 sawtooth and it has a a complicated mode structure[1]. However the pellet-enhanced phase is not terminated by a crash in all discharges, and in the absence of a tearing mode it is difficult to know how the q profile could be changed quickly enough to explain the eventual loss of the enhanced phase. In shot 16228 there was a smooth transition from the pellet-enhanced regime to the normal regime as the peaked density profile slowly diffused away[2]. That shot also differed in that only χ_i was enhanced, while χ_e remained unaffected.

While further work remains, the analysis so far confirms that the improvement in χ is correlated with steeper density gradients. This suggests that further improvements in plasma performance might be possible if the density gradient could be steepened over a broader range of the plasma rather than just in the core.

ACKNOWLEDGEMENTS: Insight on wave propagation provided by J. Jacquinot is gratefully noted. This work was conducted as part of the JET/USDOE pellet collaboration and was supported in part by U.S. DOE contract No. DE-AC02-76CH03073.

[1] G.L. Schmidt and the JET Team, Plasma Physics and Controlled Nuclear Fusion Research (Proc. 12th Int. Conf. Nice, 1988), IAEA-CN-50/A-IV-1.
[2] S.L. Milora et.al., this conference.
[3] D.N. Smithe, P.L. Colestock, R.J. Kashuba, T. Kammash, Nucl. Fus. **27** (1987) 1319.
[4] G.W. Hammett, Ph.D. Thesis, Princeton University (1986), available from University Microfilms, Ann Arbor MI 48106 (USA).
[5] A. Taroni et.al., Plasma Physics and Controlled Nuclear Fusion Research (Proc. 12th Int. Conf. Nice, 1988), IAEA-CN-50/A-7-1.
[6] P.M. Stubberfield et.al., this conference.

Fig. 1.

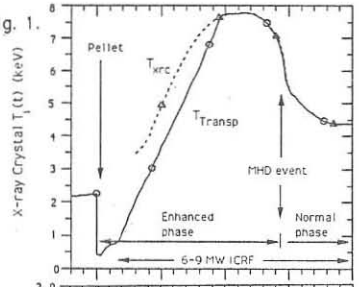

Fig. 2.

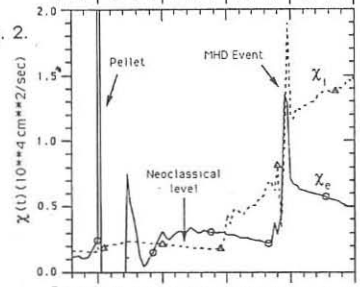

Fig. 3.

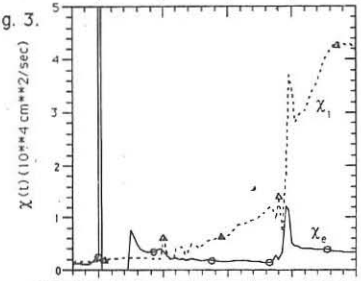

Fig. 4.

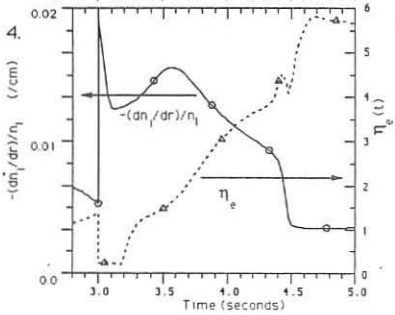

Fig. 5.

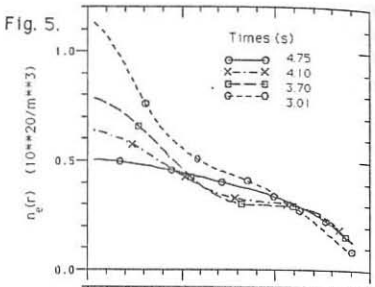

Fig. 6.

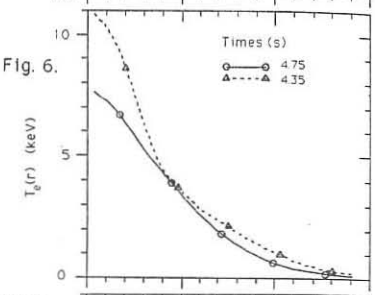

Fig. 7.

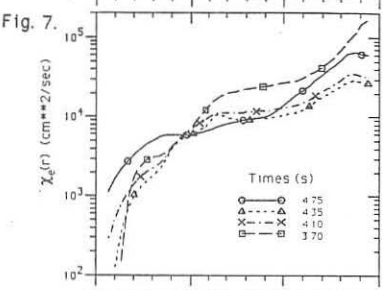

Fig. 8.

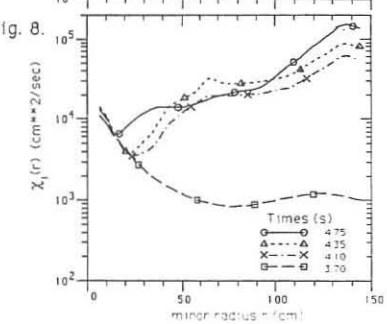

HELIUM PLASMAS RESULTS IN OHMIC FT DISCHARGES

G. Bracco

Associazione EURATOM-ENEA sulla Fusione, C. R. E. Frascati,
C.P. 65 - 00044 - Frascati, Rome, Italy

INTRODUCTION

A series of plasma discharges using helium as filling gas has been completed in FT in the range $3<q<6$, $0.5<n_e<2.5\times10^{14}\,cm^{-3}$ at $B_T=6\,T$ where q is the safety factor at the limiter n_e is the line averaged density and B_T the toroidal field.

The main task of the helium operation has been the study of the dependence of both the limits of tokamak operation and the scalings of the main plasma parameters on the ion mass/charge.

The use of helium as filling gas in FT has not presented major operation problems. The only limitation has been a more difficult plasma start-up compared to hydrogen and deuterium due to the higher ionization potential. An attempt to work at $B_T=4\,T$ has not been successfull, probably due to the higher stray field importance at lower toroidal

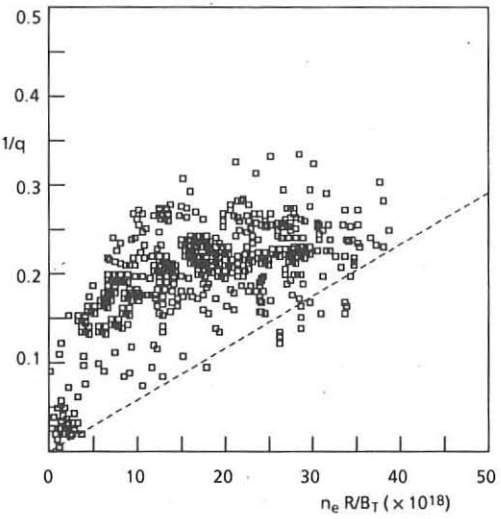

Fig. 1 - He discharges in the Hugill diagram (--) deuterium density limit

field. It has been observed that the helium operation demands a reduction in gas feed needed to reach a given density of a factor 2 compared to deuterium which implies a different recycling behaviour. Several points corresponding to helium discharges are shown in Fig. 1 on the Hugill operation diagram where the standard density limit for FT is also shown [1]. The density limit then does not seem to be increased by the operation in helium. No evidence of MARFE phenomena as been found up to now in helium operation, while they occur frequently near the density limit in deuterium plasma [2]. The residual deuterium fraction has been monitored by the analysis of the emission of both neutrons and D_α line in order to check if the deuterium contamination could affect the helium results. The neutron and D_α results agreed with a residual deuterium fraction between 5% and 15% of the total electron density. This fraction changes with the previous story of tokamak operation and with the wall and limiter temperature, but no evidence of correlation with the main plasma results has been found.

The electron temperature profile has been measured by Thomson scattering. In deuterium discharges performed in the same period, the peak electron temperature was found to depend linearly on the parameter $B_T^{1.3}/q^{0.4}n_e^{0.6}$. In Fig. 2 the peak electron temperature for deuterium and helium is shown as a function of the previous parameter and the He discharges have a 20% higher value compared to deuterium. In Fig. 3 the ratio between peak electron temperature and volume average is shown as a function of q showing no relevant difference between deuterium and helium. The sawtooth period is also similar in deuterium and helium discharges at the same q and density. The plasma resistive voltage is 20% higher for He discharges than in comparable deuterium plasmas providing an increased ohmic input power.

In the actual Thomson Scattering configuration, no absolute density calibration is available so a fixed parabolic density profile has been used in the plasma data analysis. The line averaged density is measured by a single point HCN interferometer.

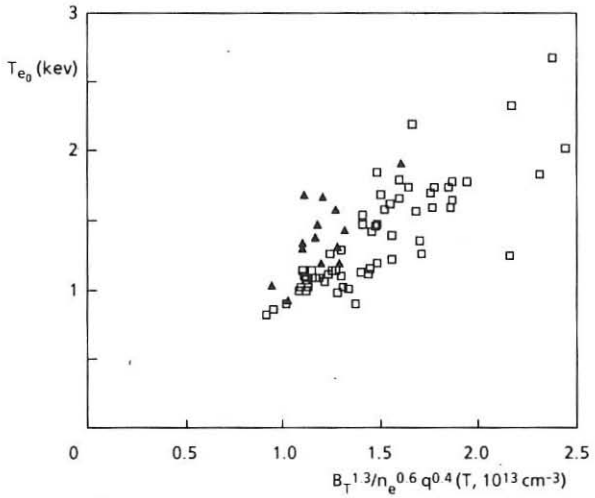

Fig. 2 - Peak electron temperature (▲) helium (□) deuterium

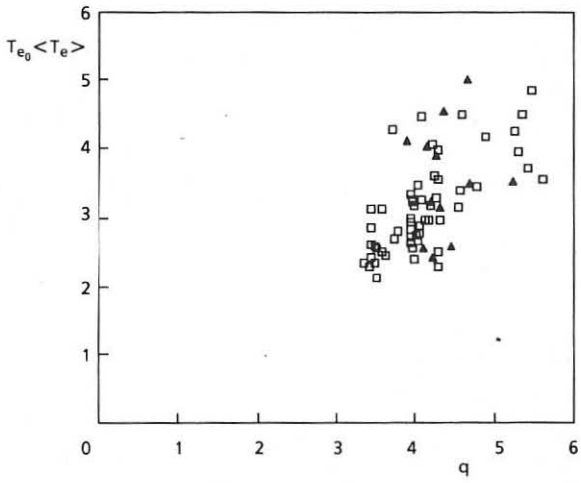

Fig. 3 - Ratio between volume averaged and peak electron temperature (▲) helium (□) deuterium

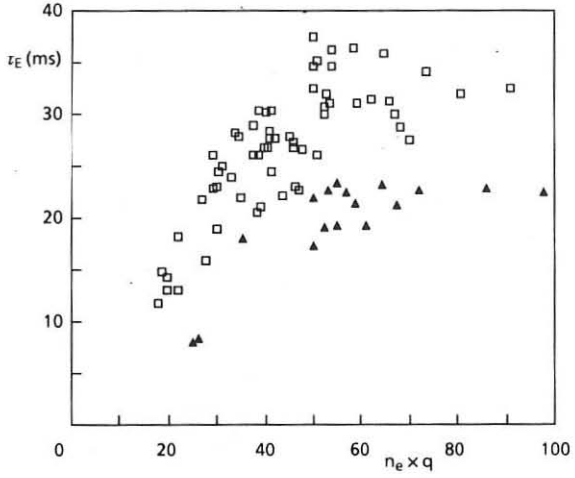

Fig. 4 - Global energy confinement time (▲) helium (□) deuterium

The global power balance results are shown in Fig. 4 where the total energy confinement time τ_e, neglecting radiation, is plotted as a function of $n_e q$ for helium and deuterium discharges of the same period. Due to the lack of experimental ion temperature measurements, the ion energy content has been computed solving the ion power balance equation using the neoclassical ion thermal conductivity [3]. In deuterium operation operation the ion thermal conductivity is equal to the neoclassical one, within the experimental errors [4]. The τ_e value for He is lower than for deuterium due essentially to a similar electron term, but a reduced ion contribution due to the lower ion density. Some results from CO_2 scattering on density fluctuation suggest that the level of $\delta n/n$ is similar in helium and deuterium discharges.

In conclusions, the overall comparison between helium and deuterium discharges in FT shows a similarity between the two species which seems to be stronger in FT than in other tokamaks where both gases have been used.

REFERENCES

[1] F. Alladio and FT Group: Nucl. Fusion **25**, 1069 (1985)
F. Alladio and FT Group: Proc. XIV Europ. Conf. on Contr. Fusion and Plasma Physics (Madrid, 22-26 June, 1987) **1**, 73
[2] F. Alladio et al.: Phys. Lett. **90A**, 405 (1982)
[3] C.S. Chang, F.L. Hinton: Phys. Fluids **29**, 3316 (1986)
[4] G. Bracco, S. Podda, V. Zanza: Proc. 15th Europ. Conf. on Contr. Fusion and Plasma Physics (Dubrovnik, 16-20 May 1988) **1**, 175

ANALYSIS OF HIGH-FREQUENCY MAGNETIC FLUCTUATIONS ON THE FT TOKAMAK

F. Crisanti, M. Marinucci, C. Nardone*

Associazione EURATOM-ENEA sulla Fusione, C. R. E. Frascati,
C.P. 65 - 00044 - Frascati, Rome, Italy

INTRODUCTION

We have investigated the magnetic signals of the FT tokamak ($R = 83$ cm, $a_L = 20$ cm) at the plasma edge using two coils to detect $\dot{B}_\theta$ placed 3.5 cm apart from each other in the shadow of the poloidal limiter at the external upper side of the torus. The measured frequency response of the two 4-winding coils, 1 cm long and radius 0.45 cm, shows a roll-off of -3 dB at about 300 kHz, well above the range of frequency considered (< 200 kHz). The electronic chain is composed of two amplifiers with an optical decoupler between them to isolate the coils, short-circuited with the liner, from the control room devices. The signals were sampled typically at a frequency of 2 MHz for a time window of 8 ms and were then integrated numerically to obtain $\tilde{B}_\theta$.

SPECTRA

The spectra observed for most of the signals examined show a low-frequency part characterized by a strong peak at about the Mirnov frequencies (for the $m = 2$ mode ~ 10-15 kHz), sometimes accompanied by the second and third harmonic peaks. The high-frequency part has a fairly typical broadband incoherent aspect and exhibits an $f^{-\alpha}$ dependence from about 20 kHz to 200 kHz, with α ranging between 2.0 and 3.0 (Fig. 1) and no apparent dependence on the macroscopic parameters of the plasma discharge.

The cross-coherence [1] between the signals of the two coils is very high at frequencies which include Mirnov oscillations, up to 30 kHz (Fig. 2). At higher

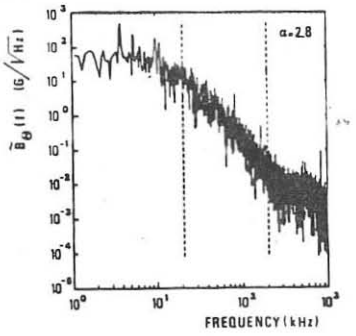

Fig. 1 - Fourier amplitude of a magnetic signal

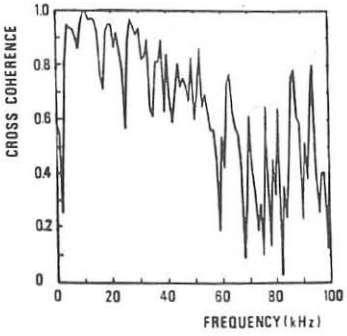

Fig. 2 - Cross-coherence between the signals of the two coils

frequencies the level of coherence decreases indicating that the high frequency turbulence is fairly localized, at least in the plane perpendicular to B_T.

SCALING WITH MAIN PLASMA PARAMETERS

More than 200 shots in hydrogen or deuterium plasma were considered, widely distributed over the space of the main plasma parameters. The ranges examined are as follows: $\bar{n}_e$ from 0.2×10^{14} to 2×10^{14} cm^{-3}; plasma current I_p from 150 to 500 kA; toroidal field $B_T = 40$, 60 and 80 kG, $q_{edge} = 3.3 \div 10.0$.

The amplitude of the signals, mainly at high frequency (> 20 kHz), was found to be very sensitive to the plasma position; therefore, a severe selection on the set of examined shots was performed in order to collect a homogeneous subset of about 50 discharges with a permitted spread in the plasma position of not more than 0.4 cm. These shots covered about the same parameter ranges as described above and were used to investigate the behaviour of the magnetic fluctuations amplitude in the $20 \div 50$ kHz band. The fluctuation amplitude at the high frequency regime ($20 \div 50$ kHz) exhibits no dependence on the average plasma density $\bar{n}_e$ for all the values of the plasma current. This allows us to study the scaling with the plasma current taking into account all the selected shots. A clear dependence of the high-frequency amplitude on the plasma

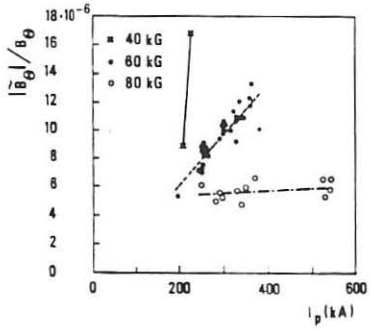

Fig. 3 - Fluctuation amplitude in the frequency range $20 \div 50$ kHz vs plasma current

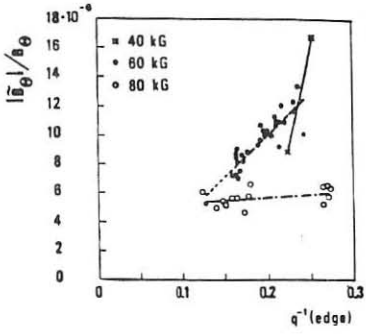

Fig. 4 - Fluctuation amplitude $|\tilde{B}_\theta|/B_\theta$ ($20 \div 50$ kHz) vs q^{-1}_{edge}

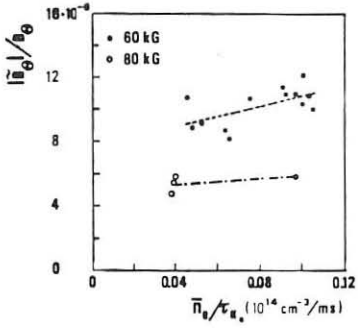

Fig. 5 - Fluctuation amplitude $|\tilde{B}_\theta|/B_\theta$ ($20 \div 50$ kHz) vs $(\tau_{E_e}/\bar{n}_e)^{-1}$

current results, but even more evidently the type of dependence appears correlated with the toroidal field (Fig. 3). This last circumstance would suggest that a dependence on q^{-1}_{edge} as a universal parameter for all the shots could be taken into account, but, as Fig. 4 reveals, this is not the case.

Due to amount of available data, it was not possible to explore a sufficiently wide range of variation in the electronic energy confinement time in order to confirm the dependence of confinement on magnetic turbulence [1]; nevertheless, there seems to be a weak dependence of $|\tilde{B}_\theta|/B_\theta$ on $\tau_{E_e}^{-1}$ (normalized with $\bar{n}_e$ to take into account the neo-Alcator scaling) (Fig. 5).

FRACTAL DIMENSIONS

In order to detect the possible existence of a strange attractor due to the nonlinear interaction of a limited number of coherent modes (presumably MHD Mirnov modes), the correlation dimensions of the magnetic signals were calculated for all the selected shots by means of the Grassberger-Procaccia algorithm [2]. The algorithm consists in calculating the correlation exponent $\nu(m)$ for increasing values of m (embedding space dimension), where the fraction $C_m(r)$ of pairs of points in the embedding space less than r distant is given by

$$C_m(r) \sim r^{\nu(m)}$$

If $\nu(m)$ eventually converges, the limit ν will be the correlation dimension of the signal; values of $\nu(m)$ increasing with m indicates that deterministic chaos is not a peculiar aspect of the phenomenon observed.

A lack of caution in applying the algorithm can lead to misleading results, therefore, we believe it useful to discuss it briefly. First, the maximum m is related to mantaining a sufficient statistics in the evalutation of $\nu(m)$. A rough evalution of the maximum m is given by

$$m < 2 \log N ;$$

in our case N~10000 so that m<7. Second, particular care must be taken in choosing the time delay Δt to avoid systematic errors in the evaluation of $\nu(m)$; the best choice is given by the time corresponding to the first minimum of the mutual information of the signal, $I(\Delta t)$ [3], which, in our case, is roughly the autocorrelation time (~ 20 μs). Third, we used a slight modification of the original algorithm in order to avoid the correlations

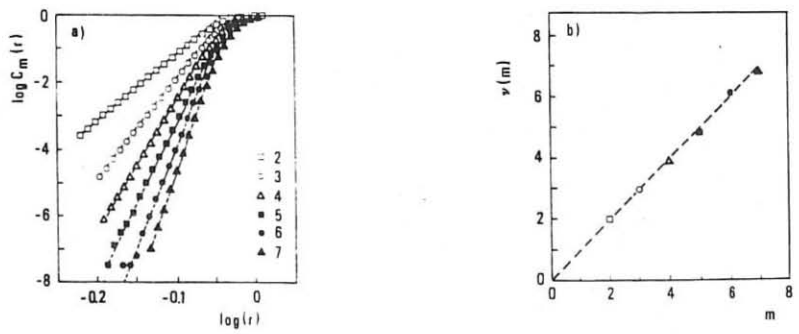

Fig. 6 - Shot # 16308. (a) Log $C_m(r)$ vs log(r) and (b) $\nu(m)$ vs m ($t_s = 2.5$ μs, $\Delta t = 10 \times t_s$, N = 8000)

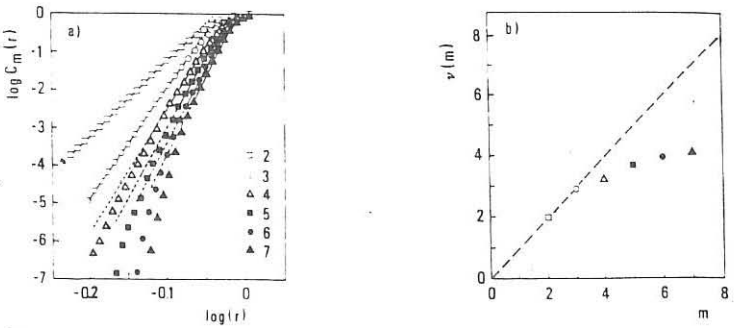

Fig. 7 - Shot # 17155. (a) Log $C_m(r)$ vs log(r) and (b) $\nu(m)$ vs m ($t_s = 0.5$ μs, $\Delta t = 45 \times t_s$, N = 11500)

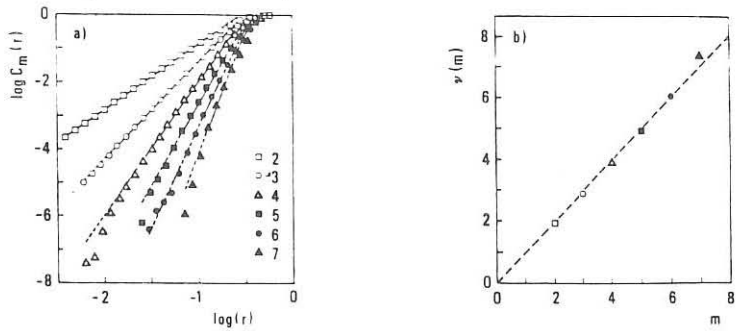

Fig. 8 - Shot # 17155 with band 13 ÷ 15 kHz filtered off. (a) Log $C_m(r)$ vs log(r) and (b) $\nu(m)$ vs m ($t_s = 0.5$ μs, $\Delta t = 45 \times t_s$, N = 11500)

among points in the embedding space too close in time, which can generate erroneous evaluations of $\nu(m)$ [4].

In most of the shots analysed we did not find any saturation of $\nu(m)$, as shown in Fig. 6. In a few cases with enhanced Mirnov activity a saturation of ν to a value near 4 is obtained (Fig. 7), but we retain that this is due to the dominant effect of the coherent oscillation, as can be demonstrated by calculating again the correlation dimension of the same signal filtered in a narrow band (13 ÷ 15 kHz) around m = 2 peak, which shows no saturation of $\nu(m)$ (Fig. 8). Our results agree with previous ones [5], obtained with the same reservations.

FOOTNOTE AND REFERENCES

* ENEA Guest

[1] M. Malacarne, P.A. Duperrex: Nucl. Fusion 27, 2113 (1987)
[2] P. Grassberger, I. Procaccia: Phys. Rev. Lett. 50, 346 (1983
[3] A.M. Fraser, H.L. Swinney: Phys. Rev. 33A, 1134 (1986)
[4] J. Theiler: Phys. Rev. 34A, 2427 (1986)
[5] C.W. Simm, M.L. Sawley, F. Skiff, A. Pochelon: Helv. Phys. Acta 60, 510 (1987)

MICROINSTABILITIES IN FT TOKAMAK

D. Frigione, S. Goetsch*

Associazione EURATOM-ENEA sulla Fusione, C. R. E. Frascati,
C.P. 65 - 00044 - Frascati, Rome, Italy

1. INTRODUCTION

Density fluctuations in the low K region (2-5 cm^{-1}) are measured by CO_2 scattering in deuterium quasi-stationary discharges covering a wide range of nq parameters (line average density times safety factor at the limiter) and energy confinement times. The data show a correlation between the inverse energy confinement time and the relative fluctuation level $(\tilde{n}/n)^2$ in the region where τ_e linearly increases with nq. For higher nq values, where τ_e saturates, the correlation is lost. No evident effect of RF heating power (LHR 8 GHz, 230 kW) has been observed in most of the discharges: in some low density shots ($n_e \sim 6\times10^{13}$ cm^{-3}) a modification of the frequency spectrum takes place, with a sharp reduction of the signal autocorrelation time. Finally, a fractal analysis of the data shows that many degrees of freedom are involved (high demensionality), thus confirming the high turbulent nature of the phenomenon.

2. EXPERIMENTAL SET UP

A 3W, 10 μm, gaussian CO_2 laser beam is weakly focused by a concave mirror to a beam waist of 5 mm in the plasma center. After 20 m path, a central portion of the beam is sent onto a CuGe photoconductive detector. In such a configuration, electron density fluctuations falling in the K range illustrated in Fig. 1 are probed [1]. The signal is analysed by bandpass rms detectors covering the frequency range 10-100 kHz and recorded during the whole discharge. In addition, two Le Croy 2264 AD converters are used for numerical analysis. The scattering volume is a cylinder with 5 mm radius covering a whole plasma vertical diameter so that only poloidally propagating waves are probed.

3. RESULTS

On the basis of previous experiments on density microinstabilities in tokamaks [3,4], we selected a K range as low as possible where probably most of the spectral density is located. In Fig. 2 we plot the inverse energy confinement time vs $(\tilde{n}/n)^2$, integrated over the whole frequency interval, for a set of ohmic sawtoothing discharges: the m=2 mode was absent and data were taken in quasi stationary phases of the discharge. The confinement time was obtained assuming a neoclassical behavior for the ions [5]. The data are clearly divided in two groups: one of them, including shots with $nq \leq 4\times10^{13}$ cm^{-3}, shows an approximately linear correlation of the inverse confinement time with the fluctuation level. The trend is more evident in Fig. 3 showing the same points on an expanded scale and agrees with the result found in Ref. 6. The second group, relative to high nq discharges, extends over a wide region of fluctuation levels, while the confinement time keeps practically constant. In Figs. 4, 5 we plot $(\tilde{n}/n)^2$ and τ_e vs nq for the same discharges: it can be seen that around nq =

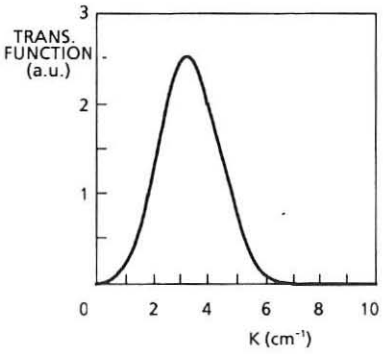

Fig. 1 - K vector range selected by the scattering system

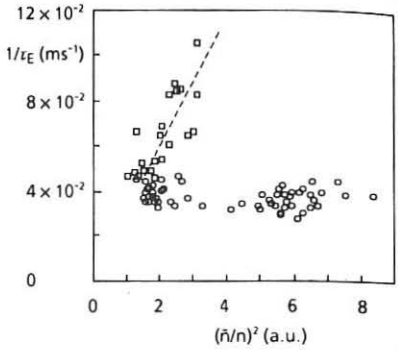

Fig. 2 - Inverse energy confinement time vs the mean square relative fluctuation level. Squares: shots with $nq \leq 4 \times 10^{14}$ cm^{-3}. Circles shots with $nq > 4 \times 10^{14}$ cm^{-3}

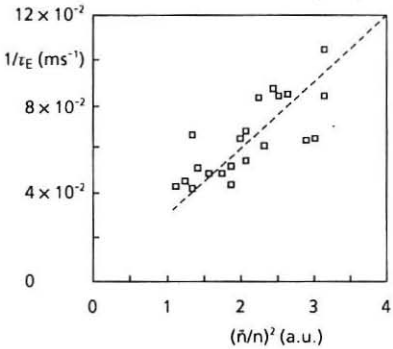

Fig. 3 - Inverse energy confinement time vs the mean square fluctuation level for shots with $nq = 4 \times 10^{14}$ cm^{-3}

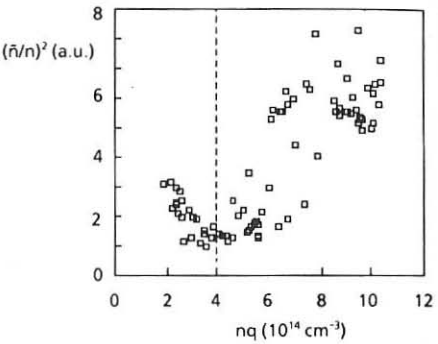

Fig. 4 - Mean square fluctuation level vs nq

4×10^{13} cm^{-3}, both quantities enter a new regime. The confinement time saturates and the fluctuation level, which was decreasing, starts increasing up to very high values.

The behavior of density fluctuations during RF heating has also been studied. Usually RF power (LH, 8 GHz, 230 kW) does not produce any effect on the CO_2 signal: in some low density shots, we observe a modification of the frequency spectrum with a decrease of the signal autocorrelation time (Fig. 6).

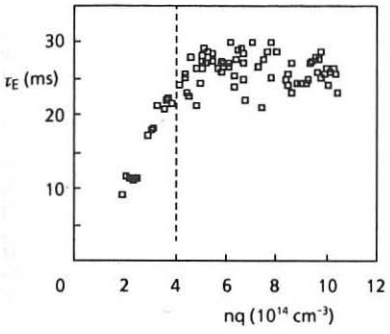

Fig. 5 - Energy confinement time vs nq

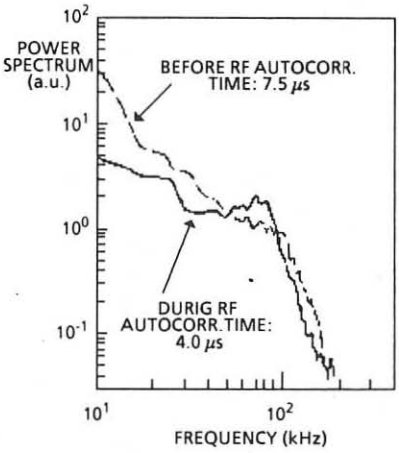

Fig. 6 - Frequency spectra of the scattering signal taken before (dashed line) and during the RF heating phase of the same shot ($n_e = 6 \times 10^{13}$ cm^{-3}; $I_p = 400$ kA; $B_T = 80$ kG)

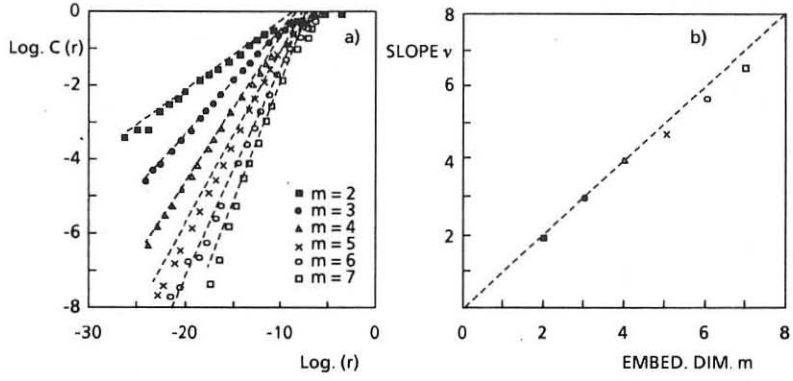

Fig. 7 - a) Correlation function C(r) vs r in log.log scale and slope of C(r) vs the embedding dimension

Finally, we used the data sampled by the AD converters for a study of the dimensionality of the signal. For each shot, the data base included 10000 points taken at

a sampling rate of 4 MHz: for the numerical analysis we used the Grassberger-Procaccia algorithm [7]. In Fig. 7a we plot the correlation function C(r) vs r for different embedding dimensions m. The slope of each curve vs m is plotted in Fig. 7b: no saturation is observed, thus indicating that the data have a fractal dimensionality at least greated than 5.

4. SUMMARY

The present study of density fluctuations on FT can be summarised in three points: a) the mean square relative fluctuation level in the measured range (2-5 cm^{-1}; 10-1000 kHz) is linearly correlated with the inverse confinement time in the low nq region where τ_e is linear. At higher nq values, in coincidence with the saturation of τ_e, the fluctuations start to increase and the correlation is lost. b) RF heating power at LHR does not usually produce any effect on the scattering signal: in some low density shots a modification of the frequency spectrum is observed. c) A fractal analysis of the signal shows an high dimensionality ($m>5$), confirming the high turbulent nature of the phenomenon.

FOOTNOTE AND REFERENCES

* ENEA Student

[1] The response, of the sytem to density fluctuation is calculated on the basis of far forward scattering theory reported in Ref. 2, and will appear in a next paper
[2] D.E. Evans, M. Von Hellermann, E. Holzhauer: Plasma Phys. **24**, 819 (1982)
[3] P. De Simone, D. Frigione, F. Orsitto: Plasma Phys. **28**, 751 (1986)
[4] G. Dodel, E. Holzhauer: 15th European Conf. on Controlled Fusion and Plasma Physics (Dubrovnik, 1988) **1**, 43
[5] G. Bracco, S. Podda, V. Zanza: 15th European Conf. on Controlled Fusion and Plasma Physics (Dubrovnik, 1988) **1**, 175
[6] TFR Group and A. Truc: CEA Report, EUR-CEA-FC-1284
[7] P. Grassberger, I. Procaccia: Phys. Rev. Lett. **50**, 346 (1983)

OBSERVATION OF SYNCHROTRON RADIATION FROM RUNAWAY DISCHARGES

K.H. FINKEN[1], J.G. WATKINS[2], D. RUSBÜLDT[1], W.J. CORBETT[3], K.H. DIPPEL[1], D.M.GOEBEL[3], R.A. MOYER[3]

[1]KERNFORSCHUNGSANLAGE JÜLICH GMBH, ASSOCIATION KFA - EURATOM, WEST GERMANY
[2]SANDIA NATIONAL LABORATORIES, ALBUQUERQUE, USA
[3]UNIVERSITY OF CALIFORNIA, LOS ANGELES, USA

Abstract

It has been observed on TEXTOR that in low density discharges the electrons gain enough energy to emit relativistic synchrotron radiation in the 3 - 6 μm IR - range, and this radiation is due to electrons with energies up to 30 MeV. The momentum in perpendicular direction amounts to about 1/10 of the longitudinal one. The total number of runaways is of the order of 10^{16} electrons, and they carry a current of about 20% of the total plasma current.

Introduction

So far runaways have been diagnosed mainly via reactions after they have left the plasma and have hit material components. The result of these reactions is hard X - ray Bremsstrahlung and (γ,n) - processes as secondary reactions from the Bremsstrahlung. Therefore runaway loss mechanisms are well investigated. On the other hand, the properties of the runaways in the plasma and their spatial distribution could not be evaluated. We present here a method for studying runaways in the plasma so that their growth in number and energy and their spatial distribution can be directly observed if the number of energetic electrons is high enough. This method is based on the detection of synchrotron radiation from the highly relativistic electrons. In the following, some basic properties of the synchrotron radiation are discussed first, then the measurements are described and a summary of the results is presented.

Properties of the Synchrotron Radiation

If electrons with sub-relativistic energies gyrate they emit radiation with a dipole characteristic in the plane perpendicular to the direction of acceleration. The cyclotron emission of electrons spinning around a magnetic field with an emission maximum at ω_{ce} is well known. If the electron becomes relativistic more and more harmonics are generated which finally merge to a continuous emission band. Also the emission characteristic changes from the dipole characteristic to emission in the direction of instantaneous velocity. The opening angle for the emission cone is roughly $\Delta\varphi \approx 1/\gamma$, where γ is the relativistic energy factor. For electrons with energies in the range of 50 MeV this angle amounts to only a few mrad.

The synchrotron spectrum for electrons moving in a circle with radius R has been derived by J. Schwinger /2/. The spectral intensity is given by:

$$P^{s}_{\lambda}(\gamma) = (4\pi/3^{1/2}) \cdot (m_o c^3 r_e/\gamma^2\lambda^3) \cdot \int_{w}^{\infty} K_{5/3}(x)\, dx$$

$$w = 4\pi R/3\lambda\gamma^3; \qquad r_e = 2.82 \cdot 10^{-15}\ \text{m}$$

where m_0 is the rest mass of the electron, λ the wavelength, R the radius of curvature of the electron's path and K the modified Bessel function of the order 5/3. In the short wave length limit i.e. for w >> 1 the spectrum can be written as

$$P_\lambda^S \approx \pi m_0 c^3 r_e \cdot (2/R\lambda^5\gamma)^{1/2} \cdot \exp(-4\pi R/3\lambda\gamma^3)$$

The spectrum depends on the energy of the electrons with a power of three in the exponent and on the radius of curvature with the first power. Fig. 1 shows a spectrum of synchrotron radiation for different energies of the electrons and a radius of curvature of 1.75 m which corresponds to the major radius of TEXTOR. The spectrum decays strongly in the short wavelength limit and is relatively flat at long wavelengths. For $\gamma \leq 20$ the emitted energy is undetectably low for the IR set-up, and for $\gamma \geq 80$ the spectrum extends up to 1 μm where a CCD - camera becomes sensitive. In the very long wavelength limit the radiation becomes independent of the electron's energy.

Experimental Observations

Under normal discharge conditions, two IR cameras record the radiation which is emitted only from the limiters or the vessel walls. The emission from the plasma is negligible because of the low emission coefficient for Bremsstrahlung. The temperature increase of the limiter due to the discharge is typically 40^0 C starting from about 150^0 C. After the discharge the surface temperature changes only very slowly during the following minutes. The details of the temperature evolution depend on the power flux and the exposure time.

The observations during runaway discharges are very different. This type of discharge is limited to line averaged electron densities below $1.0 \cdot 10^{13}$ cm^{-3}. When looking with the camera against the electrical current direction the IR picture appears normal for the first second of the discharge. Then an elliptical or nearly circular spot develops in the plasma. The brightness of the spot increases during the next second of the discharge and then overexposes the picture. The spot is the brightest object in a TEXTOR discharge and it stays nearly unchanged in shape but overexposed from $t \approx 2$ s to the end of the discharge. At the end of the discharge, it vanishes from one TV - frame to the next, i.e. within 20 ms. The brightness of the IR picture depends critically on the electron density. One example of runaways was observed where the density was just below the critical value. Here the spot appeared with a one second delay and the image was not overexposed. The extraordinarily rapid decay of the bright spot is a clear indication that the light is not thermal radiation from solid material in TEXTOR, but originates from the plasma interior.

The light is only emitted in the electron drift direction and not in the ion drift direction. During the time where the pictures are not overexposed the contrast ratio to the background thermal radiation is roughly constant between 3 and 6 μm as has been tested by inserting an interference filter for a comparison. The spectral dependence of the thermal radiation is included in fig.1.

Interpretation

The observation of the highly directed emission of radiation under the given conditions is only compatible with synchrotron radiation. In the wavelength interval between 3 - 6 μm the thermal radiation curve (T=400 K; see fig. 1) drops by nearly an order of magnitude and from the contrast argument given above the synchrotron radiation curve must have nearly the same slope there. A comparison of the slopes in fig. 1 in the wavelength region of interest provides a rather precise method to determine the energy of the runaways. According to these estimates, the relativistic energy factor amounts to $\gamma \approx 70$ or to an energy of 35 MeV. The accuracy of this estimate is better than 10% even if the contrast ratio of thermal radiation to synchrotron radiation is only accurate within a factor of two.

A systematic error can arise from the fact that the electron's path is not a simple circle along the B_T - field. The real path is a superposition of the guiding center orbit and a cyclotron motion around this line. The deviation of the guiding center path from a pure toroidal one does not change significantly the radius of curvature which enters in formula (1). Therefore the synchrotron spectrum is not altered by this effect. The cyclotron motion, however,affects the spectrum. For this motion it is assumed that it's frequency is fixed to ω_{ce}/γ and the velocity is selected such that the observed divergence of the IR - spot is reproduced. This divergence amounts to about 100 mrad and is nearly ten times larger than the divergence for a purely toroidal path. The slope of the helix corresponds to the ratio of the velocity component perpendicular to the drift orbit relative to the parallel one. The above mentioned 100 mrad yield a value of 0.1 for the ratio of the velocity components. When calculating the radius of curvature for this composed path of the electrons, an average value of roughly half the major radius is found. A re-calculation of the synchrotron spectrum with this new radius of curvature reduces the energy of the electrons to 25 - 30 MeV. An additional averaging over a velocity distribution function of the runaways does practically not change the maximum energy of the runaways. The distribution function is assumed to be flat but has a cut-off limit because electrons need a finite time for their acceleration. The perpendicular momentum amounts to $6 \cdot m_0 c$. This is by a factor of two larger than predicted by Besedin and Pankratov /3/ where already a scattering of the runaways with the background gas was taken into account.

The number of runaways is derived from the absolute value of the intensity. The number obtained here is not as accurate as the one for the energy. The reason for this is that the intensity changes very strongly with the runaway energy. So only the order of magnitude can be obtained. Including the perpendicular motion of the electrons and a flat distribution function, a number of about 10^{16} fast electrons is deduced. These electrons carry an electrical current of 64 kA which is 20% of the total plasma current. A detailed description of the evaluations will be presented elsewhere.

Concluding Remarks

The synchrotron radiation detection technique allows to deduce properties of the runaways which are not obtainable by the methods used up to now. It is found that the electrons are steadily accelerated up to late in the discharge, i.e. for several seconds. This long acceleration time requires that the runaway particle confinement time is of the order of seconds, and this means very much longer than energy or particle confinement time of the thermal plasma. The maximum energy of the runaways is close to 30 MeV. Their distribution function must be rather flat because otherwise they would carry too much electrical current; already with a flat distribution function, about 20% of the current must be attributed to the runaways. The momentum in a direction perpendicular to the guiding center orbits is rather high, and so effects are obscured which otherwise would be produced by the motion along the guiding center orbits. Therefore an analysis of these orbits and a comparison with theory seems to be impossible.

References:

/1/ H. Knoepfel, D.A. Spong, S.J. Zweben, Phys. Fluids, **20** (1977) 511
/2/ J. Schwinger, Phys. Rev. 75 (1949) 1912
/3/ N.T. Besedin, I.M. Pankratov, Nucl. Fusion, 26 (1986) 807

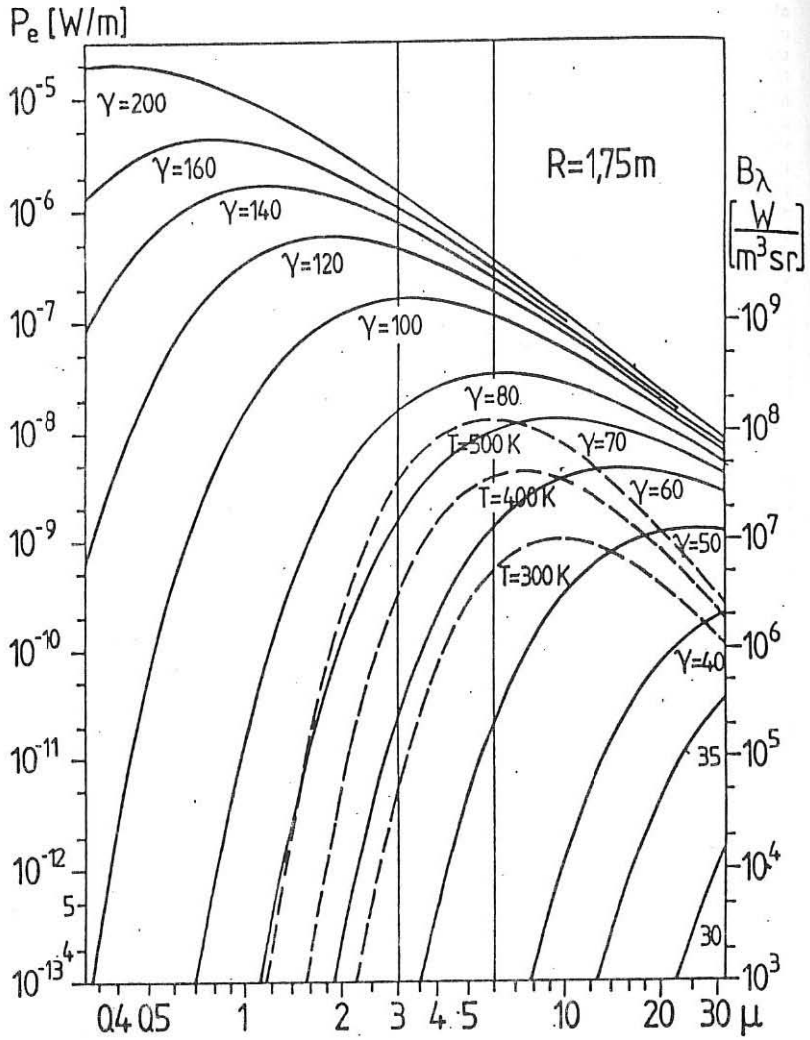

Synchrotron spectrum (solid lines, left scale) for different relativistic energy factors γ. The spectrum is presented in double-logarithmic scale. The broken lines (right scale) are the thermal spectrum for comparison.

IONIZATION LENGTHS, RADIATION PROFILES AND CONFINEMENT IN DETACHED PLASMAS IN TEXTOR.

U. Samm and R.R. Weynants*,

Institut für Plasmaphysik, Kernforschungsanlage Jülich GmbH, Association EURATOM-KFA, D-5170 Jülich, FRG.

and

Laboratoire de Physique des Plasmas - Laboratorium voor Plasmafysica
Association "Euratom-Etat belge" - Associatie "Euratom-Belgische Staat"
Ecole Royale Militaire - B 1040 Brussels - Koninklijke Militaire School

Abstract: The paper reviews various definitions of plasma detachment which are then confronted with detailed measurements describing the onset and evolution of detachment in ohmic deuterium plasmas in TEXTOR. The extent of the concomitant plasma response is best quantified by the radial variation of the peak of D_α emission, itself a measure of the ionization lengths of incoming neutrals. The peak of the total radiation (from bolometry) is found to be a less reliable monitor for detachment. Detachment also leads to a confinement deviation from Neo-Alcator scaling, the scope of which is discussed.

Introduction: The confinement of ohmic tokamak discharges is usually characterized by a linear $\bar{n}_e$ dependence of the global confinement time τ_E at low line averaged density $\bar{n}_e$, known as Neo-Alcator scaling, and a τ_E saturation or "roll-over" at high density. This change in behaviour could be due to the onset of turbulence, such as η_i modes, at high density. In this paper we deal with an alternative or additional mechanism for deviation from Neo-Alcator scaling: plasma detachment.

Well below the density limit, the plasma in a limiter tokamak leans onto, i.e. is attached to, the limiter. When, for otherwise constant machine conditions, the density is increased, the plasma starts to detach, i.e. a pronounced reduction in n_e and T_e at the edge develops resulting in penetration of wall released neutrals to smaller plasma radii leading to an inward shift of the ionization and, possibly, of the radiation layer surrounding the plasma. Earlier work can be found in [1-6].

A prerequisite for demonstrating the connection between detachment and confinement appears to be the establishment of a reliable definition of detachment, or even better, a parametrization capable of quantifying the intensity of the detachment phenomenon. In this paper, we review earlier definitions of detachment and propose a more stringent characterization. The relation of this definition to the earlier ones is demonstrated for a series of deuterium discharges in TEXTOR which also establishes a clear link between detachment and confinement deterioration.

The tokamak usually runs under all-carbon conditions : carbon limiters and a carbonized Inconel liner. During the experiments described here the plasma is limited by the fully toroidal belt limiter ALT-II. All other limiters are situated at least two centimeters in the shadow of ALT-II. The liner radius is 55 cm. The device parameters

---

* Research Director at NFSR, Belgium

for the experiments reported here are : a = 46 cm, R = 175 cm, B_T = 2 T, 250 kA < I_p < 350 kA, 1.5 x 10^{13} < $\bar{n}_e$ < 4.5 x 10^{13} cm^{-3}, 0.6 < $T_{e,o}$ < 1.5 keV.

Definition of detachment : The following characterizations of detachment can be found in the literature:

(1) It is generally agreed that a condition should be reached whereby the radiated power P_{rad}, mainly emitted from the boundary region, should rise close to the total input power P_{tot}. The ratio $\gamma = P_{rad}/P_{tot}$ should then almost be unity [1].

(2) When the above condition is reached, the plasma radius, then equated to the radius of the maximum of the radiative layer [2,3], is smaller than the limiter radius, i.e. the plasma is detached.

(3) Under these circumstances, the particle and heat fluxes to the limiter decrease and those to the wall increase [4]. The edge density and temperature are both depressed.

(4) The (maximum of the) particle recycling (mainly deuterium ionization) zone moves away from the limiter and is turned into a diffuse, poloidally and toroidally symmetric belt, detached from the limiter. It is worthwhile noting that this, to our best knowledge, constitutes the earliest definition of detachment [5].

These criteria are rather different in their capability to identify a given discharge as being detached: (1) is too vague; (3) only discriminates by comparison with an attached situation; (2) and (4) appear to be better adapted as they could quantify the very notion conveyed by the word detachment.

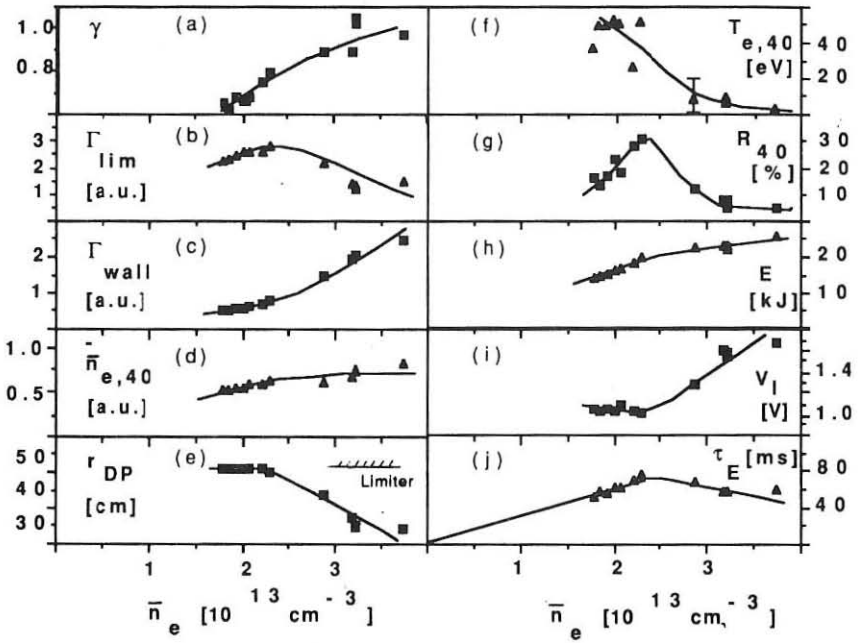

Fig. 1 Except in (j), all lines are mere fits to the data points.

Detachment in TEXTOR discharges: Figure 1 documents a density scan at I_p = 255 kA. Gasprogramming assures an $\bar{n}_e$ flat top from t = 1.0 to 1.6 s. The measurements are made at the end of this phase. The signals shown give (a) the radiation fraction γ (from bolometry, with an estimated error of about 10 %); (b) and (c) the particle fluxes to the limiter Γ_{lim} resp. to the walls Γ_{wall}; (d) the line density along the chord at r = 40 cm $\bar{n}_{e,40}$; (e) the radial position of the maximum of the profile of D_α emission r_{DP} ; (f) the electron temperature at r = 40 cm measured by laser scattering $T_{e,40}$; (g) the procentual contribution to the total radiation of the edge zone between r = 40 cm and r≈ 50 cm R_{40} ; (h) the total energy content E ; (i) the loop voltage V_l; (j) the energy confinement time τ_E.

At a density $\bar{n}_e$ = 2.25 .. 2.5 x 10^{13} cm^{-3} , the plasma detaches according to whatever criterium used : the peak of D_α emission strongly moves away from the limiter (e); the characteristic particle flux and edge behaviour is observed (b-d, f); the radiation originates from deeper inside the plasma (g). One notes that γ increases gradually over the experimental $\bar{n}_e$ range equalling 0.75 to 0.8 at the onset of the detachment phenomenon.

Our experience shows that the measurement of the position of the maximum of D_α emission r_{DP} probably constitutes the best monitor for identifying detachment, thus suggesting the following definition: *As soon as (a - r_{DP}) equals 2 cm or more in a device of the size of TEXTOR, a plasma is detached.* Furthermore, the extent of the concomitant plasma response increases monotonically with a - r_{DP} .

The alternative based on definition (2) must be used with care on TEXTOR. In Fig. 2 we show a dynamic situation in which gas puffing (Q) causes the plasma to detach from t ≈ 0.85 s on, to reach the density limit at t = 1.5 s. Figure 2(a) shows the temporal evolutions of γ , r_{DP} and $\bar{n}_e$ (I_p = 345 kA). The peak of D_α moves gradually away from the limiter, reaching r ≈ 34 cm at the moment of disruption which, within the errorbars, is reached at γ = 1. Figure 2(b) shows the simultaneous changes in the bolometric radiation profile: the peak of the emission moves slightly outwards until t = 1 s and then equally slightly inwards. At no rate is the motion as monotonic and pronounced as that of the D_α peak.

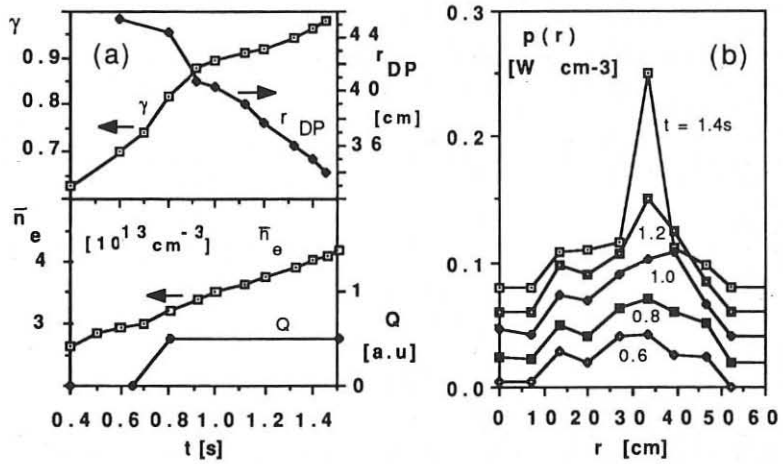

Fig.2 Please note the upshift by 0.02 of consecutive power profiles in (b).

The spatial resolution of the bolometer is typically ± 3 cm. R_{40} however decreases gradually from 28 % at t = 0.6 s to 11 % at t = 1.4 s: the radiation indeed originates from deeper inside the plasma due to the edge profile modifications. The significant change in the width of the profile can be explained by the observed increase of the density gradient at mid radius.

Confinement:. Simultaneously with the onset of detachment the plasma confinement is affected as seen on Fig.1 (h-j). The loopvoltage increases sharply and the energy turns over. As a result τ_E sharply bends away from the Neo-Alcator behaviour. The line fitted through the experimental points in Fig. 1(j) expresses the Neo-Alcator law pertaining to Textor [7] $\tau_E \sim \bar{n}_e\, a\, R^2\, q^{0.8}$, with the ansatz $a = r_{DP}$. Realizing that ($\bar{n}_e$ a) is representative of the line integral of the density, and evaluating q at the "new" plasma radius, the confinement time finally reads

$$\tau_E \sim \text{line integral}(n_e) \cdot r_{DP}^{1.6} \,. \qquad \text{Eq. (1)}$$

It should furthermore be noted that the $\bar{n}_e$ values plotted in the abscissa of Fig. 1 are actually the measured line integrals divided by the limiter diameter.

Discussion: (i) The data of Fig. 1 is particularly illustrative as the density range over which detachment prevails is rather wide at the relatively low current of 255 kA. As the plasma current increases, the separation between detachment onset and the density limit narrows [4]. (ii) The correlation between detachment and confinement degradation is not always as striking as shown above. We can find conditions in deuterium discharges where a mild deviation (up to15 %) from Neo-Alcator is already apparent before detachment (according to the r_{DP} criterium) sets in. In helium discharges a much stronger saturation is found which can not be accounted for by detachment. This mass dependence is under further study. (iii) The interference of competing saturation mechanisms might be the reason why Eq.(1) does not perform equally well under all circumstances. (iv) It is also important to recall that, when a detached plasma is auxiliarly heated, a substantial amount of extra incremental energy can be obtained in case of reattachment [6].

Conclusions: We propose the above introduced r_{DP} criterium as a reliable benchmark for defining detachment. Its usage also offers reasonable prospects for quantifying the inherent confinement degradation.

Acknowledgement: The help of J. Schlüter and the Textor diagnostic team and helpful discussions with J.D. Strachan, A.M. Messiaen and P. E. Vandenplas are highly appreciated.

References:

[1] Strachan, J.D., et al., Proc. 12th Eur. Conf. on Contr. Fus. and Pl. Phys., 1985, Vol.1,339.
[2] Lipschultz, B., J. Nucl. Mat. 145-147 (1987) 15.
[3] Strachan, J.D., et al., J. Nucl. Mat. 145-147 (1987) 186.
[4] Samm, U., et al., Plasma Phys. and Controll. Fusion, 29 (1987) 1321.
[5] Waltz, R.E. and K.H. Burrell, Nucl. Fusion 17 (1978),1001.
[6] Weynants, R.R., in Plasma confinement in attached and detached limiter tokamaks, Rep. 88, LPP-ERM/KMS, Brussels,1988; also Vandenplas P.E.,Proc. of Inv. Pap. of Int. Conf. on Pl. Phys. 1987, Kiev, Vol. 2, 1162.
[7] Weynants R.R., et al., Proc. 14th Eur. Conf. on Contr. Fus. and Pl. Phys., 1987, Vol. 1, 197.

THERMAL TRANSPORT DURING ELECTRON CYCLOTRON HEATING IN THE TEXT* TOKAMAK

D. C. Sing, M. E. Austin† , R. V. Bravenec, J.A. Boedo, J.Y. Chen††, G. Cima†††, M. Foster, R. Gandy†, K.W. Gentle, L.K. Huang§, W. H. Miner Jr., P.E. Phillips, A. Ouroua, B. Richards, B.A. Smith§§, W.P. West§§§, J.C. Wiley, A.J. Wootton, Z.M. Zhang††

The Fusion Research Center, The University of Texas at Austin, Austin TX 78712, USA.

Electron Cyclotron Heating (ECH) experiments have been performed on the TEXT tokamak (R_0 = 1 m, a = .26 m) using a Varian 60 Ghz, 200 kW gyrotron. Pulses as long as 89 ms have been delivered to the plasma. The TE_{11} mode is launched along the midplane with the O-mode polarization at 10° from perpendicular to B_T. Typical gyrotron power is 200 kW, which combined with the transmission and mode conversion efficiencies results in 157 kW launched into the tokamak. Experiments have been performed in two regimes; a low-q (I_P~200 kA, B_T~1.9-2.4 T, q(a) ~ 3, n_e~1.5-2.5 x 10^{19} m^{-3}) sawtoothing discharge, and a high-q (I_P ~110-140 kA, B_T~1.9-2.4 T, q(a)~5-6, n_e~1.5-2.0 x 10^{19} m^{-3}) non-sawtoothing discharge.

Figure 1 shows the changes in $T_e(0)$ (as measured by ECE) for typical low-q (I_P = 120 kA) and high-q (I_P = 200 kA) discharges with central ECH heating applied. The density drop usually associated with ECH in tokamaks is compensated by additional gas puffing to keep the line averaged density nearly constant at 1.6 x 10^{19} m^{-3}. The loop voltage drops 0.2 V (from 1.6 V to 1.4 V) in the low-q discharge and 0.4 V for the high-q discharge. For both cases P_{oh} decreases by ~40 kW. $T_e(0)$ for the low-q case shows a moderate increase (~30%), and the temperature sawteeth increase in amplitude by a factor of 3. For the high-q discharge $\Delta T_e(0)$ is much larger (~80%). Sawteeth occasionally occur after the ECH pulse turns off.

The T_e profiles for central ECH heating as measured by Thomson scattering are shown in Fig. 2a for low-q (with n_e = 2.5 x $10^{19}m^{-3}$ and in Fig. 2b for high-q (n_e = 1.8 x 10^{19} m^{-3}) discharges. In low-q discharges $T_e(0)$ increases but the shape of the profile remains similar to the pre-ECH case. The application of ECH to the high-q discharge changes the electron profile shape considerably, as well as increasing the central electron temperature as much as 80%. The increase due to ECH drops off rapidly

from the plasma center; outside of $\rho \equiv (r/a) \sim 0.2$ the increase of T_e is much smaller. The variation in $\Delta T_e(0)$ with resonance position depends on I_P; for low-q discharges $\Delta T_e(0)$ remains nearly constant when the resonance is within the mixing radius (~7 cm), and disappears when the resonance is moved outside of that radius. For the high-q discharge large ΔT_e's are obtained only when the resonance is within 3 cm of the magnetic axis.

Changes in electron thermal transport

The measured profiles of T_e, n_e, p_{rad}, and the central $T_i(0)$ and the changes in V_{loop} and I_P are used to determine the changes in χ_e by power balance analysis. The ECH power density was calculated using the TORAY ray tracing code [1] coupled with the measured gyrotron power output and known transmission and mode conversion losses. A lower limit to p_{ech} is calculated assuming single pass absorption (typically 75%) of a Gaussian beam by the plasma. The upper limit to p_{ech} is calculated assuming the remaining 20 to 30% is absorbed by the plasma according to the absorption profile shape calculated assuming uniform illumination of the plasma.

Figure 3 shows the χ_e profile determined by power balance analysis of the low-q discharge with central ECH heating. The heat transport inside the mixing radius ($\rho \sim 0.3$) is dominated by sawteeth and χ_e is not shown for $\rho < 0.3$. In the confinement region ($\rho \sim 0.5$) χ_e is increased by 35%. Measurement of $\chi_{e,HP}$ by the sawtooth heat pulse propagation method is possible for the low-q discharge and provides an independent measure of changes in confinement with ECH. Figure 4 shows the variation in $\chi_{e,HP}$ versus density for the low-q regime. As is usually observed, $\chi_{e,HP} > \chi_e$ from power balance. On average, $\chi_{e,HP}$ increases by 25% with on-axis ECH, which is comparable to the change in χ_e measured by power balance analysis, given the uncertainties in the χ_e measurements.

Figure 5 shows χ_e as measured by the power balance method for the non-sawtoothing high-q discharge. Also shown are the χ_e profiles used with the CHAPO [2] transport code to simulate the ohmic and ECH discharges. The power balance χ_e increases with ECH, but the error bars are large, primarily due to large uncertainties in computing dT_e/dr. The CHAPO calculated T_e profile and the measured T_e profile are shown in Figure 6. A 30% increase in χ_e from the ohmic case is required to match the $T_e(0)$

changes, which is consistent with χ_e scaling as $\sqrt{T_e}$. The agreement between the calculated and measured T_e profiles is reasonable, although the data (see Figure 2b) shows an inflection point in the T_e profile between ρ = 0.1 and 0.2.

Changes in the current density profile

Calculation of the q profile based on Spitzer resistivity indicates that q(0)~0.6 for the high-q ECH heated discharge. Sawtooth oscillations do not develop during the ECH pulse. A poloidal B-field profile measurement was undertaken to directly measure q(0) in a centrally heated (2.16 T) high-q discharge (I_P = 115 kA, q(a) = 5.7). The measurement of the poloidal field is obtained by polarization analysis of the 6708Å line emitted by neutral Li atoms in a beam injected into the plasma. A circular polarimeter was used to determine the pitch angle of the magnetic field lines at the point of observation [3]. The on-axis safety factor as measured by this method was near 0.5 on both experimental runs for which the measurement has been made, consistent with q(0) expected from Spitzer resistivity. In comparison, q(0) for sawtoothing discharges is consistently measured to be near unity by this method.

Conclusions

Moderate degradation of electron energy confinement is observed with ECH heating in the TEXT tokamak. This is observed for sawtoothing and non-sawtoothing discharges. Sharp T_e profiles are produced in high-q discharges by extremely localized central ECH power deposition coupled with the lack of sawtooth driven transport. Measurements of the q profile by polarimetry show that q(0) is significantly less than unity in a stable non-sawtoothing ECH discharge.

REFERENCES

[1] A.H. Kritz, et al., in "Heating in Toroidal Plasmas", vol.2, 707 (1982).
[2] J. C. Wiley, "CHAPO, A One Dimensional Transport Code", FRC report 328, The University of Texas Fusion Research Center, Austin TX(1988)
[3] D. Wroblewski, et al., Rev.Sci. Instr., vol. 59, 2341, (1988).

*Operated by The University of Texas at Austin under DOE grant No. DE-FG05-88ER53267.
† Auburn University, Auburn AL. ††Institute of Plasma Physics,Academia Sinica, Hefei, PRC. ††† Consiglio Nazionale Delle Ricerche, Milano, Italy. § Johns Hopkins University, Baltimore, MD. §§ Supported by a USDOE Magnetic Fusion Energy Fellowship administered by Oak Ridge Associated Universities. §§§ General Atomics Inc., San Diego, CA.

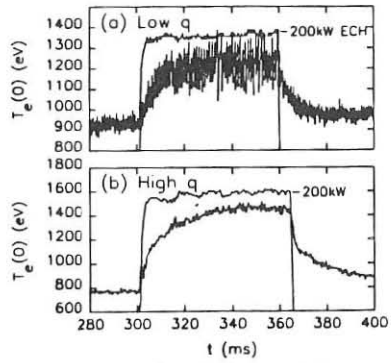

Fig. 1. $T_e(0)$ vs. time.(a) Low-q. (b) High-q

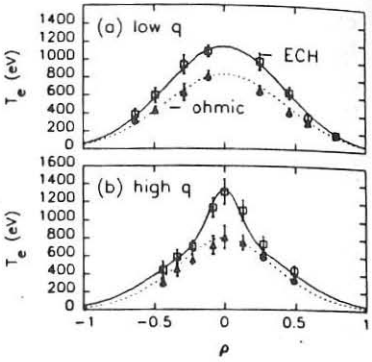

Fig. 2. T_e profile. (a) Low-q (b) High-q

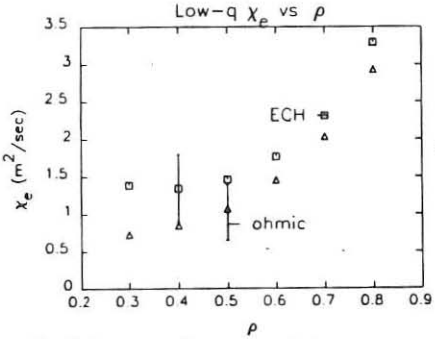

Fig. 3. Low-q χe from power balance

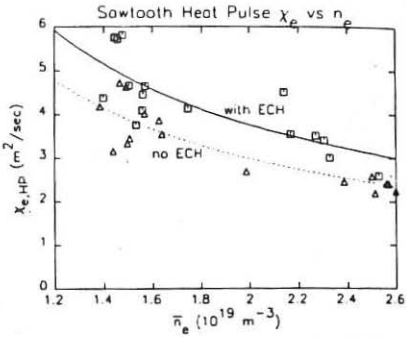

Fig. 4. Low-q $\chi e,HP$ vs. density from heat pulse propagation

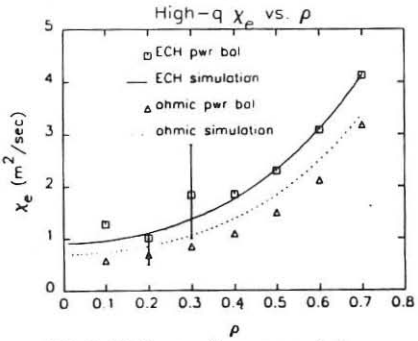

Fig. 5. High-q χe from power balance and simulation

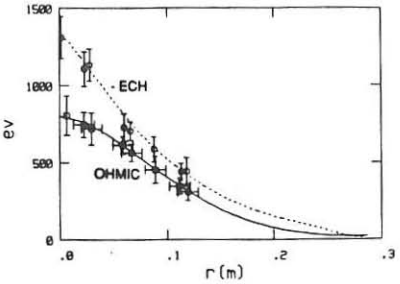

Fig. 6. Transport code T_e profile

EFFECT OF ECRH ON PARTICLE TRANSPORT IN THE TEXT TOKAMAK*

K.W. Gentle, B. Richards, D.L. Brower†, M.E. Austin††, G. Cima†††, N.C.Luhmann†, W.A. Peebles†, P.E. Phillips, W.L. Rowan, D.C. Sing, A.J.Wootton

Fusion Research Center, University of Texas, Austin, TX 78712

INTRODUCTION

Beginning with the some of the earliest experiments using electron cyclotron resonance heating (ECRH) on tokamaks [1], it has been observed that application of ECRH generally reduces the density. This effect has been explored in low-power ECRH experiments in the TEXT tokamak ($P_{ech} \leq P_{oh}$), where decreases in density, in spite of increased H_α, and changes in profiles have been observed both with the cyclotron resonance placed on axis and off axis. Furthermore, the effects on density occur both at low densities ($\langle n \rangle \leq 2 \times 10^{19}/m^3$), where the heating efficiency is good, and at higher densities, for which little heating is observed. For central resonance with good central heating efficiency, the density drop is caused by an increase in particle diffusion coefficient in the outer half of the plasma. The particle transport coefficients (particle diffusion coefficient and inward convection velocity) have been determined by gas-feed modulation experiments [2].

EXPERIMENT

TEXT is a conventional tokamak of 1 m major radius, 0.26 m minor radius, and full poloidal TiC-coated graphite limiter [3]. Typical operating parameters, which were used for the experiment reported here, are a toroidal field of 2.1 T, 200 kA plasma current, and an average density of $2 \times 10^{19}/m^3$; the central electron temperature is approximately 800 eV for reasonably clean hydrogen discharges. These are typical low-β sawtoothing discharges, $\beta_p \leq 0.2$. The ECRH is provided by one 60 GHz gyrotron which supplies 200 kW for 80 ms and is coupled to the plasma with an O-mode

outside-launch antenna. Total coupling efficiency is estimated to be approximately 70%. Heating efficiency is good for central resonance at this density; T_{eo} increases by 25% (cf. companion paper by D.C. Sing, *et al*, at this meeting).

For this case, the line-averaged density typically decreased by 10% while H_α increased by a similar amount. However, the density could be maintained constant by an appropriate modest adjustment of the gas feed. Such effects could be the result of changes in plasma transport, or they might reflect primarily changes in edge conditions: recycling, limiter pumping, etc. To determine if genuine changes in particle transport were induced by ECRH, gas-feed modulation experiments were performed to measure the transport coefficients. A modulation frequency of 31 Hz was sufficient to provide two full periods of quasi-equilibrium modulation during the ECRH pulse. Typical traces are shown in Fig.1. The amplitude and phase of the density modulation were constructed from multi-chord FIR interferometry. The instrument could be moved to scan the region from 20 cm inside the major radius to the limiter outside. By combining results from several discharges, chord integrals of the flux-surface averaged density perturbation over the range of minor radius from 0 to 18 cm could be obtained.

The transport coefficients are extracted by fitting the data with a model which includes both diffusion and convection and a realistic model of the source near the edge. The coefficients have independent values in the interior and exterior region of the plasma and make a linear transition in between. The values of the coefficients as well as the radii which bound the constant regions are adjusted for best fit to the data. To avoid errors which would be associated with quantitative source measurements, both the model calculation and the experimental data are normalized: the amplitude is unity and the phase zero for the central chord. A typical fit to the data during ECRH is shown in Fig. 2, which shows the amplitude and phase of the perturbation as observed at 6, 9, 12, 15, and 18 cm together with the curves from the model calculation of best fit. In addition, the bottom panel shows the equilibrium (chord-integrated) density profile implied by the transport coefficients deduced from the modulation experiment together with the experimental points. The fits to the preceding ohmic phase are even better because the longer time interval permits better extraction of the modulation amplitude and phase. The fits are excellent.

The transport coefficients which provide these fits for the ohmic and ECRH plasmas are plotted in Fig. 3. Although the ECRH resonance is at the center and the heating is strongly peaked within q=1, the particle transport coefficients are unchanged in the central region. The principal change is an

increase of more than 25% in the peripheral particle diffusion coefficient. (There is also a slight decrease in peripheral convective velocity in this case, but that is not consistently seen for all cases analyzed; the increase in D is always found.) The increase in diffusion occurs in the entire outer portion ($r \geq 15$ cm) of the plasma; it is not purely an edge effect. In fact, since the analysis uses data only out to 18 cm, purely edge effects have little influence on the result. The strongest evidence that the increase in D is uniform in the outer region is that fact that the increase in D deduced here is consistent in magnitude with the reduction in global particle confinement time inferred from H_α, which is largely determined by D in the edge source region.

Furthermore, the amplitude of the H_α modulation remains constant from OH to ECRH during the discharge, but the absolute magnitudes of the density perturbations decrease during ECRH, suggesting the same increase in D near the edge during ECRH. (Since only the profile of relative perturbation amplitudes is used in the analysis above, this effect is independent of those results.)

CONCLUSION

The application of central ECRH power induces an increase in the particle diffusion coefficient in the outer region of the plasma, but no significant effect in the interior. This is certainly consistent with the decrease of density generally associated with ECRH. The specific mechanism, however, remains an enigma, for the outer region seems the region least affected, either directly or indirectly, by the ECRH. The local parameters are very slightly changed. Similar density decreases are observed at higher densities, for which central heating no longer occurs, and with off-axis heating. Additional experiments of this type will be required to confirm if the same increase in particle diffusion is responsible in these cases as well.

* Supported by the US Department of Energy, Contract No. DE-FG05-88ER53267.
† University of California, Los Angeles, USA.
†† Auburn University, Auburn, AL, USA.

[1] R.M. Gilgenbach, et al. Phys. Rev. Lett. **44**, 647 (1980).
[2] K.W. Gentle, B. Richards, F. Waelbroeck, Plasma Physics and Controlled Fusion **29**, 1077(1987).
[3] R.V. Bravenec, et al. Plasma Physics and Controlled Fusion **27**,1335 (1985).

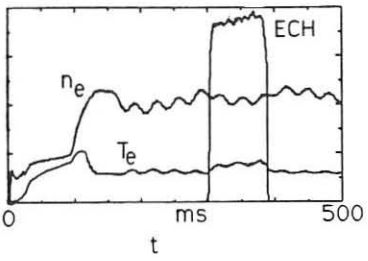

Fig. 1. Time traces of the modulated gas feed experiment. The central interferometer chord, central electron temperature from ECE, and ECRH power are shown.

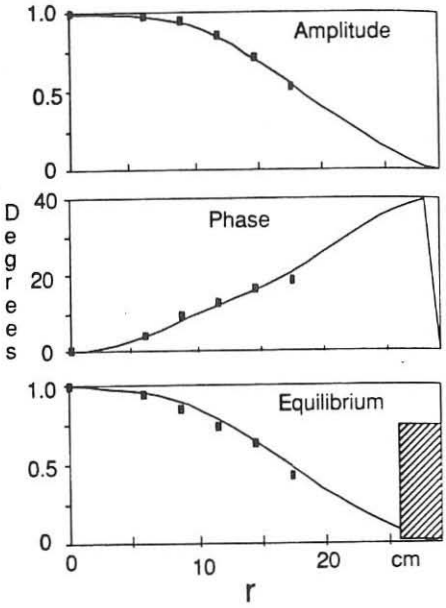

Fig. 2. Calculated fits to the amplitude and phase of the density modulation and the equilibrium profile using the transport coefficients which best fit the modulation data.

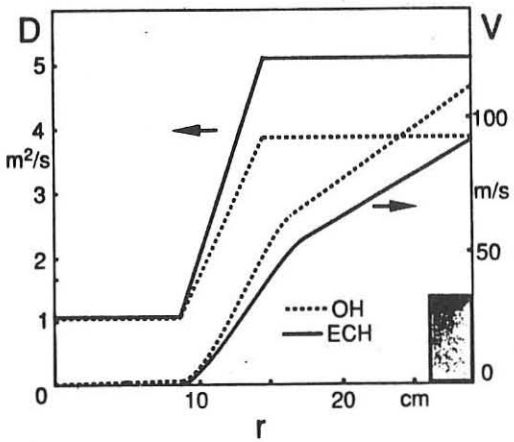

Fig. 3. The model transport coefficients, D(r) and V(r), which best fit the data of Fig. 2.

INVESTIGATION OF THE DENSITY TURBULENCE IN OHMIC ASDEX PLASMAS.

G. Dodel and E. Holzhauer, Institut für Plasmaforschung, Universität Stuttgart, FRG.

L. Giannone, H. Niedermeyer and ASDEX-Team, MPI für Plasmaphysik, EURATOM Association, Garching, FRG.

A 119 μm homodyne laser scattering experiment is used on ASDEX to investigate wavenumber and frequency spectra of the density fluctuations occurring in the different operational conditions of the machine. Details of the scattering system are described in [1]. It allows shot-to-shot spatial scans in three horizontal and two vertical channels which traverse the plasma at distances of 0, 10.5, 25, 30 and 39.5 cm from the plasma centre (minor plasma radius = 40 cm). The wavenumber range accessible is $2.5\ cm^{-1} < k_\perp < 25\ cm^{-1}$ and can be scanned within one shot. For $k_\perp < 10\ cm^{-1}$, where the dominant part of the fluctuation spectrum is found, the measurements are chord-averaged.

The changes of the density turbulence caused by additional heating are of primary interest with regard to a possible correlation to anomalous transport. Therefore, in the current experiment particular emphasis is placed on these investigations. On the other hand it is the ohmic phase which constitutes the least complicated physical situation in a tokamak and is therefore best suited to reveal the basic physical nature of the density turbulence. In the following we present a summary of our findings in the ohmic phase and make an attempt to compare these findings with what would be expected from the simplest model of density-gradient-driven driftwave turbulence saturated at the mixing-length level.

1. Density scaling of the density turbulence.

The rms value of the frequency integrated scattered power scales linearly with the mean electron density, as illustrated in Fig. 1 for a density ramp with two plateaus. This was established for $\bar{n}_e < 5\times10^{13}cm^{-3}$ in the important $k_\perp$ range and in different spatial chords. Since the shape of the density profiles (and hence the gradient length L_n) during density ramping remained fairly similar, our result suggests that $\tilde{n}_e/n_e$ is constant. This scaling is consistent with a fluctuation level determined by the mixing length criterion $\tilde{n}_e/n_e \propto (k_\perp L_n)^{-1}$. The linear dependence of the fluctuation level on line density was observed both in the SOC (standard ohmic confinement) and IOC (improved ohmic confinement) regimes. Note that the homodyne system presently used does not allow to determine the propagation direction of the fluctuations. This leaves open the possibility of the existence of the η_i-mode travelling in the ion diamagnetic drift direction.

2. Isotope scaling of the density turbulence.

The maximum of the frequency integrated $k_\perp$ spectrum shifts towards lower $k_\perp$ and its value increases when the gas filling is changed from pure hydrogen to

an approximately 1:1 mixture of hydrogen and deuterium at constant electron density (Fig. 2). Both the shift of the maximum and the increase of the fluctuation level are consistent with $k_\perp^{max} \cdot \rho_s$ = const. and $\tilde{n}_e/n_e \propto (k_\perp^{max} \cdot L_n)^{-1}$ as suggested by driftwave turbulence theory. The quantity ρ_s constitutes a characteristic length scale and is given by $\rho_s = (k_B T_e/m_i)^{1/2}/\omega_{ci}$, where $\omega_{ci} = ZeB/m_i$ (m_i - ion mass; Ze - ion charge). Note that the global confinement time increases with atomic mass in ASDEX [2]. Hence the increase of the fluctuation level is in contrast to what would be expected if the confinement were determined predominantly by the density fluctuation level.

3. Scaling of the density turbulence with toroidal magnetic field.

In a series of discharges in deuterium the toroidal magnetic field was varied from 1.9 T to 2.8 T while keeping the line electron density and the safety factor constant (q(a)=3). The shape of the density and temperature profiles remained practically unchanged. The electron temperature on the axis increased from $T_e(0)$= 1.1 keV at B_T = 1.9 T to $T_e(0)$ = 1.7 keV at B_T = 2.8 T. The frequency integrated $k_\perp$ spectra are shown in Fig. 3. The clear decrease of the fluctuation level with increasing field is consistent with the mixing length model. No definite statement can be made about a possible ρ_s scaling of the $k_\perp$ spectra expected from the relation $k_\perp^{max} \propto \rho_s^{-1}$, since no maximum is observed in deuterium at these temperatures even at the highest achievable toroidal field.

4. Scaling of the density turbulence with electron temperature.

In "cold" hydrogen discharges a maximum of the frequency integrated $k_\perp$ spectra is observed as can be seen in Fig. 4 for $T_e(0)$ = 650 eV. The maximum shifts towards lower wavenumbers with increasing electron temperature. This is consistent with the T_e dependence of the ρ_s-scaling. A value $k_\perp^{max} \cdot \rho_s \approx 0.3$ is inferred from the "cold" shot under the assumption that the main contribution of the scattered radiation originates from the gradient region.

5. Frequency spectra.

In the central chord which sees primarily poloidally propagating fluctuations a maximum of the scattered power is observed around ~ 100 kHz in the dominant $k_\perp$ range. This is on the order of the diamagnetic drift frequency evaluated in the gradient region of the discharge. In the outer vertical chord which sees predominantly radially propagating fluctuations the frequency spectra are significantly narrower [1].

In a preliminary heterodyne experiment a frequency shift of 45 kHz for the local oscillator was achieved with a rotating diffraction grating. This was sufficient to observe both the positive and negative frequency components of the narrow spectrum in the outer vertical channel close to the separatrix. The spectra were found to be symmetric. Similar results have been reported for the radial components of the fluctuations close to the limiter in TEXT [3].

A clear correlation was observed between the Mirnow coil signals at frequencies of a few kHz. This indicates a principal complication for the interpretation of frequency and wavenumber spectra, because it becomes difficult to distinguish between microturbulence and macroscopic MHD phenomena.

Conclusions

The aim of the investigation in the ohmic phase was the determination of the effect of a systematic variation in plasma parameters on the density turbulence, with the view to identifying the nature of the fluctuations. The interpretation of the results is complicated by the fact that one-parameter-scans are inherently impossible. Nevertheless, there is strong evidence for a drift wave origin of the fluctuations observed under ohmic conditions.

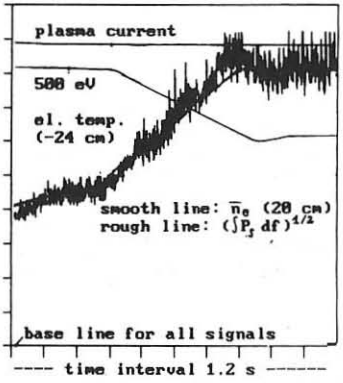

Fig.1: Density scaling of the rms scattering signal $(P_s)^{1/2}$ illustrated in a shot with a density ramp and two plateaus ($k_\perp = 3\ cm^{-1}$, r = 0 cm).

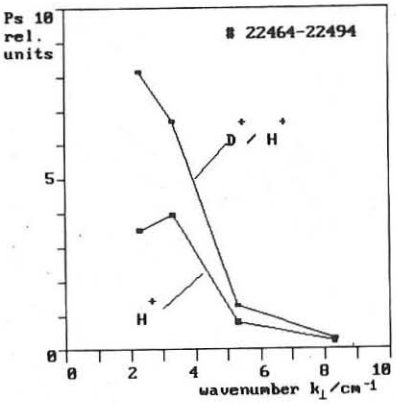

Fig.2: Change of the wavenumber spectra with gas filling. Note: Same vertical scale for both curves.

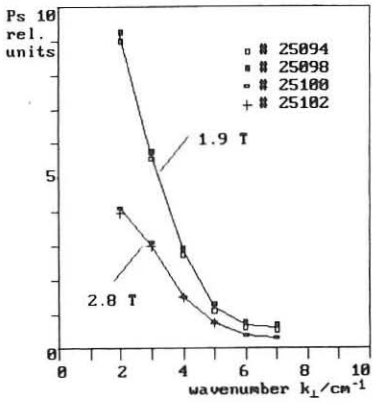

Fig.3: Wavenumber spectra in ohmic discharges with low and high toroidal magnetic field ($n_e(0) = 4x10^{13} cm^{-3}$, D^+). Note: Same vertical scale for both curves.

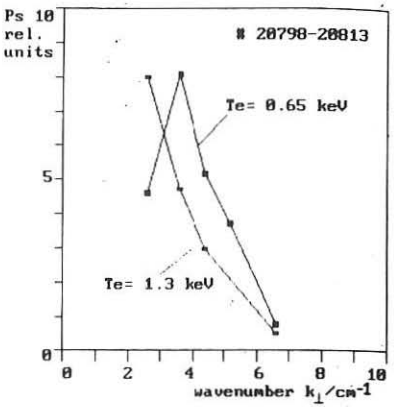

Fig.4: Wavenumber spectra in "hot" and "cold" ohmic hydrogen plasmas. The densities in the center are $1.75x10^{13}$ cm^{-3} and $4.8x10^{13}$, respectively. Signals are normalized to maximum value.

References

[1] G. Dodel, E. Holzhauer, H. Niedermeyer, K. McCormick, ASDEX-, ICRH-, NI-, and Pellet-Teams, Proc. 15th European Conf. on Controlled Fusion and Plasma Heating, Dubrovnik, 1988, Part I. p. 43.

[2] F. Wagner, M. Bessenrodt-Weberpals, G. Dodel, O. Gehre, L. Giannone, O. Gruber, E. Holzhauer, V. Mertens, H.D. Murmann, H. Niedermeyer (this conference).

[3] C.P. Ritz, D.L. Brower, T.L. Rhodes, R.D. Bengtson, S.J. Levinson, N.C. Luhmann, Jr., W.A. Peebles, E.J. Powers, Nuclear Fusion, vol. 27, p. 1125 (1987).

COMPARISON OF PARTICLE TRANSPORT FOR TARGET GAS AND IMPURITIES IN ASDEX UNDER SATURATED AND IMPROVED OHMIC CONFINEMENT

O. Gehre, G. Fußmann, K. W. Gentle[+], K. Krieger

Max-Planck-Institut für Plasmaphysik
EURATOM Association, 8046 Garching, Fed. Rep. of Germany

INTRODUCTION: Particle transport in ASDEX was investigated for Ohmic deuterium plasmas under saturated (SOC) and improved (IOC) confinement conditions. Transport in the target plasma was analyzed, using oscillating gas-puff experiments. The results are compared to transport of impurities evaluated from impurity gas-puffing and laser blow-off experiments under similar plasma parameters.

METHOD FOR THE TARGET PLASMA: The determination of particle transport coefficients is based on the solution of the particle conservation equation

$$\partial n/\partial t = -\nabla\cdot\Gamma + P, \quad \Gamma = -D\nabla n - V n$$

including an ionization production term P and a general particle flux Γ with both diffusion D and convection V. This equation is linearized for small sinusoidal perturbations from equilibrium, giving an equation for the perturbed density, which can be brought into a form suited to direct numerical solution. As an improvement to the previously used analytical method /1/, /2/, this allows a better description of the radial dependences of D and V, which are evaluated by fitting the calculated values for the complex perturbation amplitude to the values measured at different interferometer chords.

TRANSPORT RESULTS: Using this scheme, particle transport can be best modelled by a constant value for D in the inner plasma region and a different, normally higher value in the confinement zone. The transition between both regions takes place within 10 to 30 % of the full radius, typically starting outside the q=1 surface. A similar dependence is found for the convective inward term, where an additional linear increase with radius has to be superimposed.

Transport parameters determined this way for hydrogen plasmas allow a good description of the measured equilibrium profiles at all densities. In deuterium this holds for densities in the linear range of τ_e (LOC), but for higher values the calculated profiles are normally more peaked than the measured ones. A possible explanation could be the substantially stronger modulation of the profile shape, found in deuterium for the same relative line density perturbation. To get a good agreement with the measured equilibrium profile for these cases, the central inward convection has to

---

[+] University of Texas, Austin, USA

be fixed at a low value, while the other transport parameters are evaluated by the fitting procedure. The central diffusion and the edge values of D and V are only slightly altered by this modification, which has been used for deuterium, at the expense of a somewhat lower fitting accuracy with respect to the measured perturbation amplitudes.

In Figs. 1 and 2 the changes of the central and edge diffusion, respectively, are shown versus density. Both quantities decrease by approximately an order of magnitude between the lower and higher end of the LOC. In the SOC, D(0) and D_e remain constant, a further decrease, however, is obtained if IOC conditions are reached. In Fig. 3 the radial dependences of all transport parameters are shown for a case of beginning SOC and an IOC case. The absolute values for inward convection are nearly equal for both regimes, only the transition from low central to higher edge V seems to be shifted to larger radii in IOC. The main changes occur in the diffusive transport, which is reduced by about a factor of 3 in the outer part of the plasma for IOC and, to a less extent, also in the central region. The corresponding increase of V/D is in accordance with the steeper density gradients measured for the peaked IOC profiles /3/.

METHOD FOR THE IMPURITIES: The transport coefficients of the impurities were determined by means of sinusoidal modulated gas-puffing of SiH_4 and H_2S and, for metallic impurities like Al, Ti and Cr, using the laser ablation method. With gas puffing, the phase shift to the gas valve and the amplitude of spectroscopic signals are measured. Values for the diffusion coefficient are determined by analyzing the phase shift at a given modulation frequency and alternatively from amplitude ratios for different frequencies. Additional information about the convection velocity can be obtained by analyzing the radial profile of the fourier amplitude. The profiles of phase shift and amplitude are measured by radial scan of a spectrometer in a series of equivalent shots.

With laser ablation the characteristic times for maximum emission and exponential decay are evaluated. The transport coefficients are determined using an analytical model for anomalous transport and, for more sophisticated transport models, using an impurity transport code.

TRANSPORT RESULTS FOR IMPURITIES: For the comparison of SOC and IOC regime only the laser ablation was used so far. In first studies the transport parameters for the target plasma were inserted in the impurity transport code, but no satisfactory agreement of predicted and measured decay times could be derived. A better fit to experimental results was obtained by using the ansatz for anomalous impurity fluxes $\Gamma_z = - D\ \partial n_z/\partial r + V\ n_z$ with D = const. and $V = V_a\ r/a$. We found $D \approx 0.69\ m^2/s$ in the SOC regime and a strongly reduced value of $D \approx 0.33\ m^2/s$ in the IOC regime. The inward drift velocity was found to be nearly the same for both SOC and IOC with $V_a \approx 0.25$ m/s.

Figure 4 shows these parameters as a function of radius. Figure 5 shows the measured and predicted time development of the Ti XX signal for SOC and IOC regime.

In a further study we used a model with neoclassical transport and an additional anomalous diffusion term. In this case we found slightly higher values for diffusion correspdonding to the stronger neoclassical inward

drift. With the model of pure anomalous transport we obtained, however, a better agreement of predicted and measured time development of signals.

CONCLUSION: A comparison of the transport parameters for electrons and impurities leads to the result that the diffusion of the impurities is substantially higher in the SOC as well as in the IOC regime. The radial dependences of D and V, however, are similar and the ratio V/D shows the same behaviour for electrons and impurities, where we see an increase at the transition from SOC to IOC regime for both species.

References:

/1/ K.W. Gentle, B. Richards, et al., Plasma Physics and Controlled Fusion 29, 1077 (1987).
/2/ O. Gehre, K.W. Gentle, et al., Proc. of the 15th European Conference on Contr. Fusion and Plasma Physics, Dubrovnik (1988), Vol. 1, p. 7.
/3/ F.X. Söldner, E.R. Müller, et al., Phys. Rev. Lett, Vol. 61, No. 9, 1105.

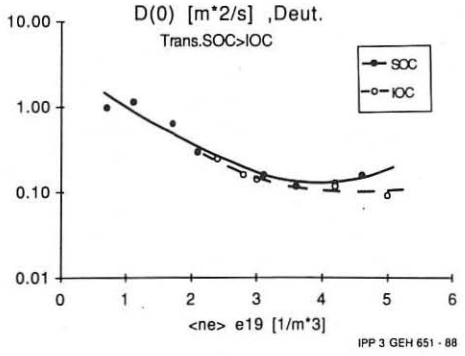

Fig. 1: Behaviour of the central diffusion, when the average density is increased through the linear range to SOC respect. IOC values. (The open circles mark the series, where, due to wall conditions, the transition SOC → IOC was possible).

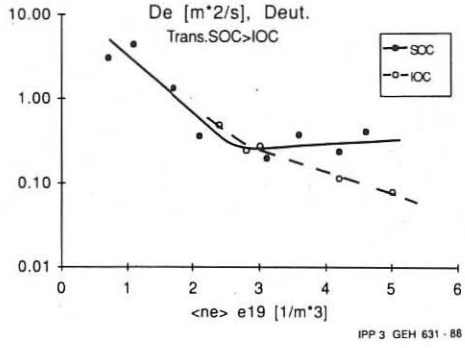

Fig. 2: Behaviour of the edge diffusion, shown for the same series of discharges as in Fig. 1.

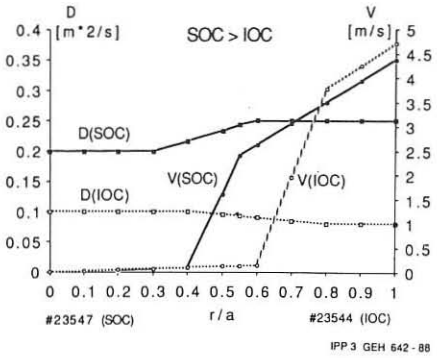

Fig. 3: Diffusion D and inward drift velocity V in deuterium versus normalized plasma radius, shown for a SOC and an IOC case within a series.

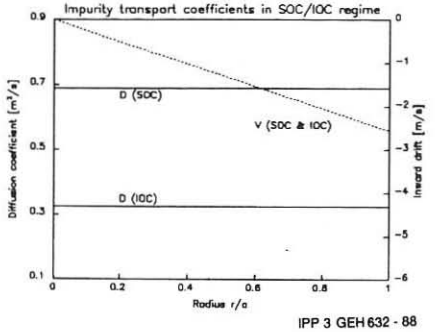

Fig. 4: Impurity transport coefficients as a function of radius.

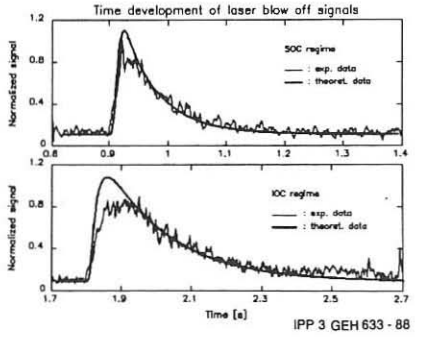

Fig. 5: Time development of measured and predicted TiXX signal for the SOC and IOC regime, respectively. In the SOC shot #23608 laser blow off was performed at t=0.9s, in the IOC shot #23610 at t=1.8s.

Ion and Toroidal Momentum Transport with Flat (Co-NBI) and Peaked (Ctr-NBI) Density Profiles in ASDEX

O. Gruber, A. Kallenbach, H.-U. Fahrbach, H. Herrmann, O. Vollmer

Max-Planck-Institut für Plasmaphysik, EURATOM Association, D-8046 Garching

1.Introduction

Strongly peaked electron density profiles have been obtained in ASDEX by different refuelling methods: pellet fuelling (ohmic and co-injection heating), NBI counter-injection and recently by reduced gas puff fuelling scenarios /1/. These discharges show in common an improvement of the particle and energy confinement. Local transport analyses indicate that the improved energy transport can be explained by reduced ion heat conductivity with values close to the neoclassical ones. The different results for the ion transport with flat and peaked density profiles agree with those expected from a superposition of neo-classical and ion-temperature-gradient driven turbulence (η_i-mode) contributions to χ_i. Consistently all cases showing confinement improvement through density peaking correspond to η_i(and η_e)<1 over a large part of the plasma cross- section. The thermal ion losses are of comparable magnitude of the electron thermal ones in both ohmic and L-mode discharges except at low densities /1/.

Toroidal momentum confinement studies are an additional tool to gain insight into the nature of ion transport, and have the advantage to isolate ion and electron transport compared with energy confinement studies, since momentum is carried almost entirely by the ions. In this paper we compare the ion and toroidal momentum transport in ASDEX discharges with nearly tangential Co and Ctr neutral beam injection using - besides the T_e and n_e-profiles measured with a 16-channel YAG-Thomson scattering system - T_i- and plasma rotation velocity V_φ-profiles measured by passive and active neutral CX analyzers and CX resonance spectroscopy /2/, respectively, at up to 5 radial positions and the TRANSP analysis code /3/.

2. Global Confinement results

We concentrate on two deuterium discharges having both I_p=420 kA, B_t=2.0 T (q(a)=2.25), and a beam heating power of .9 MW(40 keV H^0). Up to the start of the beam heating at 1.05 s (beam turn-off at 2.2 s) both discharges are nearly identical, but in the Ctr discharge the particle content increases despite of the external gas feed closed after 1.2 s. Simultaneously the density profile

- described by the ratio of the central $n_e(0)$ to the volume averaged $<n_e>$ values in Fig.1a - is gradually peaking, the energy confinement time τ_E is increasing (Fig.1b) and V_φ increases too up to values of $1.7 \cdot 10^5$ m/s. This is shown in Fig.1a for the toroidal angular rotation frequency Ω, which is obtained from V_φ measured in the outer plasma midplane under the assumption of constant Ω on a flux surface. The momentum confinement time $\tau_\varphi = L/(\Gamma - dL/dt)$, with a beam torque Γ of about 1.1 N/m derived from MC beam deposition and slowing down calculations and the plasma angular momentum L, improves in spite of the increasing density and inertial momentum, respect., and even exceeds the maximum τ_E values ($\tau_\varphi \leq 0.1$ sec). The decrease of τ_E in the later phase of the discharge and the final disruption are caused by the increasing radiation losses due to the improved impurity confinement and the disappearance of sawteeth at 1.4 sec. Correspondingly the Z_{eff} profiles are peaking as well /4/.

In the Co-NBI L-mode discharge with nearly stationary flat density profiles ($n_e(0)/<n_e> \approx 1.4$) only degraded energy confinement compared with the ohmic heating phase is observed and impurities do not accumulate (see Fig.2a and b). The rotation velocity is nearly stationary after about .2 sec and has a slightly more peaked profile than in the Ctr discharge. τ_φ is nearly a factor of 2 smaller than τ_E ($\tau_\varphi \leq 0.03$ sec).

3. Local Analysis of Energy and Heat Transport

Local analysis of the momentum transport shows that CX drag and convective terms (assuming that cross-diffusing particles carry the local average velocity) are small and the diffusive part is dominating.The viscous ion heating due to the damping of rotational energy (the latter one being less than 6% of the plasma energy even in the Ctr discharge with the higher densities and rotation veloci- ties) is small compared with the full ohmic and beam heating powers. It increases to about 100 kW in the Ctr discharge, and is a factor of 2 smaller in the Co discharge. The resulting change of the heating power density profile is not essential in these discharges.

During the density peaking with Ctr NBI the momentum diffusivity χ_φ shows a reduction over the whole plasma cross-section exhibited in Fig.1b at r=2a/3. A comparison with the ion heat diffusivity χ_i calculated by the sum of the neo-classical value χ_{CH}, given by Chang and Hinton, and the η_i-mode contribution $\chi_{\eta i}$, given by Lee and Diamond (see /6/ and /1/), shows good agreement in the time behaviour at the same radius. But one has to remember that χ_{CH} is nearly time independent,whereas $\chi_{\eta i}$ is actually decreasing due to reduced η_i values coming close to 1. There exists within the error bars of such analyses - which have to be further ascertained - a factor of 2 to 4 diference between χ_φ and $\chi_{\eta i}$. A similar relation holds if radial profiles are compared (Fig.1c). In the central part of the plasma $\chi_{\eta i}$ is zero as the η_i-mode threshold is enhanced due to long density decay lengths.

In the Co-NBI L-mode discharge with flat density profiles and degraded confinement an increasing χ_e is largely responsible for the confinement degradation going from ohmic to NBI heating. χ_i is anomalous all the time (η_i>1.5) and the ion diffusivity shown in Fig.2b is almost purely anomalous, i.e. $\chi_{\eta i} \approx 0.7\ \chi_i$. χ_φ is strongly enhanced compared with the results of Ctr- discharges, but is again correlated to $\chi_{\eta i}$ within a factor of 2 to 3 (Fig.2b). This is also revealed by the radial profiles of the diffusivities shown in Fig.2c. The enhancement of χ_i and χ_e for r/a<0.4 is due to the action of sawteeth at the low q(a)=2.5 as profiles time averaged over the sawteeth have been used.

4. Conclusions and Comparison of Momentum Diffusivity with Theory

In beam heated ASDEX discharges ion heat and toroidal angular momentum transport are strongly improved by a peaking of the density profile. For the ion transport it has already been found that χ_i can be described by a superposition of neo-classical and η_i-mode driven contributions within experimental error bars. The results given above show also a close relation of the momentum diffusivity with the η_i evolution.

Comparing the deduced χ_φ -profiles with theoretically predicted values first conclusions can be given. Classical perpendicular viscosity damping is by at least an order of magnitude too small and has the wrong radial dependence. It may contribute in the plasma centre. Gyroviscosity theory /5/ gives about the right magnitude, but would yield the same χ_φ values for the Co and Ctr discharges. As $\chi_\varphi(\text{gyrovisc}) \sim T_i^2/Z_{eff}$ also the temperature and Z_{eff} time behaviour is not reproduced in the derived χ_φ values. There exists finally a theory based on η_i-mode driven shear viscosity which predicts $\chi_\varphi = \chi_{\eta i}$ in a slab fluid model /6/. Our experimental results indicate indeed a similar radial and time behaviour of both diffusivities, but rather a $\chi_\varphi \approx (2+4)\ \chi_{\eta i}$.

References

/1/ O. Gruber, et.al., Plasma Physics and Controlled Fusion **30** (1988) 1611
/2/ A. Kallenbach, et.al., this conference
/3/ R.J. Goldston, Bas. Phys. Proc. of Tor. Fus. Pl., **1**, EUR-10418-EN, CEC, Brussels(1986)165
/4/ R. Nolte, G. Fussmann and O. Gruber, this conference
/5/ W.M. Stacey and D.J. Sigmar, Phys. Fluids **28** (1985) 2800
/6/ N. Mattor and P.H. Diamond, Phys. Fluids **31** (1988) 1180

Figure Captions

Fig. 1 and 2 correspond to a Ctr and a Co, respectively, beam heated $H^0 \rightarrow D^+$ discharge (I_p=420 kA, B_t=2.0 T, 0.9 MW NBI from 1.05 to 2.2 s).

a) Time behaviour of volume averaged electron density n_e and toroidal angular rotation frequency Ω and of their profile peaking factors.
b) Time behaviour of energy (τ_E) and toroidal momentum (τ_φ) confinement times and of ion heat diffusivity χ_i, η_i-mode driven contribution $\chi_{\eta i}$ and toroidal momentum diffusivity χ_φ at r=2a/3.
c) Radial profiles of the ion heat (χ_i , $\chi_{\eta i}$), electron heat (χ_e) and toroidal momentum (χ_φ) difusivities.

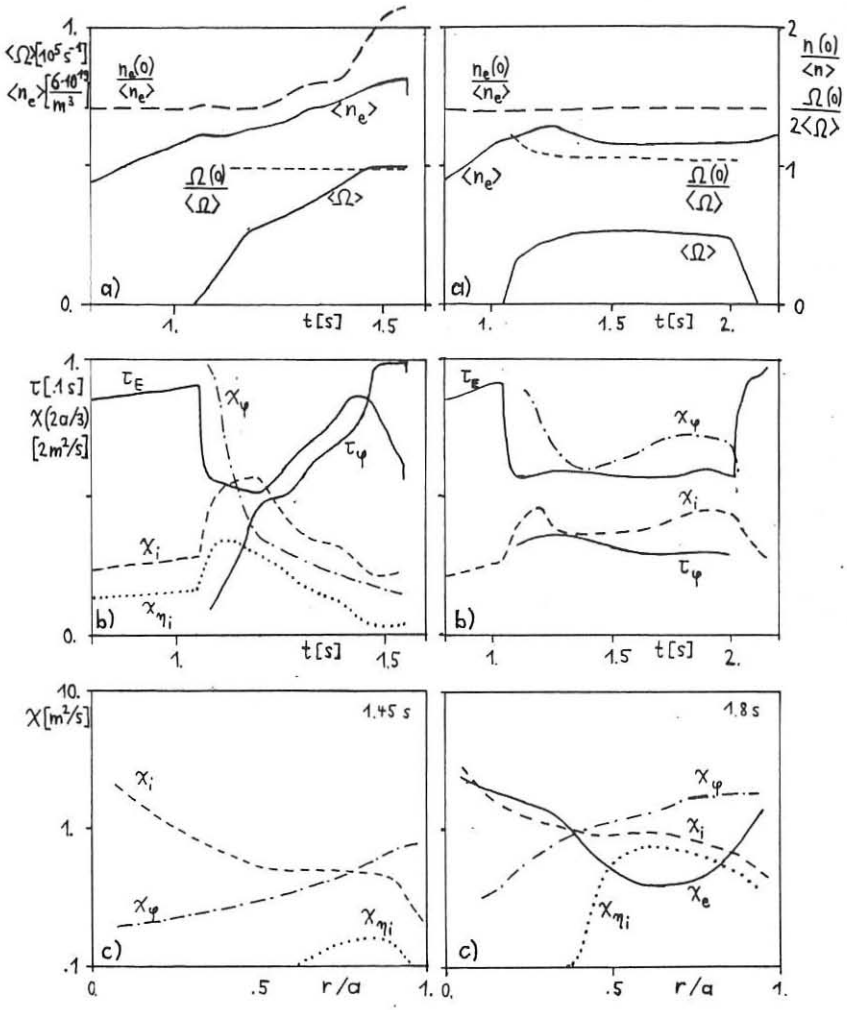

Fig.1 Ctr-discharge

Fig.2 Co-discharge

MOMENTUM CONFINEMENT STUDIES ON ASDEX

A. Kallenbach, H.M. Mayer, K. Brau+, G. Fussmann, and ASDEX-, NI-, ICRH- and Pellet Teams

IPP Garching, EURATOM Association, Fed. Rep. of Germany

1. Introduction

The toroidal plasma rotation induced by unbalanced neutral beam injection is a measure of plasma confinement, especially ion confinement. Since rotation velocities are experimentally easier accessible than ion temperatures, and the physics of momentum transport permits the neglection of electron transport effects, the study of momentum confinement is an effective diagnostic tool. We have investigated the rotational behaviour of the ASDEX plasma under different neutral beam heating schemes using charge exchange recombination (CXR) spectroscopy on up to five lines of sight [1]. Comparing the momentum confinement times derived from rotational profiles with the corresponding energy confinement times derived from β_{pol} measurements, the main differences and common features of momentum and energy confinement are discussed.

2. Experimental procedure

The plasma bulk rotation was determined from the Doppler shift of the CXR-excited C^{5+} (343.4 nm) line after subtraction of a cold, edge excited blending feature from the measured line profile. Five lines of sight in the outer plasma midplane have been used simultaneously, which intersect the northwest neutral beam line at r/a= 0.125, 0.375, 0.625, 0.875 and 1. In order to reduce the number of data points and to obtain a comparative figure, global momentum confinement times were deduced by integrating the momentum of the particles with respect to the whole plasma volume. To facilitate this, an exponential fit has been applied to each radial rotation (half-) profile which was extended to the inner part of the plasma under the assumption of constant angular rotation frequency of a flux surface [2]. For steady state conditions, the global momentum confinement time can be calculated as the quotient of plasma angular momentum, L, and beam torque, Γ: $\tau_\Phi = L/\Gamma$.

3. Results

Figure 1 shows the typical rotational behaviour of the ASDEX plasma with co and counter neutral beam injection under identical experimental conditions. Although the density rises during the counter NI, the plasma speeds up to a considerable higher velocity, which is an expression of improved confinement of momentum. Parallel to the observed improvement of momentum confinement, the energy confinement time increases as well [3].

The temporal and spatial development of the angular rotation frequency with D^0 injection under similar conditions as those of Fig. 1 are plotted in Figure 2. The corresponding rotation speed has slightly raised against that achieved with H^0 injection due to the higher torque of the deuterium beam in comparison with the hydrogen beam at the same injection power.

+ on leave from MIT, Cambridge, USA

In order to reduce the thermal load of the divertor plates and the erosion of copper, CD_4 is puffed into some ASDEX discharges. This measure increases considerably the duration of the counter NI discharges. As illustrated in Fig. 3, the additional CD_4 puffing slows down the rotation speed and prevents the plasma from further acceleration as observed from the counter NI discharges without methane puffing. A comparison of the temporal development of the momentum confinement times of a standard discharge, a discharge with pellet fuelling and the discharge with CD_4 puff is given in Fig. 4a, the corresponding energy confinement times are plotted in Fig. 4b. Although the two quantities scale in the same way, the change of confinement comes out much more clearly in the momentum confinement time than in the energy confinement time. It should be noted, that the steepest rise in momentum confinement without CD_4 puffing appears just when the sawteeth disappear in these discharges (t≈1.25 s), whereas the sawteeth do not disappear with CD_4 puffing and τ_ϕ stays at a lower level [4]. Pellet fuelling does not affect the momentum confinement drastically. While τ_ϕ is slighly improved during the pellet fuelled discharge, at its end this improvement stops. At the same time, the energy confinement begins to degrade until a disruption occurs.

Another example for the sensitivity of momentum confinement against changes of discharge parameters is given in Fig. 5. Here, at t=1.0 s, the number of active beamlines has been reduced from 3 to 1 and, additionally, CD_4 puffing has been reduced. As a result, τ_E increases moderately, but τ_ϕ is drastically improved, in contrast to the normally observed independence of τ_ϕ from the applied torque. The discharge is able to maintain the high angular momentum even with one third of the primary input torque over many of the (old) momentum confinement times.

The opposite behaviour is obtained, when additional ICRF heating is applied to the plasma with counter NI. As to be seen in Fig. 6, with ICRH the usually strong improvement of momentum confinement with counter injection fails to appear and τ_ϕ remains at a comparatively low level in the vicinity of τ_E. An interesting feature appears near the end of the discharge: A minor disruption causes the plasma to lose a part of its mass and the energy confinement time is pushed near zero. But while τ_E recovers in part after the event, the rotation of the plasma does not reappear although the torque of the neutral beams is still applied. In fact, such exceptional situations are the only occasions where momentum confinement times significantly smaller than the corresponding energy confinement times were found in ASDEX, in contrast to the results obtained with limiter machines, where τ_ϕ has typically half the value of τ_E [5].

4. Conclusion

The global momentum confinement time derived from rotational profiles of the plasma has been found to be a sensitive detector for changes in plasma confinement, with variations arising in the energy confinement time generally coming out more pronounced. A number of features in the rotational behaviour have been found, which still have to be explained: The strong increase of τ_ϕ during ctr.-NI, its degradation by ICRH and the strong influence of CD_4 puffing on the confinement of momentum. Since at the moment no theory of plasma viscosity exists which is able to describe the transport of momentum in detail, a simple analysis in terms of momentum diffusion seems to be appropriate. Comparing the momentum

confinement behaviour with that of the energy or particle confinement times, new insight may be gained concerning the overall plasma development.

References

[1] D.E. Roberts, H.M. Mayer et al. , Proc. 15th Europ. Conf. on Contr. Fusion and Plasma Phys., Dubrovnik, (1988) Part I, 15-18

[2] K.H. Burrell, R.J. Groebner, H. St. John, R.P. Seraydarian Nucl. Fus. **28**, (1988) 3-15

[3] O. Gruber et al., this conference

[4] R. Nolte et al., this conference

[5] S.D. Scott et al., presented on 12th Conf. on Plasma Phys. and Contr. Nucl. Fusion Research, Nice (1988)

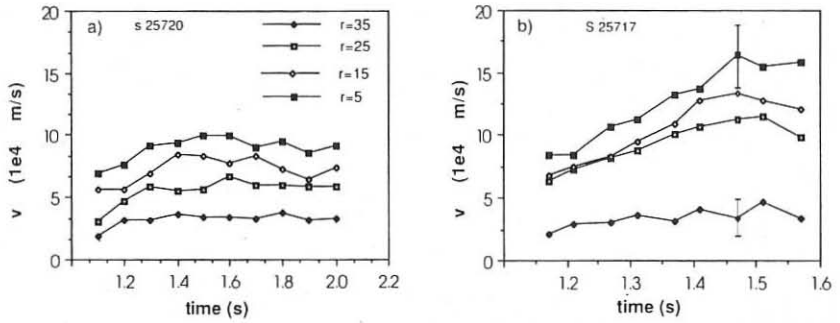

Fig. 1 Rotational behaviour with co and ctr. H^0 ->D^+ injection.
a) co injection. **b)** counter injection.

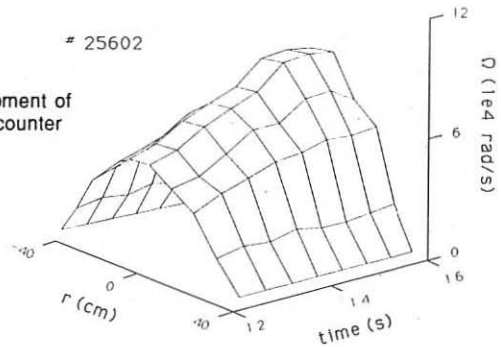

Fig. 2 Temporal and spatial development of the angular rotation frequency with counter injection, D^0->D^+.

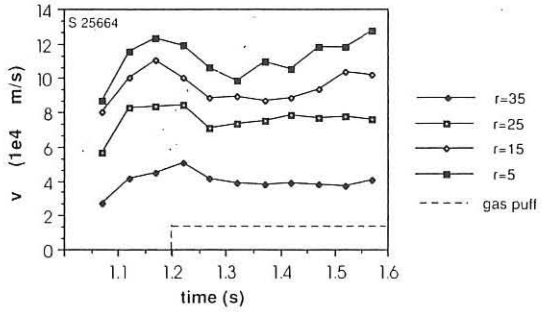

Fig. 3 Temporal development of the rotation at different plasma radii when CD_4 is puffed into the ctr-NI discharge.

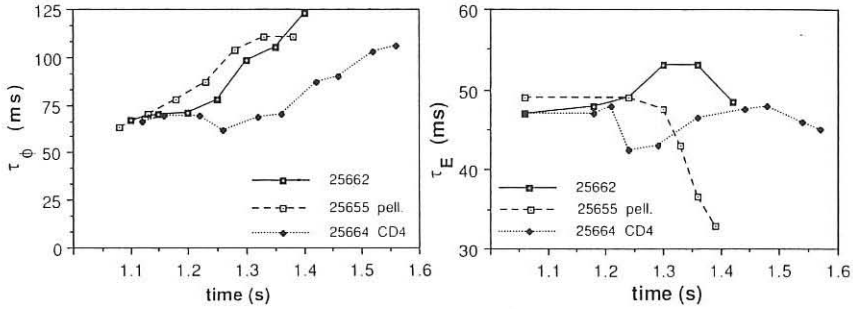

Fig. 4 a) Comparison of counter injection momentum confinement times with standard fuelling, pellet fuelling and additional CD_4 puffing. **b)** corresponding energy confinement times.

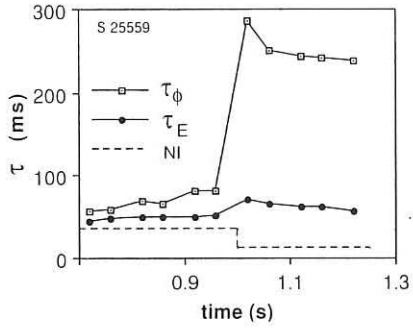

Fig. 5 Improvement of momentum confinement by the reduction of ctr.-NI and CD_4 puffing.

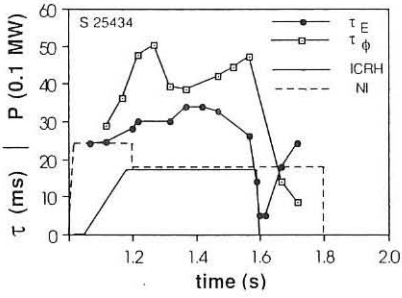

Fig. 6 Momentum confinement with ICRH and counter injection D^0->D^+.

PELLET PENETRATION IN ASDEX: A COMPARISON OF RESULTS COMPUTED BY MEANS OF THE ORNL ABLATION MODEL WITH MEASURED DATA

L.L. Lengyel, K. Büchl, and W. Sandmann

Max-Planck-Institut für Plasmaphysik, EURATOM Association,
D-8046 Garching, Fed. Rep. of Germany.

The neutral gas plasma shielding (NGPS) ablation model recently proposed by Houlberg et al. /1/ has been extensively tested on pellet penetration depths measured in JET /2/. The best fit among calculated and measured penetration depths was obtained by assuming a shielding cloud radius 1 mm larger than the local pellet radius: $R_{cl} = r_p + 1mm$, yielding maximum shielding at the end of the pellet lifetime ($r_p = 0$).

Recently, a model was developed that describes the time evolution of particle clouds in plasmas /3/. With the help of this model, the ionization radius, i.e. the radius of the shielding cloud, can be calculated as a function of the local ablation rate. The results of these calculations show that the shielding cloud radius is proportional to the number of particles locally deposited. The cloud expansion code can be combined with the ORNL ablation model with an R_{cl} feedback option between the two models.

Calculations are performed here for a number of randomly selected pellet-fuelled ASDEX shots. The pellet penetration is calculated for the measured $T_e(r)$ and $n_e(r)$ profiles by means of the ORNL ablation code with and without R_{cl} feedback active.

Eight ASDEX shots were selected for which the temperature and density data sets are complete (the radial distributions of T_e and n_e were reconstructed by fitting the data measured at 16 points and stored in the ASDEX data bank 'DABA' by means of spline functions). The central T_e and n_e values ranged in these shots from 0.5 to 0.75 keV and from 0.5 *to* 1.7 $(\times 10^{20})$ m^{-3}, respectively ($a = 0.4\ m$). The pellet penetration depths were measured by two different means: H_α radiation emission (constant pellet velocity assumption) measurements and direct photography in the visible light range. The pellet injection velocity was 650 m/s in all eight cases (centrifuge was used as pellet injector). The pellet sizes and the equivalent (spherical) pellet radii used in the calculations are displayed in Table 1. The plasma data were recorded during pellet injection (a string of approximately 20 pellets injected) typically at every 17 ms. The quantity Δt_{pre} represents the time delay between pellet injection and the nearest previous recording time. The quantity Δt_{post} is the time delay between the nearest recording time following pellet injection and the injection time. The particle content of the discharge is computed at every recording time by volume-integrating the measured density distribution (data evaluation program still under development). The ratio $\Delta N_{pla}/N_{pel}$ is supposed to show the fraction of pellet particles actually recovered in

the plasma. This quantity, also displayed in Table 1, shows unusually large scattering, unrelated to Δt_{post}, which makes the value of the effective pellet mass estimated on the basis of this ratio rather uncertain. (For example, the value given for shot #18711/#12 is in clear disagreement with the results of some auxiliary diagnostic checks.) Further quantities displayed in Table 1 are the experimental penetration depths determined by two different means and the one calculated on the basis of the ORNL ablation model with *Rcl* feedback active, and the calculated value of the shielding radius R_{cl} at the location of the maximum ablation rate. Finally, the central electron temperature and the maximum temperature 'seen' by the pellet at the end of its lifetime are also displayed. Because of the large scattering in the mass fraction values specified and the associated effective pellet radii, the calculations were repeated with an ad hoc constant mass fraction (=0.75). The resulting data are displayed in Table 2. In the same table, the pellet penetration depths calculated with the ad hoc assumption $R_{cl} = r_p + 1\ mm$ are also displayed (the values in parentheses). In spite of the substantial uncertainties regarding the actual pellet masses affecting the plasma, the following conclusions can be made:

(1) The penetration depths calculated by means of the NGPS ablation model with the R_{cl} feedback active lay within the range of the measured values.

(2) The duration of the H_α trace (in combination with the assumption of constant pellet velocity) does not always suffice for reliable determination of the pellet penetration depth.

(3) The effective shielding cloud radius at the location of the maximum ablation rate (i.e. close to the end of the pellet lifetime) is between 2.5 to 3.5 mm for the ASDEX plasma parameter ranges tested.

(4) The magnitude of the shielding cloud radius significantly affects the ablation rate and thus the penetration depth. The empirical or effective shielding cloud radii do not seem to be transferable from machine to machine (or from parameter set to parameter set). The replacement of the shielding radii calculated here with those stemming from the (JET) assumption $R_{cl} = r_{pel} + 1\ mm$ yields, under the ASDEX conditions tested and with the uncertainities described, penetration depths substantially different from the measured ones.

(5) Reliable validation calculations require at least a few shots with the following sets of experimental data:

5.1 Electron temperature and density distribution recordings immediately (i.e. with the minimum possible time delay) before and after the moment of pellet injection.

5.2 Reliable particle balances at the same time instants.

5.3 Measurement of the mass and velocity of the pellet just before its entry into the plasma and control of the pellet velocity during the flight time (checking its constancy), particularly at the time of maximum ablation rate.

5.4 Accurate determination of the pellet lifetime and of the associated penetration depth, if possible, by two independent means.

One will note that the sets of experimental data analyzed here did not in all cases simultaneously satisfy all the conditions (5.1 to 5.4) specified .

Shot No. / Pellet No.	N_{pel} (10^{19})	r_{pel} (mm)	$\frac{\Delta N_{pla}}{N_{pel}}$	r_{peff} (mm)	Δt_{pre} (ms)	Δt_{post} (ms)	Penetration depth (cm) H_α	Photo	Calc.	R_{cld} (mm)	$T_e(0)$ (keV)	T_{abl} (keV)
18710												
#1	2.9	.484	.46	.373	6.4	11.	17	25	18.5	3.4	.740	.528
#11	2.8	.479	.15	.254	10.8	7.0	19	26	16.1	2.5	.646	.396
#12	4.8	.573	.77	.524	7.7	9.0	24	27	32.1	3.0	.706	.649
18711												
#1	3.5	.516	1.0	.516	8.8	9.0	19	27	25.7	3.6	.746	.649
#11	4.4	.556	.60	.469	12.9	5.0	29	28	32.1	2.6	.553	.533
#12	4.2	.548	.10	.254	8.5	10.	25	26	17.7	2.2	.541	.346
18717												
#1	4.2	.548	1.0	.548	1.3	16.	18	27	28.9	3.6	.756	.676
#11	4.3	.552	.13	.282	7.8	9.0	25	29	18.5	2.5	.543	.404

Table 1

The ASDEX shots with pellet injection analyzed. The mass loss fraction computed by the ASDEX data analysis program was used to estimate $(r_p)_{eff}$.
Notation: N_{pel} - number of D atoms in the pellet, ΔN_{pla} - particle (electron) increment detected in the plasma following pellet injection, $(r_p)_{eff}$ - effective spherical pellet radius used in the ablation calculations; $\Delta t_{pre}, \Delta t_{post}$ - time delays before last data recording prior to and first data recording after pellet injection in relation to the pellet injection time, R_{cl} - calculated shielding cloud radius. $T_e(0)$ - central electron temperature, T_{abl} - electron temperature "seen" by the pellet at the end of its lifetime.

Shot No. / Pellet No.	N_{pel} (10^{19})	r_{pel} (mm)	$\frac{\Delta N_{pla}}{N_{pel}}$	r_{peff} (mm)	Δt_{pre} (ms)	Δt_{post} (ms)	Penetration depth (cm) H_α	Photo	Calc.	R_{cld} (mm)	T_{abl} (keV)
18710											
#1	2.9	.484	.75	.440	6.4	11.	17	25	21.7 (29.7)	3.6	.583
#11	2.8	.479	.75	.435	10.8	7.0	19	26	26.5 (34.5)	2.8	.549
#12	4.8	.573	.75	.520	7.7	9.0	24	27	31.3 (40.9)	3.0	.638
18711											
#1	3.5	.516	.75	.468	8.8	9.0	19	27	23.3 (32.1)	3.5	.614
#11	4.4	.556	.75	.506	12.9	5.0	29	28	35.3 (51.3)	2.6	.545
#12	4.2	.548	.75	.498	8.5	10.	25	26	36.9 (52.1)	2.5	.535
18717											
#1	4.2	.548	.75	.498	1.3	16.	18	27	25.7 (35.3)	3.5	.631
#11	4.3	.552	.75	.502	7.8	9.0	25	29	34.5 (50.5)	2.6	.543

Table 2:
The same shots as those displayed in Table 1, but with constant ad hoc mass fraction (=0.75) assumed. Numbers in parentheses represent penetration depths based on the $R_{cl} = r_p + 1mm$ assumption in the ablation rate calculations.

/1/ W.A. Houlberg et al., Nucl. Fusion **28** (1988), 595.
/2/ M.L. Watkins et al., Proc. 14th Eur. EPS Conf., Madrid, **11D**, (1987) 201.
/3/ L.L. Lengyel, Phys. Fluids **31** (1988), 1577.

PARTICLE TRANSPORT AND SAWTOOTH ACTIVITY IN PELLET-FUELLED ASDEX L-MODE PLASMAS

V. Mertens, K. Büchl, O. Gruber, M. Kaufmann, M. Kornherr, R. Lang, H. Murmann, W. Sandmann, K.H. Steuer, O. Vollmer

Max-Planck-Institut für Plasmaphysik, EURATOM Association, D-8046 Garching, Fed. Rep. of Germany

1. Introduction

Long-lasting enhancement of the performance of ASDEX (R = 1.65 m, a = 0.40 m) divertor discharges has been obtained by repetitive pellet injection. This regime is characterized by markedly centrally peaked electron density profiles, reduced sawtooth activity, central impurity radiation, enhanced density limit and improved global energy confinement time [1]. Almost independently of the heating power maximum densities of $\bar{n}_e = 1.4 \cdot 10^{20} m^{-3}$ are attained.

Pellet fuelling is applied with purely ohmic heating as well as with co-neutral beam injection (NBI) up to 2.6 MW (L-mode). The deuterium pellets, each contributing $3 \cdot 10^{19} m^{-3}$ to the volume-averaged plasma density, reach penetration depths of typically half the plasma radius. The investigation of diffusion coefficients D and inward pinch velocities V concentrates on discharges with carbonized walls and B_t = 2.2 T, I_p = 380 kA ($q_a = 2.7$).

2. Sawtooth Dynamics

Standard gas puff-fuelled (GP) discharges in ASDEX with ohmic and co-NBI heating show very regular behaviour of the sawtooth activity. The sawtooth repetition time normally increases with density and heating power in the range between ≈10 and 100 ms. The inversion ($q = 1$) radius and the corresponding sawtooth mixing zone shrinks with increasing q at the plasma boundary. The net inward motion and the correlated electron profile shape depends sensitively on the details of the sawtooth dynamics.

During pellet injection the sawteeth typically continue but their repetition time increases and the inversion radius shrinks culminating sometimes in the complete suppression of sawteeth. Figure 1 shows, for example, the time history of some characteristic plasma parameters of a 0.5 MW NBI-heated, pellet-refuelled discharge. With the start of pellet injection the inversion radius contracts slightly (fig. 1b). The radially shifting "sawtoothing zone" marks the region which is affected by the sawtooth activity according to the chord-integrated soft X-radiation. This radiation is also used to estimate the violence of the sawtooth activity A_{ST}. After the last pellet the sawtooth dynamics vanishes for about 0.1 s and simultaneously there is a dramatic increase of the central radiation. The plasma pressure β_p reaches its maximum during this phase. Parallel to the rise of the central radiation strong m=1 MHD oscillations are observed around r ≈ 0.07 m which disappear when the SX-radiation saturates. At t ≈ 1.28 s sawtooth-like behaviour starts affecting only the radial region between r ≈ 0.1 and 0.25 m, which apparently does not hinder the accumulation of impurities [2].

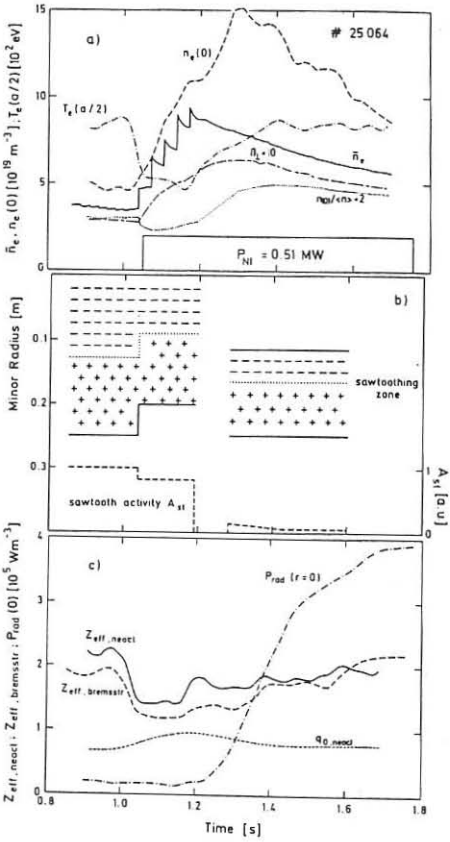

Fig. 1: Figure a) shows the reconstructed $\bar{n}_e$-trace and the smoothed $n_e(0)$, $T_e(a/2)$, β_p and the profile peaking factor $n_e(0)/\langle n_e \rangle$ vs. time. Figure b) indicates the radial zone affected by sawteeth according to SX-ray line integrals. The regions of dropping (-) and rising (+) amplitude are separately marked. Figure c) shows the measured (by means of infrared bremsstrahlung) and the neoclassically calculated radius-averaged Z_{eff}, $q(0)_{neocl}$ and the central radiation power density $P_{rad}(0)$.

3. Particle Transport

Pellet injection gives rise to strong peaking of the electron density profile also inside the deposition radius of the pellet particles and the neutrals (fig. 2). With GP only and with normal sawtooth activity, the peaking factor $n_e(0)/\langle n_e \rangle$ is below 1.5 and depends little on the total input power P_{tot} (fig. 3). When the sawteeth disappear in ohmic discharges, the peaking factor rises to 2. The highest peaking of about 2.6 was reached in sawtooth free OH phases after pellet injection. With auxiliary heating, the peaking parameter is gradually reduced from 2.6 to 1.6 if one compares the peaking at the end of repetitive pellet injection; but if the sawteeth are completely vanished, a maximum peaking of $\approx$2.5 is observed after the last pellet also with strong NBI heating. These profile changes reflect an alteration of the particle transport properties. In parallel the electron temperature profile shape is not changed by the pellet injection [3].

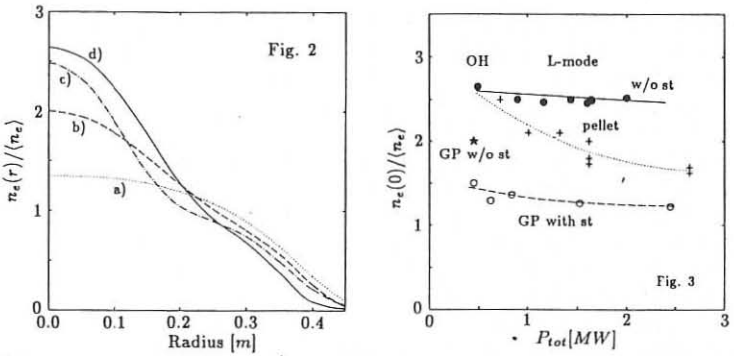

Fig. 2: Volume average normalized density profiles for a standard sawtoothing GP L-mode (a), sawtooth free GP OH (b), sawtooth free pellet L-mode (c) and sawtooth free pellet OH discharge (d).

Fig. 3: Density profile peaking factor $n_e(0)/\langle n_e \rangle$ as a function of P_{tot} of pellet and GP D^+ discharges.

If we describe the electron flux by the ansatz $\Gamma_e = -D \cdot \nabla n_e + V \cdot n_e$, we consequently find - during nearly stationary sawtooth free density phases - an increase of the ratio of the inward velocity to the diffusion coefficient $|V/D|$ in the inner half of the plasma of the order of 50 % when comparing pellet-fuelled OH discharges with the corresponding GP case.

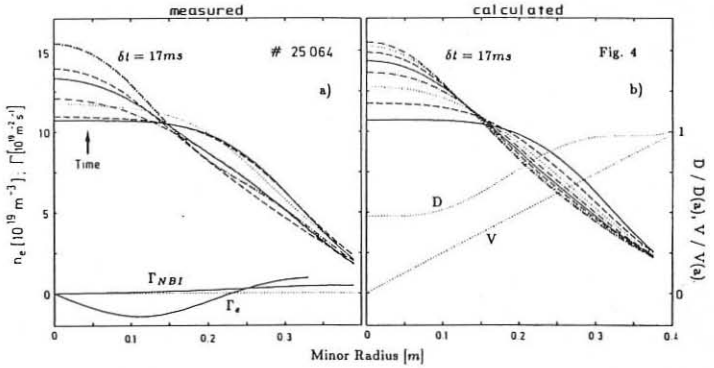

Fig. 4: Density evolution measured by Thomson scattering a) and calculated b) after pellet injection. The time between each profile is $\approx$ 17 ms. The electron flux Γ_e deduced from the measured profiles is averaged over the whole time interval of 120 ms. The electron flux Γ_{NBI} reflects the electron source due to the NBI. The normalized radial dependence of the model transport coefficients is plotted in figure b).

Since separate information on V and D can be gained from the analysis of dynamic phases, we investigated a number of sawtooth free post pellet phases where the electron profile develops from a relatively broad shape to a peaked one using a 1-D particle transport model. These profile changes happen typically on a time scale of 80 to 150 ms. The inquiry covers a density range from $\bar{n}_e = 5 \cdot 10^{19} m^{-3}$ to $1.2 \cdot 10^{20} m^{-3}$. Figure 4 compares the density evolution measured by a 16-channel Thomson scattering system which provides data every 17 ms and the calculated profile history using the radial dependence of the transport coefficients indicated in fig. 4b. The uncomplete knowledge of the boundary sources restricts the analysis to $0 < \frac{r}{a} < \frac{3}{4}$. The error of the coefficients is estimated to be $\pm$ 20 %. The deduced coefficients D and $|V|$ increase with rising heating power (fig. 5), whereas the concomitant decrease of the ratio $|V(\frac{2}{3}a)/D(\frac{2}{3}a)|$ reflects the influence of the electron source produced by the NBI. The diffusion coefficient D($\frac{2}{3}$a) of the OH and the $P_{tot} \approx 1.6$ MW discharges consistently exhibits half the value of the thermal diffusivity $\chi_e(\frac{2}{3}a)$ of a detailed TRANSP analysis of similar ASDEX discharges [4]supporting a common physical mechanism for both diffusivities. The resulting velocities V exceed the neoclassical pinch ($V_W(\frac{2}{3}a) \approx 0.15 \frac{m}{s}$) in the outer region by a factor of more than three. The observed power dependence of V is well in line with the assumption that the anomalous inward pinch is driven by the anomalous diffusivity. Unfortunately it is not possible within the actual experimental accuracy to unravel possible differences in the coefficients between pellet-fuelled and GP L-mode shots to clarify the better confinement of the pellet discharges.

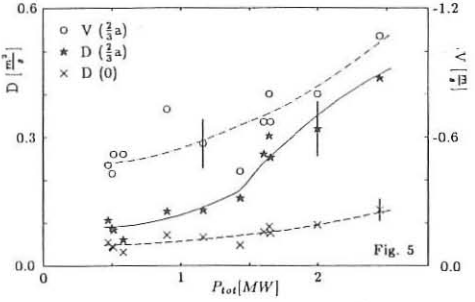

Fig. 5: Particle transport coefficients deduced from dynamic sawtooth free post pellet phases at different densities vs. total heating power P_{tot}.

References :

[1] M. Kaufmann et al., Proc. 12th Int. Conf. Plasma Phys. and Contr. Fusion (Nice, 1988) IAEA-CN-50/A-4-2

[2] V. Mertens et al., IAEA Techn. Com. Meeting on Pellet Injection and Toroidal Confinement (Gut Ising, 1988), to be published

[3] M. Kaufmann et al., this conference

[4] O. Gruber et al., Plasma Physics and Controlled Fusion, **30** (1988), 1611

TRANSITIONS BETWEEN REGIMES OF IMPROVED AND DEGRADED CONFINEMENT WITH OH AND NI HEATING

F.X.Söldner, H.U.Fahrbach, O.Gehre,V.Mertens, E.R.Müller, H.D.Murmann, H.Niedermeyer, A.Stäbler,F.Wagner

Max-Planck-Institut für Plasmaphysik,EURATOM Association
D-8046 Garching, Fed. Rep. of Germany

Introduction

A new class of improved confinement regimes characterized by peaked density profiles has been identified in recent studies on ASDEX /1/. Gas fuelled ohmic discharges pass into the **IOC** (improved ohmic confinement) regime upon reduction of the external gas flux at high density. Improved particle and energy confinement are then obtained with an unsaturated rise of the energy confinement time with density, $\tau_E \sim \overline{n}_e$, up to the density limit /2/. A similar improvement is achieved when the density is raised with fuelling from **pellet injection** /3/. In both cases the improvement in energy confinement correlates with a peaking of the density profile. The same correlation is found in **counter-NI** heated discharges /4/. There, a reduction of the gas puff rate triggers a continuous rise in β_p together with a gradual peaking of the radial density profile $n_e(r)$.

Transitions between IOC and SOC Regimes

The transitions between the different ohmic confinement regimes have been studied with discharges as shown in Fig.1. It contains three density plateaus, at $\overline{n}_e = 2.5 \times 10^{13}$ cm^{-3} in the linear ohmic confinement (LOC) regime, at $\overline{n}_e = 3.9 \times 10^{13}$ cm^{-3} and at $\overline{n}_e = 4.8 \times 10^{13}$ cm^{-3} , both in the IOC. The density is ramped up between the plateaus by increasing the gas flux Φ_{gas} for short durations of about 0.2 s. During the first phase of enhanced gas puffing, β_p remains constant while $\overline{n}_e$ increases. The discharge passes there from LOC to SOC. Immediately after reduction of Φ_{gas}, β_p starts to rise and steady state IOC conditions are attained after a slow transition of about 0.3 s. At 1.5 s, the gas flux is increased again. This triggers now a transition from IOC back to SOC as seen from the degradation in β_p with increasing $\overline{n}_e$. At the start of the transition, Φ_{gas} is much smaller than at the begin of the preceding transition from SOC to IOC. This indicates that the rate of change of Φ_{gas} seems to provide the trigger for the transition between the confinement regimes. Upon a second reduction of the gas feed rate at 1.7 s, another IOC transition is triggered. The form of the density profile during these multiple transitions between confinement regimes is monitored by the ratio of central to peripheral line integrated density, $Q_N = N_e(0)/N_e(0.75a)$. During the SOC phases Q_N drops and the $n_e(r)$-profile is broadening. With begin of the IOC transitions, Q_N starts rising and $n_e(r)$ therefore is peaking. The peakedness increases with increasing density /5/.

The changes in β_p occur on the same long time scale as the changes in the form of the electron density profile. The duration of the transition to a new steady state increases with increasing density. The improvement in confinement in the IOC regime can be consistently described by a reduction of anomalous heat conduction due to η_i-modes /6/. Both, SOC and IOC regimes are treated with the same ansatz for χ_i , summing up neoclassical and anomalous transport. The η_i-modes are destabilized in the gradient region if the ratio $\eta_i = (d\ln T_i/dr)/(d\ln n/dr) = L_n/L_{T_i}$ exceeds a threshold value η_i^*. According to drift wave theories the critical value should be of order η_i^*=1-2. In the experiment, radial profiles of η_i and η_e are determined from the radial profiles of $n_e(r)$, $n_e(r)$,$T_e(r)$ and $T_i(r)$. The temporal evolution of the radial positions with η_e=1.5 and η_i=1.5 is plotted in the lower part of Fig.1. In the regions with smaller radii, $\eta_{e,i}$>1.5 holds and η_i-modes should be unstable. During the SOC phases the unstable regions are expanding. With begin of the IOC transitions, the unstable region begins to shrink and at the highest density it disappears completely. The gradual improvement of confinement in IOC might therefore be explained by the expansion of the plasma region not affected by η_i-modes. As the excitation of these modes depends on the local form of the plasma profiles, the time scale of profile redistributions (and not of the growth time of the modes) should determine the time scale of changes in confinement. This could then explain the long time scales characteristic for the IOC transition.

Transitions from SOC/IOC to Pellet Injection

Pellet injection at high density and the IOC regime present many similarities. The improvement in confinement in both regimes is clearly correlated to the peaking of the density profile. In transport code calculations the improved confinement could be explained by the same mechanism, the suppression of η_i-modes. Transitions between the two regimes are investigated in order to understand better the role of the plasma profiles. The variation of τ_E with $\bar{n}_e$ is shown for two discharges in Fig.2. In #25645 (solid line) the IOC regime was established with τ_E=105 ms after passage through the SOC phase. Pellet injection into the fully developed IOC regime drives the energy confinement time up with density. No improvement is achieved beyond the scaling $\tau_E \sim \bar{n}_e$, already recovered in the IOC regime. Pellet injection rather extends this scaling to higher densities. As in the IOC regime the whole plasma region was already stable against η_i-modes, no additional improvement was expected from further peaking of $n_e(r)$ with pellet injection.The experimental result seems to confirm the assumed transport model. With pellet injection into an SOC target plasma (#25648,dotted curve in Fig.2) with flat density profile, $n_e(r)$ starts peaking and the region with $\eta_i > \eta_i^*$ is shrinking. The larger gain in τ_E during the initial phase of pellet injection in this case could therefore be explained by the suppression of η_i-modes.

Neutral Beam Injection into SOC /IOC Target Plasmas

With neutral beam injection (NI), transitions between confinement regimes can be studied in both directions: Co-NI into IOC was investigated up to P_{NI}=2 MW. At high NI power, normal L-mode confinement is regained. Ctr-NI into SOC plasmas leads to improved confinement /4/. With ctr-NI into IOC, improved confinement is maintained. In Fig.3 the three cases are compared for P_{NI}=0.6 MW. Co-NI into IOC leads to a further transient peaking of $n_e(r)$. During this phase, β_p, rises and the region with η_e>1.5 shrinks rapidly. About 50 ms after begin of NI, η_e<1 in the whole plasma region. Then large sawteeth trigger a flattening of $n_e(r)$, leading to a decrease of β_p and an expansion of the region with η_e>1.5, starting from the center. A new steady state with degraded confinement is attained 0.2 s after begin of NI. With ctr-NI into SOC, Q_N rises strongly in the begin and then continuously throughout the NI pulse. The increase in β_p correlates with this peaking of $n_e(r)$. The large region with η_e>1.5 starts shrinking while $n_e(r)$ is peaking resulting in $\eta_e \approx 1$ over the whole radius after 0.3 s. Then the region with η_e>1.5 begins to expand again, now starting close to the periphery. This degradation is caused by strong radiation cooling due to impurity accumulation /1/. Ctr-NI into IOC leaves the already peaked $n_e(r)$ profile nearly unchanged in the beginning and leads to a continuous peaking in the later phase similar to ctr-NI into SOC. The initial β_p increase is small due to larger orbit losses with ctr-NI. The radial profile of η_e does not change from IOC to ctr-NI until impurity radiation becomes dominant again in the late phase.

Summary

The investigation of transitions between improved confinement regimes with peaked density profiles and degraded regimes in ohmic and NI-heated plasmas clearly demonstrates the close link between the energy confinement time and the form of the electron density profile. Pellet injection into IOC plasmas and ctr-NI into IOC target plasmas show that no additional improvement results from further peaking of the $n_e(r)$ profile once it is peaked such that $\eta_{e,i} \approx 1$ over a large plasma region. The correlation of confinement improvements with a shrinking of the plasma region unstable against η_i-modes suggests strongly that the stabilization of these modes by the peaking of $n_e(r)$ is the common mechanism in the whole class of improved confinement regimes characterized by peaked density profiles.

References

/1/ Fußmann, G., et al., 12th Int. Conf. on Plasma Physics and Controlled Nuclear Fusion Research, Nice, IAEA-CN-50/A-3-1 (1988).
/2/ Söldner, F.X., et al., Phys. Rev. Lett. **61**, 1105 (1988).
/3/ Kaufmann, M., et al., Nucl. Fusion 28,827 (1988).
/4/ Gehre, O., et al., Phys. Rev. Lett. **60**, 1502 (1988).
/5/ Söldner,F.X., et al., IAEA Tech.Meeting on Pellet Injection and Toroidal Conf.,Ising (1988).
/6/ Gruber,O., et al., Plasma Phys. and Contr. Fusion 30, 1611 (1988).

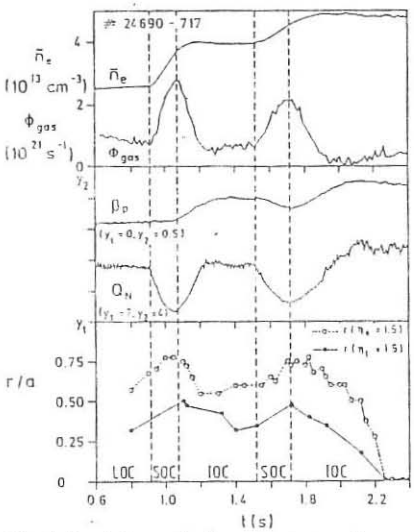

Fig.1: Evolution of plasma parameters during transitions between ohmic confinement regimes in a deuterium discharge with 3 density plateaus. I_p=380 kA, B_t=2.17 T, q_a=2.75.

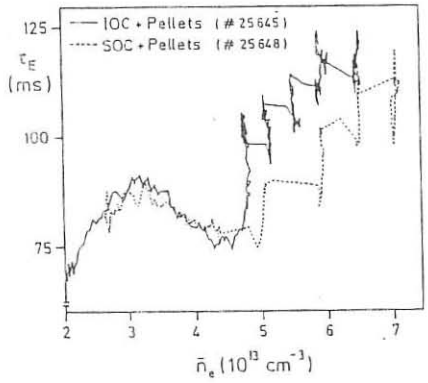

Fig.2: Variation of the energy confinement time with density in SOC and IOC phases and with subsequent pellet injection. I_p=380 kA, B_t=2.17 T.

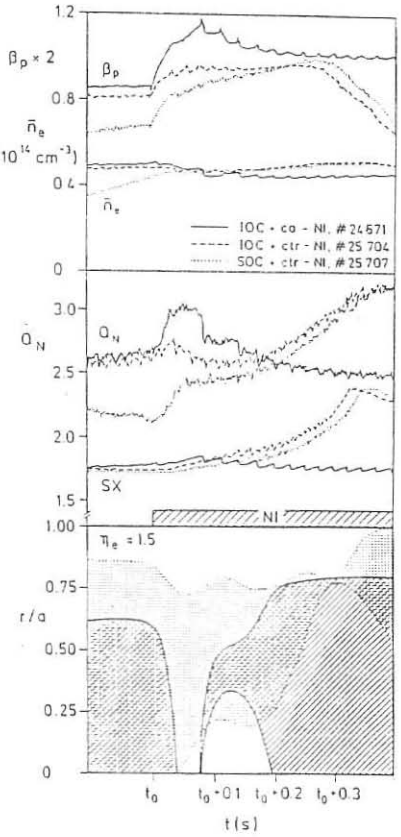

Fig.3: Temporal evolution of plasma parameters with NBI in co and ctr direction, resp., into IOC and SOC target plasmas. The lower part shows the radial extent of the region with $\eta_e > 1.5$ for co-NI into IOC (solid boundary lines) and for ctr-NI into SOC (dotted boundary lines). I_p=380 kA, B_t=2.17 T, q_a=2.75. P_{NI}=.6 MW.

IMPURITY ACCUMULATION AND Z_{eff} PROFILES IN ASDEX HIGH CONFINEMENT REGIMES

K.-H. Steuer, H. Röhr, G. Fussmann, G. Janeschitz,
A. Kallenbach, H.D. Murmann, ASDEX-, NI- and Pellet-team

Max-Planck-Institut für Plasmaphysik
EURATOM Association, D-8046 Garching, Fed. Rep. of Germany

1. INTRODUCTION.

During the past years a large effort has been undertaken to overcome the degradation of energy confinement in auxiliary heated plasmas. Considerable improvement of confinement times is found in H-mode plasmas, in pellet refuelled discharges, in counter NI heated plasmas and more recently in the IOC-regime.

In the following we show that regimes of high energy confinement are accompanied by an improvement of particle confinement leading in some cases to strong impurity accumulation in the plama centre. The improved confinement of the background plasma makes the density control more difficult and can become a severe problem under high recycling conditions (carbonized walls, large areas of graphite).

The improvement of the impurity confinement is, of course, even more critical: high-Z impurities lead to large central radiation losses and can cause radiation collapse. Low-Z impurities as carbon and oxygen in the range of several per cent lead to high Z_{eff} values on axis which can result in unacceptable fuel dilution. Information on the important question whether impurities accumulate can be obtained from Z_{eff} profile measurements. Results for high confinement regimes in ASDEX will be presented.

2. Z_{eff} DIAGNOSTICS.

Z_{eff} profiles are determined across the entire minor radius of ASDEX from the intensity of plasma bremsstrahlung in the near infrared, where both recombination and impurity line radiation are in general negligible. We use the detection system of the Nd-YAG laser scattering equipment to measure the absolute value of bremsstrahlung along 16 chords simultaneously in 3 different wavelength bands between 750 and 1000 nm /1/.

The results are compared with those obtained from VUV spectroscopic measurements. The absolutely measured line radiation of relevant impurity species like Cu, Fe, C, O is used in a transport code to calculate impurity density profiles which are taken to derive a spectroscopic Z_{eff}. The agreement between the spectroscopic Z_{eff} and the bremsstrahlung Z_{eff} is within 20% /2/. In addition, carbon and oxygen density profiles are absolutely measured by charge exchange recombination spectroscopy during beam injection. This method delivers an independent crosscheck for the low Z impurity densities derived from the VUV.

3. EXPERIMENTAL RESULTS AND DISCUSSION.

3.1 Pellet Injection

Repetitive injection of pellets has been successfully applied in ASDEX to improve substantially energy confinement in ohmically and NI-heated plasmas /3/. A characteristic feature of the high confinement phase is a nearly complete disappearance of sawtooth activity and a pronounced peaking of the electron density profile. Maximum densities of up to $1.4 \times 10^{14} cm^{-3}$ are attained. Figure 1 shows a 3-dimensional plot of the time evolution of the radial Z_{eff} profiles within half the radius of a well analyzed pellet discharge /4/. After the last injected pellet (t = 1.18 s) Z_{eff} is about 1.3 and nearly constant over the radius. The Z_{eff} profile starts to peak at about 1.25 s. From spectroscopic and bolometric measurements we know that Z_{eff} is mainly determined by light impurities as oxygen and carbon. The resulting concentrations during the accumulation phase amount to 2 % carbon and 0.8 % oxygen, whereas the concentration of of metals like Cu which is the new divertor plate material, is only 0.08 %.

The measured time evolution of the Z_{eff} profiles in the main plasma region (s. Fig. 2) can fairly well be described by neoclassical transport calculations assuming a strong reduction of the anomalous diffusive term ($D_{an} = 0.05 m^2/s$) which is a consequence of the general improvement of confinement /5/.

In the outside region (r > a/2) the measured Z_{eff} values rise again to about 2.5 at the plasma edge indicating a weaker radial decrease of impurity density as compared to the electron density. This fact is supported by measurements of carbon and oxygen densities via CXRS. The increase of Z_{eff} towards the plasma boundary is observed in all discharge types.

3.2 IOC/Ccunterinjection

Peaked impurity profiles have also been found under the improved ohmic confinement conditions (IOC) and counter injection heating. In both regimes the improved particle confinement causes an accumulation of impurities in the plasma centre. Under carbonized wall conditions Z_{eff} is in both cases determined by low-Z impurities. The IOC regime, however, differs from the accumulation phase in ctr NI heated discharges and in pellet refuelled plasmas in one important aspect. While in those cases sawteeth are either absent or vanish during the accumulation process, they appear enhanced during the IOC phase. This leads to a less pronounced impurity accumulation and gives only a slight peaking of the Z_{eff} profile. $Z_{eff}(o) = 3$ and $Z_{eff}(a/2) = 2.7$ are found /6/.

3.3 H-Regime

In the H-mode the improvement of energy confinement results in the broadening of the density profiles. With the 16 channel Z_{eff} diagnostic we are able to analyze the impurity behaviour in a quiescent H discharge in the new ASDEX divertor configuration /7/. The global parameters are: I_p = 380 kA, B_T = 2.2 T, neutral beam heating (1.3 MW D^0 in D^+) for $1.0 \leq t \leq 1.8$ s, slightly carbonized walls. The transition from L to H and back to L occurs at t = 1.18 s and 1.34 s, respectively.

Figure 3 shows the time dependence of the volume averaged $\langle Z_{eff} \rangle$ which determines the ratio of plasma current to loop voltage. $\langle Z_{eff} \rangle$ increases during the L phase and decreases in the H phase but starts to increase again at the end of the H-mode. In order to get more insight into the impurity behaviour Fig. 4 shows the radial development of Z_{eff} profiles at different times: OH (t = 0.9 s), L (t = 1.17 s) and H (t = 1.3 s). In OH and L the radial profiles are relatively flat, whereas in the H-phase strong accumulation occurs. The actual accumulation region is found to be within $r \leq 12$ cm. From spectroscopic, bolometric and soft X-ray measurements we know that in the H-regime Z_{eff} is mainly determined by high Z impurities in contrast to the previous cases. The concentration of Cu and Fe amount to about 0.5 %.

Analogue to the other improved confinement regimes the observed accumulation process and the central Z_{eff} values can be explained by the neoclassical inward drift which becomes essential when the anomolous diffusion is suppressed. It should be noted that the high central Z_{eff} is of little importance for the volume averaged $\langle Z_{eff} \rangle$ which yields a relatively low value of about 3 for the H-phase, whereas the same quantity is as high as 4.5 during the preceeding L-phase.

4. CONCLUSIONS

Z_{eff} profile measurements show clearly that an improvement of energy confinement is accompanied by an improvement of particle confinement. In all four high confinement regimes more or less peaked Z_{eff} profiles are found demonstrating impurity accumulation. In high density cases low-Z impurities are responsible for the measured Z_{eff} profiles, whereas in the H-regime the strong peaking of Z_{eff} is mainly determined by metallic impurities which accumulate within less than 0.1 s to concentrations of up to 0.5 %. The present results can be explained by neoclassical inward drifts assuming that the anomalous diffusion is sufficiently suppressed which is a consequence of the improved confinement.

References

/1/ H. Röhr, K.-H. Steuer, Rev. Sci. Instrum. 59(8), 1875 (1988)
K.-H. Steuer et al. Proc. 15th Europ. Conf. on Contr. Fusion and Plasma Phys., Vol. 12 B, 31 (1988).
/2/ G. Janeschitz et al., this conference
/3/ M. Kaufmann et al., Nucl. Fus. 28, 5 (1988)
/4/ V. Mertens et al., this conference
/5/ G. Fußmann et al., IAEA workshop, Gut Ising (1988), to be published.
/6/ F.X. Söldner et al., Phys. Rev. Lett. 61, 1105 (1988).
/7/ E.R. Müller et al., this conference.

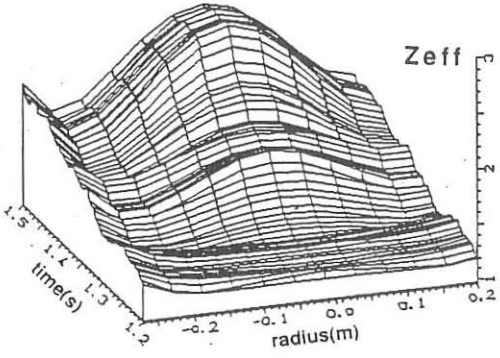

Fig 1 Time evolution of radial Zeff profiles in a pellet fuelled discharge. The accumulatior phase starts at about 0.1s after the last pellet.

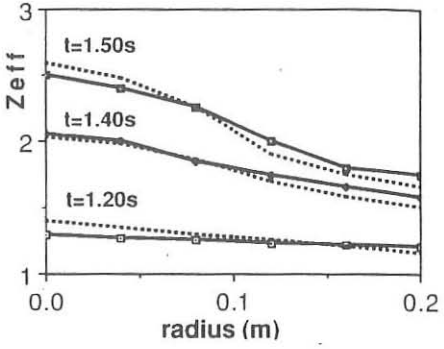

Fig 2 Comparison of measured and calculated(dotted line) at three different times during the accumulation phase.

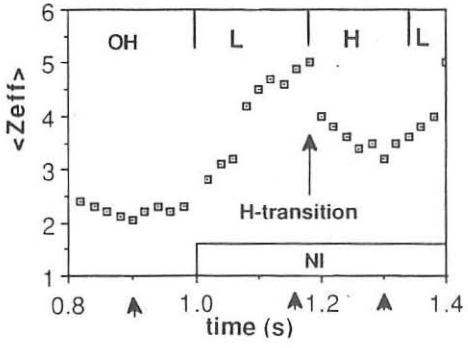

Fig 3 Time development of volume averaged <Zeff> of a neutral beam heated plasma in the sequence from OH to L to H to L.

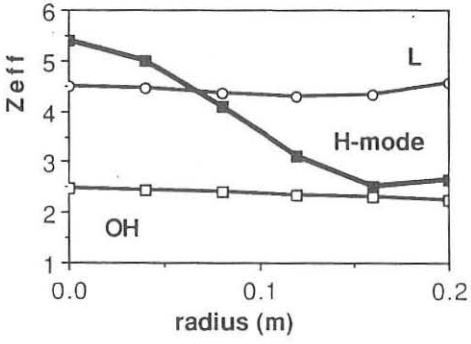

Fig 4 Radial Zeff profiles in OH, L and H phase at the times marked in Fig 3

Isotope Dependence of Ohmic Discharge Parameters of Asdex

F. Wagner, M. Bessenrodt-Weberpals, H.U.Fahrbach, O. Gruber, W. Hermann, P. McCarthy, K. McCormick, H.D. Murmann, K.H. Steuer, H. Verbeek

Max-Planck-Institut für Plasmaphysik
Garching, FRG
Euratom Association

Abstract

This paper summarizes results of regression analyses of various discharge parameters of ohmic hydrogen and deuterium plasmas of Asdex. Special emphasis is put on the dependence on the ion mass A_i. Besides the confinement time the highest sensitivity on A_i is shown by the central electron temperature, the sawtooth repetition time, and the edge electron density and temperature. The possible role of the electron density profile shape on the confinement and its A_i -dependence is discussed in detail.

Introduction: The motivation for studying the isotope effect on confinement comes (1) from the observation that τ_E improves with A_i and that A_i is the only scaling parameter observed in all confinement regimes of Asdex / 1 / and (2) from the fact that theory does not yet explain it. A_i is a scaling parameter in regimes which are dominated by electron transport (like the OH - linear regime or the L - mode) , in ion transport dominated regimes (like the saturated SOC regime), in degraded or improved regimes (L - or H - modes) at low or high β, or at low or high collisionality.

Experimental details: Two sets of ohmic discharges were carried out on Asdex - one in deuterium the other in hydrogen - for the single purpose of studying the dependence of various ohmic plasma parameters on the external parameters I_p, B_t, $\overline{n}_e$, Z_{eff}, and A_i.(Z_{eff} is regarded as an external parameter though it was not varied externally.) During a discharge the line density was kept constant but - to reduce the number of discharges - the current was increased in steps. Up to three current plateaus were possible in a discharge. The length of each plateau was sufficient for the loop voltage to reach steady state. Single plateau discharges were carried out for control purposes. A total of 244 (120) data points were collected for D_2 (H_2). The external parameters were varied in the following ranges: 150 kA $\leq I_p \leq$ 440 kA, 1.9 T $\leq B_t \leq$ 2.45 T, ($2.3 \leq q_a \leq 8.4$), 0.8×10^{13} cm^{-3} $\leq \overline{n}_e \leq 5.5\times10^{13}$ cm^{-3}. For control of the plasma impurities and to remain in the SOC regime also with deuterium operation, the vessel walls were carbonized; oxygen was removed from the

discharge by Ti - gettering in the outer divertor chambers. β_p was measured with equilibrium coils (Λ+1) and from a well compensated diamagnetic loop (β_p^{dia}). l_i / 2, necessary to determine β_p^{equ} (= Λ + 1 -l_i / 2) was obtained from a statistical analysis of the ohmic T_e - profiles of Asdex. For D_2, l_i = 0.7 +0.45×ln(q_a). The electron energy content β_p^e was determined from the quasi-stationary Thomson system on Asdex; the kinetic β_p^{kin} was determined from β_p^e and the central ion temperature T_{io} (passive and active charge exchange). Z_{eff} is measured via Bremsstrahlungsradiation in the infra-red. Z = 6 is assumed in the calculation of the proton density n_i. The three β_p - values give an average value β_p^{av} which is used in the determination of τ_E and the total energy content E_o. A fit to the experimental l_i (= 2×(Λ + 1 - β_p^{av}) - values gives : l_i = 0.75 + 0.46×ln(q_a) - in excellent agreement with the l_i- result from the T_e - profile analysis.

Results: The results of the regression analysis for the global parameters is given in table I for the linear (1a) and the saturated (1b) confinement regime. Because of the potential importance of the edge parameters for the isotope effect of confinement, edge parameters are anaysed in great detail. The results are summarized in table 2 for the SOC regime only.

Discussion: T_{eo}, the sawtooth repetition time τ_{st}, and the edge electron density n_e(a) show the most sensitive dependence on A_i. The dependence of T_{eo} on A_i does not seem to be the corollary of the A_i scaling of τ_{st}. Also T_e calculated at the respective q = 1 surface (the pivot point of the sawtooth oscillation) increases with A_i. τ_E depends in both regimes an A_i. In the linear confinement regime, the A_i dependence is weaker than in the SOC regime. However, at low density the species composition is less controlled. It is interesting to note that the ion mass affects the electron transport as seen from the A_i dependence of τ_E in the linear regime or of the electron temperature T_e or energy content E_e. The moderate A_i scaling of T_e affects both the energy content E_o and the ohmic heating power P_{OH} and leads to the strong dependence of τ_E on A_i. In the SOC regime, A_i is the only scaling parameter of τ_E. The strong dependence of the edge electron density on A_i is shown independently by the Thomson and the Li-beam results. This dependence exists obviously only at the plasma edge and quickly disappears further in. The density fall-off length does not depend on A_i; obviously the ion mass just cancels in the two competing movements - parallel drift and perpedicular diffusion - which determine the radial extent of the scrape - off - layer. A possible A_i dependence of the edge electron temperature is not well recovered. Nevertheless, the clear increase of the mean energy $<E_{cx}>$ of the low energy charge exchange flux indicates that the edge ion temperature increases. The analysis of the A_i scaling of various

plasma parameters does not reveal a clear origin for the dependence of the heat transport on the ion mass. Nevertheless, an interesting relation between edge and central parameters is observed.

Further results of the regression analysis are the close to linear relation between plasma current and the energy content (electrons and total) or the ohmic heating power, respectively. In the τ_E determination, the current as the leading scaling parameter just cancels and τ_E depends on secondary paramters only. This is clearly shown by the regression coefficients. $R^2 = 0.95$ and $= 0.93$ for E_o and P_{OH}, respectively, but drops to $R^2 = 0.73$ in the τ_E regression (saturated regime).

The linear current scaling of E_o and P_{OH} applies both to plasmas in the linear and saturated regime. For a q_a scaling of τ_E - as frequently observed in the linear regime - the linear current scaling of E_o has to be overcompensated by P_{OH}. Instead of a q_a scaling of τ_E in the linear regime we observe a Z_{eff} dependence (using the independently determined Bremsstrahlungs - Z_{eff}). In the linear regime, Z_{eff} varies strongly with $\overline{n_e}$ and I_p. This strong Z_{eff} variation enters P_{OH} and thereby τ_E. On the other hand Z_{eff} decreases strongly with decreasing I_p possibly introducing a fictitious q_a scaling in τ_E. If we substitute the Bremsstrahlungs - Z_{eff} by the Spitzer - Z_{eff} which, however, is no independently measured quantity we indeed obtain a slight q_a dependence of τ_E in the linear regime ($\tau_E \propto q_a^{0.25}$). Z_{eff} does not show a dependence on A_i which is not in agreement with previous experience but which might be typical for carbonized wall conditions.

A strong similarity in the scaling of τ_{st} and τ_E is observed.

The hypothesis that the diffusivity itself does not depend on A_i but the onset condition of an instability does, has been studied for the density profile in a separate investigation. Such a condition exists for the η_i mode which is expected to cause the ohmic τ_E to saturate. A low q_a value was chosen ($q_a = 2.5$) to fix the n_e-profile as much as possible by the large $q = 1$ radius (the ratio in the density profile shape parameter is $n_{eo} / < n_e > \propto A_i^{-0.017}$). Furthermore, $\overline{n_e}$ was as high as possible (3% below the density limit; $M = 5.5$) to reduce the electron contribution to the heat conduction as much as possible. Nevertheless, the same A_i dependence of the various parameters as at lower density and higher q_a was observed. ($P_{OH} \propto A_i^{-0.23}$, $E_o \propto A_i^{0.34}$, $E_e \propto A_i^{0.2}$, $\tau_E \propto A_i^{0.58}$, $T_{eo} \propto A_i^{0.2}$, $T_{eo} / <T_e> \propto A_i^{0.12}$). These results indicate that the isotope effect is not caused by the impact of the density profile on transport (because in the chosen case it is the same for D_2 and H_2) and that it exists also under the extreme condition of maximal ion heat transport.

/ 1 / H.D. Murmann, F. Wagner et al. Proc. 15.th Europ. Conf. Contr. Fusion and Plasma Heating, Dubrovnik, 1988, Part 1, p 3.

table 1a

	const	Ip		Bt		ne		Zeff		Ai		R
Poh	9.93E-04	1.02	0.036	-0.45	0.068	0.26	0.046	0.24	0.046	-0.09	0.026	0.96
E o	2.43E-02	1.12	0.038	-0.18	0.072	0.56	0.048	-0.14	0.049	0.21	0.027	0.97
E e	1.69E-02	1.12	0.037	0.00	0.000	0.38	0.047	-0.11	0.046	0.18	0.026	0.97
τ E	3.73E+01	0.00	0.000	0.27	0.115	0.39	0.058	-0.28	0.055	0.31	0.043	0.80
T eo	4.13E+01	0.49	0.046	0.73	0.088	-0.36	0.058	0.14	0.058	0.24	0.032	0.88
< T e >	6.14E+00	0.77	0.043	0.21	0.083	-0.37	0.055	0.12	0.055	0.17	0.031	0.92
Teo/<Te>	6.83E+00	-0.27	0.041	0.51	0.110	0.00	0.000	0.00	0.000	0.00	0.000	0.54
n eo	4.02E+00	-0.14	0.027	0.00	0.000	0.85	0.035	-0.25	0.035	0.02	0.000	0.97
< n e >	2.31E-01	0.33	0.040	-0.17	0.077	0.68	0.051	-0.25	0.051	-0.12	0.029	0.93
neo/<ne>	1.49E+01	-0.46	0.028	0.24	0.073	0.16	0.028	0.00	0.000	0.20	0.027	0.83
T io	5.75E+01	0.40	0.026	0.36	0.067	0.10	0.026	0.00	0.000	0.00	0.000	0.81
τ SZ	5.64E+01	-0.43	0.079	0.00	0.000	0.81	0.064	0.00	0.000	0.25	0.056	0.83
Z eff	2.03E-01	0.56	0.043	0.00	0.000	-0.82	0.042			0.00	0.000	0.86

table 1b

	const	Ip		Bt		ne		Zeff		Ai		R
Poh	7.93E-04	1.09	0.034	-0.40	0.061	0.24	0.039	0.00	0.000	-0.22	0.027	0.96
E o	5.74E-02	0.99	0.034	-0.13	0.063	0.43	0.048	-0.16	0.047	0.28	0.026	0.97
E e	1.40E-02	1.14	0.031	0.00	0.000	0.35	0.038	0.00	0.000	0.27	0.026	0.97
τ E	5.76E+01	0.00	0.000	0.18	0.075	0.00	0.000	-0.27	0.052	0.50	0.032	0.86
T eo	1.53E+02	0.31	0.030	0.79	0.057	-0.63	0.037	0.00	0.000	0.36	0.025	0.94
< T e >	5.92E+00	0.84	0.050	0.19	0.093	-0.62	0.061	0.00	0.000	0.19	0.041	0.88
Teo/<Te>	5.62E+01	-0.67	0.039	0.66	0.074	0.00	0.000	0.00	0.000	0.11	0.033	0.87
n eo	4.66E+00	-0.21	0.028	0.14	0.055	0.84	0.036	-0.11	0.036	0.10	0.023	0.93
< n e >	9.68E-02	0.42	0.030	-0.26	0.058	1.01	0.038	-0.10	0.038	-0.12	0.024	0.97
neo/<ne>	3.73E+01	-0.59	0.027	0.37	0.048	-0.17	0.030	0.00	0.000	0.25	0.021	0.94
T io	1.13E+02	0.29	0.051	0.55	0.095	-0.28	0.067	0.00	0.000	0.16	0.044	0.72
τ SZ	1.57E+01	0.00	0.000	0.00	0.000	0.00	0.000	-0.61	0.085	0.54	0.049	0.82

Given are the results of the regression analysis in the form const × Ip × Bt^{β} .... .The column following the power gives its standard error; R is the regression coefficient. Table 1a shows the results for the linear range ($n_e \leq 2.5 \times 10^{13}$ cm^{-3}), table 1b for the saturation regime.

table 2

	const	Ip		Bt		ne		Zeff		Ai		R
ne 39.4	2.26E-02	0.44	0.054	0.00	0.000	1.32	0.048	0.00	0.000	-0.81	0.043	0.94
ne 35.3	6.10E-03	0.73	0.043	-0.18	0.072	1.21	0.042	0.00	0.000	-0.13	0.038	0.95
ne 31.2	4.45E-03	0.89	0.048	-0.44	0.077	1.12	0.049	-0.09	0.022	0.00	0.000	0.95
ne (a)	8.03E-04	1.14	0.060	-0.32	0.129	0.67	0.081	-0.12	0.035	-0.85	0.062	0.90
Te 39.4	1.25E-01	1.27	0.062	-0.37	0.086	-0.74	0.051	-0.09	0.024	0.35	0.044	0.90
Te 35.3	6.86E-02	1.61	0.053	-0.40	0.086	-0.58	0.052	-0.06	0.024	-0.53	0.043	0.95
Te 31.2	1.22E-01	1.56	0.044	-0.43	0.074	-0.58	0.046	-0.06	0.021	-0.21	0.038	0.95
< E cx >	3.62E+00	1.09	0.047	-0.96	0.095	-1.30	0.077	-0.07	0.028	0.89	0.046	0.94
λ	1.78E+02	-0.97	0.055	0.93	0.115	0.34	0.075	0.08	0.032	0.00	0.000	0.82

ne 39.4, Te 39.4 are density and temperature as measured by Thomsonscattering at r = 39.4 cm; ne(a) is the separatrix density as measured by Li-beam; <Ecx> is the average charge exchange energy as measured by time-of-flight; λ is the s.o.l. density fall-off length.

INDUCED VOLTAGE AND EDDY CURRENT IN THE PBX-M STABILIZING SHELL

H. W. Kugel, N. Asakura, R. Bell, M. Chance, P. Duperrex, J. Faunce, R. Fonck, G. Gammel, R. Hatcher, P. Heitzenroeder, A. Holland, S. Jardin, T. Jiang, R. Kaita, S. Kaye, B. LeBlanc, M. Okabayashi, Y. Qin, S. Paul, N. Sauthoff, S. Schweitzer, S. Sesnic, and H.Takahashi

Plasma Physics Laboratory, Princeton University
Princeton, New Jersey 08543, USA

1.Introduction.

The Modified Princeton Beta Experiment (PBX-M) has a close-fitting, conducting, passive plate, stabilizing shell which nearly surrounds highly indented, bean-shaped plasmas. This magnetic configuration, together with a closed divertor, 7 MW of neutral beam auxiliary heating, several transport-dependent profile control techniques, and a unique array of diagnostics is designed to exploit the influence of its stabilizing properties on confinement at high-ß, and to explore access to the 2nd stability regime. In the pursuit of this experimental program, PBX-M [1] is addressing several associated hardware issues that are also of direct relevance to proposed tokamaks, and future directions of tokamak development. These tokamak hardware issues include the characterization of disruptions with a close-fitting shell, the measurement of induced voltage and eddy currents, the characterization of insulator breakdown, tokamak insulator design criteria, optimum cleanup procedures, the characterization of low-Z and high-Z impurities and associated plasma impurity issues, divertor power handling, plasma control methods for bean-shape profiles, and the capabilities of independent coils and passive systems for MHD stabilization at high-ß. Studies related to these issues are in progress and will be presented later. In this work, we discuss preliminary results from measurements of voltage and eddy currents induced in the passive stabilizing shell during the initial PBX-M operating phase, and comparisons with theoretical simulations in progress.

2. The PBX-M Passive Plate, Stabilizing Shell.

Fig. 1 shows the internal PBX-M magnetic configuration and an equilibrium flux plot for a highly indented PBX-M plasma. During the PBX-M initial startup, typical plasma parameters for similar equilibrium conditions were I_p = 550 kA, dI_p/dt = 0.5 MA/sec, B_t = 1.2 T, R = 1.65 m, a = 0.35 m, indentation = 25%, q_{mhd} = 3.7, $n_e = 5 \times 10^{13}$ cm^{-3}. Such discharges are initiated with circular plasmas and then quickly deformed into elongated, indented plasmas. Shown in Fig. 1 are (1) the indentation coil system, (2) the equilibrium field coil system, (3) the divertor coil system, (4-7) the T1-T4 trimming coil systems, (A) the active feedback radial field system, and (P) the close-fitting, conducting, passive plate, stabilizing shell.

The passive plate system is the primary element for stabilizing n=1 kink modes, which have been shown to be an important instability responsible for limiting access to the 2nd stability regime in PBX [2]. This system is composed of five pairs of electrically isolated plates, positioned above and below the magnetic axis as shown in Fig.2a. The outer two

pairs (1-2) act to stabilize primarily n=1 external kink modes. The three inner pairs (3-5) perform stabilization of the n=0 vertical modes. The plates of the outer pair are connected electrically via busses at 11 locations (Fig. 2b) to facilitate the flow of eddy currents, and reduce the effect of the 40 cm midplane gap required for auxiliary heating, and diagnostic access. The upper and lower plates of the four inner pairs are connected together electrically via busses to form saddle coils as shown in Fig. 2c. The plates consist mostly of 2.5 cm thick aluminum (6061-T6) with a thin explosively bonded layer of stainless steel (304) facing the plasma. Toroidal gaps in each element provide the requisite OH electrical isolation (Fig.2b and 2c). Each of the toroidal gap segments is aligned and fastened with an electrically insulated bridge plate. The individual plate elements are supported from the vacuum vessel wall, and electrically floated via mica and organic insulators. Wires from each of the five plate elements are connected to the vacuum vessel through 500 Ω resistors, which are external to the vessel. At eight toroidal locations, 12 poloidal graphite limiters are positioned on the passive plates (Fig.1). The graphite limiters are 2 cm high and electrically insulated from the passive plates by mica. Preliminary results for the effects of the passive stabilizing shell on PBX-M plasmas are given elsewhere [1,3].

3. The Effects of PBX-M Plasmas on the Passive Stabilizing shell.

In PBX-M, geometrical constraints, static loading during normal operations, dynamic impact loading during disruptions, induced voltage and current effects, and edge plasma interactions, have established narrow requirements for the structural supports and insulators of the passive plate system. In some support locations, for example, ceramic insulators with superior and recoverable high voltage standoff capabilities have failed mechanically under the effects of the impact loading. In the same locations, easily machinable, organic insulators with high yields under impact loading have failed electrically, in an irreversible manner. The nature of these failures is still under investigation. Candidate mechanisms include surface charring and tracking, unipolar arcing, and intense localized electric field effects. The failure of critical insulators has also caused tightly placed structural members to conduct large currents. The damage of the support structure indicates that, in addition to asymmetric current due to plasma vertical motion, closed poloidal current may have flowed on the passive stabilizer through the vacuum vessel, even though the passive stabilizer plates are electrically insulated from each other, toroidally and poloidally, and connected to the vacuum vessel only at one point.

In order to understand the features of an axisymmetric, vertically asymmetric, disrupting plasma in PBX-M, and its effects on the close-fitting passive plate stabilizing shell, we have performed a series of simulations using the Tokamak Simulation Code (TSC). The plasma model is fully free boundary and non-linear, and contains both ideal and resistive effects. Each passive aluminum plate is divided into 10-20 independent conductors in parallel, with the plate gaps modeled by imposing a zero net current constraint on the sum of the currents in a top-bottom pair. We also allow for a "halo" plasma of finite conductivity to exist in the plasma scrapeoff region just outside the surface intersecting the limiter or separatrix. In the calculation, a disruption is initiated by suddenly increasing the plasma thermal conductivity by a factor of between 10^3 and 10^4. This leads to the plasma/vacuum interface sequence shown in Fig.3a,b. The rapid increase in thermal conductivity causes the plasma-ß to suddenly drop (thermal quench). This causes the plasma to suddenly move radially inward into a region of more negative field index which is also less coupled to the stabilizing conducting plates, and, on a slower time scale, for the current to begin to decay (current quench). Even before much current decay has occurred, the plasma can become ideal MHD unstable, and displace downward (or upward) with velocities approaching 5×10^4

m/sec. Since this rapid instability motion also has a significant radial component , large induced toroidal voltages of 50 kV or more appear across the plate gaps for a period of several μsec as the plasma moves by. If the halo plasma is present, toroidal induced currents will appear in this halo as the plasma moves. These halo currents will also develop a poloidal component to remain force-free. If the halo region intersects two separate passive plates, the poloidal currents in the halo provide a mechanism for current to flow from one plate to another. Fig.4 shows the poloidal current flow in the plasma halo for a simulated disruption.

4. Induced Voltage and Current Measurements.

Voltage and current measurements have been initiated, in order to characterize eventually the voltage and eddy currents induced in the PBX-M passive plate stabilizing shell over the full range of operating conditions. Pairs of wires from the five passive plate elements, their respective toroidal gaps, the inter-element gaps, and two of the outer poloidal graphite limiters are brought to the outside of the vessel. A total of 16 signals are connected externally to an array of voltage dividers, and the reduced output voltage waveforms are digitized at 40 kHz and archived. Preliminary voltage waveforms obtained for typical OH plasmas typically exhibit up to 2.5 kV at the disruptions of 100-450 kA plasmas.

Eddy current measurements are performed simultaneously with the above voltage measurements using Rogowski coils placed on the respective passive plate saddle coil connectors illustrated in Fig. 2b,c. Preliminary results indicate comparable currents in adjacent plates which are in the range from 1-8 kA, but which sometimes exhibit phase differences characteristic of sawtooth activity.

5. Discussion.

The measured induced voltages for initial PBX-M plasmas are considerably less than the large multi-kV voltages predicted by the disruption model described above. This may be due in part to the relatively narrow range of low power plasmas measured to date, an undetected very fast transient voltage, or possibly the short-circuiting of intense induced electric fields via arcs from the passive plates to the plasma. Measurements incorporating voltage peak detection and fast digitization are in progress, and may reveal the presence of very fast transient voltages in less benign plasma regimes. Arcing phenomena, if present, may be revealed by impurity correlations and characteristic time and current signatures. The measured eddy currents are found to be consistent with the perturbed poloidal B field measured by Mirnov coils located on the outside surface of the passive stabilizer.

Acknowledgment

We wish to acknowledge the technical contributions of L. Gereg, S. Hand, and the PBX-M Technical Staff headed by J. Semler. The PBX-M project is supported by the U.S. DoE under Contract No. DE-AC02-76-CHO-3073.

References

[1] M. Okabayashi *et al.*., in Proc.12th Int. Conf. on Plasma Physics and Controlled Nuclear Fusion Research, Nice, 1988, IAEA-CN-50/A-2-2.
[2] K. Bol *et al.*, Phys. Re. Lett. 57 (1986) 1891.
[3] S. Kaye *et al.*, in these Proceedings.

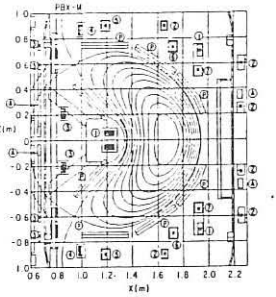

Fig.1 Schematic view of PBX-M. Refer to text for coil identification

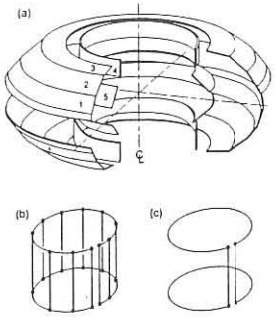

Fig.2(a) Schematic view of PBX-M Passive Stabilizer. (b) Circuit for upper and lower plates No. 1. (c) Circuit for plates 2-5.

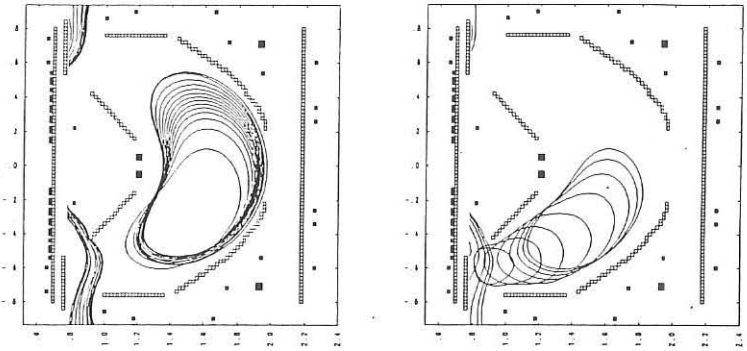

Fig. 3 (a) Initial phase of a simulated disruption. (b) Later phase of the same simulated diruption.

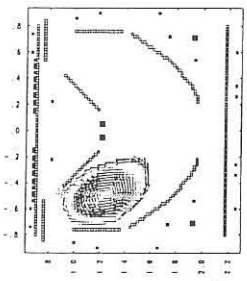

Fig.4 Poloidal current flow in the plasma halo for a simulated disruption.

IMPURITY BEHAVIOR DURING ECH IN THE TEXAS EXPERIMENTAL TOKAMAK

W. L. Rowan, M. E. Austin[1], R. V. Bravenec, J. Y. Chen[2], R. F. Gandy[1], G. Cima[3], K. W.Gentle, R. L. Hickok[4], S. C. McCool, A. G. Meigs, W. H. Miner, Jr., P. E. Phillips, B. Richards, P. M. Schoch[4], D. S. Sing, B. A. Smith, J. C. Wiley, A. J. Wootton, X. Z. Yang[5]

Fusion Research Center, The University of Texas at Austin, Austin, TX; [1]Auburn University, AL; [2]Institute of Plasma Physics, Academia Sinica, Hefei, PRC; [3]Consiglio Nazionale Delle Ricerche, Milano, Italy; [4]Rensselaer Polytechnic Institute, Troy, NY; [5]Institute of Physics, Academia Sinica, Beijing, PRC

INTRODUCTION

Electron cyclotron heating (ECH) in the Texas Experimental Tokamak (TEXT) causes an increase in central impurity emission. Thus far in our studies, we have traced this to an increase in the edge impurity source, but we also found that ECH induces an increase in impurity diffusion for $\rho > 0.7$, where ρ is the plasma radius normalized to the plasma boundary radius. Although as yet unexplained, enhanced diffusion is correlated with shorter working particle confinement time and increased edge plasma potential. Further study of this phenomenon may lead to the isolation of an impurity transport mechanism thus improving our understanding of impurity transport and perhaps suggesting a mechanism for impurity control. The purpose of this paper is to describe both the increase in source and the change in impurity transport.

EXPERIMENT

For these experiments, a 60 GHz, 95% O-mode electron cyclotron wave was launched from the low field side of the tokamak into the midplane of a sawtoothing, hydrogen plasma. The plasma major radius was 1 m, the minor radius was 0.26 m. The toroidal magnetic field, $B\phi = 2.2$ T, was selected to provide a central ECH resonance. The plasma current was 200 kA, and the chord-averaged electron density was 2×10^{19} m^{-3}. About 100 kW of power was deposited in the plasma. A ray tracing calculation[1] implies that all of the power is deposited within $\rho = 0.5$, while half is absorbed within $\rho = 0.2$.

The evidence for an increase in concentration of ambient impurity in the plasma center is quite convincing. The typical behavior of a central, metallic impurity is shown in figure 1. Both the impurity emission increase which is observed after ECH is turned on and the decrease after ECH is turned off occur on a time scale that is characteristic of impurity transport in TEXT OH discharges.

(The measurement of the transport time scale is described in the next section.) After the ECH is turned off, the impurity emission returns to its pre-ECH value on a time scale which is slower than either the time scale for atomic processes or the time scale of the electron temperature decay. The impurity emission increase is thus due to an impurity concentration increase rather that to an ECH-induced variation in electron temperature or density. These results are consistent with an increase in the edge impurity source during ECH, and there is also some indication that the central impurity transport is unaffected by ECH.

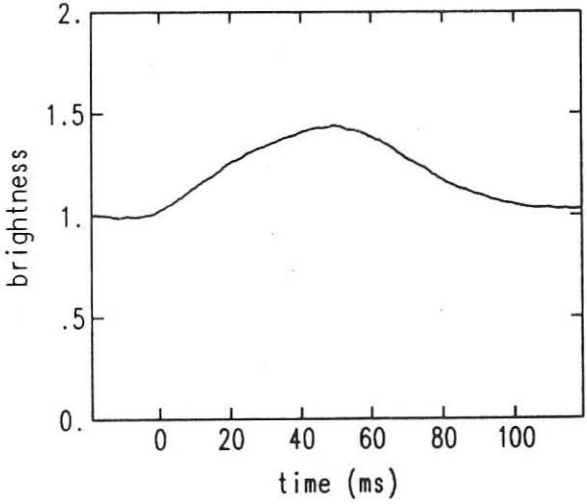

Figure 1. Typical chord-averaged emission from Ti^{+17} during ECH. ECH is turned on at t = 0 and off at t = 50 ms. The observed central impurity increase can be simulated with a 40% increase of the edge source.

ANALYSIS OF IMPURITY BEHAVIOR

The impurity behavior during ECH will be interpreted as due to a change in the edge impurity source and a change in impurity transport. Characterization of impurity transport required an additional set of experiments. A small quantity of a test impurity was injected into the plasma, and the time evolution of the emission from various stages of ionization was observed. In a simulation of this type of experiment using CHAPO[2], the UT transport code, the transport flux, Γ, was assumed to be of the form

$$\Gamma = -D\frac{\partial n_z(r)}{\partial r} - V\frac{r}{a}n_z(r)$$

where n_z is the density of impurity ionization state z, r is the plasma radius, a is the limiter radius, D is a diffusion coefficient and V is the inward-directed convective velocity. The impurity transport for a particular discharge is characterized by finding D and V such that the impurity emission predicted in the simulation agrees with that observed. These two parameters were determined before ECH was

turned on, at various times during the ECH pulse, and after ECH was turned off. Scandium was chosen as the injected test impurity since it may be expected to transport much like the impurity of principal interest, titanium. The simulation was also used to test the sensitivity to uncertainties in T_e and n_e. With the transport thus well defined through determination of D and V, an additional simulation which employs those parameters can be used to estimate the ECH induced source change by reproducing an ambient impurity observation such as that in figure 1.

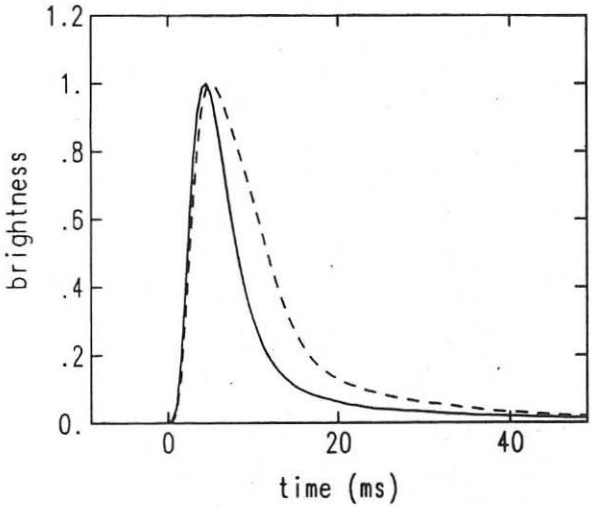

Figure 2. The observed time evolution of the chord-averaged emission from a Sc^{+12} transition following injection of a short pulse of scandium into an OH discharge (– –) and into an ECH discharge (——). In ECH discharges, the Sc^{+12} emission decays more rapidly than in OH discharges.

An example of the result of the injection experiment is shown in figure 2. The figure shows two sets of data for Sc^{+12}. In one case, the impurity was injected into an ECH discharge, while in the other, the impurity was injected into a similar discharge without ECH. The principal difference in the two cases occurs during the decay of the emission signal. The decay times differ by about 40% with the more rapid decay occurring for the ECH case. The ions studied in this way were Sc^{+10} through Sc^{+18}. The decay times differences vary smoothly from about 50% for Sc^{+10} to zero for Sc^{+17} and Sc^{+18}. For reference, the Sc^{+12} ion emission peaks near $\rho = 0.7$.

The simulation results are shown in figure 3 for the OH discharge and for the ECH discharge. In addition, there are results for the ECH discharge with variation of D to demonstrate the sensitivity of the results to choice of D. From a comparison of figures 2 and 3, it follows that without ECH, D = 1.0 $m^{-2}s^{-1}$ and with ECH D = 1.5 $m^{-2}s^{-1}$. ECH appears to increase the diffusion coefficient by about 50% for Sc^{+12}. Clearly, there is a change in the edge impurity transport.

Using the transport coefficients determined in the laser injection experiment, the ECH induced source can be inferred. To reproduce observations such as those in figure 1, it was necessary to increase the edge impurity source by approximately 40% during ECH.

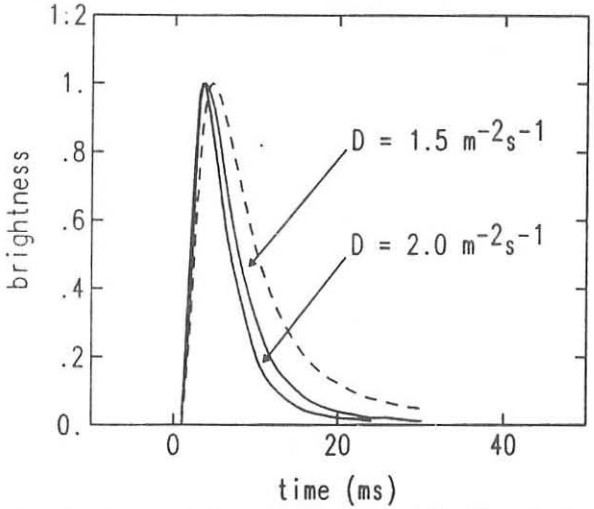

Figure 3. Simulation of the chord-averaged Sc^{+12} emission following injection of scandium. OH and ECH discharges with various transport coefficients are simulated: OH n_e and T_e profiles, D = 1.0 $m^{-2}s^{-1}$, V = 10 m/s (– –); ECH profiles with V = 10 m/s and for various D (——).

CONCLUSION

In TEXT, the ECH-induced changes in edge impurity source and in impurity transport were studied by comparing observations of ambient impurities with observations of injected test impurities. During ECH, there is a net increase in impurity concentration in the plasma center which is due to a substantial increase in edge impurity source. Central impurity transport is unaffected, but there is an increase in impurity diffusion for $\rho > 0.7$. Further study of this result may lead to the isolation of an impurity transport mechanism and perhaps even to suggestions for impurity control.

ACKNOWLEDGEMENTS

This work was supported by the U. S. Department of Energy under Grants DE-FG05-88ER53267 and DE-FG05-88ER53266. Support for one of the authors (BAS) was provided by the Magnetic Fusion Science Fellowship Program, Oak Ridge Associated Universities.

REFERENCES

1. D. C. Sing , M. E. Austin, R. V. Bravenec, J. A. Boedo, et al., (this conference)
2. J. C. Wiley, CHAPO, "A One-Dimensional Transport Code," FRC Report 328, The University of Texas Fusion Research Center, Austin (1988).

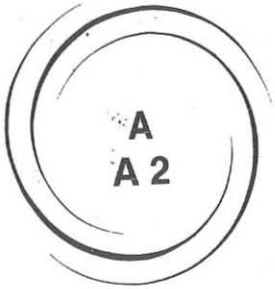

TOKAMAKS

H-MODE

BEHAVIOUR OF IMPURITIES DURING THE H-MODE IN JET

R. Giannella , K. Behringer, B. Denne, N. Gottardi, N.C. Hawkes* , M. von Hellermann, K. Lawson* , P.D. Morgan, D. Pasini, M.F. Stamp

JET Joint Undertaking, Abingdon, Oxon, U.K.

*UKAEA/Euratom Association Culham Laboratory, Abingdon, Oxon, U.K.

INTRODUCTION

In additionally-heated tokamak discharges, the H-mode phases are reported to display, together with a better energy confinement, a longer global containment time for particles. In particular, steep gradients of electron density and temperature are sustained in the outer region of the plasma column. This enhanced performance is observed especially in discharges in which the activity of edge localized modes (ELMs) is low or absent. High confinement and accumulation of metallic impurities, which quickly give rise to terminal disruptions have been described under similar conditions /1/. In JET H-modes very long impurity confinement times are also observed. However the experimental condition is somewhat more favourable since quiescent H-modes are obtained lasting much longer than the energy confinement times and the radiation from metals is generally negligible. The dominant impurities are normally carbon and oxygen, the latter generally accounting for half or more of the power radiated from the bulk plasma. During the X-point operation the effective influx of carbon into the discharge, which is normally in close correlation with that of deuterium /2/, is substantially reduced while the influx of oxygen, whose production mechanism is believed to be of a chemical nature, does not show significant variations.

EXPERIMENTAL EVIDENCE

Long duration (< 4 sec) H-mode phases that are free from ELMs are easily obtained at JET. An example of such discharges is illustrated by fig. 1. During these phases the power radiated from the bulk plasma is observed to increase at a rate which is constant or slightly increasing with time. A similar time behaviour is also shown by the intensities of lines emitted by the hydrogen-like ions of oxygen and carbon while for the lower ionization stages of these impurities, whose radiation is localized outside the magnetic separatrix, no important intensity variations are observed. Nickel lines emitted at various radii inside the separatrix are also seen to increase continuously during these phases, but the contribution of metals to the radiated power is usually marginal (< 10%). Their concentration, estimated from the absolute intensities of lines radiated by different ionization states, is generally lower than 10^{-4} of the electron densities.

The bolometric measurements indicate that the radiation is emitted during these phases in very thick (0.4 to 0.6 m) external layers with substantial emission from regions with very high electron temperature (1 to 2 keV) where the typical coronal emissivity of light impurities is very much reduced with respect to its maxima. The soft X-ray emission profiles (fig. 2) indicate rather uniform distributions of the light impurities within a radius of 0.5 m from the magnetic axis. Measurement from charge-exchange recombination spectroscopy also give hollow profiles of carbon density (fig. 3) steadily increasing with time while conserving the shape during the whole ELM free phase. These results are in agreement with the Z_{eff} profiles deduced from the bremsstrahlung measurement in the visible spectrum.

The evidence of very long confinement times for impurities is confirmed by experiments involving the injection of impurities /3/. The results of these tests also indicate the rapid formation, after the injection of metal impurities, of a hollow profile of their concentration whose decay time appears to be much longer than the few seconds available before the collapse of the high confinement plasma configuration.

The ELM-free H-mode terminates when the power radiated from the bulk plasma reaches a substantial fraction ($\approx$ 60%) of the input power P_{inp} or when the total radiation (including

radiation from the X-point region) exceeds P_{inp} : at the present levels of impurity influxes, this limits this phase to durations shorter than 4 secs. However, longer lasting H-modes or trains of H-modes are achieved if a mechanism sets in that may result in a quenching of the radiation. Intermittent short phases of i) ELM activity or ii) L-mode can substantially extend the duration or improve the performance of H-modes. These two mechanisms are different in several respects including the particle transport and their efficiency in depleting the plasma of impurities. In the **first** case while the plasma makes a transition from the quiescent H-mode to a phase of frequent ELMs the radiated power from the bulk plasma rapidly stops increasing and begins to decrease at a comparable rate. The line radiation from the metal ions emitting in the central plasma, however, keeps increasing for several hundred milliseconds at the same rate as during the ELM-free phase: the ELM activity only affects the plasma outer regions while their transport in the inner plasma is not varied. This is interpreted as evidence of a reduced diffusivity for impurities in the inner plasma during the H-mode with respect to the L-mode values. The **second** case is also illustrated in fig 1. The H-L transition is generally marked by a very strong spike in the radiated power from the X-point region followed by a very fast decrease of the radiation from all the plasma while the average density is only slightly reduced. In both cases, due to the reduction of the radiated power, the ELM-free H-mode is often resumed after a short (0.3 to 0.5 sec) interruption but with an important difference. While in the ELM phase case the impurity content is only reduced in the plasma periphery and the transport of impurities in the centre continues unperturbed, in this second case an effective depletion of the impurities all over the plasma has taken place allowing, in the subsequent ELM-free phase, lower levels of radiation at the same values of electron density and temperature.

Very long quasi stationary H-modes can also be produced by provoking a continuous ELM activity. Such discharges are obtained when the clearance between the separatrix and the inner wall or the belt limiters is small. In these cases the influx of carbon into the discharge is higher and the relative contribution of this element to the radiation is of greater importance but the oxygen contribution is also much reduced. In these circumstances the impurity confinement times are smaller and a moderate increase of the radiation (as well as of the density) can be achieved. In those cases where the electron density reaches a stationary level, the radiation level also is seen to settle or slowly decrease. The radiation pattern during these phases displays thin (< 20 cm) emitting layers at the extreme periphery of the plasma column. In these cases there is no apparent increase in the total content of impurities in the discharge.

TRANSPORT ANALYSIS

The very long temporal scale of the radiation signals originating inside the separatrix from intrinsic and injected impurity ions is clear evidence that the impurity containment time is much longer than the global energy confinement time($\leq$ 1 sec) in JET quiescent H-modes. This has the practical implication that in the present experimental conditions it is not possible to observe the stationary distribution of impurities (a reduction of a factor of five or larger in the effective impurity influxes would be required with respect to the present values to run quiescent H-mode discharges). In particular it is not possible to clarify at present whether the hollowness of the impurity distribution across the discharge is simply a transient feature or if there is any active mechanism sustaining the positive gradients of their densities. Neoclassical effects connected to the positive gradients of the background plasma density, or to the exchange of momentum between the plasma and the co-injected netral beams /4-5/, could in fact justify an outward-directed convection in the internal regions of the discharge.

In order to account for the bolometric profiles observed, displaying a very substantial shift of the light impurities total emission from its natural "locus" (T_e = 100 to 300 eV for oxygen) to a region of the plasma with temperature much higher, a strong ratio is required between the total impurity density at $\approx$ 20 cm inside the magnetic separatrix and at the scrape-off region. Such a pronounced shaping of density profile cannot be described by diffusion, but

requires a dominant convective mechanism localized at the plasma periphery, just inside the separatrix itself. This inward convection zone has to be restricted to a rather limited region in order to allow for the experimental hollow profiles of radiation and impurity densities. A strong ratio between the inward convective velocity v and the particle diffusivity D in this outer zone is also required by the observed long confinement times. Values of v/D of 0.5 cm^{-1} or larger are needed if the thickness of this convective zone is about 20 cm. In fig. 4 a velocity profile used to simulate these data is shown. The impurity density profile obtained after 2 sec of transport using this velocity and uniform diffusion coefficient D = 1500 cm^2 /sec is also shown. The corresponding computed bolometric radiation and soft X-ray emission profiles for the case of oxygen are also shown and compared with the experimental data for the JET pulse illustrated in fig. 1 at t = 13 sec. The neoclassical convective velocity profiles computed from the experimental density and temperature are generally quite similar both in shape and absolute values to the one assumed shown in the figure. It should be observed, however, that a detailed quantitative comparison is not justified in this case because of the large experimental uncertainties in the gradients of T_e and n_e and on the q profile.

A very similar convection and diffusion scheme also describes the time behaviour of different ionization stages of a metallic impurities, both injected /3/ and intrinsic, under similar experimental circumstances.

CONCLUSIONS

Enhanced confinement of the impurities is observed during quiescent H-mode phases in JET neutral-beam heated discharges. This effect is due to the formation of a convective layer at the plasma periphery. The shape and absolute value of the convective velocity are comparable to those expected from the neoclassical theory. The diffusion coefficient also appears to be reduced during these phases. Spontaneous or provoked ELM activity can stop (and reverse) the continuous buil-up of impurities in the plasma periphery that, at the present level of the impurity influxes, leads to a termination of the quiescent phase after a few seconds.

REFERENCES

/1/ E.R. Müller, G. Janeschitz, P. Smeulders, G. Fussmann, Nucl. Fus. **27** (1987) 96.

/2/ B. Denne et al. 14th Europ. Conf. on Contr. Fus. and Plasma Phys. (Madrid, Spain, 1987) vol. 11D,I 109.

/3/ N.C. Hawkes et al. this conference.

/4/ W.M. Stacey, D.J. Sigmar Nucl. Fus. **19** (1979) 1665.

/5/ R.C. Isler et al. Nucl. Fus. **23** (1983) 1017.

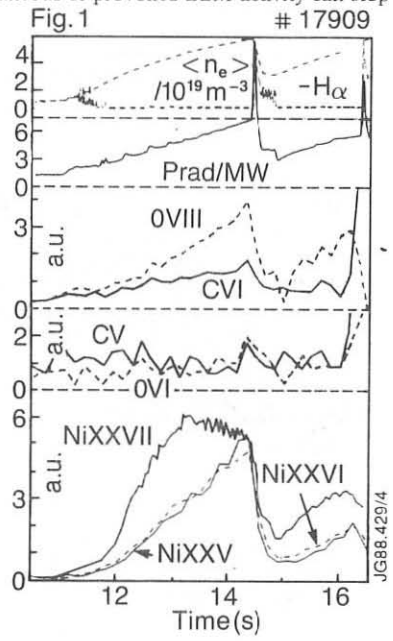

fig. 1 Time evolution of the average electron density, Hα intensity, total radiated power P_{rad} and of the radiation from different ionization stages of carbon, oxygen and nickel. Two quiescent H-mode phases are separated by a short L-mode phase.

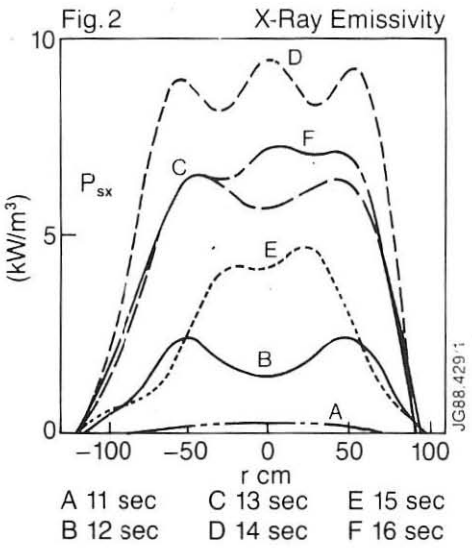

fig. 2 Soft X-ray emission profiles at different times during the the pulse displayed in figure 1.

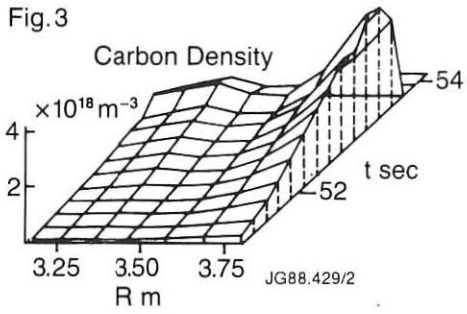

fig. 3 Carbon density measured by charge exchange recombination spectroscopy in the pulse displayed in figure 1.

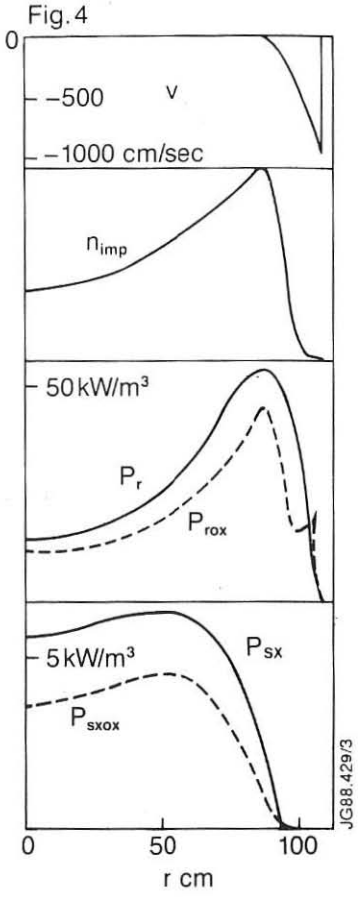

fig. 4 Shape of the convective velocity assumed for the simulation of the pulse displayed in fugure 1 and profile of the impurity density after 2 sec of transport. The corresponding computed total radiation and soft X-ray emission profiles for the case of oxygen (4% of the electron density at the plasma centre) are also shown and compared with the experimental profiles.

IMPROVED CONFINEMENT IN PEAKED DENSITY PROFILE ON JFT-2M

M. Mori, H. Aikawa, K. Hoshino, T. Kawakami, S. Kasai, H. Kawashima, T. Kondoh*, T. Matsuda, H. Matsumoto, Y. Miura, I. Nakazawa**, C. R. Neufeld***, K. Odajima, H. Ogawa, T. Ogawa, K. Ohasa, H. Ohtsuka, S. Sengoku, T. Shoji, N. Suzuki, H. Tamai, Y. Uesugi, T. Yamamoto, T. Yamauchi, and H. Maeda

Japan Atomic Energy Research Institute
Naka-machi, Naka-gun, Ibaraki, 319-11 Japan
* On leave from University of Tsukuba, Ibaraki, Japan
** On leave from Mitsubishi Electric Co., Tokyo, Japan
*** On leave from Hydro-Quebec, Varennes, Quebec, Canada

Introduction

H-mode is well studied experimentally in some tokamaks. However it is not obtained in stationary state, so far. One way to achieve stationary H-mode is to control edge localized modes (ELM). Another possibility to achieve improved confinement modes in the stationary state has been reported in JFT-2M experiments(1). This type of improved confinement modes has been obtained after H-L transition in both divertor and limiter discharges. Edge phenomenon are similar to those in the L-mode rather than the H-mode, and density profile is highly peaked. Therefore we call this mode Improved L-mode(IL-mode). Further investigations on the IL-mode have been performed in JFT-2M experimentally.

Time Behavior

One example of the IL-mode is obtained with H_e-beam co-injection heating(300kW/24kV) into single null open divertor deuterium plasmas (B_T=1.25T, I_p=255kA, R=1.28m, a=29cm, $\kappa \sim 1.4$). The plasma cross section and a temporal evolution of plasma parameters are shown in figure 1. The distance between a graphite divertor plate and a null point is around 6cm. Gas-puffing is kept almost constant during NBI. An ordinary H-mode is obtained from 30msec after the injection, and an H-L transition occurs 120msec after the injection. The line emission of D_α jumps up abruptly at the H-L transition. The peripheral electron temperature(r/a=0.95) measured by 90GHz electron cyclotron emission(ECE) drops. The density, the stored energy, and the total radiation loss decrease in this L-mode phase. Rapid increase of a soft X-ray measured by SBD(Surface Barrier Diode) along a central chord also stops. Following this L-mode, the third transition happens 140msec after the injection. The D_α emission decreases, but the level of the emission is higher than the first H-mode. This phase (IL-mode) is different from the ordinary H-mode in many points. The averaged electron density does not increase and keeps nearly constant level without the burst of D_α for more than 100msec. A quasi-stationary state of the density, which can never be obtained in the ordinary H-mode without ELMs is obtained in the IL-mode. The total radiation loss is not as high as that of the H-mode. The stored energy begins to increase again. It does not reach saturation level during heating phase in this case. The stored energy reaches 28kJ and exceeds 25kJ of the H-mode. The loop voltage is also decrease again in the IL-mode. The internal inductance(l_i), which is estimated from a difference between the diamagnetic poloidal β_p and the equilibrium $\Lambda (= \beta_p + l_i/2 - 1/2)$, decreases in the

H-mode and returns to that of the L-mode in the IL-mode as shown in Fig. 1. This tendency is also seen in the temporal evolution of the elongation factor with fixed poloidal field coil currents, where larger elongation factor indicates broader current profile. Therefore the decrease of the loop voltage is not due to a decrease of the internal inductance but due to a decrease of Z_{eff} and/or an increase of the average electron temperature.

Density and Electron Temperature Profiles

The density profile is always peaked in the IL-modes. Peaking factors, which is defined by n(-4cm)/n(-18cm) with two different chord averaged density, in various modes are plotted in Fig. 2(a) as a function of the averaged electron density. Stored energy is also plotted in Fig. 2(b) as a function of the density. Since these L-mode

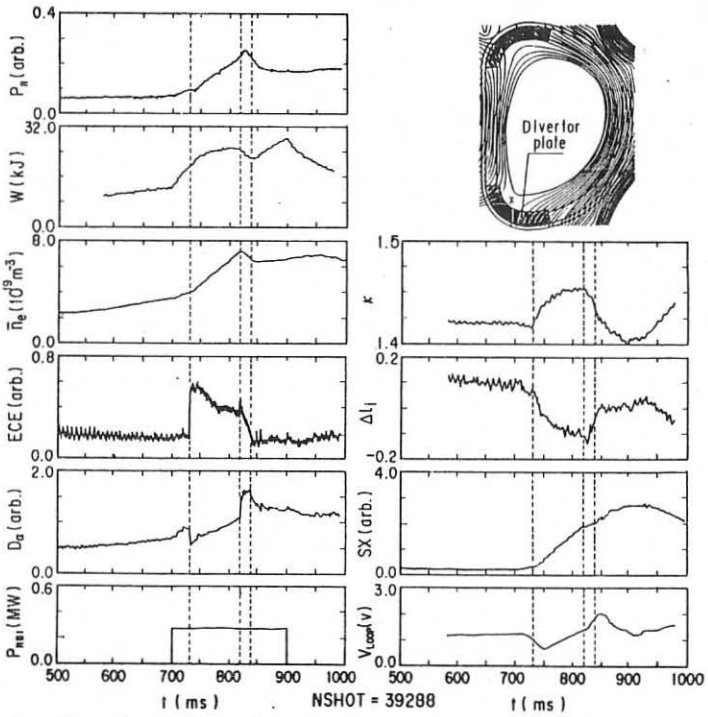

Fig. 1 Temporal evolutions of the plasma parameters in the single null divertor configuration (I_p=255kA, B_T=1.25T). Helium beam injected tangentially into a deuterium plasma from 700msec to 900msec. An ordinary H-mode is observed from 730msec to 820msec, and the transition to the IL-mode is occurs at 840msec. After this new transition, the density is kept nearly constant, and the plasma stored energy begins to increase again. Plasma cross section is also shown in this figure.

discharges in this figure are obtained by reducing the divertor length from 6cm to 0cm with same NBI power (570kW Co-injection and 170kW Counter-injection) and same positions, plasma cross section is smaller in H- and IL-mode discharges than the L-mode discharges by ~13%. In spite of reduction of the stored energy by this volume effect, confinement in the IL-mode is improved compared with that in the L-mode. Three modes belongs to different groups in Fig. 3(a), that is, the IL-mode, H-mode, and the L-mode correspond to the most peaked profile, the broadest profile, and medium profile, respectively. The peaked density profile seems to be very important to achieve the IL-mode.

Electron temperature profiles of the H and IL modes in a limiter discharge are shown in Fig. 3. (I_p=270kA, B_T=1.25T, R=1.28m, a=0.32m, κ=1.4, H^0[1.8MW/32kV]→D^+). The values of the stored energy in the H-mode and the IL-mode are same in this case. The line averaged density is increasing slowly during the IL-mode, although increasing rate is reduced compared with that in the H-mode. The peripheral electron temperature is low in the IL-mode compared with the H-mode. Since the density profile is highly peaked in the IL-mode, a pressure gradient at the core region (r/a(0.8) is larger in the IL-mode than in the H-mode. On the other hand, energy and particle confinements at the peripheral region seems to be poor. Improvement of the energy confinement is realized in the core region. Peaked pressure profile has a benefit to get high fusion output efficiently.

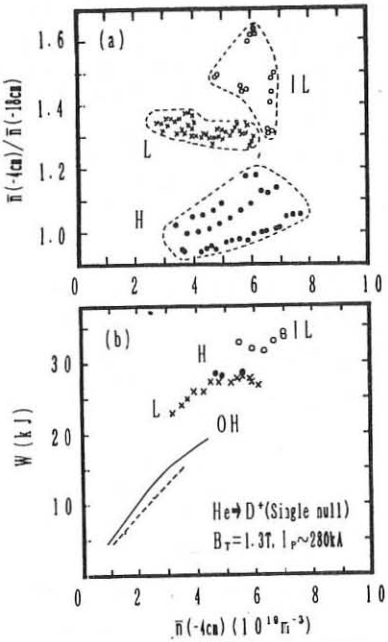

Fig. 2 Peaking factor of the density and the stored energy in H-mode, L-mode, and IL-mode. The L-mode is obtained by changing the divertor length from ~6cm to ~0cm. The stored energy in both Ohmic heating cases is presented. (solid line→~6cm, dashed line →~0cm)

Power Dependence

Power dependence of the stored energy in the IL-mode is similar to that in the ELM free H-mode as shown in Fig. 4. It can be seen clearly in this figure again that the confinement is improved in the IL-mode compared with the L-mode. Roughly speaking, the stored energy increases offset-linearly, and incremental energy confinement time is same to that in the L-mode.

Conditions to Achieve IL-mode

Conditions to obtain this mode has been surveyed experimentally. Wall condition seems to be one of critical conditions, because day-by-day reproducibility is not quite good. High plasma current and high toroidal magnetic field make it easier to obtain this mode. Gas puffing is also one of important components of control an

onset of this mode. Without gas puffing, density decreases to very low level in some cases, and stored energy also decreases to the level of the L-mode and does not recover. In such cases, strong sawteeth occur frequently. With an adequate gas puffing, the density in the L-phase after the H-phase is maintained with a little decrease, and the stored energy recovers again. Sawteeth is suppressed or reduced in such cases. Therefore, the peaked density profile without sawteeth activities seems to be important in order to improve confinement properties without edge H-mode phenomenon. In some IL-mode discharges, long period sawteeth (~50ms) are observed, and a m=1 oscillation appears in the density and soft X-ray emission. This MHD behavior in the IL-mode resembles a monster sawteeth in JET(2).

Acknowledgments

The authors would like to thank all members of JFT-2M machine group and heating group for their helps in experiments. We also wish to acknowledge continuous encouragements of Drs. M. Yoshikawa, M. Tanaka, and S. Shimamoto.

References

(1) M. Mori, N. Suzuki, Y. Uesugi, et al., Nucl. Fusion 28(1988)433

(2) D. J. Campbell, P. A. Duperrex, A. W. Edwards et al., Proc. 11th Int. Conf. on Plasma Phys. and Controled Nuclear Fusion Research(Kyoto), Vol. 1, (1987)433

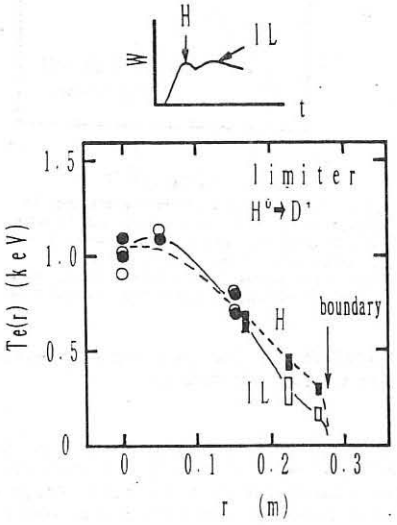

Fig. 3 Electron temperature profiles of the H-mode and IL-mode in a limiter discharge. Circle and square correspond to temperature measured by soft X-ray pulse height analysis and electron cyclotron emission, respectively. Closed and open symbols represent the H-mode and the IL-mode, respectively.

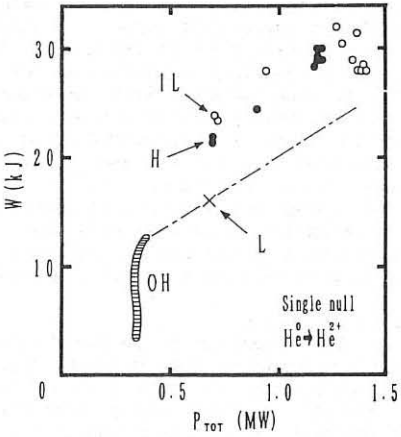

Fig. 4 Power dependence of the stored energy in three modes and Ohmic heating case. Helium beam is injected into Helium single null divertor plasmas. Open and closed circles represent the IL-mode and the H-mode, respectively. Cross represents the L-mode.

Impurity Behavior during H-mode Phase in JFT-2M

H.Ogawa, S.Kasai, H.Aikawa, K.Hoshino, T.Kawakami, H.Kawashima, T.Kondoh*, H.Maeda, T.Matsuda, H.Matsumoto, Y.Miura, M.Mori, I.Nakazawa**, C.R.Neufeld***, K.Odajima, T.Ogawa, K.Ohasa, H.Ohtsuka, S.Sengoku, T.Shoji, N.Suzuki, H.Tamai, Y.Uesugi, T.Yamamoto, and T.Yamauchi

Department of Thermonuclear Fusion Research,
Japan Atomic Energy Research Institute,
Tokai-mura, Naka-gun, Ibaraki-ken 319-11, Japan

1. Introduction

In JFT-2M, the characteristics of the high confinement mode (H-mode) have been studied in the various plasma conditions[1]. The results of these studies indicates that the quiescent H-mode (H-mode without ELM's) phase was terminated by the large increment of radiation losses during the quiescent H-mode phase. Thus, it appears that the impurity problem is one of the most serious problem to obtain the longer duration of the quiescent H-mode phase.

In this paper we present the experimental results concerned with the impurity behavior during the quiescent H-mode phase by using spectroscopic method in JFT-2M.

2. Apparatus

The JFT-2M tokamak has a D-shaped vacuum vessel made of the stainless steel with a major radius of 1.31m and minor radii of axb=0.475x0.595m. Both the limiters and the diverter plates are made of graphite. And the inside wall of the vacuum vessel is covered by the graphite plates. Titanium gettering is used to obtain the clean plasma. So, the main light impurity species is carbon and the metal impurities such as iron and titanium are not negligible in the JFT-2M plasma. Two heating neutral beam (NB) are injected near tangentially (both co- and counter-injection). The acceleration voltage is about 34kV and the maximum power is 0.8MW of each.

The impurity behaviors were measured by using the 3m grazing incident monochromator (3-60nm) and the radial profiles of the line emission were measured by tilting the monochromator. The visible monochromator was also used to measure the H-like carbon line (CVI, 343.4nm) excited by the charge exchange recombination (CXR). The radial profiles of the radiation losses were measured by the bolometer array. The radial profiles of the electron temperature and the electron density were measured by the Thomson scattering apparatus. The electron cyclotron emission (ECE) was also used to measure the radial profile of the electron temperature. The line-averaged electron density (n_e) was measured by 2mm μ-wave interferometer and 3-channel FIR interferometer.

3. Experimental Results

3.1 Impurity behavior during the quiescent H-mode phase

The typical time evolution of the plasma parameter during the quiescent H-mode phase in the deuterium plasma with the diverter configuration are as follows; n_e, P_{rad} and the soft x-ray intensity by the surface-barrier detector increased linearly with time. The time evolution of t he central electron temperature measured by the soft x-ray analyzer is almost the same as that in the discharge

* On leave from University of Tsukuba, Ibaraki, Japan
** On leave from Mitsubishi Electric Co., Tokyo, Japan
*** On Leave from Hydro-Quebec, Varennes, Quebec, Canada

with the only L-mode but the electron temperature during the H-mode phase decreased slightly by the end of the H-mode phase. The electron temperature and the electron density at the plasma periphery (just inside of the separatrix) rapidly increased just after the H-transition. These time evolution indicates that the electron temperature and the electron density profiles have a pedestal at the plasma periphery. The radial profiles of radiation losses became a centrally-peaked. The details were appeared in ref.1.

Typical time evolution of the emissions from impurity ions in the deuterium discharge with the diverter configuration were shown in Fig.1. The emission of the highly-ionized metallic lines such as TiXV increased linearly with time during quiescent H-mode phase although those of less-ionized species such as TiXI rapidly decreased just after the H-transition in comparison with the L-mode phase. The intensity of CVI line excited by CXR also increased linearly with time during the quiescent H-mode phase [2] although the intensity of the CIV line emitted from plasma periphery rapidly decreased just after the H-transition. This experimental result indicates that the fully stripped carbon ion density at the plasma center increased during the H-mode phase and suggests that the large increment of the emissions of the highly-ionized metallic ion lines is due to the large increment of the higlhly ionized ion densities. These impurity behaviors are same in both the light and the metal impurity species.

In order to understand the difference of the impurity behavior in the L- and the H-mode phase, the radial profiles of the iron ion densities were measured. This experimental results indicate that the less-ionized ion density is almost the same in both the L- and the H-mode phase but the highly-ionized ion density increase and spread whole of the plasma in the H-mode phase in comparison with the L-mode phase. Thus it appears that the influx of the iron is same in both the L- and the H-mode phase and the impurity accumulation was due to the enhancement of the particle confinement during the H-mode phase.

3.2 Comparison between the hydrogen and deuterium discharges

Figure 2 shows the time evolutions of the plasma parameters in the hydrogen and the deuterium discharges with the quiescent H-mode phase. In the hydrogen discharges increments of n_e and Prad in the H-mode phase were less than those in the deuterium discharges. The one-turn voltage in the hydrogen discharge did not increase during the H-mode phase. The electron temperature at the plasma periphery is about the same in both discharges. The stored energy in the hydrogen discharge did not decrease at the end of the H-mode phase in comparison with that in the deuterium discharge.

Figure 3 shows the radial profiles of radiation losses which were the line-integrated value during the OH, L- and H-mode phase in both discharges. During the OH and L-mode phase, the radiation losses have a hollow-profiles and the intensities were about the same in both discharges. But during the H-mode phase the radiation loss profile was a centally-peaked in the deuterium discharge and not centrally-peaked in the hydrogen discharges and the intensity at the center in the hydrogen discharge was about the half in the deuterium discharges.

The intensities of the highly ionized metallic ion lines such as FeXVIII were about the talf of those in the deuterium discharges, although those of the less-ionized ion lines were about the same in both discharges as shown in Fig.4. The intensity of the CVI line excited by CXR in the hydrogen discharges is also about the half of that in the deuterium discharges although the intensity of the CIV line is about the same in both discharged. This indicates that the fully ionized carbon ion density at the plasma center in the hydrogen discharges were about the half of the deuterium discharges during the H-mode phase.

In order to understand the difference of the impurity behavior between in the hydrogen and the deuterium discharges during the quiescent H-mode phase, the radial profiles of iron ion densities in both discharges were estimated by using the radial profile of the iron ion lines and the radial profile of the electron density and electron temperature measured by the Thomson scattering method. The excitation rate coefficient used in this experiment is proposed by Mewe and the Abel inversion is also used to obtain the emissivity of the spectral lines. Figure 5 shows the radial profiles of the Fe^{17+} and Fe^{9+} ion densities in the hydrogen and the deuterium discharges. The less-ionized ion density (Fe^{9+}) is the same in both discharges but the higher-ionized ion density (Fe^{17+}) in the deuterium discharge was about twice as large as those in the hydrogen discharge. These experimental results indicate that the influx of both discharges is about the same but the difference of the higher-ionized ion density in both discharge is due to the difference of the particle confinement in the core region of plasma.

4. Summary

The impurity behavior during the quiescent H-mode phase was studied by the spectroscopic method and the following results are obtained;

(1). During the quiescent H-mode phase, the impurity ions accumulate in the center of the plasma and there is no difference of this impurity behavior between the light and the metal impurities.

(2). These impurity behavior was due to the enhanced particle confinement in the quiescent H-mode phase.

(3). The impurity accumulation in the hydrogen discharge is less than that in the deuterium discharge which is due to the difference of the enhancement of the particle confinement between both discharge during the quiescent H-mode phase.

Acknowledgement

Authors would like to thank all the member of JFT-2M operation group. They are also grateful to Drs. A.Funahashi, Y.Tanaka, M.Tanaka, S.Shimamoto, M.Yoshikawa and S.Mori for their continuous encouragement.

References

[1] N.Suzuki, et al.: in Plasma Phys. and Controlled Nucl.Fusion Res. (Proc. 12th Int. Conf. Nice, 1988) IAEA-CN-50/A-II-3 (1988).

[2] H.Ogawa, Y.Miura and S.Kasai: Rev. Sci. Instrum. **59** (1988) 1506.

Figure Captions

Fig.1 Time evolution of the emissions of impurity ion lines during the quiescent H-mode phase.

Fig.2 Time evolution of the plasma parameters during the quiescent H-mode phase in the hydrogen(solid lines) and the deuterium (dash line) discharges.

Fig.3 The radial profiles of the line-integrated radiation losses during the OH, the L- and the H-mode phase in the hydrogen(solid lines) and the deuterium (dash line) discharges.

Fig.4 Time evolution of the emission of the impurity ion lines during quiescent H-mode phase in the hydrogen(solid lines) and the deuterium (dash line) discharges.

Fig.5 The radial profiles of the iron ion densities (Fe^{17+} and Fe^{9+}) in the hydrogen and the deuterium discharges.

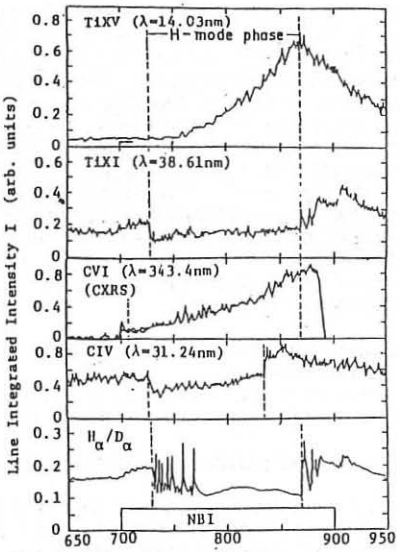

Fig. 1

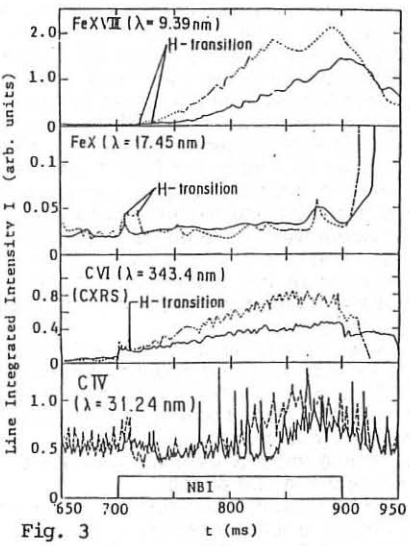

Fig. 3

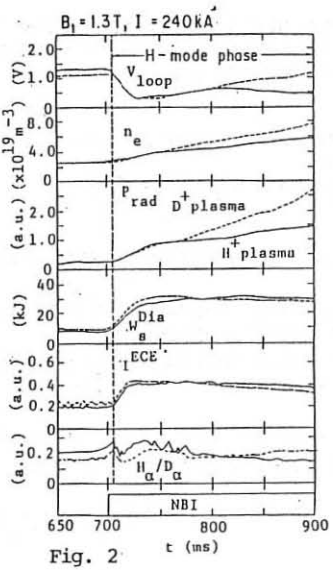

Fig. 2

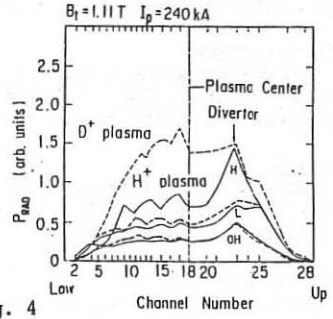

Fig. 4

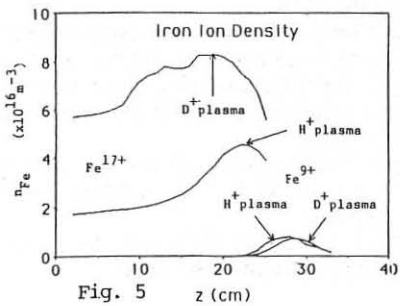

Fig. 5

LIMITER H-MODES IN THE JIPP T-IIU TOKAMAK

K. Toi, K. Adati, R. Akiyama, A. Ando, R. Ando, T. Aoki, D.G. Bi[1], J. Fujita, Y. Hamada, S. Hidekuma, S. Hirokura, K. Ida, H. Ikegami, K. Kadota, E. Kako[2], O. Kaneko, A. Karita, K. Kawahata, T. Kawamoto, Y. Kawasumi, S. Kitagawa, M. Kojima, S. Kubo, R. Kumazawa, T. Kuroda, K. Masai, K. Matsuura, A. Mohri, S. Morita, K. Narihara, A. Nishizawa, Y. Ogawa, K. Ohkubo, Y. Oka, S. Okajima[3], S. Okamura, T. Ozaki, A. Sagara, M. Sakamoto, M. Sasao, K. Sato, K.N. Sato, T. Sato, T. Seki, F. Shimpo, S. Tanahashi, Y. Taniguchi, T. Tsuzuki, T. Watari and H. Yamada

Institute of Plasma Physics, Nagoya University, Nagoya 464-01, Japan
1) Southwestern Institute of Physics, People's Republic of China
2) National Laboratory for High Energy Physics, Tsukuba 305, Japan
3) Department of Applied Physics, Chubu University, Kasugai 487, Japan

1. Introduction

Recent research of the tokamak confinement is focused on identifying turbulent fluctuations[1] and finding improved confinement regimes such as H-mode[2]. The H-mode is successfully obtained in the divertor and limiter configurations[3]. We have observed the H-mode in a circular cross-section plasma bounded by a limiter on JIPP T-IIU ($R \simeq 91$ cm, $a \simeq 23$ cm, and $B_{to} \simeq 2.7 - 3.0$ T)[1]. This H-mode is achieved in the smallest tokamak and also in the highest density regime up to $\bar{n}_e \simeq 10^{14}$ cm^{-3}.

2. Experimental Conditions

Carbon limiters and torus wall have been conditioned by pulsed helium ECR discharge cleaning (for about two weeks long with 0.1 Hz repetition rate). We use titanium gettering between shots to suppress an unfavorable density rise. A deuterium plasma with hydrogen minority (~10 %) is heated by ICRF power up to $P_{RF} \simeq 2.5$ MW, and neutral beam injected nearly perpendicularly up to $P_{NI} \simeq 0.7$ MW.

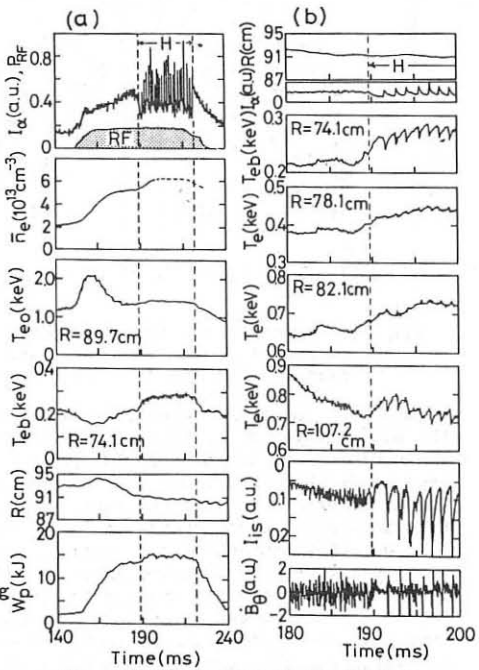

Fig.1 Time behaviour of the limiter H-mode discharge(a) and its enlarged traces (b), where $P_{RF} \simeq 1.8$ MW, $I_p \simeq 200$ kA, and $B_{to} \simeq 2.85$ T.

3. Experimental Results

Figure 1 shows a typical H-mode discharge with a constant plasma current (Type-1). About 40 ms later from the beginning of the RF pulse, the H-mode transition occurs with a sharp depression in H_α/D_α emission (I_α), and obvious rises in edge electron temperature T_{eb} (at $r/a \simeq 0.75$) and $\bar{n}_e$. Moreover, the electron density in a scrape-off layer measured by Langmuir probes (I_{is}: ion-saturation current) suddenly drops just after the transition. These characteristics are as same as those observed in other divertor tokamaks[3]. The H-phase is sustained for ~30 ms which is as long as four times of an energy confinement time. The degree of the confinement improvement is not so significant, i.e., $\Delta W_p/W_p \simeq 10$ - 15 %. This may be due to the frequent occurence of edge localized modes (ELM). The threshold power to the H-mode transition (P_{th}) is studied over the wide parameter range: $\bar{n}_e$ = 4 - 10 $\times 10^{13}$ cm^{-3}, B_{to}= 2.7 - 3.0 T, I_p= 110 - 270 kA, and P_{RF}= 0.5 - 2.5 MW, and $P_{NI} \simeq 0.7$ MW.

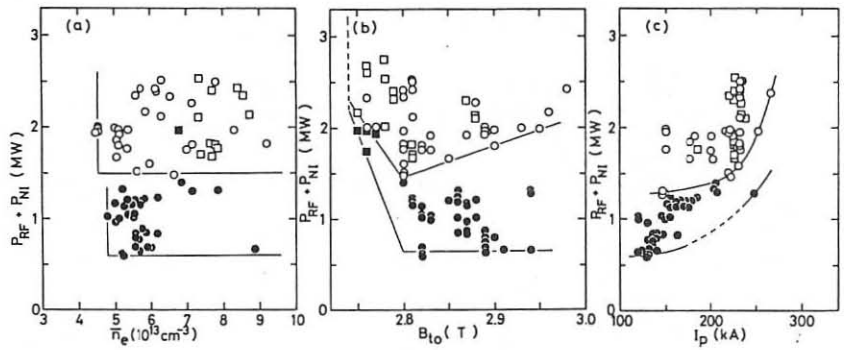

Fig.2 Dependence of the threshold power on $\bar{n}_e$, B_{to} and I_p which are estimated at the transition, where ○: RF alone, □: RF+NI, open symbols: for Type-1, and closed symbols: for Type-2.

Figure 2(a) shows the dependence of P_{th} on $\bar{n}_e$, where open symbols indicate the data in Type-1. This figure shows that there is a lower limit in $\bar{n}_e$ ($\simeq 4.5 \times 10^{13}$ cm^{-3}), but for more than it P_{th} is independent of $\bar{n}_e$. In this type of discharges, P_{th} has the minimum at $B_{to} \simeq 2.8$ T (Fig.2(b)). This feature seems to reflect the heating mechanisms of ICRF heating. The threshold power also depends on I_p, as shown in Fig.2 (c).

We study the effect of a rapid current ramp-down during the additional heating (Type-2). The modulation of the I_p-waveform may modify the current density profile near the plasma edge. When the heating power is set at that below the P_{th} obtained in Type-1 discharges, the rapid current ramp-down successfully triggers the H-mode transition(Fig.3). These data in Type-2 are also plotted in Fig.2 with solid symbols. As seen from Fig.2(c), P_{th} is obviously reduced by 30 - 50 % from that in Type-1 with the low I_p. Therefore, the results suggest that the H-mode is triggered by the mechanism related to the skin effect which is induced by the rapid

ramp-down, i.e., the decreasing rate in a plasma current $\dot{I}_p$ instead of I_p. For the higher heating power, the transition occurs with the smaller $\dot{I}_p$.

The H-mode plasma is characterized by the region with the steep ∇n_e or ∇T_e near the plasma edge ("transport barrier")[4]. The electron densities measured by six-channel FIR-interferometer rapidly rise or decrease just after the H-mode transition, depending on the measuring position. Figure 4 shows the radial dependence of the relative change in n_e for the H-mode discharges of Type-1 and Type-2, where the points in r/a >1.0 are obtained by the Langmuir probes. For both types, the transport barrier is formed near the plasma edge, but inside the limiter (r/a ≃0.8 - 0.9).

It is thought that the edge electron temperature is a crucial parameter to the H-mode transition. However, it is difficult to distinguish this possibility from closely related probable roles of other edge parameters, such as ion temperature and current density. In the H-mode discharge shown in Fig.5 with the rapid current ramp-down, the H-mode transition is initiated without any sawtooth event and without any rise in T_{eb} prior to the transition. The results suggest that the detailed shape of the current density profile near the plasma edge is a crucial factor. The rapid current ramp-down may induce a reverse current near the edge or decrease the current density sharply there, which enhances a magnetic shear.

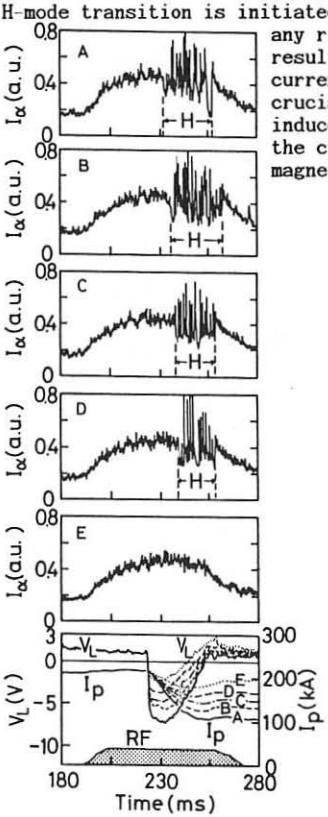

Fig.3 The effect of a rapid current ramp-down during additional heatings on the H-mode transition, where $P_{RF} \simeq 1.2$ MW.

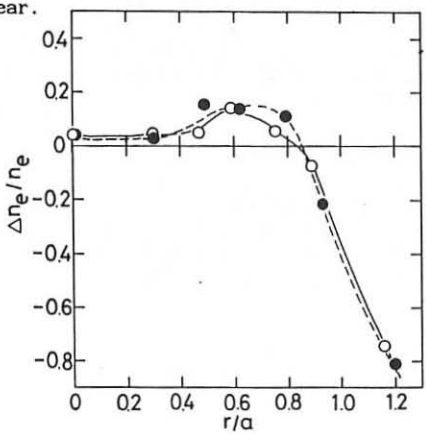

Fig.4 Radial variation of the relative change in n_e across the H-mode transition, where ○ is for Type-1, and ● for Type-2.

This moderate enhancement of the shear near the edge may block the outward flows of heat and particles effectively, and may lead to the H-mode. The high heating power flow may maintain the moderately high shear region for a long time. This region may act as a "virtual separatrix". This conjecture seems to fit for Fig.4. Note that between L- and H-phases there is no clear difference in the ion temperature and toroidal rotation velocity near the edge (r/a $\lesssim$0.8) which are measured by 50-channel charge-exchange recombination spectrometer.

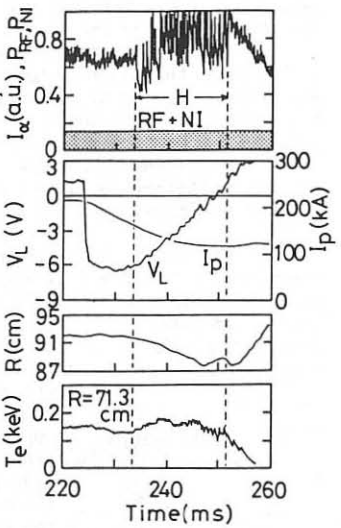

Fig.5 H-mode transition triggered by the rapid current ramp-down in the discharge with a decaying T_{eb}, where $P_{RF}\simeq$1.3 MW and $P_{NI}\simeq$0.6 MW.

4. Conclusions

In a circular cross-section plasma bounded by a limiter, H-mode is achieved in the high density regime up to 10^{14} cm^{-3} for two types of discharges without and with the rapid current ramp-down. The rapid current ramp-down reduces the threshold power P_{th} by 30 - 50 %, compared with that in Type-1, and successfully triggers the H-mode transition even in the case without any rise in T_{eb} prior to the transition. The current ramp-down may produce the moderately high shear region near the plasma edge through the skin effect.

References

1)K. Kawahata et al., in Proc. of 12th IAEA Conf., Nice, 1988, paper No. IAEA-CN-50/A-5-3-1.
2)F. Wagner et al., Phys. Rev. Lett. 49, 1408(1982).
3)M. Keilhacker, Plasma Phys. and Controlled Fusion 29, 1401(1987).
4)F. Wagner et al., Phys. Rev. Lett. 53, 1453(1984).

AN INTERPRETATION OF THE STRUCTURE OF ELMS AND THE H TO L TRANSITION ON JET

P Cripwell*,A Edwards,R Galvao,N Gottardi,P Harbour,P Haynes@,T C Hender@,
E H Joffrin,M Malacarne,P Mantica#,N Salmon,
J A Snipes,A Tagle,D Zasche+

JET Joint undertaking,Abingdon,Oxon,OX14 3EA,U.K.
* Imperial College of Science,Technology,and Medicine,University of London,U.K.
@ UKAEA Culham Laboratory,Abingdon,Oxon,U.K.
# Istituto di Fisica del Plasma,EURATOM/ENEA-CNR Ass.,Milano,Italy
+ Max-Planck Institut fur Plasmaphysik,D-8046,Garching,F.R.G.

Introduction

Edge localised modes play an important role in H-mode confinement and stability /1/. Recent studies have identified precursors to the H to L transition rotating in the opposite direction to co-injected neutral beams /2/, and proposed that the H to L transition is triggered by a giant ELM /3/. Tearing modes driven by edge current density and ballooning modes driven by pressure gradient have been put forward as possible explanations for these precursors.

Initial studies on JET /4/ have described the characteristics of edge fluctuations in X-point plasmas and their effects on energy and particle confinement.

In this paper we perform a detailed magnetic analysis of ELMs and their precursors, and make a comparison with the H to L transition. These magnetics results correlate with those of other diagnostics such as the microwave reflectometer and X-point langmuir probes. Localization of ELMs and H to L transition spike is determined with the soft X-ray camera, and particle transport estimated by an H-alpha detector. Finally possible theoretical explanations for ELMs are discussed.

Structure of ELMs and precursors

The ELM structure is examined poloidally by two sets of coils (10kHz cut-off, 6dB roll-off) near the X-points and toroidally by lower frequency response coils (10kHz cut-off, 12dB roll-off).

Typical ELMs during an H-mode are presented fig(1a). ELMs are visible by all the diagnostics mentioned above. In addition a significant magnetic fluctuating toroidal component was observed (typically, larger than one tenth of the fluctuating poloidal component : $\tilde{b}_\theta/B_{pol} \cong 5.10^{-4}$). The ELM spike has predominantly an n=0 component with an n=1 contribution of typically 30%. The poloidal component is predominantly m=1, with a phase inversion about the X-point for both single null and double null plasmas. In the single null case, the second phase inversion does not occur in a reproducible location.

ELMs are preceded by precursors and also often followed by postcursors (fig(1b)). Typically precursors start at about 0.5ms before the ELM, and postcursors stop 1ms after. Both are identical except that the amplitude of postcursors ($\tilde{b}_\theta/B_{pol} \cong 3.10^{-5}$) is often two or three times higher than the amplitude of precursors.

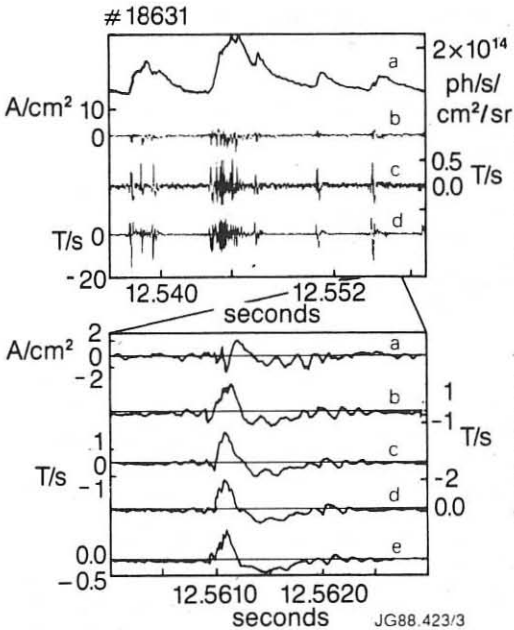

Fig 1a : ELMS for pulse 18631 (q at the edge : 9)
a) H-alpha channel viewing the X-point.
b) Langmuir probe signal.
c) Toroidal magnetic component near the X-point.
d) Magnetic coil near the X-point.

Fig 1b : Poloidal correlation of coils showing the propagation (m = 9) of the oscillations before and after an ELM.
a) Langmuir probe.
b to e) poloidal array of coils near the X-point.

Because of this small amplitude they are only detected by the magnetics and the langmuir probe. Toroidal correlations show an n = 1 component rotating opposite to the co-injected neutral beam direction with a frequency of about 6 to 8kHz. The frequency of precursors has been found to be close to the electron diamagnetic drift frequency calculated in the high shear region (≅10kHz). Poloidal mode numbers in the range of 5 to 10 have been estimated for the ELM precursors. Such high m (n = 1) modes are resonant very near the separatrix in the high shear boundary region.

Soft X-rays have verified /4/ that ELMs originate near the edge, and also exhibit an inversion radius at about 5 to 10 cm inside the plasma indicating the enhanced particle and energy transport in this region when ELMs occur. To explain this large transport during the ELMs the island width has been calculated in the high shear region for two neighbouring surfaces, assuming a tearing mode model for the precursors. Within the range of uncertainties over the edge shear and poloidal mode number of the precursors, overlap appears possible for the measured amplitude of ELM ($b/B_{pol} \cong 5.10^{-4}$), thus leading to a stochastic field topology and enhanced transport. To support this interpretation, reflectometry measurements of n_e near the inversion radius have been made during and in between ELMs. Preliminary results show at all frequencies an increased level of density fluctuations (by a factor two or three) during ELMs.

Differencies have also been noticed on toroidal correlations, but more complete analysis is required.

Comparison with the H to L transition

A similar magnetic analysis has been carried out for the H to L transition (fig(2)). Unlike ELMs, the spike that occurs at the H to L transition has dominantly an n = 1 structure with a strong n = 0 contribution of about 40%. The poloidal structure is also m = 1 predominantly but the phase inversions does not occur at the X-point. However this n = 0 m = 1 component is probably due to the fast displacement of the plasma (~1cm radially,~2cm vertically) when the transition occurs.

In addition, the H to L transition is also often preceded by precursors for about 1ms. They again rotate in the electron diamagnetic drift direction with a frequency of 6 to 8 kHz, and exhibit a predominantly n = 1, and m = 5 to 10, structure, indicating that they are localized near the separatrix.

The edge localization of the H to L transition is corroborated by the soft X-ray reconstruction shown fig(3). The spike of the transition does not affect the center of the plasma, and is a much faster phenomenon (~100 μs) than the ELM spike (~0.5 ms).

Given the identical precursors observed before the ELMs and the H to L transition, it seems that they may both have the same underlying cause. However, a decisive conclusion cannot be drawn due to differences in the modes structure and the duration.

Interpretation and conclusion

As the ELMs during H-modes are accompanied by n = 1 m = 5 to 10 precursor structures, high n ballooning activity would seem to be precluded as an explanation of their origin. It seems likely that in the high shear edge region, n = 1 instabilities with a broad spectrum of coupled poloidal harmonics are destabilized. The observed rotation of the precursors in the electron diamagnetic drift direction with approximately the electron diamagnetic drift frequency is in agreement with the tearing theory /5/.

The magnetic fluctuation level during ELM spikes may be sufficent to give island overlap in the high shear region.This overlapping could lead to ergodization of field lines and enhanced edge transport /4/, reducing the edge pressure gradients. Thus, tearing modes are a possible candidate to explain the precursors and would lead to stochastic transport during ELMs.

The H to L transition spike is preceded by similar precursors, but its different mode structure and shorter duration make it difficult to identify the transition as a giant ELM.

References

1. M. Malacarne et al, Plasma Physics and Controlled Fusion 29 (12) (1987) 1675-1686.
2. K. Toi et al, IPP III/135, May 1988.
3. N. Ohyabu et al, Proc of the XV EPS conf on Contr Fus and Pl Heat, Dubrovnik, May 1988, Vol I, p 227-230.
4. A. Hubbard et al, Proc of the XV EPS conf on Contr Fus and Pl Heat, Dubrovnik, May 1988, Vol II, p 651-654.
5. R. D. Hazeltine, D. Dobrott, and T. S. Wang, Phys Fl. 18 (75) 1778.

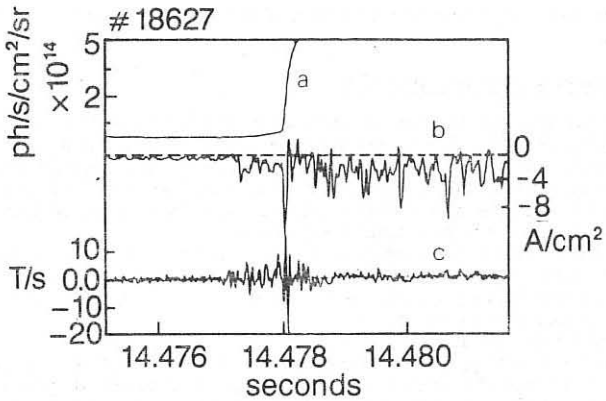

Fig 2 : H to L transition showing the precursors.
a) H-alpha channel viewing the X-point.
b) Langmuir probe signal near the X-point.
c) coil near the X-point.

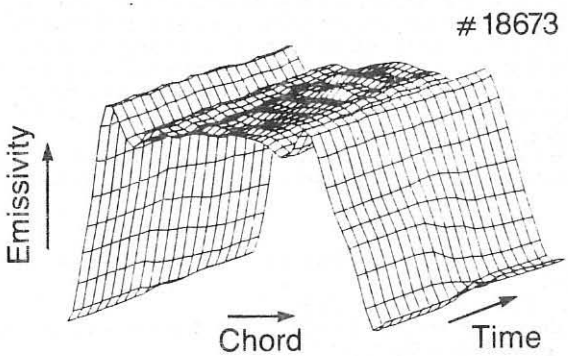

Fig 3 : Reconstructed X-ray emissivity of an H to L transition spike over 0.5ms along the vertical chord (Z = -1.6 to Z = 1.6).

BALLOONING STABILITY ANALYSIS OF JET H-MODE DISCHARGES

D.P. O'Brien, C.M. Bishop#, R. Galvao,
M. Keilhacker, E. Lazzaro, M.L. Watkins

JET Joint Undertaking, Abingdon, Oxon. OX14 3EA, UK
#UKAEA Culham Laboratory, Abingdon, Oxon. OX14 3DB, UK

1. Introduction

Previous studies [1] of the stability of a large aspect ratio model equilibrium to ideal MHD ballooning modes have shown that across the bulk of the plasma there exist two marginally stable values of the pressure gradient parameter α. These define an unstable zone which separates the first (small α) stable region from the second (large α) stable region. Close to the separatrix, however, the first and second regions can coalesce when the surface averaged current density, Λ, exceeds a critical value. The plasma in this region is then stable to ballooning modes at all values of the pressure gradient. In this paper we extend these results to JET H-mode equilibria using a finite aspect ratio ballooning formalism, and assess the relevance of ideal ballooning stability in these discharges. In particular we analyse shot 15894 at time 56 sec. which is 1.3 s into the H-phase.

2. Equilibrium and Stability

Stability information is obtained by solving the ballooning equation separately on each flux surface. The geometry of the surface, and the distribution of poloidal field, are obtained from an equilibrium reconstruction using the IDENTC code. This code generates a best fit to the experimental magnetic and kinetic data, subject to the constraints of MHD equilibrium [2]. However, since the reconstruction procedure requires zero current density of the boundary, values for Λ have been taken from transport calculations performed by the TRANSP code [3]. This gives a profile of current density J from which Λ can be calculated using

$$\Lambda = 2\bar{J}/\langle J \rangle$$

where $\bar{J}$ is the surface average of J, and $\langle J \rangle$ is the average of J over the enclosed volume. A plot of Λ against minor radius for shot 15894 is shown in Figure 1. In the edge region of an H-mode plasma the dominant contribution comes from the bootstrap current due to the presence of a steep density gradient [4]. The corresponding steep edge gradient in the electron pressure is clearly seen from the ECE and FIR interferometer data, and LIDAR data (Figure 2). In the ballooning equation the pressure gradient parameter α is treated as an eigenvalue for each flux surface, and the equation solved to give the marginally stable value of α.

3. Results of the stability analysis

Figure 2 shows a plot of α versus minor radius for the H-mode discharge #15,894. In the interior of the plasma we see the existence of first and second stable regions separated by an unstable zone, while close to the separatrix the first and second regions coalesce. It is important to note that this graph has been plotted using the experimental value of Λ on each flux surface, as given by Figure 1. The second stability boundary is very sensitive both to Λ and to the modulation of the poloidal field around the flux surface. For increasing values of the flux surface label ψ the second marginally stable α increases initially as Λ falls. Closer to the edge, however, the combined effects of poloidal field modulation (due to proximity to the separatrix), together with an increasing Λ, cause the second stable α to fall sharply, so that coalescence occurs in the edge region.

The effects of varying Λ (while retaining the flux surface shape and poloidal field) are shown in the α-Λ diagram of Figure 4. The vertical line shows the experimental value of Λ in the H-mode. At smaller values of Λ, as would occur in L-mode plasmas (which do not exhibit the steep edge density gradient) there is no coalescence, and the first and second regions are separated by a large unstable zone.

4. Comparison with experimental pressure profiles

These results have been compared with experimental values of the pressure gradient determined from the LIDAR Thomson scattering diagnostic, with electron pressures scaled by a factor 2 to account for the ion pressure contribution. Over the bulk of the plasma these give values of α = 0.2 which lie, as expected, in the first region of stability. Near the separatrix, however, the steep pressure gradients (electron pressure gradients $\simeq$ 150 kPa m^{-1}) lead to experimental values of α which increase sharply towards those determined for the first stability boundary, so that at r = 0.9m we obtain α = 0.75. This shows the relevance of ideal ballooning stability in H-mode discharges. Although these results do not show edge gradients in the coalesced region, as considered in ref.[1], it should be noted that because of limited spatial resolution (0.09 m using the convolution technique), the LIDAR diagnostic may be unable to measure the very short gradient scale lengths which appear to be characteristic of the edge region of an H-mode plasma. In particular the edge gradient of the LIDAR profile shown in Figure 2 has a scale length of about 0.1 m. The experimental values of pressure gradient in the edge region should therefore be regarded as lower bounds on the true values. Furthermore, the values of Λ close to the edge are determined by the bootstrap current, and hence by the density gradient, and so may also have been underestimated.

Conclusions

We have analysed the ballooning stability properties of JET H-mode shot 15894. Across the bulk of the plasma there exist two stable regions separated by an unstable zone. Close to the separatrix, however, we have found that the current density exceeds the critical value required for coalescence of the first and second stable regions. It has been suggested [1] that this coalescence phenomenon is associated with the transition from L-mode into H-mode. Experimentally determined values of the pressure gradient in the edge region lie somewhat below the coalesced region. However, these values may have been underestimated due to the limited spatial resolution of the LIDAR diagnostic.

REFERENCES

[1] C.M. Bishop, Nucl. Fusion 26 (1986) 1063.
[2] J. Blum, J. Gilbert, B. Thooris, JET contract JT3/9008 (1985).
[3] P. Stubberfield et al., This Conference.
[4] J.G. Cordey et al., Plas. Phys. and Contr. Fus., 30 (1988) 1625.

Figure Captions

Fig. 1 Current density parameter Λ as a function of normalized flux from centre to edge of plasma.

Fig. 2 Comparison of electron pressure profiles from ECE (used as input for TRANSP) and from the LIDAR diagnostic (upper curve) for shot 15894.

Fig. 3 Pressure gradient parameter α as a function of normalized flux from $\psi = .5$ to $\psi = 1$ (plasma edge).

Fig. 4 Sensitivity analysis of α as a function of Λ on a surface approximately 1 cm from edge of plasma.

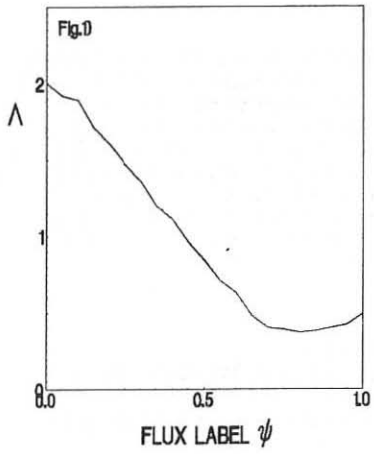
Fig.1)
Λ
2
1
0
0.0
0.5
1.0
FLUX LABEL ψ

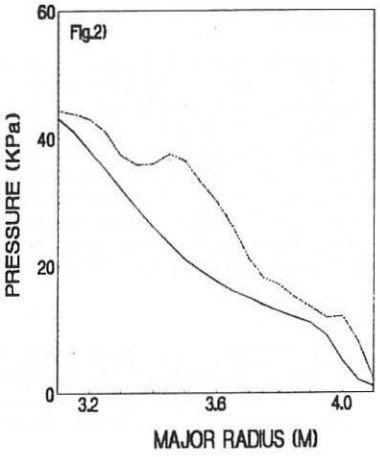
Fig.2)
PRESSURE (KPa)
60
40
20
0
3.2
3.6
4.0
MAJOR RADIUS (M)

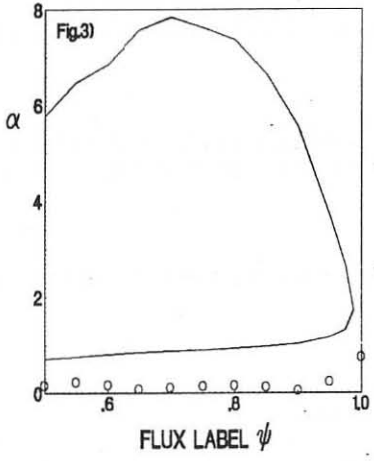
Fig.3)
α
8
6
4
2
0
.6
.8
1.0
FLUX LABEL ψ

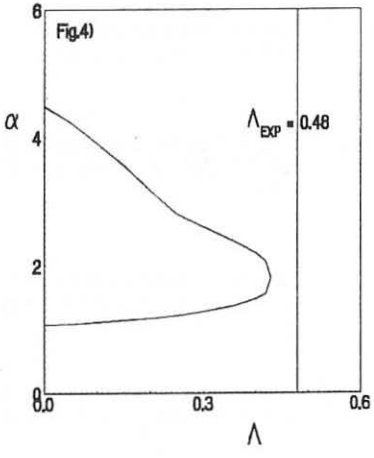
Fig.4)
α
6
4
2
0
Λ_{EXP} = 0.48
0.0
0.3
0.6
Λ

OFFSET-LINEAR DESCRIPTION OF H-MODE CONFINEMENT

K Thomsen, J D Callen*, J P Christiansen, J G Cordey,
M Keilhacker, D G Muir, M L Watkins

JET Joint Undertaking, Abingdon, Oxon, OX14 3EA, UK
*University of Wisconsin, Madison, WI 53706, USA

1. Introduction

The formulae for interpreting auxiliary heating data in terms of local transport models [1] apply to steady state plasmas with negligible edge temperatures. However, in JET H-mode discharges edge temperatures above 500eV are observed and the plasma does not normally reach a steady state [2]. An energy evolution equation for plasmas with non-zero edge temperatures based on local transport models is proposed in Section 2. In previous work [1] it was found that a suitable form for the total heat diffusion coefficient χ corresponds to $\chi_L(r) = \chi_0/(1-\alpha r^2/a^2)$ in L-mode plasmas. Analysis of JET discharges with the time dependent energy balance code TRANSP [2] suggests that a flatter profile for χ during the H-mode is appropriate, e.g. $\chi_H(r) = \chi_0$. Section 3 presents results obtained by applying the energy evolution equation to JET L and H-mode data using χ_L and χ_H respectively. The conclusions are given in Section 4.

2. Energy Evolution Equation

The local power balance equation for plasmas with density $n = n_e = n_i$ and temperature $T = T_e = T_i$ is $3\frac{\partial}{\partial t}nT = -\nabla\cdot\vec{q} + Q$, where Q is the net heating rate. The total heat flux $\vec{q}$ is assumed to be well represented by a diffusive term proportional to the temperature gradient ∇T and a negative non-diffusive flow term which represents a heat pinch or a critical temperature gradient, i.e. $\vec{q} = -n\chi\nabla T - \vec{q}_{pinch}$. The flux surface averaged power balance equation is integrated 3 times (see [1] for details) to give the following equation for the time evolution of total stored energy $W = 3\int d^3x nT$:

$$\tau_\chi \eta_w^* \frac{d}{dt} W = - W + W_p + \tau_\chi \eta_Q P_{in} + W_0 \qquad (1)$$

The pedestal energy W_p appears naturally in this formalism for plasmas with non-zero edge temperatures $T(a) \neq 0$, i.e. $W_p = 3T(a)\int d^3x n$. The power P_{in} represents a simple volume integration $\int d^3x$ of Q and W_0 is the usual offset term [1]. The remaining quantities depend on the radial profile of $\chi(r)$ as described in [1] with τ_χ denoting the 'ideal' incremental confinement time and η_Q the heating effectiveness. The effectiveness η_w^* in (1) is defined as η_Q with the local value of $3\partial nT/\partial t$ replacing Q.

In the present calculations we have assumed that the profile of $\partial nT/\partial t$ varies slowly with time, i.e. $\partial nT/\partial t = nT/\tau$, where τ is constant in radius; this assumption corresponds to $\eta_w^* \approx \eta_{nT}$, the latter being defined as η_Q with 3nT replacing Q. In this paper η_{nT} replaces η_w^* of Eq. (1).

3. Results

The aim of the analysis is to establish whether Eq.(1) can adequately describe JET L and H-mode data obtained for plasmas with X-point configurations and currents of 3 to 5 MA. The JET data shows that at fixed current and power the total energy W in the L and H-modes can differ by a factor 2 to 3. Our analysis suggests that the confinement in the central plasma region is the same in L and H-modes; the difference is therefore mainly due to different confinement properties in the outer region, i.e. for $\rho > 0.9$, where ρ denotes a normalised flux surface label $o \leq \rho \leq 1$. We have carried out calculations of the various terms of Eq.(1) using JET L and H-mode data as follows.

W and dW/dt are measured by the diamagnetic loop; the pedestal energy W_p is derived from kinetic measurements of T_e and n_e assuming $T_i = T_e(\rho=.95)$, $n_e = 2n_i$. The parameters η_Q and η_{nT} are evaluated following the prescription in [1]; for simplicity we assume a flat density profile $n(\rho) = n_o$; two types of heat diffusivity profiles are used, the first with $\chi_H(\rho) = \chi_o$, the second with $\chi_L(\rho) = \chi_o/(1-\rho^2)$. The results from our calculations are shown in Figures 1-4.

The effectiveness η_{nT} associated with the pressure profile is found to be systematically higher for H than for L-mode data. Fig. 1 shows that η_{nT} does not vary with power P, current I and toroidal field; the values for the entire H-mode data are approximately 20% above the L mode values. The 20% difference in η_{nT} arises mainly because χ_H has been used for H-mode data and χ_L for L-mode data. A similar difference in η_Q is found between H and L-mode values. Figure 2 demonstrates that for NBI heated plasmas η_Q depends mainly on the absolute value of density which determines beam penetration and thus the beam power deposition profile $Q(\rho)$. There is an implicit variation of η_Q with beam power and current which both indirectly determine the plasma density. Thus when we combine two terms of Eq.(1) the net effective power P_{eff} for both L and H-mode data can be represented by

$$P_{eff} = \eta_Q P_{in} - \eta_{nT} \frac{dW}{dt} = 0.5 \left(P_{in} - \frac{dW}{dt}\right). \qquad (2)$$

Figures 1 and 2 therefore serve to illustrate how the parameters η_{nT} and η_Q depend upon the models χ_H or χ_L for heat diffusivity profiles.

Indeed, if only one diffusivity profile, e.g. χ_H, is used to evaluate η_{nT} and η_Q, then the 20% difference between L and H-mode values disappears. The effectiveness parameters depend mainly on the χ profile. If the assumed constant density profile $n(\rho) = n_o$ is replaced by measured profiles then the effectiveness parameters for L and H-mode data may differ.

The calculated values of the pedestal energy W_p from H-mode data are shown in Figure 3 against the net total input power $P_{in} - dW/dt$ (The L-mode values of W_p are scattered in the 0 - 1 MJ range with no dependence upon power and hence they have not been included in Figure 3). There is a pronounced dependence upon power which may be expressed as

$$W_p(\text{H-mode}) \approx \tau_{edge} (P_{in} - dW/dt), \text{ with } \tau_{edge} = 0.4\text{s}. \qquad (3)$$

Up to 4 MJ of pedestal energy W_p (or edge energy) are found in H-modes and there is no apparent degradation of W_p with power. It is the pedestal energy W_p which gives rise to the observed large difference (a factor 2 to 3) between the confined energy W for H and L- modes. The remaining energy content $W-W_p$ does not exhibit such a large difference as shown in Figure 4. The variation of $W-W_p$ with P_{eff}, i.e. the slope $d(W-W_p)/dP_{eff}$ of the data points in Figure 4, represents the ideal incremental confinement time $\tau_{\bar{\chi}}$ of Eq.(1). The latter is related [1] to a volume-density weighted average $\bar{\chi}$. It is shown in [1] that $\bar{\chi}_H = \frac{1}{2} \bar{\chi}_L$ implying that for consistency $\tau_{\bar{\chi}}(\text{H-mode}) = 2\tau_{\bar{\chi}}(\text{L-mode})$. The present data shown in Figure 4 does however not fully support such a difference of a factor 2 of the slopes through the data points, since these show too much scatter. The scatter of the data points in Figure 4 is caused by several simplifying assumptions:

1) The choice of a fixed value $\rho = 0.95$ used to estimate W_p;
2) constant density n_o used to evaluate η_Q, η_{nT};
3) experimental uncertainties in determining edge values of T_e, T_i, n_e, n_i etc.

4. Conclusions

The interpretation methods in [1] have been extended to non-stationary plasmas with non-zero edge temperatures. This has led to a new form of a time dependent energy equation which is suitable for the analysis of H-mode plasmas. Two models for heat diffusivity have been used to assess the sensitivity of the results to variations in the diffusivity profile. The results from the analysis of JET H-mode data confirm that the main improvement in confinement in the H-mode is in the edge plasma leading to a pedestal energy W_p which increases with effective heating power.

References

[1] Callen, J.D. et.al. Nucl.Fus.27 (1987) 1857.

[2] The JET team (Presented by M. Keilhacker). IAEA-CN-50/A-111-2 (1988)

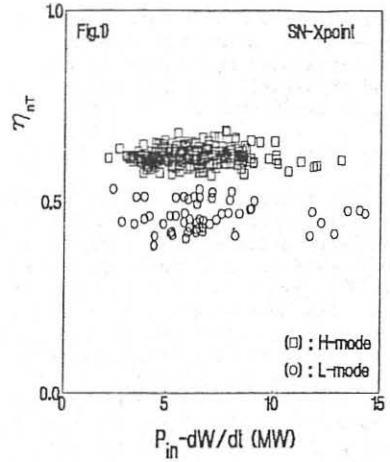

Fig. 1 Effectiveness of pressure profile η_{nT} versus net total input power for SN-X-point plasmas with I_p=3-5MA and B_T=2-3.4T (□) H-mode, (○) L-mode.

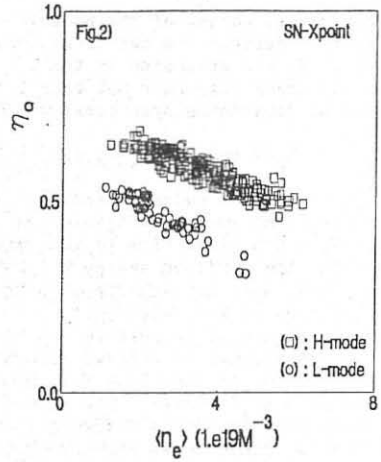

Fig. 2 Heating effectivness η_Q (without radiation correction) versus volume average electron density $\langle n_e \rangle$ for SN-X-point plasmas with I_p=3-5MA and B_T=2-3.4T. (□) H-mode. (○) L-mode.

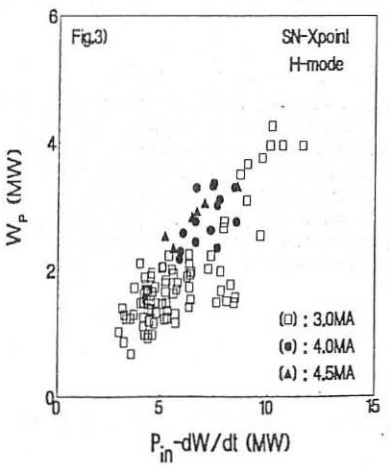

Fig. 3 Pedestal energy $W_p(\rho=0.95)$ versus net total input power for H-mode in SN-X-point plasmas. (□) I_p=3MA, (●) I_p=4MA, (▲) I_p=4.5MA.

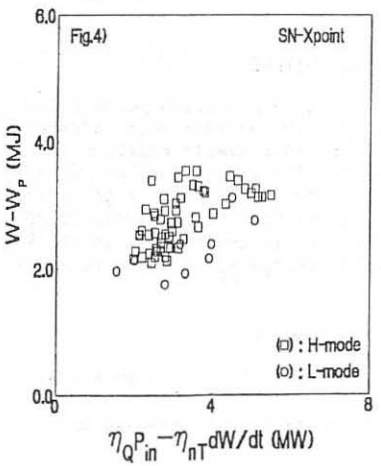

Fig. 4 Core energy W-$W_p(\rho=0.95)$ versus net effective input power in SN-X-point plasmas with I_p=3MA; B_T=2-2.2T. (□) H-mode, (○) L-mode.

DOUBLE NULL X-POINT OPERATION IN JET WITH NBI AND ICRH HEATING

B. Tubbing, V. Bhatnagar, D. Boyd[1], M. Bures, D. Campbell, J. Christiansen, J. Cordey, G. Cottrell, A. Edwards, R. Giannella, J. Jacquinot, M. Keilhacker, C. Lowry, P. Lallia, D. Muir, P. Nielsen, D. Start, A. Tanga, P. Thomas, F. Tibone

JET Joint Undertaking, Abingdon, Oxon, OX14 3EA, UK
[1]University of Maryland, College Park, MD20742, USA

1. INTRODUCTION In this paper we report on a selection of experiments on H-modes, in 3 and 3.5MA discharges, in the double null X-point configuration. The first experiment, section 2, is an attempt to couple ICRH power to H-modes. Here we also report on a rather unique H-mode with a smaller than usual distance between plasma and limiter. The second experiment, section 3, is on H-modes in the low density, hot ion regime.

2. ICRH COUPLING TO MEDIUM DENSITY H-MODES The aim of the experiment is to increase central temperature by central ICRH deposition. Further, an attempt was made at generating an H-mode with ICRH only [1]. The magnetic configuration is a double null X-point, in a deuterium plasma, with I_p = 3MA, B_t = 2.45T, elongation K = 1.8, and volume average density $\langle n \rangle \approx 2\ 10^{19} m^{-3}$ before the L-H transition. The distance to the belt limiter is about 30mm, to the antennae about 85mm. The ICRH details are: monopole antenna phasing, at a frequency of 33.5MHz, using hydrogen minority. ICRH coupling resistances of 4Ω were obtained.

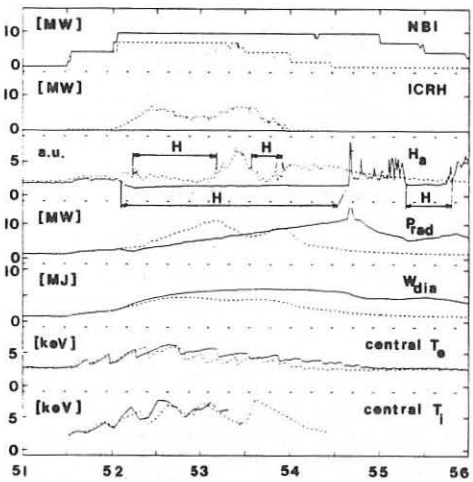

Figure 1: comparison between H-modes with NBI only (#17386, solid line) and an H-mode with combined NBI/ICRH heating (#17391, dashed line).

With ICRH heating only, weak H-mode signatures were observed on the H_α and edge magnetic fluctuations. However, we did not observe 'H' confinement (see figure 2), nor the characteristic enhanced density increase rate. Before excluding the option of ICRH only H-modes in JET, however, we will have to operate the ICRH at power

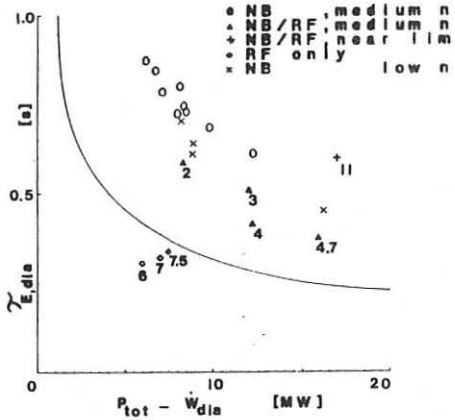

Figure 2: confinement overview, τ_E vs net input power, based on the diamagnetic measurement. The solid line represents the Goldston scaling. Data taken at 800ms after the L-H transition, except for the 'near limiter' case (350ms), and the 'ICRH only' cases. The numbers indicate the coupled ICRH power at the time of the data.

levels which are more clearly above the L-H power threshold.

With combined NBI/ICRH power, elm free H-modes were obtained. During these the density, the effective ion charge Z_{eff}, and the radiated power increase with time. The H-modes are terminated when the total radiated power (appr. 70% of which is from the bulk plasma and 30% from the X-points) equals the input power. In figure 1 we compare an H-mode with 8MW NBI and 7MW ICRH to a similar case with 10MW NBI only. The increase of the radiated power P_{rad} is 5MW/s for the NBI case, vs 10MW/s for the NBI/ICRH case (up to 18MW/s in a bad case).

The enhanced radiation is dominantly due to nickel contamination, as is apparent from an analysis of Ni line intensities. It is further confirmed by the observation that Z_{eff} shows no significant increase. The primary sources of Ni are the ICRH antenna screens. It is expected that future installation of Beryllium screens on the ICRH antennae will alleviate the problem.

The confinement overview is show in figure 2. It is apparent that the combined heating cases have somewhat lower confinement times than comparable NBI only cases. However, this can, to the first order, be accounted for by the difference in radiated power.

Central electron and ion temperatures are not increased by the ICRH, as is illustrated in figure 1. The results are an important improvement over earlier (1986) attempts to couple ICRH to 3MA, single null X-point, H-modes.

Recently a 3.5MA, 3.2T H-mode was obtained in the same (double null X-point) configuration but with a distance between plasma and limiter of only 10mm. This discharge (#18773) has excellent ICRH coupling properties. Hitherto, it was believed that the limiter clearance should be at least 30mm [2]. The pre-heating target was pellet fuelled (3 × 2.7mm pellet, before beam-on) and a 3 to 3.5MA current ramp was executed. The pre-heating target density is $\langle n \rangle = 1.4\ 10^{19} m^{-3}$. 10MW of ICRH is coupled, on top of 15MW NBI, with a coupling resistance of 6Ω (monopole phasing, 48MHz, H minority). The rate of increase of P_{rad} is low (5MW/s), indicating that the Ni influx is negligible. The confinement time (diamagnetic)

is about 600ms, the D-D reaction rate is $1.9\ 10^{16}s^{-1}$. Both electron and ion temperatures are about 10keV. The peculiarities of this discharge are not understood, (see also [5], but clearly this scenario looks very promising and deserves further investigation.

3. H-MODES IN THE HOT ION REGIME The primary aim of the experiments described here was the study of hot ion modes [3][4], using the double null configuration to obtain low density. Figure 3 shows a comparison between a low density and a medium density discharge, in similar plasma conditions, both with 10MW NBI. In the low density discharge there is a delay between beam-on (52s) and the L-H transition (53s). During this delay the plasma is in the hot ion regime (the density is below the L-H transition density threshold, see below) Concentrating on the H phase of the two shots, it is apparent that the low density case has desirable characteristics; while it has almost the same $n_e T_i \tau_E$ product, it has a 50% higher D-D reaction rate [5] because of the higher ion temperature and the longer slowing down time.

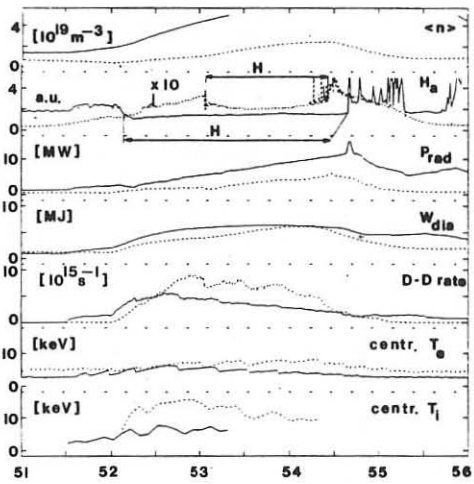

Figure 3: comparison between an H-mode at medium density (#17386, solid line) and one at low density (#18757, dashed line. Both discharges have 10MW NBI from 52s. Note that the H_α signal for the low density case is multiplied by 10.

The rate of increase of the density is lower in the low density discharge: $\langle\dot{n}\rangle = 1.3\ 10^{19}m^{-3}s^{-1}$ vs $\langle\dot{n}\rangle = 2.6\ 10^{19}m^{-3}s^{-1}$, averaged from 100 to 600ms after L-H). Note that the beam fuelling accounts for $0.8\ 10^{19}m^{-3}s^{-1}$. The rate of rise of the radiated power is also lower ($P_{rad} = 3.0MWs^{-1}$ vs $P_{rad} = 4.5MWs^{-1}$). The lower density increase rate is probably associated with the deuterium inventory of the X-point tiles rather than with the low density as such.

Penetration of the NBI (80keV D) is much improved and the density profiles remain more peaked. The rate of increase of Z_{eff} is higher in the low density discharge. In fact, it appears that the carbon influxes are approximately of equal magnitude, $\langle\dot{n}_C\rangle \approx 2\ 10^{18}m^{-3}s^{-1}$. The problem of deuterium dilution is thus more severe.

The low density target discharges also provide information on the L-H transition density threshold. It is observed that for discharges with a pre-heating density below $\langle n\rangle \leq 1\ 10^{19}m^{-3}$, the L-H transition is delayed

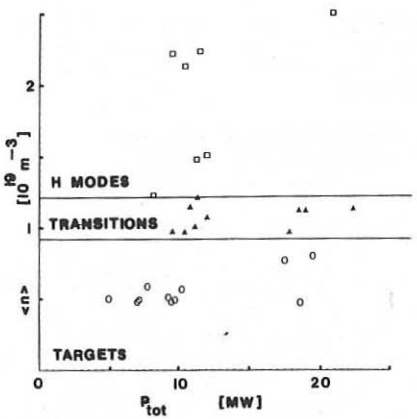

Figure 4: illustration of the L-H transition threshold density. This This threshold is independent of input power P_{TOT}.

with respect to beam-on (up to 1s, see fig. 3, while for normal medium density H-modes this is ≤ 200ms). During the delay time, the beam fuelling increases the target density to the density threshold of about 1 $10^{19}m^{-3}$. This is illustrated in figure 4, where we plot the pre- heating target density and the density at the transition vs the total input power. It appears that the density threshold is rather independent of the input power. A similar plot of electron temperature (at r/a ≈ 0.7) vs input power shows appreciably more scatter.

The potential of the low density H-modes lies in the benefits of the hot ion regime. With the present 80keV NBI system, the window for the hot ion regime is between $\langle n \rangle \approx 0.5\ 10^{19}$ and $1.5\ 10^{19}m^{-3}$. This allows only a small overlap with the H-mode density window, $\langle n \rangle \geq 1 \cdot 10^{19}m^{-3}$. With the near future upgrade of the NBI to 140keV, this overlap should be appreciably wider.

4. CONCLUSIONS On the ICRH coupling experiments: significant ICRH power has been coupled to H-modes generated with NBI and a plasma to limiter distance of 30mm. In these discharges, there is a Ni influx problem. The increased radiated power limits the confinement, and the central temperatures. No H-modes have yet been observed with ICRH only, although weak H-mode signatures have been observed. More recently an H-mode has been observed with a plasma limiter separation of about 10mm. This configuration allowed excellent ICRH coupling, and showed no significant Ni influxes. 11MJ stored energy was obtained in a 3.5MA plasma with 25MW input power.

On the low density H-modes: H-modes have been obtained at low densities $\langle n \rangle \geq 1\ 10^{19}\ m^{-3}$ where there is an overlap with the hot ion regime. These discharges have several desirable properties. The low density H-modes have similar $n_e \tau_E T_i$, but a higher D-D rate than medium density ones.

[1] D. Start et al, proc. 12th IAEA conference, Nice, 1988.
[2] M. Keilhacker and JET team, proc. 12th IAEA conference, Nice, 1988. See also report IAEA-CN-50/A-111-2.
[3] P. Thomas et al, proc. 12th IAEA conf. Nice, 1988.
[4] C. Lowry et al, this conference.
[5] F. Tibone et al., this conference.

H-MODE TRANSITION STUDIES IN DIII-D

T.N. Carlstrom, M. Shimada,* K.H. Burrell, J. DeBoo, P. Gohil,
R. Groebner, C. Hsieh, H. Matsumoto,* and P. Trost

General Atomics, P.O. Box 85608, San Diego, California 92138-5608 U.S.A.
*Japan Atomic Energy Research Institute JAPAN

INTRODUCTION

Determining the conditions necessary for the H-transition is important not only for scaling this important confinement regime to future machines but also to aid the understanding of H-mode physics with the hope of further exploiting H–mode confinement. We have done systematic scans of I_P, $\bar{n}_e$, B_T, and the X-point to divertor plate distance δ, in single-null diverted discharges, to ascertain their influence on the threshold power required for the L-H transition. During each of these scans, the neutral beam power ($H^0 \rightarrow D^+$) was increased in a staircase fashion and the power required for the transition was noted. Over the ranges of: $1 < I_P$ (MA) < 2, $1 < B_T$(T) < 2, $3 < \bar{n}_e$ (10^{19} m^{-3}) < 8, and $1 < \delta$ (cm) < 23, the threshold power scales as $\bar{n}_e B_T$, independent of I_P, and is reduced when δ is small. This method also provided an L-mode power scan over the various plasma conditions, in which we looked for changes in the L-mode plasma, particularly in the edge region, that might trigger the H-transition. Over the range of conditions studied, we found that T_e $(r/a = 0.97)/B_T$ approached a critical value before each L-H transition. Various theories have been put forth to explain the bifurcation observed at the L-H transition. We show that the predictions of several of these theories are inconsistent with the observations on DIII-D.

KEY FEATURES OF THE L TO H TRANSITION

There are several general observations of the L-H transition and its dynamics that are important to consider when evaluating mechanisms for the H-mode transition. It is a rapid event, not a slow, gradual improvement in confinement. Although a certain threshold power is required to obtain H-mode, once the transition has taken place, the power requirement to maintain the H-mode can be less than the transition threshold power. This power hysteresis is best demonstrated by the fact that power to the edge plasma from a sawtooth crash can trigger an H-transition and the plasma remains in H-mode even after this transient power subsides. Both of these transition features suggest a bifurcation of the plasma transport.

In addition to NBI, H-mode plasmas have also been obtained with ECH [1] and with Ohmic heating alone [2]. H-mode periods up to 165 msec have been produced in low field (B_T=0.8 T), high current (I_P=1.25 MA), discharges without auxiliary heating. The threshold power for ECH and Ohmic H-modes is slightly lower than NBI produced H-modes at similar conditions. The appearance of H-mode using a variety of heating methods leads us to conclude that the physics of the H-mode transition is independent of the heating method.

At the transition there is a reduction of both the magnetic and density edge fluctuations as an edge transport barrier is formed [3]. The time dependence of the drop

in the H_α signals located around the plasma suggest that the transition starts at the outboard midplane [3].

During L-mode there is a strong asymmetric power flow to the divertor, with the outer separatrix hit spot receiving up to five times the power of the inner hit spot. This asymmetry is reduced by a factor of 2 to 3, to near the ohmic level, after the H-transition [4]. These observations suggest that the anomalous losses associated with L-mode are concentrated near the outboard midplane and that these losses are greatly reduced at the H-transition.

The magnetic configuration is important in determining the threshold power. Hinton [5] has shown that the direction of the ion ∇B drift in the scrape-off-layer can influence the ion heat flux across the separatrix. Jackson, et al. [6], have recently observed that good H-mode confinement times can be obtained in elongated plasmas limited on the inner wall. However, limited plasmas and the wrong direction of the ion ∇B drift increase the threshold power for H-mode up to a factor of 3. In double null configurations, the threshold power is about twice the single null case. These observations indicate that processes in the scrape-off-layer and edge plasma are important for understanding the H-mode transition.

PARAMETRIC DEPENDENCE OF THE H-MODE POWER THRESHOLD

For single-null discharges with the ion ∇B drift toward the X-point, we find that the total input power (Ohmic + absorbed NBI) required for the H-transition is proportional to $\bar{n}_e B_T$, independent of I_P, and increases with the X-point to divertor plate distance δ, in an offset linear manner. Systematic scans of the total input power as a function of B_T, $\bar{n}_e$, δ, and I_P are shown in Fig. 1. The data were all taken during the L-phase of the discharge as the neutral beam power was increased by adding individual sources every 300 msec in a staircase fashion. The data were taken at the end of each power level or just before the L to H transition. The threshold power shows a roughly linear dependence on B_T as shown in Fig. 1a. This could also be interpreted as a q dependence. However, the I_P scan shown in Fig. 1d, shows the power is insensitive to I_P as B_T is fixed. This result is in contrast to JFT-2M where the B_T and I_P dependence of the threshold power could be reduced to a q dependence [7]. The $\bar{n}_e$ dependence shown in Fig. 1b, indicates a substantial increase in threshold power at high $\bar{n}_e$. The data point that remains L-mode at the lowest density shown suggests a density threshold as reported earlier [8]. However, presence of locked modes prevented operation at lower density for these conditions and no clear density threshold for the H-transition was found. The vertical position of the X-point also influences the threshold power as shown in Fig. 1c, with the lowest power occurring at the lowest X-point position.

CRITICAL EDGE PARAMETER FOR THE H-TRANSITION

Over the wide range of conditions studied for the parameter scans, the ratio of the edge T_e to B_T was found to be approximately 115 eV/T in the L-phase at power levels that obtain H-mode. Fitted profiles to the Thomson scattering data were used to analyze the edge density and temperature behavior. Fig. 2a shows the edge T_e dependence at $r/a = 0.97$ as a function of B_T for plasmas that obtain H-mode and those that remain L-mode. There is a roughly linear dependence between T_e and B_T for plasmas that obtain H-mode. Ohmic and H-mode plasma points, shown for comparison, indicate that that the H-mode T_e exceeds this value and the Ohmic T_e is below. This result indicates that the edge T_e needs to exceed a certain value for the H-transition, and that value depends linearly on B_T.

The edge T_e increases with increasing input power but the value obtained for a given power depends on the density. This result is shown in Fig. 2b where the edge T_e

at $r/a = 0.97$ is plotted against the total input power for various line-average densities. For the plasmas that obtain H-mode, the edge T_e is roughly the same regardless of the density. However, the power required to achieve the same T_e increases with density. The results that the edge T_e required for the H-transition is a function of B_T and that T_e decreases with line-average density are consistent with the observed $P_{th} \propto \bar{n}_e B_T$ scaling. As yet, due to our limited data set, we have not discovered how the X-point height affects the edge plasma and the threshold condition.

Several theories on the L to H transition require certain conditions to exist at the plasma edge. Just prior to the L-H transition, we observe that near the edge region of the plasma ($r/a = 0.97$), $T_e = T_i$ and ν_{*i} is in the range of 1 to 5 over the range of conditions studied. These observations conflict with transport bifurcation theories that require $T_e \neq T_i$ at the plasma edge [9], and indicate that ion orbit losses may not be important in establishing a radial electric field as required by other bifurcation theories [10]. More recent calculations [11] have shown that ν_{*i} as high as 5 may be accommodated by the theory of Ref.[10]. At the transition, edge ion rotation consistent with a negative E_r is observed [12], in conflict with Ref.[13]. After the transition, the plasma remains in the first stability regime for ideal ballooning modes [14], indicating the L-H transition is not a switch into the second stability regime [15]. Further discussion of H-mode related theories can be found in Ref.[16].

SUMMARY

Conditions leading to the L-H transition in single-null, NBI heated ($H^\circ \rightarrow D^+$) discharges in DIII–D were investigated through systematic scans of plasma parameters. The threshold power scales with $\bar{n}_e B_T$, independent of I_P, and increases with the X-point to divertor plate distance δ. As NBI power was increased during the L–phase of the discharge, T_e $(r/a = 0.97)/B_T$ approached a critical value before each L to H transition. Just prior to the L-H transition, $T_e = T_i$ and $1 < \nu_{*i} < 5$ at $r/a = 0.97$.

This is a report of work sponsored by the U.S. DOE under contract DE-AC03-84ER51044.

REFERENCES

[1] Lohr, J.M., *et al.*, Phys. Rev. Lett. **60** (1988) 2630.
[2] Osborne, T.H., *et al.*, General Atomics Report GA-A19362 (1988).
[3] Burrell, K.H., *et al.*, in 12th Inter. Conf. on Plasma Physics and Controlled Nuclear Fusion Research, Nice, 1988.
[4] Hill, D.N., *et al.*, General Atomics Report GA-A19101 (1988).
[5] Hinton, F.L., Nucl. Fusion **25** (1985) 1457.
[6] Jackson, G.L., *et al.*, Bull. Am. Phys. Soc. **33** (1988) 1963.
[7] Suzuki, N., *et al.*, in Proc. 14th Eur. Conf. on Cont. Fusion and Plasma Heating, Madrid (1987) 217.
[8] Burrell, K.H., *et al.*, Phys. Rev. Lett. **59** (1987) 1432.
[9] Rebut, P.H., *et al.*, in Proc. 15th Eur. Conf. on Cont. Fusion and Plasma Heating, Dubrovnik (1988) 247.
[10] Shaing, K.C., *et al.*, in 12th Inter. Conf. on Plasma Physics and Controlled Nuclear Fusion Research, Nice, 1988.
[11] Shaing, K.C., private communication (1988).
[12] Groebner, R.J., *et al.*, this conference (1989).
[13] Itoh, I.S. and Itoh, K.I., Phys. Rev. Lett. **60** (1988) 2276.
[14] Gohil, P., *et al.*, Phys. Rev. Lett. **61** (1988) 1603.
[15] Bishop, C.N., Nucl. Fusion **26** (1986) 1063.
[16] Burrell, K.H., *et al.*, this conference (1989).

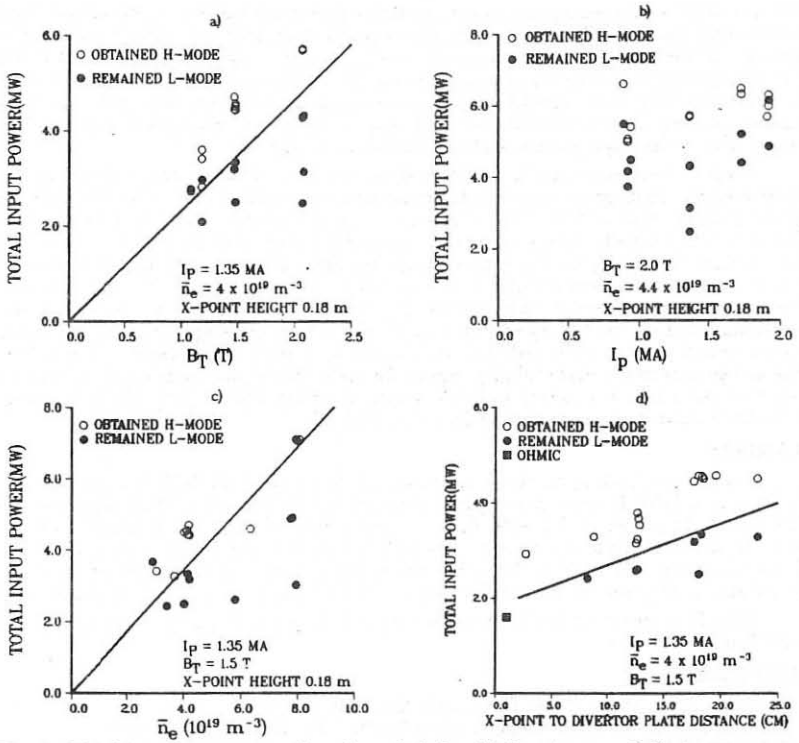

Fig. 1. Total input power as a function of a) B_T, b) I_P, c) $\bar{n}_e$, and d) the X-point to divertor plate distance δ.

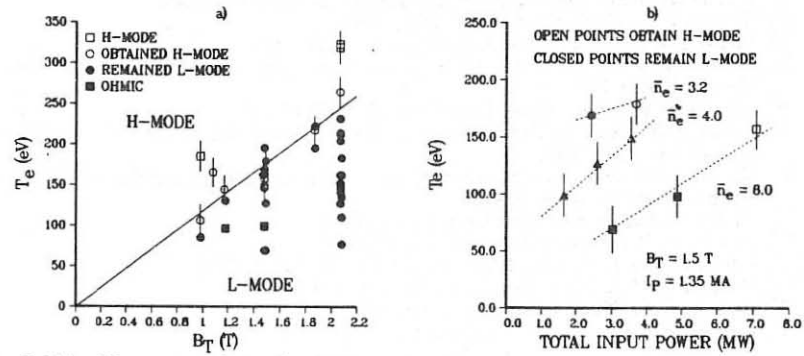

Fig. 2. Edge T_e measured at r/a=0.97 as a function of a) B_T, and b) total input power.

PLASMA ROTATION AND ELECTRIC FIELD EFFECTS IN H-MODE IN DIII-D

R.J. Groebner, P. Gohil, K.H. Burrell, T.H. Osborne, R.P. Seraydarian, H. St. John

General Atomics, San Diego, California 92138-5608, U.S.A.

INTRODUCTION

Poloidal rotation has been observed near the separatrix of H-mode discharges in the DIII-D tokamak. This rotation persists throughout the entire time of the H-phase and is a general characteristic of all H-mode discharges studied to date. The force balance equation for a single ion species shows unambiguously that the poloidal rotation is produced by a negative radial electric field. Field strengths of at least 200-300 V/cm have been inferred 1-3 cm inside the separatrix, and the electric field may extend across the separatrix into the scrape-off layer. This paper discusses the techniques used to measure poloidal rotation and the salient features of the rotation.

DIAGNOSTICS

The Doppler shift of the He II 4686 Å line is used to measure poloidal and toroidal rotation in the DIII-D tokamak. Measurements are made with two 8-chord CER (Charge Exchange Recombination) spectrometer systems.[1] As illustrated in Fig. 1, one of these systems has a horizontal view of the plasma and is used to measure toroidal rotation velocity profiles $v_{\rm tor}(r)$; the other system has a vertical view and is intended to measure poloidal rotation $v_{\rm pol}$.

The spectrum of the He II 4686 Å line is composed of three distinct components. One of these components is excited by charge transfer between the fast hydrogen atoms of a neutral beam and helium nuclei and is used for spatially resolved measurements of $T_{\rm i}$ and rotation velocity in the bulk of the plasma.[2] There are two additional components, one with a temperature of 10-20 eV ("cold" component) which is excited by electron impact collisions and one with a temperature of 70-400 eV ("warm" component). The warm component has been previously observed on the JET tokamak.[3] The excitation mechanism for the warm component is unknown but is probably charge transfer of thermal neutrals with helium nuclei. With the assumption that $T_{\rm i} = T_{\rm e}$ near the plasma periphery, the locations in the plasma from which the cold and warm components are emitted can be determined by comparing $T_{\rm i}$ of the components with the $T_{\rm e}$ profile from a multipoint Thomson scattering system. In general, these comparisons show that the warm component lies just inside (within 1-3 cm) of the separatrix and the cold component lies in the scrape-off layer. The assumption that $T_{\rm i} = T_{\rm e}$ inside the separatrix is well supported by comparisons of $T_{\rm i}$ from the CER data and $T_{\rm e}$ from Thomson scattering and by the fact that the transfer time between the ions and electrons is only a few ms due to the high densities and low temperatures in the outer half of H-mode discharges in the DIII-D tokamak.

ROTATION DATA

The poloidal rotation is mostly clearly manifested by an abrupt Doppler shift of the warm He II component at the times of the L-H transition, the occurrence of giant ELMs (edge-localized modes) and at the H-L transition. A typical example is illustrated in Fig. 2. For this discharge, about 1 MW of NBI power was applied prior to 1.0 s and the power was increased in stages to 5 MW between 1.2 and 1.4 s. As determined by an H_α detector, the L-H transition occured at 1.364 s and the first ELM occurred at 1.908 s. The toroidal rotation velocity of the warm component [Fig. 2(a)] was 10–15 km/s during the L-phase and increased to about 30 km/s during the H-phase. As shown in Fig. 2(b), the velocity $v_{\rm vert}$ of the warm component along the line of sight of the edgemost vertical chord was about 8 km/s during the L-phase and increased to about 25 km/sec within 40 ms after the L-H transition. For this chord, which has an angle of 75 degrees with respect to the toroidal direction, only about 1/3 of the observed Doppler shift at the L-H transition can be attributed to toroidal rotation. With this correction, $v_{\rm pol}$ was about 18 km/s during the H-phase. During the H-phase, $v_{\rm pol}$ remained approximately constant during the 1.6 s duration of the H–mode with the exception that it abruptly returned to nearly the L–mode level at the occurrence of each giant ELM. The ELMs also modulated $v_{\rm tor}$ of the warm component (and also $v_{\rm pol}$ and possibly $v_{\rm tor}$ of the cold component). The direction of $v_{\rm pol}$ was up near the outer edge of the plasma (Fig. 1). For deuterons at the location of the warm peak, the thermal velocity was about 90 km/s.

The poloidal rotation is sometimes also observed in the Doppler shift of the cold component. However, for the discharge displayed, $v_{\rm tor}$ and $v_{\rm pol}$ of the cold component maintained roughly a value of zero during the L and H-phases with the exception of transients observed at the L-H transition and at ELMs. The initial direction of these transient motions is consistent with a radial negative electric field, but there are other possible explanations.

For the analysis used here, the reference for zero poloidal rotation is known unambiguously because the rotation provides a blue shift for the downwards-viewing vertical chords (Fig. 1) and a red shift for the upwards-viewing chords. Calibration data obtained with a Hg source show the relative locations of the lines on the detector for the case in which there is no rotation. The cold line always has $v_{\rm pol}$ equal to zero during the ohmic and L-phases of the discharges. For $v_{\rm tor}$, the wavelength in the ohmic and L-phases of the cold line is used to obtain the reference for zero rotation velocity. No shift of the cold line in the toroidal direction has ever been observed between the ohmic and L-phases of a discharge.

Although numerous systematic effects could produce small spurious shifts of the He II components, the authors are aware of no effect which could produce the magnitude of the shifts observed. One qualitative feature of the data defies explanation by systematic effects. For the example presented here, the neutral beams which provide signals for the vertical and horizontal CER systems were not turned on, so the He spectra consisted of the cold and warm components only. Two of the upwards-viewing and the two downwards-viewing vertical chords share the same multichannel detector. At the L-H transition, both of the He components exhibited red shifts on the upwards-viewing chords (Fig. 1) and blue shifts on the downwards-viewing chords. This behavior can only be due to a true rotation of the plasma.

The poloidal rotation velocities imply inward-directed radial electric fields $E_{\rm r}$ with magnitudes of at least 200–300 V/cm. $E_{\rm r}$ is calculated from the force balance equation for a single ion species. With collisions neglected, the equation is

$$\vec{E} = \frac{1}{n_I Z_I e}\vec{\nabla} P_I - \vec{V}_I \times \vec{B} \quad .$$

where E is the electric field, n_I is the ion density, Z_I is the charge of the ion, e is the electronic charge, P_I is the ion pressure, V_I is the ion flow velocity and B is the magnetic field. With the observation that $\vec{\nabla} P_I$ is negative (pressure decreasing with minor radius), the magnetic field directions (Fig. 1) and the force balance equation indicate that a negative electric field produced the observed poloidal rotation. The contribution of the $\vec{\nabla} P_I$ term to E_r is unknown because the density profile for the He II ions is not measured. For $v_{pol} = 18$ km/s and $B_t = 1.5$ T, the contribution of the $\vec{V}_I \times \vec{B}$ term to E_r is - 260 V/cm, and this field was measured 1–3 cm inside the separatrix. Inclusion of the $\vec{\nabla} P_i$ term would increase the calculated value for E_r.

The major weakness of the data set is the lack of independent spatial localization of the cold and warm components and the lack of fine spatial resolution of v_{tor} and v_{pol} near the plasma edge. Comparison of v_{pol} from the warm and cold He II components suggests that the radial electric field changes rapidly in magnitude within a few cm at the plasma edge.

CONCLUSIONS AND IMPLICATIONS FOR THEORY

Poloidal rotation has been observed in every H–mode discharge which has been studied, and the parameter range includes I_p of 0.34 to 1.5 MA, co-injected neutral beam powers of up to 9.5 MW and the ohmic H–mode. Data are not yet available for counter-injection or the ECH H–mode. Negative radial electric fields near the separatrix appear to be characteristic of at least some classes of H–mode discharges. These observations have significant implications for theories developed to explain the H–mode. Ohkawa and Hinton[4] suggested that the development of a negative radial electric field due to ion orbit losses was an essential ingredient for H–mode plasmas. The bifurcation theory of Itoh and Itoh,[5] requiring a positive electric field at the plasma edge during the H-phase, is not consistent with the poloidal rotation data. The theory of Shaing, et al.,[6] requires that a negative electric field at the plasma edge suddenly becomes more negative at the L-H transition. This direction is consistent with the measurements discussed here. At present, the experimental time scale for the change of the electric field is not clear. The rise time for v_{pol} after the L-H transition varies from less than the 10 ms, the minimum time resolution of the instrument, for some discharges to 40 ms for other discharges. It is not clear whether the rise time is controlled by a changing electric field or by viscosity. This is an area requiring further research.

ACKNOWLEDGMENTS

This work was sponsored by the U.S. Department of Energy under Contract No. DE-AC03-84ER5l044. R.J.G. acknowledges useful conversations with F.L. Hinton and T.N. Carlstrom.

REFERENCES

1. Seraydarian, R.P., and Burrell, K.H., Rev. Sci. Instrum. **57** (1986) 2012.

2. Fonck, R.J., Darrow, D.S., Jaehnig, K.P., Phys Rev. A **29** (1984) 3288.

3. Carolan, P.G., Forrest, M.J., Hawkes, N.C., Peacock, N.J., Proceedings of 12th European Conference on Controlled Fusion and Plasma Physics, Budapest, Hungary, Vol. 1, 263 (1985).

4. Ohkawa, T., and Hinton, F.L., Proceedings of the 11th International Conference on Plasma Physics and Controlled Fusion Research, 1986, IAEA, Kyoto, Japan, Vol. 1, 221 (1987).

5. Itoh, I.S., and Itoh, K.I., Phys. Rev. Lett. **60** (1988) 2276.

6. Shaing, K.C., *et al.*, Proceedings of 12th International Conference on Plasma Physics and Controlled Nuclear Fusion Research, Nice, 1988.

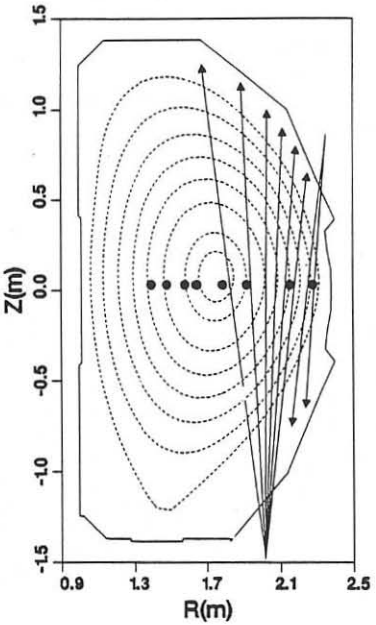

Fig. 1. CER systems shown in reference to typical H–mode equilibrium. Six chords view vertically upwards, 2 chords view vertically downwards and 8 chords view horizontally (out of the paper). B_t points out of the paper and I_p points into the paper. Beam injection is in the direction of I_p.

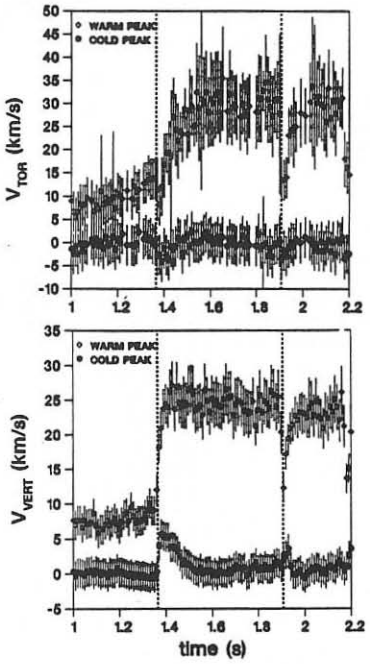

Fig. 2. Rotation velocities. (a) Toroidal rotation velocity of cold and warm He II components observed by edgemost horizontal CER chord. (b) Poloidal rotation velocity of cold and warm He II components observed by edgemost vertical CER chord. Vertical lines show L-H transition at 1.364 s and first ELM at 1.908 s.

ATTAINMENT OF QUASI STEADY-STATE H-MODE PLASMAS IN THE DIII-D TOKAMAK

M. Ali Mahdavi, A. Kellman, P. Gohil, N. Brooks, K.H. Burrell, R. Groebner, G. Haas,* D. Hill,† G. Jackson, G. Janeschitz,* T. Osborne, M.E. Perry,‡ T. Petrie, M. Rensink,* M. Shimada,§ G. Staebler, R. Stambaugh, and R. Wood†

General Atomics, San Diego, California 92138-5608, U.S.A.
*Max Planck Institut für Plasmaphysik, Garching, FRG
†Lawrence Livermore National Laboratory, Livermore, California, U.S.A.
‡John Hopkins University, Maryland
§Japan Atomic Energy Research Institute, Japan

ABSTRACT

We report the results of experiments on DIII-D where quasi steady-state H-mode plasmas with low amplitude Edge Localized Modes (ELMs) were maintained for 5 seconds. Within one second from the onset of the H-mode, most plasma parameters reach their asymptotic values ($\bar{n}_e \approx 7 \times 10^{13}$ cm^{-3}, $\tau_E \simeq 100$ ms, $Z_{eff} = 1.7$) and the electron density and temperature profiles are no longer evolving. By this time, frequent ELMs and effective helium wall conditioning limit the rate of increase of $\bar{n}_e$ ($\leq$10% of the beam fueling rate) and maintain the total radiated power from impurities at a constant level.

FEATURES OF THE LONG PULSE H-MODE

The experiments reported here were all performed in plasmas consisting of $\simeq$30% deuterium and $\simeq$70% hydrogen, with $I_p = 1.25$ MA, $B_T = 1.40$ T, and $\bar{n}_e = 2.8 \times 10^{13}$ cm^{-3} before NBI. Seven MW of neutral beam power with an approximate isotopic mixture of 25% D° and 75%H°, approximately the target plasma composition, was injected one second after the plasma initiation. The H-mode transition occurs shortly after the start of NBI, and the H-phase lasts for 5 sec until the end of the NBI (Fig. 1). After an initial rapid rise, the rate of line-averaged density rise decreases to 0.7×10^{13} cm^{-3} s^{-1}, despite an average beam fueling rate of $\sim 7 \times 10^{13}$ cm^{-3} s^{-1} [Fig. 1(c)]. Regularly spaced ELMs at a frequency of $\sim$30 Hz occur during the H-mode phase [Fig. 1(d)]. Each ELM expels $\approx$10% of the plasma stored energy and a similar fraction of the plasma particles. At these NBI powers, no significant change was observed in ELM behavior for different X-point heights above the divertor plates, in contrast to previously observed behavior at lower NBI powers. The energy confinement time, deduced from magnetic measurements, is shown in Fig. 1(e).

Except for an initial rapid rise after the L-H transition, line intensities of the high charge states of metallic impurities [Fig. 1(f)] decrease into the H-mode while those of the lower charge states increase [Fig. 1(g)]. In agreement with these observations the gross radiated power increases rapidly during the first ELM-free period, and then is nearly constant for the remaining duration of the H-mode, with the radiation profile

becoming more hollow. This behavior may be explainable by a combination of neoclassical impurity transport, a nearly flat density profile, and ELM activity. Within a few centimeters of the separatrix, neoclassical impurity fluxes would be inward, whereas, further in the interior of the plasma, due to a strong temperature gradient term, the impurity fluxes would be outward. As a result impurities may be concentrated in the plasma periphery where they are periodically expelled by ELM activity.[1]

DENSITY BEHAVIOR

A key factor for the attainment of long pulse H–mode plasmas is particle control, since an uncontrolled rise in electron density or impurity content of the plasma will ultimately lead to radiation collapse. In DIII–D, during the ELM free periods, the rate of density rise is typically 2–3 times the sum of the cold and energetic particle sources. In contrast the average rate of density rise during the H-mode is typically $\simeq$10% of the fueling rate by the neutral beams. From these observations we deduce: (a) the divertor plate surfaces act as particle reservoirs with a characteristic particle confinement time which is of the same order as the plasma particle confinement time so that the density equilibrium results from balancing significant particle transfers between the plasma and the plates, and; (b) particle loss during ELMs is a key factor in the reduced rate of density rise observed in the later phase of the H–mode.

In an attempt to explain the H–mode density behavior we have used a simple model of the particle balance in a system consisting of: the main body of the plasma within the closed flux surfaces; the scrape-off layer and divertor plasmas, and; the graphite divertor target plates, all with their respective particle confinement times of τ_P, τ_D and τ_W. The divertor plasma is the interface between the target plates and the main body of the plasma. The high divertor plasma density allows only a small fraction, α, of the particles recycling at the target plates, or particles released by the plates, to penetrate the main body of the plasma. In this model, neglecting terms of the order τ_D/τ_P and N_D/N_P, and averaging over events of a time scale $\gtrsim \tau_D$, the particle content of the plasma is given by

$$N_P(t) \simeq \frac{1}{\gamma\tau_W}\left[N_T(o) + \Gamma t\right] + \left[N_P(o) - \frac{N_T(o)}{\gamma\tau_W}\right] e^{-\gamma t} + \frac{\Gamma}{\gamma^2\tau_W}\left(1 - \gamma\tau_W\right)\left(e^{-\gamma t} - 1\right) \ , \quad (1)$$

where $\gamma = \frac{\alpha\tau_P + \tau_W(1-R)}{\alpha\tau_P\tau_W}$, R is the particle reflectivity of the divertor plates, Γ is the beam particle source, $N_T(0)$ is the initial total particles in the system. The quantity $\gamma^{-1}\tau_W^{-1}$ in the first term of Eq. (1) is interpreted as the fueling efficiency of the plasma. The parameter γ is the particle equipartition time constant between the plasma volume and the target plates. The last term in Eq. (1) is due to the time delay in the redistribution of the particles during fueling which is of no consequence for our present discussion.

The initial rate of density rise at the L-H transition, in excess of the beam fueling rate, arises from a sudden increase in particle confinement time, $\tau_p(H)$, relative to $\tau_p(L)$. This rate of density rise is given by the second term in Eq. (1):

$$\frac{dN_p}{dt} \simeq \frac{N_T(o)}{\tau_W}\left(1 - \frac{\gamma_H}{\gamma_L}\right) \simeq \frac{N_T(o)}{\tau_W}\left[1 - \frac{\tau_P(L)}{\tau_P(H)}\right] \quad ,$$

where we have used $\alpha \simeq 0.1$ (see Ref. 3) and $R \approx 0.5$, and assumed $\tau_P \approx \tau_W$. Since $\tau_p(H) \gg \tau_p(L)$, the initial rate of density rise is due to plasma absorbing all the particles released by the wall. Later in the H-mode when $\gamma t \gg 1$, $\langle (dN_P)/(dt) \rangle \simeq \Gamma/(\gamma \tau_W)$. Using the measured value of $\langle (dN_p)/dt \rangle \simeq 0.1\ \Gamma$, we obtain $\tau_P \approx 0.5\ \tau_W$, verifying the earlier assumption of $\tau_P \approx \tau_W$.

In the intervals between ELMs, the net rate of density rise is $\cong$40 Torr liters/sec, whereas the average rate of density rise is $\cong$2.1 Torr liters/sec. Neglecting particle transport during the ELM free periods compared to the average particle outflux due to ELMs, yields an effective particle confinement time of 0.5 sec, and $\tau_W \approx 1$ sec.

ELM BEHAVIOR

ELMs are an essential factor in the attainment of the long pulse H-mode plasmas, because they not only limit the rate of density rise, but are also responsible for reducing the impurity content of the plasma. It has been shown[4] that ELMs occur when the edge pressure gradient is near the ideal ballooning mode limit, which scales as I_P^2 . In DIII-D, the ELM frequency decreases with increasing I_P and decreasing power. This tendency is greatly accelerated when a significant fraction of the input power is radiated in the core plasma. This is because radiative losses reduce the rate of pressure buildup, thus reducing the ELM frequency, which in turn results in more density and impurity buildup and even greater radiative losses. This phenomenon is demonstrated in Figs. 1 and 2, where the ELM behavior of two discharges with different heating power but otherwise identical external parameters are compared. In Fig. 2, the ELM frequency of a discharge with 40% lower heating power is a factor five lower than that of the reference discharge (Fig. 1). Furthermore each ELM event is followed by a 20–50 msec long L-mode period. Ultimately, due to excessive radiation, the discharge of Fig. 2 reverts to the L-mode.

Consequently, in the absence of an active particle control technique to mitigate the rate of density rise and radiative losses, it is desirable to increase the heating power or lower the plasma current. The ELM behavior in the second discharge of Fig. 2 is similar to that of JET H-mode plasmas, where the ELM free periods are long and ELMs are followed by L-mode periods. Relative to DIII-D, JET is a low power density device. Therefore JET observations[5] are consistent with the above description of the ELM behavior in DIII-D at low NBI power.

SUMMARY AND CONCLUSIONS

We have demonstrated that H-mode confinement can be sustained without impurity accumulation or confinement deterioration for times much longer than all the plasma characteristic time scales. It is shown that ELMs in conjunction with graphite divertor plates reduce the rate of density rise and radiative losses, which enable the long pulse sustainment of these discharges.

This work was supported by U.S. Department of Energy under Contract No. DE-AC03-89ER51114.

REFERENCES

1. Content, D., *et al.*, General Atomics Report GA-A19288, August 1988 (submitted for publication in Nuclear Fusion).

2. Jones, T.T.C., *et al.*, Journal of Nuclear Materials **163–165** (1988).

3. Allen, S.L., Rensink, M.E., Hill, D.N., *et al.*, Journal of Nuclear Materials **163–165** (1988).

4. Gohil, P., Mahdavi, M. Ali, Lao, L., *et al.*, Phys. Rev. Lett. **61**, 1603 (1988).

5. Tanga, A., *et al.*, Proceedings of the 15th European Conference on Controlled Fusion and Plasma Heating, Dubrovnik, Yugoslavia, May 16–20, 1988.

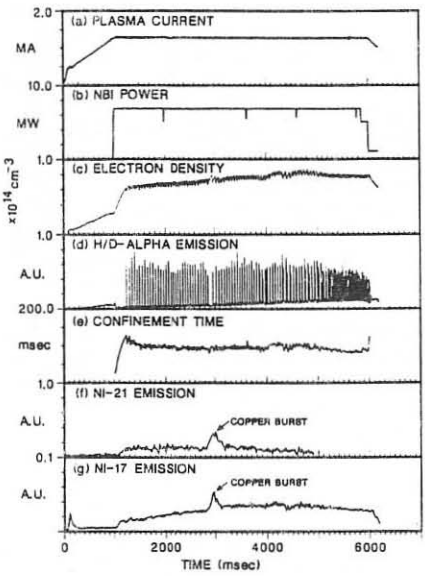

Fig. 1. Time histories of plasma parameters for quasi steady-state H–mode: (a) plasma current; (b) NBI power input; (c) line-integrated electron density; (d) H_α/D_α plasma emission from plasma divertor; (e) confinement time; (f) line emission from Ni-21 impurity near plasma center; (g) line emission from Ni-17 impurity near plasma edge.

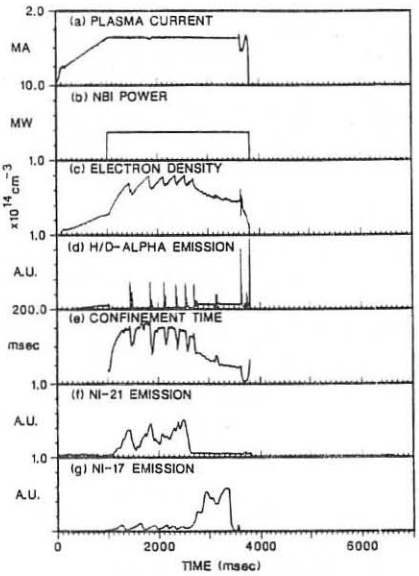

Fig. 2. Time histories of plasma parameters for a similar plasma discharge to Fig. 1 but with reduced NBI power input. Figure quantities are the same and have the same units and scales as in Fig. 1, except for the Ni-17 line emission [(g)] which is 10 times greater than in Fig. 1.

ON GLOBAL H-MODE SCALING LAWS FOR JET

O. Kardaun°, K. Thomsen, J. Christiansen, J. Cordey, N. Gottardi, M. Keilhacker
K. Lackner°, P. Smeulders, the JET Team

JET Joint Undertaking, Abingdon, Oxon OX14 3EA, UK
°Max-Planck-Institut für Plasmaphysik, 8046 Garching, BRD

Investigation of the scaling of the energy confinement time τ_E with various plasma parameters has since long been an interesting, albeit not uncontroversial topic in plasma physics. Various global scaling laws have been derived for Ohmic as well as (NBI and/or RF heated) L-mode discharges [1-5]. Due to the scarce availability of computerised, extensive and validated H-mode datasets, systematic statistical analysis of H-mode scaling behaviour has hitherto been limited. A common approach is to fit the available H-mode data by an L-mode scaling law (e.g., Kaye-Goldston, Rebut-Lallia) with one or two adjustable constant terms. In this contribution we will consider the alternative approach of fitting all free parameters of various simple scaling models to two recently compiled datasets consisting of about 140 ELM-free and 40 ELMy H-mode discharges, measured at JET in the period 1986-1988. From this period, approximately all known H-mode shots have been included that satisfy the following criteria: D-injected D^+ discharges with no RF heating, a sufficiently long ($\geq$ 300 ms) and regular P_{NBI} flat-top, and validated main diagnostics. Normally, 3 time points per discharge were selected. For future reference, we call these two datasets in this paper *ELMF* and *ELMY*, respectively.

We start our discussion with the empirical JET scaling law presented last year by Keilhacker [6] at the IAEA Conference in Nice:

$$\tau_{dia} = (0.63 \pm .02) I_p^{.75\pm.08} B_t^{.5\pm.08} \langle n_e \rangle^{.2\pm.1} (P_{tot} - \dot{W}_{dia})^{-.7\pm.05}, \qquad (1)$$

This law is based on a large subset of *ELMF*, consisting of those single null (SN) shots from 1986 and 1988, in which during some time interval $\dot{W}_{dia}/P_{tot} < 0.30$ (i.e. without relatively early disruptions), and containing some, but not all of the very latest 1988 5 MA shots. The regression was made taking only one timepoint per shot, where W_{dia} approximately reached its maximum value. The global energy confinement time is defined by $\tau_{dia} = W_{dia}/P_c$, where W_{dia} is the diamagnetically determined energy content, P_c is an abbreviation for $P_{tot} - \dot{W}_{dia}$, P_{tot} is the ohmic plus the NBI-injected power, B_t is the toroidal magnetic field, I_p the plasma current, and $\langle n_e \rangle$ the volume averaged electron density, all quantities being evaluated at the selected time point. The errors indicate one std (estimated standard deviation) of the estimated coefficients. The units used in formula (1) are: τ_{dia} (sec), I (3 MA), B_t (2.5 T), $\langle n_e \rangle$ ($4.10^{19}\mathrm{m}^{-3}$), and P_c (10 MW). These units correspond roughly the average values in the dataset. After a logarithmic transformation, a linear model was fitted. This approach presumes that a constant level of statistical errors exists on logarithmic scale (or, equivalently, constant relative errors on ordinary scale). The usual flaw of ordinary least squares, namely the assumption that only the response variable and none of the 'explanatory variables' are measured with statistical error, was avoided by presuming, not very differently from [7], 10% measurement error on τ_{dia} and W_{dia}, and 5% on $\langle n_e \rangle$ and P_c, and applying

special regression techniques [8] based on theory of 'functional relationships' [9-12]. (The reader may have noted that, by definition of τ_{dia}, the above assumption on the errors implies that the errors in $\log \tau_{dia}$ and $\log W_{dia}$ are correlated with correlation coefficient $r = 0.875$.) Obviously, one gets an equivalent scaling law for W_{dia} by just adding $+1$ to the coefficient of $P_{tot} - \dot{W}_{dia}$ in (1). The assumed measurement errors in τ_{dia} and W_{dia} are more or less consistent with the residual rmse (root mean squared error) of 8% from ordinary regression.

To classify the various types of scaling laws, it seems useful to distinguish between 'scientific' scaling laws, in which the dependence of the energy confinement time τ_E on physically relevant, though possibly not directly controllable parameters (like the axis temperature $T_e(0)$ or a descriptor of the ELM activity, Δ_E) is analysed, and engineering ones, in which only directly controllable parameters (like heating power, refuelling rate, wall conditioning, etc.) are taken as independent variables. In practice, scaling laws are often of a hybrid type, in which the two objectives are mixed. In fact, looking at (1), one can see that the inclusion of P_{tot} instead of the electron temperature T_e implies an engineering aspect. The scaling law is, however, not a fully engineering one, since for instance $\langle n_e \rangle$ during H-mode is not an independently controllable parameter.

In table 1, the results are presented of an empirical analysis of the datasets from a more strictly engineering point of view. In this table, $\langle n_{ohm} \rangle$ denotes the volume-averaged electron density during the stationary ohmic discharge phase just before the onset of NBI. From the descriptive statistics one can see that the continuous variables were, generally, varied over quite a large range, B_t being changed least. However, from the correlation matrix it clear that the 'controllable' variables were not at all varied independently. The determinant $|R|$ of this matrix (i.e. the product of its eigenvalues) is some measure of the global dependency. In fact, under the hypothesis of independence, for large normal samples, $X = -N \log |R| \sim \chi^2_{p(p-1)/2}$. In our case, obviously, $X = 623 \gg \chi^2_{6;\alpha}$ for any reasonable level α. Clearly, less correlation between the independent variables at roughly the present ranges, which may be feasible to achieve, even if one takes into account operational machine limits, would have a beneficial effect on the precision and the robustness of the regression. The two binary variables Δ_{DN} and Δ_{87} indicate whether ($\Delta = 1$) or not ($\Delta = 0$) the shot was double null and/or run in 1987. In the scaling law section, coefficients and their std's are given that correspond directly to expressions like (1). Ordinary least squares [13] has been used for simplicity. (The presence of interaction terms destroys the linearity in the functional relationship model. The measurement errors tend to increase the absolute values of the estimates and certainly increase their std's. Experience with the simple model (1) suggests by 5 to 10% and 50 to 100%, respectively.) The quantity τ_{mhd} represents the equilibrium-based confinement time, in which the parallel as well as the perpendicular thermal and beam energy contributions are taken into account, whereas τ_{dia} is obtained from the perpendicular contributions. The subscript $_{rc}$ denotes a rough correction for radiation ($\tau_{rc,dia} = W_{dia}/(P_c - \alpha P_{rad})$), where P_{rad} denotes the total radiated power (from the central plasma as well as the X-point) and α was taken to be 30%. From an analysis of a few shots, this approximation appeared not too bad, although of course P_{rad} and P_{NBI} depend both on density. Obviously, a standard implementation of a more accurate radiation correction would be desirable. From this simple approximation, one can see however that the engineering scaling laws are, except for their constant terms, not very sensitive to the radiation correction. In order to keep the scaling law an engineering one, no radiation correction was applied to the independent variable P_c. In a scientific approach, one may do so, in order to get a better fit, or at least to have the same scaling laws for τ_{rc} and W.

The reader might object that the laws in table 1 are not purely engineering ones, because of the presence of $\dot{W}$. The relationships presented can however be interpreted as applying to the quasi-stationary state where $\dot{W} = 0$, which is reached in many JET

discharges. The more serious objection that knowledge on the presence of ELM's is not yet an engineering quantity, is encountered by making an appropriate discriminant analysis, the details of which will be presented on a poster. It has been known for some time that the shots from 1987 were somewhat worse than the other H-mode shots. This is quantified in column Δ_{87}, where one can see that the overall degradation ranges between 20% and 30%. After some searching for the cause, it turned out that during and prior to the period (december 1987) in which these 18 H-mode shots were run, the He wall conditioning was stopped for 6 weeks and the condition of the wall was directly influenced by a number of disruptions. Hence, from an engineering point of view, one might interpret the absolute values of these exponents as 'the gain in H-mode confinement time due to careful wall conditioning'. In table 1, $I_p \otimes I_p$ denotes an interaction term, which is simply a quadratic term on logarithmic scale. On ordinary scale we have, in our units, $\tau_{dia} \sim I_p^{.67-.46 \log I_p}$, i.e. for $I_p = 3$ MA the exponent is .67, which diminishes by .23 if the current is a factor $\sqrt{e} = 1.65$ larger, i.e. at $I_p \simeq 5$ MA. The presence of more interaction terms has been investigated, but only the significant ones have been retained in the table.

Compared to the ELM-free shots, the ELMy shots have a worse degradation with power and a smaller exponent for I_p. However, no significant saturation with current was found in *ELMY*. A remarkable fact is the difference in (I_p, B_t) dependence between τ_{dia} and τ_{mhd} in *ELMY*. As $I_p^a B_t^b \sim I_p^{a+b} q_{cyl}^b$, this can be interpreted as difference in q_{cyl} dependence at constant I_p. One might be concerned about the difference in power dependence between (1) and table 1. It should be remembered, however, that in (1) this exponent has to be interpreted at constant instantaneous $\langle n_e \rangle$, and in table 1 at constant $\langle n_{ohm} \rangle$. As P_c and $\langle n_e \rangle$ are positively correlated, a larger $\langle n_e \rangle$ from more power, at constant $\langle n_{ohm} \rangle$, counteracts the power degradation in (1). Of course, the quadratic term has been chosen as a simple expedient for describing the deviation from linearity, and the scaling law should not be extrapolated too far from the experimental range. The saturation with current is obvious for the ELM-free shots. It is not perfectly clear, however, whether this is due to intrinsic machine limitations, or to the fact that the 5 MA H-mode shots were not yet fully optimised. In the future, it is intended to compare the present scaling laws with other types of scaling laws at JET, and to make similar analyses for ASDEX.

References

[1] HUGILL, J., SHEFFIELD, J., Nucl. Fusion **18** (1978) 15-22.

[2] CONNOR, J.W., TAYLOR, J.B., Nucl. Fusion **17** (1977) 1047-1055.

[3] PFEIFFER, W., WALTZ, R.E., Nucl. Fusion **19** (1979) 51-67.

[4] CORDEY, J.G., In: CEC publ. EUR 1048 EN (1986), Luxemburg.

[5] CRISTIANSEN, J.P., CALLEN, J.D., CORDEY, J.G., THOMSEN K., Nucl. Fusion **28** (1988) 817.

[6] The JET Team, presented by M. Keilhacker, IAEA XII, Nice, 1988.

[7] The JET Team, compiled by M.L. Watkins and M. Keilhacker, JET-IR(88) 12.

[8] PANTULA, S.G., Factor Analysis Program, written in SAS (1984), NC State Univ.

[9] FULLER, W.A., *Measurement error models* (1987), Wiley, New York.

[10] HILLEGERS, L.T.M.E., PhD Thesis (1986), Tech. Univ. of Eindhoven.

[11] ANDERSON, T.W., The 1982 Wald Memorial Lectures, Ann. Stat. **12** (1984) 1-45.

[12] FERRE, L., Lab. de stat. et prob. N° 01-88 (1988), Univ. P. Sabatier, Toulouse.

[13] SAS, User's Guide: Statistics, Version 5 (1985) SAS Inc., Cary, NC.

Acknowledgements

The authors are grateful to Drs. H. Jensen, D. Muir, and M. Watkins for several helpful discussions, to M. Johnson for providing the disruption dates, and to the JET Data Management Group for support in extracting and maintaining the datasets.

Table 1. Engineering scaling laws for the global energy confinement time of JET H-mode shots, from ordinary least squares regression.

descriptive statistics

	units	av.	std	(min,max)
Dataset ELMF (ELM-free, D into D^+, NBI only, 140 shots, N = 420 datapoints)				
τ_{dia}	sec	0.81	0.17	(0.4, 1.45)
I_p	MA	3.4	0.7	(2.0, 5.2)
B_t	T	2.4	0.4	(1.7, 3.5)
P_c	MW	7.2	2.5	(1.4,16.7)
$\langle n_{ohm} \rangle$	$10^{19}/m^3$	1.6	0.5	(0.8, 3.1)
Δ_{87}		13%		(0,1)
Δ_{DN}		6%		(0,1)

correlation matrix R (on logarithmic scale)

	I_p	B_t	P_c	$\langle n_{ohm} \rangle$
I_p	1			
B_t	**.49**	1		
P_c	.22	**.40**	1	
$\langle n_{ohm} \rangle$	**.78**	**.56**	.24	1

eigenvalues: 2.4, 0.9, 0.5, 0.21

Dataset ELMY (with ELM's, D into D^+, NBI only, SN, 40 shots, N = 120 datapoints)

τ_{dia}	sec	0.75	0.18	(0.4, 1.14)
I_p	MA	4.1	0.7	(3.0, 5.2)
B_t	T	2.7	0.4	(1.7, 3.5)
P_c	MW	8.7	3.3	(1.4,16.7)
$\langle n_{ohm} \rangle$	$10^{19}/m^3$	2.0	0.5	(1.0, 3.1)

	I_p	B_t	P_c	$\langle n_{ohm} \rangle$
I_p	1			
B_t	.43	1		
P_c	**.55**	.43	1	
$\langle n_{ohm} \rangle$	**.75**	**.48**	**.47**	1

eigenvalues: 2.5, 0.7, 0.6, 0.24

scaling laws: ELMF

	C	I_p	$I_p \otimes I_p$	B_t	P_c	$\langle n_{ohm} \rangle$	Δ_{87}	Δ_{DN}	rmse
τ_{dia}	.705	.67	−.46	.36	−.50	.16	−.18	−.04	7.0%
	(.008)	(.03)	(.06)	(.04)	(.02)	(.03)	(.01)	(.015)	
$\tau_{rc,dia}$	.890	.77	−.55	.28	−.44	.12	−.20	−.06	8.8%
	(.012)	(.04)	(.07)	(.04)	(.02)	(.03)	(.01)	(.02)	
τ_{mhd}	.690	.45	−.55	.57	−.46	.14	−.32	−.08	7.7%
	(.008)	(.03)	(.06)	(.04)	(.01)	(.03)	(.01)	(.015)	
$\tau_{rc,mhd}$	.870	.57	−.64	.50	−.43	.11	−.36	−.10	10 %
	(.015)	(.04)	(.07)	(.05)	(.02)	(.04)	(.02)	(.02)	

scaling laws: ELMY

	C	I_p	B_t	P_c	$P_c \otimes P_c$	$\langle n_{ohm} \rangle$	rmse
τ_{dia}	.610	.27	.34	−.87	−.52	.26	10.5%
	(.020)	(.08)	(.08)	(.04)	(.08)	(.06)	
$\tau_{rc,dia}$	.795	.23	.35	−.75	−.50	.28	11.3%
	(.030)	(.09)	(.09)	(.04)	(.08)	(.06)	
τ_{mhd}	.585	−.32	.89	−.85	−.59	.25	14.5%
	(.030)	(.11)	(.11)	(.05)	(.10)	(.08)	
$\tau_{rc,mhd}$	.745	−.30	.92	−.74	−.57	.25	15.2%
	(.035)	(.12)	(.12)	(.05)	(.11)	(.08)	

In this table, av. stands for average, std for estimated standard deviation, P_c for $P_{tot} - \dot{W}_{dia}$ or $P_{tot} - \dot{W}_{mhd}$, and τ_{rc} for a roughly radiation corrected confinement time. The units for the scaling laws are: τ (sec), I_p (3 MA), B_t (2.5 T), P_c (10 MW), and $\langle n_{ohm} \rangle$ ($2.10^{19} m^{-3}$). The std's of the estimated coefficients are given in parentheses. The correlations in bold-face are at least 8 (for *ELMF*) or 5 (for *ELMY*) times as large as their std under the (unlikely) hypothesis that the corresponding true correlation is zero.

QUENCHING OF THE QUIESCENT H-PHASE IN ASDEX

E.R. Müller, G. Fussmann, G.Janeschitz, H.D. Murmann, A. Stäbler
and the ASDEX- and NI-Teams

Max-Planck-Institut für Plasmaphysik
EURATOM Association, D-8046 Garching, Fed. Rep. of Germany

Introduction

Highest energy confinement during neutral-beam heating is obtained when the discharge is in the quiescent, ELM-free H-mode. The improved energy confinement is linked to higher particle and also impurity confinement / 1 /. In the original ASDEX DV-I divertor configuration and with stainless-steel vessel walls, this resulted in an accumulation of metallic impurities. The excessive radiation power losses terminated the H-phase after about 100 ms / 2 /. After carbonization of the walls aimed at reducing the metallic impurity content and, secondly, the prolongation of the ASDEX NI-heating pulse in the new DV-II divertor configuration / 3 /, much longer quiescent H-phases could be expected. This, however, was not achieved. After a quiescent phase of less than 150 ms, the H-mode converts back into the L-mode.

Plasma parameter evolution

Fig.1 shows the time evolution of various plasma parameters during discharge # 24939 which exhibits an ELM-free H-phase from 1.19 to 1.325 s (I_p = 380 kA, B_t = 2.36 T, $\bar{n}_e(0.95\ s) = 3.7 \times 10^{13}$ cm^{-3}, P_{NI} = 1.3 MW, $D^o \rightarrow D^+$ co-injection, DV-II divertor configuration in single-null operation, slightly carbonized walls).The L-phase between 1.0 and 1.19 s does not become fully stationary (see gas feed rate). There are three characteristic times during the H-phase : Firstly, the L- to H-mode transition at 1.19 s, indicated by the sharp drop in the D_α-signal, is triggered by a sawtooth (see soft X-ray intensity). The improved energy and particle confinement result in rising β_p and $\bar{n}_e$ (the gas valve switches off). Global radiation power losses (P_{RAD}) and local radiation power losses at the plasma centre ($P_{RAD}(0)$) start to grow as well. This is only partly due to the density rise but also due to impurity accumulation, as is demonstrated by the increasing $Z_{eff}(0)$ value at the plasma centre ($Z_{eff}(a/2)$ decreases / 4 /). The time evolution of $P_{RAD}(0)$ is closely correlated with that of soft X-ray and metallic impurity line intensities, which are emitted from the plasma core. The OVI line intensity, more representative of the impurity influx at the plasma edge, is fairly constant. At 1.27 s, the second characteristic time, β_p saturates at a value of 1.2. While density and radiation losses continue to grow, $T_{e,0}$ and $Z_{eff}(0)$ begin to decline. In contrast, $T_e(a/2)$ (see Fig. 2) and $Z_{eff}(a/2)$ go up. Sawteeth are visible on the soft X-ray signal over the entire H-phase. At 1.325 s, the third time mark, the H-mode is terminated by sudden collapse producing simultaneous dips or peaks on most centre and edge signals. While the discharge falls back into the L-mode, it develops transiently its highest $P_{RAD}(0)$ and $Z_{eff}(0)$ values. At about 1.70 s, a really stationary L-mode is reached with much lower values of $T_{e,0}$ and β_p and much higher ones of $P_{RAD}(0)$ and loop voltage (U_L) than during the first L-mode at 1.15 s.

As usual, in the H-mode the n_e profiles are broader and the T_e profiles are higher at the edge than in the L-mode (Fig. 2). But, with the more open DV-II divertor configuration /3 /, the n_e profiles of the H-mode are even flatter in the centre and steeper at the edge than those obtained with the more closed DV-I configuration.

Impurity accumulation at the plasma centre

Fig. 3 shows the central peaking of the P_{RAD} profile during the quiescent H-mode, which is only partly caused by the increase of the n_e and the decrease of the T_e profiles (Fig. 2), but which mainly reflects the accumulation of metallic impurities with medium-Z value at the plasma centre (accumulation of low-Z elements cannot be excluded). Copper originates from the new divertor target plates, iron from the weakly carbonized walls. Accumulation has been simulated quantitatively using the model described in Ref. / 5 / : The influx of metals ($\Phi_{Cu} = 1.5 \times 10^{19}\ s^{-1}$) does not change at the L- to H-mode conversion. But the anomalous diffusion coefficient drops by an order of magnitude ($D_{an} = 0.9 \rightarrow 0.1\ m^2/s$) over the whole plasma cross-section, thus suppressing the impurity outward flow. Since neoclassical inward drift ($v_{Fe}(a/2) = 0.8$ m/s) is not counteracted any more, this leads to impurity accumulation. At the β_p maximum (1.27 s), metal concentrations of 0.5 % are atttained at the plasma centre, with equal contributions of iron and copper.

The extremely high central radiation values ($P_{RAD}(0)$ in Fig. 3) can be sustained stationary during the second L-phase (1.70 s) in association with lower $T_e(r)$ (Fig. 2). In contrast to the first L-phase at 1.15 s, the second L-phase is sawteeth-free.

Quenching of the quiescent H-mode by central radiation losses

Fig. 4 presents the time variation of the global power balance and Fig. 5 of the local one for the plasma centre. Neutral-beam power depositions have been calculated with the FREYA code. The power deposition onto the divertor target plates was not measured, which may explain the missing power in some global balances. The blocking of the energy flow into the divertor during the quiescent H-mode / 6 / is less perfect with the present DV-II divertor (see RAD_{div}) than the former DV-I . Radiation power losses volume-integrated over the outer plasma half-radius (RAD_{edge}) always dominate over radiation losses from the inner half-radius (RAD_{center}). But, it is mainly the enhancement of RAD_{center} by a factor of 5 that raises the global radiation power losses, $RAD_{center} + RAD_{edge}$, from 46% of the total heating power in the ohmic and L-phase(s) to 82 % at the collapse of the H-mode. For compensation of such high radiation losses and the power losses into the divertor, energy is taken from the plasma ($dW/dt < 0$).

The local power balance at the plasma centre reveals, that the quiescent H-mode is quenched when the central radiation power losses $P_{RAD}(0)$ reach 1 $W \cdot cm^{-3}$ which is almost exactly hundred per cent of the local heating power ($P_{OH}(0) + P_{NI}(0)$). Power for transport losses must be drawn from the energy reservoir of the plasma ($dW(0) / dt < 0$).

Conclusion

During the ELM-free H-mode, impurity accumulation in the plasma core occurs as a consequence of improved confinement. The exponentially growing radiation power losses at the plasma centre become as high as the local power input and, thus, quench the H-mode. The β_p saturation (1.27 s) cannot be attributed to radiation power losses from the plasma centre ($r < 20$ cm); perhaps, radiation losses at outer radii play a role.

References

/ 1 / M. Keilhacker, et al., 10th Int. Conf. London 1984 , IAEA 1 (1985) 71.
/ 2 / E.R. Müller, et al., Nucl. Fus. 27 (1987) 1817.
/ 3 / H. Niedermeyer, et al., Pl. Phys. and Contr. Fusion 30 (1988) 1443.
/ 4 / K.H. Steuer, et al., this conference.
/ 5 / G. Fußmann, et al., 8th PSI conference, to be published in Journ. Nucl. Mat.
/ 6 / E.R. Müller, et al., Journ. Nucl. Mat. 121 (1984) 138.

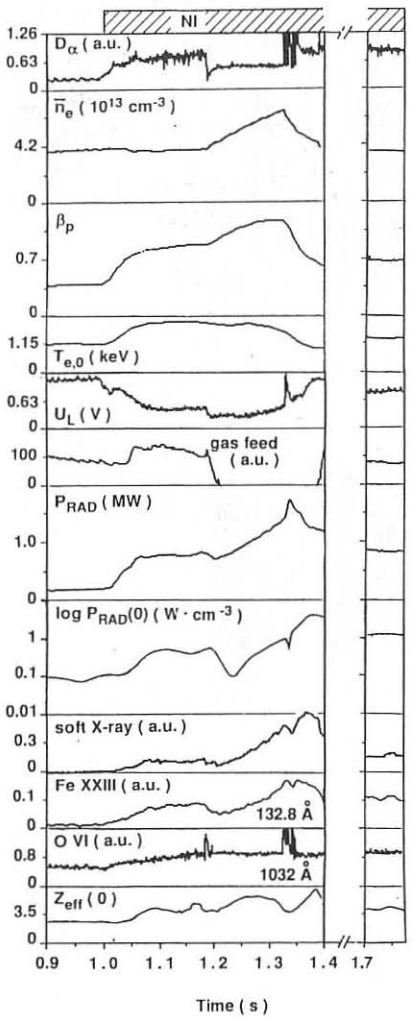

Fig.1 : Time evolution of various plasma parameters during discharge # 24939 which shows an ELM-free H phase.
(I_p = 380 kA, B_t = 2.36 T, P_{NI} = 1.3 MW, $D^o \rightarrow D^+$, DV-II divertor configuration in single-null operation (Δz= 2cm), carbonized walls)

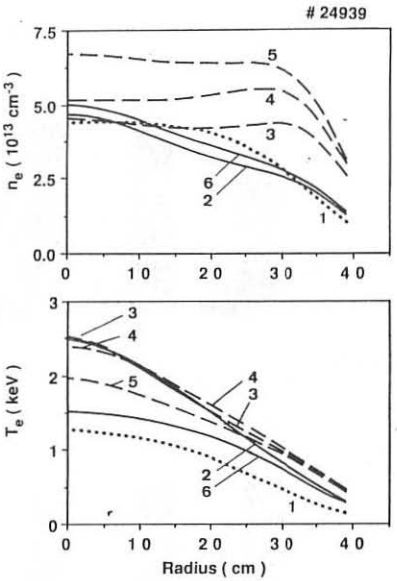

Fig.2 : Radial profiles of electron density n_e and temperature T_e at typical times during discharge # 24939 (the L or H mode character is indicated behind the time value).
(1) t = 0.950 s
(2) t = 1.150 s (L)
(3) t = 1.210 s (H)
(4) t = 1.270 s (H)
(5) t = 1.325 s (H)
(6) t = 1.700 s (L)

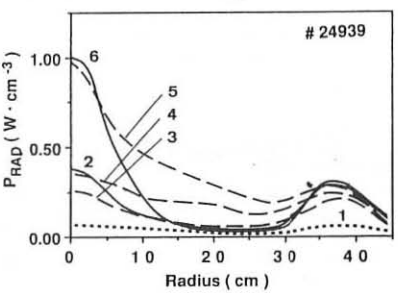

Fig.3 : Bolometrically determined radial profiles of radiation power density (at same times as in Fig. 2).

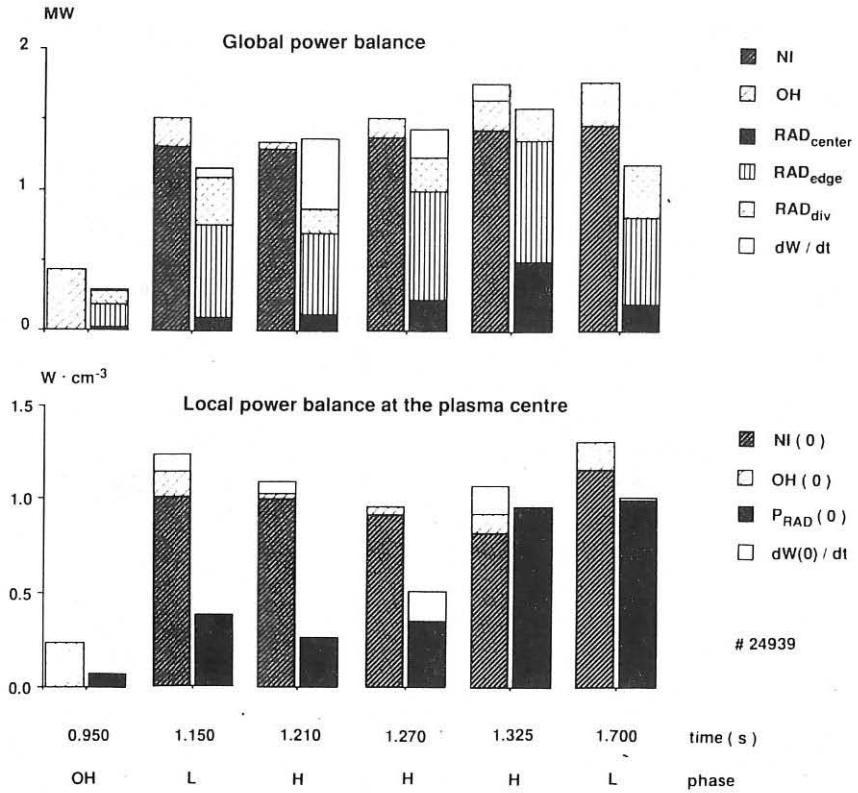

Fig. 4 (above) :
Time evolution of the global power balance of discharge # 24939 :

Power input channels : the neutral-injection heating power (NI) and the Ohmic heating power (OH).
Power loss channels : bolometrically determined radiation and neutral particle power losses, volume-integrated over the inner plasma half-radius (RAD_{center}) and over the outer half-radius (RAD_{edge}), and the volume power losses of the plasma within the divertor chambers (RAD_{div}), determined by bolometers as well.

Fig. 5 (below) :
Time evolution of the local power balance at the plasma centre of discharge # 24939 :

$P_{RAD}(0)$ denotes the bolometrically determined local radiation power losses at the plasma centre, and NI(0), OH(0), dW(0)/dt represent also local values.

Dependig on their sign, the time derivatives of the respective plasma energy contents, dW/dt and dW(0)/dt, are added to the input or loss channels.

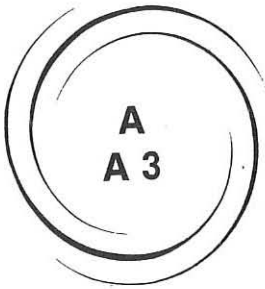

TOKAMAKS
THEORY

A3

ON THE ACCESSIBILITY TO THE SECOND REGION OF STABILITY IN TFTR-LIKE PLASMAS*

M.S. CHANCE and K.M. McGuire

PRINCETON PLASMA PHYSICS LABORATORY
P.O. BOX 451, PRINCETON, NJ 08543

Access to the second region of stability to ballooning modes at moderate aspect ratios generally requires a finite amount of triangularity and probably some degree of elongation. These requirements are contrary to the design parameters of the TFTR configuration and although the size and flexibilty of the machine, and perhaps minor hardware modifications could allow for some of these effects, it seems worthwhile to consider whether stable equilibria exist and whether accessibility to these can be achieved in the present configuration. (An obvious technical advantage is the absence of the vertically axisymmetric instability.) One way to do this is to raise the value of q(0) as is evidenced by theoretical predictions [1-3] and the results of the DIII-D device [4]. This method fortunately parallels the recognition and development of various forms of current-broadening schemes such as, for example, beam-driven, or bootstrap currents, lower hybrid, and current ramping.

Some of the results of numerical optimizaton studies presented in [3] indicate that second stability operation should be possible for a circular cross-section plasma with an aspect ratio of 3, provided q(0) is substantially above unity. The problem of accessibility is more delicate. To facilitate this study we make use of the CAMINO code [5] which is based on the perturbative method of [6] to generalize the familiar s-α diagram [7] to arbitrary toroidal geometry. Applying the code to a specified equilibrium generates a three-dimensional space in (p',q',ψ) within which the equilibrium can be seen in its own stability environment, and thus the profiles can be iterated as desired in order to avoid the unstable regions. It should be pointed out that in most cases the concept of the 'second region' is nebulous since both the first and the second region are simply connected, especially when accessibility is being acheived. However, a benefit of our method is that the relation of the plasma with respect to these regions becomes clear.

To begin this study we first attempt to find equilibria which lie in the second region. We choose a plasma with a circular cross-section of radius 83 cm. centered at a major radius of 250 cm. This is chosen to roughly fill the TFTR chamber so as to maximize the current and also to enable the plasma to be situated near the vacuum shell to provide for some stabilization against surface modes. The largest plasma possible in TFTR would actually be centered at 262 cm. with radius 97 cm. Other fixed parameters for the equilibria studied are q(0)=2.5, q(1)=7.5 and q'(0)=0.5, where q'(y)=dq/dy and $y=\psi/\Delta\psi$. Some relevant parameters are shown Table 1. for three equilibria labelled A, B, and C. β_p is defined with respect ot the square of the curent, I, and the stability notation in the table refers only to ideal, infinite n ballooning modes. The results of applying the CAMINO code are presented graphically as 3-D s-α plots. Three projections, i.e., s-α, α-ψ, and s-ψ, are shown for each equilibrium. S and

$\propto$ are normalized values of q' and p'. Where similar pairs are shown these are to be viewed stereoscopically, i.e, by looking at both figures simultaneously so as to merge them together. The space curve of the equilibrium is depicted as the heavy solid line. To aid in the visualization the magnetic axis 'o' is labelled, and the unstable region of this line is crossed in several of the figures. The two net-like surfaces are the first and second stability boundaries. Although the latter are actually connected along a common curve near their low shear boundary, we have not extrapolated the data to show this connection. The grid seems relatively coarse in the figures, but the stability of each case is verified with our standard ballooning code on a much finer scale.

In the projections of Fig. 1 a substantial portion of the outer half of the plasma of case A is unstable. The stability seen at the axis and edge of the plasma is consistent with the pressure profile chosen, i.e., $p(y)=p\ (1-y^2)^2$, so that p' vanishes at the origin and at the edge of the plasma. It's clear from the figure that accessibility to the second region may be attained by going under the instability barrier, i.e., by lowering the shear. This remains to be shown. We now increase the pressure. As seen in Fig. 2 for case B, this places a large central portion of the plama in the second region. However the equilibrium curve intersects the instability boundaries as it tracks back to small p' at the plasma edge. On the other hand the figure suggest that decreasing the shear from its value of q'(1)=20 at the outer edge of the plasma may put the unstable portion of the equilibrium under the instability barrier. The stable results for case C in Fig. 3 shows that this is achieved when the shear is decreased so that q'(1) is 12.0. The case where q'(1)=15.0 was still unstable and is not shown here. Moreover, by comparing Fig. 2 and 3 it is seen that the instability barrier actually also rises as the shear is decreased. This tendency for the instability near the edge and its dependence on the shear there may have some relevance to the edge relaxation phenomena commonly observed in H-mode plasmas in tokamaks.

Present TFTR results shows a poloidal beta limit at $\approx$ 2 with values of $\varepsilon\beta_p \approx 0.7$. For these discharges the lack of sawteeth suggests that q(0) is above 1. In addition, averaged betas of $\approx$ 1% have been obtained with $B_0 \approx$ 2.2T. For present TFTR parameters, case A seems obtainable and even though it is unstable over part of the profile, it is getting close to the second region. Case C has a large $\langle\beta\rangle_0$ % $\approx$ 2.37 and substantially exceeds the Troyon limit, so it seems reasonable that the best possibility of getting close to the second region is by high poloidal beta operatioin on TFTR. However, with judicious profile control techniques these limitations may be relaxed enough for achieving second stability.

We have found a relatively high beta equilibrium considered to be in the second stability region and which is compatible with the TFTR geometry. The question of accessibility to such equilibria is being addressed. The use of the CAMINO code should prove useful in finding possible paths under the instability boundaries.

*This work supported by US DoE Ccntract # DE-ACO2-76-CHO3073.

[1] Sykes, A., and Turner, M. F., in Controlled Fusion and Plasma Physics (Proc. 9th European Conf. Oxford, 1979) UKEA, Culham Lab., Abingdon (1979) 161.
[2] Coppi. B., Comments in Plasma Physics. 6,109 (1981).
[3] Sabbagh, S.A., Phillips, M.W., Navratil, G.A., and Todd, A.M.M., U.S.-Japan Workshop on Kinetic Modifications of MHD modes, Second Stability, and Alpha Particles in Toroidal Systems, January 9-13,1989, PPPL Princeton.
[4] Simonen, T.C., et al., Phys. Rev. Lett. 61, 1720 (1988).
[5] Chance, M.S., in Theory of Fusion Plasmas (Proceedings, Varenna, Italy, September,

1987).
[6] Greene, J. M., and Chance, M. S., Nucl. Fusion 21 (1981) 453.
[7] Connor, J. W., Hastie. R. J., and Taylor, J. B., Proc. R. Soc. London A365 (1979) 1.

TABLE 1.

	$q'(1)$	I/B_o	$\langle\beta\rangle_o$%	β_{pc}	$\langle\beta\rangle_o aB_o/\mu_o I$	Stability
A	15.0	0.26	0.75	1.72	1.94	Unstable
B	20.0	0.356	2.78	3.12	5.28	Unstable
C	12.0	0.335	2.37	2.98	4.77	Stable

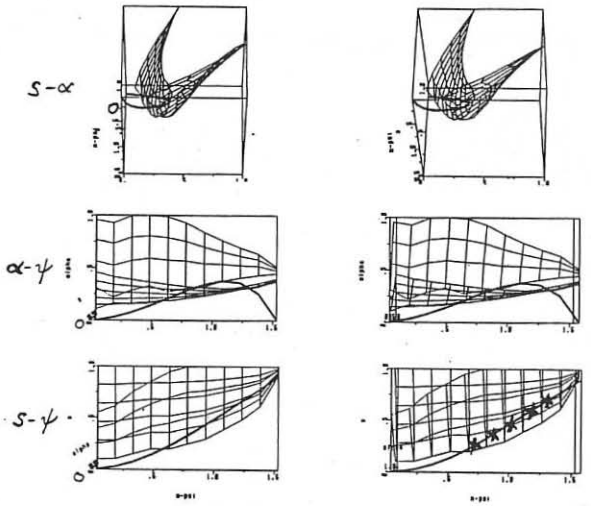

Fig. 1. Case A. Unstable within a large central portion of the plasma.

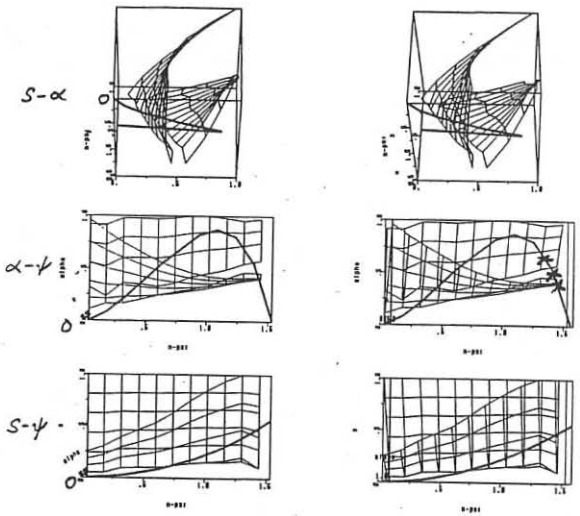

Fig. 2. Case B. A high beta case mostly in the second region but still unstable near the edge.

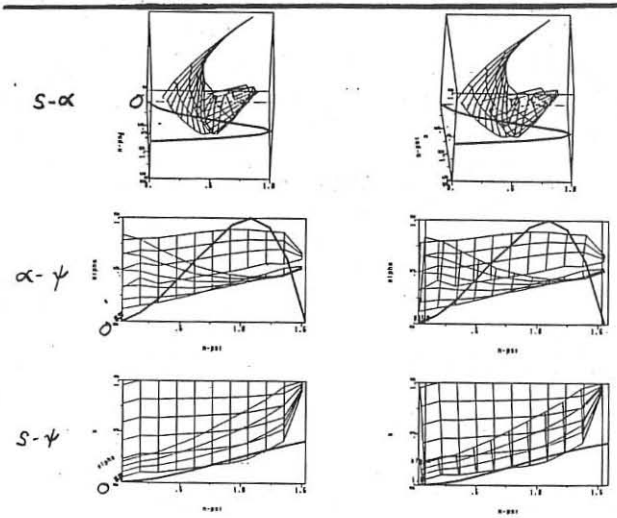

Fig. 3. Case C. A high beta case stabilized by decreasing the shear at the edge.

COLLISIONLESS FAST IONS DYNAMICS IN TOKAMAKS

A. Becoulet, D.J. Gambier, P. Grua, J-M. Rax, J-P. Roubin

Association EURATOM-CEA sur la Fusion Contrôlée,
CEN Cadarache B.P. n°1, 13108 Saint-Paul-lez-Durance, France

INTRODUCTION

In thermonuclear plasmas of the next Tokamak generation, the dynamics of fusion products needs to be understood as it could well influence the reactor performances. In such a low collisionnality regime, a careful analysis of the associated transport and relaxation processes is required. For this program to be completed, the effect of a perturbating field on fast particle individual motion must be precisely evaluated. This imposes to address the question within the Hamiltonian mechanics. In this framework, resonances of particle trajectories with low frequency fields arise naturally as a potential mechanism for transport and relaxation. The latter processes result from the destruction of adiabatic invariants when a stochasticity threshold is reached. Then, the quasi-linear theory is applicable, and diffusion coefficients can be derived. In the following, the method will be briefly reviewed and two reactor relevant situations analysed : heating of energetic ions under the effect of a compressionnal wave and alpha-particle losses induced by the toroidal field ripple.

HAMILTONIAN DESCRIPTION OF COLLISIONLESS TRANSPORT

In an axisymmetric unperturbed tokamak magnetic configuration, the particle trajectory is integrable and described by a set of three action-angle variables $\{J_k,\Phi_k\}$. Its hamiltonian $H_0(J_k)$ depends only on the action variables and the motion is quasi-periodic : the actions remain constant and the angles rotate linearly ($\Phi_k = \omega_k(J_k)t + \Phi_{0k}$). Essentially, the effect of low frequency perturbations is to disrupt this adiabatic behaviour in regions of the phase space where an efficient coupling (i.e. resonances) between fields and particles occurs. In order to identify those regions, the hamiltonian perturbation is expanded as a Fourier series :

$$\delta H = \sum_{n_k} h_{n_k} \exp(in_k\Phi_k + i\omega t) + \text{complex conjugate}$$

Resonant interaction takes place when the phase of the perturbation is stationnary along the unperturbed trajectory. For a given triplet of integers $\{n_k\}$, the location of the resonance surfaces is defined by : $\Omega = n_k\omega_k(J_k) + \omega = 0$. Around these surfaces an island like structure emerges and above a stochastic threshold (S >1) [1], resonance overlapping destroys this regular behaviour; S is the product of the island width $2\Delta\Omega_I = 4\sqrt{2\alpha h_{n_k}}$, ($\alpha = n_k n_l \dfrac{\partial^2 H_0(J)}{\partial J_k \partial J_l}$) by the density of resonant surfaces. The stochastic behaviour legitimates the random phase approximation and the quasi-linear theory.

COMPRESSIONNAL WAVE HEATING OF ENERGETIC IONS

In the case of ICRF, wave particle resonance occurs when the cyclotron frequency of the particle matches the RF frequency at some points along its trajectory. An irreversible transfer of energy (heating) is possible if the phase of the particle get randomised in between two successive resonance crossings. For low energy ions, the randomisation is insured by both collisions and intrinsic stochasticity [2]. When the wave spectrum contains only one toroidal number N, the fast ion population recovers its adiabatic behaviour, but when a full toroidal wave spectrum is considered, stochastic heating reappears.

To demonstrate that point, we focus on passing particles. Their motion is represented by the following set of action-angle variables for the cyclotronic, poloidal and toroidal motions :

$$J_1 = -\frac{m}{e}\mu \qquad J_2 = e\Phi_T(J_3/e) + q(\Psi_P)R_0 m v_{//} \qquad J_3 = e\Psi_P + mR_0 v_{//}$$

$$\Phi_1 = \phi_c + \frac{r_G \bar{\omega}_c}{R_0 \omega_2}\sin(\theta) \qquad \Phi_2 = \theta \qquad \Phi_3 = \phi$$

with the magnetic poloidal and toroidal fluxes Ψ_P, Φ_T; major radius R_0; poloidal and toroidal angles θ and ϕ; safety factor $q(\Psi_P)$ and for the particle : charge e; mass m; guiding centre radius r_G; magnetic moment μ; parallel velocity $v_{//}$; cyclotronic phase and averaged pulsation ϕ_c, $\bar{\omega}_c$.

The compressional field is taken as a radially running wave with one toroidal harmonic N and :

$$\delta H = e\, v_r\, a \exp i(\omega t + kr) \exp(iN\Phi_3) + c.c.$$

The fundamental harmonic resonance ($n_1 = 1$) gives rise to a family of resonances in the phase space, labelled by $(1, n_2, N)$, of density $1/\omega_2$. The stochasticity threshold is :

$$S = 4\frac{q}{v_{//}}\left(N + \frac{n_2}{q}\right)\sqrt{2\frac{e a v_\perp}{m}}\sqrt{\frac{2}{\pi x}}$$

where $2x = 2r_G/R_0\ (\bar{\omega}_c/\omega_2)$ is the number of effective resonances.

If for the low energy particles, S is greater than 1 and stochastic heating is effective, it is no longer the case for highly energetic ones as S scales with $v^{-1/4}$. For a field strength of 50 V/cm, stochasticity disappears for alpha-particles of energy typically greater than 100 keV.

However for a wave toroidal spectrum, the resonance families are superimposed leading to a higher resonance density and to a destruction of the regular trajectories (Fig.1). Applied to α-particles in a reactor, ICRH continues to take place, allowing the use of the quasi-linear theory. This gives confidence in the use of 2-D ICRF modelling even for high energetic particles and to the further Fokker Planck calculations.

STOCHASTIC INSTABILITY OF ENERGETIC TRAPPED IONS IN THE T.F. RIPPLE

In the transport regime relevant for α-particles in a reactor, i.e. the ripple banana drift regime, the neoclassical diffusion coefficient scales as the particle collisionnality and is consequently very low. As already pointed out [3,4], collisionless effects may dominate the α transport. In the hamiltonian analysis, the trapped α-particle motion in presence of a ripple perturbation

$\delta B\cos(N_c\phi)$ is strongly influenced by the existence of resonant surfaces. For this class of particles, many resonances appear because the bounce frequency $\omega_b=\partial H_0/\partial J_2$ and the precession frequency $\omega_p=\partial H_0/\partial J_3$ are of the same order. Here J_2 and $J_3=e\Psi_p(r)$ ($r=r_G$) are the invariants associated respectively to the bounce (Φ_2) and precession (Φ_3) motions. The Fourier expansion of the perturbation writes :

$$\delta H = \sum_{n_2=-\infty}^{+\infty} \frac{1}{2}\mu\,\delta B\, J_{n_2}(N_c q\,\theta)\exp(iN\Phi_3+in_2\Phi_2) + \text{complex conjugate}$$

where $J_{n2}(N_cq\theta)$ reflects the averaging over the bounce motion (θ is the banana tip poloidal angle). The resonant surfaces are given by $\Omega=N_c\omega_3+n_2\omega_2=0$ and their radial positions for a typical reactor case are shown on Fig.2. Using first order ε expansions ($\varepsilon=r/R_0$) of the action-angle variables, the stochasticity threshold takes the following form :

$$S = f(s,\theta)\,\frac{N_c q^2}{\varepsilon}\frac{\rho_c}{r}\,\sqrt{\delta(r)\,J_{n_2}(N_c q\,\theta)}$$

where ρ_c is the larmor radius, $\delta(r)=\delta B/B$ the ripple value and f a function of the shear parameter $s=r/q(dq/dr)$ and of the banana tip poloidal angle θ (f is of order of one and for strongly trapped particles $f = 4\,(3s/2 - 1)^{1/2}$). The critical value of δ scales as ρ_c^2 and can be very low for energetic particles. This scaling is quite different from the one proposed in [4]. However, for 3.5 MeV α-particles in an INTOR-like device, we obtain the same critical value ($\delta\approx10^{-3}$). This expression has been successfully confirmed by Poincaré maps (fig.2). Above this threshold, i.e. above a critical minor radius, the motion becomes stochastic and leads to a radial diffusion at constant energy and magnetic momentum. The diffusion coefficient is given by the quasi-linear theory. For typical trapped particles ($\theta\approx1$ and $N_cq\theta > n_2$) :

$$D_{QL} = \frac{\sqrt{2}}{4}N_c\delta^2\rho_c^2\frac{\nu}{\theta\, r}\frac{q^2}{\varepsilon^{3/2}}$$

Under typical reactor conditions, values of order 10 m^2s^{-1} are easily reached for fusion products with $\delta=10^{-3}$, leading to fast losses.

CONCLUSIONS

We have investigated two reactor relevant situations where collisionless processes dominates the dynamics of fast ions population :

- Concerning ICRF, provided that a realistic wave spectrum is considered, intrinsic stochasticity allows for the use of the quasi-linear theory even for very energetic ions.
- Concerning the TF ripple, we have shown that this perturbation dominates the trapped α-particles transport as soon as $\delta\approx10^{-3}$.

Such kind of stochastic behaviour is of major importance for the next tokamak generation and gives constraints on the forthçoming fusion reactor designs.

REFERENCES

[1] Chirikov B.V., Physics Report 52 (1979) 265.
[2] Gambier D.J., Samain A., Nucl. Fus. 25 3 (1985) 283.
[3] Goldston R.J., White R.B., Boozer A.H., Phys.Rev.Lett. 47 (1981) 647.
[4] White, R.B. et al., 12th Int. Conf. on Plasma Physics, Nice (1988) IAEA, paper D-2-4.

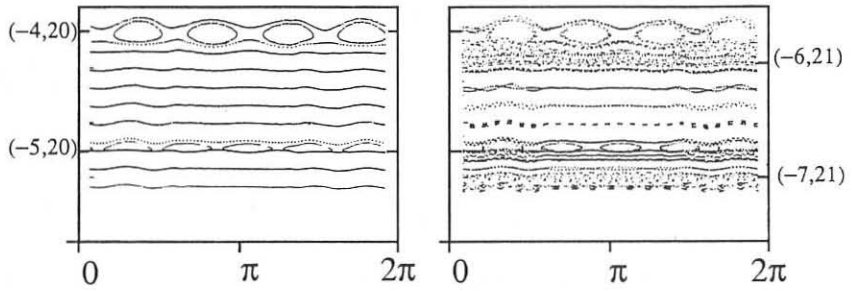

Figure 1: Poincaré maps representing $J_1(\Phi_2)$ for 500 keV α-particles in presence of an ICRF field. Resonant surfaces are labelled by (n_2,N). Left : with a single N=20 harmonic, no resonance overlapping is achieved. Right : a second N=21 harmonic is superimposed, leading to overlapping and stochastic areas.

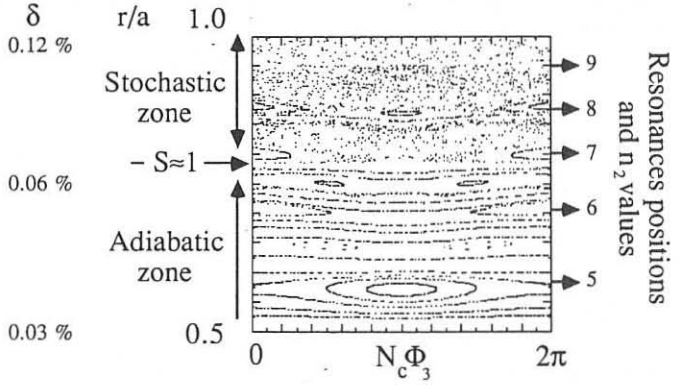

Figure 2 : Poincaré map for α-particles in a reactor case with low ripple ($R_0/a=4$, $\rho_c/a=0.04$, $\theta=1$, $q_{edge}=3$, $N_c=12$, $\delta_{edge}=0.12$ %, $\delta(r) \propto R^{N_c}$) : the radial positions of the particles (related to the invariant J_3) are plotted as a function of their precession angle Φ_3 when they cross the equatorial plane. The figure also displays the resonances and the ripple values. Two different regimes can be clearly identified: stochastic (r/a>0.8) and adiabatic (r/a<0.7).

STUDY OF THE BEHAVIOUR OF CHAOTIC MAGNETIC FIELD LINES IN A TOKAMAK

M. Hugon, J.T. Mendonça and P.H. Rebut

JET Joint Undertaking, Abingdon, Oxon, OX14 3EA, UK

1. INTRODUCTION

One plausible explanation for the observed anomalous energy losses in tokamaks is the existence of a confinement region in the plasma, where magnetic islands coexist with stochastic magnetic field lines [1]. It is the purpose of the present work to elucidate the statistical behaviour of the stochastic field lines. This is done by numerically integrating the field line equations. Assuming $2N_0 + 1$ magnetic island chains centered at radial positions $x_N = N/m$, where m is the poloidal mode number, the field line equations are:

$$\frac{dx}{dz} = \frac{B_x}{B_z} = \frac{\gamma^2}{16m} \sum_{N=-N_0}^{+N_0} \sin(Nz - my + \phi_N); \quad \frac{dy}{dz} = \frac{B_y}{B_z} = x \qquad (1)$$

γ is the overlapping parameter and ϕ_N are the phase shifts, which are assumed to be randomly distributed among the island chains. In Eqs. (1), x is normalised to $\Delta = 1/m$ and the poloidal and toroidal variables, y and z, are in radians. Note that, in the limit $N_0 \to \infty$ and for $\phi_0 = \ldots = \phi_N = \text{const}$, Eqs. (1) exactly reduce to the standard map [2].

2. CROSS SECTION OF STOCHASTIC FLUX TUBES

Let us call $\sigma(N)$ the normalised cross section of the flux tubes associated with the stochastic field lines which leave the 0th island chain and attain the Nth island chain. It is defined by the expression [1]:

$$\sigma(N) = \frac{2}{S} \iint \frac{B_x(\gamma)}{B_z} H(B_x)\, H^N_{cross}\, dydz; \qquad S = \iint dxdy \qquad (2)$$

where $H(B_x)$ is the Heaviside function and H^N_{cross} is equal to 1 if the field line attains the Nth island chain and zero otherwise. The numerical results obtained from Eqs. (1) and (2) with 9 island chains can be described by:

$$\sigma(1) = A(\gamma - \gamma_c)^B \qquad (3)$$

where $A = 0.47 \pm 0.13$, $B = 2.50 \pm 0.23$ and $\gamma_c = 0.75 \pm 0.05$ for $\gamma_c \leq \gamma \leq 2$. The error bars are not due to numerical errors but to deviations induced by the particular choices of ϕ_N.

Using a recurrence analysis, it is possible to show that:

$$\sigma(N) = \sigma(1)\ [1 + (N - 1)(1 - \alpha)]^{-1} \qquad (4)$$

where α is the fraction of the stochastic field lines which cross one island chain. Eq. (4) was checked numerically, using for α the arithmetical mean of the values $\alpha(N) = N(N-1)^{-1} - [\sigma(1)/\sigma(N)]^{cal}(N-1)^{-1}$. The results are summarised in Table I, which shows that the recurrence relation is very well satisfied.

3. STOCHASTIC VOLUME

The normalised volume filled by the stochastic field lines, V_s, and the normalised volume occupied by the magnetic islands, V_i, is defined by:

$$V_{s,i} = \frac{1}{S} \iint \frac{B_x(r)}{B_z} H(B_x)\ L_{s,i}\ dydz \qquad (5)$$

where the lengths $L_{s,i}$ are:

$$L_s = 2H^{1}_{cross}[z(x=1) - z_0(x=0)]/2\pi + 2H^{0-1}_{cross}[z_1(x=0) - z_0(x=0)]/2\pi + H^{1-1}_{cross}[z_2(x=0) - z_0(x=0)]/2\pi$$

$$L_i = [1 - (H^{1}_{cross} + H^{0-1}_{cross} + H^{1-1}_{cross})][z_2(x=0) - z_0(x=0)]/2\pi$$

H^{0-1}_{cross} (resp. H^{1-1}_{cross}) is equal to 1, if the field line attains the island chain -1, (resp. $+1$ or -1) after having crossed the plane $x = 0$ once (resp. more than once), and zero otherwise. $z(x = 1)$ is the toroidal coordinate of the field line in the plane of the chain $+1$ and $z_i(x = 0)$ are the toroidal coordinates of the field line in the plane of the chain 0 after i crossings of this plane.

The computation of Eqs. (5) using Eqs. (1) indicates that the relation $V_s + V_i = 1$ is verified. For $\gamma < \gamma_c$, the island volume V_i is shown to increase with γ according to $2\gamma/\pi$, as expected. For $\gamma > \gamma_c$, the magnetic surfaces of the island are destroyed by stochasticity and V_i decreases until it reaches 0, when γ is close to 1.5.

4. DIFFUSION COEFFICIENT

The mean number of turns in the toroidal direction to cross N island chains is determined by $T(N) = V(N)/\sigma(N)$, where $V(N)$ is defined by an expression formally identical to Eqs. (5), but with $L(N) = 2H^{N}_{cross}[z(x = N) - z_0(x = 0)]/2\pi$. The numerical results for $T(N)/T(1)$ are represented in figure 1 as a function of N, for different values of γ. $T(N)$ is very close to $N^2T(1)$ for $\gamma = 1.3$ and 1.35, which is characteristic of a diffusion process across the island chains. However, for $\gamma \geq 1.8$, there is a slight deviation from the diffusion, since $N < T(N)/T(1) < N^2$. These effects are described by a kinetic equation for the field lines containing a diffusion and a propagation term [3].

The diffusion coefficient is defined as $D = 1/T(1)$. The average of

the numerical values obtained for D from Eqs. (1) with different phases ϕ_N is given in figure 2 as a function of γ. Also shown is a fit of the computed results valid for $\gamma_c \leq \gamma \leq 2$:

$$D = A'(\gamma - \gamma_c)^{B'} \qquad (6)$$

where A' = 1.25 ± 0.30 and B' = 2.10 ± 0.40. Figure 2 shows that Eq. (6) is in good agreement with the data obtained for D = 1/T(1) using the standard map, D^{SM}, for $\gamma_c \leq \gamma \leq 1.1$, indicating that the standard map provides a good approximation of the exact field line calculation for values of γ close to γ_c. However, D^{SM} departs from Eq. (6) for larger values of γ and follows the quasi-linear diffusion coefficient $D^{QL} = \pi^2\gamma^4/128$ before starting to saturate for $\gamma \geq 1.75$. The saturation is due to the fact that, for the standard map, T(1) can never be less than 1. A proper definition of D prevents the well known strong oscillations of D^{SM} around D^{QL} [4].

5. CONCLUSION

The recurrence relation (4) on $\sigma(N)$ has been numerically tested by integrating the field line equations. The same computation has shown that the behaviour of the stochastic field lines is close to a diffusion process, when islands are in equilibrium with a stochastic region. The diffusion coefficient for the stochastic field lines D is defined as the inverse of the average number of toroidal turns to cross one island chain. The computation of D from Eqs. (1) is valid for values of γ up to 5. The island and stochastic volumes have been also defined and computed, ensuring that the equality $V_i + V_s = 1$ is satisfied.

ACKNOWLEDGEMENTS

We would like to thank Dr. M. Brusati for his help in developing the numerical code.

Table I

Comparison between the numerical results $[\sigma(N)/\sigma(1)]^{cal}$ and those obtained through Eq. (4), $[\sigma(N)/\sigma(1)]^{rec}$, using for α the arithmetical mean α^{av} of $\alpha(N) = N(N-1)^{-1}-[\sigma(1)/\sigma(N)]^{cal}(N-1)^{-1}$.

γ	1.30		1.35		1.80		3.00	
α^{av}	0.461		0.438		0.524		0.629	
$\frac{\sigma(N)}{\sigma(1)}$	cal	rec	cal	rec	cal	rec	cal	rec
N = 2	0.651	0.650	0.642	0.640	0.679	0.678	0.671	0.729
3	0.473	0.481	0.465	0.471	0.497	0.512	0.589	0.574
4	0.390	0.382	0.376	0.372	0.425	0.412	0.496	0.473
5							0.448	0.402

REFERENCES

[1] P.H. Rebut et al, in Plasma Physics and Controlled Nuclear Fusion Research (Proc. 11th Int. Conf. Kyoto, 1986), Vol.2, IAEA, Vienna, 187(1987).
[2] B.V. Chirikov, Phys. Reports 52, 265 (1979).
[3] M. Hugon, J.T. Mendonça and P.H. Rebut (1989) - to be published.
[4] Y.H. Ichikawa, T. Kamimura and T. Hatori, Physica 29D, 247 (1987).

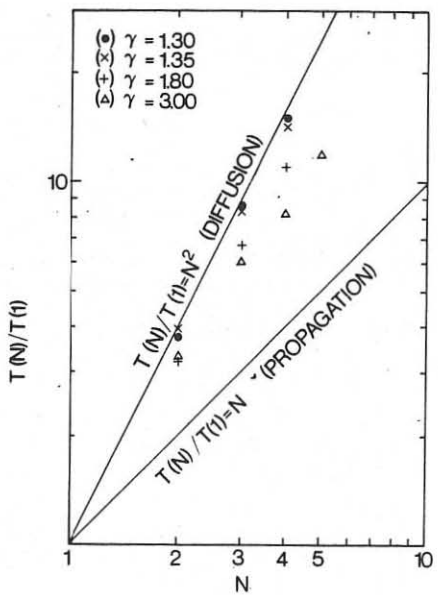

Fig. 1

Mean number of turns T(N) in the toroidal direction for a stochastic field line to cross N island chains.

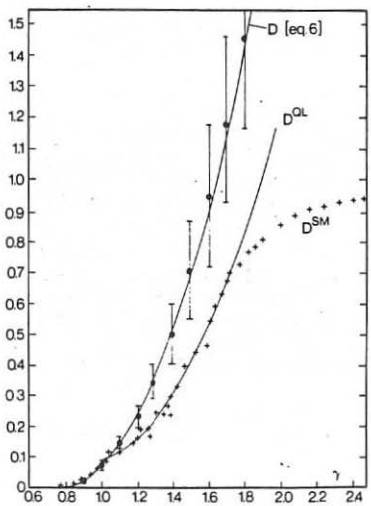

Fig. 2

Diffusion coefficient. The numerical results (♠) computed from eq. (1) are compared with eq. (6) with the quasi-linear curve D^{QL} and with those obtained from the standard map, D^{SM}.

LIMIT ON β_p DUE TO GLOBAL MODES IN IGNITED PLASMAS

F. Pegoraro and F. Porcelli

JET Joint Undertaking, Abingdon, Oxon., OX14 3EA, UK

B. Coppi and S. Migliuolo

MIT, Cambridge, Mass. 02139, USA

ABSTRACT

It is shown that fusion produced α-particles can lead to stable values of β_p that are considerably larger than those predicted by the ideal MHD theory. The stabilising mechanism is effective if a combined criterion is met, involving among others, the area of the plasma cross-section where q is below unity and the ignition temperature. The implications of this criterion are discussed in terms of envisaged ignition scenarios.

INTRODUCTION

Internal MHD modes, such as sawteeth and fishbone oscillations, affect the central hottest part of the plasma column and can damage the plasma performance, hindering the achievement of ignition conditions. These modes cause a repetitive failure of the central plasma confinement leading to a spatial redistribution of the plasma energy. In addition, these modes spread, and possibly expel from the plasma, the α-partices which are produced at the centre of an ignited D-T plasma. On the other hand this loss of confinement can also be beneficial, e.g. in avoiding ^{4}He ash accumulation at the plasma centre once the plasma is ignited, or in preventing the fusion thermal runaway. Control over the onset of the internal modes becomes particularly important for plasmas where the magnetic winding parameters q is expected to fall below unity over a sizeable portion of the poloidal cross-section.

In this paper we show, along the analysis of Refs. [1,2] that the α-particles produced by the fusion reactions, naturally exert a controlling influence. This can enhance the stable values of the poloidal beta β_p of the bulk plasma by as much as three times its threshold value, as determined within the ideal MHD approximation. However, this control turns out to be ineffective if the area where q is below one is large (say $r_o/a \gtrsim 1/2$, with $q(r_o) = 1$ and a the mean radius of the plasma column). Besides r_o/a, key parameters are the ratio between the magnetic curvature + ∇B drift frequency of the α-particles and the Alfvén frequency, which scales as $n^{1/2}/(r_o B^2)$, and the central ignition temperature T_o ($T_{eo} = T_{io}$ is assumed). The latter controls the ratio between the α-particle $\beta_{p\alpha}$ at ignition and β_p. If ignition is to be achieved at high values of T_o (say $T_o \gtrsim$ 20-25keV) the effect of the α- particles on internal modes may turn from stabilising to destabilising. This resurgent instability [3] interacts with the newly born, fully energetic α's, and can thus affect the ignition energy balance severely.

STABILITY DOMAIN

The relevant dispersion relation, which governs internal m = 1 modes in the presence of energetic particles, as derived e.g. in [1], reads

$$[\omega(\omega-\omega_{di})]^{1/2} = i\omega_A[\lambda_H + \lambda_K(\omega)] \qquad (1)$$

where $\omega_{di} = [(k_\theta\, c/en\, B)(dp_i/dr)]_o$ is the bulk ion diamagnetic frequency at $r = r_o$, $\lambda_H \equiv \gamma_{mhd}/\omega_A \sim O(\epsilon_o^2\, \beta_p)$ is the ideal driving term, $\epsilon_o = r_o/R_o$ and $\omega_A = V_A/R_o\sqrt{3}$ is the Alfvén frequency. The complex function $\lambda_K(\omega) \sim O(\epsilon_o^{3/2}\, \beta_{p\alpha})$ gives the contribution of the α-particles and can be approximated by

$$\lambda_K(\omega) \simeq (\epsilon_o^{3/2}\beta^*_{p\alpha}/s_o)\ \lambda_K(\omega/\bar\omega_{D\alpha}), \qquad (2)$$

where $s_o = d\ \ell n\ q/d\ \ell n\ r|_{r=r_o}$, $\beta^*_{p\alpha} = -[8\pi/B_p^2(r_o)] \int_o^1 dx\ x^{3/2}\ (dp_\alpha/dx)$, $\bar\omega_{D\alpha}$ is the bounce averaged magnetic drift frequency at $r = r_o$ of deeply trapped α-particles with energy $\epsilon = 3.5$Mev, and the form factor λ_K, which is shown in Fig. 1, is largely independent of the plasma parameters. An isotropic slowing down distribution function has been assumed.

Solving (1) for $\omega = \omega_R \equiv$ Re ω, we obtain the marginal stability curve in the $\lambda_H - \beta_{p\alpha}$ plane where

$$\lambda_H = (\omega_A\ \lambda_H/\bar\omega_{D\alpha}) \equiv \gamma_{mhd}/\bar\omega_{D\alpha}, \qquad \beta_{p\alpha} = (\omega_A\ \epsilon_o^{3/2}/\bar\omega_{D\alpha}\ s_o)\ \beta^*_{p\alpha} \qquad (3)$$

This curve is plotted in Fig. 2 for $\omega_{di}/\bar\omega_{D\alpha} = 5\times10^{-2}$. The portion of the unstable domain, immediately above the stability curve to the left of its maximum, corresponds to fishbone oscillations [4] with $\omega \sim \omega_{di}$ which resonate with slowed down α-particles. The portion to the right of the

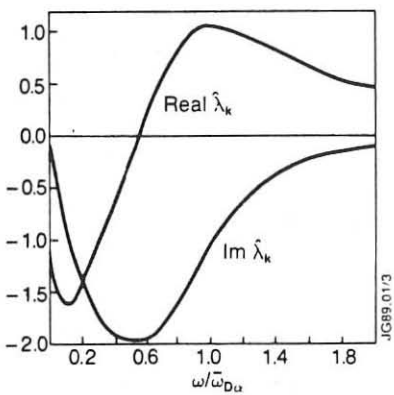

Fig. 1: Real and imaginary parts of λ_K defined in Eq. (2).

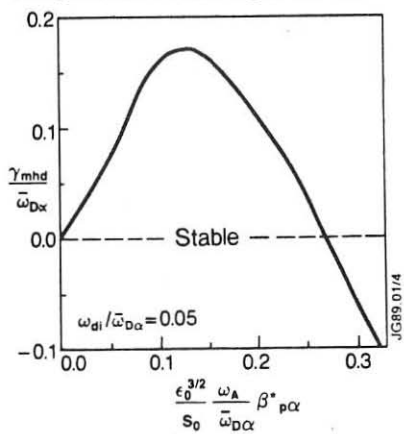

Fig. 2: Stability domain in the $\lambda_H - \beta_{p\alpha}$ plane (see Eq. (3)).

maximum corresponds to fishbone oscillations [3] with $\omega \sim \bar{\omega}_{D\alpha}$, driven by the precessional motion of the α-particles. Further within the unstable domain, almost purely growing internal m = 1 modes occur. The stability curve in the $(\omega_{di}/\bar{\omega}_{D\alpha})$ - $\beta_{p\alpha}$ plane is shown in Fig. 3 for $\gamma_{mhd}/\bar{\omega}_{D\alpha} = 0.05$ and 0.1. These curves indicate that above a maximum value of $\gamma_{mhd}/\bar{\omega}_{D\alpha}$, and/or of $\omega_{di}/\bar{\omega}_{D\alpha}$ no stabilisation is possible.

The stability domain in the λ_H-$\beta_{p\alpha}$ plane [5] is essentially independent of the plasma parameters, once the ratio $\omega_{di}/\bar{\omega}_{D\alpha}$ is fixed. In an ignited plasma the latter is characteristically $\gtrsim 10^{-2}$. A more explicit form of the stability criterion can be obtained by expressing λ_H and $\beta_{p\alpha}$ in terms of β_p, for chosen values of the geometrical and profile plasma parameters and of the central ignition temperature T_o.

For convenience, we adopt the simplified, even though rough, model

$$\lambda_H = (3\pi/2)\ \epsilon_o^2[\beta_p^2 - \beta_{p,mhd}^2] \tag{4}$$

where

$$\beta_p = [8\pi/B_p^2(r_o)][\langle p(r_o)\rangle - p(r_o)], \tag{5}$$

with $\langle p(r_o)\rangle$ the average of p inside the q = 1 surface. The ideal mhd threshold $\beta_{p,mhd}$ varies characteristically between 0.1 and 0.3, being smallest for elongated configurations and for large r_o/a. This leads to the following estimate of the maximum stable value $\beta_{p,max}$

$$\beta_{p,max}^2 - \beta_{p,mhd}^2 = 5.6\times10^{-3}\ \frac{\bar{\omega}_{D\alpha}}{\omega_A}\left(\frac{R_o}{r_o}\right)^2\ (1 - 5.5\ \frac{\omega_{di}}{\bar{\omega}_{D\alpha}}) \tag{6}$$

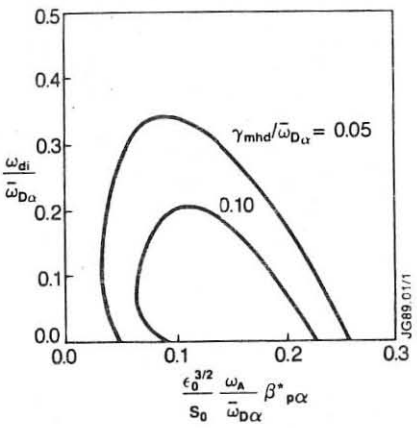

Fig. 3: Stability domain in the $(\omega_{di}/\bar{\omega}_{D\alpha})$ - $\beta_{p\alpha}$ plane.

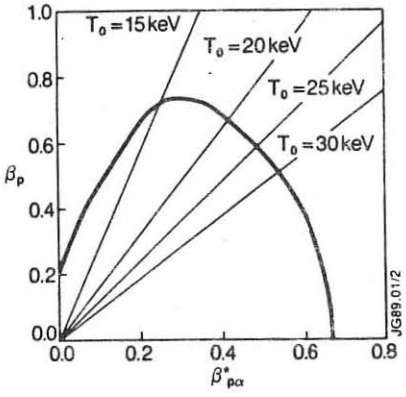

Fig. 4: Stability domain in the β_p - $\beta^*_{p\alpha}$ plane (see definition below Eq. (2)).

where the r.h.s. decreases approximately as r_o^{-3}. For $\beta_{p,max} >> \beta_{p,mhd}$, $\beta_{p,max}$ scales approximately as

$$\beta_{p,max} = 0.5 \frac{[n_i(r_o)/10^{15}\ cm^{-3}]^{1/4}}{(9\ r_o/R_o)(r_o/50cm)^{1/2}(B/10T)} \qquad (7)$$

The stability domain in the β_p-$\beta^*_{p\alpha}$ plane is shown in Fig. 4 where we have chosen $\beta_{p,mhd} = 0.2$. An increase of r_o from $r_o/a = 0.36$, shown in Fig. 4, to $r_o/a \simeq 0.6$ brings $\beta_{p,max}$ down from approximately 0.7 to 0.35, while the largest value of $\beta^*_{p\alpha}$ on the stability curve decreases from 0.67 to 0.2.

At ignition, the ratio $\beta^*_{p\alpha}/\beta_p$ is determined by the central plasma temperature T_o and by a profile factor. For fixed profiles, the rapidly increasing temperature dependence is shown by the slopes of the straight lines in Fig. 4, corresponding to the ratio $\beta_p/\beta^*_{p\alpha}(T_o)$. This ratio has been evaluated for the following profiles: $p = p_o(1 - r^2/a^2)^\sigma$, with $\sigma = 2$ for the thermal plasma and $\sigma = 6$ for the alphas. These lines indicate that the largest stabilisation is obtained at relatively low ignition temperature. If ignition is sought at higher values of T_o, the enhanced stability is largely lost and, as r_o/a is increased above the value shown, the instability threshold may fall below its ideal mhd value, as fishbones with $\omega = \bar{\omega}_{D\alpha}$ can be excited.

CONCLUSIONS

These results indicate that fusion α-particles can indeed help in controlling the onset of internal modes in an ignited plasma. However, this control is most effective when the area where $q < 1$ is not too large, i.e. when the consequences of these modes would be less damaging. The most effective strategy, besides keeping β_p small, is to approach ignition conditions at relatively low temperatures and large values of $n^{1/2}/(r_o B^2)$. Higher temperatures can be expected to lead to fishbone oscillations with $\omega \sim \omega_{D\alpha}$ and, consequently, to scattering of fully energetic α-particles. Fishbone oscillations with $\omega \sim \omega_{di}$ can occur if ignition is approached at $\beta_p \gtrsim \beta_{p,mhd}$, but $\gamma_{mhd} < \omega_{di}/2$, and $\beta_{p\alpha}$ is still small. However, these oscillations resonate with slowed down α's and are not expected [6] to affect the energy balance significantly. In fact they may even be beneficial in easing the problem of ash accumulation.

REFERENCES

[1] B. Coppi, J. Hastie, S. Migliuolo, F. Pegoraro and F. Porcelli, Phys. Lett. A132, 267 (1988).

[2] F. Pegoraro, F. Porcelli, B. Coppi, P. Detragiache and S. Migliuolo, XII Int. Conf. Plasma Phys. & Contr. Fus., Nice, (1988) paper IAEA-CN-50/D-4-6.

[3] L. Chen, R.B. White, M.N. Rosenbluth, Phys. Rev. Lett. 52, 1122 (1984)

[4] B. Coppi, F. Porcelli, Phys. Rev. Lett. 57, 2272 (1986).

[5] B. Coppi, S. Migliuolo, F. Pegoraro and F. Porcelli, "Global modes and high-energy particles in ignited plasmas", to be published.

[6] B. Coppi, F. Porcelli, Fusion Tech. 13, 448 (1988).

HEAT PULSE ANALYSIS IN JET AND RELATION TO LOCAL ENERGY TRANSPORT MODELS

J.C.M. de Haas*, W. Han, N.J. Lopes Cardozo*, C. Sack, A. Taroni

JET Joint Undertaking, Abingdon, Oxon., OX14 3EA, UK
*FOM, "Rijnhuizen", The Netherlands

INTRODUCTION

The evolution of a perturbation $\hat{T}_e$ of the electron temperature depends on the linearised expression of the heat flux q_e and may be not simply related to the local value of the electron heat conductivity χ_e [1]. It is possible that local heat transport models predicting similar temperature profiles and global energy confinement properties, imply a different propagation of heat pulses.

We investigate here this possibility for the case of two models developed at JET [2,3]. We also present experimental results obtained at JET on a set of discharges covering the range of currents from 2 to 5MA. Only L-modes, limiter discharges are considered here. Experimental results on the scaling of χ^{HP}, the value of χ_e related to heat pulse propagation, are compared with those of χ^{HP} derived from the models.

DERIVATION OF χ^{HP} AND EXPERIMENTAL RESULTS

The value of χ^{HP} is derived from the electron temperature traces following [4]. The velocity of the heat pulse and the radial attenuation are given by:

$$v = (d(t_p)/dR)^{-1} \tag{1}$$

$$\alpha = -\ 10a\ \frac{d}{dR}\ (\log_{10} A) \tag{2}$$

Here R is the major radius where the time t_p, at which the peak of $\hat{T}_e$ is reached, is measured; A is the amplitude of $\hat{T}_e$. The corresponding "cylindrical" quantities, used in [4], are given in first approximation by $v_{CYL} = \sqrt{\kappa}\ \frac{a}{a-s}\ v$ and $\alpha_{CYL} = \frac{a-s}{a}\ \alpha$, a being the horizontal minor radius, s the Shafranov shift and κ the plasma elongation.

The analysis in [4] shows that an approximate heat pulse diffusion coefficient

$$\chi^{HP} = 4.3\ a_{CYL}\ v_{CYL}/\alpha_{CYL} \tag{3}$$

can be introduced for the description of the heat pulse propagation in JET. Here $a_{CYL} = \sqrt{\kappa}\ a$.

The JET discharges in the period 1986-1988 for which χ^{HP}_{exp} has been derived following Eqs.(1-3) are summarised in Table 1. The geometry was practically the same for all analysed discharges: major radius R_o = 3m, horizontal minor radius a = 1-1.2m and elongation κ = 1.3-1.5. The analysis has been performed only in high field discharges because the

signal to noise ratio of the signal from the diagnostic, a 12-channel ECE grating polychromator [5], is proportional to B^3. The remaining discharge parameters, current I, total input power P_{tot}, effective charge Z_{eff}, volume average density $\langle n_e \rangle$ and peak temperature T_{eo} cover a wide range. The dependence of χ_{exp}^{HP} on these parameters is investigated. The main problem is related to the non-complete independence of the parameters. For example one expects some internal relationship among n_e, P_{tot} and Z_{eff} or n_e, T_e, P_{tot} and I. A study of the correlation matrix shows that the correlation between pairs of the parameters is not too strong and a regression analysis is carried out. There is a coupling between the radial position $x = r^{HP}/a$ where χ^{HP} is measured and the mixing radius $r_{mix} \propto a/q_a$, q_a being the cylindrical safety factor at the boundary. This implies that one cannot distinguish between variations of I and x^{HP}. Here it is assumed that any effect is related to variations of x^{HP} and not of I; a dependence of I can be introduced by a correspondent variation in the dependence on x^{HP}. Fitting a power law model for χ^{HP} to the data yields:

$$\chi_{exp}^{HP} = (2\pm0.5)(x^{HP})^{2.1\pm0.2} Z_{eff}^{0.6\pm0.1} T_e^{0.5\pm0.2} P_{tot}^{0.0\pm0.1} \langle n_e \rangle^{0.0\pm0.1} \quad (4)$$

The mean square root of the fit (Fig. 1) is $0.328 m^2/s$ which is comparable to the estimated error on χ_{exp}^{HP}. The correlation coefficient with the largest value (-0.84) is that between the constant and T_e. Fits with less variables show that the main dependences are those shown in Eq. 4. The dependence on Z_{eff} has been checked separately for the subsets of discharges with I = 2-4MA and with I = 5MA (which shows the largest variation in Z_{eff}). The fits yield the same results within error bars.

Keeping in mind its limitations, this analysis confirms [1] that the dependence of χ_{exp}^{HP} on P_{tot} is either absent or weak (possibly via T_e) and shows a rather strong dependence on Z_{eff}. A separate dependence on I and x cannot be derived.

RESULTS OF TRANSPORT CODE SIMULATIONS

The space and time evolution of T_e following sawtooth crashes has been computed by means of the full 1½ D transport code JETTO [6]. We consider here two local energy transport models proposed at JET: the so-called Rebut-Lallia (or critical electron temperature gradient) model [2] and the critical pressure gradient model related to resistive instabilities proposed by P. Thomas [3]. The velocity of the heat pulse and its attenuation have been derived from the computed results, (Fig.2) using Eqs.(1) and (2). The coefficients χ_{RL}^{HP} and χ_{PT}^{HP} have been evaluated using Eq.(3). Discharges at 2 and 5MA have been studied so far.

An example of results obtained with the code is given in Table 2. Here the first line refers to a JET discharge at 2MA, with 4MW of ICRF additional power. The other lines are the results of computational experiments corresponding to variations of the input power, Z_{eff} and the position at which χ^{HP} was evaluated. The numerical results are consistent with those expected from the study of the linearised expressions of the heat fluxes. This confirms the validity of Eq.(3), even in the case of highly nonlinear models such as those considered here. As shown in Table 2, one finds $\chi_{PT}^{HP} = \gamma \chi_{PT}$, with $\gamma \approx 1.5$, consistent with $\chi_{PT} \propto \nabla p$ and $p_e \lambda$

p_i, where p indicates the pressure. This implies that χ_{PT}^{HP} is too low for ohmic discharges (see lines 3 and 4 in Table 2 and Fig. 2). The dependence of χ_{RL}^{HP} is weaker and compatible with the experimental results also in the ohmic cases. Table 2 also shows that χ_{RL}^{HP} does not depend on Z_{eff}, contrary to experimental indications. This could indicate that a factor $(1 + Z_{eff})^{\frac{1}{2}}$ has been neglected in the expressions of χ_{RL} derived so far [7]. Some increase of χ_{PT}^{HP} with Z_{eff} is observed. It is, however, weaker than observed experimentally.

Both models predict an inverse dependence of χ^{HP} on the current I. They also predict that χ^{HP} depends weakly on x in the region $x \lesssim .8$ and increases sharply in the boundary region. This is qualitatively consistent with the experimental results but quantitative comparisons have not been possible so far.

CONCLUSIONS

We have shown that the numerical simulation of heat pulse propagation with a full 1½D transport code can be used to assess local energy transport models. The experimental results obtained so far in JET plasmas indicate that χ^{HP} has a weak or no dependence on the input power. This important feature is better simulated by a transport model producing confinement degradation through a transport threshold at a critical value of the electron temperature gradient [2] than by a model producing degradation via a nonlinear dependence of the heat flux on the pressure gradient [3]. The relatively strong dependence of χ^{HP} on Z_{eff} implied by the analysis of the experimental data, seems to indicate a stronger dependence of the local χ on Z_{eff} than predicted, showing a possible line of improvement for the models.

More work is required for a quantitative comparison of predicted and experimental results on the dependence of χ^{HP} on the plasma current and the radial position, possibly extending the study to "controlled" heat pulses, generated by the time modulation of auxiliary power deposited at chosen values of x in a set of reference discharges.

REFERENCES

[1] B.J.D. Tubbing, et al., Nucl. Fusion 27 (1987) 1843.
[2] P.H. Rebut, et al., 12th IAEA Conf., Nice, France (1988), CN50/D-4-1.
[3] P. Thomas, et al., Proc. XV EPS Conference, Dubrovnik, 1988, Vol.I, p.127.
[4] N.J. Lopes Cardozo, et al., Nucl. Fus. 28 (1988) 1173.
[5] B.J.D. Tubbing, et al., Proc XII EPS Conference, Budapest, 1985, Vol.9F-I, p.215.
[6] G. Cenacchi and A. Taroni, JET-IR(88)03.
[7] P.H. Rebut, Private communication.

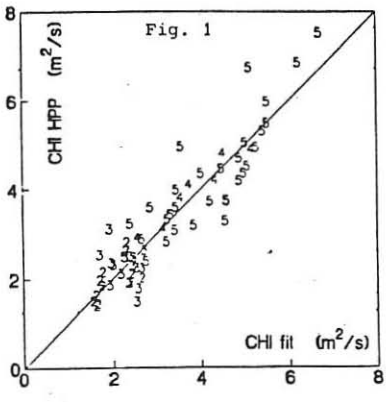

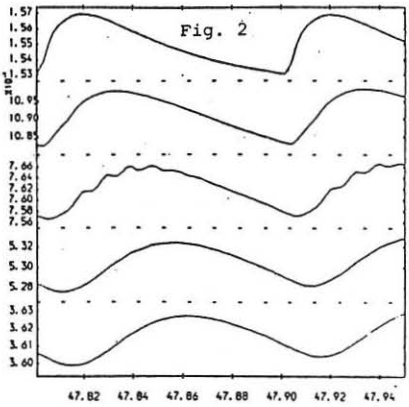

Fig. 1: Plot of the measured χ^{HP} vs the fitted χ^{HP} according to Eq. 4 for the full data set.

Fig. 2: Time (sec) evolution of T_e(keV) computed with the RL model. Channels corresponding to ρ/ρ_{max} = 0.5, 0.6 ... 0.9 are shown. The parameter of the discharges are I = 2MA, $P_{tot_{HP}} = P_{OH}$ = 1MW, Z_{eff} = 2.2, $\langle n_e \rangle$ = $2.1 \times 10^{19} m^{-3}$, T_{eo} = 3.6keV. One derives χ^{HP}_{RL} = 1.6 at R = 3.7. Equation 4 gives χ^{HP} = 1.8

TABLE 1

I(MA)	B_t(T)	$\langle n_e \rangle (m^{-3})$	P_{tot}(MW)	Z_{eff}	x = r/a	T_{eo}(keV)	N° of Pulses
2.0	3.5	2.0±0.2	2.5-5.0	2.2-3.5	0.52	4.1-5.5	12
3.0	2.9-3.5	1.8-4.0	2-14	2.6±0.2	0.6-0.7	3.1-4.3	16
4.0	2.9	1.9-3.3	3.2-6.7	2.0-3.5	0.8	3.2-5.0	7
5.0	3.5	1.6-4.0	4.0-16.0	1.5-5.0	0.78	3.1-5.3	31

TABLE 2 - Values of χ^{HP}_{RL} and χ^{HP}_{PT} derived from numerical "experiments" simulating heat pulse propagation at I = 2MA and different values of $P_{tot_{HP}}$, Z_{eff} and R. The first line in the table corresponds to JET pulse 15020 for which χ^{HP} = 1.05 was determined experimentally at R = 3.65. Values of $\chi = q_e/n_e \nabla T_e$ are also given.

I(MA)	Z_{eff}	P_{tot}(MW)	R(m)	$\chi^{HP}_{RL}(m^2/s)$	$\chi_{RL}(m^2/s)$	$\chi^{HP}_{PT}(m^2/s)$	$\chi_{PT}(m^2/s)$
2	2.2	4.6	3.68	1.9	1.0	1.8	1.1
2	2.2	4.6	3.9	3.0	1.5	2.1	1.4
2	2.2	1	3.68	1.6	0.5	1	0.6
2	2.2	1	3.9	3.1	0.7	1.2	0.8
2	2.2	16	3.68	2.3	1.3	2.3	1.5
2	2.2	16	3.9	3.2	2.3	3.2	2
2	1	4.3	3.68	2.0	1.0	1.5	1.0
2	4	4.8	3.68	1.8	1.0	2.0	1.3

ION THERMAL CONDUCTIVITY AND CONVECTIVE ENERGY TRANSPORT IN JET HOT-ION REGIMES AND H-MODES

F.Tibone, B.Balet, J.G.Cordey, G.Corrigan, D.F.Düchs, A.Galway, H.Hamnén[1], G.Maddison[2], G.Sadler, W.Stacey[3], T.Stringer, P.Stubberfield, M.L.Watkins

JET Joint Undertaking, Abingdon, Oxon., OX14 3EA, UK
[1] Chalmers University of Technology, Gothenburg, Sweden
[2] UKAEA, Culham Laboratory, Abingdon, Oxon. UK
[3]Georgia Institute of Technology, Atlanta, Georgia 30332, USA

INTRODUCTION

Local transport in a recent series of JET experiments has been studied using interpretive codes. Auxiliary heating, mainly via neutral beam injection (80keV $D^0 \rightarrow D^+$), was applied on low-density target plasmas confined in the double-null (DN) X-point configuration (I_p = 3-3.5MA, B_t = 2.5-3.2T). This has produced two-component plasmas with high ion temperature and neutron yield and, above a threshold density, H-modes characterised by peaked density and power deposition profiles. H-mode confinement was also obtained for the first time with 25MW auxiliary power, of which 10MW was from ion cyclotron resonance heating. Operational aspects and global performance of these experiments are discussed in [1].

We have used profile measurements of electron temperature T_e from electron cyclotron emission and LIDAR Thomson scattering, ion temperature T_i from charge-exchange recombination spectroscopy (during NBI), electron density n_e from LIDAR and Abel-inverted interferometer measurements. Only sparse information is, however, available to date concerning radial profiles of effective ionic charge and radiation losses. Deuterium depletion due to high impurity levels is an important effect in these discharges, and our interpretation of thermal ion energy content, neutron yield and ion particle fluxes needs to be confirmed using measured Z_{eff}-profiles.

Electron and ion energy balances can be clearly separated at these low plasma densities, thereby allowing a reliable estimate of the ion thermal conductivity χ_i. Bulk plasma radiation amounts to 30-40% of the total input power; the uncertainty on its radial distribution strongly affects the determination of χ_e when ion heating is dominant.

HOT-ION REGIME

A peak ion temperature of 18keV and D-D neutron rates of 10^{16}/s are produced by 20MW NBI into a low-density target plasma ($\langle n_e \rangle$ = 0.5 $10^{19}m^{-3}$, Z_{eff} = 4). Excellent beam penetration leads to a centrally peaked density profile ($n_{eo}/\langle n_e \rangle$ = 2), and an even more strongly peaked ion temperature profile (Fig.1A; the large central value of $\eta_i \equiv \nabla \ell n T_i / \nabla \ell n n_i$ is shown in Fig.1C).

The transient hot-ion phase is dominated by fast ion dynamics. TRANSP calculations involving sophisticated treatment of beam-plasma interaction [2] show that W_{fast} accounts for half of the total stored energy, with a nearly isotropic fast ion velocity distribution. The observed time evolution of D-D neutron yield is well reproduced (Fig.1B), showing that 90% of the neutrons come from beam-beam and beam-plasma reactions.

The strongly peaked ion source predicted is found to be compatible with the measured electron density only if the Z_{eff}-profile is significantly hollow, with $Z_{eff} \lesssim 2$ near the plasma center (where $n_{fast} > 0.5\ n_e$ during the first 0.5 sec of NBI).

Low density and high temperature make thermal exchange between electrons and ions a minor effect, and the two energy balances can be unambiguously separated. Main transport losses for the thermal plasma are through the ion channel: χ_i (Fig. 1C) increases with radius and is larger than χ_e by an order of magnitude. For $\rho > 1/4$ ($\rho \equiv$ normalised radial coordinate) χ_i is larger than the neoclassical prediction by at least a factor 20. For both electrons and ions, the convective heat flux (here $q_{cv}=3/2\Gamma T$, Γ being the particle flux) accounts for more than half of the net heat flux near the plasma center. Viscous energy transport associated with the damping of toroidal rotation is a small fraction (<10%) of the ion losses.

HIGH- AND LOW-DENSITY H-MODES WITH 10 MW NBI

Analysis of ELM-free JET H-modes at medium/high density ($\langle n_e \rangle > 2.5\ 10^{19} m^{-3}$) in the DN configuration yields similar results to those obtained for single-null cases [3]. Beam deposition and plasma density profiles are flat or even hollow, and W_{fast} is a minor fraction ($\lesssim$ 10%) of the total stored energy. Although the e-i thermal exchange term is uncertain, the observation that at medium density $T_i(\rho) = T_e(\rho)$ while ion heating is predominant implies $\chi_i \gtrsim \chi_e$. The "effective" thermal conductivity $\chi_{eff} \equiv - q_{cd}/n_e \nabla T_e$, q_{cd} being the total conductive heat flux, is $\sim$ 1-1.5m²/s for $\rho < 0.8$ (Fig.2).

In recently obtained low-density H-modes [1] the beam deposition profiles remain centrally peaked throughout the H-phase, $T_i > T_e$ and the L/H transition is significantly delayed until the plasma density has built up. The phase preceding the transition is a hot-ion regime of the type discussed, dominated by fast ions and with $\chi_i \gtrsim 2\ \chi_e$ for the thermal plasma. χ_{eff} appears to be decreasing in time during the L-phase, and settles on an H-mode value $\sim$ 1 m²/s (Fig.2).

Quiescent H-modes are characterized by significantly improved particle confinement. The electron flux Γ_e, which is outwards throughout the plasma in L-regimes, remains such near the edge (where the recycling source dominates) but is reversed in the inner plasma (Fig.3), corresponding to the formation of a shoulder in the density profile. In the low-density H-mode, Γ_e remains positive also near the plasma center.

The corresponding reversal of convective heat flux may have a bearing on the intepretation of the improved energy confinement at the L→H transition. If $\Gamma_i \equiv \Gamma_D + \Gamma_{imp} \sim \Gamma_e$, the effect on the total energy balance could be significant, with q_{cv}/q_{tot} up to +25% in L-modes and down to -10% in H-modes. However, with the impurity concentrations typical of these plasmas ($n_{imp}/n_e \sim 5\%$) such effect is very sensitive to Γ_{imp}: if Γ_e is mostly a consequence of impurity flows, then Γ_i may well be opposite to Γ_e, and dominant. On the other hand, the effect would be enhanced if impurities were counterflowing with respect to electrons. Profile measurements of Z_{eff} are necessary in order to resolve this issue.

H-MODE WITH STRONG COMBINED AUXILIARY HEATING

The pulse shown in Fig. 4 is so far a unique example of H-mode obtained with 15MW NBI and 10MW ICRH heating a target plasma fuelled by multiple pellet injection. Power deposition is predicted to be mostly on ions for NBI and mostly on electrons for ICRH. The measured electron density profile is only moderately peaked, and $T_e \sim T_i$. Estimated fast ion energy content is $\sim \frac{1}{3} W_{tot}$ initially, then decreases but still contributing significantly to the global energy confinement. The electron convective heat flux is again found to be inwards over most of the plasma, and $\sim 15\%$ of the net electron heat flux. The effective thermal conductivity for the background plasma is $\chi_{eff} \sim 3$ m²/s (Fig.2), supporting the conclusion that confinement is degrading with increasing input power [3].

CONCLUSIONS

Non-thermal ions play a dominant role in the hot-ion regime in JET. 90% of the observed neutron yield is due to beam-beam and beam-plasma reactions. The background plasma is characterized by $\chi_i \gg \chi_e$, apparently not correlated with η_i.

Low-density H-modes (featuring peaked density profiles) appear to have transport properties similar to higher density ones. The reversal of local particle fluxes during H-phases, associated with increased particle confinement, may influence the energy balance and could explain part of the improvement in energy confinement with respect to L-modes. Thermal plasma confinement in the H-mode appears to degrade with increasing input power.

The anomalous nature of ion energy transport [4] is confirmed, and $\chi_i \gtrsim \chi_e$ is found in all cases where the energy balances can be decoupled.

REFERENCES

[1] B.J. Tubbing et al., this conference.
[2] R.J. Goldston et al., Journal Comp. Physics 43 (1981) 61.
[3] M. Keilhacker et al., IAEA-CN-50/A-III-2, Nice 1988.
[4] A. Taroni et al., Proc. EPS Conf., Madrid 1987, 11D (Pt. I) 97.

FIGURE CAPTIONS

Fig. 1 Hot-ion regime:
A) density and temperature profiles
B) time evolution of measured and computed D-D neutron yield
C) $T_{io}(o)$, χ_i (solid line) and η_i (dashed, assuming similar profile shapes for n_i and n_e) at (a) $\rho=1/3$, (b) $\rho=1/2$ vs time.

Fig. 2 "Effective" thermal conductivity for various JET H-modes:
(a) medium n, SN 8MW NBI (#14832/15894); (b) high n, DN 10MW NBI (#17386);
(c) low n, DN 10MW NBI (#18757); (d) medium n, DN 25MW NBI+ICRH (#18773).

Fig. 3 Measured dn_e/dt and predicted electron source S_e for:
(a/b) low density plasma (L/H-phase); (c) high density H-mode

Fig. 4 Overview of H-mode with $P_{aux} \sim 25$MW, pulse #18773 (open circles = computed kinetic energy)

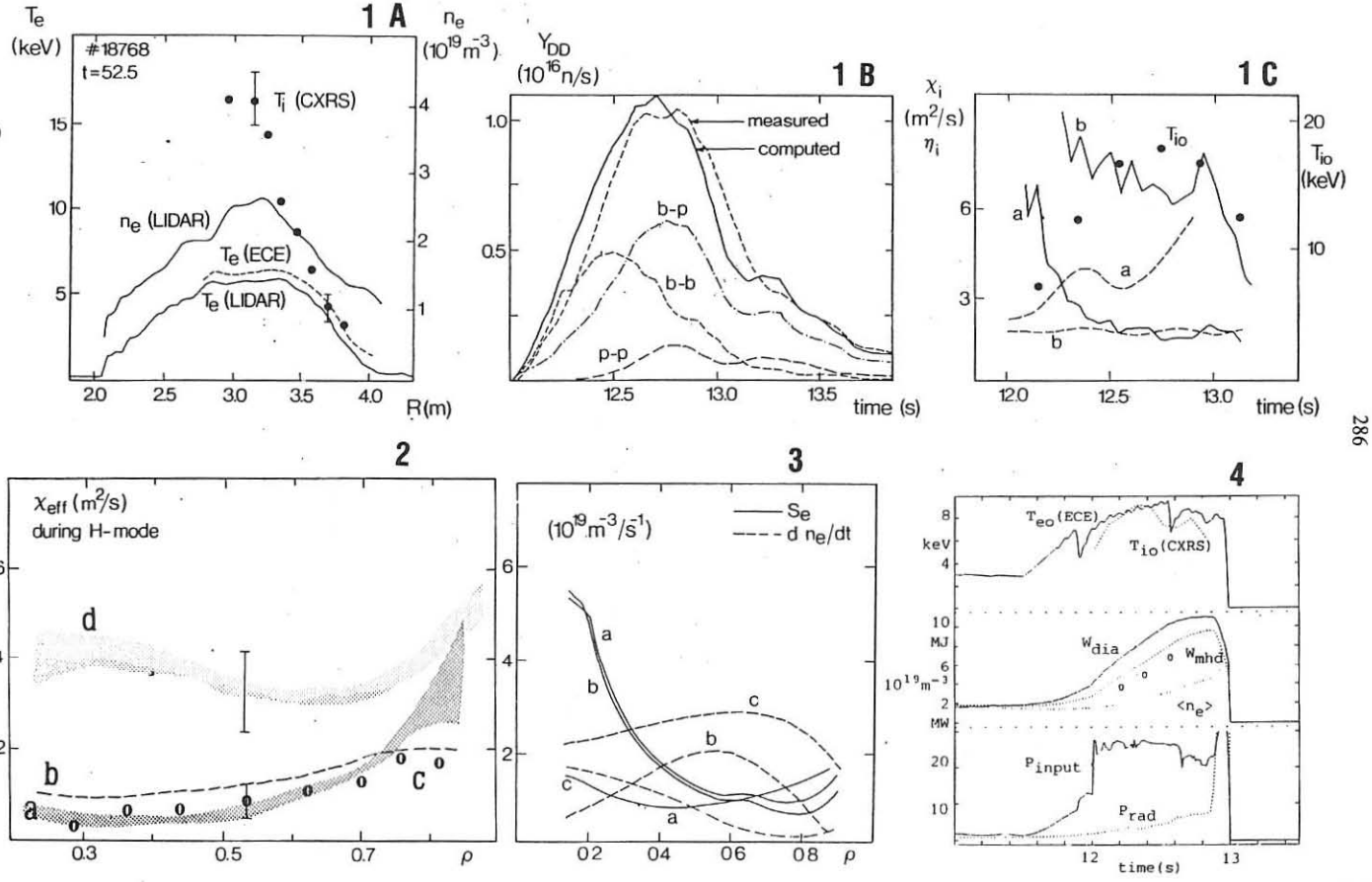
1 A
T_e (keV)
n_e (10^{19} m^{-3})
#18768
t=52.5
T_i (CXRS)
n_e (LIDAR)
T_e (ECE)
T_e (LIDAR)
R(m)
1 B
Y_{DD} (10^{16} n/s)
measured
computed
b-p
b-b
p-p
time (s)
1 C
χ_i (m^2/s)
η_i
T_{io}
T_{io} (keV)
time (s)
2
χ_{eff} (m^2/s)
during H-mode
ρ
3
(10^{19} m^{-3}/s^{-1})
S_e
d n_e/dt
ρ
4
T_{eo} (ECE)
T_{io} (CXRS)
keV
W_{dia}
W_{mhd}
$<n_e>$
MJ
10^{19}m^{-3}
P_{input}
P_{rad}
MW
time (s)

MAGNETODRIFT TURBULENCE AND DISRUPTIONS

Jean ANDREOLETTI

CEA - DRFC - CEN CADARACHE (FRANCE)

A qualitative model has been recently reported [1] for sawtooth relaxation in Tokamaks. Here we also discuss minor and major disruptions.

MAGNETODRIFT TURBULENCE

As proposed in that model, magnetodrift motions (md) are a particular type of motions with exceptional properties. They can exist only in configurations having along $\underline{B}$ lines a sufficient large scale asymmetry of the local magnetic shear.

In order that the kink motion can fully develop, the mhd flux conservation constraint has to be broken by some parallel electric field. In a hot plasma, the electron pressure term is dominant since the ratio of $\nabla_{//}p_e / en_e$ by $\eta J_{//}$ varies as T^3.

In a low β plasma any perpendicular fluid velocity field is almost divergence free, and so $\nabla \wedge \underline{V} \neq 0$ almost everywhere. Then during the disruption, strong turbulence must develop in spite of the magnetic shear. Thus the corresponding motions must be free of that constraint, which means that $\delta(\underline{J} \wedge \underline{B})$ must be weak. Therefore we would have $d/dt\ (\nabla \wedge \underline{V}) \sim 0$ and the perpendicular spectrum will be quasi-isotropic. From this property we deduce $k_{//} \sim 2\pi s_*/qR$ where s_* is a local value of the shear parameter.

An asymmetry of the local magnetic shear produces a variation of $k_{//}$ along the $\underline{B}$ lines. When this asymmetry is sufficient, ω exists such that:

- In the region where s_* is weak, $\omega/k_{//} > Ve$, the electron continuity equation is dominated by its perpendicular part, and mhd dynamics is valid with $\delta E_{//} \sim 0$.
- In the region where s_* is strong, $\omega/k_{//} < Ve$, the electron continuity equation is dominated by its parallel part, and drift wave dynamics is valid with $\delta E_{//} \sim \nabla_{//}p_e / en_e$. These motions can tap the mhd free energy (∇p versus curvature) and become free of the global magnetic shear constraint trough disposal of several wavelenghts before toroidal closure.

MAGNETIC RELAXATION

Magnetodrift turbulence will produce fast transport. Braiding of magnetic lines (mhd + non mhd $\delta \underline{B}$) and non equilibrium forces due to $\nabla p \longmapsto 0$ will result in a tendency of J/B to become constant in the turbulent domain.

SAWTOOTH DISRUPTION

Magnetodrift turbulence is the main ingredient of the model proposed for the sawtooth relaxation D1 (disruption near and inside q=1). It triggers a fast transition from resistive kink to quasi-mhd kink and it allows a catastrophic increase and a full developement of this convective motion. This effect of the turbulence is obtained by relaxing asymmetrically the current density spikes associated with the $B_\theta(r)$ field distorded by compression-expansion. An increase of the shear parameter s_1 near q =1 results. It produces an enhancement of the ξ_2 (m/n=2/1) harmonic of the kink motion and thus an increase of the instability. Therefore the system enters a positive feedback loop which constitutes the trigger mechanism.

When the symmetry is sufficiently broken by the helical deformation, a strong burst of this turbulence produces the collapse of the density and temperature profiles and flattens the current density profile in some annular domain.

Various experimental aspects of D1 (cold bubble, crescent shape of the core, twisting, precursor and successor oscillations, partial sawteeth, snake motion) fit naturally in that model.

Experimental measurements of the specific fluctuations associated with the sawtooth relaxations in TFR plasmas [2] show several similarities with the proposed magnetodrift turbulence.

ROTATION AND HELICAL DEFORMATIONS

The experimental observation that the various particle and energy transport coefficients have similar numerical values whatever the particle mass and energy, strongly suggests that fluctuations of the electric drift velocity is the main turbulent transport process. Since collisional transport is much larger for ions than for electrons, the plasma will generally develop a negative charge density. The resulting radial electric field produces a poloidal rotation, which is slower in the central part because of the sawtooth relaxations which reduce the potential gradient.

Helical current pertubations can develop around the resonnant magnetic surfaces with the most simple ratios m/n=q due to tearing instability. When the resulting islands of neighbouring resonnances interact, their spatial phases are no more independent. The potential energy W of the configuration depends on their relative phase. The value of this phase which minimize W will be imposed to the system through non equilibrium forces acting on the relative toroidal rotation.

As an exemple, a strong 1/1 deformation inside a 2/1 "cavity " will have a toroidal phase such that the 1/1 displacement directed outwards takes place in the poloidal plane where the flux surfaces are streched along the equatorial direction by the 2/1 deformation. This particular phase permits the 1/1 displacement to be stronger in the direction of low magnetic field than in that of high field. In this situation the poloidal and toroidal rotations combine in such a way that the coupled helical deformations rotate toroidically at the same frequency.

Another noteworthy exemple is the coupling of two island systems, one due to plasma tearing current pertubations and one due to symmetry imperfections in the external currents. The common toroidal frequency for strong coupling is zero, which means that for a sufficiently large amplitude the plasma helical deformation will appear as blocked.

SOFT MINOR DISRUPTION

When the maximum of J" (= $\partial^2 J/\partial r^2$) is near the resonnant radius r_2 (q = 2) the J(r) profile is favorable to 2/1 tearing instability. The plasma evolves to this situation either by an increase of density (atomic losses displaced inwards) or by an increase of the current (r_2 displaced outwards).

The island helical deformation of the configuration produces an asymmetry of the local magnetic shear s_* which for $r \lesssim r_2$ is weakened near the hyperbolic axis and is enhanced near the ventral segment. On these magnetic surfaces near the separatrix, while the relative poloidal rotation of magnetic lines with respect to the island system is accelerated beside the ventral segment, it is reduced near the X point where they accompany the hyperbolic axis for several turns. There the poloïdal rotation of lines is more regular than in the unpertubed equilibrium, and a weak ballooning of the pertubation is sufficient to tape the mhd free energy. An eventual enhancement of this effect can be produced by a 4/2 mhd harmonic induced by nonlinearity. Indeed this harmonic produces variations of the island angle that can result in an enlargement of the stagnation azimutal domain.

We suppose that, from these geometrical properties, md motions or d (drift wave) motions coupled to the mhd free energy (depending on the actual asymmetry of the local shear) become unstable in a small annular domain near and inside ($r \lesssim r_2$) the inner branch of the separatrix.

The resulting turbulence that initiates the D2 disruption (near and inside q=2) will not be azimutally localized as in the case of D1 because the local shear asymmetry is weaker and the poloïdal period is smaller. Density and temperature transport, and current density relaxation will result and favour an inward spreading of turbulence. This inward 2/1 deformation of the magnetic configuration will induce by toroïdal coupling a 1/1 displacement of the central core.

HARD MINOR DISRUPTION

If the 1/1 displacement is sufficiently pronounced it will permit the development of md turbulence near and inside r_1 mainly localized in the wake of this displacement. Then the resulting magnetic relaxation allows a fast growth of the internal kink motion.

Meanwhile the two main helical distorsions 2/1 and 1/1 generate second order and high order islands by toroïdal and nonlinear couplings. Thus transition to global stochasticity of magnetic lines [3] which are hamiltonian trajectories in real space can be reached.

Transport of electron energy and current relaxation will result producing an evolution of the magnetic structure. The time varying stochasticity can be considered as a particular sort of low frequency turbulence. Density and ion temperature will not be much affected because electric drift velocity is not a basic element of that turbulence. On the contrary, the electron temperature profile is expected to shift down as a whole for $r<r_2$, and the current density profile to become somehow flattened inside r_2 and stepened outside.

If the energy loss is important, the toroidal equilibrium is lost and the plasma ring contracts producing an increase of the total current and a decrease of the voltage, by inductance reduction. Scraping off by the inner limiter will enhance the edge steepening of the J(r) profile.

MAJOR DISRUPTION

If the current density profile is sufficiently enlarged, external mhd kink can become unstable [4, 5]. Considering a situation with $2< q_a <3$, the 3/1 unstable kink will develop a three petal-like deformation of the plasma edge. Scraping-off by the limiter will steepen the J(r) profile near the edge and thus make the kink more unstable.

When the plasma edge, transfered inwards by scraping-off reaches the q=2 surface, the 2/1 external kink will in turn develop. The final step will be the 1/1 external kink propelling the remaining plasma to the wall.

More direct routes to major disruption can be given by any process generating an enlarged and edge steepened current density profile. Skin effect due to fast current rise, ballooning mode turbulence near the β limit, strong plasma wall interaction, are three possible mechanisms.

REFERENCES

[1] J. Andreoletti- International Workshop on " Turbulence in mhd flows" Cargèse (France) July 1988 (to be published by Elsevier).
[2] Equipe TFR, A. Truc - C. R. Acad. Sc. Paris, t.304, série 2, n° 7 (1987) and in this Conference (P2-A4-6).
[3] A. Lichtenberg, M. Lieberman - Regular and stochastic motion (Springer).
[4] V. D. Shafranov - Sov. Phys. Tech. Phys. 15 (1970) 175.
[5] J. Wesson - Nucl. Fusion 18 (1978) 87.

TOROIDAL COUPLING AND FREQUENCY SPECTRUM OF TEARING MODES

D.Edery , A.Samain , A.L.Pecquet , J.C.Vallet , P.Lecoustey
Association Euratom-CEA sur la fusion controlée
DRFC- CEN Cadarache
F-13108 SAINT PAUL LEZ DURANCE

INTRODUCTION

An important problem which has been adressed since the beginning of exploitation of Tokomak devices is the precise understanding of the MHD activity.Many calculations have been performed to cover the laminar phases where the modes maintain integrability of flux lines [1,2,3],as well as the disruptive phases where stochastic effects play a leading role. The theoretical analysis we present here reconsider the former case in the spirit of a confrontation with the observed poloidal structures, growth rates and frequencies of the modes.Such data can in fact provide useful informations on the equilibrium characteristics which determine the radial structure of the various poloidal components of each unstable mode in the plasma bulk between the resonant layers , and also on the irreversible processes which, together with plasma rotation and diamagnetic effects, control the active coupling within the resonant layers.

We consider a magnetic perturbation derived from a potential vector parallel to the unperturbed toroidal field $\underline{B}_0$: $\underline{\delta B} = \underline{Rot}(\delta\psi\ \underline{B_0}/RB_0)$,$\delta\psi= \psi(r,\theta,\phi)\ \exp-i\omega t$ +c.c involving several helicities: $\psi = \Sigma_m\ \psi_m(r)\ \exp i(m\theta+n\phi)$. The mode is resonant on the magnetic surfaces $r=r_m$ where q=m/n, creating around each of them a thin island chain of half width $w_m=[8\psi_m(r_m)L_m/B_0]^{1/2}$ where $L_m^{-1}=(r\ d/dr\ (1/q))_m$. The Ampere's law is equivalent to state that the functional:

$$F(\psi,\psi^*,\omega)= -\iiint |\nabla_\perp\psi|^2 / R^2\ d^3x + \mu_0\iiint J\ .\psi^*/R\ d^3x \qquad (1)$$

is an extremum in ψ^*. Here the parallel current response $J(r,\theta,\phi)\exp-i\omega t$ +c.c is considered as a known functional of $\psi(r,\theta,\phi)$.As the functional $F(\psi,\psi^*,\omega)$ is linear in ψ^*, its extremum value in ψ^* cancells. This provides the mode frequency ω for a given geometrical structure $\psi(r,\theta,\phi)$. On the other hand, for a magnetic perturbation applied at a real frequency ω, the quantities $2\omega Im(F)$ and $2nIm(F)$ are respectively the power and the ϕ momentum rate coupled to the plasma.

TOROIDAL COUPLING AND OUTER SOLUTION

We split the functional F as given by (1) into $F_{bulk} + F_{res}$, arising from the plasma intervals outside the resonant layers and from the resonant layers, respectively.In the bulk plasma and vacuum intervals, the MHD response J applies and the functional F_{bulk} is just equivalent to the variational form of the linearized energy principle derived from the toroidal quasi-equilibrium equation [4] , namely to :

$$-\delta W = -\iiint |\underline{\nabla}_\perp \psi|^2 / R^2 \, d^3x + R_e \iiint U^* \, \underline{\delta B}.\underline{\nabla}(\mu_0 R J_{0\phi}) / R B_0 \, d^3x \qquad (2)$$

where $J_{0\phi}$ is the equilibrium current density and $U(r,\theta,\phi,t)$ is the scalar potentiel of the velocity field defined by: $\nabla_{//} U = \psi/R$ .The toroidal terms in δW proportional to β [5] have been ignored because,they are strongly divergent near the resonant surfaces r_m, and in fact belong to F_{res}.The fact that δW is real means that it contributes to no secular transfer of energy or ϕ momentum to the plasma.The extremal value of δW gives the slope jumps $[\underline{n}.\underline{\nabla}\psi]$ of ψ across the resonant layers r_m ; we have:

$$\delta W = -\Sigma_m \iint \psi^* [\, \underline{n}.\underline{\nabla}\psi \,] / R^2 d\sigma \qquad (3)$$

where ψ is the solution of the Euler equation of (2) and $\underline{n}$ is the unit vector normal to the equilibrium resonant surfaces r_m=cst

In principle, the extremal value (3) could depend on all the values $\psi_{m'}(r_m)$ $m \neq m'$; however it is found that linear relations exist between $[\psi'_{m'}(r_m)]$ and $[\psi'_m(r_m)]$, just leaving δW as a functional of $\psi_m(r_m)$ only:

$$-\delta W = \Sigma_{mm'} T_{mm'} \psi_m(r_m) \psi^*_{m'}(r_{m'}) \qquad (4)$$

In cylindrical geometry $T_{mm'} = \Delta'_m \delta_{m,m'}$, Δ'_m being the classical logarithmic slope jump. The matrix elements $T_{mm'}$ specify through (3) the slope jumps corrected by the toroidal effects.Expending δW to the second order in the small parameter $\varepsilon = r/R$ leads to analytical values $T_{mm'}$, with $m' = m \pm 1$, involving the cylindrical tearing profiles $\psi^c_m(r)$ and the usual characteristics of the toroidal equilibrium: β_{pol} , L_i , Λ ,etc.

RESONANCES AND INNER SOLUTION

The ψ solutions within the outer regions of the plasma are connected to the resonant inner layer solutions through alternate expressions of the slope jumps derived from integration of the resonant parallel current responses $\underline{J}$ .These resonant currents determine the contribution

$\iiint J.\psi^* /R\, d^3x$ of each resonant layer r_m in F_{res} .They are calculated in the frame rotating in the toroidal direction at the same velocity $R_e(\omega)/N$ as the islands, supposing a non linear regime where the electrons reach thermodynamical equilibrium over each perturbed magnetic surface.This regime applies for observable modes, for which the parallel transit frequency $K_\theta w_m V_{the}/RL_m$ is larger than the diffusion rate D_e/w_m^2 assumed larger than the mode frequency ω. This situation imposes the detailed density , temperature and electrostatic potential profiles in terms of the unperturbed diamagnetic frequencies ω^*_n ,ω^*_T and of the island velocity $R_e(\omega)$ /N -Ω in the plasma frame.The parallel current $\underline{J}$ is then determined from the charge continuity equation:

$$\mathrm{div}(\underline{J}) = -\mathrm{div}(\underline{J}_\perp) \qquad (5)$$

where the expression of the tranverse current is $\underline{J}_\perp = e(\underline{\Phi}_e - \underline{\Phi}_i) + \underline{J'}_\perp$, $\underline{\Phi}_e$ and $\underline{\Phi}_i$ being the diffusion electron and ion transverse fluxes due to the small scale turbulence present in the plasma , while $\underline{J'}_\perp$ is due to the drift curvature and to the ionic effects of inertia , F.L.R. and viscosity [6].To complete the determination of $\underline{J}$,so that it represents the deviation from the Rutherford current $\underline{J}_R$,a further constraint on average value of J over each perturbed magnetic surface must be imposed: the inductive electric field , proportional to the mode growth rate γ must balance the ohmic friction in the average.If we assume ambipolarity of the local diffusion i.e. $\underline{\Phi}_e = \underline{\Phi}_i$ then the deviation of $\underline{J}$-$\underline{J}_R$ is simply $\underline{J'}_\perp$ and the electron diamagnetism does not influence the mode frequency.However , if the turbulent modes which determine $\underline{\Phi}_e$ and $\underline{\Phi}_i$ exchange momentum with the plasma over a radial range larger than the island width , the ambipolarity condition must be removed , resulting in a largely dominant contribution of $e(\underline{\Phi}_e - \underline{\Phi}_i)$ compared to $\underline{J'}_\perp$. The calculations [7] then give :

$$F_{res} = \Sigma_{m\,m'}\, \delta_{mm'} K_m \psi_m(r_m) \psi^*_{m'}(r_{m'}) \qquad (6)$$

where K_m is an explicit complex non linear function of already defined quantities: $D, \omega^*_n, \omega^*_T$ for both electrons and ions and γ , $R_e(\omega) - N\Omega(r_m)$,$\psi_m(r_m)$. The mode consistency is expressed by matching the outer and inner solutions .This is equivalent to extremalize $F_{bulk} + F_{res}$ in $\psi^*_m(r_m)$ where, $F_{bulk} = -\delta W$ and F_{res} are given by (4) and (6) respectively. This yields the following non linear system of equations for the growth rate γ, the frequency $R_e(\omega)$ and the normalized amplitudes $\psi_m(r_m)$:

$$\sum\{T_{m'm''} - K_{m'}(\gamma, R_e(\omega), \psi_{m'})\,\delta_{m'm''}\} \quad .\psi_{m''}(r_{m''})=0 \qquad (7)$$

$m''=m,m\pm1$ $m'=m,m\pm1$

PRELIMINARY RESULTS

As a first application of the above theory we analyze the saturated Rutherford regime $\Omega=\omega^*=R_e(\omega)=0$ which corresponds in (7) to $K_m=\gamma R_m$, $R_m \approx |\psi_m|^{1/2}$.Starting from an unstable tearing mode m=2, n=1($\Delta'_2>0$) we find that: if the m=3, n=1 harmonic is cylindrically unstable, then the two harmonics m=2 and m=3 are mutually pumped with a relative phase 0 or Π depending on the sign of the coupling coefficient $T_{2,3}$; if the m=3, n=1 harmonic is stable then it can be destabilized by toroidal coupling with the same phase,at a normalised amplitude up to a/R_0.Generally, the frequency $R_e(\omega)$ compromises the friction effects within the two resonance surfaces m=2,3 (and of course within the resistive wall).Assuming $T_{3,3}<0$, $T_{2,2}>0$ one finds, in the above Rutherford situation, only one positive root $\gamma=\gamma_R$.For non vanishing Ω,ω^*, the mode may bifurcate from a state $\gamma \approx T_{2,2}/R_2 < \gamma_R$, mainly driven by the plasma velocity and diamagnetism at $r=r_2$, to a state $\gamma \approx \gamma_R$ with a frequency influenced by the frictions at $r=r_3$.

CONCLUSION

Generally the model shall provide by solving (7) the relative amplitude $\psi_m(r_m)$ from which the external mode structure may be deduced and compared to the magnetic probe datas. The model provides also the structure of the pumped internal m=1 n=1 mode by its neighbouring m=2 n=1 , which may be then compared with the soft X-ray data analysis.On the other hand the model should allow to explain the mode frequency $R_e(\omega)$ in terms of diamagnetism and plasma rotation at the resonant layers. Bifurcation in $R_e(\omega)$ could for instance explain the mode locking.

REFERENCES

[1] H.P.Furth ,J.Killeen and M.N.Rosenbluth Phys Fluids 6 ,459(1963)
[2] P.H.Rutherford Phys Fluids 16, 1903(1973)
[3] B.Basu,B.Coppi Phys Fluids 24 ,465 (1981)
[4] D.Edery,J.L.Soulé,R.Pelat Plasma Physics and Controlled Fusion Vol1 IAEA Brussels(1981)
[5] R.J.Hastie Nice, France 12-19October (1988)
[6] D.Edery and al Phys Fluids 26 5 (1983)
[7] A.Samain Plasma Physics and Controll. Fus. Vol 26 5 (1984)

MICROTEARING TURBULENCE AND HEAT TRANSPORT

X. Garbet, F. Mourgues, A. Samain

Association EURATOM-CEA sur la Fusion Contrôlée
Centre d'Etudes Nucléaires de Cadarache B.P. n°1
13108 St-Paul-lez-Durance

INTRODUCTION

Up to now, experimental results do not allow to decide whether electrostatic or magnetic turbulence is the source of anomalous transport in tokamaks. Magnetic instabilities such as microtearing modes are often dismissed, for the transport they induce is usually estimated to be small. These modes are linearly unstable in collisional regimes for reasonable $\beta_p = 2\mu_o nT / B_p^2$ corresponding to a potential vector A which is radially constant near the resonant surface. However, they induce in non linear regimes a small electron heat diffusivity D_e [1]. Indeed, the collisional impedance requires that $D_e/\delta^2 \ll \nu_c$ where δ is the mode radial scale, while a mode is stabilized by electric fluctuations unless δ is smaller than the ion Larmor radius ρ_i. In collisionless regimes, microtearing modes are linearly stable. However, preliminar results [1] show that the modes may be driven unstable by the radial diffusion they induce in non linear regimes where magnetic islands overlap. To study this effect, we use a model where the non linear action of modes on a given Fourier component of the perturbed distribution function is represented by a velocity dependent diffusion coefficient operator. This introduces a new scale $\delta_D \propto D_e^{1/3}$ which must be larger than the linear current width δ_e so that non linear destabilization takes place, and smaller than ρ_i to avoid electric stabilization. Unstable modes are found for $\beta_p \lambda \gtrsim 1$ associated with non constant A profiles. The dependence of the marginal threshold β_p on the parameters $K_\theta \delta_D$, δ_e / δ_D and ρ_i / δ_D is studied in this work.

I BASIC EQUATIONS AND NUMERICAL CALCULATION

We study in a cylindrical equilibrium a perturbed potential vector $\delta \mathbf{A} = \frac{\mathbf{B}}{B} A(r-r_l) \exp\{i(l\theta+m\varphi-\omega t)\} + cc$ and a perturbed electric potential $\delta U = U(r-r_l) \exp\{i(l\theta+m\varphi-\omega t)\} + cc$ (r_l is the radius of the resonant surface $m + \frac{l}{q(r_l)} = 0$) which induce perturbed current and charge densities

δj and $\delta\rho$. The Ampère equation and the electroneutrality constraint may be written in the linear case under a variational form whose functional

$$\mathcal{L} = -\int d_3x \, \frac{|\nabla \times A|^2}{2\mu_o} + \int d_3x \, (j.A^* - \rho U^*) \ ,$$

extremum with A^* and U^*, is derived from the usual electromagnetic action. The densities j and ρ are deduced from a Vlasov equation for each species with non linear Landau terms replaced by a linear diffusion operator [3] with a diffusion coefficient $D(v_{/\!/}) = D_T \, |v_{/\!/}/v_T|$ $\left(v_T = \sqrt{2T/m}\right)$.

It is easier to compute the particle responses in the Fourier space

$$(j(r-r_l),\rho(r-r_l)) = \int_{-\infty}^{+\infty} \frac{dK}{2\pi} \, (j(K),\rho(K)) \exp\{iK(r-r_l)\} \ .$$

leading to the following expression of $\mathcal{L}$ [2]

$$\mathcal{L} = -\frac{1}{\mu_o} \int_{-\infty}^{+\infty} \frac{dK}{2\pi} \, K_\perp^2 \, A(K) \, A^*(K) \ + \sum_{s=i,e} \mathcal{L}_s \qquad (1)$$

$$\mathcal{L}_s = \frac{n_s e_s^2}{T_s} \int_{-\infty}^{+\infty} \frac{dK}{2\pi} \, U(K) \, U^*(K) \ +$$

$$+ \ i \ \frac{n_s e_s^2}{T_s} \iint_{-\infty}^{+\infty} \frac{dK \, dK'}{2\pi} \int_{-\infty}^{+\infty} \frac{dv_{/\!/}}{\sqrt{\pi} \, v_{Ts} \left|\dot{K}_{/\!/} v_{/\!/}\right|} \exp\left(-\frac{v_{/\!/}^2}{v_{Ts}^2}\right) \int_0^{+\infty} dh_\perp \exp -h_\perp$$

$$\left(\omega - \omega_{ns}^* - \omega_{Ts}^* \left(\frac{v_{/\!/}^2}{v_T^2} + h_\perp - \frac{3}{2}\right)\right) Y\left(\frac{K'-K}{\dot{K}_{/\!/} v_{/\!/}}\right) \exp\left\{ i\frac{\omega}{\dot{K}_{/\!/} v_{/\!/}}(K'-K) - \frac{D_s(v_{/\!/})}{6\dot{K}_{/\!/} v_{/\!/}}(K'^3 - K^3)\right\}$$

$$J_0\left(K_\perp \rho_s \sqrt{h_\perp}\right) \ J_0\left(K_\perp \, q \, \rho_s \left(\frac{v_{/\!/}}{v_{Ts}} + \frac{v_{Ts}}{2} \frac{h_\perp}{v_{/\!/}}\right)\right) \ (U(K) - v_{/\!/} A(K))$$

$$J_0\left(K'_\perp \rho_s \sqrt{h_\perp}\right) \ J_0\left(K'_\perp \, q \, \rho_s \left(\frac{v_{/\!/}}{v_{Ts}} + \frac{v_{Ts}}{2} \frac{h_\perp}{v_{/\!/}}\right)\right) \left(U^*(K') - v_{/\!/} A^*(K')\right)$$

where $\omega_{ns}^*, \omega_{Ts}^* = \frac{K_\theta T_s}{e_s B} \left(\frac{\partial n_s}{n_s \partial r} \ , \ \frac{\partial T_s}{T_s \partial r}\right)$ are the diamagnetic frequencies

$$K_\theta = 1/r \quad ; \quad K_\perp^2 = K^2 + K_\theta^2 \quad ; \quad \dot{K}_{/\!/} = K_\theta / L_s$$

and Y is the Heaviside function. The Bessel averaging involving the safety factor q takes account of the drift surface shift and is correct if $K_\theta \rho_i \ll L_n/qR$ and $\frac{K}{1/r} \gg \frac{r}{q}\frac{dq}{dr}$. This variational form has been implemented in a code [2] which finds the modes by scanning over the parameters $\beta_p^* = \frac{n_e T_e}{B_p^2/2\mu_o}\left(\frac{L_s}{L_{ne}}\right)^2$ and $\frac{\omega_{Te}^*}{\omega}$.

I. STABILITY AND ANORMAL TRANSPORT

In the linear case ,i.e. $\delta_e = \omega / \dot{K}_{/\!/} v_{Te} \gg \delta_D = \left(D_{Te} / 6\dot{K}_{/\!/} v_{Te}\right)^{1/3}$, microtearing modes are stable and this is checked numerically. Considering first a magnetic mode ($\delta U=0$) in the case $\delta_e \ll \delta_D$, the main term in (1) is imaginary and vanishes if $\omega = \omega_{ne}^* + \frac{1}{2}\omega_{Te}^*$, whatever A(K) is. The following term, of order δ_e / δ_D ,is found destabilizing for profiles $A(r-r_j)$ decreasing as $\exp\{-|K_\theta(r-r_j)|\}$ outside the resonant layer and exhibiting a hollow shape around the resonant surface (figure 1a).

However, the associated electric potential has a stabilizing influence which depends on the ion resonant response. If the mode is strongly localized, i.e. $\delta_D \ll \rho_i$, the ion response is nearly adiabatic and the modes are weakly stabilized. Increasing the ratio δ_D / ρ_i , the mode do not distinguish between electrons and ions and the threshold β_p^* increases, as shown on figure 1b. This figure allows to derive for a given β_p^* the transport coefficient

$$D_{Te} = 6 \; K_\theta \delta_D \left(\frac{\delta_D}{\rho_i}\right)^2 \frac{\rho_i^2 \, v_{Te}}{L_s}$$

which increases dramatically with β_p^* . For instance , for $\beta_p^* \simeq 3$, the diffusivity D_{Te} is of order $0.04\, \rho_i^2 \frac{v_{Te}}{L_s}$ with $K_\theta \rho_i = 0.25$, $\frac{L_{ne}}{L_s} = 20\sqrt{\frac{m_e}{m_i}}$, q=2, and $dLogT_e/dLogn_e = 2$.

CONCLUSION

A simple model shows that microtearing modes can be unstable in non linear regimes for reasonable values of physical parameters. The bounds obtained on the heat transport coefficient do not allow to neglect such a turbulence and encourage to perform more accurate calculations.

REFERENCES

[1] X. Garbet,F. Mourgues,A. Samain ,Plasm. Phys. Cont. Fus. 30(1988),343.
[2] X. Garbet,L. Laurent,F. Mourgues,J.P. Roubin,A. Samain, report EUR-CEA-FC 1355 , submitted to J. of Comp. Phys. .
[3] P.H. Diamond,M.N. Rosenbluth,Phys. Fluids 24(1981),1641.

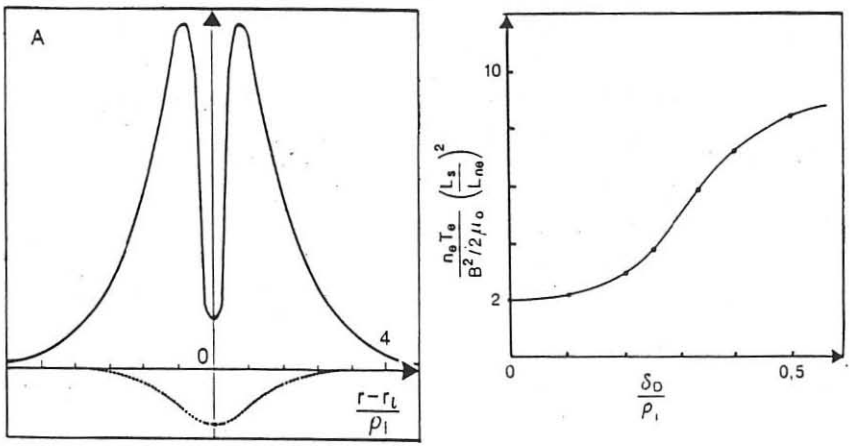

Figure 1a: Marginal profile of a magnetic mode (U=0) for $\beta_p^*=2.9, K_\theta \delta_D=0.1$ The solid and dashed lines represent the real and imaginary parts of A (the scale is $\delta_D/\rho_i=0.1$).

Figure 1b : Marginal threshold β_p^* versus δ_D/ρ_i for q=2, $\omega_{Te}^*/\omega_{ne}^*=2, K_\theta \delta_D=0.1$, $\delta_D/\delta_e = 5$.

TURBULENCE PROPAGATION DURING PELLET INJECTION

X. Garbet, L. Laurent, F. Mourgues, J-P. Roubin, A. Samain

Association EURATOM-CEA sur la Fusion Contrôlée
CEN Cadarache B.P. n°1, 13108 Saint-Paul-lez-Durance, France

ABSTRACT

It has been observed in the TFR tokamak that an injected pellet was preceded by a cold front propagating at about twice its velocity. The aim of this paper is to show that the observed phenomena can be interpreted as a manifestation of the ballooning structure of modes destabilised by the pellet.

I. INTRODUCTION

Details about experimental data during pellet injection in TFR can be found in [1,2]. The most striking features are:

- The "cold front" (position where the electron temperature starts decaying) propagates inwards with velocities ranging between 10^3 and 2 10^3 ms^{-1} outside the q=1 surface (increasing with decreasing minor radius), and much larger inside the q=1 surface.
- Between this front and the pellet which moves more slowly (0.6 10^3 ms^{-1}), there is a zone with enhanced transport ($\chi_e \approx$ 10-100 m^2s^{-1}) that broadens in time up to a width of 0.1 m (half the plasma minor radius).
- When the pellet is fully ablated the heat transport goes back everywhere to its previous value in less than 10 μs.
- The density fluctuations (measured by scattering) are greatly enhanced. The spectrum shape is similar to the one without pellet. A striking feature is that the increase in the fluctuation level starts 30-40μs after the pellet injection and stops 50 μs after the enhanced transport period.

During fast heat transport which lasts typically 150 μs, it seems that the particle transport is only weakly affected. Such a difference in the behaviour of n_e and T_e profiles has been reported by other authors [3,4]. It results that there is a turbulent zone propagating beyond the pellet.

A question addressed by these experiments is how the excited electromagnetic perturbations propagate radially. Two possible mechanisms already proposed are the spreading

of a turbulent zone by non-linear interaction [5] or linear destabilisation by local gradient at the turbulent front [2,6]. However, it should be pointed out that a radial propagation is a natural consequence of the toroidal mode coupling, as discussed in section II. In section III, we propose a scenario based of this model to explain the experimental facts.

II. A LINEAR MECHANISM FOR RADIAL PROPAGATION OF MICROINSTABILITIES

Heat transport is believed to be due to microinstabilities. They can be described by eigenfunctions localized around resonant magnetic surfaces coupled by toroidal effects. When the plasma properties are assumed to be invariant by radial translation, it can be shown that the general solution of the equations defining the instability can be written as [7] :

$$\delta\vec{E},\delta\vec{B} = \sum_{l} \vec{h}(r-r_l)\, \exp\left[i(l\theta - n\varphi - \omega t + l\delta)\right]$$

where $h(r-r_l)$ are functions localized around resonant surfaces r_l and δ is a phase factor. These surfaces are separated by a distance $d=(n\partial q/\partial r)^{-1}$. This expression is equivalent to the ballooning representation. Generally one considers solutions with $\delta=0$. All the modes $h(r-r_l)$ are oscillating in phase with a frequency ω_0. However, the general solution corresponds to arbitrary values of δ and ω is a function of δ. At scales larger than d, the perturbation behaves like a travelling wave with a wave vector $K=\delta/d$ and a frequency $\Omega=\omega(\delta)-\omega_0$. When a perturbation is excited on a magnetic surface its energy propagates at the group velocity $v_g=\partial\Omega/\partial K$ (like phonons in a crystal). When the plasma is weakly inhomogeneous, WKB theory can hold for such waves. When the mode propagates in a zone where it is stable (growth rate $\gamma < 0$), the evanescent length is given by $L=v_g/|\gamma|$.

In the general case $\omega(\delta)$ can only be computed numerically [7]. However a dimensional analysis shows that $v_g = \alpha\, \varepsilon\, v^* / s$ where ε is the inverse aspect ratio representing the mode coupling, v^* is the diamagnetic velocity, $s=(r/q)\,(\partial q/\partial r)$ the shear parameter and α is a constant.

III. A POSSIBLE SCENARIO TO EXPLAIN THE PLASMA BEHAVIOUR DURING PELLET INJECTION

a. Mode excitation

When the pellet reaches a flux tube, it creates a strong perturbation that lasts a time of order $\tau=r_{pellet}/v_{pellet} \approx 1\mu s$ [8]. When the crossed magnetic surface is rational ($q=l/n$) this excitation stays localized around a closed magnetic field line and the shear limits its radial extension Δr to values given by :

$\Delta r < \left(n^2 \frac{\partial q}{\partial r}\right)^{-1} = \frac{d}{n}$. The effect is maximum for $\Delta r \approx r_{pellet}$ i.e. $l = \sqrt{\frac{qr}{sr_{pellet}}}$

These perturbations are short ($\tau\ \omega^*<1$) and well-localized ($\Delta r < \rho_{thi}$, $l \approx 30$). They have significant projections on the plasma eigenmodes. These modes may already exist in the plasma or may be stable: in the second case the pellet creates forced oscillations.

The magnetic field is perturbed because the current is expelled out of the cold flux tubes (resistive perturbation) or because the field lines are perpendicularly displaced by the impact of the pellet (shear Alfvèn waves). The density is increased drastically in the crossed flux tubes (electrostatic drift waves). However, in the latter case, the toroidal equipartition time limited by the ambipolarity constraint is a few tens of microseconds.

From the experimental point of view, the difference between the heat and particles transports and the fact that the density perturbations are delayed suggests that magnetic perturbations are responsible for the enhanced transport.

b. Cold front propagation

According to our model, these perturbations should propagate radially. The observed velocity (1000 ms^{-1}) is compatible with our previous estimate taking $\alpha=4$. (On TFR, $v^*=2500$ ms^{-1}, $\varepsilon=0.2$ and $s=2$ at the edge). The acceleration of the cold front is compatible with the decrease of s along its trajectory. Since transport stops as soon as the pellet disappears, the excited modes are damped. The fact that the turbulent zone extends up to L=10 cm beyond the pellet imposes an upperbound for the damping rate $|\gamma| < v_g / L \approx 10^4\ s^{-1}$.

A noticeable feature is that the fast transport stops everywhere within 10 µs. This implies that the information propagates at a velocity of 10^4 ms^{-1}, no more compatible with the precedent group velocity. However, a possible explanation is that behind the cold front the plasma is strongly turbulent: in such a situation, non linear mode interaction could dominate the toroidal coupling. In the expression of the group velocity, ε (representing the toroidal effects) should be replaced by a larger factor.

In JET, a cold front propagating faster than the pellet has not been observed. This could be explained by our model in two ways:

-in large tokamaks the group velocity can be less than the pellet velocity, because the diamagnetic velocity is lower and the pellets are injected at higher speed.

-the evanescent length $L=v_g/\gamma$ is much smaller than the plasma minor radius. In this case, although the turbulence may propagate faster than the pellet, the cold front is observed to stay at a constant distance L from the pellet. This interpretation corresponds to the experimental data on JET [9] with $L \approx 5$ to 10 cm.

IV. CONCLUSION

Toroidal coupling of modes is the simplest mechanism allowing a radial propagation of low frequency modes that otherwise would remain localized near resonant surfaces. Such a phenomenon should have a strong influence on anomalous transport. For example, this scheme can explain how edge turbulence affects the plasma bulk and why the saturation levels at different radii are coupled.

The study of radial propagation of perturbations can be an useful way to test the properties of microturbulence. First, it can provide a macroscopic evidence of the ballooning structure and then gives quantitative informations about micromodes from the experimental values of L and v_g. Pellets, although not very selective for the excited modes are an useful experimental tool for such investigations.

REFERENCES

[1] TFR Group , Nucl. Fusion **27** (1987) 1975.

[2] Equipe TFR presented by L. Laurent. Plasma Physics and Controlled Fusion, **28**(1986) 85.

[3] Vlases, G., Kaufman, M., Gruber, O., et al. in Controlled Fusion and Plasma Physics (Proc. 11th Europ. Conf. Aachen, 1983), Vol.1, European Physical Society (1983) 127.

[4] Greenwald, M., Parker, J., Besen, M. et al. in Controlled Fusion and Plasma Physics (Proc. 11th Europ. Conf. Aachen, 1983), Vol.1, European Physical Society (1983) 7.

[5] Landau, L. et Lifchitz, E., Mécànique des fluides, Editions MIR (1971).

[6] Dubois, M.A., Samain, A., in Plasma Physics and Controlled Nuclear Fusion Research 1978 (Proc. 7th Int. Conf. Innsbrück, 1978), Vol.1, IAEA, Vienna (1979) 615.

[7] Garbet, X., et al., Report EUR-CEA-FC n° 1355 (1988), submitted for publication in Journal of Computational Physics.

[8] Cheetham, A.D., et al., in Controlled Fusion and Plasma Physics (Proc. 14th Europ. Conf. Madrid, 1987), Vol.1, European Physical Society (1987) 205.

[9] Pégourié, B., and Dubois, M.A., these proceedings, poster P.8 A-4-4.

THERMAL EQUILIBRIUM OF THE EDGE PLASMA WITH AN ERGODIC DIVERTOR

H. Capes, Ph. Ghendrih, A. Samain, A. Grosman, J.P. Morera

Association EURATOM-CEA sur la Fusion Contrôlée, CEN Cadarache,
F-13108 Saint Paul lez Durance, Cédex, France

1 Intoduction

The knowledge of the possible thermal equilibria of a radiating edge plasma layer is of first importance to understand the thermal plasma stability, which in turn controls various edge plasma phenomena (attached-detached plasma, density limit,etc.). The aim of this paper is to study an ergodic divertor (ED) layer in presence of radiating impurities. The main expected effect of the divertor is to build up a layer with a constant radial pressure [1] profile except in a thin layer where neutral interactions take place. We assume the electron density to be sufficiently high so that the thickness of that neutral layer can be neglected. The number of steady equilibria is discussed in terms of the incident power, impurity species and concentrations. The possibility of bifurcation between equilibrium states is discussed (S shaped diagrams). In the case of radiation in the coronal limit, we show that the standard situation exhibits only one steady state.

2 Model

We consider the peripheral plasma region $r_1 < r < r_0$ where the ergodic divertor regime is established. Assuming a slab geometry the heat equation is given by :

$$\frac{d}{dr}\Phi(r) = -C_R\, n^2\, F_R(T) \quad ; \quad \Phi(r) = -\chi \frac{dT}{dr} \qquad (1)$$

where C_R is the impurity concentration, n is the plasma density and where $F_R(T)$ describes the radiation losses. In the collisional regime [1]

$\chi = 2.10^{22}\, T_{ev}^{5/2}\, D/(qR_0)$ $(m^{-2}s^{-1})$ with $D = 2\pi qR_0(\delta B/B)^2$; q is the safety factor, R_0 the major radius and δB the magnetic pertubation created by the ED coils.

The number of equilibria is related to the boundary conditions. In the present case the heat equation has to be solved for a given heat flux from the plasma core $\Phi(r=r_1) = \Phi_1$, while $\Phi(r=r_0)=\Phi_0$ satifies the sheath conditions :

$$\Phi_0 = \gamma_1 \Gamma_0 T_0 \quad ; \quad \Gamma_0 = \gamma_2\, n_0\, (2T_0/m)^{1/2} \qquad (2)$$

where Γ_0 is the plasma flux flowing to the wall and where n_0, T_0 are respectively the density and temperature at the wall. The factor γ_1 incorporates both the effect of the electrostatic sheath potential and the energy exchange with the neutrals. Similarly γ_2 takes account of the

density and velocity variation across the neutral layer (the sheath effect yields the sound velocity dependence).The particle flux escaping from the plasma is assumed null. Finally the neutral flux from the wall is taken as the sum of two contributions $R\Gamma_0 + \Gamma_{ext}$ where Γ_{ext} is an independent source and R the wall recycling coefficient. The particle balance within the neutral layer then determines the flux $\Gamma_0 = \Gamma_{ext}/(1-R)$.

3 Equilibrium of a radiating layer

Eq. 1 allows a straightforward change to an equation of a moving body in a given potential W(u) :

$$\frac{1}{2}\left(\frac{du}{dr}\right)^2 + W(u) = \frac{1}{2}\Phi_1^2 \qquad (3a)$$

$$u = \int^T \chi\, dT \quad ; \quad W(u) = (n_0 T_0)^2\, C_R \int_u^{u_{max}} \frac{1}{T^2} F_R(T)\, du \qquad (3b)$$

The cutoff, u_{max}, which corresponds to a temperature of ~100eV, is due to the strong decrease of χ/T^2 at high temperature when the non-collisional regime is reached (χ scales as $T^{1/2}$). Finally we restrict the study to equilibria such that $u(r_1) > u_{max}$, so that $W(u(r_1))=0$.

In order to solve Eq.(3), we will calculate Φ_0, and thereby T_0 in view of Eq.2, for a given control parameter Φ_1, as done below. For a given couple (Φ_0, T_0), eq.(3) then turns into an initial value problem for which the solution is unique [2]. The number of solutions of Eq.3 for a given Φ_1 is thus entirely determined by the number of initial conditions Φ_0 to the problem. Using Eqs(2,3), the ratio $q_0=\Phi_0/\Phi_1$ is solution of the following nonlinear equation :

$$q_0^2 = 1. - \alpha\beta^{-1} q_0\, S(\beta q_0) \quad ; \quad S(\beta q_0) = \int_{\beta q_0}^{T_{max}/T^*} F_R(yT^*)\, y\, dy \qquad (4)$$

Here T^* is a normalization temperature and the paramaters α and β are given as follows in MKS units,and normalized to Tore Supra characteristic length

$\alpha = 5.3\ 10^{32}(T^*/10)^{0.5}\alpha^*$ $\quad \beta = 1.1\ 10^{23}\beta^*/(T^*/10)(r_1/0.6)(R_0/2.37)$

with $\alpha^* = C_R\,\%/\gamma_1^2\gamma_2^2$ and $\beta^* = (P/10)/(\Gamma\gamma_1/3.5\ 10^{22})$

Here P is the power in MW deposited inside the plasma core ($P = 4\pi R r \Phi_1$).

Note that Eq(4) is formally independent of $\delta B/B$ and then can be applied to study non ED situations such as those encountered in diverted plasmas [3].

4 Bifurcation of equilibria with different impurity species

We choose the coronal expression for $F_R(T)$ [4] and solve Eq(4) numerically. For carbon impurity only,the solution $q(\beta^*)$ is plotted on fig.1 for $\alpha^*=3$. Two bifurcation points are found for $\beta^*=0.86$ and $\beta^*=1$. In

the plane (α^*,β^*) the curves shown on fig.2 reproduce the bifurcation points of the function $q(\beta^*)$ for different α^* values. The two branches of this curves separate the (α^*,β^*) plane in two regions : inside the two branches Eq(4) admits three solutions,outside only one solution exists. The intersection point,A, of the two branches plays the role of a critical point below which no bifurcation can occur when α^*or β^* are varied. For instance, if α is less than 0.5 no bifurcation occurs whatever the power. The behaviour of an impurity mixture composed with carbon and oxygen where the ratio of concentrations $c_R^o/c_R^c=0.075$, is plotted on fig.3 and 4, showing a more complicated structure. The curve $\alpha^*(\beta^*)$ exhibits two distinct domains where the heat equation admits 3 steady solutions. For higher α^* and β^* values areas with 5 solutions can be found.With $\gamma_1=6$ and $\gamma_2=1$, high impurity concentration $(C_R\% \geqslant 20.)$and high power $(P \geqslant 24.\Gamma_0/3.5\ 10^{22})$ are needed to get a bifurcation.

6 Conclusion

Within the coronal hypothesis, the main conclusion is that a strong impurity concentration is requiered for bifurcation to appear when the energy flux is varied. Of great importance in this statement is the high γ_1 value imposed by the sheath physic more than the coronal hypothesis. With lower γ_1 value, lower impurity concentration will be necessary. Thus the heat equation admits generally only one equilibrium state. This practically guarantes the thermal stability of the layer except in cases of oscillating modes.

References

[1] A. Samain et al., J.Nucl. Mater, 128-129 (1984) 185.
[2] P.M. Morse, H. Feshbach, Methods of Theoretical Physics, MacGraw-Hill, (1953), 676
[3] S. Saito et al., Nucl. Fusion, 25 (1985) 828.
[4] D.E. Post et al., Atomic Data and Nuclear Tables, 20 (1977) 397.

Figure captions

Fig.1: Variation of $q_0(\beta^*)$ for $\alpha^*=2.$ with carbon impurity.

Fig.2: Bifurcation points of $q_0(\beta^*)$ for different α value and with carbon impurity only. Inside the two branches, the heat equation admits three steady solutions; A is a critical point below which no bifurcations occur.

Fig.3: Variation of $q_0(\beta^*)$ for $\alpha^*=7.45$ and for an impurity mixture of carbon and oxygen (with a relative impurity concentration $c_R^o/c_R^c=0.075$)

Fig.4: Bifurcation points of $q_0(\beta^*)$ for different α^* value, in the case of the carbon-oxygen mixture, $c_R^o/c_R^c=0,075$.

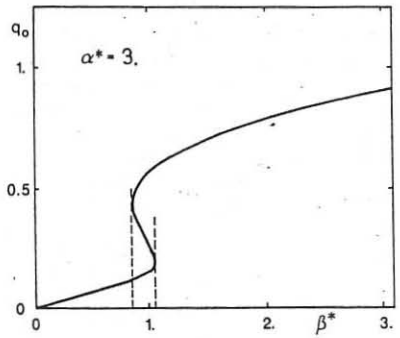

Fig.1

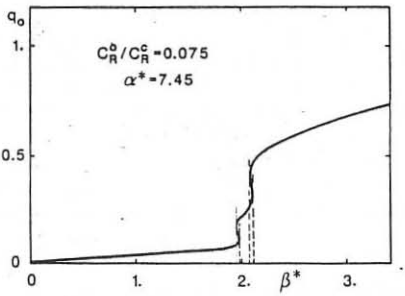

Fig.3

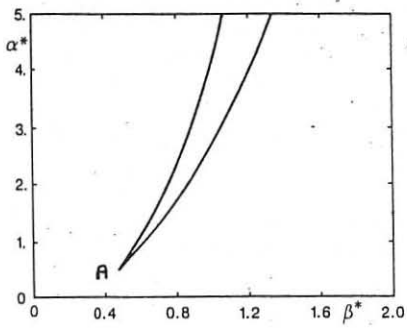

Fig.2

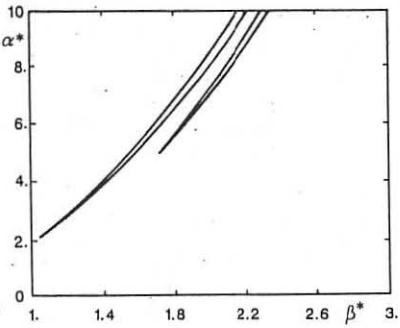

Fig.4

THE DIPOLE CURRENT COMPONENT AND ITS OUTER REGION FIELD IN A TOKAMAK

Shigeo NAGAO

Engineering School, Chubu University, Kasugai, Aichi, 487 Japan.

DIPOLE COMPONENT OF TOROIDAL CURRENT

As is well known, the plasma equilibrium in a tokamak with an axial symmetry can be described, in the toroidal coordinate system (ρ, θ, s) along the circular axis of radius R, by the magnetic field $\vec{B}$ and the current density $\vec{J}$, as follows,[1]

$$\vec{B} = I\,\vec{u} - \vec{u}\times\nabla\psi, \quad \vec{u} = \vec{e}_s/h \quad \text{and} \quad h = 1 - (\rho/R)\cos\theta \tag{1}$$

$$\mu_\circ \vec{J} = \left[I\frac{dI}{d\psi} + \mu_\circ h^2 \frac{dP}{d\psi} \right]\vec{u} - \vec{u}\times\frac{dI}{d\psi}\nabla\psi \tag{2}$$

$$= \mu_\circ \left[1 - (\rho/R)\cos\theta \right]\frac{dP}{d\psi}\vec{e}_s + \frac{dI}{d\psi}\vec{B} \quad , \tag{3}$$

where ψ is the magnetic surface function and I and P are the axial field and plasma pressure respectively, both being assumed as function of ψ .

Thus when this toroidal current density is observed near the magnetic axis at r = R, it is obvious that the current density given by eq.(2) or (3) contains some component, which is assymetric regarding to the vertical on the magnetic axis and is called dipole current component here.

As for the second term of eq.(3) parallel to the magnetic field, it may contains some dipole component but it is of no use for the plasma confinement. Thus such a dipole component in the toroidal current density, which is useful and important for the plasma confinement, is written by

$$\vec{J}_{dp} = -(\rho/R)\cos\theta\frac{dP}{d\psi}\vec{e}_s \tag{4}$$

Thus as far as the plasma equilibrium, described by the Grad-Shafranov equation, is concerned, it has been proved that the toroidal current must contain a certain amount of dipole component being proportional to $dP/d\psi$.

Now in order to make clear the role of this dipole current component in

the tokamak equilibrium, its product with the poloidal field $-\vec{u}\times\nabla\psi$ is calculated in the preious report, as follows,

$$\vec{J}_{dp}\times(-\vec{u}\times\nabla\psi) = [-(\rho/R)\cos\theta\frac{dp}{d\psi}]\vec{e}_s\times\frac{-(\vec{e}_s\times\nabla\psi)}{1-(\rho/R)\cos\theta}$$

$$= -(\rho/R)\cos\theta\frac{\nabla p}{1-(\rho/R)\cos\theta} \quad . \tag{5}$$

By integrating this dipole current force over the toroidal plasma volume we obtain

$$\int\int\int\frac{-x[(\partial p/\partial x)\vec{e}_x+(\partial p/\partial y)\vec{e}_z]}{1-(\rho/R)\cos\theta}dx\,dz\,[1-(\rho/R)\cos\theta]d\theta$$

$$= 2\pi\int\int[-x(\partial p/\partial x)\vec{e}_x]dx\,dz = 2\pi\int\int p\,dx\,dz\,\vec{e}_x$$

$$= 2\pi^2a^2<p>\vec{e}_x \tag{6}$$

Here a and $<p>$ are the average plasma radius and the average plasma pressure respectively. Now it must be emphasized that eq.(6) means that the expandining force of the annular plasma column is balanced with the vector product force of the dipole current times the poloidal magnetic field.

OUTER REGION FIELD DUE TO DIPOLE CURRENT COMPONENT

Since the dipole current component of the toroidal current is shown in the above to be necessary for the equilibrium of a finite beta plasma, it may be interesting to estimate the magnetic field in the outside region of plasma column due to this dipole component for the experiment to verify its finite beta equilibrium. In the MHD theory of a tokamak, given by V.S. Mukhovatov and V.D.Shafranov,[2] the magnetic surface of outer region is assumed as follows,

$$\psi = -\frac{\mu_0 I}{2\pi}[\ln(8R/\rho)-2]-\frac{\mu_0 I}{4\pi R}[\ln(8R/\rho)-1]\rho\cos\omega+$$

$$(C_1/\rho)\cos\omega+C_2\rho\cos\omega+\cdots\cdots, \tag{7}$$

where the constants C_1 and C_2 are determined by the matching with the magnetic surface in the inner region and are given by

$$C_1 = -\frac{\mu_0 I}{4\pi R}(<\beta_p>+\ell_i/2-1/2)a^2 \qquad \text{and} \tag{8}$$

$$C_2 = -B_v = \frac{\mu_0 I}{4\pi R}\left[\ln(8R/a) + \ell_i/2 + <\beta_p> - 3/2\right], \qquad (9)$$

where C_1 gives the outer region field by the dipole current component and C_2 the vertical field to be applied externally.

However, according to J.M.Greene, J.L.Johnson et al.[3], C_1 is given, when the notation is altered so as to fit the present one, by

$$C_1 = \frac{\mu_0 I}{4\pi R}\left[a^2/2 + 2R(\triangle_a - a\triangle_a'/2)\right] = \frac{\mu_0 I}{4\pi R}(a^2/2) \qquad (10)$$

since $\triangle_a = \alpha a^2/2R$, where $\triangle_a$ is the inward shift of geometric center of plasma column with radius a from the magnetic axis and the suffix $'$ denotes the derivative with respect to a. This discrepancy of C_1 between eq.(8) and eq.(10) might induce some confusion in the tokamak physics and so has be explained reasonablly. Obviously it is caused by the difference of inner surface function assumed by them, though in Ref.[3] any functional form of the magnetic surface is not given exlpicitly.

In order to clarify and solve this discrepancy, here is assumed a more general expression as written by

$$\psi = \frac{\mu_0 I}{4\pi a^2}\left[\rho^2 + \delta R\,\rho\cos\omega + (\alpha/R)\,\rho^3\cos\omega + \cdots\right], \qquad (11)$$

where $\alpha = \ell_i/2 + <\beta_p>$. C_1 of eq.(10) results from assuming $\delta = 0$, while C_1 of eq.(8) results from the assumption of a circular outermost magnetic surface of the plasma column with its center on the coordinate axis. However this is equivalent to assume $\delta = \triangle_a = \alpha = 0$, though the assumption of $\alpha = 0$ is not compatible with the model employed in this case.

Now it will be shown in the following the normal method to derive the expressions of C_1 and C_2 by the connection of eq.(7) and eq.(10) on the outermost magnetic surface of the plasma column. Because the geometric center of this surface does not always coinside with the origin of the coordinate system, it is assumed here at first that the former is shifted inwards by $\triangle$ from the latter and so the coordinate system is transformed by the following equations.

$$\rho\cos\omega = \rho'\cos\omega' + \triangle \quad \text{and} \quad \rho\sin\omega = \rho'\sin\omega' \qquad (12)$$

Then the condition that the poloidal field B_ω on the outermost magnetic surface $\rho' = a$ and $\omega' = 0$, given by eq.(7) and eq.(11) must be equal one another requires that

$$\frac{\mu_\circ I}{2\pi a}\left(1+ a\triangle/2R +\cdots\right) = \frac{\mu_\circ I}{2\pi a}\left(1+ 2\alpha\ a\triangle/R+\cdots\right) \qquad (13)$$

and we obtain $\triangle = 0$ unless $\alpha = 1/4$ (14)

Another condition regarding the poloidal field is the equal dependency upon the azimuthal angle ω' on the surface $\rho' = a$. Moreover the plasma column given by both eq.(7) and eq.(11) must be circular. Through all these conditions are obtained C_1 of eq.(8) but not of eq.(10) and C_2 of eq.(8), when $\delta R + \alpha a^2/R = 0$ and $\alpha \neq 1/4$ (15)

Now the inner magnetic surface eq.(11) becomes of Mercier type [4] with $\delta = -\alpha(a/R)$. It is easy to show that when the coordinate origin is shifted outward by $\delta R/2$ to the location of magnetic axis, the expression of C_1 becomes of eq.(10). Since in both cases the expression of B_v is kept unaltered, as is given by eq.(9) and so the part of the revision proposal of the classical formula in the previous report should be withdrawn.

And by the way, it may be interesting to note that in the case of $\alpha = 1/4$ $\triangle$ becomes indefinite, which suggests the possibility of a helically perturbed center core, as measured in ASDEX by G. Lisitano [5] with a Schlieren techniques.

CONCLUSION

It was shown that the outer field due to the dipole component necessary for a finite beta equilibrium of a tokamak plasma, which makes the current profile a little assymetric to the vertical on the magnetic axis will play an interesting role, if measured, for the verification of its equilibrium.

ACKNOWLEDGEMENTS

This work has been supported partly by the Special Research-Aid Funds of Chubu University and partly by the Grant-in-Aid from the Japanese Ministry of Education, Science and Culture.

REFERENCES

[1] S.Nagao: 15th EPS Dubrovnik Conf. Postdeadline paper A3,A4 No. 91.
[2] V.S.Mukhovatov and V.D.Shafranov: Nuclear Fusion,11(1971) p.605.
[3] J.M.Greene, J.L.Johnson et al.: Phys.Fluid,14(1971) p.671.
[4] C.Mercier: Lecture in plasma Physics, EUR 5127 EN/1987.
[5] G.Lizitano: 14th EPS Madrid Conf. Part II p. 1334.

2-D MODEL FOR RUNAWAY DYNAMICS IN TOKAMAKS USING CONSERVATIVE NUMERICAL SCHEME. APPLICATION TO TJ-1 TOKAMAK

L. Rodríguez, R.L. Vázquez* and A.P. Navarro
Asociacion EURATOM/CIEMAT. 28040 Madrid, ESPAÑA

INTRODUCTION

Runaway electrons in tokamak plasmas have received lately a great attention due to several reasons : a) the capability of enhancement the ECH absorption in the presence of a suprathermal tail in the electron distribution [1], and b) the possibility to study electromagnetic turbulence by measuring the runaway flux fluctuations and its energy spectra [2]. In this paper we are presenting a numerical scheme for the development of a 2D model for runaway dynamics and its application to the interpretation of Hard-X-ray spectra. First, a single electron is considered and the obtained results are later extended to the case of maxwellian distribution in the plasma, solving the dynamics equation in a faster and simpler way by using a conservative numerical scheme instead of Fokker-Planck equations.

The properties of the motion of a particle in a force field are related to the existence of certain conservation laws and symmetries. Due to their importance, it is highly desirable that numerical schemes should show a discrete analogous of the conservation laws, symmetries and stability properties of the underlying continuous equations. Otherwise, the scheme can show numerical chaos and the solutions exhibit unphysical properties [3]. In this framework of ideas, we give a new numerical scheme to integrate the equations of motion of a relativistic charge in an electric field either with dissipation or without it.

TWO DIMENSIONAL MODEL

a) Single particle case.

Motion equations for a single electron in a fully ionized plasma for a force field with Coulomb collisions can be expressed as:

$$\begin{cases} \dot{x} = \dfrac{p_x}{\sqrt{m_0^2 + \vec{p}^{\,2}}} \quad ; \quad \dot{y} = \dfrac{p_y}{\sqrt{m_0^2 + \vec{p}^{\,2}}} \\ \dot{p}_x = -\dfrac{\partial U}{\partial x} - \alpha v_x \quad ; \quad \dot{p}_y = -\dfrac{\partial U}{\partial y} - \alpha v_y \end{cases}$$

where, (we use the natural units c=1), m_0 is the rest mass of the particle and , $\vec{p}$ the momentum, U(x) the potential energy of the particle and α the total electron momentum loss collision frequency with relativistic corrections and

$$U = -e\vec{E}\vec{x}, \quad \vec{E} = (E_x, E_y, 0)$$

To solve this system we apply a two dimensional conservative scheme [4] to the fol-

lowing modified discrete equations:

$$\begin{cases} \dfrac{x_{n+1}-x_n}{\tau} = \dfrac{\sqrt{m_0^2+(p_x^2)_{n+1}+(p_y^2)_n}-\sqrt{m_0^2+(p_x^2)_n+(p_y^2)_n}}{(p_x)_{n+1}-(p_x)_n} \\ \dfrac{y_{n+1}-y_n}{\tau} = \dfrac{\sqrt{m_0^2+(p_y^2)_{n+1}+(p_x^2)_{n+1}}-\sqrt{m_0^2+(p_y^2)_n+(p_x^2)_{n+1}}}{(p_y)_{n+1}-(p_y)_n} \\ \dfrac{(p_x)_{n+1}-(p_x)_n}{\tau} = -\dfrac{U(x_{n+1},y_n)-U(x_n,y_n)}{x_{n+1}-x_n}+\alpha\dfrac{(x_{n+1}-x_n)/\tau}{v_n^3} \\ \dfrac{(p_y)_{n+1}-(p_y)_n}{\tau} = -\dfrac{U(x_{n+1},y_{n+1})-U(x_{n+1},y_n)}{y_{n+1}-y_n}+\alpha\dfrac{(y_{n+1}-y_n)}{v_n^3} \end{cases}$$

where:

$$v_n = \frac{\sqrt{(p_x^2)_n+(p_y^2)_n}}{\sqrt{m_0^2+(p_x^2)_n+(p_y^2)_n}}$$

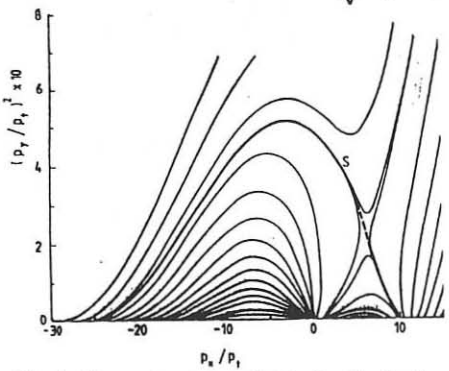

Fig. 1: Momentum-space plot for E_x=E_y=2 v/m, T_e=600 eV, Z_{eff}=1.

The electric field has a main component E_x parallel to v_x and to the magnetic field lines. As initial conditions we take $-1<(v_x)_0<1$, and $(v_y)_0=0$. All calculations are normalized for p using $p=p/p_t$, where p_t is the momentum for the electron temperature T_e. For different values of T_e, Z_{eff} and electric fields E_x and E_y we obtain momentum-space trajectories as is shown at figure 1. We can define two regions in the momentum-space plot, delimited by a separatrix S. With our scheme we can approximate qualitatively the trajectory corresponding to S, calculating trajectories above and below it. The value of the intersection of S with axis x is called p_r. An electron lying on a trajectory above S will gain energy, then runaway, and an electron lying on a trajectory inside S will lose energy and stay thermal. Therefore S represents a trajectory of constant energy. Electrons with negative momentum can become runaway, when their trajectory is above S.

b)Electron distribution functions.

As it was done in [5] for the one dimensional case, we apply our single particle two dimensional model to an electron population with a maxwellian energetic distribution function. We consider that the tail of the maxwellian distribution losses e times runaway electrons in a time τ_r that we call runaway electron confinement time, and the initial maxwellian distribution is restaured in the thermal equilibration time given by:

$$\tau_{eq} = \frac{\sqrt{m_0 T_e^3}}{\sqrt{2}\,\pi n_i e^4 \ln\lambda}$$

For the conditions of figure 1, we obtain the electron distribution function in the phase space shown at figure 2. In figure 3, we represent the distribution function along axis v_x.

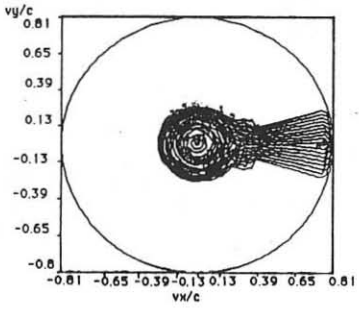

Fig:Electron distribution for T_e=600eV, Z_{eff}=1, E_x=2 V/m, E_y=1.e-3 V/m and τ_r=1.e-4 s.

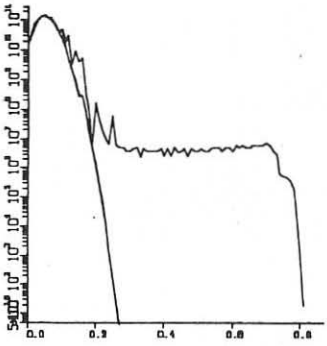

Fig 3: Distribution function along axis v_x

HARD-X-RAY SPECTRUM SIMULATION AND CONFINEMENT TIME.

For each electron distribution function we obtain the hard-x-ray intensity spectrum P(k), using as cross section the expresion given in [6]. In figure 4, we represent hard-X-ray photon and intensity spectra for the conditions of figure 2.

For different values of the runaway confiment time we obtain intensity spectra with different slope α. In figure 5, the relation between α and τ_r is shown.

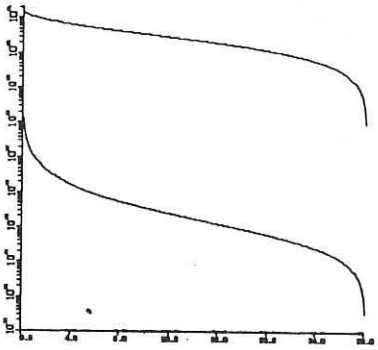

Fig 4: Photon and intensity spectra for conditions of fig 2.

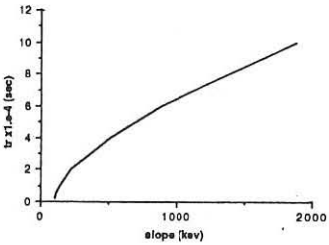

Fig 5: Runaway confinement time versus slope of intensity spectra.

CONCLUSIONS

A 2D model for runaway electron dynamics have been developed based in the solution of a conservative numerical scheme. Results for TJ-I tokamak are in agreement with those obtained with a previous 1-D model. The bidimensional character of the model enables to study situations where other component in addition to the toroidal one can be important such as ECR heated or stellarator plasmas.

REFERENCES

1. C. Alejaldre, Nucl. Fusion 28 (1988) 849.
2. F. Wagner et al. Proc. 14th EUR. Conf. on Contr. Fusion and Plasma Phys., 11D (1987) I 222.
3. W.A. Strauss and L.Vázquez, J. Comp. Phys. 28 (1978) 271.
4. L.Rodriguez R., and A.P. Navarro, Proc. 13th Conf. on Contr. on Contr. Fusion and Plasma Physics, 10D, I, 272, 1986.
5. L. Rodriguez, R., L. Vazquez and A.P. Navarro "2-D model for runaway dynamics in tokomaks. Using a conservatrive numerical scheme". Submitted for publication to J. Comp. Phys.
6. E. Hisdal, Phys. Review,105 ,(1957) 1821.

ATTRACTOR-LIKE BEHAVIOUR OF A TEMPERATURE PROFILE FOR A MAGNETIC CONFINEMENT FUSION PLASMA

H. WILHELMSSON

Laboratoire de Physique des Milieux Ionisés, UPR 65 du C.N.R.S.
Ecole Polytechnique, 91128 Palaiseau, France

In plasma physics there is a considerable interest in phenomena which can be described by reaction-diffusion equations[1]. Recently, various types of reaction nonlinearities of either annihilating type or creative type, leading to explosive growth, and occasionally also to collapse or anti-collapse solutions, have been considered[1,2].

It is the purpose of the present paper to study a particular case of energy transport, which can be formulated in terms of a reaction-diffusion equation, and which exhibits some interesting features concerning the evolution of the temperature profile in a magnetized plasma.

Typical radial shapes of density and temperature profile in H-mode tokamak fusion plasmas indicate a flat distribution in density for the central region, whereas the temperature distribution may be more peaked.

A particular solution for a reaction-diffusion equation which takes into account beside diffusion also bremsstrahlung losses and heating effects, describes the spatial temperature profile and its evolution under the assumption of a flat density distribution for a magnetic confinement fusion plasma. The dynamic response of this profile to deviations of the initial profile is discovered to exhibit attractor-like behaviour, i.e. "nearby" states have a tendency to adjust dynamically to the particular temperature profile.

Assuming the plasma density to be approximately constant in space and time a model equation for the electron temperature T may be written

$$\frac{\partial T}{\partial T} = \frac{a}{x^{\gamma}} \frac{\partial}{\partial x} \left(x^{\gamma} D(T) \frac{\partial T}{\partial x} \right) - cT^{1/2} + S(T), \qquad (1)$$

where γ determines the dimension, $d = 1+\gamma$, assuming here radially symmetrical cases ($\gamma = 1,2$, $x \to r$ for 2D and 3D situations).

The first term on the RHS of Eq. (1) represents diffusion, for which, in the presence of a magnetic field and for perpendicular diffusion we may take $D \sim T^{-1/2}$, the next term accounts for bremsstrahlung losses, and the last term relates to a heating source representing, e.g. heating by alpha particles. Neglecting ohmic heating ($\sim T^{-3/2}$) as well as radiation losses (line and recombination losses) other than bremsstrahlung and, furthermore, modelling the heating source as $S(T) \sim g(t)T$ the model equation to be

studied here is settled. The radially symmetric situation is here first assumed to be infinitely extended, i.e. the effects of spatial boundaries are initially neglected.

Being aware of the fact that the model thus defined admits solutions which are separable in space and time, it is convenient to introduce the transformations

$$\hat{T} = T \exp\left[-\int_0^t g(t')dt'\right], \quad \tau = \int_0^t \exp\left[-\frac{1}{2}\int_0^{t'} g(t'')dt''\right] dt'. \qquad (2,3)$$

By applying the reaction-diffusion theory[1] one obtains a particular solution, namely

$$\hat{T} = \tau_c - \tau)^2 \; \Phi_o \; \text{sec h}^{\alpha}(x/L_\alpha), \qquad (4)$$

where

$$\Phi_0 = \left\{3/[2(2-\gamma)]\right\}^2, \quad \alpha = (4/3)(3+\gamma), \quad L_\alpha^2 = \alpha(2-\gamma),$$

and $\tau = \tau_c$ corresponds to a finite time $t = t_c$ where $\hat{T} = 0$.

For spatial deviations of $\hat{T}$ from the form of the particular solution (4) one may write $\hat{T}$ in a generalized form

$$\hat{T} = A\, F(x/L) \qquad (5)$$

where A and L are now both functions of time : $A = A(\tau)$ and $L = L(\tau)$.

By using an expansion of (5), taking for F the space-functional form (4) and matching constant and x^2-terms in the normalized form of Eq. (1) one obtains two coupled nonlinear equations in time for A and L^2, namely

$$\frac{1}{A}\frac{dA}{d\tau} = \frac{-1}{A^{1/2}}\left[\frac{4(1+\gamma)}{L^2} - 1\right], \qquad (6)$$

$$\frac{1}{L^2}\frac{dL^2}{d\tau} = \frac{1}{2A^{1/2}}\left[\frac{4(2-\gamma)}{L^2} - 1\right]. \qquad (7)$$

One finds by integration from Eqs. (6) and (7) :

$$A/A_o = (L^2/L_o^2)^{2(1+\gamma)/(2-\gamma)} \left[(L^2-L_c^2)/(L_o^2-L_c^2)\right]^{6/(2-\gamma)}, \qquad (8)$$

where A_0 and L_0^2 refer to the initial state and $L_c^2 = 4(2-\gamma)$ to the final state where $A = 0$.

An attractor-like behaviour of the temperature profile follows from Eqs. (6-8). Only for sufficiently small S(T) and in the absence of ohmic heating the t_c will be finite, so that the condition $\tau = \tau_c$, necessary for $T = 0$, can be reached. The tendency of attraction will, however, persist even if a full approach to a solution of the form (4) will not occur.

In the presence of a finite boundary the free solution has to be modified. This is not a trivial matter as a result of the nonlinear nature of Eq. (1). A suitable extension of the spatial part of the particular solution can, however, be written

$$\Psi(r) = \sec h^{\alpha}(r\sqrt{c/a}/L_\alpha) - \epsilon r^2/r_a^2 - (1-\epsilon)(r^4/r_a^4)\sec h^{\alpha}(r_a\sqrt{c/a}/L_\alpha), \qquad (9)$$

where $\Psi(o) = 1$, $\Psi(r_a) = 0$, r_a denoting the radial boundary, and ϵ being a constant.

Experimentally one notices that temperature profiles of large tokamaks, e.g. JET or TEXTOR may be expressed as $\Psi_{exp} = (1-r^2/r_a^2)^{\beta}$ with β of the order of 2-4. Expanding this form to fourth order in r and matching terms up to the same order in the expression (9), making also a configurational modeling of the tokamak by taking $\gamma = 3/2$, i.e. dimension 2 1/2 D, one obtains with $r_a = 1$ and $c/a = 1$ the constant $\epsilon = 3.249$ and the value for $\beta = 2.264$.

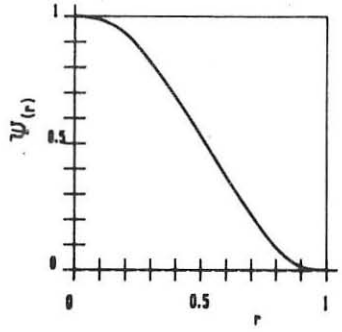

Figure 1 : Radial temperature profile according to the formula (9) with $r_a = 1$ and $c/a = 1$ $\epsilon = 3.249$, $\beta = 2.264$.

The value here obtained for β is in agreement with the value obtained from JET experimental data (β ~ 2.3) for a flat density special case[3]. In fact, the detailed profile shape agreement is so good that the discrepancy is less than a few percent over the whole radial interval[3]. The ratio of the diffusion and bremsstrahlung coefficients may thus be estimated with the aid of expression (9).

[1] H. Wilhelmsson, Phys. Rev. A, 35, 1957 (1987) ; Phys. Rev. A, 36, 965 (1987) ; Phys. Rev. A, 38, 1482 (1987) ; Phys. Rev. A, 38, 2667 (1988).
[2] H. Wilhelmsson, M. Benda, B. Etlicher, R. Jancel and T. Lehner, Physica Scripta, 38 (in print) (1988).
[3] J. Weiland (private communication).

SOME MATHEMATICAL PROPERTIES OF DIFFUSION AND HEAT CONDUCTION IN cylindrical and toroidal plasmas

M.P.H. Weenink

Eindhoven University of Technology, P.O. Box 513, 5600 MB Eindhoven, The Netherlands

The diffusion equation for a perturbation n_1:

$$\partial_t n_1 = \frac{D}{r}\,\partial_r(r\,\partial_r n_1), \tag{1}$$

is solved as an initial value-boundary value problem for a cylindrical plasma.

1°. For an infinite domain ($0 \le r$) with as initial condition

$$n_1(r,0) = Pe^{\alpha r^2} - Qe^{\beta r^2} \qquad 0 \le r \le r_0 \tag{I.1}$$

and $n_1(r,0) = 0$ for $r_0 \le r$. P, Q, α and β can be determined by the requirements that $\partial_r n_1 = 0$ at $r = 0$, $\int_0^{r_0} n_1(r,0)\,r\,dr = 0$, and the least square deviation from the measured $n_1(r,0)$. Even with three free parameters (taking $\beta = 0$) good agreement could be obtained. The solution for this latter case reads

$$n_1(r,t) = \frac{P}{4\theta}\,e^{-\frac{\rho^2}{4\theta}} \sum_{k=0}^{\infty} \frac{1}{(k!)^2}\left(\frac{\rho}{4\theta}\right)^{2k} I_k + Qe^{-\frac{\rho^2}{4\theta}}\left[e^{+\frac{\rho_0^2}{4\theta}} - 1\right]. \tag{I.2}$$

for $\rho\rho_0/4\theta < 1$, and

$$n_1(r,t) = \frac{1}{4\theta\sqrt{\pi\rho}}\left[P\int_0^{\rho_0} d\rho' \sqrt{\rho'}\, e^{\alpha\rho'^2 - \frac{(\rho-\rho')^2}{4\theta}} - Q\int_0^{\rho_0} d\rho' \sqrt{\rho'}\, e^{-\frac{(\rho-\rho')^2}{4\theta}}\right] \tag{I.3}$$

for $\rho\rho_0/2\theta \gg 1$. Here ρ and θ are dimensionless length and time variables and I_k integrals that can be calculated analytically.

Note that the solutions obtained of eq. (1) are completely transferable to solutions of the equation for heat conduction, provided that both the unperturbed density and the heat conductivity K are constants. Even with the inclusion of a loss term (representing e.g. radiation losses or heat transfer losses to the ions) proportional to the temperature perturbation, the equation for the temperature can be transformed into an equation equivalent to eq. (1): the equation

$$\frac{3}{2} n_0\,\partial_t T_1 = \frac{1}{r}\,\partial_r(r\,n_0\,K\,\partial_r T_1) - \frac{n_0}{\tau} T_1 \tag{I.4}$$

becomes an equation of type eq. (1) by the transformation

$N = T_1 e^{\frac{2t}{3\tau}}$ and $K = \frac{3}{2} D$.

The effect of a loss term $n_0 T_1 / \tau$ in a heat pulse like solution on the velocity of the maximum of the $T_1(r,t)$ curve has been determined for a few model solutions. Also the effect on the decay rate of the maximum for the same models has been calculated. These decay rates do not just have an exp-t/τ dependence.

2°. The evolution in time of the density at the axis ($r = 0$) is obtained by setting $r = 0$ in the well-known solution of the initial-value problem:

$$n_1(0,t) = \frac{1}{2Dt} \int_0^\infty dr' r' n_1(r',0) \exp(-r'^2/4Dt). \qquad (II.1)$$

The integral can be considered as a Laplace transform of $\tilde{n}_1(\sqrt{x},0)$ with respect to $x = r'^2$ and $s \equiv 1/(4Dt)$ as Laplace variable. So we may state that the evolution of the density at the axis is related to the initial density perturbation as a function of r by means of a Laplace transform.

3°. Solution of eq. (1) for a finite domain ($0 < p < r < q$) when the boundary conditions at $r = p$ and $r = q$ are periodic functions of time:

$$n(p,t) = \sum_0^\infty f_K e^{iK\omega t}, \quad n(q,t) = \sum_0^\infty g_K e^{iK\omega t}. \qquad (III.1)$$

The solution is found by a straightforward Laplace transform in terms of ber and bei functions:

$$n(r,t) = \sum_0^\infty A f_K \exp i \{\theta_0(\beta_K r)\phi_0(\beta_K q) - \theta_0(\beta_K q)\phi_0(\beta_K r) - K\omega t\} +$$

$$\sum_0^\infty B g_K \exp i \{\theta_0(\beta_K p)\phi_0(\beta_K r) - \theta_0(\beta_K r)\phi_0(\beta_K p) - K\omega t\}. \qquad (III.2)$$

where A and B are rational functions of the ber and bei functions, and θ_0 and ϕ_0 their argument functions [1].

For $\sqrt{\omega\rho^2/D} \gg 1$ eq. (III.2) simplifies to

$$n(r,t) \simeq \frac{\ln(q/r)}{\ln(q/p)} f_0 + \frac{\ln(r/p)}{\ln(q/p)} g_0 +$$

$$\sqrt{\frac{p}{r}} \sum_1^\infty \frac{\sinh(q-r)\sqrt{K\omega/2D}}{\sinh(q-p)\sqrt{K\omega/2D}} f_K \cos\left\{K\omega t - \frac{\pi}{4}(r-p)\sqrt{\frac{K\omega}{2D}}\right\} +$$

$$\sqrt{\frac{q}{r}} \sum_1^\infty \frac{\sinh(r-p)\sqrt{K\omega/2D}}{\sinh(q-p)\sqrt{K\omega/2D}} g_K \cos\left\{K\omega t - \frac{\pi}{4}(q-r)\sqrt{\frac{K\omega}{2D}}\right\}. \qquad (III.3)$$

This result can be interpreted as a superposition of waves emanating from the boundaries p and q. Note that the amplitude of the waves travelling from p towards q vanishes at q and vice versa, independent of the wave number k. The phase velocity of the waves is

$$v_k = \frac{4\sqrt{2}}{\pi}\sqrt{k\omega D}\ , \qquad k \gtrsim 1 \tag{III.4}$$

For $\sqrt{\frac{k\omega q^2}{D}} \ll 1$ eq. (III.2) becomes the quasistatic approximation:

$$n(r,t) \simeq \frac{\ln(q/r)}{\ln(q/p)}\, f(t) + \frac{\ln(r/p)}{\ln(q/p)}\, g(t), \tag{III.5}$$

which means that the density between p and q momentarily adjusts itself to the prescribed boundary conditions. Note that this approximation breaks down for high values of k. The influence of their contributions, however, decays very rapidly with the distance from the boundary. This section is applicable as a model for diffusion in a cylindrical plasma in which the diffusion time $(q-p)^2/D$ is larger than, or of the same order as the saw tooth period $2\pi/\omega$.

4°. The "mirror" perturbation of the density.

In this section we construct a mirror image density perturbation for $r > a$ (a = plasma radius) that forces the density perturbation to be and remain zero at $z = a$. We thus eliminate the necessity of imposing the boundary condition $n(a,t) = 0$. Once this mirror perturbation has been determined ($\tilde{n}_1(r,0), r>a$) the solution of eq. (1) reads:

$$n_1(r,t) = \int_0^\infty dx\, x\, \{n_1(x,0)H(a-x) + \tilde{n}_1(x,0)H(x-a)\} I_0\left(\frac{rx}{2Dt}\right) e^{-\frac{r^2+x^2}{4Dt}} \frac{1}{2Dt}, \tag{IV.1}$$

where H is the Heaviside unit step function.

By requiring $n_1(a,t) = 0$, (IV.1) becomes an integral equation for $\tilde{n}_1(x,0)$. The solution is found to be a Bromwich type integral:

$$\tilde{n}_1(a+a\sqrt{y},0) = \frac{\sqrt{y}}{\pi i\sqrt{(1+\sqrt{y})}} \int_{\sigma-i\infty}^{\sigma+i\infty} d\theta e^{y\theta}\sqrt{4\pi\theta}\ F(\theta) e^{-\theta^2}, \tag{IV.2}$$

where

$$F(\theta) = \int_1^\infty dx\, x \frac{n_1(ax,o)}{\sqrt{4\pi x\theta}} \exp -\theta x^2 + 2\theta x\,. \tag{IV.3}$$

5°. Diffusion with inclusion of the pinch effect.

For this case the diffusion equation becomes:

$$\partial_t\ n_1 = \frac{D}{r}\partial_r(r\,\partial_r n_1) - \frac{1}{r}\partial_r(r\ V(r) n_1). \tag{V.1}$$

The Laplace transform of this equation with respect to time yields a Whittaker equation both for a V = constant and a V inversely proportional to r, so that the solution of the Laplace transform of eq. (V.1) can be expressed in terms of integrals containing the initial perturbation multiplied by Whittaker functions as kernels. To obtain a solution of eq. (V.1) the inverse Laplace transform has to be applied.

In stead of using this cumbersome method we try to eliminate the pinch term by means of a coordinate transformation: $r' = r-Vt$ (and neglecting the term n_1/r with respect to $\partial_r n_1$). Eq. (V.1) now becomes:

$$\partial_t \tilde{n}_1(r',t) = \frac{D}{r'+Vt}\,\partial_{r'}\{(r'+Vt)\partial_{r'}\tilde{n}_1(r',t)\} \qquad (V.2)$$

where $\tilde{n}_1(r',t) \Leftrightarrow n_1(r,t) = n_1(r'+Vt,t)$.

Eq. (V.2) is still not of the same form as eq. (1), because t still occurs in the right hand side. Only by making a further assumption, $Vt \ll r'$ eq. (V.2) reduces to eq. (1) with r replaced by r'. To obtain a more accurate solution a systematic expansion in Vt/r can be applied, which is justified as long as $Vt/r \ll 1$.

6°. Diffusion in a cylindrical plasma taking into account the finiteness of $D_\perp/D_{//}$, and assuming a diagonal diffusivity tensor.

The diffusion eq.

$$\partial_t n = \nabla.(\bar{\bar{D}}.\nabla n) \qquad (VI.1)$$

is split into an eq. for the average $\langle n(r,t)\rangle$ of n over the azimuthal angle φ and the length of the cylinder h:

$$\langle n(r,t)\rangle = \frac{1}{2\pi h}\int_0^h dz \int_0^{2\pi} d\varphi\, n(r,\varphi,z,t), \qquad (VI.2)$$

and an eq. for the deviation $N(r,\varphi,z,t)$ from $\langle n\rangle$.

For $\langle n\rangle$ we thus obtain an equation equal to eq. (1) with D replaced by $D_\perp$, with the well-known solution

$$\langle n\rangle = \int_0^\infty dx\, x\,\frac{n(x,0)}{2D_\perp t}\, I_0\left(\frac{xr}{2D_\perp t}\right)\, \exp-(x^2+r^2)/4D_\perp t. \qquad (VI.3)$$

The eq. for N is solved by Fourier analysis with respect to φ and z. In the equations for the Fourier coefficients the r-dependence of the equilibrium magnetic field enters. In general these equations have to be solved numerically. However, by using an expansion in $D_\perp/D_{//} = \varepsilon$ ($\varepsilon \ll 1$) we find to lowest significant order:

$$N^{(0)}_{m,\kappa}(r,t) = N^{(0)}_{m,\kappa}(r,0)\exp -D_{//}\frac{(mB_\varphi + krB_z)^2}{B^2 r^2}t. \qquad (VI.4)$$

Note that the higher the mode number the faster it decays. Note also that to this order in ε the diffusion of $\langle n\rangle$ and N are independent of each other. Only in first order the solution for N starts to depend on the solution $\langle n\rangle$. The procedure used here can also be applied to a truly toroidal plasma with arbitrary cross section of the magnetic surfaces.

Reference: [1] M. Abramowitz and I.A. Stegun, Handbook of Mathematical Functions, section 9.9 and 9.10 on Kelvin functions.

Acknowledgement. Part of this work was performed at J.E.T. Undertaking in Culham during a leave of absence from the Eindhoven University of Technology in the summer period of 1988.

ENERGETIC PARTICLE EFFECTS ON THE INTERNAL KINK MODES IN TOKAMAKS*

C.Z. CHENG

PRINCETON PLASMA PHYSICS LABORATORY
P.O. BOX 451, PRINCETON, NJ 08543

The analytical studies of the energetic particle effects on the internal kink modes have shown that if $|\langle\omega_D\rangle/\omega| >> 1$ and $(\omega_*/\langle\omega_D\rangle) > 0$, the ideal branch is stabilized for $\beta_h > \beta_{h1}$, but a resonant fishbone branch is destabilized with $\omega \lesssim \langle\omega_D\rangle$ for $\beta_h \gtrsim \beta_{h2}$, where $\beta_{h2} \geq \beta_{h1}$. Numerical studies by the NOVA-K code [1], which computes kinetic-MHD stability of realistic numerical tokamak equilibria with neutral beam injection have confirmed these qualitative conclusions, but give quantitatively very different values of β_{h1} and β_{h2} (can be an order of magnitude larger). In addition a necessary condition for exciting the resonant fishbone branch requires that the total plasma $\beta > \beta_c$ where β_c is the ideal MHD critical β. This is contrary to the analytical analysis that only $\beta_h > \beta_{h2}$ is required. Therefore, we obtain a stability window in the $\beta - \beta_h$ diagram for the n=1 internal kink even in the absence of FLR effects (finite ω_{*i}) of core plasma ions. Since the bounce-averaged $\langle\omega_D\rangle$ may change sign for different flux surfaces and different trapped particle pitch angles, the stability of the internal kink modes must be computed by the NOVA-K code. For alpha particles generated in the ignited tokamaks, the stability of the internal kink modes is weakly influenced because the alpha particle distribution is isotropic in pitch angle and sampling of trapped alpha particles with $\langle\omega_D\rangle$ of different signs almost averages out the alpha contribution to δW. This result is different from the previous conclusion of alpha-particle stabilization of the internal kink obtained from the simple assumption that $\omega_*/\langle\omega_D\rangle > 0$ for all trapped alpha particles.

I. Introduction

The n=1 ideal MHD internal kink mode is usually unstable for tokamak plasmas with $\beta > \beta_{crit}$ and $q(0) < 1$ so that the $q = 1$ surface lies within the plasma. The stabilization of the internal kink and ballooning modes by an energetic particle component mirror-trapped on the unfavorable-curvature side of the tokamak has been proposed by Rosenbluth et al. [2]. Their stabilization mechanism requires that the hot particles drift across field lines rapidly i.e., $\langle\omega_d\rangle >> |\omega|$ and $(\omega_*/\langle\omega_d\rangle) > 0$. The stabilizing kinetic energy of the hot particles may bring the plasma into the second stability region, where the stability may improve with increasing β. Chen et al. [3] further showed that for $\beta_h > \beta_{hcrit}$ and $(\omega_*/\langle\omega_d\rangle) >> 1$, the trapped energetic ions can resonantly destabilize a new branch of internal kink mode (called fishbone mode) with a real

frequency comparable to $\langle\omega_d\rangle$ and that the growth rates are of the same order as the ideal internal kink values. This fishbone mode was used to explain the experimental observations of large amplitude bursts of m=n=1 MHD fluctuations in tokamak experiments with high-power, nearly perpendicular neutral beam injections.

These previous analytical theories [3] of energetic particle effects on the internal kink mode were performed for large aspect ratio tokamak plasmas with circular, concentric magnetic surfaces, and the radial plasma displacement ξ_r was taken as the cylindrical solution of the m = n = 1 mode with ξ_r = constant for $q \leq 1$ (or $r \leq r_s$), and $\xi_r = 0$, otherwise. In addition, there are other approximations made in calculating energetic particle contributions to δW, such as, 1-q(0)=0, $(\omega_*/\langle\omega_d\rangle) > 0$ for the whole minor radius, and no toroidal couplings of neighboring poloidal harmonics. Those approximations can be quite erroneous for realistic finite aspect ratio tokamaks. Therefore, the analytical theory, although it predicted the excitation of the fishbone mode, failed to give quantitative predictions of the critical β_h for both the stabilization of the internal kink and the excitation of the fishbone mode.

II. Energetic Particle Effects on the Internal Kink

In this section we will present numerical studies of the effects of energetic particles on the n=1 internal kink mode by using the NOVA-K code [1]. We consider an equilibrium with circular plasma surface computed from a flux equilibrium code. The equilibrium parameters are $\Delta\psi$ = 0.061, $\langle\beta\rangle_{av}$ = 0.625%, R = 1.43, R/a = 3.4, P_o = 0.018, q(0) = 0.8, q(1) = 2.85, q'(0) = 13.82 and q'(1) = 106.6. For a given pitch angle Λ_o, $\langle\omega_d\rangle$ may change from being negative to positive as r changes, which means that $(\omega_*/\langle\omega_d\rangle)$ also varies from being positive to negative. If the trapped particles are destabilizing to a certain MHD mode for $(\omega_*/\langle\omega_d\rangle) > 0$ in certain radial region, the trapped particles in the radial region with $(\omega_*/\langle\omega_d\rangle) < 0$ would be stabilizing. Thus, the net effect of hot trapped particles must be integrated over the entire hot particle population with proper weightings of different poloidal harmonics. For neutral beam heated plasmas, F_{oh} is taken as a slowing-down distribution in energy and a delta function in pitch angle. Since both ω_* and $\langle\omega_d\rangle$ are proportional to T_h or (ε_b), we will introduce a temperature scaling factor C_T in ω_* and $\langle\omega_d\rangle$. For $C_T \to \infty$, the eigenmode equations correspond to the case studied by Rosenbluth et al.[2]. We will set $n_h(\psi)T_h = \alpha_h P_c(\psi)$, and vary α_h to change the hot particle pressure. Λ_o=1.1 is the pitch angle of the injected beam ions. For this equilibrium, the volume averaged hot particle beta, $\beta_h \equiv 2\langle p_h\rangle/\langle B^2\rangle$, is related to the total volume averaged beta, $\beta = 2\langle p\rangle/\langle B^2\rangle$, by $\beta_h = 1.38\,\alpha_h\beta$ where $\beta = 0.625\%$. In varying β_h (or α_h) we will keep the total β fixed so that as β_h is increased, the core plasma β_c is decreased by the same amount.

In Figs. 1(a) and 1(b), the growth rates and the negative real frequencies, respectively, versus the hot particle pressure scaling factor

α_h are plotted for several values of the hot particle injection energy scaling factor C_T. For $C_T \lesssim 0.4$, the hot particle pressure is stabilizing for small values of α_h, but becomes destabilizing as α_h becomes larger ($\alpha_h > 0.036$). The destablizing effect is accompanied by an increase in $|\omega_r|$ and is associated with $\omega - \langle\omega_d\rangle \simeq 0$ resonance. However, when C_T becomes larger with $C_T \simeq 1$, the ideal branch is stabilized for $\alpha_h \gtrsim \alpha_{h1} \simeq 0.036$ (for $C_T \simeq 1$). But the resoant fishbone branch is destabilized for $\alpha_h > \alpha_{h2} \simeq 0.06$ for $C_T = 1$. For larger C_T, α_{h1} is smaller, but α_{h2} becomes larger. Note that the broken curves in Fig. 1(a) are obtained by employing the extrapolation scheme due to numerical difficulties near marginal stability with $|\gamma/\omega_r| \ll 1$ or $|\gamma/\omega_A| \ll 1$ when the eigenfunction ξ_ψ becomes singular.

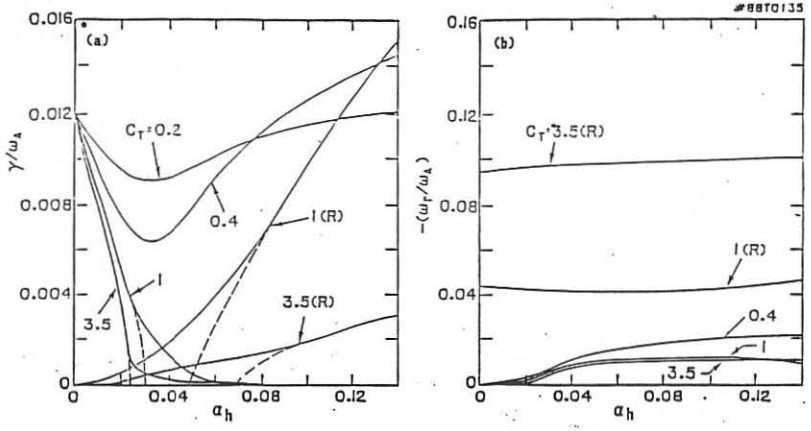

Fig. 1 (a) The growth rates, (γ/ω_A), versus α_h for both the ideal and the resonant branches for several values of C_T which scales $\langle\omega_d\rangle$ and ω^*. (b) The corresponding negative real frequencies, $-(\omega_r/\omega_A)$, versus α_h.

The results presented in Figs. 1(a) and 1(b) are qualitatively similar to those obtained from the following analytical dispersion relation for the neutral-beam-injected energetic particle distribution:

$$-i\left(\frac{\omega}{\omega_A}\right) = \left(\frac{\gamma_{MHD}}{\omega_A}\right) - \frac{9}{8}\hat{\beta}_h \left\{\frac{\omega_*}{\omega_d} + \frac{\omega}{\omega_d}\left(\frac{\omega_*}{\omega_d} - 1\right)\left[\ell n\left(1-\frac{\omega_d}{\omega}\right) + i\pi\sigma\right]\right\} \quad , \quad (*)$$

where $0 < \mathrm{Re}(\omega) < \omega_d$, $\sigma = 0$ for $\mathrm{Im}(\omega) > 0$, $\sigma = 1$ for $\mathrm{Im}(\omega) = 0$, and $\sigma=2$ for $\mathrm{Im}(\omega) < 0$. ω_* and ω_d are the typical hot particle diamagnetic drift frequency and the bounce-averaged magnetic drift frequency, respectively. $\hat{\gamma}_{MHD}$ is the ideal MHD growth rate in the absence of hot particles, and $\hat{\beta}_h$ is proportional to the hot particle β_h. Equation (1) predicts

that if $\gamma_{MHD} > 0$, the ideal branch will be stabilized for $\hat{\beta}_h > \hat{\beta}_{h1}$, where $\beta_{h1} = (8\gamma_{MHD}\omega_d/9\omega_A\omega_*)$. At $\beta_h = \beta_{h1}$, $\omega = 0$. The resonant fishbone branch will be destabilized for $\beta_h > \beta_{2h}$, where $\beta_{h2} = 8\omega_d/[9\pi\omega_A(\omega_*/\omega_d - 1)]$. At $\beta_h = \beta_{h2}$, ω is purely real. For $(\omega_*/\gamma_{MHD}) \geq \pi(\omega_*/\omega_d - 1)$ (i.e., $\beta_{h1} > \beta_{h2}$), the ideal branch is unstable for all β_h. For $\beta_{h1} < \beta_{h2}$, there is a stability window for $\beta_{h1} \leq \beta_h \leq \beta_{h2}$.

Next, we examine the validity of the approximations made in the analytical theory of Chen at al.[3]. Our calculations show that although the analytical theory gives qualitatively correct results, it fails to provide the correct values of the critical hot particle betas for both the stabilization of the ideal branch and the destabilization of the resonant fishbone branch. To make comparisons on the values of critical β_h, we impose similar approximations, as done in Ref. 3 in computing the perturbed hot particle pressures. The analytical approximations have produced an error in β_{h1} and β_{h2} by roughly a factor of 4 in this particular example. The error is mainly due to the omission of higher poloidal harmonics in $\delta\hat{p}$.

Another important result that is different from that of Chen et al. [3], is that a necessary condition to excite the resonant fishbone mode is $\beta > \beta_c$, where β_c is the ideal MHD critical β for the n=1 internal kink. From the analytical dispersion relation, the critical β_h for excitation of Fishbone mode is independent of γ_{MHD}, and there is no constraint on the total plasma β. Our conclusion is derived by computing the stabilities of several equilibria with decreasing β. As β is decreased, the growth rates of both the ideal branch and the resonant fishbone branch also decrease. For $\beta \leq \beta_c$, no instabilities are found by the NOVA-K code.

Finally, the NOVA-K code has been employed to study the energetic particle effects on the internal kinks, external kinks, and toroidicity induced shear Alfvén [4] waves for various types of MHD equilibria and energetic particle distributions. For example, our results show that the α-particle has very little effect on the n=1 internal kink mode for Compact Ignition Tokamak type equilibria. This is contrary to the results of several analytical calculations which either made a very improper approximation of keeping only the m=1 poloidal harmonic or failed to integrate over the α-particle pitch angle with self-consistent equilibria.

*This work was supported by U.S. DoE Contract No. DE-AC02-76-CH03073.

[1] Cheng, C.Z., PPPL-2575 (1988).
[2] Rosenbluth, M.N., S.T. Tsai, J.W. Van Dam, and M.G. Engquist, Phys. Rev. Lett. 51 (1983), 1967.
[3] Chen, L., R.B. White and M.N. Rosenbluth, Phys. Rev. Lett 52(1984), 1122.
[4] Cheng, C.Z., G.Y. Fu, and J.W. Van Dam, PPPL-2585 (1988).

ALPHA PARTICLE DESTABILIZATION OF SHEAR ALFVÉN WAVES IN IGNITED TOKAMAKS*

C.Z. CHENG, G.Y. FU†, and J. VAN DAM†

PRINCETON PLASMA PHYSICS LABORATORY
P.O. BOX 451, PRINCETON, NJ 08543

The effects of alpha particles on the stability of the shear Alfvén waves are investigated for realistic numerical toroidal equilibria with noncircular flux surfaces by employing a nonvariational kinetic-MHD stability code (NOVA-K). [1] Both the low-n and the high-n toroidicity-induced shear Alfvén eigenmodes (TAE) [2,3] were shown to exist with frequencies lying in the gaps of the shear Alfvén continuum spectrum due to toroidal couplings of neighboring poloidal harmonics. The TAE modes can be strongly destabilized via transit resonance with alpha particles when the inverse Landau damping associated with the alpha particle pressure gradient becomes larger than the velocity space Landau damping. On the other hand, the global Alfvén eigenmode (GAE), whose frequency lies just below the minimum of the continuum, are shown to remain stable.

1. Introduction

Ignition tokamak experiments will contain alpha particles with very high energies and in neither coordinate nor velocity space will they be in thermodynamic equilibrium. Consequently, "thermonuclear" instabilities could be driven by the expansion free energy associated with the spatial gradient of the alpha particle pressure, ∇P_α, which enters the dynamical equations that describe the plasma behavior through the alpha particle diamagnetic frequency $\omega_{*\alpha}$. For typical ignition parameters the alpha particle velocity $v_\alpha = (\varepsilon_\alpha/M_\alpha)^{1/2} = 9\times 10^8$ cm/sec for an energy of 3.5 MeV is comparable to the Alfvén speed $V_A = B/(N_i M_i)^{1/2}$. Thus, the transiting alpha particles could destabilize shear Alfvén waves via inverse Landau damping through the $\omega \simeq k_\parallel v_\parallel$ wave-particle resonance. To satisfy the resonance condition, it requires that $v_\alpha > v_A$. To overcome the Landau damping by the inverse Landau damping associated with $\omega_{*\alpha}$, it requires that $\omega_{*\alpha} > \omega_A$.

In this work, we will investigate two global types of shear Alfvén waves with low mode numbers n and m. The first type of global shear Alfven wave is a regular, spatially nonresonant wave whose frequency lies just below the minimum of the continuum, i.e. $\omega < k_\parallel V_A$ and $k_\parallel \neq 0$. This wave is called the Global Alfvén Eigenmode (GAE). Previous theoretical analysis of this mode was limited to cylindrical geometry, where it was found that transit wave-particle resonant interaction with super-Alfvénic alpha particles could destabilize it, although with weak growth rates

[4]. When finite toroidicity is included, GAE modes with different poloidal mode numbers will become coupled. We will show that toroidal coupling tends to stabilize the GAE modes completely. Another type of global shear Alfvén wave, is called Toroidicity-Induced Alfvén Eigenmode (TAE) and exists only in toroidal geometry. Its frequency lies within "gaps" in the shear Alfvén continuum that are created due to toroidal coupling. We find that this TAE mode can be strongly destabilized by alpha particles in a burning tokamak plasma [5].

2. Stability of Global Alfvén Eigenmodes

In toroidal geometry, finite toroidicity can stabilize the GAE modes via coupling to electron Landau damped sideband modes that resonate with the shear Alfvén continuum [6]. The theoretical framework is contained in the general wave equation, written in the form

$$\nabla \times \nabla \times \underline{E} - \frac{\omega^2}{c^2} \underline{\underline{\chi}}_f \cdot \underline{E} = \frac{\omega^2}{c^2} (\underline{\underline{\chi}}_k + \underline{\underline{\chi}}_\alpha) \cdot \underline{E} \quad . \tag{1}$$

Here, $\underline{E}$ is the perturbed electric field, and the susceptibility tensor has been separated into three parts: $\underline{\underline{\chi}}_f = (c/V_A)^2(\underline{\underline{I}}-\underline{bb})$ for the plasma fluid response, $\underline{\underline{\chi}}_k$ for the core plasma kinetic response (including ion FLR and parallel electron dynamics, but in the low frequency limit $\omega/\omega_{ci} < 1$), and $\underline{\underline{\chi}}_\alpha$ for the drift-kinetic alpha particle response.

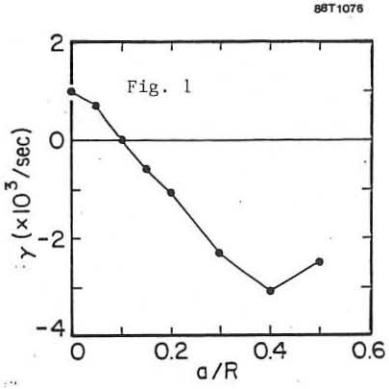

Fig. 1 shows the growth rate of the n=1, m=-2 GAE mode coupled to the sidebands (1,-1) and (1,0), as a function of the inverse aspect ratio. At a/R=0 (i.e., in the cylindrical limit), alpha particles excite this mode to be unstable. However, as toroidicity is introduced, the mode becomes stable for aspect ratios $R/a < 10$. Fig. 1 was computed for $L_\alpha/a = 0.25$. The real frequency of the mode is $\omega_r = 7.95 \times 10^6\ s^{-1}$. The n=0 GAE mode is found to be stable in toroidal geometry in fully toroidal numerical calculations, performed with the NOVA-K code. This result will be discussed in the theoretical interpretation given in Sec. 4.

3. Stability of Toroidicity-Induced Alfvén Eigenmodes

The stabilities of the TAE modes were solved in a general toroidal flux coordinate system for realistic numerical equilibria by the NOVA-K code [1]. The alpha particle equilibrium distribution function, $F_{o\alpha}$, was taken to be isotropic in pitch angle Λ and slowing down in energy ε. The alpha particle density is taken to be proportional to 3.5 power of the total plasma pressure $P(\psi)$.

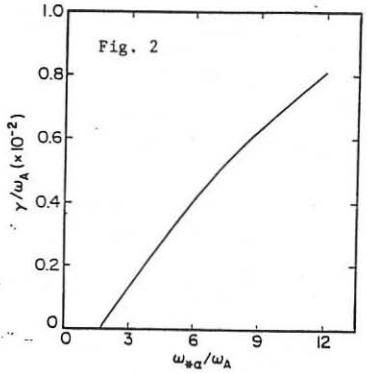

Figure 2 shows the growth rate for the n=1 fixed boundary TAE mode as a function of the alpha particle diamagnetic drift frequency $\omega_{*\alpha}$ (evaluated at $y^{1/2} = 0.5$ and for m=1) normalized to $\omega_A = V_A(0)/q(a)R$, for a numerical equilibrium with a circular plasma boundary. The pressure profile is $P(y) \propto (1-y^2)^2$, with $y=\psi/\Delta\psi$ the normalized poloidal flux. The other parameters for Fig. 2 are $q(0) = 1.05$, $q(a) = 2.3$, $R/a = 4$, $\langle\beta_{total}\rangle = 1.89\%$, and $\langle\beta_\alpha\rangle = 0.4\%$. The real frequency of the mode is $\omega_r/\omega_A = -0.705$, which lies within the continuum gap formed by the toroidal coupling of the m=1 and m=2 modes at q=1.5. Figure 2 shows that $\omega_{*\alpha}$ is large enough to overcome the usual Landau damping when $\omega_{*\alpha}/\omega_A \gtrsim 1.5$ and that beyond this threshold the growth rate γ is approximately linearly proportional to $\omega_{*\alpha}$. For typical ignition parameters, the growth rate of the n=1 TAE mode can be about one order of magnitude larger than the GAE mode growth rates (evaluated at small a/R).

4. Theoretical Interpretation

From the eigenmode equations one can construct the quadratic form

$$\omega^2 \delta K = \delta W_f + \delta W_\alpha \quad . \tag{2}$$

Here, δK is the inertial energy, δW_f is the fluid-like potential energy, and δW_α is the potential energy of the kinetic alpha particles (including their transit and bounce resonances). For the mode frequency, we write $\omega = \omega_r + i\gamma$ and assume that the growth rate is small ($|\gamma| \ll |\omega_r|$). Then Eq. (2) yields

$$\gamma \tilde{=} -\mathrm{sgn}(\omega_r)\int d\psi d\Lambda \left(\frac{9\pi^2 \hat{\tau}_t}{4\ \delta K}\right) P(\psi) \sum_{m,m';p=-\infty}^{\infty} \frac{\left[\omega_r - \omega_{*\alpha}^{(m)}\left(\frac{\omega_r/\omega_t}{p-nq}\right)^2\right]}{(p-nq)^2 \omega_t^2} \mathrm{Re}\left[\langle G_{m',p}\rangle^* \langle G_{m,p}\rangle\right], \quad (3)$$

where $G_{m,p} = F_m(\Lambda,\theta)\exp\{i[(m-nq)\theta-(p-nq)\omega_t \hat{t}]\}$, $F_m(\Lambda,\theta)$ depends on the pitch angle, the equilibrium θ-variation and the mode amplitude, t is the time-like variable measuring alpha particle position along a field line, ω_t and τ_t are the alpha particle transit frequency and transit time, respectively, and $\langle G_{m,p}\rangle$ is the transit average of $G_{m,p}$. The transit harmonic number is p, where p values close to m contribute the most. We define $\omega_{*\alpha}^{(m)} = m\omega_{*\alpha}$, where $\omega_{*\alpha}$ is the diamagnetic frequency for m=1.

Equation (3) shows that the instability condition is $\omega_{*\alpha}^{(m)} \geq \omega_r$; here the alpha particle free energy drive overcomes usual Landau damping. This marginal stability condition agrees with the numerical result, shown in Fig. 2, for which $\omega_{*\alpha}/\omega_A \simeq 1.5$ is marginal. Above this threshold, Eq. (3) indicates that the growth rate γ will tend to scale linearly with $\omega_{*\alpha}$, which again agrees with Fig. 2.

The form of Eq. (3) also shows why the n=0 GAE mode is stable in toroidal geometry. Since the alpha particle effects are perturbatively small, to a good approximation the mode structure is given by the ideal MHD toroidal wavefunctions. Being self-adjoint, these wavefunctions have the symmetry property $|G_{m,p}|^2 = |G_{-m,-p}|^2$ for n=0. Thus, the alpha particle excitation terms $\omega_{*\alpha}^{(m)}$ and $\omega_{*\alpha}^{(-m)}$ are seen to tend to cancel in Eq. (3), so that the n=0 GAE mode is stable.

The results of this paper indicate that the global Alfvén eigenmodes (GAE) will not be problematic in ignition tokamaks. Toroidicity tends to stabilize the n≠0 GAE modes for a/R > 0.1, and the n=0 GAE mode is stable when the ± m mode coupling is taken into account. Therefore, primary attention should be focused on the toroidicity-induced shear Alfvén eigenmodes (TAE), which can be strongly destabilized by alpha particles. It should be noted that if the edge plasma density value is reduced, the toroidicity-induced mode may possibly resonate with the shear Alfvén continuum near the plasma periphery, an effect which could be stabilizing and should be investigated.

†Permanent address: Institute for Fusion Studies, University of Texas at Austin, Austin, TX 78712

*DoE Contract No. DE-AC02-76-CH03073 with Princeton University and DoE Contract No. DE-FG05-80ET-53088 with the University of Texas.

[1] C.Z. Cheng, in Theory of Fusion Plasmas (Societa Italiana di Fisica - Editrice Compositori, Bologna, 1988), p. 185.
[2] C.Z. Cheng and M.S. Chance, Phys. Fluids 29, 3695 (1986).
[3] C.Z. Cheng, L. Chen, and M.S. Chance, Ann. Phys. (NY) 161, 21 (1984).
[4] Y.M. Li, S.M. Mahajan, and D.W. Ross, Phys. Fluids 30, 1466 (1987).
[5] C.Z. Cheng, G.Y. Fu, and J.W. Van Dam, PPPL-2585 (1988).
[6] G.Y. Fu, Ph.D. Thesis, University of Texas at Austin, Institute for Fusion Study Report No. 325 (1988).

ALPHA PARTICLE LOSS IN TOKAMAKS*

R.B. WHITE and H.E. MYNICK

Princeton University, Plasma Physics Laboratory,
P.O. Box 451, Princeton, NJ 08543 USA

Rapid alpha particle loss has been examined for tokamaks, and the dominant mechanism found to be ripple induced stochastic trapped particle diffusion.[1,2,3] A very simple loss criterion allows the rapid estimation of total alpha particle loss. The results agree reasonably with guiding center calculations.

Stochastic ripple loss is easily understood. The banana tip position of a toroidally precessing trapped particle is modified by the ripple. When the toroidal bounce position is modified by an amount comparable to a ripple period, the ripple phase of the drifting banana decorrelates in a bounce time, and stochastic collisionless diffusion results. The field magnitude at the banana tip is conserved, so the tip diffuses approximately vertically until the banana is large enough to intersect the wall. The diffusion constant is large enough to result in particle loss in a time which is short compared to the slowing-down time. The approximate condition on the ripple magnitude $\delta = \delta B/B$ (peak to average) for stochastic diffusion is, in a circular cross section,[3]

$$\delta > \left(\frac{\varepsilon}{\pi N q}\right)^{3/2} \frac{1}{2\rho q'} \qquad (1)$$

where N is the number of ripple coils, q the safety factor, ρ the gyro radius, ε the inverse aspect ratio, and $q' = dq/dr$.

This identification of stochastic ripple diffusion as the dominant loss mechanism makes it possible to very quickly calculate an estimate for alpha-particle loss, using an analytic criterion. We have investigated global ripple loss due to stochastic diffusion using the code RIPLOS. This code reads numerically generated equilibria, which can have arbitrary cross-sectional shape and pressure and current distributions. It then produces a Monte-Carlo-generated alpha-particle distribution, and numerically evaluates the local stochastic threshold condition, which is a generalization of Eq. (1) to an arbitrary equilibrium. Shown in Fig. 1 is the domain for stochastic loss given by this criterion for an INTOR equilibrium. Because the ripple magnitude is much larger near the field coils, the condition given by Eq. (1) defines a loss domain bounded by a curve C. Thus trapped particles can be

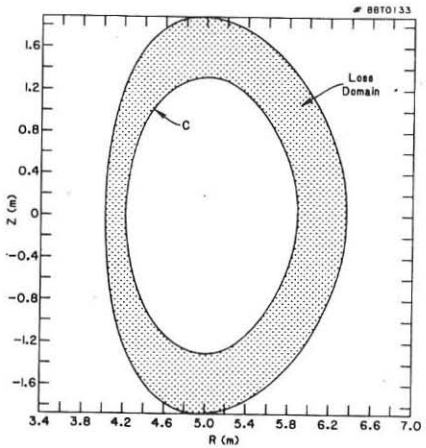

Figure 1. Loss domain for stochastic ripple diffusion.

counted lost if their banana tip is located outside the curve C. This very simple code allows a rapid examination of alpha-particle loss as a function of equilibrium parameters. Comparison of the results with a full guiding-center calculation[4] shows that reasonable confidence can be given to this method, with a saving in computing time of approximately four orders of magnitude. The dependence of the loss fraction for fusion-product alpha particles in INTOR and TFTR as a function of the safety factor q at the limiter is shown in Fig. 2. Equilibrium scaling is used, with the entire q-profile increasing with q-limiter. The ripple at the plasma edge is 1% in INTOR and 2% in TFTR. The very strong q-dependence arises from the sensitivity of the threshold condition to q and the steepness of the alpha distribution. As the curve C of Fig. 1 moves inward it causes rapidly increasing losses. The flattening of the loss curve for very large q, reflects the fact that all trapped particles are lost. The curves in Fig. 2, each consisting of ten equilibria and using 40,000 particles per distribution, took two minutes of computing time on the CRAY, whereas a single point generated by the guiding-center code, using only 500 particles, took several hours for low q-values.

The loss mechanism produces a localization of the lost particles near the midplane. This is because the particles are shifted from confined orbits to lost orbits by a small radial shift at the last bounce point. They thus make impact with the wall near the point of maximum banana width, with the size of the impact zone determined by ripple magnitude and profile, alpha particle distribution, banana width, and geometrical factors. The loss is quite uniform toroidally because ripple induced toroidal orbit excursions are small compared to the shift produced at the bounce point, and the impact points are distributed toroidally because of the distribution in pitch. The concentration of

the loss near the midplane produces an intensification of the wall loading by about a factor of 20, which must be taken into account in design limitations. The high energy alpha particle wall loading can be a much more significant restriction than that given by simple

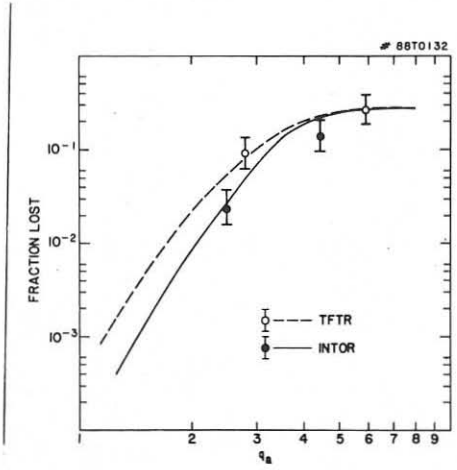

Figure 2. Alpha particle loss in INTOR and TFTR as a function of q-limiter. The points were obtained with the guiding center code ORBIT and the curves with RIPLOS.

considerations of the effect of the lost energy on ignition margin. In this regard one must also take into account the production of bursts of alpha particles produced by magnetic perturbations such as sawteeth. A magnetic perturbation converts a stored population of barely passing particles into trapped particles, and some of these will be on prompt loss orbits and others will be in the stochastic loss zone. Because of the strong dependence of these effects on the alpha particle density profile and the q profile, as seen in Fig. 2, one cannot design a machine to operate close to the safety margins dictated by these effects.

Acknowledgment

*Supported by U.S. Department of Energy Contract No. DE-AC02-76-CH03073.

References

[1] R.B. White and H.E. Mynick, Phys. Fluids, to be published.
[2] R.B. White, M.S. Chance, J.L. Johnson, H.E. Mynick, F.W. Perkins, and A.H. Reiman, 12th. Intl. Conf. on Plasma Physics and Controlled Nuclear Fusion Research, Nice, France 1988, paper IAEA-CN-50/D-2-4.
[3] R.J. Goldston, R.B. White, and A.H. Boozer, Phys. Rev. Lett. 47, 647 (1981).
[4] R.B. White and M.S. Chance, Phys. Fluids 27, 2455 (1984).

In questa Maniera la State ne' gran Caldi si va' ai Freschi per li canali della Citta' la sera fino a meza notte con Musiche di voci, e diversi istromenti, con grandissimo diletto, con le Signore Cortegiane, e spesso anco si Cena in barca con mirabil piacere
franco forma con privilegio

OPTIMIZED STARTUP OF ELONGATED PLASMAS IN THE TCV TOKAMAK

F. Hofmann, C. G. Schultz

Centre de Recherches en Physique des Plasmas
Association Euratom-Confédération Suisse
Ecole Polytechnique Fédérale de Lausanne
21, Avenue des Bains, CH 1007 Lausanne, Switzerland

1. Introduction

TCV is a new tokamak under construction at CRPP, Lausanne. It is designed to produce vertically elongated plasmas of various shapes with $I_p \leq 1.2$ MA and $\kappa \leq 3$. The optimal programming of shape evolution, plasma current and density rampup during the startup phase is a difficult problem. One of the difficulties stems from the fact that, in highly elongated plasmas, axisymmetric stability is favoured by low values of q_s [1], whereas kink stability requires relatively high values of q_s [2]. Whether the two stability domains can be made to overlap is not at all obvious. In this paper we consider a variety of startup scenarios, and we show that there are indeed classes of equilibria, with elongation $\kappa = 3$, which are both kink stable and whose vertical resistive growth rates are low enough to be stabilized by an active feedback system.

2. Vertical Instability Growth Rates with Resistive Walls

Under the assumption that the plasma is vertically stable with an ideally conducting shell, the time constant, τ_p , of the unstable motion in a resistive shell can be expressed as

$$\tau_s / \tau_p = \Omega_v^2 / \Omega_s^2 \qquad (1)$$

where τ_s is the resistive decay time of the induced currents in the shell (for the particular mode under consideration), Ω_s is the stable oscillation frequency of the plasma in a perfectly conducting shell, and Ω_v is the unstable growth rate in the vacuum field, without any shell. Eq.(1) implies that the effect of the poloidal field coils is negligible compared with the effect of the vacuum vessel, as is the case in TCV. Ω_s is computed by using the FBT code [3]. Approximate values of Ω_v can be obtained from

$$\Omega_v^2 = (2\pi R_0 I_p / M)\,(\partial B_R / \partial z) \qquad (2)$$

where R_0 is the major radius, I_p the plasma current, M the plasma mass and the radial field gradient is evaluated on the magnetic axis. The plasma mass, of course, also appears in Ω_s^2 and cancels out in Eq.(1). We note that, when the plasma approaches marginal stability on the fast time scale, Ω_s tends to zero and τ_s/τ_p diverges. In any given tokamak, τ_s/τ_p must be below a certain value, depending on machine parameters and on the bandwidth of the active feedback system. In TCV, $\tau_s = 6.7$ ms and τ_s/τ_p must be less than about 20.

3. Typical Startup Scenario

Let us consider a startup evolution in which a circular plasma is first created in the upper half of the vessel, close to the top wall. The shape then evolves according to a predetermined scenario (Fig.1), while current and density are ramped up simultaneously. Successive equilibria are generated as solutions of the Grad-Shafranov equation with the source functions:

$$p' = A + Bx^a + Cx^{a+1}$$
$$ff' = D + Ex + Fx^b + Gx^{b+1} \qquad (3)$$

where x is the normalized flux, $x = (\psi_{ax} - \psi)/(\psi_{ax} - \psi_{lim})$, ψ_{lim} and ψ_{ax} are the poloidal fluxes at the limiter and on the magnetic axis, respectively, and the constants a,b and A through G are assumed independent of elongation. In Fig.2a, we show the global plasma parameters as a function of elongation for a typical case. Current, pressure and q-profiles of the final plasma (κ=3) are also shown. The normalized vertical growth rate, τ_s/τ_p, is computed using the method described in the previous section. We consider two different versions of this scenario: The first is up-down asymmetric, as shown in Fig.1. The second version is up-down symmetric, i.e., the magnetic axis stays on the equatorial plane of the machine. We note that, in the asymmetric case, the maximum vertical growth rate is seen at the end of the scenario (κ=3), whereas in the symmetric case, the maximum appears at κ=2.6, and its value is twice the value at κ=3. In TCV, where normalized growth rates greater than 20 cannot be stabilized, the symmetric version of this scenario would be limited to κ=2.2. The asymmetric version, on the other hand, can go up to κ=3.

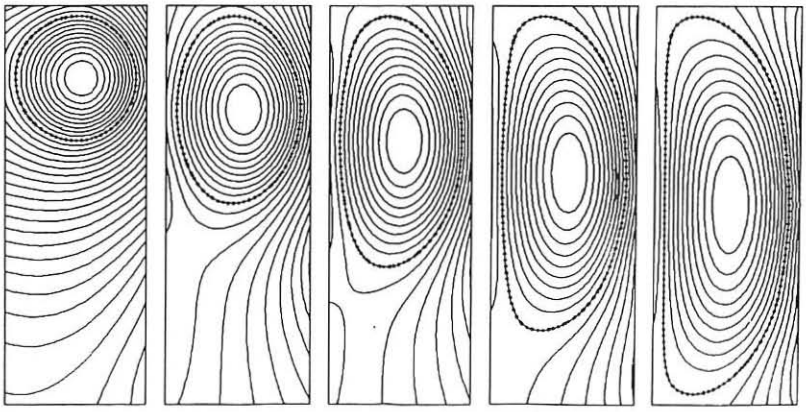

Fig.1. Typical plasma shape evolution during startup phase of TCV

4. Profile Optimization

A systematic study of the effects of profile variations has shown that, for a given plasma shape, the vertical growth rate depends primarily on two parameters, i.e., the internal inductance, l_i and the poloidal beta, β_p. For D-shaped plasmas with κ=3, the growth rate increases with increasing l_i, but it decreases with increasing β_p. This suggests that, from the point of view of axisymmetric stability, a high-beta startup is advantageous, i.e., the plasma density should be ramped up during, not after the current rise. Furthermore, we observe that, for given values of q_0, q_s and β_p, it is possible to reduce the vertical growth rate by modifying the current profile in such a way that l_i decreases. A startup scenario based on such current profiles is shown in Fig.2b. The shape evolution is the same as in Fig.1. Source functions are again assumed independent of elongation, and the current, pressure and q-profiles at κ=3 are also shown (Fig.2b). We note that the symmetric scenario now becomes feasible, since τ_s/τ_p <20. However, it is not at all clear whether current profiles such as the ones considered here can actually be produced in an experiment.

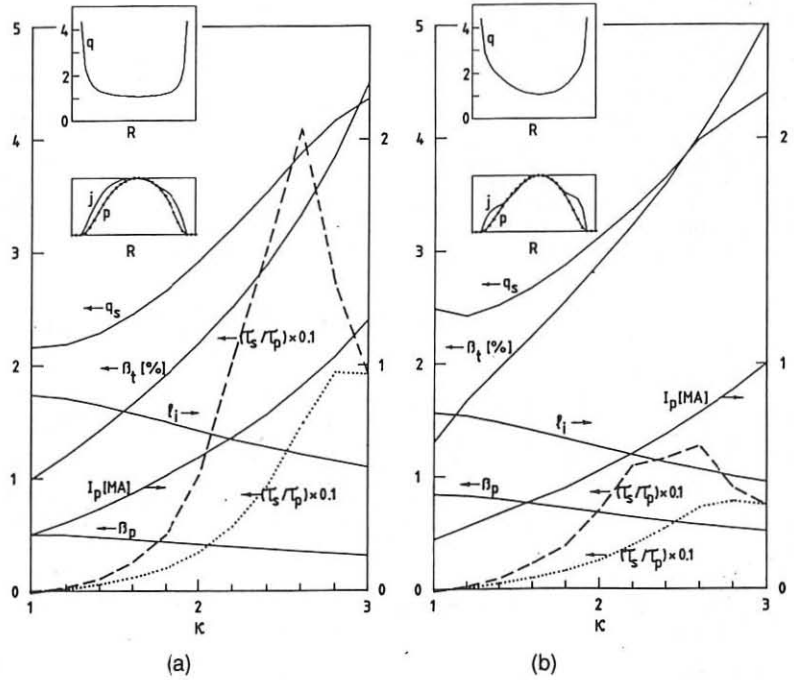

Fig.2. Global plasma parameters and vertical instability growth rates vs. elongation for up-down symmetric (dashed line) and asymmetric (dotted line) startup scenarios in TCV: (a) standard current profile, (b) bell-shaped current profile. q_0=1.05, B_0=1.5 T.

5. n=1 Kink Stability

In this section, we consider D-shaped plasmas with elongation $\kappa=3$, and triangularity $\delta^*=0.4$, corresponding to the rightmost equilibrium of Fig.1. We compute growth rates of the most unstable n=1 mode, using the ERATO code [4]. The effect of the conducting shell is not taken into account in these calculations. We assume $\beta=0$, $q_0=1.05$, $q_s=3.5$. The source functions are given in Eq.(3). A systematic parameter scan shows that, under these conditions, the n=1 growth rate depends essentially on the internal inductance, as shown in Fig.3. Note that n=1 growth rates below 10^{-4} are considered to be stable. It is interesting to see that n=1 stability is only possible in a narrow l_i-window, $0.42 < l_i < 0.46$. The n=0 vertical growth rates, τ_s/τ_p corresponding to this window, are far below the critical value of 20, and should be easily stabilized in TCV. The current profile in the n=1 stable range is very similar to the one shown in Fig.2b.

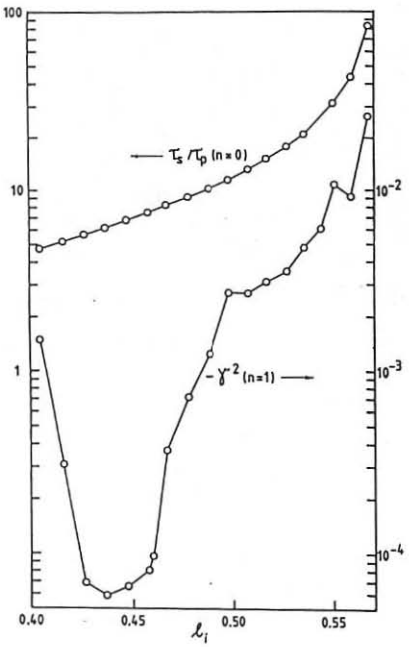

Fig.3. n=1 growth rate without shell (γ^2) and vertical growth rate with resistive shell (τ_s/τ_p) vs. l_i

6. Conclusions

The gain in axisymmetric stability resulting from an up-down asymmetric startup, as compared to a symmetric one, is important and perhaps crucial for reaching $\kappa=3$ in TCV. Resistive vertical growth rates can be reduced, at constant q_0 and q_s, by using bell-shaped current profiles. Finally, n=1 kink calculations for a D-shaped plasma with $\kappa=3$, $\beta=0$, $q_0=1.05$ and $q_s=3.5$ show that there is a stable window in l_i-space and that the corresponding n=0 vertical growth rates appear to be controllable in TCV.

Acknowledgements

Fruitful discussions with Professors A. Bondeson, F. Troyon and Drs. F.B. Marcus and G. Tonetti are gratefully acknowledged.

References

[1] Hofmann,F., Jardin,S.C., Marcus,F.B., Perez,A., Turnbull,A.D., Fusion Technology 1986 (Proc. 14th SOFT Avignon, 1986), I, 687 (Pergamon Press).
[2] Turnbull,A.D., Roy,A., Sauter,O., Troyon,F.S., Nucl. Fusion 28 (1988)1379.
[3] Hofmann, F., Comput. Phys. Commun. 48 (1988) 207.
[4] Gruber, R., et al., Comput. Phys. Commun. 21 (1981) 323.

Beta limits - MHD Stability Analysis for NET / ITER

C. G. Schultz, A. Bondeson, F. Troyon, A. Roy

Centre de Recherches en Physique des Plasmas
Association Euratom-Confédération Suisse
Ecole Polytechnique Fédérale de Lausanne
21, Avenue des Bains, CH 1007 Lausanne, Switzerland

1. Introduction

For the next generation of large Tokamaks, operation at β of a few percents is essential in order to reach ignition and maintain it. It has become accepted that only elongated cross-sections will allow the required β. The problems that remain are to quantify the gain brought by elongation and shaping and identify eventual penalties that might be associated with them such as reduced operational space, a greater sensitivity to the current profiles or even pathological current profiles which would require costly profile control systems.

The beneficial effect of elongation on β can be understood from the scaling law [1]

$$\beta[\%] < g\, I_N \ , \quad I_N = \mu_0 I / a B \tag{1}$$

which gives the maximum value of β, derived from numerical optimizations, and which is found to reproduce well all the experimental data [1], with a g factor between 2.2 and 3.0. Higher elongations allow higher current I for a fixed plasma half-width a.

Here we report on an optimization in progress of the influence of triangularity δ and elongation κ on the ideal MHD β-limit for plasmas with a boundary specified by

$$r/a = A + \cos(\theta + \delta \sin\theta) \ , \quad z/a = \kappa \sin\theta \tag{2}$$

The study is limited to free-boundary n=1 (kink) and n=∞ (ballooning) modes.

2. Profiles

Several studies have been made concerning the influence of triangularity on the ideal-MHD β-limit [3-7], however, the picture emerging from these studies is rather incoherent. It appears that the discrepancies are due to different choices of plasma profiles, in particular the pressure profile $p(\psi)$. To gain some understanding of the dependence on plasma profiles, we have carried out a detailed optimization of the pressure and current profiles for a noncircular plasma with κ=2 and δ=0.6. The study has been restricted to current profiles for which the surface averaged toroidal current I' is non-negative and vanishes at the plasma edge, and the safety factor q is everywhere above unity. (Note that the definition of I' differs from that used by Todd [5]).

In the circular case [8], the highest β-values are reached with a

top-hat current (Shafranov) profile with q_0 slightly above unity and low shear in the centre. The pressure gradients are localized in the external high-shear region where I'=0. With increasing triangularity, the optimum current profile remains essentially unchanged, however, the q-profile becomes rather strongly modified as $q(\psi)$ shoots up increasingly rapidly near the edge. An important effect of triangularity is to improve ballooning stability in the central region by a combination of increased shear and shaping.

Thus, for large triangularity, the optimum pressure profile has finite gradients in the central region of flat I', i.e., is more peaked than in the circular case. As the optimum profile depends on triangularity, it is clear that a full optimization must allow considerable freedom in $p(\psi)$ and that discrepancies between different β-limit studies have resulted from different restrictions on the pressure profiles. Furthermore, it is useful to specify the current rather than the q-profile, in particular, as the latter choice may lead to non-zero currents at the plasma edge, which strongly influences the stability of external modes.

A typical case of profiles $p'(\psi)$ and $I'(\psi)$ optimized for $n=1$ and $n=\infty$ stability and $\kappa=2$, $\delta=0.6$ is shown in Fig. 1. This case has $q_0=1.07$, $q_s=4.2$ and $\beta=6\%$ at an aspect ratio A=3.7. The current profile is somewhat broader than a top-hat, however, it is still flat in the centre and has I'=I''=0 at the edge. The pressure gradient in Fig. 1 is essentially proportional to the ballooning stability limit on each flux surface.

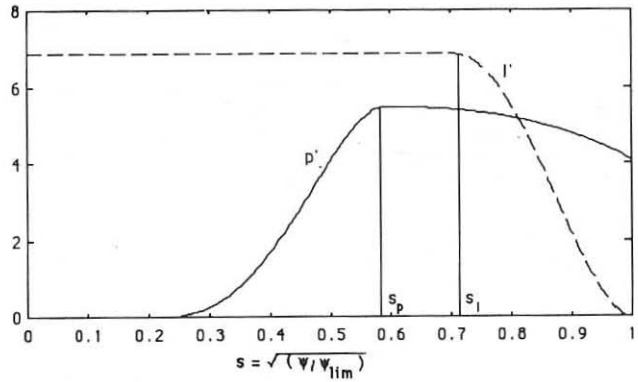

Fig. 1 Optimized pressure and current profiles for $\kappa=2$, $\delta=0.6$, A=3.7 and β about 6%

3. Results $\beta_{max}(q_s, q_0)$ for $\delta=0.6$ and $\kappa=2$

Using the ERATO stability code, we have computed the β-limit for equilibria of the type shown in Fig. 1, changing s_p and s_I. The result is shown in Fig. 2 as $\beta_{max}(q_s)$ for different values of q_0.

Several interesting features are seen in this diagram. The most striking result is that the β-limit is only weakly dependent on q_s between 2 and 5, in particular when q_0 is close to unity. Contrary to other studies [5,7] we do not find a pronounced deterioration of the β-limit for $q_s<3$, if q_0 is maintained close to unity. In addition, we note the absence of the so-called ravines observed in [5,7] when q_s is slightly below integer values. It appears that these two features depend on the choice of current

profile. For example, by comparison with cylindrical theory, we infer that the ravines are caused by finite current gradients I'' at the plasma surface. The sensitivity to the choice of current profile is well illustrated by the fact that the current profile in Fig. 1 avoids difficulty for $q_s<3$ as well as the ravines and instead gives rise to a β-limit which is very weakly dependent on q_s for $2<q_s<5$.

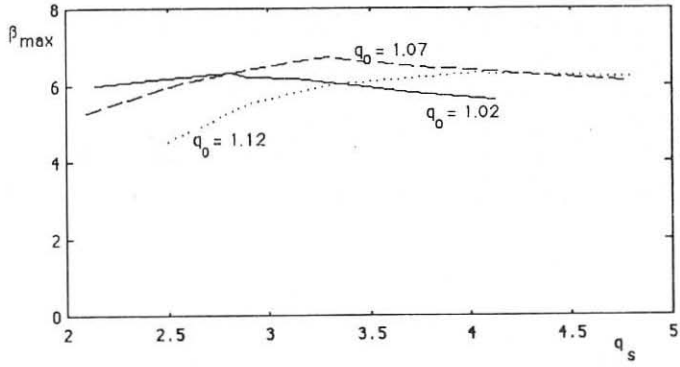

Fig. 2 Maximum β for varying q_s at three different values of q_0 and κ=2, δ=0.6 and A=3.7.

Since β_{max} is almost independent of the current in this range, g decreases with increasing current. At q_s=4.5, the maximal g reaches 3.0 The value for g is not decreased from the circular value even at the low values of q_s. We note that g comes out the same as for circular plasmas for which one has used the same kind of optimized current profiles [8], the values being higher than previously reported [1]. We also note that for $q_s>4$, the β-limit is not sensitive to the value of q_0. It is seen, however, that if q_0 is far above unity, the β-limit deteriorates at low q_s. The gain for an elongation of 2 has come in β: in the circular case one finds a maximum β of 2.5%, with κ=2 the maximum β is 6.7%, a gain by a factor of 2.7. At the same time the normalized current I_N has increased by a factor of 3 from the circular value.

From the particular case we have studied, κ=2 and δ=0.6, triangularity appears to open the possibility of operation at relatively high β and q_s at moderate current with a very high value of g without an excessive sensitivity to plasma conditions in the centre. Further studies of the dependence on ellipticity and triangularity as well as for the more realistic case of true free-boundary equilibria [9] are underway.

References

[1] Troyon, F., Gruber, R., Saurermann, H., Semenzato, S., Succi, S., Plasma Phys. Controlled Fusion 26 (1984) 209
[2] Stambaugh, R. et al., Plasma Phys. Controlled Fusion 30 (1988) 1585
[3] Todd, A.M.M., Manickam, J., Okabayashi, M., Chance, M.S., Grimm, R.C., Greene, J.M., Johnson, J.L., Nucl. Fusion 19 (1979) 743
[4] Yasseen, F., Cooper, W.A., Turnbull, A.D., Troyon, F., Roy, A., LRP 333/87 "MHD stability analysis for NET and INTOR", NET contract 242/86-6
[5] Phillips, M.W., Todd, A.M.M., Hughes, M.H., Manickam, J., Johnson, J.L., Parker, R.R., Nucl. Fusion 28 (1988) 1499
[6] Naitou, H., Yamazaki, K., Nucl. Fusion 28 (1988) 1751
[7] Hogan, J., presented at the ITER workshop on operational limits, IPP Garching, June 1988
[8] Roy, A., Troyon, F., "Ideal MHD stability of a circular cross-section tokamak", in Proceedings of the joint Varenna-Lausanne workshop on Theory of Fusion Plasmas, October 1988
[9] Hofmann, F., Schultz, C.G., these proceedings

SEMICOLLISIONAL MICROINSTABILITIES IN THE PRESENCE OF A MAGNETIC SEPARATRIX

S. Briguglio, F. Romanelli

Associazione EURATOM-ENEA sulla Fusione, C. R. E. Frascati,
C.P. 65 - 00044 - Frascati, Rome, Italy

1. INTRODUCTION

An improved confinement regime, known as H-mode, has been observed since 1982 in several auxiliary-heated Tokamaks. Common features of these experiments seem to be, among the others, the presence of a magnetic separatrix quite close to the plasma boundary, the existence of a threshold in the edge electron temperature for the achievement of the H-mode, and the observation of electron density and temperature profiles rather flat over the whole radius with marked pedestals at the edge.

These features indicate that the role of good confinement region is possibly played by the region beyond the q=2 surface. Therefore, in order to understand the global confinement properties of the discharges, it is necessary to investigate the mechanisms which can determine the transport in such region. Due to the high edge temperature values, the role of microinstabilities in contributing to the anomalous transport coefficients may be important, in principle, differently from the ohmic and L-mode cases. Moreover microinstabilities may still be relevant in determining transport in the internal region where the reduced gradients may be consistent with the locally improved confinement.

The aim of this paper is to examine if the stability of toroidal semicollisional modes, belonging to the electrostatic drift branch, destabilized by ion temperature gradients and trapped electron dynamics, may be affected by the presence of a magnetic separatrix.

The relevant integro-differential eigenvalue equation for a model equilibrium with magnetic separatrix [1] comes out to be [2], in the fluid-ion limit

$$\left[\frac{d^2}{d\theta^2} + Q(\theta)\right]\phi = II\,\frac{\Omega^2 q_0^2 b_{\theta_0}}{\varepsilon_n^2}\left(\frac{h}{b_p}\right)^{3/2} \cdot \tag{1}$$

$$\cdot \sum_{-\infty}^{+\infty} P \int_0^1 \frac{d\kappa^2}{4\hat{R}(\kappa)}\,\hat{g}(\kappa,\theta-2\pi p)\int_{-\infty}^{+\infty} d\theta' h(\theta')\,\hat{g}(\kappa,\theta')\,\phi(2\pi p-\theta')\left[\frac{h(2\pi p-\theta')}{b_p(2\pi p-\theta')}\right]^{1/2}$$

with the same notation introduced in Ref. 2 and boundary conditions of outgoing wave energy. Two parameters specify the shape of the magnetic surface: γ, the poloidal coordinate of the x-point; and k, ranging from 0 to 1 in going from circular surfaces to the separatrix.

2. ION TEMPERATURE GRADIENT MODES

In this section we examine the effects of the considered equilibrium on the stability of the η_i-modes, i.e. the modes driven unstable by the ion temperature gradient. We neglect here the trapped electron response by taking the $\varepsilon \to 0$ limit of Eq. (1). The effect of the magnetic separatrix on the stability of the mode shows a qualitative dependence on the ε_n value. From the numerical solution of Eq. (1) it can be seen that the eigenfunction exhibits a fair localization at $\theta \approx 0$. This fact suggests that the η_i threshold for instability can be more satisfactorily determined through the local kinetic approximation, which yields in the large ε_n limit

$$\eta_i > \eta_{i_{th}} = -\frac{\omega_{Di}(0)}{\omega_{*e}}(1+\tau) \qquad (2)$$

It is easy to verify that $-\omega_{Di}(0)$ is, at fixed γ, an increasing positive function of k and, at fixed k, a decreasing function of $|\gamma|$. This is shown in Fig. 1, where the threshold value of η_i is plotted vs ε_n at $k=0$ and at $k=0.9$ for $\gamma=0$ and $\gamma=-\pi/2$ (note that Eq. (2) yields for $\gamma=\pi$ the same threshold as the circular surface case, independent of k). In Fig. 1 the threshold value obtained from the numerical solution of Eq. (1) is also shown for comparison. It may be seen that, notwithstanding the expected quantitative disagreement, the same trend emerges from the two approximations: a strong stabilization of the mode for equilibria with the x-point in the outer part of the torus becoming weaker and weaker as the x-point is moved toward the inner part of the torus, causing the mode to feel weaker principal curvature. This trend could be correlated with the experimental observation of improved local thermal confinement in the interior zone of the plasma which is characterized, during the H-phase, by flat density profiles (large ε_n values).

Regarding the small ε_n limit, which is typical of the H-phase steep-gradient edge region, the η_i threshold vs ε_n, obtained from the solution of Eq. (1), is shown in Fig. 2 for the usual values of k and γ. The local threshold, which in this limit is given by

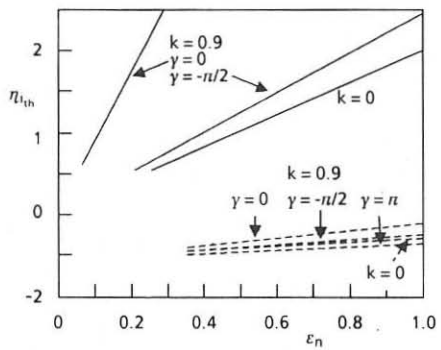

Fig. 1 - η_i-threshold for the onset of instability at large ε_n for different magnetic surfaces, obtained in the local kinetic limit (solid lines) and from Eq. (1) (dashed lines).

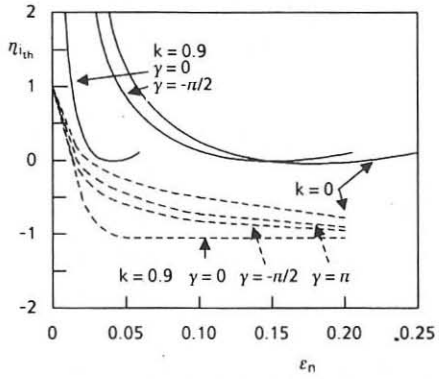

Fig. 2 - η_i-threshold for the onset of instability at small ε_n for different magnetic surfaces, obtained in the local limit (solid lines) and from Eq. (1) (dashed lines).

$$\eta_{i_{th}} = -\frac{\omega_{D_i}(0)\tau}{\omega_{*_e}}\left[2 + \frac{\tau}{4}\left(1 + \frac{\omega_{*_e}}{\omega_{D_i}(0)\,\tau}\right)^2\right] - 1, \tag{4}$$

is also plotted, showing the same trend. The effect of the separatrix, at fixed ε_n, is apparently destabilizing, the threshold becoming lower with increasing k and decreasing $|\gamma|$. Note however that this is not in contrast with the improvement of confinement in the edge region and with the consequent formation of pedestals in temperature profiles. Indeed, in going from the L-phase to the H-phase, ε_n changes, in the edge region, from values ~0.1 to values ~0.01. It may be seen that, due to the strong dependence of the threshold on ε_n, this corresponds to moving toward more stable conditions. Moreover the dependence of the threshold on γ at fixed k and ε_n could advantage configurations with the x-point on the top or inside the plasma, rather than outside the plasma.

3. TRAPPED ELECTRON MODES

In this section we analyze the effects of the separatrix on the stability of the trapped electron modes by solving Eq. (1) in the cold ion limit ($\tau \gg 1$), which makes the effects associated to finite ion temperature gradient negligible.

In Fig. 3 the effect of trapped electron dynamics on the separatrix-modified electron mode is compared, for configurations with the x-point on the equatorial plane, with the circular surface case results, by plotting the growth-rate of the mode vs ε, for $\tau = 100$, $\eta_i = 0$, $\nu_{ei}/\omega_{*e} = 0.1$, $\eta_e = 1$ and the usual values for the other parameters. It may be seen that the destabilization driven by trapped electrons is only slightly reduced for configurations with the x-point inside the torus but it is strongly reduced if the x-point is outside the torus. Also in the case of intermediate position of the x-point the effect of the separatrix is remarkably stabilizing, as shown in Fig. 4.

This is due to the fact that in the latter cases, differently from the former, the sharp modulation in the poloidal field distribution close to the x-point causes the trapped electron contribution to be strongly localized around the x-point and therein overwhelmed by the term $Q\phi$ in Eq. (1). Consequently, both the structure of the

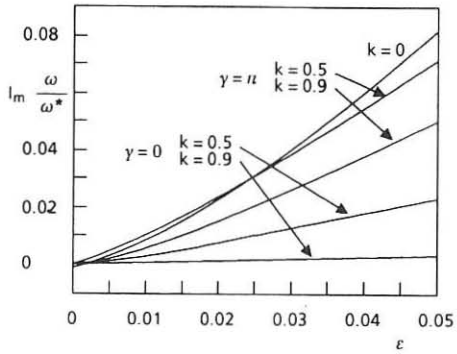

Fig. 3 - Growth-rate vs ε at $\iota = 100$, $\eta_i = 0$, $\nu_{ei}/\omega_{*e} = 0.1$, $\eta_e = 1$, for different magnetic surfaces.

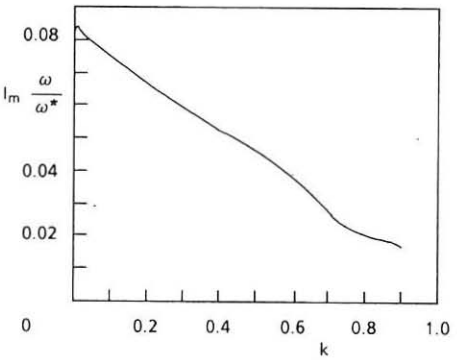

Fig. 4 - Growth-rate vs k for $\gamma = -\pi/2$, at $\varepsilon = 0.05$ and the other parameters as in Fig. 3.

eigenmode and the eigenvalue hardly experience the destabilizing trapped electron dynamics.

REFERENCES

[1] C.M. Bishop, P. Kirby, J.W. Connor, R.J. Hastie, J.B. Taylor, Nucl. Fusion **24**, 1579 (1984)

[2] S. Briguglio, in Proc. Joint Varenna-Lausanne Int. Workshop on "Theory of Fusion Plasmas" (Lausanne 1988)

TOKAMAK CONFIGURATION ANALYSIS WITH THE METHOD OF TOROIDAL MULTIPOLES

P. Micozzi, F. Alladio, F. Crisanti, M. Marinucci, A. Tanga*

Associazione EURATOM-ENEA sulla Fusione, C. R. E. Frascati,
C.P. 65 - 00044 - Frascati, Rome, Italy

INTRODUCTION

In the study of tokamak machines able to sustain plasmas of thermonuclear interest (JIT, IGNITOR, NET, CIT, ET), there is a strong quest for engineering optimization of the circuital components close to the plasma.

We have developed a semianalytical axisymmetric MHD equilibrium code based on the technique of the poloidal ψ flux function expansion in toroidal harmonic series [1].

This code is able to optimize the necessary currents in the poloidal circuits in order to sustain a plasma of fixed shape (also x-point configuration), toroidal current and poloidal β.

EQUILIBRIUM CODE AND BEST FIT METHOD

The solution of the Grad-Shafranov equation, which in cylindrical coordinates (R,Z, ϕ) is

$$\frac{\partial^2\psi}{\partial R^2}+\frac{\partial^2\psi}{\partial Z^2}-\frac{1}{R}\frac{\partial\psi}{\partial R}=-2\pi\mu_0 R J_\phi(R,\psi)=-4\pi^2\mu_0 R^2\frac{dP(\psi)}{d\psi}-\frac{\mu_0^2}{2}\frac{dI^2(\psi)}{d\psi} \qquad (1)$$

(J_ϕ toroidal current density, P plasma pressure, I poloidal plasma current), can be expanded, in full toroidal coordinates [3] ($\theta,\bar{\omega},\phi$), as follows:

$$\psi=\frac{1}{\sqrt{ch\theta-cos\bar{\omega}}}\left\{\sum_0^\infty{}_m\left|M_m^{i,c}(\theta)f_m(ch\theta)+M_m^{e,c}(\theta)g_m(ch\theta)\right|cos(m\bar{\omega})+sinus\,Part\right\}+C \qquad (2)$$

θ is a radial-like coordinate, and $\bar{\omega}$ is similar to an ordinary poloidal angle.

In (2) C is an arbitrary constant, $f_m(ch\theta)$ and $g_m(ch\theta)$ are the Fock functions [2] and the $M_m(\theta)$ are the radial behaviours of the multipolar moments that can be expressed as integrals of the toroidal current $J_\phi(\theta,\bar{\omega})$ [1]; therefore, the code solves the equation (1) with a 1-dimensional fast iterative method on the multipolar moments $M_m(\theta)$.

This code can work prescribing both a free, as well as a fixed boundary: in both cases we must give the total plasma current I_p, the poloidal beta β_p and the functional forms of $P(\psi)$ and $I^2(\psi)$. Moreover, in the free boundary case, we must provide the poloidal currents external to the integration domain: on the other hand in the fixed boundary case, we do not provide these currents, but we must choose the contour of the last plasma magnetic surface as a set of points in which $J_\phi(\theta,\bar{\omega})=0$.

In the first option, the output is the flux function $\psi(\theta,\bar{\omega})$, while in the second case, as a result we also have the vacuum magnetic field able to substain the required plasma shape.

Our method reproduces this vacuum field on the plasma zone by means of the currents in a prescribed set of poloidal coils used as fit parameters. In more detail, the complete procedure is the following.

i) A fixed boundary case is run with selected plasma parameters (and, in the first step, without coils inside the mesh). ii) The vacuum ψ resulting from this run is fitted on a prescribed contour enclosing the plasma boundary; the currents of all the available poloidal coils (internal and external to the integration mesh) are used as best fit parameters. iii) One can check the goodness of the fit running a free boundary case with the currents obtained in (ii) flowing in the chosen set of coils.

The set of equations to be fulfilled is

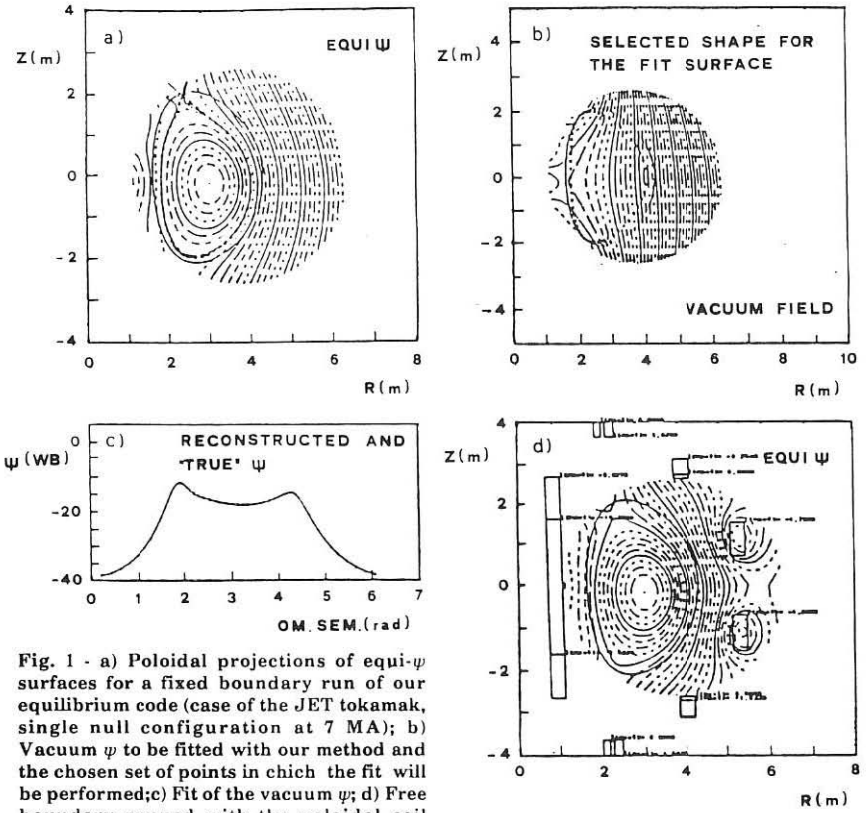

Fig. 1 - a) Poloidal projections of equi-ψ surfaces for a fixed boundary run of our equilibrium code (case of the JET tokamak, single null configuration at 7 MA); b) Vacuum ψ to be fitted with our method and the chosen set of points in chich the fit will be performed;c) Fit of the vacuum ψ; d) Free boundary runned with the poloidal coil currents obtained from the fit of Fig. 1c

$$\sum_{l}^{N_c} {}^{l}\psi_n \cdot I_l = \psi(\theta_n, \omega_n) \quad (n = 1, 2 \ldots\ldots, N_m) \tag{3}$$

Here N_C is the number of coils, I_l the current in each coil and N_m the number of points $(\theta_n \omega_n)$ on a selected surface enclosing the plasma zone to be used in the best fit; the vacuum ψ is the result of the fixed boundary run and ${}^{l}\psi_n$ is the flux function produced by the l-th coil in the n-th point for unitary current, $N_m \gg N_C$, so that the system [3] is overdetermined and can be solved with a least square method.

Since the ψ in (1) is defined with an arbitrary constant C, we can subtract, without changing the equilibrium propriety, the flux generated by an ideal transformer from the vacuum ψ in order to minimize (for instance) the magnetic energy of the system [4]. This produces a set of currents I_l^T that gives an almost null magnetic field in the plasma region and then we minimize the quantity

$$E(\alpha) = \sum_{l}^{N_c} L_l (I_l + \alpha I_l^T)^2 \tag{4}$$

where L_l are the magnetic selfinductances of the coils and α is the minimization parameter. So the new currents in the coils will be

$$I_l^{NEW} = I_l + \alpha_{min} I_l^T \tag{5}$$

We can observe the results of the points (i-iii) in Fig. 1(a-d) for the case of the JET without an iron core transformer (our method has not yet been extended to treat materials with a magnetic permeability different from 1).

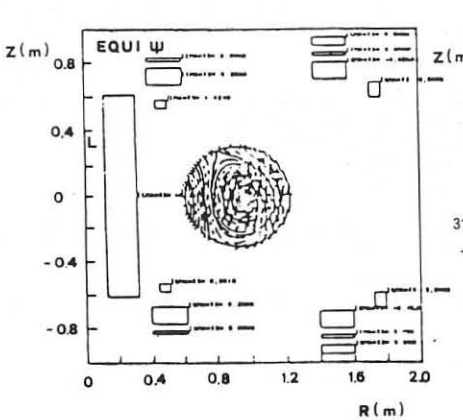

Fig. 2 - Single null configuration for the FTU Tokamak ($I_p = 0.5$ MA)

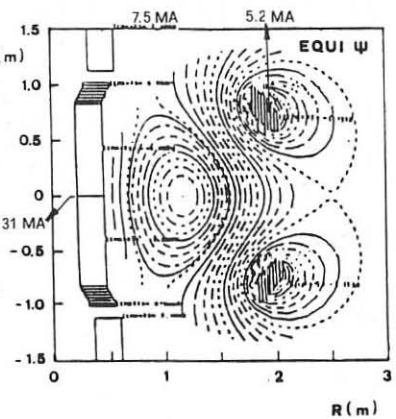

Fig. 3 - Elongated configuration for the IGNITOR tokamak ($I_p = 12$ MA), using a preliminary set of poloidal coils

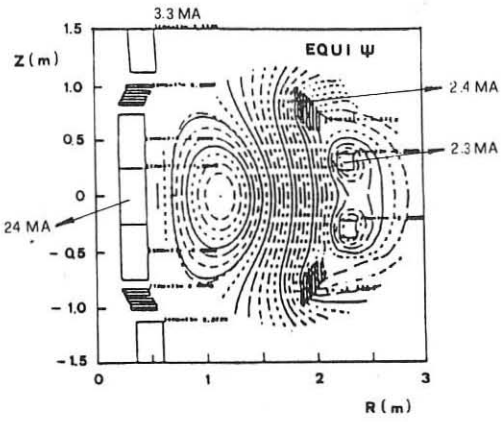

Fig. 4 - Elongated configuration for the IGNITOR tokamak ($I_p = 12$ MA), using a different set of poloidal coils

APPLICATION OF THE METHOD

Figure 2 shows a single null configuration in FTU (Frascati Tokamak Upgraded). As we can note, also at a low plasma current of 0.5 MA (the maximum expected current is about 1.6 MA on this machine), the currents that one has to feed in the poloidal circuitry are very high because the x-point is too far from the coils (FTU has not been designed for elongated plasmas). In Fig. 3 we can see an example of an elongated plasma (k=1.8) for a given configuration of the IGNITOR poloidal coils (using a preliminary version of this machine) Fig. 4 shows that with a different distribution of coils, it is possible to pull down the poloidal field currents that are a critical parameter in a machine with very high plasma current like IGNITOR ($I_p \simeq 12$ MA, $B_t = 13$ T, $k = 1.8$).

FOOTNOTE AND REFERENCES

* Present address: JET, Culham Laboratory, Abingdon (GB)

[1] F. Alladio, F. Crisanti: Nucl. Fusion 26, 1143 (1986)
[2] V.A. Fock: Fiz. Zh Sovietunion 1, 215 (1832)
[3] P.M. Morse, H. Feshbach: Method of Theoretical Physics (Mc Graw-Hill, New York, 1953)
[4] F. Alladio, F. Crisanti, M. Marinucci: Proc. 12th European Conf. on Controll. Fusion and Plasma Phys., Budapest (1985) Part. I, p.171

NUMERICAL SIMULATION OF TOROIDAL η_i TURBULENCE

M. Ottaviani, F. Romanelli, R. Benzi*, M. Briscolini†, P. Santangelo†, S. Succi†

Associazione EURATOM-ENEA sulla Fusione, C. R. E. Frascati,
C.P. 65 - 00044 - Frascati, Rome, Italy

Small scale turbulence induced by the combined effect of ion temperature gradients and the unfavourable magnetic curvature (toroidal η_i modes) is commonly considered a strong candidate for explaining the high density saturation of ohmic confinement time [1-2].

Anomalous transport models are generally based on turbulent transport coefficients obtained from quasilinear theory together with a mixing length estimate of the fluctuation level.

In this work, extensive numerical simulations of η_i turbulence have been performed in order to investigate the validity of simple analytical estimates, as well as the scaling of heat transport with the relevant plasma parameters, such as forcing and dissipation.

A fluid model of the nonlinear evolution of η_i modes has been derived directly from the Braginskij equations [3]. The resulting set of equations describes the coupled evolution of the electric potential and of the ion pressure in the local approximation:

$$\partial_t \phi + (1 - 2\varepsilon_n)\partial_y \phi - 2\varepsilon_n \partial_y p - \partial_t \nabla^2 \phi - [\phi, \nabla^2 \phi] = - D_1 \nabla^4 \phi \tag{1}$$

$$\partial_t p + [\phi, p] + 2\varepsilon_n \partial_y \phi - \frac{20}{3} \varepsilon_n \partial_y p = D_2 \nabla^2 p + S \tag{2}$$

where x corresponds to the radial coordinate, y to the poloidal coordinate, and parallel dynamics has been entirely neglected. In the above equations, the electric potential ϕ and the ion pressure p are normalized to $\rho_s/L_n T_e/e$ and $\rho_s/L_n nT_i$ respectively, ρ_s and L_n being the ion Larmor radius evaluated at the electron temperature and the typical density gradient length. Moreover, we have set $T_e = T_i$ for simplicity, $\varepsilon_n = L_n/R$ is a measure of toroidicity, D_1, D_2 are normalized ion viscosity and heat conductivity, S is a suitable energy source and $[A,B] = \partial_x A \partial_y B - \partial_x B \partial_y A$ as usual.

Equations (1-2) have been solved by a spectral code with periodic boundary conditions [4]. Typical runs have been performed on a 128 × 128 grid in the wavenumber range chosen to be the interval $1/16 \leq k_\perp \rho_s \leq 4$. The box size is therefore of order 10^2 Larmor radii, while the maximum wavenumber is appropriate to the typical magnitude of the dissipation $D_1 \sim D_2 \sim 10^{-1} \div 10^{-2}$. Note the somewhat arbitrary extension of the model beyond the fluid wavenumber range, required to simulate the effects of dissipation, at least qualitatively.

Two types of simulations have been performed: In the first, the equilibrium pressure gradient is held fixed, then $S = - (1 + \eta_i) \partial_y \phi$ is the usual driving term of η_i instabilities, while p in Eqs. (1-2) is the difference between the total pressure and the

equilibrium pressure; in the second, the energy source is taken as $S = - S_0 \cos k_0 x$ where k_0 is the lowest available wavenumber. In this case p is the difference between the total pressure and the average pressure in the box, while S is to be considered as a source of pressure gradients, which are, therefore, allowed to evolve consistently with energy transport.

An example of the first type of simulation is shown in Fig. 1 where the grid averaged heat flux $F_x = - \int p \partial_y \phi dV$ is plotted vs time for two different cases belonging

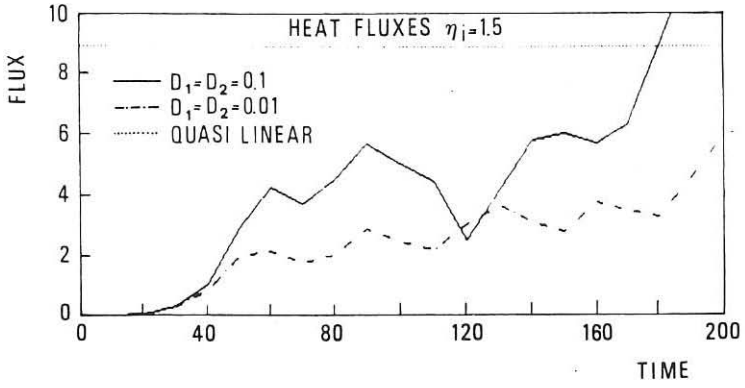

Fig. 1 - Heat fluxes $\eta_i = 1.5$

to the same $\eta_i = 1.5$ but with different dissipation $D_1 = D_2 = 10^{-1}$ (continuous line) and $D_1 = D_2 = 10^{-2}$ (dashed line). The horizontal dotted line represents the quasilinear level estimated by the following expression:

$$F_x = < k_y \sin\theta >_{lin} |p|_{num} |\phi|_{num} \qquad (3)$$

Here $|p|_{num}$ and $|\phi|_{num}$ are the exact mean quadratic values of pressure and potential obtained from the simulation to avoid the uncertainties in the fluctuation level obtained from the mixing length estimate, while $< k_y \sin\theta >_{lin}$ is a spectral average obtained from linear theory, θ being the phase difference of the Fourier amplitudes of p and ϕ. Note the reduction of the actual flux with respect to the estimate (3). This effect, which is systematically recovered in both types of simulations, results more pronounced as the dissipation lowers.

The phenomenon is understood by looking at the scatter plot of Fig. 2, where the pressure is plotted against the potential for each grid site. The strong build-up of coherence is apparent: the ion pressure results approximately proportional to the potential. This means that large regions are occupied by coherent structures characterized by $[\phi, p] \approx 0$. In these regions the quasilinear expression (3) breaks down, since $\sin\theta \approx 0$; therefore the heat flux is almost zero within the structures and only

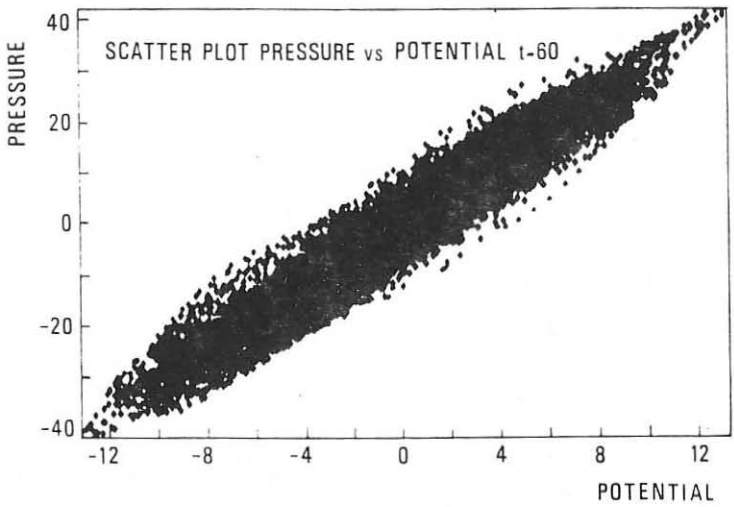

Fig. 2 Scatter plot pressure vs potential $t = 60$

some fraction of the fluid volume is available for energy transport. Moreover, since coherent structures are stationary solutions of the inviscid equations, they tend to be destroyed by dissipation. This explains the observed dependence of the total heat flux on the dissipation.

Indeed, by taking $\partial_t p$ and $D_2 = 0$ in Eq. (2) with type I source, one gets the following functional relation:

$$p = \frac{2\varepsilon_n + 1 + \eta_i}{\frac{20}{3}\varepsilon_n}\,\phi \tag{4}$$

The slope of Eq. (4) results in good agreement with the simulations performed for different values of η_i.

Heat fluxes obtained from type II simulations are shown in Fig. 3, where a reference case ($S_0 = 1/40$, $D_1 = D_2 = 10^{-1}$, dotted line) is compared to a case with much smaller dissipation ($D_1 = D_2 = 10^{-2}$, dashed line) and a case with much larger forcing ($S_0 = 1/4$, continuous line). Note the reduction of the flux associated with lower dissipation. On the other hand, a much larger forcing leads to large energy losses, so that the final departure from marginal stability is sufficiently contained. The assumption of marginal stability for global transport modelling is therefore reasonably supported.

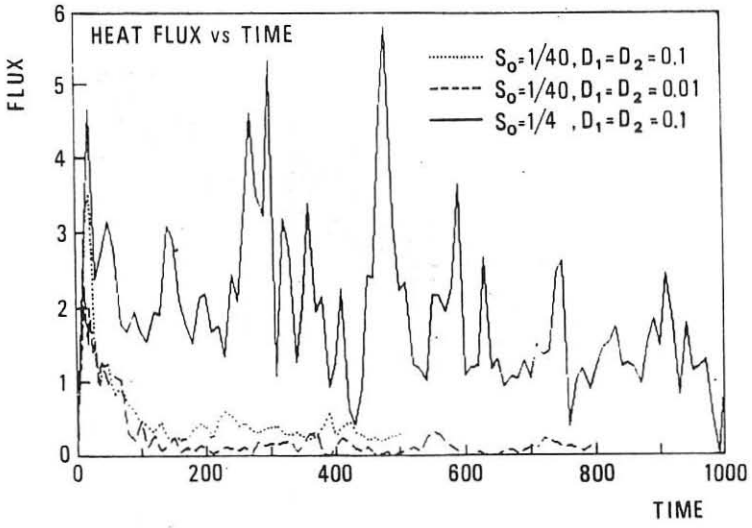

Fig. 3 - Heat flux vs time, type II simulation

REFERENCES AND FOOTNOTES

*University of Rome II "Tor Vergata", Rome, Italy
†IBM - ECSEC, European Center for Scientific and Engineering Computing, Rome, Italy

[1] F. Romanelli, W.M. Tang, R.B. White: Nucl. Fusion 26, 1515 (1986)
[2] R.R. Dominguez, R.E. Waltz: Nucl. Fusion 27, 65 (1986)
[3] M. Ottaviani et al.: submitted to Phys. Fluids
[4] M. Ottaviani et al.: Proceedings of the Joint Varenna Lausanne International Workshop on Theory of Fusion Plasmas, Chexbres, Switzerland (1988)

TOROIDAL SEMI-COLLISIONAL MICROINSTABILITIES AND ANOMALOUS ELECTRON AND ION TRANSPORT

F. Romanelli, S. Briguglio

Associazione EURATOM-ENEA sulla Fusione, C. R. E. Frascati,
C.P. 65 - 00044 - Frascati, Rome, Italy

Tokamak plasmas are characterized by strongly anomalous particle and thermal fluxes. Microinstability based models have been proposed in the past in order to explain such anomalies [1-3]. These models rely on the effect of the semicollisional microinstabilities destabilized by trapped electrons and ion temperature gradients (η_i-modes, with $\eta_i = d\ln T_i/d\ln n$). Numerical simulations have shown good agreement with the experimentally determined trends of the global confinement time [3].

In the present paper we reconsider the problem of the stability of η_i-modes in the presence of the nonadiabatic electron response associated to the trapped particle dynamics.

The dispersion relation, derived in Refs. [4,5], is

$$D(\omega) = \frac{1}{\tau}\left[1 + \delta_T(\omega)\right] + 1 - \int d^3v\, F_M J_0^2(\beta)\, \frac{\omega - \omega_{*T_i}}{\omega - \omega_{Di}} = 0 \qquad (1)$$

where $\tau = T_e/T_i$ and

$$\delta_T(\omega) \equiv -\frac{2}{n^{1/2}}(2\varepsilon)^{1/2} \int_0^\infty \frac{dE}{T_e}\left(\frac{E}{T_e}\right)^{1/2} \frac{\omega - \omega_{*T_e}}{\omega - \langle\omega_{De}\rangle + i\nu_{eff}(T_e/E)^{3/2}}\, F_M \qquad (2)$$

We refer to Ref. [4] for the notation.

A convenient starting point for the discussion of Eq. (1) is the fluid ion approximation which has been used in Ref. [6] to discuss the effects of the trapped electrons on the η_i-mode stability

$$\tau - \tau(1 - 2\varepsilon_n)\frac{\omega_*}{\omega} + 2\left[1 + \eta_i - \frac{10}{3}\varepsilon_n\right]\left(\frac{\omega_*}{\omega}\right)^2 \varepsilon_n + \tau\delta_T(\omega) = 0 \qquad (3)$$

Upon neglecting the nonadiabatic electron dynamics ($\varepsilon = 0$), Eq. (3) yields two distinct roots given by

$$\frac{\omega}{\omega_*} = \frac{\omega_\pm}{\omega_*} = \frac{1 - 2\varepsilon_n \pm \Delta^{1/2}}{2} \qquad (4)$$

with $\Delta = (1-2\varepsilon_n)^2 - \frac{8\varepsilon_n}{\tau}\left(1+\eta_i - \frac{10}{3}\varepsilon_n\right)$.

Both these roots satisfy the condition for the validity of the fluid approximation in the limit $\varepsilon_n \to 0$, $\eta_i \gg 1$ and indeed may be recovered by the numerical solution of the general dispersion equation, Eq. (1). Below the η_i threshold, the two roots are purely real and correspond to modes propagating in the electron diamagnetic direction. As η_i decreases at fixed ε_n, ω_+ increases, while ω_- decreases eventually going to zero on a curve which has to be determined using the kinetic ion response and which corresponds to $\eta_i = \eta_{io} = [1 - 2/3\,(1+1/\tau)\,\varepsilon_n]$ and $\varepsilon_n < \varepsilon_{nc} = [2\,(1+1/\tau)]^{-1}$. With further decreasing η_i and then increasing ε_n at fixed η_i, ω_+ also decreases, finally vanishing for $\eta_i = \eta_{io}$ and $\varepsilon_n > \varepsilon_{nc}$. The two modes coalesce on the marginal stability curve and above threshold correspond to a stable and unstable mode respectively. With increasing ε_n at fixed η_i, value the modes change the direction of propagation from the electron to the ion diamagnetic velocity and the unstable root reaches a second marginal stability boundary which in the fluid approximation would correspond to

$$\eta_i \approx \left(\frac{5}{3} + \frac{\tau}{4}\right) 2\varepsilon_n \tag{5}$$

However at this point the condition for the validity of this approximation is not satisfied because $\omega/\omega_{Di} \leq 1$ and the result given in Eq. (5) can be considered only as indicative. The most important effect which is missed in deriving Eq. (3) is the ω_{Di} resonance which occurs, in going from the first to the second stability boundary, as the frequency of the mode changes sign. The actual marginal stability curve can be analytically determined by making the approximation $v_\perp^2/2 + v_\parallel^2 \to 4/3\,(v_\perp^2 + v_\parallel^2)$ in the ω_{Di} expression, which yields

$$\eta_{ic} = \frac{4}{3}\left(1 + \frac{1}{\tau}\right)\varepsilon_n \tag{6}$$

Note that the boundaries given by Eqs. (5) and (6) roughly coincide for $\tau \approx 1$. Nevertheless, for $\tau \ll 1$ (as in the hot ion regime) the true η_i threshold, given in Eq. (6), is significantly larger than the fluid threshold. Below η_{ic} the effect of the resonance is stabilizing and both the roots are now damped.

When the nonadiabatic electron dynamics is considered ($\varepsilon > 0$), a significant change in the results can be expected when the mode propagates in the electron diamagnetic direction because in this regime the effect of trapped electrons can be destabilizing and the ω_{Di} resonance plays no role. Again it is convenient to consider first the fluid limit. At the lowest order in $\varepsilon^{1/2}$ the eigenvalue is given by the fluid approximation Eq. (3), while, upon keeping the correction due to the δ_T term, evaluated with the lowest order eigenvalue, the following result is obtained as the mode is not too close to threshold

$$I_m \frac{\delta\omega_\pm}{\omega_*} = \mp \frac{(\omega_\pm/\omega_*)^2}{\Delta^{1/2}}\,\delta_T^{(i)} \tag{7}$$

with $\delta_T^{(i)}$ being the imaginary part of δ_T. As the ω_+ root corresponds to a positive energy wave, it is destabilized if $\delta_T^{(i)} < 0$, while the ω_- root which corresponds to a negative energy wave is destabilized by $\delta_T^{(i)} > 0$.

Specifically, in the collisionless case ($\nu = 0$), the following expression is obtained by considering the effect of the electron magnetic drift resonance

$$I_m \frac{\delta\omega_\pm}{\omega_\pm} = \pm \frac{4\omega_\pm/\omega_{*_e}}{\tau\alpha\Delta^{1/2}} \pi^{1/2}(2\varepsilon)^{1/2}\left(\frac{2z_\pm}{\tau\alpha}\right)^{1/2} e^{-\frac{2z_\pm}{\tau\alpha}}\left(\frac{\eta_e}{\alpha\varepsilon_n} - 1\right)(z_\pm - z_e) \tag{8}$$

with $z_\pm = \omega_\pm/\omega_d$, $\omega_d = 2k_y T_i/(eBR)$ and $z_e = \tau\alpha/2\,(1 - 3/2\,\eta_e)/(\alpha\varepsilon_n - \eta_e)$. For $\eta_e > 2/3$ and $\eta_e > \alpha\varepsilon_n$, the z_+ root is unstable for $z_+ > z_e$, and the z_- root for $z_- < z_e$. As the real frequency of the z_- mode approaches zero, the growth rate decreases and, finally, below the boundary $z_- = 0$ the mode is stable.

For sufficiently low values of ε, no significant change of the toroidal η_i-mode growth rate is expected.

With increasing collisionality the trapped electron response changes character but the behaviour of the $\omega_\pm$ roots can again be discussed in the fluid limit by using Eq. (7) which yields

$$I_m \frac{\delta\omega_\pm}{\omega_\pm} = \mp \frac{(\omega_\pm/\omega_*)}{\varepsilon_n \Delta^{1/2}} 2\frac{\tau}{\pi^{1/2}} \frac{(2\varepsilon)^{1/2}}{\nu}\left[\frac{\omega_\pm}{\omega_*} - \left(1 + \frac{3}{2}\eta_e\right)\right] \tag{9}$$

with $\nu = \nu_{eff}/\omega_d$.

The mode corresponding to the ω_- root becomes completely stabilized by collisions because, $\delta_T^{(i)}(\omega_-) < 0$ at sufficiently high values of ν (for typical values of the parameter the mode is already stabilized at $\nu = 0.1$). The ω_+ root is unstable as far as the mode propagates in the electron diamagnetic direction and the stabilizing effect associated to the ω_{Di} resonance plays no role. As the mode propagates in the ion diamagnetic direction the stability boundary is approximately given by Eq. (6), valid for $\varepsilon = 0$, because at large collisionality values the effect of trapped electrons is negligible. The stability boundaries for the dissipative regime are shown in Fig. 1.

A complete discussion of the implication of the proposed diffusion coefficients needs a transport code numerical analysis which is beyond the scope of the present paper. Here we focus the attention on the consequencies which can be expected for the ion transport on the basis of the presented theory. The general expression of the quasilinear fluxes can be found in Ref. [4].

On ALCATOR-C [7] a consistent reduction of the ion transport has been observed during pellet injection. In order to compare this result with the present analysis, we consider the model profiles $T_i = T_{io}(1 - r^2/a^2)^{\alpha_{T_i}}$, $n = n_0(1 - r^2/a^2)^{\alpha_n}$. Upon assuming $\varepsilon = 0.08$, $\tau = 1$, $\eta_e = \eta_i$, $\nu = 10$ and α_{T_i} fixed, we obtain the ion heat flux shown in Fig. 2. It is possible to see that for $\alpha_n \simeq 2$ the diffusivity changes by a factor 2 to 3 in agreement with the experimental finding. For $\alpha_n > 2$ the ion thermal conductivity is due to the effect of trapped electrons and, due to the large value of collisionality typical of ALCATOR-C, its magnitude is relatively low. Note however that this is not necessarily the case for a low collisionality machine. Upon assuming $\varepsilon = 0.25$, $\nu = 1$ and the other parameter the same as in the latter case (a JET-like situation), there is no significant change in the same range of α_n. This is again illustrated in Fig. 2 where the corresponding behaviour of the ion thermal conductivity is shown. Only at very large α_n values ($\alpha_n > 6$), the reduction in the heat flux is significant due to the very small driving effect of the ω_{De} resonance.

Consistent reduction in the ion transport has also been observed in the TFTR supershots [8] with very high ion temperatures $T_i \sim 30\,keV \gg T_e \sim 6\,keV$. A possible

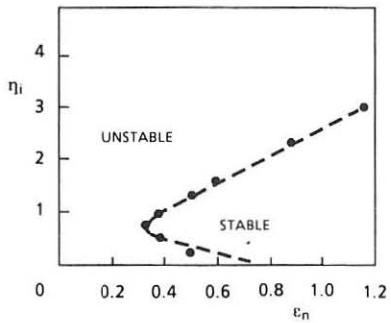

Fig. 1 - Stability boundaries in the η_i vs ε_n plane for $\eta_e = 4$, $\nu = 10$ $\iota = 1$ and $\varepsilon = 0.05$

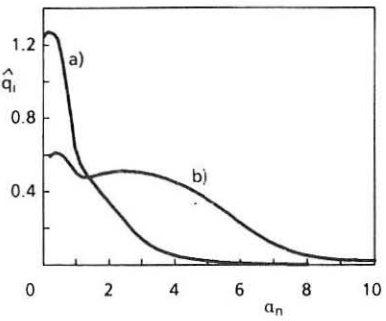

Fig. 2 - Ion thermal conductivity vs α_n for ALCATOR-C (a) and JET (b)

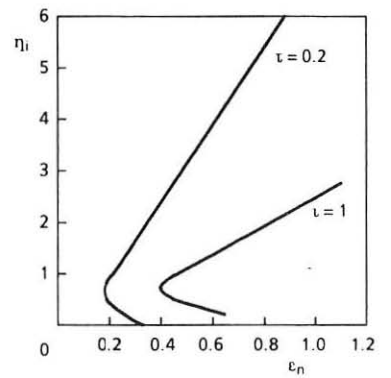

Fig. 3 - Stability boundaries in the η_i vs ε_n plane for $\varepsilon = 0.2$, $\eta_e = 1$ and $\nu = 1$ (TFTR supershots)

explanation of this regime can be found by noting that for $\iota \ll 1$ the adiabatic electron response becomes very large, raising the stability boundary of the mode. This is illustrated in Fig. 3 where the stability diagram in η_i vs ε_n plane is shown for $\iota = 0.2$, $\varepsilon = 0.2$, $\eta_e = 1$ and $\nu = 1$. Note the strong reduction of the unstable region in the low ι case.

Helpful discussions with Dr. F. Pegoraro are gratefully acknowledged. This work has been supported by the task agreement on "Theory and models of anomalous transport" between JET and the EURATOM-ENEA Association.

REFERENCES

[1] W.M. Tang: Nucl. Fusion **26**, 1605, (1986)
[2] F.W. Perkins: 4th Int. Symp. on Heating in Toroidal Plasmas (Rome, 21-28 March 1984) **2**, 977.
[3] F. Romanelli, W.M. Tang: R.B. White, Nucl. Fusion **26**, 1515 (1986)
[4] F. Romanelli, S. Briguglio: JET-P(88)31
[5] F. Romanelli: JET-IR-16 (1987). Submitted to Phys. Fluids.
[6] B. Coppi, F. Pegoraro: Nucl. Fusion **17**, 5 (1977)
[7] M. Greenwald, D. Gwinn, S. Milora, J. Parker, R. Parker et al.: Phys. Rev. Lett. **53**, 352 (1984)
[8] R.J. Goldston, V. Arunasalam, M.G. Bell, M. Bitter, W.R. Blanchard et at.: in Plasma Phys. and Controlled Nucl. Fusion Research (IAEA, Kyoto 1986) **1**, 75

INFLUENCE OF ENERGETIC ION POPULATION ON TOKAMAK PLASMA STABILITY

R.B. White*, F. Romanelli, M.N. Bussac**

Associazione EURATOM-ENEA sulla Fusione, C. R. E. Frascati,
C.P. 65 - 00044 - Frascati, Rome, Italy

Recent experiments in JET [1] have indicated that an energetic particle component has a strong stabilizing influence on sawtooth oscillations. The high energy particles, by precessing faster than the growth rate of the mode, average the potentials associated with the perturbation and give rigidity to the plasma. Investigations of the fishbone mode [2,3] showed that the ideal internal kink mode can be completely stabilized.

More recently, the stabilizing influence on the resistive internal kink mode was demonstrated [4,5,6] and a domain of operating parameters was found such that both the resistive internal kink and the fishbone mode are stable [6]. In order to understand the relation with different analyses [5,7], we investigate here different limits of the dispersion relation.

The plasma is considered to consist of two components, a warm background treated with resistive MHD, and a low density hot component treated with the gyrokinetic formalism. The resulting dispersion relation is [4]

$$\delta W_c + \delta W_k - \frac{8i\,\Gamma\left[\frac{(\Lambda^{3/2}+5)}{4}\right]\left|\omega(\omega-\omega_{*_i})\right|^{1/2}}{\Lambda^{9/4}\,\Gamma\left[\frac{(\Lambda^{3/2}-1)}{4}\right]\omega_A} \tag{1}$$

where $\Lambda \equiv -i\,[\omega(\omega-\omega_{*e})\,(\omega-\omega_{*i})]^{\frac{1}{3}}/\omega_R$, $\omega_R = \omega_A\, S^{-\frac{1}{3}}$, ω_A is the shear Alfven frequency, ω_{*j} are the diamagnetic frequencies, δW_c is the minimized ideal variational energy first calculated by Bussac et al. [8], and the notation is the same as in Ref. 4. The quantity δW_k is the kinetic contribution coming from the trapped particle distribution, which, for a slowing down distribution, takes the form

$$\delta W_k = \frac{\beta_h}{\varepsilon}\,\frac{\omega}{\omega_{dm}}\,ln\,(1-\frac{\omega_{dm}}{\omega}) \tag{2}$$

while, for a Maxwellian distribution, it is

$$\delta W_k = \frac{3}{4}\,\frac{\beta_h}{\varepsilon}\,\frac{\omega}{<\omega_d>}\left[\frac{1}{2}+\frac{\omega}{<\omega_d>}+\left(\frac{\omega}{<\omega_d>}\right)^{3/2} Z\left((\frac{\omega}{<\omega_d>})^{1/2}\right)\right] \tag{3}$$

with Z being the plasma dispersion function. In both cases a single pitch distribution function has been considered The behavior of the roots in the complex ω plane depends on the value of the parameters $\gamma_I \equiv -\delta W_c \omega_A$ and ω_{*}. Considering for simplicity the ideal case with a slowing down distribution function, we have the following possibilities

a) For $\gamma_I > \omega_{*i}/2$ and $\gamma_I < \gamma_M$, with $\gamma_M \approx 0.1\, \omega_{dm}$, at $\beta_h = 0$ the internal kink mode is instable. With increasing β_h the mode is stabilized and at larger values of β_h a second branch becomes unstable corresponding to the fishbone mode. The third root of Eq. (1) is unphysical because the corresponding eigenfunction is not well behaved in the inertial layer.
b) For $\gamma_I > \omega_{*i}/2$ and $\gamma_I > \gamma_M$, the kink and fishbone branches coalesce and no stable window is found.
c) For $\gamma_I < \omega_{*}/2$ and $\gamma_I < \gamma_M$, at $\beta_h = 0$ two marginally stable modes exist, a low frequency mode $\omega \ll \omega_{*i}$, corresponding to the kink branch, and a high frequency mode $\omega \approx \omega_{*i}$, corresponding to the ion branch. With increasing β_h the kink branch is stabilized. The ion branch is first destabilized and then stabilized. At larger values of β_h the fishbone branch becomes unstable.
d) For $\gamma_I < \omega_{*i}/2$ and $\gamma_I > \gamma_M$, the ion and fishbone branches coalesce and again no stable window is possible.

The behavior of the roots in the complex ω plane is shown in Fig. 1. Resistive corrections do not alter the behavior of the fishbone branch. On the contrary, the kink branch is destabilized by resistivity and the ion branch is stabilized by resistivity yielding resistivity-dependent threshold β_h values for the internal kink stabilization and the ion branch destabilization, as shown in Ref. 8. On the contrary, the threshold β_h value for the internal kink stabilization is almost independent of resistivity for case a), first investigated in Refs. 2 and 3.

The stability domain in the γ_I vs β_h plane, for case a) has a triangular shape as shown in Fig. 2. The stability boundaries in practical units are the following

a) Fishbone boundary

$$n_h \ll n_{hc} = 20\, \beta_{hc}\, \frac{n^{\frac{1}{2}} \left(10^{14}\, cm^{-3}\right) s \left(\frac{m_i}{m_p}\right)^{\frac{1}{2}}}{R(m)}\, 10^{11}\, cm^{-3} \tag{4}$$

with the constant β_{hc} being $\beta_{hc} = 1.2$ for a Maxwellian distribution function and $\beta_{hc} = 0.4$ for a slowing down with $\mu/E = 1$.

b) Kink-fishbone boundary

$$\gamma_I \leq \hat{\gamma}_M \frac{n_h}{n_{hc}} \langle \omega_d \rangle \tag{5}$$

with $\langle \omega_d \rangle = c \langle E \rangle / (e\, B\, r_s\, R)$. The quantity $\hat{\gamma}_M \equiv \gamma_M / \langle \omega_d \rangle$ is plotted in Fig. 3.

c) Resistive boundary

$$\gamma_I > \gamma_R \tag{6}$$

For $\gamma_R > \hat{\gamma}_M \langle \omega_d \rangle$ the stable triangle disappears. The corresponding value of resistivity is given by

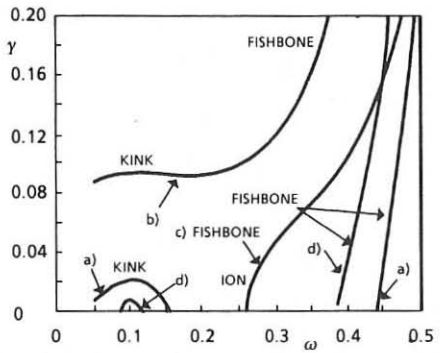

Fig. 1 - The complex ω plane

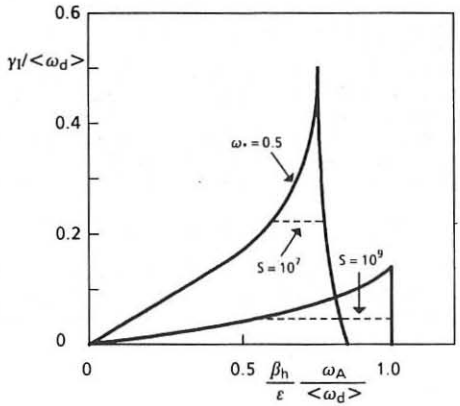

Fig. 2 - Stable domain in γ_I vs β_h plane for a Maxwellian distribution function and two values of ω_*. The dashed line is the resistive boundary

$$S \geq S_c = \frac{10^3}{\gamma_M^3} \left| \frac{B^2(T)\, r_s(m)\, Z_n}{s\left(\frac{m_i}{m_p}\right)^{\frac{1}{2}} n^{\frac{1}{2}}\left(10^{14}\, cm^{-3}\right) <E(keV)>} \right|^3 \qquad (7)$$

and is plotted in Fig. 3 vs ω_*/ω_d. However the resistive threshold is very mild as the growth rate of the mode is very low for $S<S_c$.

The above results have been verified by means of a Monte Carlo integration which allows the evaluation of δW_k for arbitrary distribution functions.

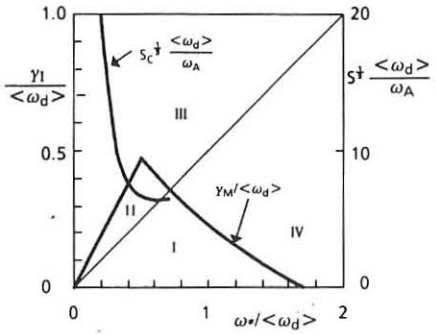

Fig. 3 - Maximum ideal growth rate γ_M and corresponding critical magnetic Reynolds number S_c vs ω_*;

FOOTNOTES AND REFERENCES

* Permanent address: Plasma Physics Laboratory, Princeton University, P.O. Box 451, Princeton N.I. 08543

** Permanent address: Ecole Polytechnique, 91128 Palaiseau, Cedex, France

[1] J. Jacquinot et al. in Plasma Phys. and Controll. Fusion Research 1986 (IAEA Vienna 1987) **Vol. 1**, p, 449

[2] L. Chen, R.B. White and M.N. Rosenbluth: Phys. Rev. Lett. **52**, 1122 (1984)

[3] R.B. White, L. Chen, F. Romanelli and R. Hay: Phys. Fluids **28**, 178 (1985)

[4] R.B. White, P.H. Ruterford, P. Colestock and M.N. Bussac: Phys. Rev. Lett. **60**, 2030 (1988)

[5] B. Coppi, R.J. Hastie, S. Migliuolo, F. Pegoraro and F. Porcelli: Phys. Lett. A **132**, 267 (1988)

[6] R.B. White, M.N. Bussac and F. Romanelli: submitted to Phys. Rev. Lett.

[7] B. Coppi and F. Porcelli: Phys. Rev. Lett. **57**, 2272 (1986)

[8] M.N. Bussac, R. Pellet, D. Edery and J.L. Soulè: Phys. Rev. Lett. **35**, 1638 (1975)

HIGH FIELD TOKAMAKS: THE WHY'S AND HOW'S

A. Sestero

Associazione EURATOM-ENEA sulla Fusione, C. R. E. Frascati,
C.P. 65 - 00044 - Frascati, Rome, Italy

I - FROM SCALING LAWS TO MERIT FACTORS AND COSTS

After expressing the input power into the plasma through the energy confinement time τ_E (by invoking thermal equilibrium), and in turn expressing τ_E through the LAWSON parameter L, power-law type scalings can be manipulated into the form

$$G(L,T,m) = M(a,B,A,q,\beta) \tag{1}$$

where G and M are monomial functions of their arguments. The function G can be labelled *goal factor* in that by assigning numerical values to its arguments L (Lawson's parameter), T (temperature) and m (ion mass), one is typically identifying specific goals on the way to fusion. Conversely, the function M can be labelled *merit factor* in that, whichever merit exists in the discharge parameters appearing as its arguments, it is expressed by the particular combination of values that M represents. Please note that, of the usual variables appearing in scaling laws, the minor radius a and the magnetic field B are maintained as such in relation (1), while the major radius R, the plasma current I and the plasma density n are respectively expressed in terms of the aspect ratio A, the safety factor q and the plasma β: consequently, arguments of M are one *extensive* variable (namely a) and one *intensive* variable (namely B), plus a set of three dimensionless variables (namely A,q,β). If desired, other quantities can be selected to play the role of *extensive* variables in place of a - such as, e.g., the plasma current, or the total magnetic energy content within the plasma volume (the latter quantity being particularly interesting, as we shall see, in that it is believed to represent a good index of experimental costs).

As an application of the concept of *goal factor*, one can consider, e.g., the objective of reaching ignition. Hence, among the arguments of G, m is to be given the value 2.5 and L becomes a function of T. Then one can look for the value of T which makes the function $G(T)$ a minimum. Such a value of T defines, thus, the optimal ignition temperature (the latter, of course, being found different for different scaling laws).

As an application, in turn, of the concept of the merit factor, one can consider, e.g., the issue of the cost involved in the reaching of certain fusion goals - such goals being translated into the assigning of certain numerical values to the independent variables appearing in the left-hand side of Eq. (1). To such an end, it is convenient to select the magnetic energy content E as the *extensive* variable (thus expressing a in terms of E in Eq. (1)). Subsequently, the relation obtained can be solved with respect to E - presumed to be a good index of experimental costs - thus revealing how cost supposedly depends on the discharge parameter B,A,q,β. Most interesting is the dependence of cost on the *intensive* variable B: for all the most credited scaling laws, **cost is found to be a sensitively decreasing function of** B, comprised between two

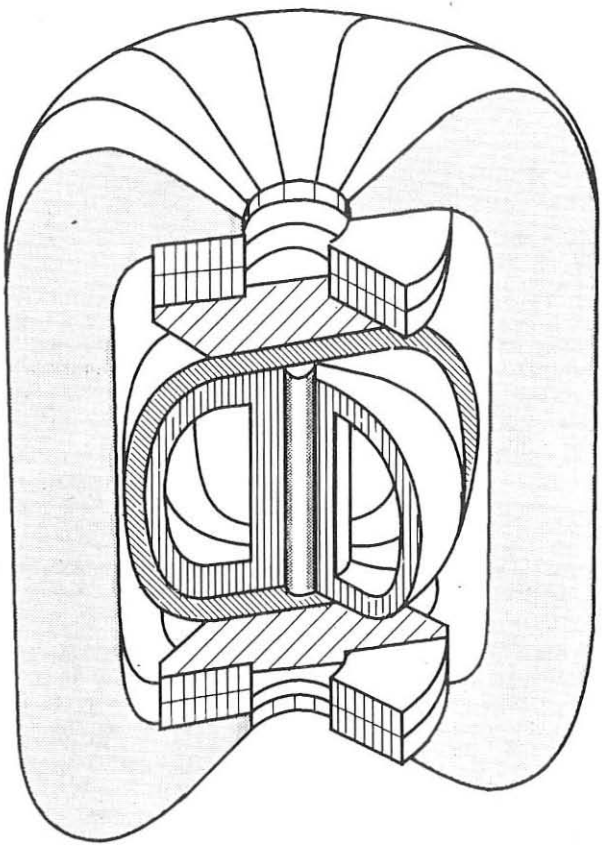

Fig. 1 - Schematic view of magnet plus press system of the OMITRON tokamak

limits, corresponding respectively to the so-called *Goldston scaling* (cost $\propto B^{-1.41}$) and *Kaye-All-Complex scaling* (cost $\propto B^{-6.10}$).

It is to be noted, finally, that one is sometimes interested in assessing machine performance under conditions of pure ohmic heating. The requirement that the input power be due essentially to ohmic heating results hence in a constraint, which is to be added to Eq. (1), and which can be exploited to eliminate one of the independent variables in it (e.g., most conveniently, the variable β). For this case too, the same steps seen before can be retraced, leading to similar results. In particular, the scaling of the cost with B is, if anything, still more favourable for the high magnetic fields than it was in the previous circumstances.

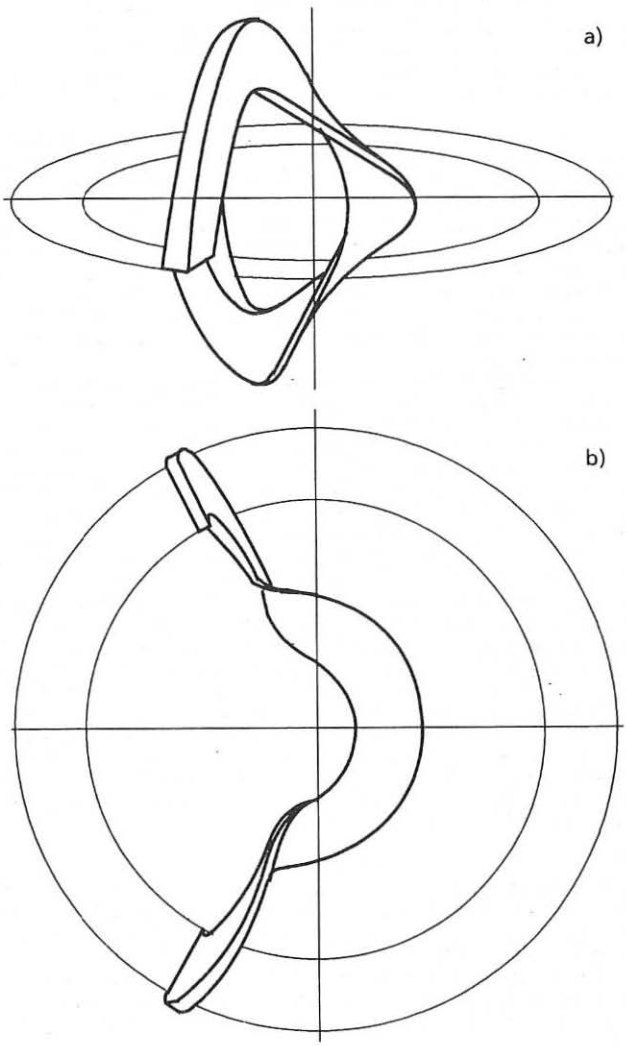

Fig. 2 - Schematic drawing of single turn in the tilted winding concept, with viewing direction nearly horizontal (a) and, respectively, nearly vertical (b)

II - ADVANCED SOLUTIONS FOR HIGH-FIELD TOKAMAKS

One is actually witnessing, at present, a surge of interest in high-field tokamaks as a consequence of the soaring costs of the more conventional approaches. Moreover, the high field appears to be the only hope, for the moment, of ever going beyond the D-T option to the burning of the more advanced D-^{3}He and catalized D-D thermonuclear fuels.

In order to fully exploit the advantages of the high field, however, one has to resort to innovative ideas in the mechanical engineering of the toroidal magnets. One concept in particular, which has in the recent past proven worthy, relies on an active mechanical support scheme implemented by way of a press. Such a solution was first conceived during the working out of the OMITRON proposal [1,2,3] - whose design still today embodies the fullest implementation of the press concept. Some variations of the same idea have subsequently found their way into some other proposed experiments, namely, IGNITOR, CIT, and above all IGNITEX (in the latter, indeed, the press support scheme having the same fundamental importance that it has in OMITRON). By way of an example, a schematic view of the magnet plus press support system of the OMITRON tokamak is shown in Fig. 1.

Equally promising appears to be an alternative recipe requiring the tilting of the turns of the toroidal magnet, in the most critically loaded *throat* region, by a suitable amount with respect to the meridian plane [4,5,6]. The resulting configuration brings about a number of favourable consequences, namely: (i) in the *throat* region, the magnetic pressure of the toroidal field is to a large extent compensated by the magnetic pressure of the poloidal field which is generated in the magnet *doughnut hole* due to the geometry of the tilted winding, (ii) the spring-like behaviour of the helicoidally-tilted inner segments of the turns is helpful in reducing also those components of the mechanical strain which originate from the non-compensated part of the toroidal field pressure; (iii) the helical pattern of the current flow in the magnet *throat* substantially reduces the *skin effect* there and hence lightens its unfavourable consequences; (iv) with reference to the tokamak configuration, the flux variation associated with the poloidal magnetic field can drive the bulk of the toroidal plasma current (thus providing a *built-in transformer*); (v) the geometry of the stress distribution is such as to allow (if desired) the fitting of cooling ducts between adjacent turns without substantially weakening the mechanical performance of the magnet assembly; (vi) finally, the strong and easily accessible poloidal magnetic field that is generated in the region of the *doughnut hole* is an asset which, in principle, could also lead to worthwhile applications in areas other than thermonuclear research. By way of an example, Fig. 2 shows the peculiar configuration that a *single turn* may assume in one particular embodiment of the considered solution.

REFERENCES

[1] A. Sestero: Proc. of the XII Symp. on Fusion Technology, **Vol. 2**, 909 (1982)
[2] A. Sestero: Comments on Plasma Phys. and Controlled Fusion **8**, 31 (1983)
[3] See also U.S. Patent no 4,475,096 of October 2nd, 1984, priority based on Italian Patent Application no 48482-A/81 of October 14th, 1981
[4] A. Sestero: Proc. of the XIV Symp. on Fusion Technology **Vol. 2**, 1669 (1986)
[5] A. Sestero: Comments on Plasma Phys. and Controlled Fusion **11**, 27 (1987)
[6] See also Italian Patent Application no 47795-A/86 of March 20th, (1986)

EXPECTED IGNITOR PERFORMANCE

Airoldi A.(+), Cenacchi G.(*)

(+) Istituto di Fisica del Plasma CNR - Milano (Italy)
(*) Centro Ricerche Energia ENEA - Bologna (Italy)

Introduction

In this work we study the influence of a few parameters on the ignition conditions to be attained in Ignitor. The explicit goal of this machine is to reach ignition by employing a high current plasma in a high magnetic field. The basic data of the experiment are presented elsewhere (B.Coppi, 1988) and here we recall only the principal ones: $R_o = 117cm$; $a = 43.3cm$; elongation $k = 1.8$; triangularity $\delta = 0.3$; $B_T = 13.2T$; $I_p = 12MA$. Besides these peak magnetic field and current values to be achieved in a transient phase of the main Ignitor operative scenario, it is also planned an alternative situation with a current plateau lasting for about 6 sec at $I_p \simeq 10MA$ and $B_T = 11.1T$. This preliminary study refers to such a well defined plasma configuration, on account of the fact that the relevant magnetic equilibria have been extensively discussed (G.Cenacchi, B.Coppi et al., 1988). Because of the highly elongated plasma shape, typical of this device, it should be necessary to adopt the real equilibrium evaluation coupled to the transport code, in order to correctly take into account the effects due to the magnetic configuration and to obtain more plausible predictions. In our simulations we use the 1 1/2 dimensional equilibrium-transport code JETTO (G.Cenacchi and A.Taroni, 1988).

The simulation models

The equilibrium package of the code finds the magnetic equilibrium configuration by solving the Grad-Schluter-Shafranov equation given the toroidal current density profile, with the plasma boundary determined by imposing the inner limiter position. The transport module solves the diffusion equations for the electron and ion energies, for the primary ion and impurity densities, and for the poloidal field, averaged over the magnetic surfaces determined by the equilibrium package. Our primary popolation is a (50%-50%) deuterium-tritium mixture. The two considered impurity species, oxigen and carbon, give a value of $< Z_{eff} > \simeq 1.2$ in most of the simulations as it is usually obtained in high density machines. Each impurity is treated as a single type of ion whose charge is given by coronal equilibrium. Concerning the density profile two options are considered: in the first one the initial profile is held fixed, while in the second case it evolves. The parallel electrical resistivity has the neoclassical expression taking into account the trapped particle correction (S.P. Hirshman, R.J. Hawryluk et al., 1977). For the electron thermal diffusivity χ_e we have adopted the model

developed by M.H.Redi, W.M.Tang et al. (1987) in the two forms depending on the ν_{*e} value, extended to auxiliary heated cases. The ion thermal diffusivity χ_i , taken from the same reference, includes the contribution from the η_i modes added to the Chang and Hinton (1982) expression. In the central region, which we assume defined by the condition $q < q_{\min} \simeq .7$, since we do not consider sawteeth, the thermal diffusivity is enhanced in such a way to flatten temperature and density profiles. The additional power given to the electrons and ions by the produced α particles has the form

$$S_{\alpha(e,i)} = n_D n_T W_\alpha < \sigma_{DT} > f_{e,i}(T_e)\, \gamma$$

where n_D, n_T are the densities of deuterium and tritium ions, W_α is the 3.5 Mev energy with which α particles are born, $< \sigma_{DT} >$ is the cross section rate for fusion production, $f_{e,i}$ is the energy fraction delivered to the electrons or ions, according to D.J.Rose (1969) evaluations, and γ takes into account the fraction of the confined α particles. We have assumed as a conservative value $\gamma \leq .95$ because Ignitor has a very low magnetic field ripple ($\simeq$1.5%at the plasma outer edge) so that the number of promptly lost α particles should be very small. A rough model taking into account the variation of the relative D-T fraction after the ignition time has been introduced to avoid a too sharp increase in α-power.

The constraints in the (n, T) plane are the Murakami Greenwald value of the density limit, which, for our reference parameters, turns out to be $< n > \simeq 12.7 \times 10^{20} m^{-3}$ and a β_T limit in the form $\beta_T(\%) < g I_p(MA)/[a(m) B_T(T)]$ with $g \simeq 2.8$. We define, in order to assess the terminology, the ignition time , t_{ign} , as the one when the global power due to the α −particles, P_α , balances and exceeds the total plasma losses, i.e. convective and conductive losses, $P_{e+i} = (W_e + W_i)/\tau_E$, impurity radiation, P_{imp} , bremsstrahlung and syncrotron emission, P_{brem}, P_{sync} . The energy replacement time τ_E is defined by

$$\tau_E = \frac{(W_e + W_i)}{P_{ohmic} + P_\alpha - \Delta(W_e + W_i)/\Delta t}$$

Results and discussion

We illustrate the results obtained in five simulations performed under different conditions. Our reference case (Shot 1) involves a plasma equilibrium with $q_\psi(a) \simeq 3$ and $q_\psi(0) \simeq 0.9$. The total toroidal field, taking into account the paramagnetic effect, results to be $B_T = 12.1 T$. The initial temperature profile is assumed as parabolic with a peak value of 5 keV. The density profile, given in a parabolic form, with the peak value $n(0) = 12. \times 10^{20} m^{-3}$, and the volume averaged value $< n > = 6.4 \times 10^{20} m^{-3}$, is held fixed. In case 2 the density profile temporally evolves. In case 3 the central region is broadened until $q_{\min} = .8$. The influence of the equilibrium configuration is evaluated by considering a case where elliptic formulas are used for representing the magnetic surfaces (Shot 4). In case 5 the initial temperature profile is obtained from the equilibrium pressure profile.

In Table 1, for each case, are listed: the ignition time τ_{ign}, and some plasma parameters ($T_{e,i}(0)$, $< T_{e,i} >$, β_T, ohmic and α powers) relevant to this time. Besides the τ_E value given by the code, we list also the values obtained, for the same data, by using some popular scaling laws usually adopted for interpreting experimental data.

Table 1

Shot		1	2	3	4	5
t_{ign}	s	3.0	2.0	4.9	2.1	1.05
$T_e(0)$	keV	10.3	13.5	9.7	12.0	15.5
$< T_e >$	keV	3.7	3.7	4.6	3.5	3.4
$T_i(0)$	keV	9.7	12.4	9.2	11.1	13.5
$< T_i >$	keV	3.6	3.6	4.5	3.4	3.1
P_α	MW	22.2	20.6	24.3	24.9	28.5
P_{ohmic}	MW	6.5	7.2	5.3	6.7	10.1
τ_E	s	.52	.52	.58	.50	.40
$\tau_{E\ (KG85)}$	s	.44	.44	.44	.42	.35
$\tau_{E\ (NK86)}$	s	.28	.28	.28	.28	.23
$\tau_{E\ (R-L)}$	s	.33	.33	.32	.29	.25
$\tau_{E\ (G84)}$	s	.20	.19	.19	.18	.15
$< Z_{eff} >$		1.23	1.16	1.24	1.27	1.22
β_p		.18	.17	.21	.17	.22
β_T		.019	.016	.022	.018	.018

The different time evolution of the peak electron and ion temperatures in cases 1 and 2 is shown in Fig.1, where a vertical bar marks the ignition time in each case. It must be observed that the ignition is a very steep process and a tight control on the density should be provided. The results of case 3 clearly show that the ignition time depends on the size of the internal region where profiles are flattened. In case 4 the toroidal field is increased in the percentage resulting from an independent equilibrium calculation. Notice that, using the vacuum toroidal field ($B_T = 11.1T$), the ignition would not be reached. On the other side, our enhancement of B_T, results in a more favourable condition for the plasma.

The differences between the examined cases do not depend on the transport models; the same trend has been observed also in other conditions. The adopted anomalous χ_e and χ_i coefficients ($\simeq$80% of the Redi and Tang values) partially justify the differences between our confinement times and those obtained by global scaling laws. However one should consider that the scaling laws derived

from the data base relevant to actual tokamaks rely on machines operating at low densities and low magnetic fields.

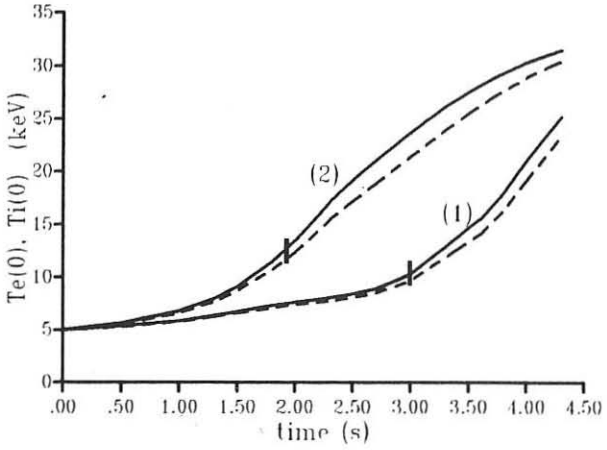

Fig.1 - Time evolution of peak electron (continuous lines) and ion (dashed lines) temperatures for cases (1) and (2). The vertical slashes indicate the ignition time.

This work was intended as a preliminary scan looking for the possibility of obtaining ignition with the parameters considered. The first purpose was to evaluate the importance of using the real equilibrium configuration. Other effects, such as sawteeth, plasma evolution after the ignition time, more realistic α- particles model, different transport models will be analyzed in the future.

References

G.Cenacchi, B.Coppi, L.Lanzavecchia and M.Rulli - MIT Report PTP - 88/12 (1988)

G.Cenacchi and A.Taroni - JET-IR(88)03, (1988)

C.S.Chang and F.L.Hinton - Phys. Fluids **23** 1493 (1982)

B.Coppi - Vuoto **XVIII** , 153 (1988)

S.P.Hirshman, R.J.Hawryluk and B.Birge - Nucl. Fusion **17** , 611 (1977)

M.H.Redi, W.M.Tang, P.C.Efthimion, D.R.Mikkelsen and G.L.Schmidt - Nucl. Fusion **27** , 65 (1987)

D.J.Rose - Nuclear Fusion **9** , 183 (1969)

IGNITION DOMAIN AND PLASMA BURN CONTROL

G. Apruzzese, A. Tanga*

Associazione EURATOM-ENEA sulla Fusione, C. R. E. Frascati,
C.P. 65 - 00044 - Frascati, Rome, Italy

INTRODUCTION

A tokamak fusion reactor should ignite at low powers and operate at high powers without thermal instability. The properties of the ignition domain and plasma thermal stability have been analysed with a zero dimensional model whose basic features are those of the POPCON code [1,2]. A mechanism of stabilizing the reactor operating region, based on the control of energy confinement sensitive parameters such as plasma current, is presented.

IGNITION DOMAIN

To analyse the ignition conditions and plasma operating regimes, a global zero-dimensional code which solves the power balance equation, both in the steady-state and with time dependent terms, has been developed.

The power balance equation is solved:

$$\frac{dW}{dt} = P_{OH} + P_{aux} + P_{\alpha} - P_{con} - P_{rad} \qquad (1)$$

where W is the plasma energy, P_{OH}, P_{aux} and P_{α} are, respectively, ohmic auxiliary and alpha power and P_{con}, P_{rad} conduction and radiation power [3].

The specific assumptions used in this model are (1) the ohmic power has been calculated considering the neoclassical correction factor in the Spitzer resistivity; (2) conduction losses have been determined by global confinement scalings ($P_{con}=W/\tau_E$); (3) the confinement time has been determined by the combination of the ohmic (neo-Alcator) value τ_{OH} and the L-mode τ_L so that $\tau_E=(1/\tau^2_{OH}+\tau^2_L)^{-1/2}$ [4]; (4) the density and temperature profiles have been assumed of the form $(1-r^2/a^2)^{\alpha_x}$, where a is the minor radius and α_x the peaking factor; for the density $\alpha_x=1.0$, while, for the temperature it has been determined by the relation between the total current, I_p, and the value of the safety factor on axis, q(0). The electron and ion temperatures have been assumed to be identical; (5) the scaling of the confinement degradation on α particle power has been assumed to be similar to any other power source.

Time independent solutions have been found by $dW/dt=0$. As an example, the contour plots of equilibrium in the space $<n>$, $<t>$ for the NET-E device are shown in Fig. 1. For D-T plasma in ignition conditions, besides the ohmic equilibrium, there are other contours of equilibrium.

The shape of the ignition domain depends strongly on the energy confinement scaling. This point is illustrated in Fig. 2 which shows the equilibrium contour plots using Goldston × 2, Kaye-Goldston and Rebut-Lallia scalings. The existence of a minimum density to achieve ignition is determined by the density dependence of the

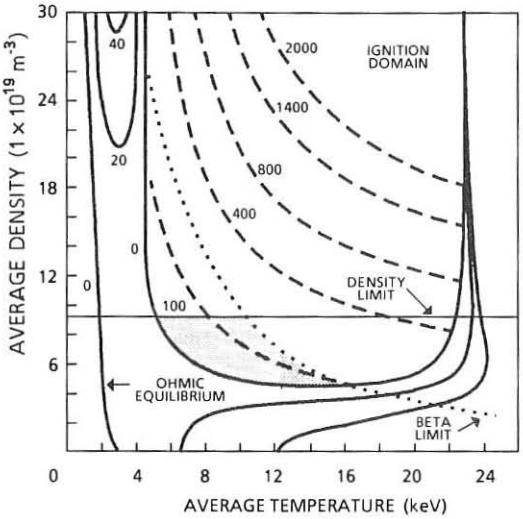

Fig. 1 - Plots of equilibrium contours (dW/dt=0) over <n>-<t> space for P_{aux} (MW)= 0,20,40 for NET-E device, with Z_{eff} (effective charge)= 1.0, q(0)= 0.8, and Goldston × 2 scaling. Horizontal line: Murakami limit, dotted line: Troyon β limit, dashed lines: P_α (MW), dotted region: operating region. Left-hand line describes the ohmic equilibrium

ohmic (neo-Alcator) confinement scaling. At high densities, instead, the dominant term becomes τ_L so that with the Kaye-Goldston scaling and the Rebut-Lallia scaling, which depend on plasma density, the ignition boundary contains a density dependence, while, with the Goldston scaling, it is simply U-shaped.

THERMAL STABILITY

A necessary and sufficient criterion for thermal stability is $\partial/\partial T(dW/dt) < 0$. The part of the equilibrium contours which satifies this criterion is the ohmic equilibrium curve and the ignition curve at the high temperature boundary. The ignition domain, limited at the left-hand side by an unstable curve and at the right-hand side by a stable curve, is unstable. The growth rate of thermal instability is strongly dependent on the energy confinement time [5].

In ignition conditions, an analytic expression for temperature evolution can be written:

$$\frac{T(t)}{T(0)} = \frac{1 - t/\tau_E}{1 - t/\tau^*} \qquad (2)$$

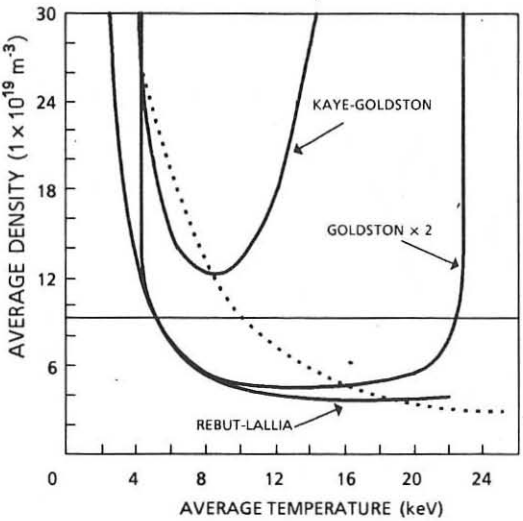

Fig. 2 - Plots of ignition contours for NET-E device, with $Z_{eff}=1.0$ and $P_{aux}=0$, using the following scalings: Goldston × 2, Kaye-Goldston and Rebut-Lallia. Dotted line: β limit, horizontal line: Murakami limit

where $\tau^* = \frac{12}{nE_\alpha T(0)} \cdot \frac{1}{<\sigma v>/T^2}$

E_α and $<\sigma v>$ are the α particle energy and the reaction rate parameter for a D-T reaction. For the temperature ranges of interest, $<\sigma v>/T^2$ is a constant. The $1/\tau_E$ dependence implies that the thermal instability growth rate is larger for good confinement than for poorer energy confinement.

PLASMA BURN CONTROL

To provide the thermal stability of the operating point, a real time control of the $n\tau_E$ parameter is required. This control can be achieved either by varying the plasma density or by varying some physical parameter functionally related to τ_E such as plasma current. In the first case, the stabilization is based on the reduction of the α power maintaining the plasma on the edge of the ignition domain, characterized by low thermonuclear powers. In the second case, it is possible to operate at any point of the ignition domain, i.e., at any power. The results obtained with a feedback, which includes proportional and derivative terms, are shown in Fig. 3. The features of this mechanism is not to operate directly on the operating point but on the ignition curve which is dependent on the energy confinement time. In fact, decreasing the plasma current, the ignition curve varies so that an ignited regime is again reached. The stabilization is reached varying the plasma current until the operating point is on the ignition curve. In

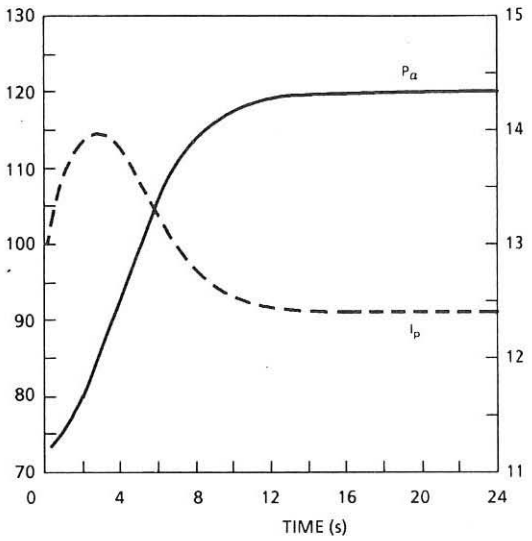

Fig. 3 - Plots of plasma current and α power time evolution during the feedback control for NET-E device, with $Z_{eff}=1.0$, $q(0)=0.8$, $P_{aux}=0$ and $<n>=8\times10^{19}$ m^{-3} using Goldston × 2 scaling

this case, the thermal stabilization is obtained without decreasing the α power, which could still be controlled independently by plasma density control.

CONCLUSIONS

The study of ignited plasma for a given device shows that the operational domain depends strongly on the confinement model. Ignited plasma is always thermally unstable up to the upper temperature limit with a characteristic time which is a function of the energy confinement time. A mechanism of stabilising the burn could be a feedback based on the control of plasma current.

FOOTNOTE AND REFERENCES

* Present address: JET Joint Undertaking, Abingdon, OX14 3EA, England

[1] T.K. Mau, E.L. Vold and R.W. Conn: Fusion Technology 12, 187 (1987)
[2] N.A. Uckan, J. Sheffield: ORNL Report ORNL/TM-9722 (1985)
[3] G. Apruzzese, A. Tanga: JET Report (to be published)
[4] R.J. Goldston: Plasma Phys. Controlled Fusion 26, 87 (1984)
[5] K. Borrass: NET Report 61, EUR-FUS/XII-80/86/612 (1986)

ANALYSIS OF THE IGNITION EXPERIMENT IGNITEX

R. Carrera, G. Y. Fu, J. Helton,* L. Hively,+ E. Montalvo, C. Ordonez, M. N. Rosenbluth,** S. Tamor, and J. W. Van Dam

The University of Texas at Austin, Austin, TX 78712, USA; *GA Technologies, Inc., San Diego, CA; +Oak Ridge National Laboratory, Oak Ridge, TN; **University of California, San Diego, CA.

The realization of an ignition experiment in a laboratory will prove the scientific feasibility of controlled thermonuclear fusion. The fusion ignition experiment IGNITEX has the potential to produce and control a self-sustained fusion reaction with relative simplicity and low cost. Relevant plasma physics aspects of the experiment are analyzed in this paper.

Introduction

The IGNITEX concept has been proposed by Marshall N. Rosenbluth, William F. Weldon, and Herbert H. Woodson (1) on the basis of Bruno Coppi's idea of a compact ignition experiment and recent technology advances in pulsed power high current systems.

The IGNITEX experiment is to be realized in a compact, high-field, single-turn-coil tokamak. At the time of ignition the plasma state can be described according to Table I. Because of the low impedance of the magnet system, pulsed power generators working at low voltages and supplying high currents are needed. Homopolar generators can provide these conditions. The effect of self-shield from neutron and gamma radiation of the single-turn-coil structure alleviates by orders of magnitude the problems of activation and waste disposal.

Ignition Margin

A typical (n,T) diagram for the IGNITEX experiment as obtained with SSIC is given in Fig. 1. An ample ignition region exists which is accessible by ohmic plasma heating. The accessibility conditions: POH > PE, T (POH ~ PE) > T (PFUS ~ PRAD), and n (POH ~ PRAD) > n (PFUS ~ PE) are satisfied for high values of B^2aK^2, which in IGNITEX is > 500. Ignition is achieved when the ignition factor $\rho(n,T,t) = PFUS / PE > 1$ or, since $\rho \sim n_0\tau_E T_0 f_\alpha$, $n_0\tau_E T_0 \geq 5 \times 10^{15}$ s keV/cm^3 and $f_\alpha \sim 1$. The ignition margin can be measured by $\Delta\rho = \rho(n_{MUR}, Tm)$; typically $T_m \sim 12$ keV (on axis).

The IGNITEX device is an Alcator-type machine. As such, its ignition margin is very high. Even assuming energy confinement degradation by alpha heating (ex,: Kaye-Goldston scaling, the IGNITEX ignition margin is over 300%). As presently defined, IGNITEX is marginal for Goldston scaling ($\Delta\rho = 1.1$ if pellet injection is used). It should be noted that the Goldston scaling is significantly based on data from low field, large size, and low density devices different ftom the Alcator-type experiments.

Ohmic Ignition

The duration of the experiment is constrained by resistive heating of the TF magnet. In IGNITEX, currents and fields are ramped up in 3 seconds and shutting down in 2 seconds. A flat top of about 10 energy confinement times (~ 5 seconds) can be maintained.

Ohmic heating to the plasma increases during the first 3 seconds. Before a significant decrease in ohmic dissipation takes place at high plasma temperatures, alpha heating becomes the dominant heating mechanism. Ignition is attained less than one second into the flat top of the discharge. Thermally stable ignited plasmas can be produced in IGNITEX. Typical discharges to ignition (simulated with TDIC) evolve well within the Hugill diagram of operation and below the Murakami and Troyon disruptive limits.

Plasma Equilibrium

A high-coupling internal inductor is employed in IGNITEX. The plasma inductance is significantly reduced by the coil structure so that flux consumption during the discharge is much lower than in conventional devices.

Equilibrium simulations using GAEQ, with free current surfaces give PF coil currents within the stress and heating limits and indicate good plasma equilibrium throughout the discharge to ignition (including null field production). Structural eddy current effects have been analyzed. During regular operation these effects are small. However during vertical displacements of the plasma column these effects significantly stabilize the plasma. 2X equilibrium configurations are easily obtained with small changes in the pulse shape of the elongation coils.

Plasma stability

The IGNITEX experiment can produce ignited plasmas far away from marginal stability. Typically at the time of ignition the volume-averaged toroidal beta is 0.6% which is much lower than the Troyon limit 3.5%. Values of elongation (1.6), edge cylindrical safety factor (2.2), and safety factor on axis (1.0) give a high stability margin. Ideal external kink modes have been analyzed with GATO. Even without plasma profile optimization and plasma-wall stabilization, beta values over 5% are possible. Since the Troyon limit is an operational tokamak limit, operation far from stability limits implies a good reproduceability and reliability of the IGNITEX ignition discharge. The shell surrounding the plasma column should stabilize ideal and resistive MHD modes, slowdown mode locking, increase pulse duration, and provide some degree of stabilization of plasma disruptions.

Plasma Transport and Plasma Wall Interaction

The relative high density of operation in IGNITEX should prevent impurity accumulation in the plasma. Typically the neutron wall load at the time of ignition is 3 Mw/m^2 and the peak value during the ignited phase is 8 Mw/m^2. Detailed transport simulations have been carried out using PROCTR. Sawteeth oscillations in the plasma core region do not seem to prevent ignition. Sputtering is maintained to acceptable levels even in high temperature discharges where Ti ~ 5O keV can be obtained. Threshold values of impurity concentration for ignition are Zeff > 2 for typical plasma impurity compositions.

Alpha Particle Containment

Alpha heating is the only additional heating mechanism to ohmic dissipation that maintains the self-sustained fusion reaction in the IGNITEX experiment. The small alpha Larmor radius and the large alpha containment factor (ratio of the plasma current to the minimum plasma current for confinement of most alpha particles according to neoclassical

orbit theory) make alpha containment in IGNITEX high. Alpha transport simulations using DESORB indicate negligible alpha loses with high-n-ripple levels up to 4%. Threshold levels of low-n-ripple losses are even higher.

Thermal Runaway Control

Thermally stable ignited plasmas can be produced in the IGNITEX experiment. Simulations with the SSIC and TDIC codes show that electron cyclotron emission can damp the thermal runaway associated to ignition conditions in the case that the electron energy confinement time follows the Neoalcator scaling. In simulations where alpha degradation of confinement is assumed, then both plasma energy losses due to cyclotron emission and alpha degradation provide the required damping of the thermal runaway. A sketch that explains the various physics regimes relevant to the experiment is given in Fig. 1. Disruptive limits can be avoided throughout the duration of the experiment.

Alpha-Driven Plasma Modes

Ideal MHD plasma modes could potentially be excited by the alpha particles during the ignited phase of the experiments with an associated energy confinement degradation. At low frequencies ($\omega \sim \omega^{\alpha}_{D} < \omega_{A}$), low-n fishbone and high-n ballooning-bone are possible for toroidal beta values above critical levels. At higher frequencies ($\omega \sim \omega^{s}_{A}$) low-n and high-n GAP modes can be excited at frequencies $\omega \sim \omega^{\alpha}_{t}$. The IGNITEX low beta operation should attenuate the negative effects of these modes.

Electron Cyclotron Emission and Absorption

The dominant radiation mechanism before ignition is bremsstrahlung emission. After ignition is reached the electron cyclotron emission becomes dominant because of the high electron temperature and the low beta value. Simulations assuming NeoAlcator electron confinement and four times neoclassical ion confinement with locally applied global theories (ex: Engelmann-Curatolo at low T and Trubnikov high T) indicate that cyclotron emission controls the thermal excursion before reaching disruptive limits. Detailed calculations of the cyclotron radiation radial transport (emission, absorption, and reflection) with SNECTR, show that wall-reflectivity effects can be outweighted by control of the plasma density.

Scientific Basis

The basic mode of operation of the IGNITEX experiment is the one of ohmically heated high field tokamaks (L-mode). This mode of operation has produced record values of energy confinement, plasma density, and plasma cleanness. Simulations with sustained ignited H-mode phases have been carried out (driven by alpha heating in 2X configurations). However L-mode of operation is preferable because it is simpler, less costly, more reliable, and sufficient for ignition.

High plasma current is presently thought to improve thermal energy balance and relax operation conditions. Present scalings indicate that values of $B^2aK^2 \sim 270$ may be required for ohmic ignition. A higher field and plasma current (with comparable plasma current density but larger plasma size) than in previous high-field tokamak experiments is predicted to open a path between the low-and high-temperature energy gain regions of the (n, T) diagram as indicated in Fig. 1.

Conclusion

A controlled self-sustained fusion reaction is a new basic physics process that could be produced and studied in the near future with a tokamak device. A compact single-turn-coil

tokamak with about twice the field conventionally available in previous high-field-tokamaks seems to offer a simple, theoretically reliable, and low cost ignition experiment.

Acknowledgements. This work is supported by the Texas Atomic Energy Research Foundation, the Texas Advanced Technology Program , and the Department of Energy.

(1) M.N. Rosenbluth, W.F. Weldon, and H.H. Woodson, "Basic Design Report for the Fusion Ignition Experiment IGNITEX," Center for Fusion Engineering Report, University of Texas at Austin (March, 1987).

TABLE I

IGNITEX EXPERIMENT		
Minor radius	47.	cm
Major radius	150.	cm
Plasma elongation	1.6	
Toroidal field on axis	20.2	T
Safety factor at the plasma edge	2.72	
Plasma current	12.	MA
Avg. plasma density	3.6×10^{14}	cm^{-3}
Avg. plasma temperature	6.5	keV
Avg. toroidal beta	0.6%	
Avg. energy confinement time	0.54	s
Confinement product	3.9×10^{14}	s/cm^3
Ignition margin (KG)	3.4	
Fusion power	149.	MW
Neutron wall load	3.	MW/m^2
Neutron production rate	5.3×10^{19}	n/s
Alpha containment factor	3.2	
$T_0 n_0 t_E$ product	4.7×10^{15}	$keV/cm^3/sec$

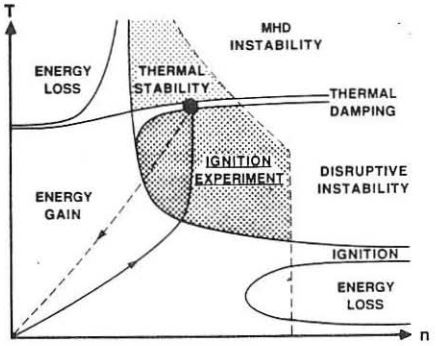

Fig. 1 Conceptual (n, T) diagram for the IGNITEX experiment

THE EFFECTS OF FINITE PRESSURE AND TOROIDICITY ON THE STABILITY OF NON-IDEAL MODES IN A TOKAMAK

J.W. Connor, R.J. Hastie, S.C. Cowley*, T.J. Martin & J.B. Taylor

Culham Laboratory, Abingdon, Oxfordshire, OX14 3DB, UK.
(Euratom/UKAEA Fusion Association)
* Princeton Plasma Physics Laboratory, Princeton, NJ, USA.

Introduction

The stability of tearing modes in toroidal geometry with realistic descriptions of the physics at the resonant layers can only be addressed by the asymptotic matching procedure.[1] The formal procedure, which allows for the presence of a number of resonant poloidal harmonics as a result of coupling due to toroidal geometry, has been described previously.[2] This approach breaks the problem into two parts, namely a treatment of the complex physics necessary for a realistic description of the tearing layers at the resonant surfaces (simplified as a result of the narrowness of the layers) and a separate treatment of the regions between resonant surfaces for which the marginal ideal mhd equations are adequate. The results of the two treatments are matched near the resonant surfaces to obtain a dispersion relation. In general this depends on two quantities $\Delta_+(\omega)$ and $\Delta_-(\omega)$ at each resonant surface corresponding to solutions of the layer equations with twisting and tearing parity respectively. For instance with only one resonant surface present in the plasma the dispersion relation takes the form[3]

$$\Delta_+\Delta_- - \frac{\epsilon}{2}(\Delta_R + \Delta_L)(\Delta_+ + \Delta_-) + \epsilon^2\Delta_L\Delta_R = 0 \qquad (1)$$

where Δ_L and Δ_R are the ratios of 'small' to 'large' solutions on the left and right respectively, i.e., near the resonant surface $x = 0$

$$\phi_{L,R} = A_{L,R}(|x|^{\alpha_+} + \Delta_{L,R}\,|x|^{\alpha_-})$$

with $\alpha_\pm$ being the Mercier indices, and $\epsilon \ll 1$ measures the narrowness of the resonant layer. If the layer solutions are such that $\Delta_-(\omega) \ll 1$, $\Delta_+(\omega) \sim 0(1)$ then one obtains

$$\Delta_-(\omega) = \epsilon\,\Delta', \quad \Delta' = (\Delta_R + \Delta_L)/2 \qquad (2)$$

which is the tearing parity dispersion relation. Conversely

$\Delta_+(\omega) << 1$, $\Delta_-(\omega) \sim 0(1)$ would lead to a twisting parity dispersion relation

$$\Delta_+(\omega) = \epsilon \Delta' \tag{3}$$

Examination of the compressible resistive mhd layer model for example, using the results of Connor et al,[4] indicates that a pure tearing mode only exists in a plasma with negligible pressure gradient at the resonant surface and near marginal stability such that $\beta > S^{-2/5} \Delta'^{6/5}$, otherwise a mixed parity mode results.

If we assume, however, that the layer physics does admit a pure tearing parity mode then it was shown in Ref 2 that the dispersion relation for a plasma with n resonant surfaces can be written in the form

$$\left| \underset{\approx}{I} + \underset{\approx}{\Delta}_-(\omega) \underset{\approx}{E} \right| = 0 \tag{4}$$

where $\underset{\approx}{\Delta}_-(\omega)$ is an nxn diagonal matrix whose elements are the values of $\Delta_-(\omega)$ at the n resonant surfaces and $\underset{\approx}{E}$ is an nxn matrix constructed entirely from a basic set of solutions of the marginal ideal mhd equations.

Realistic kinetic layer models (e.g. Ref 5) suggest $\Delta_-(\omega) >> 1$ unless $\omega = \omega_{*e}(1 + \alpha\eta_e)$ where α is a constant. Since this will only be true in general on one resonant surface, say the j^{th} surface, eqtn.(4) implies

$$\Delta_-(\omega) = E_{jj}^{-1} \tag{5}$$

and the surfaces are decoupled (although E_{jj} itself will of course depend on toroidal effects).

However, if we consider 'neutral' resonant layer models[6]

$$\Delta_-(\omega) \propto (-i\omega)^p \tag{6}$$

such as resistive mhd in the absence of interchange effects (when $p = 5/4$) or the non-linear Rutherford model (when $p = 1$), then stability is determined by the external ideal mhd solutions alone. Thus marginal stability occurs as $\left|\underset{\approx}{E}\right| \to \infty$ and a sufficient stability criterion is given by the $2^n - 1$ conditions

$$(-)^k (\underset{\approx}{E}^{(k)})_{jj} > 0 \tag{7}$$

where $\underset{\approx}{E}^{(k)}$ is a co-factor of order k. This may be considered to be the toroidal generalisation of the cylindrical Δ' criterion.

Stability of a Large Aspect Ratio Tokamak

In earlier work[6] we have described a numerical code T3 which calculates a set of basis solutions to the marginal ideal mhd equations for tearing parity modes in a large aspect ratio tokamak. This code was limited to the toroidal coupling of three poloidal harmonics, any of which could be resonant. Applications of this code, which is extremely rapid to run, to studying β limits due to tearing modes and the stability of profiles of interest for sawteeth phenomena were given previously.[6] It is also ideal for parameter surveys and has for example been applied to study the stability of a q-profile with two resonant surfaces. In this case eqtn.(4) has the form

$$(\Delta_(\omega) - \alpha)(\Delta_(\omega) - \beta) = \gamma^2 \qquad (8)$$

where the constants α, β and γ are related to the elements of the 2×2 matrix $\underset{\sim}{E}$. With a parabolic pressure profile $p = p_o(1 - r^2)$ and a q-profile $q = 1.1(1 + 2\,r^2)$, for which the tearing mode with toroidal mode number $n = 1$ has two resonant surfaces, we find a fit

$$\alpha = \Delta_{21} - 20\,\epsilon^2 + 207\left(\frac{\beta_o}{\epsilon}\right)^2 + 21\,\beta_o$$

$$\beta = \Delta_{31} - 14.5\,\epsilon^2 + 575\left(\frac{\beta_o}{\epsilon}\right)^2 - 285\,\beta_o$$

$$\gamma = 44\,\left(\epsilon - 2.5\,{\beta_o}/{\epsilon}\right)^2 \qquad (9)$$

where $\beta_o = \frac{2\,p_o}{B_o}$ and $\Delta_{21} = 3.5$ and $\Delta_{31} = -13.7$ are the cylindrical values of Δ' for the $m = 2$ and $m = 3$ modes for this q-profile.

To obtain the elements of the matrix $\underset{\sim}{E}$ to sufficient accuracy it is necessary to calculate the properties of the poloidal harmonics corresponding to all the n resonant surfaces plus their upper and lower sidebands. This could only be achieved rather inelegantly, and a little ambigiously, with T3 by repeating calculations with different triplets of harmonics. We have therefore developed an improved code Tn which permits analysis of modes with an arbitrary number of resonant surfaces, although still only keeping couplings of poloidal harmonics consistently to $O(\epsilon^2)$. This code is important for studying the stability of higher values of n when a more ballooning-like mode structure may result.

In addition, this code can be used to investigate the stability of twisting parity modes which require a different set of basis solutions to the marginal ideal mhd equation, namely ones in which the 'large' solution is not continuous at a resonant surface but changes sign.

The effect of increasing β on the stability of such modes using Tn will be presented.

References

1 R C GRIMM et al in Plasma Physics and Controlled Nuclear Fusion Research 1982 (Proc. 9th Int. Conf. Balitmore 1982) Vol 3 IAEA Vienna (1983) 35.

2 J W CONNOR et al, Phys. Fluids 31 (1988) 577.

3 A H GLASSER, S C JARDIN and G TESAURO, Phys. Fluids 27 1225 (1984).

4 J W CONNOR et al in Plasma Physics and Controlled Nuclear Fusion Research 1982 (Proc. 9th Int. Conf. Baltimore 1982) Vol 3 IAEA Vienna (1983) 403.

5 S C COWLEY, R M KULSRUD and T S HAHM, Phys Fluids 29 3230 (1986).

6 J W CONNOR et al, paper IAEA-CN-50/D-1-4, 12th Int. Conf. on Plasma Physics and Controlled Nuclear Fusion Research, Nice 1988.

CURVATURE EFFECTS ON NONLINEAR ISLAND GROWTH

T C Hender

UKAEA/EURATOM Fusion Association
Culham Laboratory, Abingdon OX143DB, UK

INTRODUCTION

Within the context of resistive MHD theory, it is known that the favourable average curvature in the tokamak, can have a strong stabilising effect on the tearing mode [1]. Analytic [2] and numerical simulations [3] show that this stabilising effect is particularly strong in low aspect ratio, high temperature devices, such as JET. Analytic studies [4,5] also show that the curvature stabilisation should persist nonlinearly, until the island exceeds a critical width. The expression given by Somon [4] is derived in cylindrical geometry and contains a modification of the basic Rutherford island growth expression [6], to account for the curvature terms:-

$$\frac{dW}{dt} = 1.6\frac{\eta}{S}\left(\Delta' + 16a_1\frac{D_c}{W}\right) \tag{1}$$

where time is normalised to the Alfven time, S is the magnetic Reynolds number, W the island width, a_1 is a pressure evolution dependent constant of $o(1)$ (eg for an adiabatic pressure law $a_1 = 1.7$) and

$$D_c = -\beta_o r_s \frac{dP}{dr}\left(\frac{q}{r_s q'}\right)^2 \tag{2}$$

with all quantities evaluated at the resonant surface, $r = r_s$. The expression by Kotschenreuther et al [5] is derived in toroidal geometry and is very similar to Eq(1):-

$$\frac{dW}{dt} = 1.6\frac{\eta}{S}\left(\Delta' W^{-2D_I} + \frac{a_2 D_R}{W}\right) \tag{3}$$

with to second order in the inverse aspect ratio, $o(\epsilon^2)$

$$D_I = \beta_o r_s \frac{dP}{dr}\left(\frac{q}{r_s q'}\right)^2 (q^2 - 1) \tag{4}$$

and

$$D_R = \beta_o r_s \frac{dP}{dr}\left(\frac{q}{r_s q'}\right)^2 \left[q^2 - 1 + \left(\frac{r_s q'}{q}\right)\frac{q^4}{r_s^2}\int_o^{r_s}\left(\frac{\hat{r}}{q^2} - \frac{\beta_o}{\epsilon^2}a^2\hat{r}^2\frac{dP}{dr}\right)d\hat{r}\right] \tag{5}$$

In Eq(3) a_2 is again a pressure evolution dependent constant, and for a particular case examined in Ref 5, $a_2 \simeq 6.3$. Both these island evolution expressions (Eqs (1) and (3)) show the curvature term dominates for 'small' island widths ($W < 16a_1 D_c/\Delta'$ or toroidally $W < (a_2 D_R/\Delta')^{1+2D_I}$) and for 'large' island widths the Δ' term dominates (and normal linear Rutherford island growth occurs [6]). It should be noted that at the transition to nonlinear behaviour ($W \sim$ tearing layer width) the linear instability criterion, $\Delta' > \Delta'_c$ [1], is consistent with the requirement for nonlinear instability determined by Eqs(1) and (3).

COMPARISON WITH NONLINEAR COMPUTATIONS

The validity of these island growth expressions (Eqs (1) and (3)) has been examined by nonlinear simulations in cylindrical geometry. To examine the effects of favourable curvature cylindrically ($D_c < 0$), it is necessary to have a positive pressure gradient at the resonant surface. This is achieved by using a pressure profile of the form [7], $P(r) = \beta_o(1-r^2)^2(1+ar^2)$. For the q-profile used, $q = 1.6(1+r^2/0.64)$, the $m = 2, n = 1$ resonant surface is at $r_s = 0.4$, and $P'(r_s) > 0$ implies $a > 3.84$. Figure 1 shows the linear m=2, n=1 growth rate (normalised to the Alfven time, τ_A) for these profiles, as a function of $\beta_o P'(r_s)$ with $S = 5 \times 10^5$, $\eta \equiv 1$ and $\epsilon = 0.2$. The close agreement between the $\beta_o = 0.25\%$ and 0.5% incompressible growth rates shown in Fig 1, confirms that the curvature effects are determined solely by the pressure gradient at r_s. It should be noted also that Δ' is a function of β, but for the β-values examined, evaluation of Δ' (as defined in Ref [1]) shows that it varies by less than 1%.

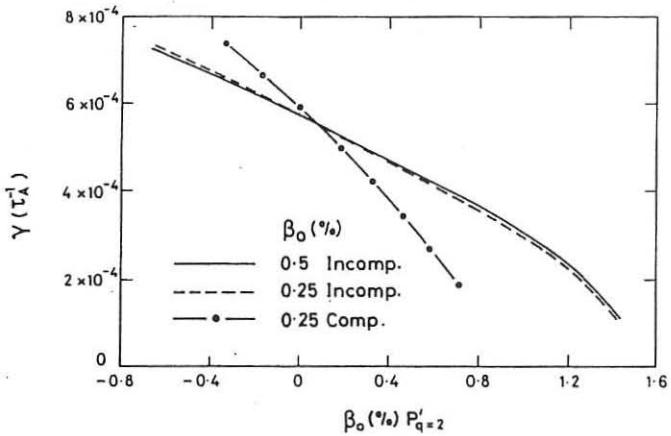

Fig1 Linear $m = 2$, $n = 1$ growth rate v pressure gradient at $q = 2$

Also shown in Fig 1 is the compressible growth rate ($C_p/C_v = 5/3$) for $\beta_o = 0.25\%$. This indicates at the larger pressure gradients that the effects of compressibility can be quite important. Beyond the highest pressure gradients shown in Fig 1 the modes become overstable (as expected [1]).

Nonlinearly, incompressible single helicity (m/n = 2/1) simulations have been made. Figure 2 shows the m=2, n=1 island width evolution, for various pressure gradients at q=2 ($\beta_o P'(r_s)$) with $S = 5 \times 10^5$ and $\eta \equiv 1$. The close agreement between the cases with $\beta_o P'(r_s) = 0$ (but different pressure gradients elsewhere) indicates nonlinearly that it is local pressure gradients (at r_s) which determine the island evolution. The evolution of the $\beta_o P'(r_s) = 0.728$ and 0.903 cases shows a tendency to saturate for $W \sim 6\%$, and then a subsequent increase in growth rate. This behaviour is consistent with Eqs(1) and (3) which show that the stabilising effect of the curvature term is diminished for $W \gtrsim 16 a_1 D_c/\Delta'$. Evaluating this for $\beta_o P'(r_s) = 0.728$ ($D_c = 0.77$) we have $W(\%) \gtrsim 7.04 a_1$ (with $a_1 \sim 1$); this result is in good agreement with the numerical simulations (which show the curvature effect is diminished for $W \gtrsim 6\%$). The $\beta_o P'(r_s) = 1.078$ result shown in Fig 2 saturates at a small island width. The saturation behaviour is not described by Eqs (1) or (3), since these are quasi-linear expressions. The remaining curves in Fig 2 ($\beta_o P'(r_s) < 1.078$) show saturation over a relatively narrow range ($10.4 < W(\%) < 13.4$) despite a variation of 2.1 in the linear growth rates.

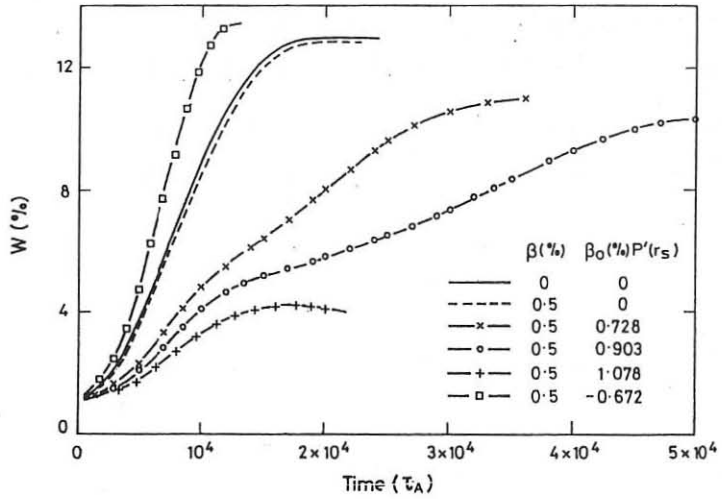

Fig 2 Quasi-linear m = 2, n = 1 island evolution for various P' at $q = 2$

CONCLUSIONS AND DISCUSSION

It has been shown that the analytic expressions for the modification to the nonlinear growth by curvature terms (Eqs (1) and (3)) are consistent with nonlinear simulations. In particular the curvature stabilisation effects are diminished for $W \gtrsim 16D_R/\Delta'$. Taking typical values for a JET size device shows that $W \gtrsim 5\%$ is required for the curvature stabilisation to be nonlinearly diminished. Thus except near the disruption boundaries (where the curvature effect is weakened, by a reduction in local conductivity temperature at $q = 2$ and an increase in Δ') it is expected that the curvature terms will remain effective in stabilising the tearing mode. A possible exception is where a large perturbation occurs (perhaps due to an injected pellet or a large sawtooth crash) which introduces a large initial island, and sufficiently weakens the curvature stabilisiation to permit growth.

References

[1] GLASSER, A.H., GREEN, J.M., JOHNSON, J. L., Phys Fluids 18 (1975) 875

[2] HASTIE, R.J., SYKES, A., TURNER, M.F., WESSON, J.A., Nucl Fusion 17 (1977) 515

[3] HENDER, T.C., HASTIE, R.J., ROBINSON, D.C., Nucl Fusion 27 (1987) 1389

[4] SOMON, J.P., Energy Research Centre, Frascati, RT/FUS/84/13

[5] KOTSCHENREUTHER, M., HAZELTINE, R.D., MORRISON, P.H., Phys Fluids 28 (1985) 294

[6] RUTHERFORD, P.H., Phys Fluids 16 (1973) 1903

[7] IZZO, R., MONTICELLO, D.A., DeLUCIA, J., PARK, W., RYU, CM., Phys Fluids 28 (1985) 903

STUDIES OF THE TIGHT-ASPECT-RATIO TOKAMAK CONCEPT

T.C. Hender, P.S. Haynes, J.K. Holt, D.C. Robinson, A. Sykes, T.N. Todd

Culham Laboratory, Abingdon, Oxon. OX14 3DB, England
(Euratom/UKAEA Fusion Association)

INTRODUCTION

Tight aspect ratio tokamaks (i.e., having an aspect ratio A = R/a < 2) have received considerable attention in recent years [1]. The interest in such devices arises partly from the changes expected in the physics behaviour at tight aspect ratio, and partly from the possible advantages these, and the near-spherical topology, might give to a tight aspect ratio reactor.

In the next section we discuss some of the physics aspects of tight aspect ratio devices and then in the following section outline details of an experiment to test the tight aspect ratio (A $\sim$ 1.2) concept.

PHYSICS ASPECTS.

Equilibrium studies have demonstrated large increases in edge safety factor due to toroidicity and natural shaping effects, which enables large increases in plasma current whilst keeping $q_a > 2$. The tight aspect ratio also means that the ratio of toroidal field current to plasma current is considerably lower than in a conventional tokamak (A $\gtrsim$ 3, [2] which may obviate the need for superconducting coils in a reactor design. Other features of tight aspect ratio plasmas include enhanced ohmic heating due to increased neo-classical resistivity, the possibilities of significant bootstrap current and a large paramagnetic increase in toroidal field under certain conditions.

Stability studies for equilibria with A=1.2, an ellipticity of 2, and triangularity of 0.4, have confirmed that the limit from ballooning and low n modes, $\beta_c = 2.8\ I(MA)/a(m)B(T)$ [3] continues to apply (where B is the axial vacuum toroidal field). Figure 1 shows for example the β-limit to ballooning modes, calculated with the ERATO code [4] for pressure profiles of the form $P' = -a\psi - b\psi^2$ with $q_a \sim 12$ (here $\beta = 2\langle P\rangle/\langle B^2\rangle$). The ballooning stable cases in Fig. 1 are also stable to n = 1 modes, with no conducting wall.

An important consideration for potential tight aspect ratio reactor designs is the neutron damage suffered by the essentially unshielded

centre column, which is dependent upon the fraction of neutrons intercepted by it. A full 3D evaluation of this fraction has been made for a wide range of neutron emission profiles and plasma geometries, showing that the simple surface-area-ratio overstates this fraction by a factor of approximately 2. The profile of neutron fluence along the core has been evaluated and typically exhibits a midplane value approximately twice that at the ends.

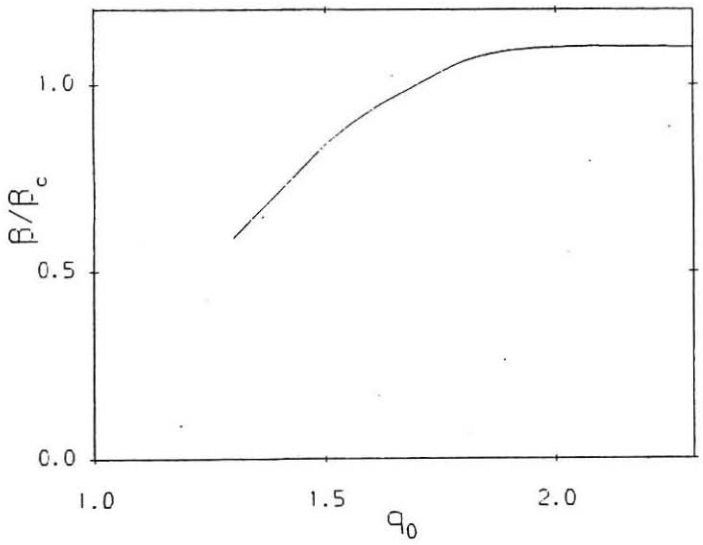

Fig 1 β-limit normalised to $\beta_c = 2.8Ia/B$ as function of central q for an equilibrium sequence with $q_a \sim 12$

SMALL SCALE EXPERIMENT

A Small Tight Aspect Ratio Tokamak (START) is being constructed at Culham. The objective of this experiment is to verify the MHD equilibrium and stability properties, with a plasma of central temperature > 200eV.

The envisaged aspect ratio of START, A = 1.2, means that inductive current drive becomes very difficult because of the required current densities in the central column solenoid. To avoid these problems a major radius compression, possibly combined with a minor radius decompression, will be used in START to achieve the tight aspect ratio. Figure 2 shows the projected compression sequence, together with details of the vacuum tank and coil locations. The 4 poloidal field (PF) coil currents are initially set to produce an approximate octupole null at R ∿ 0.65m. The current in the inner set of PF coils is then driven to zero thus inducing a plasma current of up to 60kA, while the current in the outer set provides the necessary vertical field for equilibrium. This plasma is then compressed to A = 1.2 by using the outer set of PF coils to increase the vertical field. By using this design no solenoid is required and the central column consists of just a single conductor (with a current density of ∿ 5 kA/cm²) acting as the return limb of the parallely connected TF coils. This design thus gives transient A = 1.2 plasmas, which should be sufficient to make an initial assessment of the properties of very tight aspect ratio tokamak plasmas with $q_\psi \gtrsim 3$. If these are realised then a minor upgrade would be to install a small solenoid to sustain the current flat-top at A = 1.2 for 10 → 20 ms.

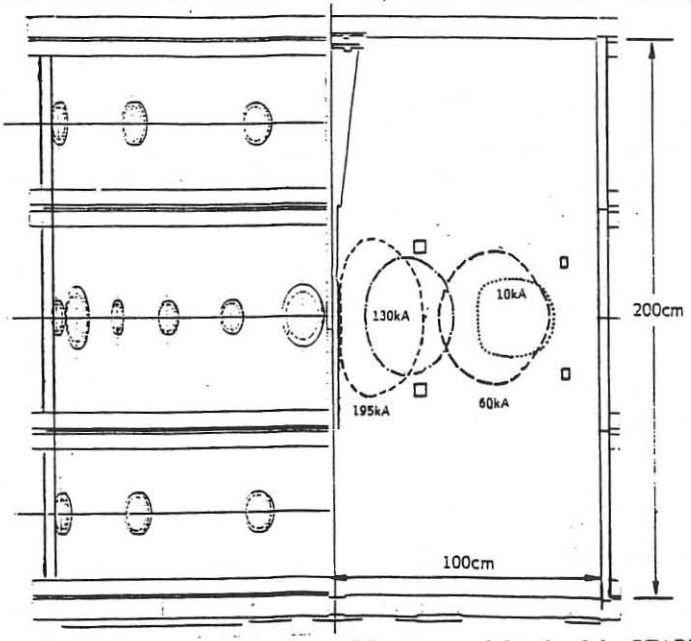

Fig 2 Equilibrium sequence showing coil locations and details of the START (formely TORSO) vacuum vessel

Preliminary transport studies have been performed for the pre-compressed and final plasma states in the START experiment. Using the simple INTOR transport model (with diffusion coefficient set to a value typical of small ohmic tokamaks) predicts central a electron temperatures of around 200 eV in the initial A = 3 plasma but over 1 keV in the final A = 1.2 plasma. This increase is partly due to the large current but also to a substantial increase of the ohmic heating power arising from increased neo-classical resistivity[5]. The INTOR model is an optimistic choice; other models predict worsening confinement at tight aspect ratio. Indeed the range of predictions for the 11 ITER scaling laws vary from 0.6ms (Merezhkin - Mukhovatov) to 2.7ms (Kaye-Goldston) for the final 200KA equilibrium, though there is a significant degree of uncertainty as the loop voltage varies between 2 and 6V depending on the neo-classical enhancement factor. This emphasises the lack of knowledge of the aspect ratio dependence with these scaling laws, and the importance of undertaking such an experiment. Should such an experiment operate at approximately half the density limit ($I/N = 10^{-14}$Am, N = nmab) then these confinement times indicate $\beta \sim 10\%$ should be obtained ohmically. If the full neo-classical resistivity enhancement is present then the critical β values can be reached.

CONCLUSIONS

The stability studies have shown the possibility of high-β at low aspect ratio and the transport studies have indicated beneficial heating and profile effects from neo-classical enhancements to the resistivity. To test this concept a small tight aspect ratio ($A \sim 1.2$) experiment (START) is being constructed. This experiment will use a major radius compression to achieve the tight aspect ratio and high β-values are predicted by even the most pessimistic confinement law.

ACKNOWLEDGEMENT

We are very grateful to M. Peng for useful comments and discussions.

REFERENCES

[1] E.A. Lazarus et al, Oak Ridge National Laboratory Report ORNL/TM - 9786 (1985).

[2] Y-K.M. Peng and D.J. Stickler, Nucl. Fusion 26 (86) 769.

[3] F. Troyon et al, Plasma Physics and Controlled Fusion 26 (84) 209.

[4] R. Gruber et al, Computational Physics Commun. 21 (1981) 323.

[5] M. R. O'Brien et al, this Conf. Paper P4 F6 4.

THE NATURE OF TURBULENT PARTICLE TRANSPORT IN TOROIDAL PLASMA CONFINEMENT

A. Thyagaraja and F. A. Haas

Culham Laboratory, Abingdon, Oxfordshire, OX14 3DB, U.K.
(Euratom/UKAEA Fusion Association)

INTRODUCTION

The purpose of this paper is to discuss certain general properties of turbulent plasma in toroidal (as opposed to open-ended) configurations. It is experimentally well-established that even under conditions when external sources and fields are maintained stationary, the particle and energy fluxes in pinches and tokamaks are anomalous. These anomalous fluxes are far larger in magnitude than those expected from classical or neoclassical theory and are thought to arise from plasma turbulence. Although the details of origins and scalings appropriate to such "anomalous transport" remain mysterious, it is our aim to show that certain very general statements regarding turbulent particle fluxes can be deduced from classical electrodynamics of charged particles. Previously, several authors (KROMMES and KIM (1988), TERRY et al (1986), and WALTZ (1982), for example) considered particular plasma models such as clump theory, to demonstrate flux constraints. In the present paper we show that turbulent particle fluxes are automatically ambipolar under much more general conditions. These results are classical analogues of unitarity and gauge invariance principles of quantum theory. In particular, they do not depend on the nature or (the as yet un-understood) origin of plasma turbulence. Any nonlinear theory of plasma turbulence must take proper account of these theorems. Thus they play a role analogous to sum rules based on unitarity in quantum theory and optics. They can also be seen to generalize the well-known ambipolarity results of neo-classical plasma theory (HIRSHMAN and SIGMAR (1981)), in the sense that the kinetic equations we discuss include those used in neo-classical theory as a special case. We also demonstrate the importance of compressibility and the role played by nonlinearities in turbulent particle transport. Specifically we show that if incompressibility of either electrons or ions is assumed the particle flux is significantly lower for a given fluctuation amplitude. In particular, non-linear interactions are needed to give a significant non-adiabatic correlation between density and potential fluctuations as observed (SCHOCH et al 1987).

PARTICLE TRANSPORT DUE TO ELECTROMAGNETIC TURBULENCE

We consider a pure, electron-ion plasma in a region R. The complete dynamical description of such a fully ionized system is given by the electromagnetic fields $\underline{E}(\underline{r},t)$, $\underline{B}(\underline{r},t)$ and the distribution functions $F_{e,i}(\underline{r},\underline{v},t)$. The sources of the Maxwell equations are the charge density $\rho(\underline{r},t)$ and the current density $\underline{j}(\underline{r},t)$. Whatever equations $F_{e,i}$ obey, we must always have the relations,

$$\rho(\underline{r},t) = Z_i e \int F_i d^3\underline{v} - e \int F_e d^3\underline{v} \tag{1}$$

$$\underline{j}(\underline{r},t) = Z_i e \int F_i \underline{v} d^3\underline{v} - e \int F_e \underline{v} d^3\underline{v} \tag{2}$$

$$\frac{\partial \rho}{\partial t} + \nabla . \underline{j} = 0 \tag{3}$$

If the turbulence is such that $\rho(\underline{r},t)$ is a bounded function (this is true for example in stationary tokamak turbulence), and we define the average,

$$< \underline{j}(\underline{r},t) > \equiv \lim_{T \to \infty} \int_o^T \underline{j}\, dt \tag{4}$$

Equation (3) shows that

$$\nabla . <\underline{j}> = 0 \tag{5}$$

Integrating over any closed (flux) surface $\Psi_o(\underline{r})$ (used by experimentalists and not intersecting material boundaries such as limiters) we get from (5),

$$< \int_{S\Psi_o} n_i \underline{v}_i . d\underline{\sigma} > = < \int_{S\Psi_o} n_e \underline{v}_e . d\underline{\sigma} > \tag{6}$$

where n_i, n_e, $\underline{v}_i$, $\underline{v}_e$ denote the usual moments of $F_{e,i}$. Equation (6) is an expression of the ambipolarity of the time-averaged turbulent particle fluxes evaluated over mean magnetic flux surfaces (or pressure surfaces). If the wave lengths and frequencies of the electromagnetic turbulence in the system are compatible with quasi-neutrality, we may set $\rho \simeq 0$ in Eq.(3). In this case, we get the instantaneous ambipoliarity result,

$$\int_{S\Psi_o} n\underline{v}_i . d\underline{\sigma} = \int_{S\Psi_o} n\underline{v}_e . d\underline{\sigma} \tag{7}$$

That these results are completely independent of the mechanisms of turbulence and the precise forms of the kinetic equations satisfied by $F_{e,i}$ is easily seen by the observation that any set of kinetic equations with particle conserving collision terms (they may otherwise be arbitrary) and consistent sources led to the charge conservation law (3). Thus, our proof of the ambipolarity of turbulent particle fluxes is completely general and depends either on stationarity of turbulence or quasi-neutrality. It is similar to the "automatic" ambipolarity theorems of neo-classical theory.

ROLE OF COMPRESSIBILITY AND NONLINEARITY

Consider quasi-neutral turbulence with mean magnetic surfaces Ψ_o such that $\underline{B}_o.\nabla\Psi_o = 0$. From the electron continuity equation

$$\frac{\partial n_e}{\partial t} + \nabla.n_e\underline{v}_e = S_e(\underline{r}) \tag{8}$$

$$\int_{S(\Psi_o)} <n_e\underline{v}_e>.d\underline{\sigma} = \int_v S_e(\underline{r})\ d^3\underline{r} \tag{9}$$

If $\underline{v}_e$ is assumed incompressible, we get the identity (assuming $\underline{v}_{oe}.\nabla\Psi_o = 0$; where, $n_e \equiv n_o(\Psi_o) + \tilde{n}_e$, $\underline{v}_e \equiv \underline{v}_{oe} + \tilde{\underline{v}}_e$ with $<\tilde{n}_e> = 0 = <\tilde{\underline{v}}_e>$)

$$\int_{S(\Psi_o)} <\tilde{n}_e\tilde{\underline{v}}_e>.\nabla n_o \left|\frac{ds}{\nabla\Psi_o}\right| = -\int_S \nabla.<\tilde{\underline{v}}_e \frac{\tilde{n}_e^2}{2}> \left|\frac{ds}{\nabla\Psi_o}\right| .$$

Thus, $$-\int_S \left|\frac{1}{\nabla n_o}\right| \nabla.<\tilde{\underline{v}}_e \frac{\tilde{n}_e^2}{2}> ds = \int_v S_e(\underline{r})\ d^3\underline{r} \tag{10}$$

This, and its ion counterpart show that for significant (second order in amplitude) transport to occur $\nabla.\underline{v}_e$, $\nabla.\underline{v}_i$ must not be zero (parallel electron motion, ion polarization drift). If they are vanishing non-linear effects are needed to get significant phase shifts between $\tilde{n}_e$ and $\nabla\tilde{\phi}$ (non-adiabaticity).

The results derived above are consequences of the equation of continuity (9) and are independent of the specific mechanisms of turbulence. They show clearly that assuming (for example)

$$\tilde{\underline{v}}_e = \frac{-c\ \nabla\phi \times \underline{B}_o}{B_o^2} \tag{11}$$

with $\underline{B}_o$ uniform cannot lead to non-zero particle transport and non-adiabaticity between $\tilde{n}_e$ and $\tilde{\phi}$. In this respect, statements in the literature (Mannheimer (1977)) can be misleading.

CONCLUSIONS

Particle transport in turbulent plasmas is constrained by certain sum rules which apply in the interior of toroidal confinement devices. Such constraints are manifestly independent of the mechanisms responsible for the turbulence but are consequences of continuity equations, quasi-neutrality etc. In general, energy and momentum fluxes need not be constrained in the same way by ambipolarity.

REFERENCES

HIRSHMAN, S.P. and SIGMAR, D.J. (1981) Nuclear Fusion, 21, p.1079.
KROMMES, J.A. and KIM, C.(1988) Phys. Fluids, Vol.31, No.4.
MANNHEIMER, W.M. (1977) An Introduction to trapped-particle instability in tokamaks. ERDA, TID-27157. Nat. Tech. Inf. Service, Springfield, Virginia, U.S.A. p.17.
SCHOCH, P.M. et al. (1987) Proc. 14th Euro.Conf. on Controlled Fusion, Madrid, 1, p.126.
TERRY, P.W., DIAMOND, P.H. and HAHM, T.S.(1986) Phys.Rev.Lett.57, 1899.
WALTZ, R.E.(1982) Phys. Fluids 2 (7), p.1269.

THE STOCHASTIC COLLISIONLESS DIFFUSION AND RADIAL ANTIDIFFUSION OF ALPHA PARTICLES IN TOKAMAK

K.GAC, A.GACEK

Institute of Plasma Physics and Laser Microfusion.
00-908 Radiowa, p.o.Box 49 Warsaw, POLAND.

One of the serious problem in Tokamaks is loss of fast particles. Among different kinds of losses the stochastic collisionless diffusion of bananas induced by TF ripple is more dangerous [1]. The fast particles diffusion strong depends on amplitude of ripple and may be used as a burn control method. There are some ways of reduction of the alphas losses. The first one is optimalizing of the plasma current profile and arising its amplitude. The another one is based on increase of number of the toroidal field coils. In this work a new method of reduction is proposed. This method is based on small modification of the TF coils [2] or on including additional poloidal current circuit [3].
For this magnetic curcit we can approximate B field in the form [2]:

$$B_\phi = \frac{B_o R_o}{R} + \delta_{\phi 1}(R,Z)\cos N\phi + \delta_{\phi 2}(R,Z)\cos\frac{N\phi}{2}$$

$$(1)\quad B_\theta = B_{\theta o}(R,Z) + \delta_{\theta 1}(R,Z)\sin N\phi + \delta_{\theta 2}(R,Z)\sin\frac{N\phi}{2}$$

$$B_r = B_{ro}(R,Z) + \delta_{r1}(R,Z)\sin N\phi + \delta_{r2}(R,Z)\sin\frac{N\phi}{2}$$

Where $B_{\theta o}$, B_{ro} is magnetic field of plasma current.
In tipical tokamak one can observes the normal ripple-induced stochastis banana diffusion [1,4]. In such modificated field (1) the opposite to diffusion effect exists. We have investigated a lot of fast alpha particles trajectories in guiding-center approximation for

$$(2)\quad \delta_{\phi 1} \sim A_1 + \frac{Z}{a},$$

$$\delta_{\phi 2} \sim A_2 - \frac{Z}{a}$$

(A_1, A_2 = const) using the Monte-Carlo code "DRIFT".
The small piece of alpha particle orbit in Tokamak is shown in Fig.1. The banana trajectory has been calculated without collisions. One can see evident collisionless diffusion of bananas outside the plasma. The radial antidiffusion effect for modificated field (1) is ilustrated in Fig.2. The banana orbit moves from outside to the plasma inside after several bounce times. Initial velocities and radiuses for alphas in Fig.1 and Fig.2 are the same.
An interesting phenomenon is shown in Fig.3 where free orbit converges to magnetic axis. The radial antidiffusion (compression) of the free and banana particles is generated by uncompensated vertical drift in special structure TF ripple [2], [3].

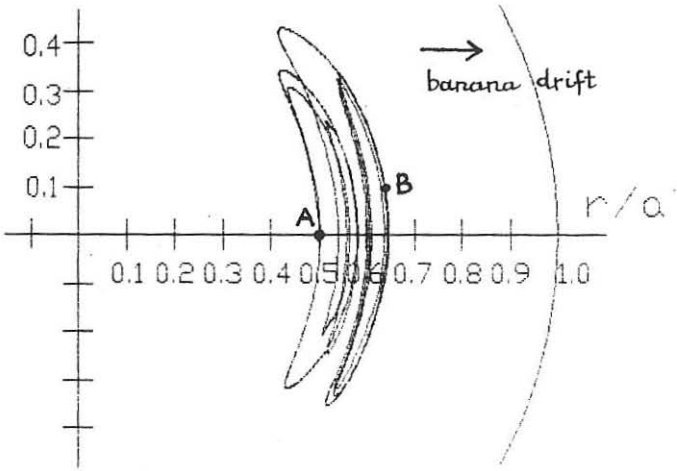

Fig.1. Trajectory of alpha particle in Tokamak. j_o=2.5 MA/m^2, a=2 m, R_o= 6.25 m. A - start point, B - alpha particle position alfer several bounce times.

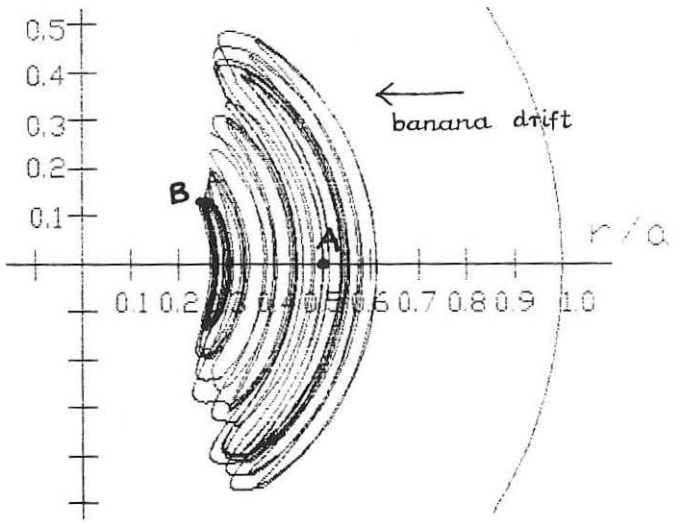

Fig.2. Trajectory of banana particle in modificated toroidal field (1) after several bounce times.

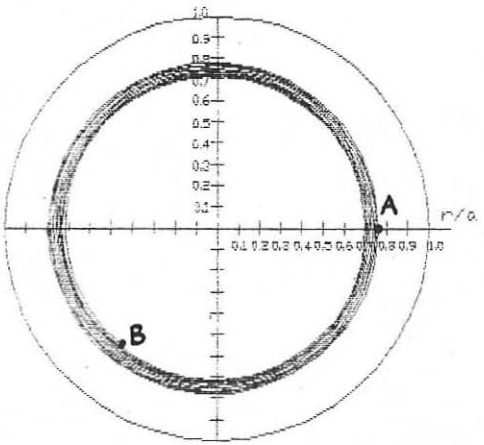

Fig.3. Trajecctory of free alpha particle in modificated B field (1) after several bounce times.

[1] R.B.White, H.E.Mynick. Alpha particle confinement in Tokamaks. Report PPPL - 2563 (November 1988)
[2] A.Gacek. The structure toroidal field for reduction of the stochastic collisionless diffusion of alpha particles. Report IPPLM. To be published
[3] A.Gacek. The concept of reduction of alpha particles losses by means additional poloidal field. IPPLM Report, to be published
[4] K.Tani, T.Takizuka, M.Azumi, M.Yamagiwa, Y.Kishimoto, K.Hamanatsu, J.J.Foit. Burn Control of Tokamak Plasma by Toroidal Field Ripple, 12th Int.Conf. on Plasma Physics and Controlled Nuclear Fusion Research Nice, France 12-19.Oct. 1988

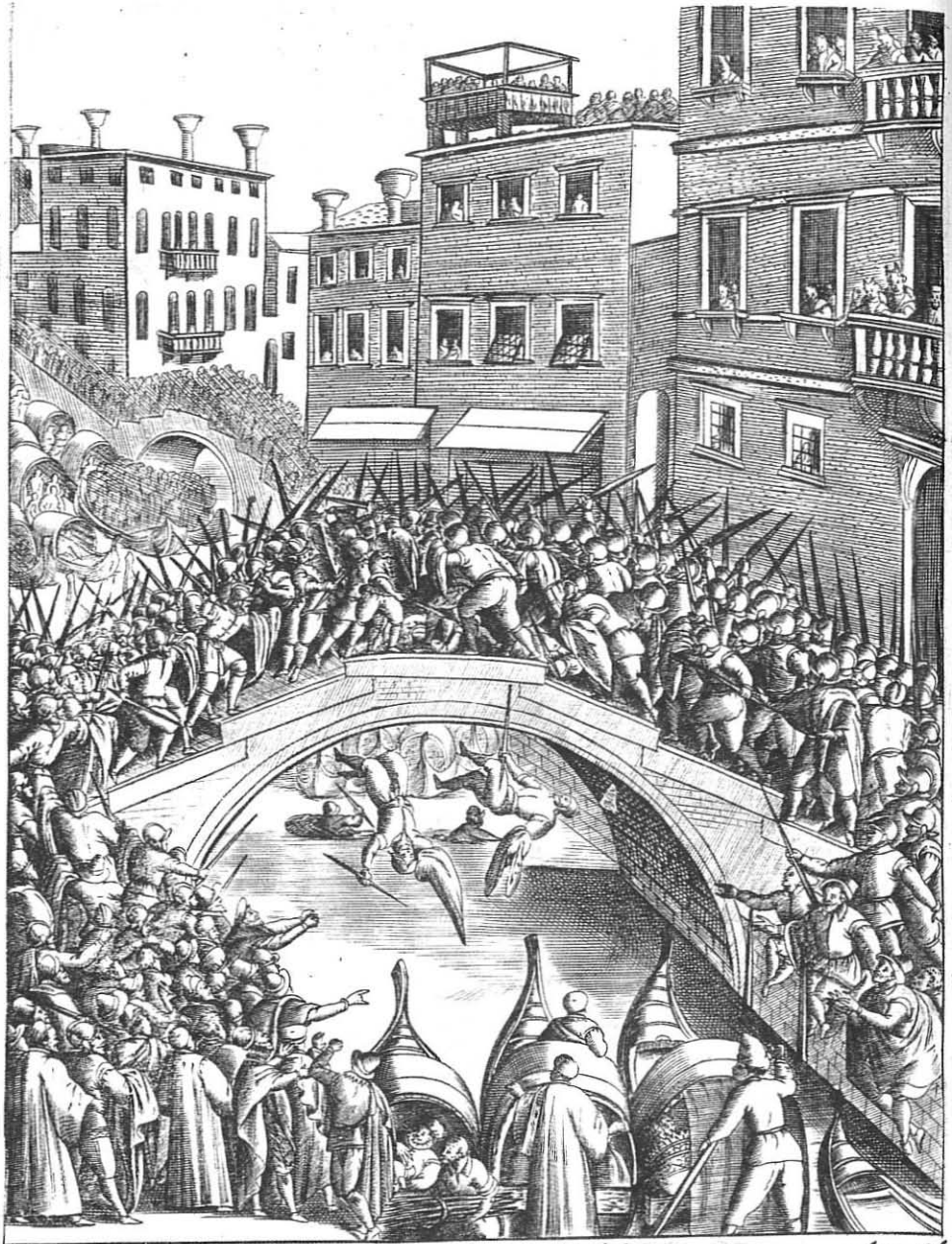

Per antico essercitio del popolo fu introdotto p decreto pub.co che l'inuerno si facesse p i ponti di Ven.a la battagliola combattendosi l'auantaggio del ponte co legni et l'una delle parti si chiama Castellana et l'altra Nicolotta

Giacomo Franco Forma con Priuilegio

THE EVOLUTION OF RESISTIVE BALLOONING MODES IN THE Banana Plateau Collisionality Regime

A.K.Sundaram and J.D.Callen[+]

Institute for Plasma Research, Bhat, India 382424

[+]University of Wisconsin, Madison, WI, 53706-1687, USA

Recently, it has been well recognized that a simple MHD description of resistive modes in a plasma is inadequate since current tokamaks operate in a high temperature regime wherein the electron mean free path much exceeds a typical connection length. For this regime, trapped particle effects and contributions from the bootstrap, the enhanced ion polarization and the Ware-pinch type currents become important. Keeping the above effects in mind, a new set of neoclassical MHD equations has been derived in the literature.[1] In this paper, we re-examine the evolution of resistive ballooning modes in the banana-plateau collisionality regimes employing the neoclassical fluid approach and show that there exists a smooth transition from Pfirsch-Schluter regime to neoclassical regimes.

We consider an axisymmetric tokamak equilibrium in which we define $\vec{B}_o = I\nabla\zeta + \nabla\zeta \times \nabla\Psi$, where Ψ,θ and ζ are the flux surface coordinates representing the poloidal flux within the magnetic surface, the poloidal angle-like variable and the toroidal angle, respectively. In the neoclassical equilibrium, we consider the presence of a finite electric field, $E_{\parallel}^{A}$ induced due to Ohmic heating transformer and a poloidal flow of electrons, besides diamagnetic drifts. The basic set of two fluid equations governing the resistive ballooning mode dynamics in the neoclassical regime is

$$\vec{v}\cdot = \frac{c}{B^2}\vec{B}\times[\nabla F + \frac{mc}{eB^2}\frac{d}{dt}(\vec{B}\times\nabla F)] - \frac{mc^2}{eB^2}I^2J\frac{d}{dt}(\frac{\partial F}{\partial\Psi})\nabla\theta\times\nabla\zeta \qquad (1)$$

$$\vec{J}_{\perp} = \frac{c}{B^2}\vec{B}\times[\nabla P + \nabla\cdot\overleftrightarrow{\pi}_{\parallel i} + \frac{\varrho_m c^2}{B^2}\frac{d}{dt}\vec{B}\times\nabla F_i] - \frac{\varrho_m c^2 I^2 J}{B^2}\frac{d}{dt}(\frac{\partial F_i}{\partial\Psi})(\nabla\theta\times\nabla\zeta)$$

$$+ \frac{CIJ}{B}(\vec{b}\cdot\nabla P)\nabla\theta\times\nabla\zeta, \qquad (2)$$

$$\frac{\partial n}{\partial t} + \nabla\cdot(n\vec{v}_{\perp e}) + \frac{\vec{B}\cdot\nabla}{B}[nv_{\parallel i} - \frac{J_{\parallel}}{en}] = 0, \frac{\partial n}{\partial t} + \nabla\cdot(n\vec{v}_{\perp i}) + \frac{\vec{B}\cdot\nabla}{B}(nv_{\parallel i}) = 0, \qquad (3)$$

$$-enBE_{\parallel} - (\vec{B}\cdot\nabla)P_e - \vec{B}\cdot\nabla\cdot\overleftrightarrow{\pi}_{\parallel e} + \vec{B}\cdot\vec{R} = 0, \qquad (4)$$

$$\varrho_m B\frac{dv_{\parallel i}}{dt} = -(\vec{B}\cdot\nabla)P - \vec{B}\cdot\nabla\cdot\overleftrightarrow{\pi}_{\parallel i}, \qquad (5)$$

where $F = \phi + \frac{T}{e}\ln n$, $\rho_m = m_i n, n_i = n_e = n$, $P = n(T_i + T_e)$, $\vec{R} = en_o(\vec{J}_\perp/\sigma_\perp + J_\parallel \vec{b}/\sigma_\parallel)$, $\vec{b} = \vec{B}/|B|$, $\sigma_\parallel \alpha_e = \sigma_\perp = ne^2/m_e \nu_e$ ($\alpha_e = 0.51$) and $\eta_\parallel = (P_\parallel - P_\perp)(\vec{bb} - I/3)$, $P_\parallel - P_\perp = -mn\mu < B^2 > \vec{v}.\nabla \ln B/ < (\vec{b}.\nabla B)^2 >$. Other symbols have their usual meanings. In Eqs.(1) and (2), the new features are the presence of enhanced ion polarization effect (namely, the $\partial F/\partial \Psi$ term) and the pinch-type current ($\vec{b}.\nabla P$) term. Eqs. (1) to (5) together with Maxwell's equations will therefore constitute the basic set for studying the evolution of resistive ballooning modes in the neoclassical regime.

In order to study the linear stability characteristics of resistive ballooning mode, we follow the standard procedure[2] and seek ballooning mode representation, $Q \sim \Sigma_\ell\, Q(\theta + 2\ell\pi, t)\, \exp\{in\, S(\Psi, \theta, \zeta)\}$, where $S = \zeta - \int_o^\theta (IJ/R^2)\, d\theta'$ is the eikonal, I is the toroidal current and J is the Jacobian. We then adopt the multiple length scale analysis and perform the poloidal flux surface averaging to derive the ballooning mode equation in inner and outer layers defined respectively by $z << 1$ and $z >> z_r >> 1$, where $z = s\theta$, s being the shear parameter and $z_r = (\omega_{pe}/k_\theta c)(\omega/\nu_e)^{1/2}$ is the resistive layer thickness. To simplify the algebra, we consider the limit $s\omega_{bi} < \omega < \omega_{bi}$, where ω_{bi} is the ion bounce frequency. Further we consider the evolution of fast resistive ballooning modes typified by $|\omega| >> c_s/qR_o$, where c_s is the sound speed and qR_o is the connection length. With these approximations, the poloidal flux surface averaged equation for the potential, $\bar{\phi}$, valid within the resistive layer can be written as

$$A\frac{d^2\bar{\phi}}{dz^2} + Bz\frac{d\bar{\phi}}{dz} + (cz + D)\,\bar{\phi} = 0, \tag{6}$$

where the expressions for A, B, C and D are defined by the relations

$$A = (\omega_{pe}/k_\theta c)^2 (\omega_1 - \omega_{*e})/(\nu_e - \mu_e)$$

$$B = -i\alpha R_o/2rs + (s/k_\theta r)(\Omega_i \omega_1/\omega_A^2)[\mu_e/(\nu_e - \mu_e)]\,[(\mu_i/3 - i\omega_1)/(\omega_1 + i\mu_i)$$

$$-i(\omega_{*e}/\omega_1)\{1 + (4|L_n|/3r) + (i\mu_i)(1/3 + \frac{1+\tau}{\tau^2})/(\omega_1 + i\mu_i)\}]$$

$$-\frac{1}{6}\frac{B_o^2}{B_\theta^2}\frac{\beta}{s}\frac{r}{|L_n|}\left(\frac{\mu_i}{\omega_1 + i\mu_i}\right)$$

$$C = \frac{B_o^2}{B_\theta^2}\left[\frac{\omega - \omega_{*i}}{\omega_A^2}\{\mu_i + i\omega_1(1 + \frac{B_\theta^2}{B_o^2})\} - \frac{1}{3}\frac{\omega_1 - \omega_{*i}}{\omega_1 + i\mu_i}\frac{(1+\tau]/\tau}{}\right.$$

$$D = \frac{i\alpha}{2s}\left(\frac{\alpha}{s} - \frac{R_o}{r}\right) - \frac{i\mu_e}{\nu_e - \mu_e}\frac{s}{k_\theta r}\frac{\Omega_i \omega_1}{\omega_A^2}\left[\frac{\omega_1}{\omega_1 + i\mu_i} + \frac{|\omega_{*e}|}{\omega_1}\{1 + \frac{4}{3}\frac{|L_n|}{r} + \frac{i\mu_i}{\omega_1 + i\mu_i}\frac{1+\tau}{\tau^2}\}\right] \tag{7}$$

In the above expressions, ω_* denotes the diamagnetic drift, $\mu_{i,e}$ is the ion/electron viscosity, $\tau = T_e/T_i$, $\omega_A = sv_A/qR_o$, $s = \Psi' d\ln q/d\Psi$, $L^{-1} = \Psi' d\ln n_o/d\Psi$, $\beta = 8\pi p_o/B_o^2$, $v_A = B_o/\sqrt{4\pi n_o m_i}$, $\alpha = -8\pi q^2 R_o p_o'/B_o^2$ and $\omega_1 = \omega + \omega_E$, ω_E being the neoclassical equilibrium drift. In the expressions (7), important neoclassical effects such as perfurbed bootstrap current, the pinch-type current and the enhanced ion polarization current, respectively enter through the terms connected with μ_e, $R_o\alpha/rs$ and $(1 + B_\theta^2/B_o^2)$. The terms proportional to $(\omega_1 + i\mu_i)^{-1}$ represent contributions from parallel ion motion.

The general dispersion relation in the neoclassical regime can easily be derived from Eq.(6) for different mode frequencies in the parameter space. In what follows, we choose a particular case in which $\mu_i > |\omega_1| > \omega_*$. In this limit, the dispersion relation yields a localized ballooning mode with growth rate, $\gamma \propto v_A |d\ln p_o/dr| (k_\theta c/\omega_{pe}) [(\nu_e - \mu_e)^{1/2}/\mu_i^{1/2}] (\beta q^2 \eta - 1)^{1/2} (\beta q^2 \eta - \frac{1}{3})^{1/2}$, where $\eta = |d\ln p_o/d\ln q|$ and $\beta q^2 \eta > 1$. The localization of this mode occurs in the close proximity of the magnetic axis. Far away from the magnetic axis, the growth rate expression for the localized mode becomes significantly modified. Thus, it turns out that γ becomes proportinal to

$$\omega_A (\mu_i/\mu_e)^{1/2} [\nu_e - \mu_e)^{1/2}/(\hat{\omega}_i)^{1/2}] (\beta\eta)^{1/2} (B_o/B_\theta).$$

Thus, we have demonstrated that a new class of localized resistive ballooning modes in the long mean free path regime is excited with growth rates dependent on pressure gradient and viscous forces. In the relevant frequency regime, $\mu_i > |\omega_1| > \omega_*$, we find that the evolution of resistive modes are purely controlled by effects associated with the perturbed bootstrap current, the enhanced ion polarization and pinch-type currents. It may be mentioned that the evolution of resistive ballooning mode becomes significantly modified when mode-width in z-space has a broad/spatial extent. These cases have not been explored in this text. Further, in arriving at the above results severe restrictions on the mode frequency regimes have been placed and the linear coupling of trapped particle modes with the ballooning modes has been omitted. These effects become important in a realistic situation and they will be investigated in detail. Pertinently it may be remarked that our calculations may be important to ISX-B experiments in explaining the degradation in electron energy confinement. With ISX-B parameters, the computed growth time of m=1 type mode turns out to be ten milliseconds while m=2 type mode or Δ' driven mode will be expected to give larger growth rates than m=1 type modes. The calculations for the m=2 type mode are currently under investigation and will be presented later. Finally it may be stated this work establishes smooth transition of the resistive ballooning mode characteristics from a classical to the neoclassical regime. In other words, the classical growth rate for the resistive ballooning mode can easily be recovered from the present analysis by setting the parameters of neoclassical regime to zero.

1. Callen, J.D. and Shaing, K.C. Phys. Fluids, 28 (1985) 1845; Callen, J.D., Qu, W.X., Siebert, K.D., Carreras, B.A., Shaing, K.C. and Spong, D.A. in Plasma Physics and Controlled Nuclear Fusion Research 1986 (IAEA, Vienna 1987) Vol.II, 157.

2. Lortz, D. and Nuhrenberg, J., Phys. Lett. 68A (1978) 49; Nucl. Fusion 19 (1979) 1207; Hazeltime, R.D. and Meiss, J.D. Phys. Reports 121 (1985) 1.

THE STABILITY OF IDEAL AND RESISTIVE BALLOONING MODES in the Presence of Equilibrium Flows

A.K.Sundaram and A.Sen

Institute for Plasma Research, Bhat, India 382424

Ideal and resistive ballooning modes have been the topic of extensive study in view of their important role in constraining plasma β or in causing degradation in electron energy confinement time. Much of these works in the literature have been done for static equilibrium. Recently several experiments on ISX, PDX and currently on TFTR and JET have demonstrated the presence of toroidal and poloidal flows due to asymmetry in the neutral beam injection (NBI). Also equilibrium flows can arise through diffusive processes in tokamak plasmas. Such flows induced by external sources or dissipative processes affect the form and location of the magnetic surfaces and also modify the density and pressure profiles in the equilibrium. In this paper, we therefore examine the effect of mass flows on the evolution of high (m,n) ideal and resistive ballooning modes using the simplified MHD equations.

In the axisymmetric tokamak equilibrium, we define $\vec{B}_o = I\nabla\zeta + \Psi'\nabla\zeta\times\nabla r$, where Ψ is the poloidal flux surface and r,θ and ζ are the Shafranov coordinates. In considering the stability of ideal ballooning modes, we assume that the plasma rotates rigidly about the axis of symmetry and incorporate the effect of centrifugal forces in Grad-Shafranov equation. In case of resistive ballooning modes, we take into consideration parallel and perpendicular flows caused by external sources (such as NBI or current drive) and diffusive processes. We assume that the perpendicular flows arise mainly from diffusive processes. The linearized equations for both ideal and resistive ballooning modes may be written in the form

$$
\begin{aligned}
&-\frac{(\vec{B}_o\cdot\nabla)}{B_o}\nabla^2 A_{\parallel} + \{4\pi\nabla p_1 + 4\pi\rho_o(\frac{\partial\vec{V}_1}{\partial t} + \vec{F})\}\cdot\nabla\times\frac{\vec{B}_o}{B_o^2} \\
&+ (\frac{\partial\vec{V}_1}{\partial t} + \vec{F})\cdot\frac{4\pi\nabla\rho_o\times\vec{B}_o}{B_o^2} - \frac{\vec{B}_o}{V_A^2}\cdot\nabla\times(\frac{\partial\vec{V}_1}{\partial t} + \vec{F}) \\
&+ 4\pi\rho_1\{(\nabla\times\frac{\vec{B}_o}{B_o^2})\cdot(\vec{V}_o\cdot\nabla)\vec{V}_o - \frac{\vec{B}_o}{B_o^2}\cdot\nabla\times(\vec{V}_o\cdot\nabla)\vec{V}_o\} + \{4\pi\nabla\rho_1\cdot\frac{\vec{B}_o}{B_o^2}\times \\
&(\vec{V}_o\cdot\nabla)\vec{V}_o\} + \frac{4\pi}{C}\vec{b}\times\nabla(J_{o\parallel}/B_o)\cdot\nabla A_{\parallel} = 0, \qquad \ldots \qquad (1)
\end{aligned}
$$

$$\vec{V}_{1\perp} = \frac{C}{B_o}\vec{b} \times \nabla\phi + \frac{V_{o\parallel}}{B_o}\nabla A_\parallel \times \vec{b}, \; - \nabla_\parallel \phi + \frac{V_{o\parallel}}{C}\nabla_\parallel A_\parallel - \frac{1}{C}\frac{\partial A_\parallel}{\partial t} - \left(\frac{\vec{V}_o \cdot \nabla}{C}\right) A_\parallel =$$

$$- (\eta C/4\pi)\, \nabla_\perp^2 A_\parallel, \qquad \ldots \quad (2)$$

$$\frac{\partial \rho_1}{\partial t} + V_{o\parallel}(\vec{b}.\nabla)\rho_1 + (\vec{V}_{o\perp}.\nabla)\rho_1 + \vec{V}_{1\perp}.\nabla\rho_o + \rho_1 \nabla.\vec{V}_o + \rho_o \nabla_\parallel V_\parallel = 0, \qquad (3)$$

$$\rho_o \left(\frac{\partial V_\parallel}{\partial t} + \vec{F}.\vec{b}\right) + \rho_1 \vec{b}.(\vec{V}_o.\nabla)\vec{V}_o = -(\vec{b}.\nabla p_1) - (\vec{B}.\nabla p_o)/B_o, \qquad (4)$$

where $p_1 = \rho_1 C_s^2$, $\vec{B} = \nabla A_\parallel \times \vec{b}$, $\vec{F} = (\vec{V}_o.\nabla)\vec{V}_1 + (\vec{V}_1.\nabla)\vec{V}_o$, $\vec{V}_o = V_{o\parallel}\vec{b} + \vec{V}_{o\perp}$, $V_{o\parallel} = \vec{V}_o.\vec{b}$, $V_\parallel = \vec{V}_1.\vec{b}$ and η is the Spitzer's resistivity. Other symbols have their usual meanings. Eq.(1) represents the $\nabla.J = 0$ condition while Eqs. (3) and (4) respectively denote the continuity and the parallel memontum balance equations. Ohm's law is described in Eqs.(2).

For ideal ballooning modes, setting $\eta = 0$, $V_{o\perp} = 0$ and $V_{o\parallel} = V_{o\zeta} = \Omega R$ where Ω is the uniform angular frequency of toroidal rotation and following the standard procedure outlined in Ref.1, the ballooning mode equation at marginal stability after some lengthy algebra reduces to

$$\frac{d}{d\theta}\left[1 + \left(s\theta - \alpha\sin\theta - \frac{\alpha\delta}{2}\sin 2\theta\right)^2\right]\frac{d\phi}{d\theta} + \alpha\,(1 + \delta\cos\theta)\left[\cos\theta + \sin\theta\,(s\theta\right.$$

$$\left. - \alpha\sin\theta - \frac{\alpha\delta}{2}\sin 2\theta\right]\phi = 0, \qquad (5)$$

where $s = d\ln q/d\ln r$ is the shear parameter, $\alpha = -\beta q^2 \Psi'(d\ln \bar{p}_o/d\Psi)\exp(\Omega^2 R_0^2/C_s^2)$, $\delta = \Omega^2 R_o (r - L_p)/C_s^2$, $L_p = d\ln P_o/dr$ and $P_o = \bar{P}_o(\Psi)\exp(\Omega^2 R^2/2C_s^2)$. In writing down the model equation (5) at marginal stability, the constraint conditions derived in Ref.2 for stationary equilibria have been assumed to be valid. The toroidal rotation of plasma introduces two major modifications in Eq.(5). Firstly, the $\alpha\delta \sin 2\theta$ term arises from the equilibrium modifications in the shape of the magnetic flux surface, namely ellipticity effects and is associated with the poloidal asymmetry in the equilibrium pressure. Secondly the $\delta\cos\theta$ term depicts the usual centrifugal force effect which causes destabilization of the ballooning mode. We have solved Eq.(5) numerically to determine the marginal stability boundary in the parametric space (s,α). For $\delta > 0$, we show that the instability zone is enhanced while for $\delta < 0$ (that is, $r < L_p$) the marginal stability boundaries in (s,α) diagram move away from the origin and thus provides a stable access to second stability regime. Therefore we conclude that ideal ballooning modes remain stable in the inner regions of a tokamak plama ($r < L_p$) and become destabilized at the plasma edge regions ($r > L_p$).

We consider now the evolution of resistive ballooning modes. Retaining the effects of resistivity and general equilibrium flows in the parallel and perpendicular directions, the eigen value equation can be

derived from Eqs.(1) to (4). In what follows, we investigate a special case when $\omega_1 >> \Omega, c_s/qR$. In this limit, the poloidal flux surface averaged equation in the resistive layer reduces to a second order differential equation in ϕ, namely,

$$\Lambda \frac{d}{dz}\left[z^2/(\Lambda + i\nu z^2)\right] \frac{d\phi}{dz} + (i\Lambda\mu s/q)\, z \frac{d\phi}{dz} + \{-(\frac{\alpha^2}{s^2} + \frac{\beta q^2}{s^2}\Delta)$$

$$+ (\mu/q)^2 (l_p + 2\alpha\varepsilon\Delta) + (i\Lambda\mu/q) + z\,[(i\Lambda\mu s/q) + \mu\nu l_I (l_p$$

$$+ 2\alpha\varepsilon\Delta)/qm^2] + z^2\,[\Lambda^2 - \Delta(\beta q^2/s^2 + \alpha\varepsilon\mu^2/q^2)$$

$$+ i\nu\Lambda l_I (1 - l_p - \varepsilon\Omega^2 R_o^2 \alpha^2/s^2)/m^2]\} \phi = 0, \qquad (6)$$

where $\Lambda = (\omega_1/\omega_A)$, $\omega_A = sv_A/qR$, $\omega_1 = \omega - (\eta c^2 k_\theta^2/4\pi m)\, zl_I$, $\nu = \eta c^2 k_\theta^2/4\pi\omega_A$, $z = s\theta$, $\mu = \Omega/\omega_A$, $\Delta = 1 + \Omega^2 R_o^2/c_s^2$, $m = k_\theta r$, $l_p = |d\ln \bar{p}_o/d\ln r|$ and $l_I = (d\ln I/d\ln r)$. As in the previous case, we have set $v_{o\parallel} = v_{o\zeta}$ for the sake of simplicity. For the resistive ballooning mode, the new effects due to equilibrium flows come from terms connected with μ and l_I. Solutions of equation (6) can be derived in a general case by employing asymptotic matching method or the variational principles. In case of pure toroidal rotation, we find that the resistive ballooning modes remain unstable with enhanced growth rates varying as $\nu^{1/3}$. Similarly the combined effects of both toroidal and radial flows lead to enhancement in the growth rate of the resistive modes.

In summary, we have shown that pure toroidal rotation provides stable access to second stability regime while the same effect gives a new pressure-gradient driven resistive mode even in the absence of normal driving term, namely (α/s). Further detailed analysis of Eq.(6) is in progress.

References

1. Hazeltine, R.D. and Meiss, J.D., Phys. Reports 121 (1985) 1.
2. Laval, G., Pellat, R., Cotsaftis, M., Trocheris, M., Nucl. Fusion 4 (1964) 25.

SHEAR AND CURRENT DENSITY EFFECT ON TOKAMAK KINK MODE INSTABILITY

Degtyarev L.M., Medvedev S.Yu.
Keldysh Institute of Applied Mathematics, Moscow, USSR

1. An effect of profiles in a plasma on stability of external kink modes is a serious problem arising in determining the β limits in tokamaks. As it is known from an analysis of stability of 1D cylindrical plasma and from numeruos calculations of stability of 2D toroidal plasma, this effect is essencial. We may note, in particular, a stabilizing role of shear [1,2]. However, a role of profiles in determining the stability boundaries of a toroidal plasma yet remains to be revealed.

The profile effect on stability of small scale ballooning modes is a simpler problem. There is a procedure for finding the pressure gradient limits in the stability of ballooning modes at the given profile of safety factor $q(\psi)$; an influence of magnetic surfaces geometry and shear has also been determined. Besides, scalings for β limits, well justified theoretically and numerically, have been obtained [2,3].

As to the scaling for β limits in stability of all ideal modes, the region of its applicability is still uncertain when geometry and profiles are changed. Under such changes the stability of external kink modes is a main source of uncertainty.

2. Ideal MHD β limits are computed by using the following two-step procedure. Equilibrium plasma boundary is prescribed by

$$R = R_0 + a\,\mathrm{Cos}(\theta + \delta\,\mathrm{Sin}\theta),$$
$$Z = a\,\varkappa\,\mathrm{Sin}\theta, \qquad 0 \le \theta < 2\pi, \qquad (1)$$
$$A = R_0/a = 3,\ \varkappa = 2,\ \delta = 0.4.$$

The safety factor profile is determined from the force-free equilibrium (β=0) with given density of toroidal current:

$$R\,j_\phi = (1 - \psi^{j_1})^{j_2}, \qquad (2)$$

where ψ is the normalized poloidal flux (ψ=0 on the magnetic axis, ψ=1 at the plasma boundary). When optimizing the pressure gradient profile $dp/d\psi$ we proceed from the $dp^{\infty}/d\psi$ limits stable against ballooning modes. At the second step of optimization we stabilize external kink modes (the toroidal wave number n=1, conducting wall at infinity) by decreasing $dp/d\psi$ in external plasma layers.

The optimization results at the given value of $q(\psi)$ on the

magnetic axis q_0=1.1 are presented in Fig.1. The limiting β values for fixed j_2=1 and j_2=2 are shown when the value of $q(\psi)$ at the boundary q_s and the normalized current $I_N=\mu_0 I/aB_0$ are varied with j_1 in formula (2). The circles mark the $\beta=\beta^\infty$ limits in ballooning modes. The solid lines connect $\beta=\beta^c$ - the results of the second optimization step. We note a decreasing ravine in the curve $\beta^c(I_N)$ for $q_s<3$ as the shear grows at the boundary (an increase in j_2). This increase in β^c is not connected with decreased density of longitudinal current at the boundary (cf. Figs 2a and 2b). Moreover, in the case of larger shear the values of β^c and β^∞ coincide for the most of q_s-values while the current density does not vanish at the plasma boundary. Computations with a different kind of second optimization step yield a clear sensitivity of β limits to the current density profile at lower shear. In this case the β limits against external kink mode stability are determined from series of equilibria with the $dp/d\psi$ profiles decreasing from the magnetic axis as compared with $dp^\infty/d\psi$, and with non-zero current density at the boundary. In this series of computations with j_2=1 the β limits are lower than β^c (dotted vs solid lines in Fig.1). It becomes noticeable at low values of $q_s<3$, especially in the instability gap when $q_s\simeq 2.9$. For j_2=2 (larger shear) and $q_s\simeq 2.9$ the difference between β limits in the both series of profiles is not great. Thus, the sensitivity of β limits in stability of external kink modes to the pressure and current profiles at the boundary reduces as the boundary shear increases.

The computations for q_0=0.9 (Fig.3) confirm the same conclusion. In this case the standard second optimization step does not yield an optimal profile. It is connected with the necessity to stabilize the internal mode m=1, n=1, which requires $dp/d\psi=0$ within the surface q=1. Therefore the slightly cut-off from the boundary profiles $dp^\infty/d\psi$ are then cut off from the magnetic axis (Fig.4). The ravines in the $\beta^c(I_N)$ with q_0=0.9 are small at both j_2=2 and j_2=1. Specifically, β^c grows as q_0 decreases from 1.1 to 0.9 when $q_s\simeq 2.9$ and j_2=1. This behavior of β^c may be explained by increasing shear at the boundary as q_0 decreases at fixed q_s and j_2. As is noted above, it leads to lower sensitivity of external kink modes to j_ϕ value at the boundary.

Another peculiarity of equilibria with q_0=0.9 is instability at β=0 for q_s close to 2 (Fig.3, j_2=2). This weak free boundary instability is generated by the toroidal coupling between external

kink mode and internal mode m=1. As shear grows the coupling leads to destabilization.

3. Influence of the pressure and current density profiles on the stability of external kink modes may be summarized in the following way: the sensitivity of β limits to this influence reduces when

(a) the shear grows at the plasma boundary;

(b) the safety factor at the boundary is slightly larger than the rational resonant values (q_s>2,3,4... at n=1). Boundary shear requirements become less stringent in this case. The opposite situation occurs when q_s gets into instability gap (q_s<2,3,4...).

(c) the q_s value increases. For low values of q_s<3 the shear and profile requirements to obtain β limits are more stringent.

It should be noted that the above considerations are valid in the case when the pressure gradients do not exceed the ballooning mode $dp^{\infty}/d\psi$ limit in the first stability zone. In particular, $dp/d\psi$ values are low in low-shear region. Large pressure gradients in this region, which are possible at partial transfer into the second stability zone, are unfavourable for the stability of both external kink and internal modes (infernal modes).

The shear influence on scalings for β and current limits is not restricted by the profile sensitivity of kink mode stability. The vast low-shear region near the magnetic axis together with large shear at the boundary lead to saturation of the ballooning mode β^{∞} limit with growing plasma current. Moreover, such a distribution of shear intensifies the destabilization due to mode coupling which results in force-free equilibria instability (β^{c}=0). The destabilization shows at low q_s, it is especially strong when q_0<1. Such scaling variations with increasing elongation and decreasing aspect ratio [4,5] may be due to growing shear at fixed current density.

References

[1] Todd A.M.M. et al.-Nucl. Fusion, 1979, v.19, p.743

[2] Degtyarev L.M. et al.-Fizika Plazmy, 1985, v.11, p.1299

[3] Sykes A. et al.-In: Proc. 11th Europ. Conf. Contr. Fusion and Plasma Phys., Aachen, 1983, v.2, p.363

[4] Degtyarev L.M. et al.-In: Proc. 14th Europ. Conf. Contr. Fusion and Plasma Phys., Madrid, 1987, v.3, p.1133

[5] Bespoludennov S.G. et al.-Fizika Plazmy, 1986, v.12, p.771

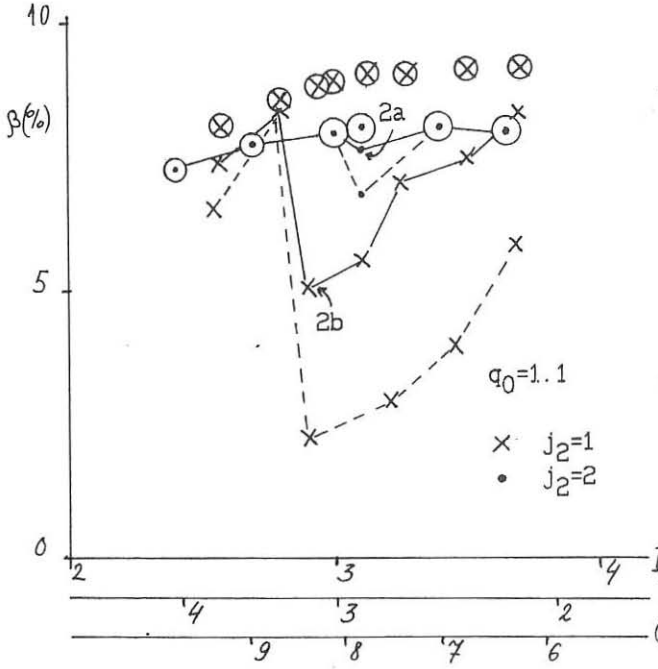

Fig. 1

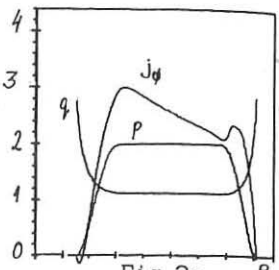

Fig. 2a

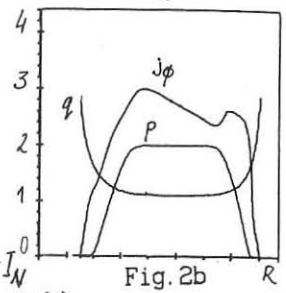

Fig. 2b

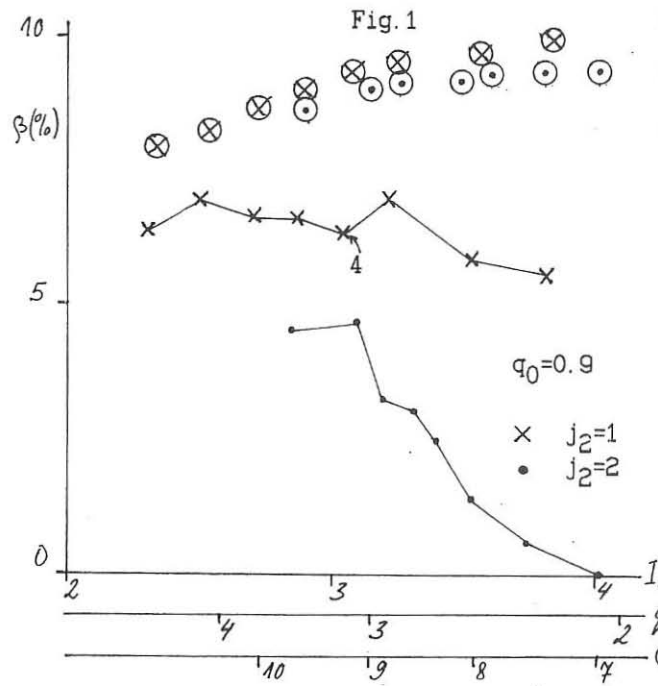

Fig. 3

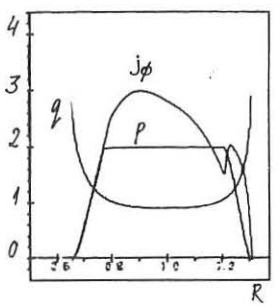

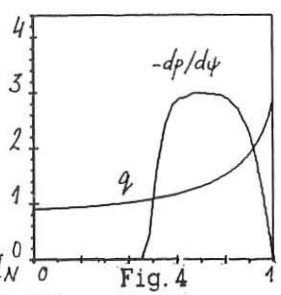

Fig. 4

THE BEHAVIOUR OF A PLASMA WITH POLOIDAL FLOWS IN TOKAMAKS

Computational problems connected with the bifurcating solutions to static and extended Grad-Shafranov-Schlüter equations (with stationary flows)

R. Zelazny, R. Stankiewicz, S. Potempski

RCC CYFRONET, The Institute of Atomic Energy
05-400 Otwock-Swierk, Poland

After a rich and long series of spectacular experimental and theoretical achievements, the present status of tokamak research encounters many challenging problems which cannot be explained satisfactorily within the framework of contemporary theory. First of all, the efforts to explain the sawtooth oscillations after seemingly initial successes connected with the ideas of Kadomtsev and quasi-interchange concepts, failed to resolve the observed complexity of those phenomena. The present state of affairs is called dramatically, a mystery /1/.

Also the additional heating has produced some unexpected results, as for example, the deterioration of the confinement time and discrepancies between the neoclassical (collisional) theory and the observed rate of momentum transfer /2-6/. On the other hand, the additional heating might be considered as being responsible for the generation of an electric field in the plasma and thus for the generation of the flows /7,8,3,4/, which may have a dramatic influence on the behaviour of the plasma /9,10,13-15,20/. There is no doubt that during discharges there are observed fluctuations in the plasma of the plasma density, temperature, electrical potential and of the magnetic field /11/. Those fluctuations have complicated structures and "morphology", and are linked with different kinds of instabilities, and even with the occurrence of strange attractors. There is, however, no agreement as to which of those instabilities are most important and can determine and explain the behaviour of the plasma. What is even more important, there is no comprehensive numerical theory which can predict unambiguously the impact of those instabilities on the transport of plasmas in axisymmetric systems /2/.

The observation of L- and H-modes with the spontaneous increase of plasma density and energy /12/, is being considered as an example of a bifurcation phenomenon, which, with small changes in the plasma parameters, may cause large changes in the overall plasma performance.

This study has originated from the idea /20/ that flows may drastically change the original equilibrium approach to the plasma behaviour and that the original static Grad-Shafranov-Schlüter (SGSS) equation might be a too drastic simplification for the description of the plasma transport in contemporary tokamak experiments with additional heating, where inevitable large toroidal flows may develop. The fact that almost sonic toroidal flows are observed may suggest that they must be correlated with smaller but still appreciable poloidal flows. Early /9,10,13/ and more recent papers /14,15/ have indicated that the extended Grad-Shafranov-Schlüter equation (with flows) starts to be a more complicated partial differential equation with many elliptic and hyperbolic domains. Thus the need to study this equation more closely, even in elliptic regions, has become evident.

Due to some claims /16-18/ that the inverse method approach and Fourier decomposition can offer some advantages over other approaches, it has been decided to see whether those advantages can be exploited also for EGSS equations.

During the performance of this research, a number of interesting and evidently important results have been obtained.

First of all, it has been found that EGSS equations offer many branches of solutions which, even for small poloidal velocity, correspond in general to two elliptic regions and two hyperbolic regions. These branches of solutions are of algebraic nature and are called the Bernoulli branches of the solution. One elliptic branch may, with the increase of poloidal velocity, pass the "sonic" barrier producing possibly "transonic" effects, as for example shock waves, which then might cause the change of the magnetic surface topology /19/.

Secondly, exploiting the nonlinear character of EGSS equations, one can claim that every elliptic branch additionally bifurcates into stable and non-stable branches, according to the general theory of nonlinear elliptic partial differential equations, thus giving a rich "zoology" of solutions. This property also characterises, as is well known, the original static GSS equation. Described phenomena for ideal MHD equations depend strongly on the shape of the characteristic profiles of defined quantities. There are five of such profiles in the case of stationary flows, whereas static equilibria are characterised only by three of them. This fact means that the properties of bifurcating solutions in the case of flows are probably much richer but, on the other hand, their calculation is necessarily much more difficult and complicated.

Thirdly, the computer program for solving both SGSS and EGSS equations using inverse method and Fourier decomposition has been prepared in its first preliminary version with an extensive discussion of computational problems connected with regularity conditions at the magnetic axis.

The program has been implemented for a given class of profiles, as functions of the magnetic surface label and can be used for studies of bifurcation phenomena in tokamak conditions. The applied shooting method for solving resulting nonlinear ODE allows to find possible multiple solutions.

The results of first test cases show that the poloidal flow causes a separation of the surfaces of constant density from the magnetic surfaces, as well as separation of the density axis from the magnetic axis. The distance between the magnetic axis and the density axis increases with the increasing of the magnitude of the poloidal flow. This fact might be of importance for the interpretation of existing diagnostics measurements based on static equilibrium assumptions and/or for the idea of the indirect measurements of the magnitude of the poloidal flow during additional heating.

The relevance of these results for JET experimental situation should be the subject of further studies.

Presented research has been done within the framework of JET Contract (JA5/0962). The grant from the Research Programme 01.10 "Diagnostics of Tokamak Plasmas" of the Ministry of National Education of the PPR is also acknowledged.

REFERENCES

/1/ J. Wesson, Theory of sawtooth oscillations, JET Report, P(87)55, to be published in Proceedings of Workshop on Theory of Fusion Plasmas, Varenna, Italy, 24-28 August 1987.
/2/ R.S. Pease, The status of function research, Proceedings of 14th EPS Conference on Controlled Fusion and Plasma Research, Plasma Physics and Controlled Fusion 29, (1987), 1187.
/3/ K. Brau et al, Nuclear Fusion 23 (1983), 1643.
/4/ R.C. Isler et al., Nuclear Fusion 26 (1986), 391.
/5/ W.M. Stacey Jr., D.H. Sigmar, Phys. Fluids 28 (1985), 2800.
/6/ J.W. Connor et al., Plasma Physics and Controlled Fusion 29 (1987), 919.
/7/ D.F. Düchs, Z. Naturforsch 42a (1987), 1193.
/8/ S. Suckewer et al., Nuclear Fusion 21 (1981), 1301.
/9/ H.P. Zehrfeld, B.J. Green, Nuclear Fusion 12 (1972), 569.
/10/ G.J. Green, H.P. Zehrfeld, Nuclear Fusion 13 (1972), 750.
/11/ D.C. Robinson et al., JET-P(85)11.
/12/ M. Keilhacker, Plasma Physics and Controlled Fusion 29 (1987), 1401.
/13/ H.P. Zehrfeld, B.J. Green, Nuclear Fusion 10 (1970), 251.
/14/ S. Semenzato, R. Gruber, H.P. Zehrfeld, Comp. Physics Report 1 (1984), 389.
/15/ E. Hameiri, Phys. Fluids 26 (1983), 230.
/16/ H.R. Hicks, R.A. Dory, J.A. Holmes, Comp. Physics Report 1 (1984), 373.
/17/ L.L. Lao, S.P. Hirschman, R.H. Wieland, Phys. Fluids 24 (1981), 1431.
/18/ L.L. Lao, S.P. Hirschman, W.A. Houlberg, R.H. Wieland, Comp. Physics Comm. 27 (1982), 129.
/19/ E. Hameiri, J. Plasma Physics 22 (1979), 245.
/20/ R. Zelazny, JET Internal Report JET-DN-T(85)18.

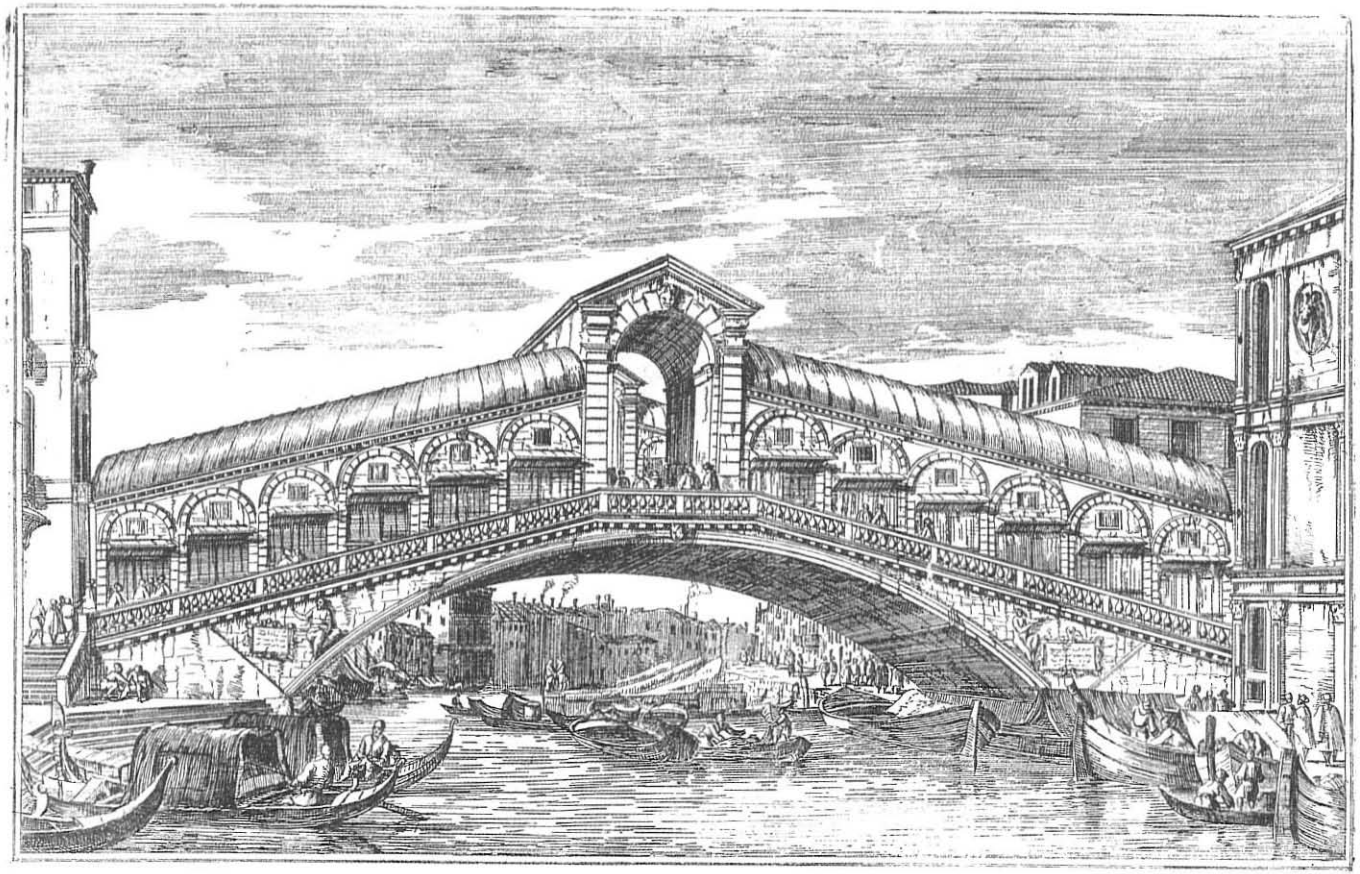

PONTE DI RIALTO

EFFECT OF THE TOKAMAK CROSS-SECTION ELLIPTICITY ON THE RIPPLE INDUCED DIFFUSION OF FAST IONS

Ya.I.Kolesnichenko, V.A.Yavorskij

Institute for Nuclear Research, Ukrainian SSR
Academy of Sciences, Kiev, USSR

Abstract. The elongation of the plasma cross-section is shown to affect the condition on the ripple amplitude for the intrinsic stochasticity of the collisionless particle motion and the value of the diffusion coefficient. It changes also the energy ranges with the various collisional diffusion regimes and the values of collisional diffusion coefficients.

1. The plasma cross-section in the reactor-tokamaks projected is elongated along the major axis of the torus. The elongation (k) reduces the particle characteristic drift velocity across the flux surfaces: $v_D = v_D^0/k$, $v_D^0 = (v^2+2v_\parallel^2)/(2\omega_B R)$ being the drift velocity in a circular tokamak, R the large radius of the torus, ω_B the gyrofrequency, $v_\parallel$ the particle velocity along the magnetic field. For this reason the banana width may be presented as follows: $\Delta r_b = 2\sqrt{2}\varkappa q \rho_L/(k\sqrt{\epsilon})$ where q is the tokamak safety factor, $\epsilon = \rho/R$, ρ the radial flux coordinate [1] , ρ_L the particle gyro radius, $\varkappa$ the particle trapping parameter. This expression for Δr_b we use to find the condition of the particle stochastic motion in the tokamak ripple field. To do it let us take into account that the motion of the main fraction of trapped particles becomes stochastic when the banana tips are in the region where the following inequality is satisfied:

$$\delta > \delta_2 \qquad (1)$$

where δ is the ripple amplitude, $\delta_2 = \delta_1 \rho/\Delta r_b$, $\delta_1 = \epsilon_*(Nq)^{3/2}$ is the characteristic ripple value which divides the plasma cross-section in two regions (where $\delta < \delta_1$ and $\delta > \delta_2$) with

qualitatively different particle orbits, the star * characterises the values in the particle turning point, N the magnetic coil number. δ_2 can be presented in the form which is similar to that one obtaned in Ref [2] for the circular tokamak:

$$\delta_2 \simeq k \left(\frac{\epsilon}{\pi N q}\right)^{3/2} \left(\rho_\perp \frac{dq}{d\rho}\right)^{-1} . \qquad (2)$$

The cross-section elongation affects the diffusion coefficient reducing it by a factor of k . This conclusion may easily be done if one take into account that [3,2]

$$D_0 \sim d^2 / \tau_b \qquad (3)$$

where D_0 is the diffusion coefficient related to the trapped particles only, d is the banana tip displacement near the turning point (d is proportional to Δr_b), τ_b is the particle bounce-period.

2. When $\delta < \delta_2$ the collisionless motion of the main fraction of trapped particles is regular and is characterized by the particle oscillations near the resonant flux surfaces with the frequency ν_r . The mentioned frequency depends on the ripple amplitude: $\nu_r \sim \mathcal{K}^{1/2} \tau_b^{-1}$ for $\delta < \delta_1$ and $\nu_r \sim \mathcal{K}_2 \tau_b^{-1}$ for $\delta > \delta_1$, where

$$\mathcal{K}_1 \sim \frac{\Delta r_b}{\rho} \quad \mathcal{K}_2 \sim \left(\frac{\Delta r_b}{\rho}\right)^2 \frac{\delta}{\delta_1} . \qquad (4)$$

It follows from Eq.(4) and definition of ν_r that $\nu_r \sim k^{-1}$.

However, the particle regular motion is destroyed by the Coulomb collisions. When collisions are weak ($\nu_{eff} \ll \nu_r$) they mainly change chaotically the particle oscillation phase. As a result the diffusion arises which is characterized by coefficient

$$D \sim \nu_{eff} D_0 / \nu_r \qquad (5)$$

where D_0 is given by Eq.(3), $\nu_{eff} \sim \nu_\perp [v_\parallel / (v \Delta\lambda)]^2$, $\nu_\perp$ is 90° deflection frequency, $\Delta\lambda = \epsilon/(Nq)$ [4] for $\delta > \delta_1$ and

$\Delta\lambda \sim (\epsilon/Nq)(\delta/\delta_1)^{1/2}$ for $\delta < \delta_1$, in the last case $\Delta\lambda$ being the resonant region width. It can be seen that the diffusion coefficient is reduced due to plasma elongation, $D \sim k^{-1}$.

When $\nu_r \ll \nu_{eff} \ll (Nq)^{3/2}\tau_b^{-1}$ (ripple-plateau regime) the collisions destroy the particle trajectories in the phase space. It leads to the diffusion coefficient which is similar to that one in the case of intrinsic stochasticity of particle motion (see Eq.(3)). Because of the plasma elongation the energy region with the ripple-plateau regime increases (since $\nu_r \sim k^{-1}$) and the diffusion coefficient decreases, $D \sim k^{-2}$.

In the regime of strong collisions ($\nu_{eff} > (Nq)^{3/2}\tau_b^{-1}$)

$$D \sim (Nq)^{3/2}(\nu_{eff}\tau_b^{-1})D_0 \sim k^{-1}$$

3. We have shown that the shape of the plasma cross-section affects essentially both the diffusion coefficient of fast ions and the conditions which should be satisfied in various regimes. In particular, the elongation increases the ripple limit δ_2 and, hence, makes more essential the role of the collisional diffusion. This circumstance is important when the weak collisional regime takes place because in this regime the diffusion coefficient is smaller than the corresponding value in the case of collisionless stochastic diffusion by ν_r/ν_{eff} times. Note that the regime of weak collisions is typical for the non-thermalized alpha particles. When comparing the fast ion diffusion in tokamaks with the circular and elliptic cross-section one should also take into account that the diffusion coefficients in various regimes drop due to elongation by a factor of k or k^2 provided the other plasma parameters and the tokamak safety factor are unchanged.

The described changes of the particle diffusion in the ripple field of the tokamak with elongated cross-section may strongly affect the confinement of fast ions because the con-

dition of the ion escaping ($\tau_n \sim a^2/D \ll \tau_s$ τ_n and τ_s are the fast ion confinement and slowing-down times) may be violated.

References.

1. Ya.I.Kolesnichenko, V.A.Yavorskij. Physica Plazmy, 5 (1979) 126
2. R.J.Goldston, R.B.White, A.H.Boozer. Phys. Rev. Leff., 47 (1981) 647
3. A.H.Boozer. Phys. Fluids, 23 (1980) 283
4. V.Ya.Goloborod'ko, Ya.I.Kolesnichenko, V.A.Yavorskij. Proc. Int. Symp. on Alpha Particles (Göteborg, 1986) Physica Scripta, T 16 (1986) 46

ANGULAR DISTRIBUTION OF ALPHA PARTICLE FLUX ON THE FIRST WALL OF A TOKAMAK

V.Ya.Goloborod'ko, V.A.Yavorskij

Institute for Nuclear Research, Ukrainian SSR
Academy of Sciences, Kiev, USSR

Toroidal field was shown to play an important role in the behaviour of the high-energy alpha particles in tokamaks [1-5]. Ripple induced diffusion can result in the losses of large fraction of the toroidally trapped alphas [2-4]. In the case of strongly inhomogeneous distribution of alpha flux over the wall the losses would have a large impact on the chamber wall. The numerical calculations carried out in Ref. [2,3] found that the ripple induced alpha flux is strongly peaked in poloidal angle for the INTOR-like plasma. In the present report we study the dependence of the angular distribution of the alpha flux on the tokamak parameters.

As the trapped alphas mainly contribute to the losses, we shall proceed from the map of the banana tip ($\vec{r}\,(V_\parallel = 0)$) motion [1,5]

$$\bar{r} = r + d\cos\chi\,, \qquad \bar{\chi} = \chi + \varphi_p(\bar{r}) + \bar{\sigma}\,\varphi_b(\bar{r}) + \bar{\nu} \tag{1}$$

Here r is the radius of banana tip; $\chi = N\varphi_t + \sigma\pi/4$; $\sigma = sgn(\sin\theta_t)$; θ_t and φ_t are the poloidal and toroidal positions of the turning point; φ_p , φ_b and ν are the changes of phase χ per half-period of bounce oscilation due to precession, motion along the field line and collisions; $d = \rho_L \delta\, (\pi N|\cos\sec\theta|)^{1/2} \cdot (q/\epsilon)^{3/2}$; ρ_L is the gyroradius; δ is the ripple magnitude; N is the number of toroidal field coils, q is the safety factor; $\epsilon = r/R$ (see Fig.1). Evidently, the radial position of the particle guiding center $r\,(\theta)$ is given by

$$r(\theta) = \bar{r} + \sigma\Delta\sqrt{\varkappa^2 - \sin^2\theta/2} \tag{2}$$

with θ the poloidal angle, $\Delta = \sqrt{2}\, q\rho_i/\sqrt{\epsilon}$, $\varkappa^2$ the particle trapping parameter. If $\bar{r}$ is the radial position of the tip of the banana orbit intersecting the wall, the former tip position $\underline{r}$ should satisfy the inequality

$$a - \varkappa\Delta - 2d < \underline{r} < a - \varkappa\Delta \qquad (3)$$

where a is the chamber wall radius. The coordinates $\underline{r}$, $\underline{X}$ and X determine the only poloidal angle θ_a at which particle hit the wall (see Fig.1)

$$a = \underline{r} + \Delta\left(\varkappa^2 - \sin^2\theta_a/2\right)^{1/2} + d\left(\cos\underline{X} + \cos X\right) \qquad (4)$$

From Eq.(4) one can see that $\theta_a(X, \underline{X}, \varkappa) \le \theta_{am}$. Assuming that ripple magnitude $\delta(r = a)$ is given by

$$\delta(\theta) = \delta_0 \exp\left\{-\eta \sin^2\theta/2\right\} \qquad (5)$$

we find [6]

$$\theta_{am} = 2.8\, \eta^{-1/8} \zeta^{-1/2} \qquad (6)$$

Here $\zeta^{-1} = A\,\delta_0\,(Nq)^{1/2}$, A is the aspect ratio. For the reasonable tokamak parameters (N =16, δ_0 =1 %, A=4, η =3÷4, q=2) we obtain $\theta_{am} \simeq 60°$.

Ripple induced diffusion results in the energy losses $\mathcal{E}_\Sigma$ given by

$$\mathcal{E}_\Sigma = \int d\vec{r}\, d\vec{V}\, \mathcal{E} Q$$

with Q the number of alpha particles coming per second into the unity of the phase space volume of the region determined by (3), and

$$d\vec{r}\, d\vec{V} = 4\pi V^2 dV \sum_{\sigma'} 2\sqrt{\epsilon}\, K(\varkappa) R\, \underline{r}\, d\underline{r}\, N^{-1} d\underline{X}\, d\varkappa^2, \quad \mathcal{E} = m_\alpha V^2/2 \qquad (7)$$

The angulas distribution of the alphas wall load (W_α) is defined by the expression [6].

$$\nu_\theta = \int d\vec{r}\, d\vec{V}\, \delta(\theta - \theta_a) Q \mathcal{E} \Big/ \int d\vec{r}\, d\vec{V}\, Q \mathcal{E} \qquad (8)$$

As follows from the Eqs. (4) and (3) θ_a is independent on $\mathcal{E}$, and on the other hand depends strongly on $\varkappa$. For this reason we can neglect the dependence $Q(\varkappa)$ in Eq.(8). As a result

it follows from Eq.(8) that [6]

$$\nu_\theta = \frac{\zeta \sin\theta}{4\pi} \int dx\, x\, K(x)(x^{-2}-1)^{1/4} e^{\eta x^2} \Phi\left(\frac{\Delta \sin^2\theta/2}{4x\alpha}\right) \quad (9)$$

where $\Phi(x) = \sin^{-1}(1-x)^{1/2}$ for the regime of weak collisions, and $\Phi(x) = 2\pi^{-1}\int_x^1 dy\, K(\sqrt{1-y^2})$ for the collisional or collisionless stochastic regime.

It is evidently from Eq.(9) that ν_θ is the function of two parameters η and ζ. In Fig.2 it is plotted the dependence $\nu(\theta)$ for different values of these parameters (curves 1÷6). For comparison these is shown the 3.5 Mev alpha particle prompt losses distribution in tokamak with I =5MA and parabolic profiles of plasma parameters and current (curve 7) [7]. One can see that the wall load peaking factor $P = W_{\alpha max}/\langle W_\alpha \rangle$ increase as η and ζ increase. Note that as δ_o decrease $W_{\alpha max}$ decrease slower than $\langle W_\alpha \rangle$ because peaking factor $P \gtrsim 2\pi\, \theta_{\alpha max}^{-1} \sim \delta_o^{-1/2}$.

As $\langle W_\alpha \rangle = 0{,}25\, W_n \nu_\varepsilon$ (here ν_ε is the alpha particle energy loss fraction, W_n is the neutron wall load) the $W_{\alpha max}$ is given by

$$W_{\alpha max} = 0.25\, W_n \nu_\varepsilon P \quad (10)$$

For the case of INTOR-like plasma $\nu_\varepsilon \sim \delta_o$ if $0{,}1\% \leq \delta_o \leq 1\%$ [2], therefore, $W_{\alpha max}$ scales as $W_{\alpha max} \sim \nu_\varepsilon P \sim \delta_o$. Let us estimate the value of $W_{\alpha max}$. For $\delta_o \sim 1\%$ we have $\nu_\varepsilon \simeq 12\%$ [2] and for the considered case η =3, ζ =4 one can finde from Fig.2 that P =11 and consequently $W_{\alpha max}$ ($\delta_o = 1\%$)$=0.3\, W_n$. For W_n =1.3MW m^{-2} we get $W_{\alpha max}$ =0.4 MW m^{-2}.

The present paper shows that the wall loading is strongly peaked in poloidal angle (the tipical value of peaking factor is about 10÷20). Note that the wall loading distribution is quite universal (it depends weakly on the tokamak parameters).

References

1. Goldston R.J., White R.B., Boozer A.H. Phys.Rev.Letters, 1981, 47, 647.
2. Tani K., Takisuka T., Asumi M., Kishimoto H. Nucl.Fusion, 1983, 23, 657.
3. Hively L.M. Nucl.Fusion, 1984, 24, 779.
4. Zajtsev F.S., Smirnov A.P., Yushmanov P.N. Nucl.Fusion, 1986, 26, 1311.
5. Goloborod'ko V.Ya., Kolesnichenko Ya.I., Yavorskij V.A. Physica Scripta, 1987, T16, 46.
6. Goloborod'ko V.Ya., Yavorskij V.A. Preprint KIYaI - 88-32.
7. Kolesnichenko Ya.I., Fursa A.D., Yavorskij V.A. Fiz. Plazmy, 1976, 2, 911.

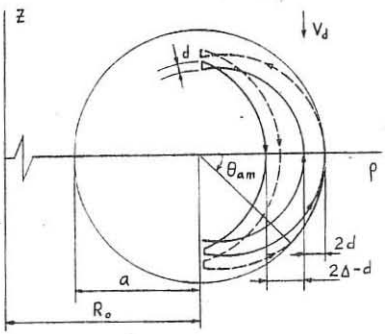

Fig.1. Qualitative shape of two banana orbits intersecting the wall with $\theta_a = 0$ (solid curve) and $\theta_a = \theta_{am}$ (dashed curve)

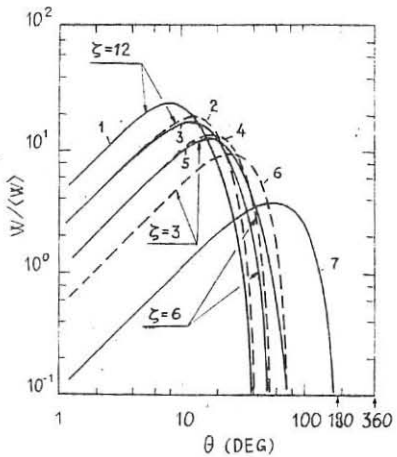

Fig.2. $W_\alpha/\langle W_\alpha\rangle$ versus poloidal angle θ. Curves 1, 3, 5 correspond to $\eta = 4$, curves 2, 4, 6 - $\eta = 3$.

SPECTRUM AND IMPEDANCE PROPERTIES OF A PLASMA IN A HELICAL MAGNETIC FIELD.

A.G.Elfimov, K.G.Komoshvili, V.P.Sidorov
(I.N.Vekua Institute of Physics and Technology, Sukhumi, USSR).

M.V.Dmitrieva, S.Yu.Medvedev, G.A.Pestryakova
(M.V.Keldysh Institute of Applied Mathematics of the USSR Academy of Sciences).

Theoretical and numerical analyses of interaction between Alfven frequency range fields and a nonhomogeneous cylindrical plasma in a helical magnetic field have been carried out (for some time), this plasma being used to simulate a tokamak plasma. By this a MHD plasma model, considering gyrotropy [1] as well as a kinetic model, considering finite ion Larmor radius effect and the thermal motion of electrons [2-4] during RF field generation, have been used. With the help of MHD and kinetic numerical codes the spectra of global and slow (kinetic) Alfven waves, fast magneto-sonic and surface waves have been well studied for small-size tokamak [1,2] with the gyrotropy parameter large enough: $\omega/\omega_{ci} \simeq 0{,}3\text{-}0{,}5$. This parameter is definitive for dispersion of global Alfven waves which always exist below the lower bound of the Alfven continuum edge $\omega_{GL} < \omega_{th} = (k_\parallel c_A(0) / \sqrt{1 + (k_\parallel^2 c_A^2(0)/\omega_{ci}^2}\,)_{min}$ for $m, n < 0$, (where ω_{th} denotes a threshold frequency). For large-scale INTOR-type devices, the gyrotropy parameter is small $\omega/\omega_{ci} \leq 0{,}1$ and the global wave "enters" the continuum, as if being dissolved among wave dispersion also begins to depend essentially upon the axial current magnitude and profile in a plasma.

In the present paper we investigate the spectra (dependence of eigenfrequencies on $k_z a = na/R$) of a global kinetic Alfven, fast magneto-sonic and surface waves, and active and reactive impedances of helical antennas [1-4] for INTOR-type tokamak plasma parameters. The following parameters have been chosen: the casing, plasma and antenna radii d=1,3 M, a=1,2M, b=1,25 M, respectively; the antenna current density $j_{\varphi,z} = j^0_{\varphi,z} \exp i(-\omega t + m\varphi + k_z z)$, the electron density $n_e = 2{,}5 \cdot 10^{14}(1-x^2)$ the axial plasma current density $j_z = j_0(1-x^2)^\alpha$; the magnetic field $B_z = 5$ T; the torus major radius R= 5 M. Fig.1 shows the dependence of eigenfrequencies which are computed by means of the MHD code according to the peaks in the impedance curves for $\alpha = 2$, $q_a = 2{,}19$, $m = \pm 1$ with the toroidal number n varied. Dispersion of fast magneto-sonic waves (F) practically does not depend on the gyrotropy, the shear and the value of q_a. The surface wave (S) behaviour essentially depends upon the signs of m and n. The signs being the same Fig.1a , on increasing n, the surface mode approaches to the lower edge of the Alfven continuum while the points of conversion

corresponding to the impedance curve maxima move close to the plasma center. For m, $n<0$ when $|n| > n_{cr}$, a global Alfven mode (GA) is established. Under these conditions, the impedance curve, within the kinetic approximation, is zigzagged with the kinetic Alfven resonance peaks and the damping length (KA) of the waves is shorter than the distance from the point of conversion to the plasma center. For other values of α and q_a, a simple interpolation formula may be derived for $n_{cr} = 14 + 10(q_a - 1{,}5) - 6(\alpha - 1)$. For m=-2, the value of n_{cr} is nearly two times that of n_{cr}(m=-1). The impedance value is highest for $|n| = n_{cr} - 1$ while the reactive part of the impedance is close to zero. Such a regime is most convenient for Alfven heating of the central plasma region. This peak of the impedance is considered to be linked with a combined resonance [4] being formed in the plasma. In the MHD model this resonance is a combination of the fast Alfven mode fields and the noneigenfield of the fast magneto-sonic mode which are linked by a local Alfven resonance. For the surface wave to be formed, there is no need in existence of the fast Alfven wave propagation domain from the plasma boundary to the point of conversion. These regimes are shown in Fig.1b.

If m, $n>0$ the surface mode (S), on increasing n, see Figs. 1a,3, approaches to the continuum threshold frequency ω_{th}, then it begins to retire slowly. For large values $n > n_{cr} = 32$, the surface mode tends to arrive at the fast magneto-sonic branch of the oscillations and at this moment, below the continuum edge, there arises the global mode (GA).

Fig.4 shows a typical distribution of the electrical field E_ξ-component under the conditions of the local resonance ($x_A = r_A/a = 0.5$) and for the kinetic Alfven resonance formation process shown in Fig.2.

For operation modes with lowest values of q_a at m =-1, the global mode, as in small-size tokamaks [1;2] may exist for all the values of $n<0$ (see Fig.5). For this case, there are no discontinuities in the dispersion curve, but the second radial global mode enters the continuum and becomes dissolved among the kinetic resonances.

CONCLUSIONS. The spectra of the eigenmodes of a cylindrical plasma column in a helical magnetic field are analyzed. The conditions are shown for forming combined and global Alfven resonances for parameters of large-scale tokamaks (INTOR-ITER) with small gyrotropies. The conditions for central plasma heating are found in a combined Alfven resonance when the reactive resistance of an antenna is small.

REFERENCES

1. K.Appert, J.Vaclavic and Villard, Phys.Fluids 27,432,(1984).
2. D.W.Ross, G.L.Chen and S.M.Mahajan, Phys.Fluids, 25, 652, (1982).
3. M.V.Dmitrieva, A.G.Elfimov, K.G.Komoshvili et al. Preprint issued by M.V.Keldysh Institute of Applied Mathematics of the USSR Academy of Sciences, N4, 1984.
4. A.G.Elfimov, K.G.Komoshvili, V.P.Sidorov. In: Proc.Contr. Pap.Intern.Conf.on Plasma Phys.,Kiev,1987,v.1,pp 22-25.

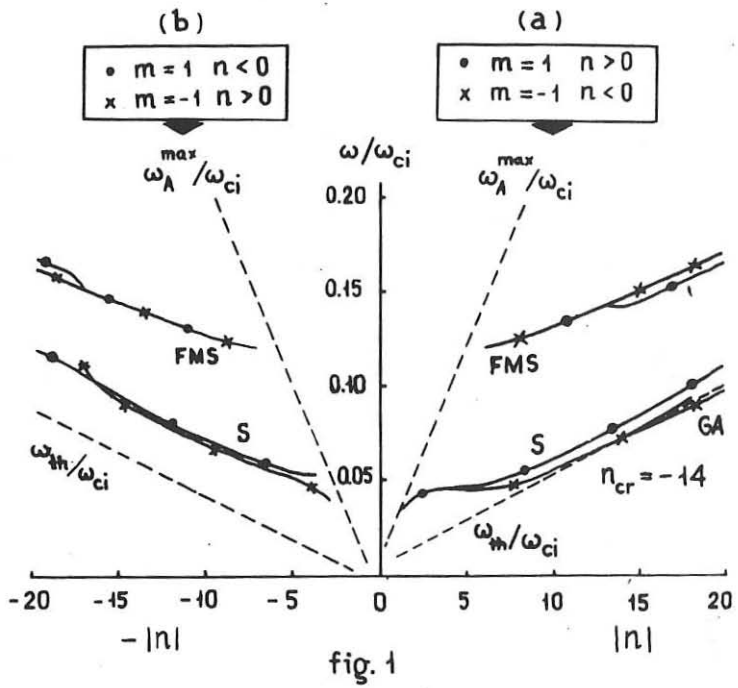

fig. 1

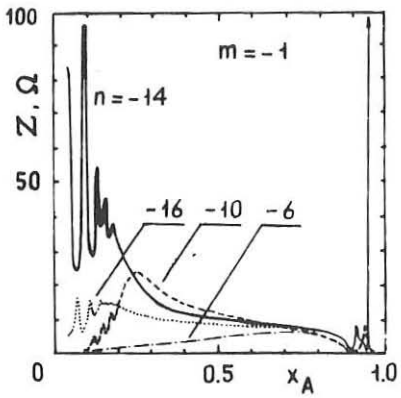

fig. 2

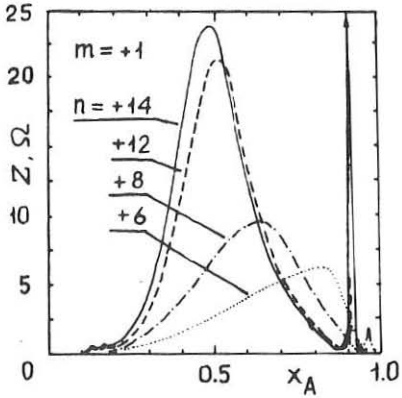

fig. 3

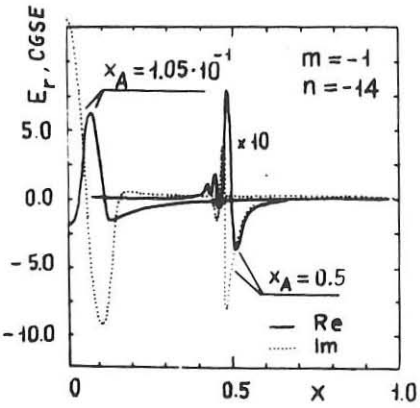

fig. 4

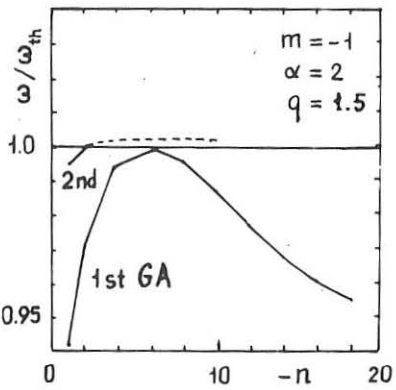

fig. 5

GLOBAL ENERGY CONFINEMENT DEGRADATION DUE TO MACROSCOPIC PHENOMENA IN TOKAMAKS*

I.D. Callen and Z. Chang

University of Wisconsin, Madison, WI 53706-1687, USA

Introduction

Discharges in tokamaks are often afflicted by one or more macroscopic phenomena (sawteeth, Mirnov oscillations, ELMs, etc.) that can reduce the energy confinement in the plasma. In this paper we develop quantitative and scaling estimates of the (slight) energy confinement degradations due to the various types of macroscopic phenomena that can occur in tokamaks. The analysis is based on the recently developed formalism [1] for determining the incremental energy confinement time τ_{inc} from a local transport model. To apply the local transport fomalism to the energy confinement degradation problem we make the fundamental assumption that heat transport outside the region where the macroscopic phenomena operates is unaffected by it. Thus, the macroscopic phenomena will have their effects on energy confinement primarily through their reduction of the effective cross-sectional area of the plasma which provides thermal insulation. This paper briefly summarizes a number of the illustrative results in their cylindrical geometry approximations; a more complete paper [2] that allows for arbitrary tokamak geometry and gives more comprehensive results will be published later.

Local Transport Model for an Ideal Plasma

Under the assumption that the heat diffusivity coefficient is parametrically constant [i.e., $\chi \neq f(T_e)$ but $\chi = \chi(r)$] the sum of the electron and ion heat balance equations can be integrated three times in the radial coordinate to yield an "offset-linear" stored energy scaling relation [1]:

$$W = W(0) + \tau_{inc} P_{in}, \tag{1}$$

where W(0) is the sum of edge boundary condition (pedestal) and heat pinch or minimum temperature-gradient effects [1], and P_{in} is the input power. The incremental energy confinement time is defined by

$$\tau_{inc} \equiv \frac{\Delta W}{\Delta P_{in}} = \eta \tau_{\chi}. \tag{2}$$

Here, η is the heating effectiveness factor [1] that takes account of the heating profile effects ($0 \leq \eta \leq 1$). For simplicity in this paper we consider the case of delta function heating on axis

($\eta = 1$). The ideal incremental energy confinement time τ_χ is defined by [1]

$$\tau_\chi = \frac{3a^2}{4\bar{\chi}}, \quad (\bar{\chi})^{-1} = 4 \int_0^a \frac{dr \int_0^r r' n(r')\, dr'}{a^2\, r\, n(r)\, \chi(r)}. \tag{3}$$

For an ideal plasma (no macroscopic phenomena present) with n = constant and $\chi(r) = \chi_0/(1 - \alpha r^2/a^2)$ for $0 \le \alpha \le 1$, τ_χ becomes [1]

$$\tau_0 = \frac{3a^2}{4\chi_0}\left(1 - \frac{\alpha}{2}\right). \tag{4}$$

This ideal value of τ_χ will be used as the reference value against which the energy degradation effects due to various macroscopic phenomena will be measured.

Sawtooth Flattening Effects

To model the effects of sawteeth [3] we take the extreme model [1] that χ is infinite inside the mixing radius r_m. This model implies that sawteeth are so frequent that there is no significant increase in the total stored energy between sawtooth crashes; the case where this is not true is treated in the penultimate section. For the present extreme model but with $\chi(r)$ and n = constant the same as before outside the mixing radius we find

$$\tau_\chi^s / \tau_0 = (1 - r_m^2/a^2)\,[1 - (\alpha/2)\,(1 + r_m^2/a^2)] / (1 - \alpha/2), \quad \Delta\tau^s/\tau_0 \sim r_m^2/a^2. \tag{5}$$

Here, $\Delta\tau^s/\tau_0$ is the fractional change in the incremental energy confinement time due to the presence of the sawteeth. Note that it is of the order of the fractional area affected by the sawteeth. For $\alpha = 1$ we have $\tau_\chi^s/\tau_0 = (1 - r_m^2/a^2)^2$, which is a formula that Bhatnagar et al. [4] have found represents the energy confinement degradation due to sawteeth for central ICRF heating of JET plasmas reasonably well.

Mirnov Oscillation and Locked Mode Effects

Mirnov oscillations and locked modes are apparently due to a magnetic island of a specific helicity being formed within the plasma [5]. We will assume that while the magnetic topology in which the transport takes place changes, the heat diffusivity coefficient will be unchanged.

Then, the radial coordinates in $\bar{\chi}$ must be converted to helical flux coordinates to take account of the presence of the island. For simplicity a thin (or slablike) island is assumed and the calculations are carried out only through first order in the ratio of the island width w to the minor radius a. After some lengthy algebra [2] we find

$$\tau_\chi^M / \tau_0 = 1 - (r_s^3 w/a^4)\ (1 + 1.83 \ln a/r_s), \quad \Delta\tau^M/\tau_0 \sim r_s^3\, w/a^4 \tag{6}$$

in which r_s is the radius of the singular surface at the center of the island. This result indicates a larger (by the logarithm factor) energy confinement degradation than was obtained from a previous "belt" model [5] in which the temperature profile was simply flattened over the radial extent of the island region. Physically, it is larger because of the greater reduction of the effective insulation area of the plasma -- mainly outside the magnetic island due to the helical magnetic flux surface geometry there. This larger effect should improve the correlation between theory and experiment [6] since the preceding belt model [5] gave the proper trend but was quantitatively too small.

Edge Localized Mode (ELM) Effects

When a tokamak plasma is operating in an H-mode [7] operating regime, edge localized modes (ELMS) can degrade energy confinement. ELMs are unfortunately not well understood as yet. The primary effect of an ELM is apparently to remove a lump of density from an outer layer of the plasma, without affecting the electron temperature in this region very much [8]. We will adopt a simple model that postulates a density decrease Δn over the region $r_E \le r \le a$ with $n\chi$ being held constant. Then, the increased χ resulting from the ELM induced density decrease causes a reduction in τ_χ given by

$$\tau_\chi^E / \tau_0 = [1 + (8/3)\,(\Delta n/n)\,(1 - r_E/a)^3]^{-1}, \quad \Delta\tau^E/\tau_0 \sim (\Delta n/n)\,(1 - r_E/a)^3. \tag{7}$$

Time-Dependent Macroscopic Phenomena Effects

For sawteeth the temperature in the central region of the plasma increases roughly linearly with time between the repetitive sawtooth "crash" phases. During this time the stored energy increment ΔW (change in W from ideal case to one with sawtooth effects, $\Delta W < 0$) changes according to an equation of the form $\tau_0 \partial \Delta W / \partial t = - \Delta W + \Delta\tau\, P_{in}$ which yields $\Delta W = - \Delta\tau P_{in} e^{-t/\tau_0}$, where t starts from zero just after a crash. Averaging this stored energy increment over the repetition time t_R of the sawtooth crashes, we find for our simple models that the $\Delta\tau/\tau$ effect calculated above for sawteeth gets multiplied by a factor dependent on the ratio of t_R to τ_0:

$$\Delta\tau/\tau_0 \Rightarrow (\Delta\tau/\tau_0)\, f\,(t_R/\tau_0), \quad f(x) = (1 - e^{-x}) / x \tag{8}$$

In the limit of rapid crashes ($t_R << \tau_0$), $\Delta\tau/\tau_0$ approaches the given in Eq. (5). However, for $t_R > \tau_0$ the time-dependence factor f becomes small and the energy degradation due to sawteeth goes away. For ELMs a similar effect should occur, but the characteristic time scale entering the differential equation for ΔW would not be τ_0, but instead would be some time scale characteristic of the edge plasma density buildup between ELMs, which is not very well understood.

Discussion and Conclusions

In this summary we have given simple estimates of the energy confinement degradation effects of the major macroscopic phenomena (sawteeth, Mirnov oscillations/locked modes, ELMs) in tokamak plasmas. Each of these effects can easily amount to some 10's of percent changes in the energy confinement time. Thus, in doing energy confinement scaling studies it is very important to either operate the discharge in a manner which eliminates the macroscopic phenomena or make some effort to compensate for their effects using formulas such as the ones given here or the more detailed ones in [2]. Also, these formulas could be used to estimate the potential energy confinement degradation effects due to macroscopic phenomena in future devices such as ITER, particularly for low q(a) and high ellipticity where the q = 1 and mixing radius become large and the sawteeth flattening effects could be significant.

ACKNOWLEDGEMENT

The authors gratefully acknowledge useful discussions with V.P. Bhatnagar, J.G. Cordey, A. Kellman and K. McGuire during the development of these various models.

*Research supported by the U.S. DOE under grant DE-FG02-86ER53218.

[1] J.D. Callen, J.P. Christiansen, J.G. Cordey, P.R. Thomas, K. Thomsen, Nuclear Fusion 27, 1857 (1987).

[2] Z. Chang and J.D. Callen, "Global Energy Confinement Degradation Due to Macroscopic Phenomena in Tokamaks," UWPR 89-1 (to be published).

[3] S. Von Goeler, W. Stodiek, N. Sauthoff, Phys. Rev. Letters 33, 1201 (1974).

[4] V.P. Bhatnagar, J.G. Cordey, J. Jacquinot, D.F.H. Start, "Effect of Sawteeth, Safety Factor and Current on Confinement During ICRF Heating of JET," JET-P(88)51 (to be published).

[5] J.D. Callen, B.V. Waddell, B.A. Carreras et al., "Magnetic 'Islandography' in Tokamaks," Plasma Phys. Cont. Nuc. Fusion Res. 1978 (IAEA, Vienna, 1979), Vol. I, p., 415.

[6] B.A. Carreras, B.V. Waddell, H.R. Hicks, Nuclear Fusion 19, 1423 (1979).

[7] F. Wagner, et al., Phys. Rev. Letters 49, 1408 (1982).

[8] See for example: M. Ali Mahdavi et al., "Modification of the Scrape-Off Layer by Edge Plasma Modes," GA-A19291, September 1988 (to be published in J. Nuclear Materials).

BOOTSTRAP CURRENT AND BALLOONING STABILITY IN ASDEX L AND H PLASMAS

G. Becker

Max-Planck-Institut für Plasmaphysik
EURATOM Association, D-8046 Garching, FRG

ABSTRACT: The effect of bootstrap and neutral-beam-driven currents on the loop voltage, toroidal current density and ideal ballooning stability was investigated in various phases of H discharges by computer simulations. It is found that the loop voltage computed with neoclassical resistivity is only compatible with the measurements if Ohmic, bootstrap and beam-driven currents are included. The sum of the bootstrap current (100 kA with broad profile) and beam-driven current (50 kA with peaked profile) reaches 47 % of the plasma current. The field diffusion effect connected with all contributions is assessed by inclusion of these currents in the B_p diffusion equation. The main effect is the adjustment of the total current density to the broader electrical conductivity profiles in the H phase on the resistive diffusion time scale of about 400 ms. The broadening due to the bootstrap current is comparatively small, so that the ideal ballooning stability is scarcely modified by this current.

INTRODUCTION: Evidence of bootstrap currents in tokamaks was recently reported from TFTR /1/ and JET /2/. The present paper explores the bootstrap and neutral-beam-driven currents, the total current density and the ideal ballooning stability in L and H plasmas of ASDEX. The simulations are carried out by modified versions of the BALDUR predictive transport code /3, 4/. Local, empirical electron heat diffusivities χ_e, diffusion coefficients D and inward drift velocities v_{in} are used to describe the anomalous energy and particle fluxes /5, 6/.

COMPUTATIONAL MODEL: The bootstrap current density is computed from an expression /7/ valid in the banana regime since in high power injection-heated ASDEX plasmas both the electrons and the ions are collisionless ($\nu_{*e} < 1$, $\nu_{*i} < 1$):

$$j_{bs} = c\,\varepsilon^{1/2}\,B_p^{-1}\left[K_{13}\left(-\frac{\partial p_e}{\partial r} - \frac{n_e}{n_i}\frac{\partial p_i}{\partial r} + \frac{1.17}{1+\nu_{*e}^2\varepsilon^2}\,n_e\frac{\partial T_i}{\partial r}\right) + (2.5\,K_{13} - K_{23})\,n_e\frac{\partial T_e}{\partial r}\right] \qquad (1)$$

Here, c is the speed of light, $\varepsilon = r/R_o$ and K_{13} and K_{23} are dimensionless transport coefficients.

The build-up of bootstrap and beam-driven currents induces return currents in the plasma which decay on the resistive time scale. This field diffusion effect is assessed by including

$$E_t = \eta\,(j - j_{bs} - j_{bd}) \qquad (2)$$

in the diffusion equation for B_p, where η is the neoclassical resistivity and E_t is the toroidal electric field induced by the OH circuit and by the bootstrap (j_{bs}) and beam-driven (j_{bd}) currents.

Ideal ballooning stability is analysed by the transport code which evaluates the local criterion /8/

$$-\frac{2\,R_0 q^2}{B_t^2}\left(\frac{\partial p}{\partial r}\right)_c = f(s) \qquad (3)$$

where $(\partial p/\partial r)_c$ is the critical pressure gradient and f(s) is a known function of the dimensionless shear $s = (r/q)\partial q/\partial r$. In the pressure gradient both the thermal pressure and the anisotropic beam pressure are taken into account, the beam contribution being derived from fast ion guiding centre distributions.

CURRENT PROFILES AND BALLOONING STABILITY: An H discharge with $\bar{n}_e = 3.3 \times 10^{13}$ cm^{-3}, $I_p = 320$ kA, $B_t = 1.85$ T and neutral co-beam power $P_{NI} = 3.45$ MW ($H^0 \rightarrow D^+$) is analysed (see Fig. 1). The L-to-H transition occurs at $t = t^*$. Transport is simulated in the whole plasma, including the scrape-off layer and the steep gradient zone (width $\Delta \simeq 2.5$ cm) close to the separatrix during the H phase. The transport model applied /9,10/ yields a good fit to the measured n_e, T_e and T_i profiles and β_p^{dia}. Neoclassical resistivity and uniform $Z_{eff} = 2$ are assumed in the computations.

The time evolution of the loop voltage is shown in Fig. 2. Obviously, the loop voltages calculated with Ohmic, bootstrap and beam-driven currents included come close to the measurements while those with Ohmic current only do not.

The current distributions in the L and H phases are given in Figs. 3 and 4, respectively. Broad profiles are found for the bootstrap current, whereas the beam-driven current is peaked like the Ohmic one. The bootstrap and beam-driven currents in the L phase are $I_{bs} = 63$ kA and $I_{bd} = 57$ kA, respectively. During the H phase $I_{bs} = 100$ kA and $I_{bd} = 50$ kA are obtained. Their sum reaches 47 % of the total current. Since the resistive time scale for current redistribution is $\tau_{res} \approx 400$ ms, very little diffusion occurs between Figs. 3 and 4. Near the separatrix, however, skin times are much shorter, so that the hump on $j_{bs}(r)$ due to the steep pressure gradient in the zone Δ becomes visible on the total current profile.

Figure 5 illustrates that the current distribution in the H phase is broader than that in the Ohmic phase. On time scales much shorter than τ_{res}, the current profile in the hot plasma is left almost unchanged by the non-Ohmically driven currents. The simulation of another H discharge has shown that the current density mainly adjusts to the broader electrical conductivity profiles in the H phase on the scale $\tau_{res} \approx 400$ ms. The broadening due to the bootstrap effect is found to be comparatively small.

Including Ohmic, bootstrap and beam-driven currents in the ballooning stability analysis yields the results presented in Fig. 6, where the pressure gradient normalized to the critical value from Eq. (3) is plotted versus the radius. In the case with Ohmic current alone results differing by just a few per cent are obtained. This is due to the almost identical j, q and s profiles in the two cases. During the L phase the

pressure gradient is everywhere below 40 % of the critical value. The edge plasma is found to be ideal ballooning stable even if bootstrap and beam-driven currents are taken into account. The steep pressure gradient in the zone Δ during the H period drives the edge plasma close to marginal stability.

Ballooning stability was also analysed in the phase prior to reaching of the beta limit, i.e. before the onset of additional transport losses. It is found that ideal ballooning stability at the β limit is modified very little by the bootstrap and beam-driven currents. It is thus concluded that the earlier results based on Ohmic current profiles /11/ are still valid.

References

/1/ Zarnstorff, M.C., Bell, M.G., Bitter, M., Goldston, R.J., Grek, B., et al., Phys. Rev. Lett. 60 (1988) 1306.

/2/ Cordey, J.G., Challis, C.D., Stubberfield, P.M., Plasma Physics and Controlled Fusion 30 (1988) 1625.

/3/ Becker, G., ASDEX Team, Neutral Injection Team, Analysis of Local Transport in Neutral-beam-heated L and H Plasmas of ASDEX, Rep. IPP III/98, Max-Planck-Institut für Plasmaphysik, Garching (1984).

/4/ Post, D.E., Singer, C.E., McKenney, A.M., BALDUR: A One-dimensional Plasma Transport Code, Rep. 33, Princeton Plasma Physics Laboratory, Princeton (1981).

/5/ Becker, G., Nucl. Fusion 24 (1984) 1364.

/6/ Becker, G., Nucl. Fusion 28 (1988) 1458.

/7/ Hinton, F.L., Hazeltine, R.D., Rev. Mod. Phys. 48 (1976) 239.

/8/ Connor, J.W., Hastie, R.J., Taylor, J.B., Phys. Rev. Lett. 40 (1978) 396.

/9/ Becker, G., in Controlled Fusion and Plasma Heating (Proc. 15th Europ. Conf. Dubrovnik, 1988), Part I (1988) 211.

/10/ Becker, G., Murmann, H., to be published in Nucl. Fusion.

/11/ Becker, G., ASDEX Team, Neutral Injection Team, Nucl. Fusion 27 (1987) 1785.

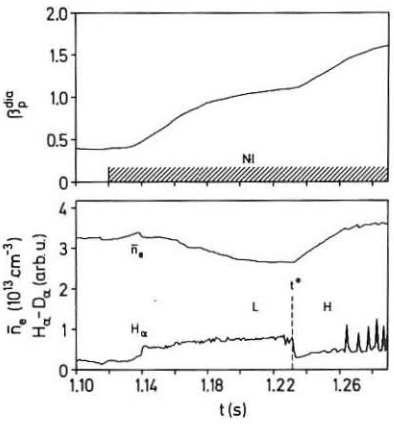

Fig. 1: Line-averaged density $\bar{n}_e$, H_α intensity and β_p in an H discharge with I_p = 320 kA, B_t = 1.85 T, P_{NI} = 3.45 MW ($H^0 \rightarrow D^+$).

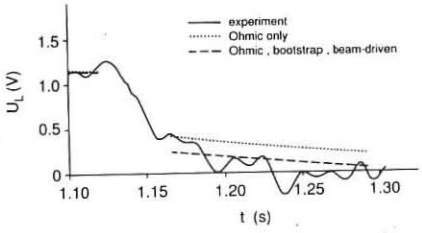

Fig. 2: Time development of measured loop voltage U_L compared with predictions from driven current models.

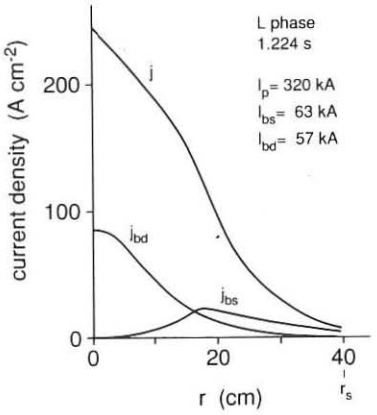

Fig. 3: Profiles of bootstrap j_{bs}, beam-driven j_{bd} and total current density j in the pre-transition L phase.

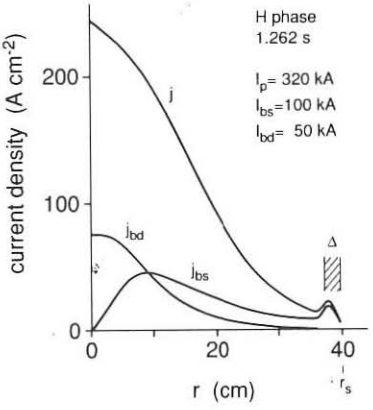

Fig. 4: As in Fig. 3, but in the ELM-free H phase.

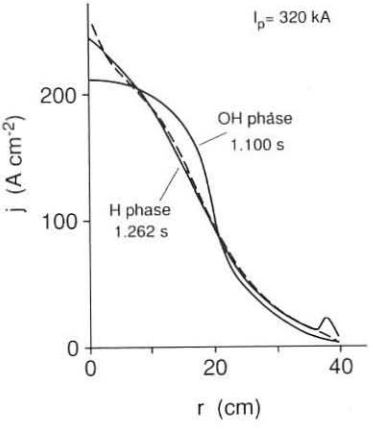

Fig. 5: Evolution of current profile with Ohmic, bootstrap and beam-driven currents (solid curves) and with Ohmic current only (dashed curve).

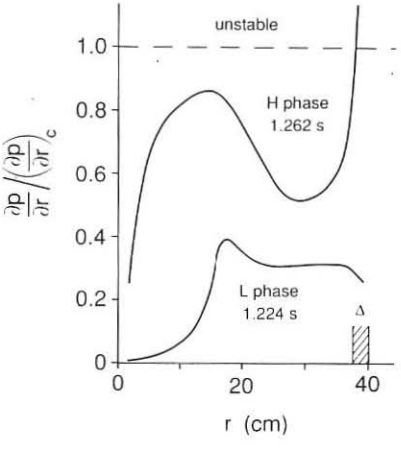

Fig. 6: Normalized pressure gradient versus radius with Ohmic, bootstrap and beam-driven currents included..

NON-LOCAL PARTICLE DEPOSITION AND PELLET WAKE EVOLUTION IN PELLET-FUELLED TOKAMAKS

L.L. Lengyel and P.J. Lalousis*

Max-Planck-Institut für Plasmaphysik, EURATOM Association,
D-8046 Garching, Fed. Rep. of Germany;
*The NET Team, c/o IPP Garching, D-8046 Garching,
on leave from Research Centre of Crete, Heraklion, Greece.

A pellet crossing a sequence of flux surfaces continuously releases neutral particles whose initial expansion velocity is considerably larger than the pellet flight velocity. The particles are ionized and confined to magnetic flux surfaces at some distance from the pellet location. The pellet thus traverses its own cloud. The particles confined to individual flux surfaces expand along the magnetic field lines, forming a characteristic wake whose state parameters are considerably different from those of the background plasma [1]. At the same time, the portion of the neutral cloud ahead of the pellet may form an effective buffer layer shielding the pellet from the incident plasma particles [2].

A numerical code is being developed that describes the time development of the state parameters of the wake behind the pellet and those of the buffer layer ahead of it (size, expansion velocity, temperature, density, bulk ionization degree, etc.) in a self-consistent manner.

The code consists of three parts: an ablation routine based on the neutral gas plasma shielding model of Houlberg et al. [3], the MHD cloud expansion model that computes the expansion and ionization of the pellet particles released at individual flux surfaces [1] and, finally, a routine that calculates the pellet mass fractions deposited at neighbouring flux surfaces in front of and behind the pellet during the residence time of the pellet at any particular flux surface [4]. The wake evolution is thus computed in the following manner: The pellet is advanced to a flux surface of given local plasma parameter values. The local ablation rate is determined [3], being assumed to remain constant during the residence time ($\tau_{res} = \Delta r / v_{pel}$, Δr being the mesh size along the pellet path, it shall be referred to hereafter as flux tube width) of the pellet at the flux surface considered. With the mass source strength (mass deposition

rate) thus prescribed, the time evolution of the ablatant cloud formed by the pellet particles locally released is calculated [1]. Next, the ionization ($\approx$ confinement) radius is determined, and the pellet mass locally released is distributed over the flux tubes affected [4] in proportion to the respective volumetric fractions. Once the mass increment ΔM is determined for each flux tube piercing the cloud ($\Delta M \equiv 0$ for all flux tubes outside the cloud boundaries) together with the associated temperature and density increments ΔT and Δn, the state parameters of the plasmoids confined to flux tubes in front of and behind the pellet location are updated for the time increment (represented by the residence time) by means of the cloud expansion routine. The pellet is than advanced to the next flux surface and the procedure is repeated. At some flux surface the pellet mass vanishes (end of the pellet lifetime) and, as of this moment, the calculation of the wake evolution is continued with zero mass source strength specified.

Representative results stemming from preliminary calculations are shown in Figs. 1 and 2. In this scenario, a D_2 pellet 3 mm in dia. is injected into a plasma of $a = 1.2$ m radius with

$$T(r) = T_1 + (T_o - T_1)[1 - (r/a)^2]^2,$$

$$n_e(r) = n_1 + (n_o - n_1)[1 - (r/a)^2]^{1/2},$$

$T_o = 3.2$ keV, $T_1 = 0.05$ keV, $n_o = 5 \times 10^{19}$ m^{-3}, and $n_1 = 5 \times 10^{18}$ m^{-3}. The assumed pellet velocity v_p is 2 km/s.

Figure 1 shows the plasmoid length measured along the magnetic field lines (wake width) as a function of the radial coordinate (pellet flight path) for a sequence of time instants. At time $t = 0$ pellet ablation begins at the plasma periphery ($r = a = 1.2$ m). As time goes on, the mass source (pellet) moves towards the plasma centre, and both the longitudinal (r) and lateral (z) dimensions of the wake steadily increase. The ablation is complete at t = 0.48 ms (the duration of the pellet lifetime, the corresponding length of the particle deposition region is, as can be seen, 96 cm). Figure 2 shows the time evolution of the plasmoid density along the centre line of the wake produced by the flying pellet. The pellet location is marked by the density maximum at any particular time instant. After the pellet ablation is completed, the peak density values continuously decrease (not shown in this plot).

[1] L.L. Lengyel, Nucl. Fusion **29** (Jan.-Febr. 1989), see also Phys. Fluids **31** (1988), 1577.

[2] L.L. Lengyel and P.J. Lalousis, Proc. IAEA Techn. Comm. Meeting on Pellet Injection, Gut Ising, Fed. Rep. Germany, Oct. 24-26, 1988.

[3] W.A. Houlberg at al., Nucl. Fusion **28** (1988), 595.

[4] P.J. Lalousis and L.L. Lengyel, in Contr. Fus. Pl. Heating (Proc. 15th Eur. Conf. Dubrovnik, 1988) **12B**, Part I, Europ. Phys. Soc. (1988) 286.

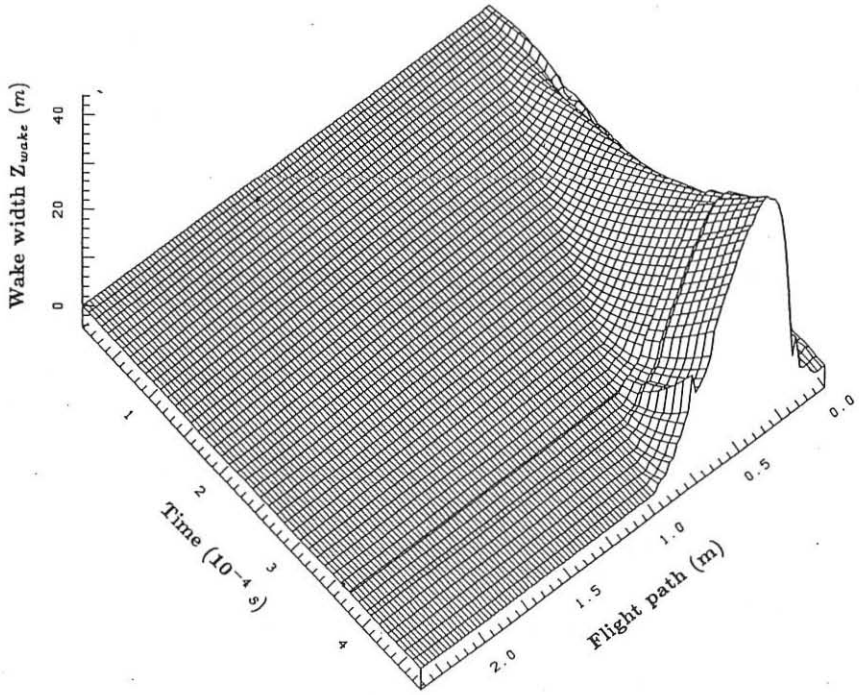

Figure 1:
Pellet wake width measured along the magnetic field lines as a function of pellet path and time.

Figure 2:
Plasmoid density in the pellet wake as a function of pellet path and time.

INSTABILITY OF TOKAMAKS WITH NON-CIRCULAR CROSS-SECTION

D. Lortz

Max-Planck-Institut für Plasmaphysik, IPP-EURATOM Association,
D-8046 Garching bei München

Abstract. The stability of external axisymmetric ideal MHD modes is considered. For a large aspect ratio equilibrium with linear profiles and with the wall infinitely far, it is shown that an arbitrary deviation from the circular cylinder is unstable. This proves a property which, hitherto, has merely been conjectured by several authors.

An axisymmetric equilibrium is described by the Lüst-Schlüter equation

$$\Delta_*\Psi + F = 0, \quad F(s,\Psi) = I'I + s^2p', \quad \Delta_* = \frac{\partial^2}{\partial s^2} - \frac{1}{s}\frac{\partial}{\partial s} + \frac{\partial^2}{\partial z^2} = s^2\nabla\cdot\frac{\nabla}{s^2}$$

for the flux function Ψ. Here, s, ϕ, z are cylindrical coordinates, $p(\Psi)$ is the pressure, and $B_\phi = I(\Psi)/s$ is the toroidal field. The poloidal field $\vec{B}_p$ is related to Ψ by

$$\vec{B}_p = \nabla\phi \times \nabla\Psi.$$

The prime denotes differentiation with respect to Ψ. Let us take $\Psi = 0$ on the plasma boundary S_f, $\Psi > 0$ in the plasma region V_f, and $\Psi < 0$ in the vacuum region V_v. The profile functions $p(\Psi), I(\Psi)$ are chosen such that

$$I'(0) = p'(0) = 0. \tag{1}$$

This choice implies that the current density vanishes everywhere on S_f. If the current density were not zero there, the system could be unstable with respect to peeling modes. If (1) is valid and, in addition, the shear does not vanish, the stability problem for axisymmetric modes can be completely described by the functional

$$\delta W_f \geq \frac{1}{2}\int_{V_f}\frac{d^3\tau}{s^2}\{|\nabla\xi|^2 + |f|^2 + \gamma pR^2|g|^2 - \frac{\partial F}{\partial\Psi}|\xi|^2\},$$

where ξ is the scalar quantity

$$\xi = \vec{\xi}\cdot\nabla\Psi$$

and the surface quantities f, g are defined by

$$f = f(\Psi) = I(\int\frac{1}{s^2}\frac{d^2S}{|\nabla\Psi|})^{-1}\frac{d}{d\Psi}\int\frac{\xi}{s^2}\frac{d^2S}{|\nabla\Psi|},$$

$$g = g(\Psi) = \left(\int \frac{d^2S}{|\nabla\Psi|}\right)^{-1} \frac{d}{d\Psi} \int \xi \frac{d^2S}{|\nabla\Psi|}.$$

If the pressure vanishes on S_f, the energy variation of the system can be written in the form

$$\delta W = \delta W_f + \delta W_v,$$

$$\delta W_v = \frac{1}{2} \int_{V_v} \frac{d^3\tau}{s^2} |\nabla\hat{\xi}|^2$$

with the boundary conditions

(2) $$\xi = 0 \text{ on the magnetic axis,}$$

(3) $$\hat{\xi} = \xi \text{ on } S_f,$$

and

(4) $$\hat{\xi} = 0 \text{ on } S_w,$$

the perfectly conducting outer wall. The minimum of δW corresponds to the eigenvalue problem [1]

(5) $$\Delta_*\xi + \left[(I'I)' + s^2p''\right]\xi + (fI)' + \gamma s^2(pg)' + \sigma\xi = 0 \text{ in } V_f,$$

(6) $$\Delta_*\hat{\xi} = 0 \text{ in } V_v$$

with the boundary conditions (2)-(4) and

(7) $$\nabla\Psi \cdot \nabla(\xi - \hat{\xi}) + fI = 0 \text{ on } S_f.$$

The condition that the lowest eigenvalue be non-negative,

$$\sigma_0 \geq 0,$$

is necessary and sufficient for stability against axisymmetric disturbances.

In this paper the eigenvalue problem (2)-(7) is solved for the straight case if both profiles are linear in Ψ, the position of the wall is infinitely far, and the fluid boundary deviates only slightly from the circle. It is shown that all these configurations are unstable. This contradicts stability investigations dealing with the so-called decay index which yields neutral stability in the large aspect ratio case. So, it has to be concluded that the decay index, which is only a crude estimate of the stability properties, does not give the correct result.
If the profiles $I'I$ and p' are linear in Ψ, conditions (1) imply that

$$I'I = (1 - \beta_p)\lambda\Psi, \quad p' = \beta_p\lambda\Psi$$

with constants $\lambda > 0$, $\beta_p \geq 0$. In polar coordinates r, Θ the equilibrium equation

$$\Delta\Psi + \lambda\Psi = 0, \quad \Delta = \frac{\partial^2}{\partial r^2} + \frac{1}{r}\frac{\partial}{\partial r} + \frac{1}{r^2}\frac{\partial^2}{\partial \Theta^2}$$

has to be solved for the boundary condition

$$\Psi = 0 \quad \text{for} \quad r = R(\Theta),$$

where $R(\Theta)$ describes the given contour and λ is considered as an eigenvalue for the equilibrium problem. If the contour deviates only slightly from the circle with radius R_0, a perturbation parameter ϵ can be introduced by

$$R(\Theta) = R_0 + \epsilon R_1(\Theta) + \epsilon^2 R_2(\Theta) + \cdots \tag{8}$$

According to (8) it is assumed that the solutions of the eigenvalue problem can also be expressed as power series in ϵ:

$$\Psi = \Psi_0 + \epsilon\Psi_1 + \epsilon^2\Psi_2 + \cdots, \quad \lambda = \lambda_0 + \epsilon\lambda_1 + \epsilon^2\lambda_2 + \cdots.$$

The solution of the zeroth-order equation

$$\Delta\Psi_0 + \lambda_0\Psi_0 = 0$$

is, in terms of Bessel functions,

$$\Psi_0 = J_0(\rho), \quad \rho = \sqrt{\lambda_0}r, \quad \lambda_0 = \frac{j_{0,1}^2}{R_0^2},$$

where

$$\rho_0 = j_{0,1} = 2.4048255577$$

is the first zero of the Bessel function $J_0(\rho)$. For the discussion of the solubility conditions the notations

$$\overline{\cdots} = \frac{1}{2\pi}\int_0^{2\pi} r\cdots|_{r=R_0}\, d\Theta$$

$$\langle\cdots\rangle = \frac{1}{2\pi}\int_0^{2\pi}\int_0^{R_0} \cdots r dr d\Theta$$

are introduced. Without restricting the generality it can be assumed that

$$\overline{R_1} = \overline{R_2} = 0, \tag{9}$$

$$\overline{R_1 exp(i\Theta)} = 0, \tag{10}$$

because if these quantities were not zero, they would describe a change of the radius or a shift but not a deformation of the circle. Conditions (10) lead to $\overline{\Psi_1} = 0$, $\lambda_1 = 0$ and in second order to

$$\lambda_2 \langle \Psi_0^2 \rangle = -\Psi_{0,r}(\overline{R_1 \Psi_{1,r}} - \frac{1}{2} R_0^{-1} \overline{R_1^2} \Psi_{0,r})(R_0).$$

The stability problem is also solved as power series in ϵ:

$$\xi = \xi_0 + \epsilon \xi_1 + \epsilon^2 \xi_2 + \cdots, \ \sigma = \sigma_0 + \epsilon \sigma_1 + \epsilon^2 \sigma_2 + \cdots.$$

The interesting eigenvalue $\sigma_0 = 0$ of the unperturbed problem is degenerate, i.e.there are two independent eigenfunctions $\xi_{(1)}, \xi_{(2)}$ belonging to it. These can be chosen as, for instance, the shift in two different directions, or in complex notation as

$$(11) \qquad \begin{cases} \xi_{(1)} = \Psi_{0,r} exp(i\Theta), \quad \xi_{(2)} = \Psi_{0,r} exp(-i\Theta), \\ \hat{\xi}_{(1)} = \dfrac{R_0 \Psi_{0,r}(R_0)}{r} exp(i\Theta), \quad \hat{\xi}_{(2)} = \dfrac{R_0 \Psi_{0,r}(R_0)}{r} exp(-i\Theta) \end{cases}$$

with the orthogonality property $\langle \xi^*_{(k)} \xi_{(l)} \rangle = \langle \Psi^2_{0,r} \rangle \delta_{kl}$, where the star denotes the complex conjugate. The unperturbed solution is a superposition

$$\xi_0 = \sum_{l=1}^{2} a_l \xi_{(l)}, \quad \hat{\xi}_0 = \sum_{l=1}^{2} a_l \hat{\xi}_{(l)},$$

whose coefficients a_l are determined in higher order. The solubility condition in first order takes the form

$$\sigma_1 \langle \Psi^2_{0,r} \rangle a_k = -\lambda_0 \sum_{l=1}^{2} \overline{\xi^*_{(k)} \xi_{(l)} R_1} a_l,$$

The system is unstable unless $\overline{R_1 exp(2i\Theta)} = 0$,wich means that the elliptical deformation of the circle must vanish. This corresponds to the result in [2]. If this is satisfied,it follows that $\sigma_1 = 0$ and the second order has to be considered, which yields the two eigenvalues $\sigma_2 = \langle \Psi^2_{0,r} \rangle^{-1}(-d \pm |c|)$ with

$$d = \lambda_0^{\frac{3}{2}} \Psi^2_{0,r}(R_0) \sum_{\nu \neq 0} |\nu| |C_\nu|^2 / \rho_0, \quad R_1 = \sum_{\nu=-\infty}^{+\infty} C_\nu exp(i\nu\Theta).$$

This completes the instability proof. More details of the theory will be published elsewhere.

References.

[1] Lortz, D., On the Stability of Axisymmetric MHD Modes, Z. Naturforsch. 43a, (1988)
[2] Haas, F.A. and Papaloizou, J.C., MHD stability of toroidal equilibria to axisymmetric modes, Nuclear Fusion 17, 721-728 (1977)

A 1+1 D MODEL OF ION-IMPURITY PFIRSCH-SCHLÜTER TRANSPORT IN A ROTATING TOKAMAK PLASMA

R. Zanino [†,*], K. Lackner [*], C.T. Hsu [‡] and D.J. Sigmar [‡]

[*] Max-Planck Institut für Plasmaphysik, EURATOM Association
D 8046 Garching, Federal Republic of Germany
[†] Dipartimento di Energetica, Politecnico, Torino, Italy
[‡] Plasma Fusion Center, Massachusetts Institute of Technology,
Cambridge (MA) 02139 USA.

Introduction

We address in this paper the question of particle and angular momentum transport in a highly collisional tokamak plasma which, 1) contains a single impurity species of sufficiently high concentration that the friction of the electrons on the ions and the impurities is negligible, and 2) is toroidally rotating with a velocity such that (at least) the impurities are supersonic. Under the latter conditions (typical of neutral beam injected plasmas) the transport analysis intrinsically requires a 2-D treatment: differently from the conventional case of small rotation, the densities and the elctric potential are no more flux surface functions, due to the action of inertial forces.

Compared to previous ones ([3,4,5] and references therein) our model [1,2] contains (all and) only the purely neoclassical contributions pertaining to the high collisionality regime (no *ad hoc* terms), and we can afford (in principle) arbitrarily large poloidal variations of the relevant plasma parameters.

Brief outline of the model

We build a hydrodynamic model by taking velocity moments of the Fokker-Planck equation, and the resulting hierarchy is truncated assuming the plasma is in the high collisionality regime (details are to be found in [1,2]). The set of moment equations is then expanded in the small parameter δ_{pi} (ratio between the ion Larmor radius in the poloidal field and a characteristic radial scale length). To each order in δ_{pi} corresponds a separate time scale, and we present here the essential features of the steady states obtained up to the second order, which describes the slowest evolution in our problem (the fastest, zero-th order time scale, being of the order of the inverse of the ion transit frequency).

Our model includes all effects related to toroidicity (in the Pfirsch- Schlüter limit), inertia and viscous stress tensor. We do not attempt here to discuss energy transport; therefore a constant uniform temperature is assumed, and its value is chosen such as to give, for densities in the experimental range, both ion species well in the Pfirsch-Schlüter regime (thermal friction should not qualitatively change our results). A low beta, large aspect ratio equilibrium with circular concentric magnetic surfaces is taken as the fixed background for this transport model.

Zero-th order time scale

To this order the plasma is described by the balance between parallel inertial, pressure, and electric forces (also, quasineutrality of the plasma is imposed). The flow is rigid toroidal separately on each magnetic surface, and species independent ($V_j^{(0)} = V_\phi e_\phi = \omega^{(0)} R e_\phi$) [5, 6, 7]. The density distribution at steady state is given by

$$n_j^{(0)}(r,\theta) = \bar{n}_j(r) \frac{A_j^{(0)}}{< A_j^{(0)} >}$$

where we defined

$$A_j^{(0)}(r,\theta) \equiv \exp\left(\frac{m_j \omega^{(0)2} R^2}{2T}\right) \left[\frac{\dot{n}_i^{(0)}(\theta=0) + Z n_Z^{(0)}(\theta=0)}{n_i^{(0)} + Z n_Z^{(0)}}\right]^{Z_j}.$$

To this order the average quantities $\bar{n}_j$ and $\omega^{(0)}$ are taken as given. Notice that the density poloidal distribution is up-down symmetric to this order, due to the absence of ion-impurity friction.

First order time scale

Ion-impurity friction drives the evolution to this order through the factor [1, 2]

$$\left(m_i - \frac{m_Z}{Z}\right) \frac{R^2}{T} \omega^{(0)} \frac{\partial \omega^{(0)}}{\partial r} + \left(\frac{\partial}{\partial r} \mathrm{Log} \frac{\bar{n}_i}{< A_i^{(0)} >} - \frac{1}{Z} \frac{\partial}{\partial r} \mathrm{Log} \frac{\bar{n}_Z}{< A_Z^{(0)} >}\right)$$

proportional to the difference in the first order diamagnetic flows. The first term is the new contribution to the transport fluxes coming from rotation, and for $\omega^{(0)} \to 0$ the driving force reduces to the well known result in the absence of rotation [8]. The mass and parallel momentum balances for ions and impurities are evolved to steady state to determine the first order poloidal distributions. The radial gradients in the driving force are taken as given quantities, because they vary on the slower, second order time scale. A typical result for an ion Mach number of 0.75 is shown in Fig.1 (ions=dashed,

impurities=solid, $\theta = \pi$ outboards), where the impurity species is Oxygen VI, as for all the other numerical examples presented in this paper. Notice that the densities (given here normalized to their respective averages) are now up-down asymmetric, due to friction; also, nonzero steady state poloidal flows are obtained.

Second order time scale and 1+1 D algorithm

The evolution of the average ion and impurity density, and of the toroidal angular momentum of the plasma is described by

$$\frac{\partial < n_j^{(0)} >}{\partial t_2} = \frac{1}{eZ_j}\frac{1}{rR_0}\frac{\partial}{\partial r}\left(\frac{r}{B_{\theta 0}} < RF_{\|j}^{(1)} >\right) + < S_j >$$

$$\frac{\partial}{\partial t_2}\left(\sum_j m_j < Rn_j^{(0)} V_{\phi j}^{(0)} >\right) = \frac{1}{rR_0}\frac{\partial}{\partial r}\left(\frac{r}{B_{\theta 0}}\omega^{(0)} \sum_j \frac{m_j}{eZ_j} < R^2 F_{\|j}^{(1)} >\right) + \sum_j < RM_{\phi j} >$$

where $F_{\|}^{(1)}$ is the first order ion-impurity parallel friction (classical contributions have been presently neglected but will be included in future numerical experiments). As boundary conditions we impose zero particle fluxes (therefore we also set $S_j = 0$ in order to get a steady state), and a flux of angular momentum proportional to the toroidal rotation velocity.

One sees that the dependence of the radial fluxes on $\bar{n}$ and $\omega^{(0)}$ is not explicitely known, differently from the low rotation case, but only implicitely through flux surface moments of the friction. The latter results in turn from the steady state reached by the fast first order evolution, whose driving force contains radial gradients evolving only on the slow second order time scale. The 1+1 D algorithm can thus be summarized as follows: 1) start with given radial profiles, 2) compute the zero-th and first order steady states on several different magnetic surfaces, 3) update the radial profiles integrating one step forward in time the second order equations, 4) go to 2) and repeat until a steady state is reached on the slowest time scale.

In Fig.2 the initial (solid) and steady state (thick) radial profiles of $\bar{n}_i$, $\bar{n}_Z$ (in m^{-3}) and ion Mach number are shown, for the case of an isolated plasma. (The dashed line indicates the profile foreseen by the theory [8] for the case of low rotation.) One notices impurity peaking towards the center, and that the whole plasma rotates in this case as a rigid body. The results corresponding to a uniform momentum source applied on the plasma cross section are shown in Fig.3. The density profiles are now sensibly different from the case of low rotation, because non zero rotation gradients are sustained by the source at steady state.

References

[1] C.T.Hsu and D.J.Sigmar, MIT Report PFC/JA-88-14 (1988), (unpublished).

[2] C.T.Hsu, D.J.Sigmar and R.Zanino, Sherwood Controlled Fusion Theory Meeting 1988, Paper 3D9, (unpublished).

[3] K.H.Burrell, T.Ohkawa and S.K.Wong, *Phys. Rev. Lett.* **47**, 511 (1981).

[4] W.M.Stacey and D.J.Sigmar, *Phys. Fluids* **27**, 2076 (1984).

[5] S.K.Wong, *Phys. Fluids* 30, 818 (1987).

[6] J.W.Connor, *et al.*, Plasma Phys. and Contr. Fusion **29**, 919 (1987).

[7] D.J.Sigmar, R.Zanino and C.T.Hsu, *Bull. Am. Phys. Soc.* **32-II**, 1917 (1987).

[8] P.H.Rutherford, *Phys. Fluids* **17**, 1782 (1974).

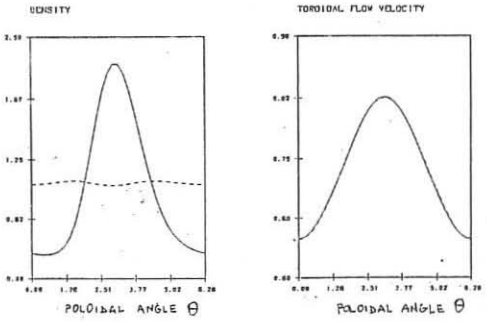

Fig. 1

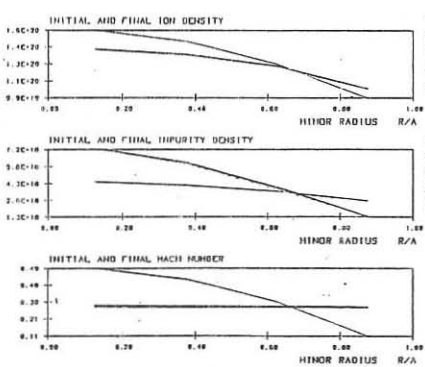

Fig. 2

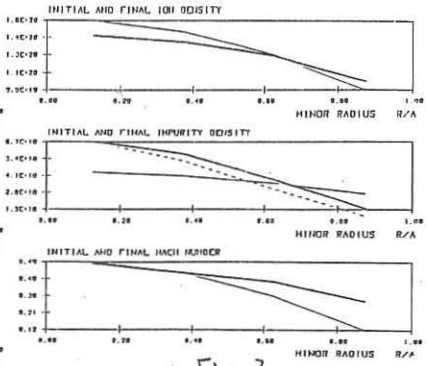

Fig. 3

AN ALTERNATIVE APPROACH TO THE ANALYSIS OF THE ACTIVE VERTICAL STABILIZATION IN A TOKAMAK

R. Albanese[1], G. Ambrosino[2], E. Coccorese[3], F. Garofalo[2], G. Rubinacci[2]

[1] IIE, Univ. of Salerno, 84081 Baronissi, Salerno, Italy
[2] DIS-DIE, Univ. of Napoli, V. Claudio 21, 80125 Napoli, Italy
[3] IICE, Univ. of Reggio Calabria, V. V. Veneto 69, Reggio Calabria, Italy

Introduction

Some of the present day experiments as well as the next generation tokamaks are based on highly elongated plasma configurations, which are unstable with respect to vertical displacements. The design of the active control system for the stabilization of these motions is usually based on the assumption that the input signal for the controller is the plasma vertical position. This quantity, which for non-rigid plasma motions requires a more precise definition, is not directly available and is usually derived from flux and field measurements.

The aim of this paper is to show how the detection system (i.e. the set of magnetic measurements) can directly be included in a mathematical model suitable for the application of the LQG-LTR stabilization technique [1]. The objective of this kind of control is to keep all the parameters of the whole system (stabilization currents and hence plasma position) as close as possible to their nominal (equilibrium) values, instead of focusing the attention on a single quantity (e.g. the plasma position).

With respect to simpler techniques (such as PID controllers based on single input single output models), this design phylosophy provides a better performance in terms of control power and settling time and guarantees wider stability margins.

The model

In the limit of zero plasma mass [2], the problem can be described [3] by the linearized dynamic equation:

$$L^{*}\dot{I} + R\,I = D\,V \qquad (1)$$

and by the linearized measurement equation

$$\Psi_s = L_s\,I \qquad (2)$$

where:

- I is the set of the stabilizing currents in the conducting structures;
- V is the set of applied voltages;
- Ψ_s is the set of flux measurements;
- L^{*} is the modified inductance matrix of the conducting structures, defined as $L^{*}_{jk}=(\partial\psi_j/\partial I_k)$ in the presence of the plasma [3];
- R is the resistance matrix of the conducting structures;
- D is an incidence matrix specifying the circuits to which the external voltages are applied;
- L_s is the matrix of mutual inductances between flux measurement coils and stabilizing circuits.

It should be noticed that, disregarding the plasma inertia, its

vertical position can be expressed as a linear combination of the stabilizing currents [2,3].

The stabilization technique

The objective of the active control is to select the input voltages that drive the currents I in the stabilizing circuits to their nominal values, corresponding with I=0 in eqns. (1)-(2), so forcing the plasma ring to occupy its equilibrium position. This objective should be accomplished trading off between the power involved in the control and the deviation from the equilibrium state. This is achieved by designing a feedback controller which minimizes a quadratic performance index of the form

$$J = \int_{t_0}^{\infty} (I^T \Theta\ I + V^T D^T \Gamma\ D\ V)\ dt \qquad (3)$$

where Θ and Γ are designer chosen weighting matrices (positive semidefinite and positive definite respectively). In particular Θ can be selected such as the first term of the performance index is the squared plasma displacement. Moreover, the feedback control is required to be robust with respect to unmodelled phenomena and external disturbances, or , equivalently, to have sufficient stability margins.

Since most of the currents in the stabilizing circuits are not directly measurable, the robust feedback control design minimizing (3) must be split into two steps [4]:

a) find an estimate of the external currents starting from the flux measurements;

b) find the optimal feedback on the assumption that the estimates of the currents are the true system state.

As regards phase *(a)* of the design, the estimator of the currents has the form

$$L^* \dot{\hat{I}} + R\ \hat{I} = D\ V + L^* K\ (\Psi_s - L_s \hat{I}) \qquad (4)$$

where $\hat{I}$ is the estimate of currents I, and K is the so called observer gain matrix. The design of the gain matrix K is critical as far as the robustness of the closed loop system is concerned.

Once matrix K has been fixed, phase *(b)* can be carried out evaluating the feedback input voltages as a combination of the estimated currents:

$$V = - \Gamma^{-1} D^T P\ \hat{I} \qquad (5)$$

where P is the positive definite solution of the Riccati equation

$$- R\ L^{*-1} P - P\ R\ L^{*-1} + \Theta - P\ L^{*-1} D^{-1} \Gamma^{-1} D^{-T} L^{*-1} P = 0 \qquad (6)$$

In order to ensure sufficiently high phase and gain margins the observer gain matrix K is given by [1]:

$$K = \Sigma\ L_s^T\ R^{-1} \qquad (7)$$

where Σ is the positive definite solution of the Riccati equation

$$- R L^{*-1}\Sigma - \Sigma R L^{*-1} + Q_o + q^2 L^{*-1} D \Pi D^T L^{*-1} - \Sigma L_s \Omega_o^{-1} L_s \Sigma = 0 \qquad (8)$$

where Ω_o and Q_o represent given process noise and measurement noise intensities, Π is any positive definite matrix, and q is a real positive parameter.

With the previous definitions, taking q=0, K is the steady state gain of a Kalman filter for system (1) with measurement equation (2); for $q \to \infty$, infinite gain margin and 60^0 phase margin can be achieved for system (1)-(2) with estimator (4) and feedback control (5).

Results and conclusions

The features of the procedure presented here are illustrated with reference to the configuration analysed in [3]. This case refers to a NET plasma configuration [5] with an idealized axisymmetric geometry of the stabilizing conductors, as shown in Fig. 1. Therefore, from the technical point of view, the results must be regarded only qualitatively, because a more precise and significant analysis requires a more detailed schematization of the conducting strustures.

The system has been stabilized on the assumption of a rigid displacement model [2,3]. Three different controllers have been designed.

The first one is a classical PD controller driven in feedback by a single input corresponding with the plasma displacement; its gains (G=20kV/m, τ_d=10ms) have been computed such as to have a good compromise between installed power and response time (measured by the eigenvalue of the closed loop system which is closest to zero).

The second one is a full state controller, based on the assumption of complete availability of the state variables; in this case the 6 state variables, i.e. the active current and the 5 passive currents, are derived by the measurements of 4 fluxes and their derivatives. The Γ matrix (which in the case under cosideration reduces to a scalar parameter) in the performance index (3) has been selected by using a trial and error procedure.

The third one differs from the second controller because only the 4 flux measurements are used; therefore the 6 state variables are estimated via an LTR designed observer.

Simulations have been performed, taking the initial conditions for the stabilizing currents according to the growth mode of the open loop system, scaled such as to correspond to a plasma vertical displacement of 1 cm.

Fig. 2 shows currents and voltage in the active coil and plasma displacement as computed using the rigid displacement model with the three different controllers, while Tab. I summarizes the main features of the closed loop systems.

The results show that the full state stabilization has a better behaviour with respect to a PD controller. The LQG-LTR controller provides an intermediate performance as far as active current and plasma displacement are concerned; the lower value of the active voltage is essentially due to the zero initial conditions of the estimated currents $\hat{I}$.

This deterioration of performance, together with the problems related to the presence of the observer in terms of system robustness, highlights the necessity of a full state approach. This can be accomplished by increasing the number of measurements or by reducing the order of the

mathematical model without dramatically reducing the consistency with the real phenomena.

References

[1] J.C. Doyle and G. Stein, "Robustness with Observers", IEEE Trans., Vol. AC-24, no. 4, 1979.
[2] INTOR GROUP, International Tokamak Reactor: Phase Two A Part II, IAEA, Vienna, 1986.
[3] R. Albanese, E. Coccorese and G. Rubinacci, "Plasma Modeling for Vertical Instabilities", to appear.
[4] H. Kwakernaak and R. Sivan, "Linear Optimal Control Systems", Wiley Interscience, 1972.
[5] E. Salpietro et al., "NET Operation Cycle", Fusion Technol., Vol. 14, 1988.

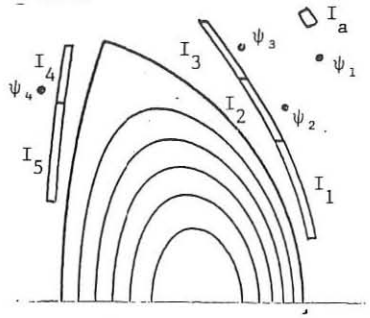

Fig.1: Geometry.

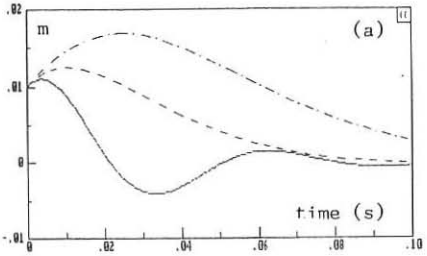

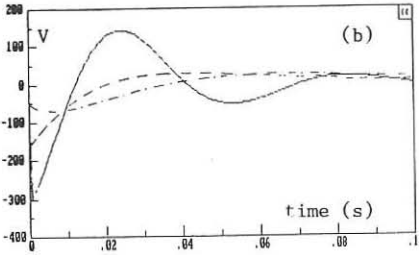

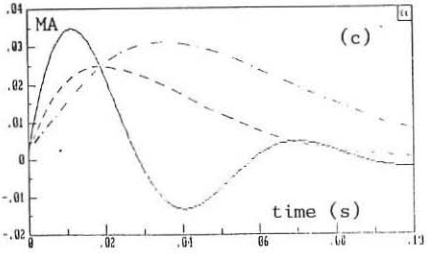

Fig.2: Plasma displacement (a), applied voltage (b) and active current (c): ———— PD, - - - - - full state, — · — · — LQG-LTR.

Tab.I: BEHAVIOUR OF THE THREE DIFFERENT CONTROLLERS

Controller	λ_{min} [s^{-1}]	V_{max} [V]	I_{max} [kA]
PD	-20.8±122.7j	301	34.8
Full state	-44.0± 26.8j	162	24.8
LQG-LTR	-35.6	70	31.0

A PERTURBATION MODEL OF TOKAMAK MHD EQUILIBRIA FOR STUDY OF PLASMA BOUNDARY CONTROL

K.Takeuchi, M.Abe, H.Fukumoto and M.Otsuka

Energy Research Laboratory, Hitachi, Ltd.
1168 Moriyama-cho, Hitachi-shi, Ibaraki-ken, 316 Japan

1. INTRODUCTION

Precise control of the plasma surface boundary is of increasing importance with regard to the reliable operation of H-mode discharges, as well as the protection of the first wall and RF launchers. In order to simulate dynamical plasma boundary deformation, we propose a new model based on a linear perturbation analysis of 2-dimensional tokamak equilibria. This model can avoid difficulties which arise from solving time evolution of positionally unstable plasma equilibria around an equilibrium. In this paper, the numerical model is presented, and its applicability to vertical position control is tested through comparison with experimental results on the Hitachi Tokamak (HT-2).

2. A PERTURBATION MODEL OF TOKAMAK MHD EQUILIBRIA

The tokamak MHD equilibria can be described by the Grad-Shafranov equation. The variation around an equilibrium is obtained by perturbation analysis of the equation assuming a small deviation, i.e.,

$$\left(\frac{\partial^2}{\partial R^2} - \frac{1}{R}\frac{\partial}{\partial R} + \frac{\partial^2}{\partial Z^2} \right) \Psi_p{}^1 + \mu_o R\, j^1 = 0 \qquad (1)$$

$$j^1 = \frac{\partial j}{\partial I_p} I_p{}^1 + \frac{\partial j}{\partial W_k} W_k{}^1 + \frac{\partial j}{\partial W_m} W_m{}^1 + \frac{\partial j}{\partial \Psi_A} \Psi_A{}^1$$

$$\Psi_A \equiv \Psi - \Psi_B = \Psi_p(I_p) + \Psi_c(I_c) - \Psi_B,$$

where R and Z are the cylindrical coordinates; Ψ is the magnetic flux function; j, the plasma current density; I, the toroidal current; W_k, the kinetic energy; and W_m the magnetic energy of plasma internal area. Superscript 1 denotes the first order perturbed quantity, subscripts P, C and B represent the plasma, other toroidal currents and the plasma surface boundary, respectively. Since the boundary value $\Psi_B{}^1$ is unknown, Eq.(1) must be solved iteratively.

Dependence of mutual inductances between plasma and other toroidal currents on plasma current distribution are evaluated by solving Eq.(1). The boundary deformation is also obtained as functions of I^1, $W_k{}^1$ and $W_m{}^1$.

Then electric circuit equations for plasma current and toroidal currents, i.e.,

$$\frac{d}{dt}(M \cdot \vec{I}) + \Omega \cdot \vec{I} = \vec{V}, \qquad (2)$$

are solved considering time evolution of the inductance M, where $\vec{I}$ and $\vec{V}$ are vectors which denote the toroidal currents and their power supply voltages, matrix Ω is the resistances. Eddy currents on the vacuum vessel are expanded into four axisymmetric eigen modes and considered as toroidal currents without power supplies.

The modal analysis of Eq.(2) gives the growth rate of plasma vertical instability as that of an unstable eigen mode of the system. The plasma boundary behavior is obtained by solving Eq.(2) according to the power supply control algorithm,

$$V = G_0 X + G_1 I, \qquad (3)$$

where V, I, X and G_i(i=0,1) are the power supply voltage, the coil current, the controlled variable and the control gains for each poloidal field coil system.

3. NUMERICAL RESULTS AND THEIR COMPARISON WITH THE EXPERIMENTS

In order to confirm the applicability of this model, the plasma behavior in vertical instability on the HT-2 is compared with the model results for growth rate and surface boundary displacement. Typical parameters of the HT-2 are listed in Table 1, and its poloidal cross section is given in Fig.1. Feed back controls are holded at the flat top of the plasma current to cause the vertical instability.

The plasma vertical position is measured by signal difference ΔB_p of two magnetic probes installed at top and bottom of the vacuum vessel. Plasma surface boundary is determined by magnetic field fitting technique [1,2]. Externally applied vertical field curvature $n \equiv -R/B_V \cdot \partial B_V/\partial R$ is evaluated at the center of the plasma current, using the poloidal field coil currents obtained by the fitting scheme.

Contours in Fig.2 show a typical equilibrium configuration of HT-2, obtained by an ideal MHD equilibrium code. The surface boundary deformation due to the current deviation in coils DCH1-2(see Fig.1), evaluated by both the perturbation model and full MHD equilibrium computation, are also indicated by arrows. The surface boundary deformation agree well with both two models, though the plasma displacements are $\Delta Zp \fallingdotseq 0.03m$ (30% of the plasma minor radius). This shows the validity of linear perturbation analysis of plasma vertical displacements.

The relation between the n-index and the instability growth rate is shown in Fig.3. The experimental results are shown by circles with error bars. The results of the perturbation model are shown by triangles and squares for the normalized internal inductance $l_i \fallingdotseq 2.2$ and 1.4,

respectively, while the result of a ring current model[3], in which the plasma is approximated by single filament loop, is shown by a solid line. The parameter $\beta_p+l_i/2$ (where β_p is poloidal beta) is fixed at 1.3 in the numerical calculation according to the experiments.

The perturbation model results for the two cases agree with that of the ring current model, which is the limit of peaked plasma current. This shows that the difference in plasma current profile does not have a serious effect on the vertical instability in the range $l_i>1.4$. The calculated growth rate dependence on n-index agrees with experimentally obtained one, and their differences are within a factor of 2. This difference is caused by localized high resistance areas for the eddy current flow, which are not considered in this axisymmetric model.

The plasma boundary displacement is also simulated and compared with experiment. Fig.4 shows time evolution of a plasma boundary position Z_{top} which is the highest point of the surface. The plasma vertical position is controlled by two poloidal coil systems (see Fig.1) throughout the discharge. The parameters in Eq.(3) are $X=I_p\triangle Z_p$ ($\propto \triangle B_p$), $G_0=2.7$ (V/Am) and $G_1=0$ for DCH1-2 and $G_1=1.0$(V/A) for ACH1-2. The instability occurs at 19ms. In the simulation, the displacement of Z_{top} is calculated for the cases of the gains $G_0=1.35$, $G_0=2.7$ and $G_0=13.5$, where the delay time 0.1ms of the power supply is assumed (for 5kHz transistor choppers). The perturbation is externally added in this calculation at 19ms. As shown in Fig.4, the amplitude and time evolution of Z_{top} displacement is well represented by the simulation for the case of actual control gain $G_0=2.7$, which shows the vertical position control system is adequately described by this model.

4. SUMMARY

A perturbation model of 2-dimensional MHD equilibria was developed and combined with the electric circuit model to study the plasma position and its surface boundary control. The model was checked through comparison with the full MHD equilibrium computation and the experiments on the Hitachi Tokamak (HT-2) for the plasma vertical instability. The agreement between the results of the perturbation model and these of the full MHD computation was good. The vertical instability growth rate obtained by this model agreed with that of the filament plasma current model, and with experimentally obtained ones within a factor of 2. The time evolution of the plasma boundary was adequately represented by this model. These results show that this model is applicable to the plasma vertical position and its surface boundary control.

REFERENCES

[1] SWAIN, D.W., NEILSON, G.H., Nucl. Fusion 22 (1982) 1015.
[2] ABE, M., et al., Kakuyugo Kenkyu 60 (1989) in press.
[3] FUKUYAMA, A., et al., Jpn. J. Appl. Phys. 14 (1975) 871.

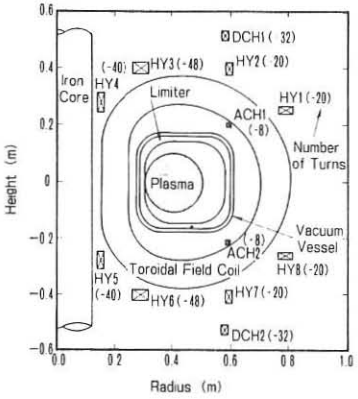

Fig.1 Poloidal cross section of HT-2. Coil connections for elongated plasmas are as follows.
HY1-2-7-8: Primitive Vertical Field Control
HY3-5, HY4-6: Radial Position and Elongation Control
DCH1-2, ACH1-2: Vertical Position Control

Table 1. Typical Parameters of HT-2

Major Radius	0.41 m
Minor Radius	0.10 m
Plasma Current	40 kA
Toroidal Field	1 T
Vertical Elongation	1.5
Plasma Duration	40 ms

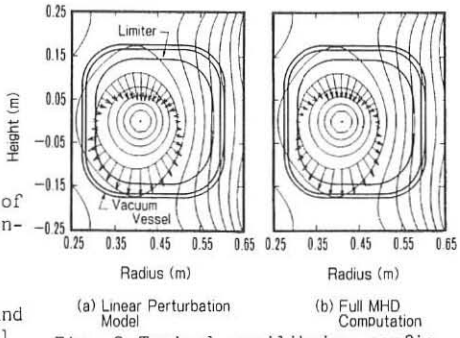

Fig. 2 Typical equilibrium configurations of HT-2. The contours show the basic equilibrium and the arrows, the deformation multiplied by a factor of 2.

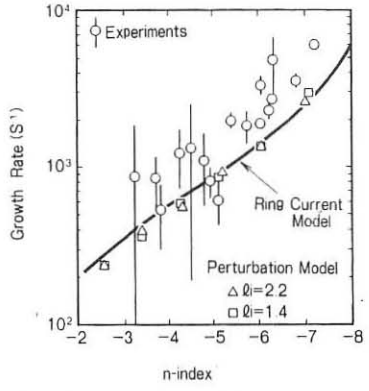

Fig. 3 Vertical instability growth rate as a function of n-index.

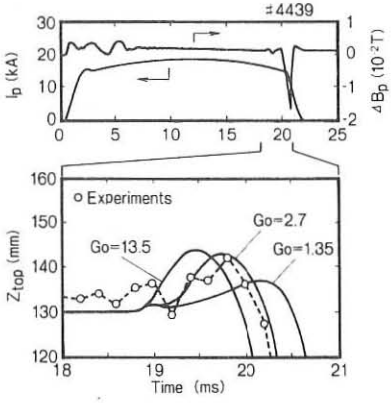

Fig. 4 Time evolution of the highest plasma boundary position.

A METHOD FOR LOCAL TRANSPORT ANALYSIS IN TOKAMAKS WITH ERROR CALCULATION

G.M.D.Hogeweij, G.Hordósy* and N.J. Lopes Cardozo

FOM Institute for Plasma Physics, Association EURATOM-FOM, 'Rijnhuizen',
P.O.Box 1207, 3430 BE Nieuwegein, The Netherlands
* on leave from Central Research Institute for Physics, Budapest, Hungary

Introduction

Global transport studies have revealed that heat transport in a tokamak is anomalous, but cannot provide information about the nature of the anomaly. Therefore, local transport analysis is essential for the study of anomalous transport. However, the determination of local transport coefficients is not a trivial affair. Generally speaking one can either directly measure the heat diffusivity, χ, by means of heat pulse propagation analysis [2,4,5], or deduce the profile of χ from measurements of the profiles of the temperature, T, and the power deposition [1,2]. Here we are concerned only with the latter method, the local power balance analysis.

For the sake of clarity heat diffusion only is considered:

$$\rho = - \text{grad}T / q \qquad (1)$$

where $\rho = \kappa^{-1} = (n\chi)^{-1}$ is the heat resistivity and q is the heat flux per unit area. It is assumed that the profiles T(r) and q(r) are given with some experimental error. In practice T(r) is measured directly, e.g. from ECE spectroscopy, while q(r) is deduced from the power deposition and loss profiles. The latter cannot be measured directly and is partly determined on the basis of models. This complication will not be considered here.

Since in Eq.(1) the gradient of T appears, noise on T can severely affect the solution ρ. This means that in general some form of smoothing must be applied. A criterion is needed to select the optimal smoothing. Too much smoothing will wipe out the details, whereas with too little smoothing the noise will distort the reconstructed profile of ρ.

Here a new method to solve Eq.(1) is presented which expresses $\rho(r)$ as a cosine-series. The coefficients of this series are given as linear combinations of the Fourier coefficients of the measured T- and q-profiles. This formulation allows i) the stable and accurate calculation of the ρ-profile, and ii) the analytical calculation of the error in this profile.

Method

The transport is treated as a 1-D problem in cylindrical geometry. It is well-known that the temperature profile in a tokamak is of a self-similar shape in practically all conditions. This suggests an expansion of the profile around this typical shape, for which a Gaussian is taken. As an educated guess for the ρ-profile ρ is taken uniform, $\rho(x) = \rho_0$, where x denotes the normalized radius, r/a. Hence we write:

$$T(x) = T_0(x) + T_1(x) \qquad T_0(x) = T_0(0)\exp(-x^2/\lambda^2) \qquad (2)$$

$$q(x) = q_0(x) + q_1(x) \qquad q_0(x) = h_0\, 2x\, \lambda^{-2}\exp(-x^2/\lambda^2) \qquad (3)$$

First λ and h_0 are determined by fitting q_0 to the deduced q-profile, secondly $T_0(0)$ is determined by fitting T_0 to the measured T-profile. In most practical cases we can satisfy the condition $q_1/q_0 \ll 1$ everywhere, so that we can make a Taylor-expansion of ρ:

$$\rho = - (T_0'/q_0)\,(1+T_1'/T_0')\,(1+q_1/q_0)^{-1} = \rho_0\,(1+T_1'/T_0' - q_1/q_0 - T_1'q_1/T_0'q_0) \qquad (4)$$

where $\rho_0 = T_0(0)/h_0$. We approximate the elements of this expression by Fourier series. To get well-behaved Fourier expansions the interval of x is extended from [0,1] to [-2λ,2λ]. The profiles are mirrored around x=0, and a continuation of the profiles beyond x=1 is made such that the derivatives vanish at $x = \pm 2\lambda$.

For T_0' and q_0 the Fourier series are calculated analytically. They are sine series. The lowest order sine is divided out and cosine series for $(T_0')^{-1}$ and q_0^{-1} are obtained by making a Taylor expansion. The Fourier expansion of the measured profiles T_1' and q_1 are determined numerically with a FFT routine. Thus ρ is expressed as :

$$\rho = \sum \alpha_n \cos(nx\pi/2\lambda) \qquad (5)$$

The α_n are complicated bilinear combinations of the Fourier coefficients of the measured profiles. An expression for α_n is given in [3].

Summarizing, the procedure is to firstly determine ρ_0, $T_0(0)$ and λ by fitting q_0 and T_0 to the measured profiles, secondly determine the Fourier coefficients of T_1' and q_1 and finally insert those in the expression for α_n to find the solution ρ with Eq.(5).

In the experimental situation one has an estimate of the noise on the measured T profile. We assume white noise for this study. Uncertainties in the determination of the q-profile will not be considered here, but can be treated analogously.

The noise level can be indicated in the Fourier spectrum of the profiles. In the computation of ρ the Fourier series of T and q should be truncated at the highest significant harmonic. This criterion can be built into a code, which then automatically calculates ρ with the maximum amount of detail that can be extracted from the measurements.

Testresults and Error Analysis

To test the method, a computer code was made that takes profiles of ρ and the power density (p) as input and computes the corresponding profiles of T and q. The generated T-profile is perturbed with random noise and subsequently the ρ-profile is reconstructed from this perturbed T-profile and the computed q-profile, following the recipe described above. The noise added to the T-profile has a Gaussian probability distribution, with a standard deviation σ_T which is given as a fraction of the central temperature. For comparison also a straightforward numerical solver is used, which calculates T' by fitting a parabola to five subsequent data-points and then evaluates Eq.(1) directly.

By making many (M) runs with the code, the variance σ_ρ^2, a measure of the quality of the reconstruction is calculated:

$$\sigma_\rho^2 = (NM)^{-1} \sum\sum [\rho_{reconstructed} - \rho_{input}]^2 \qquad (6)$$

The summations are over the different runs and the measuring points in the profile, respectively. N is the number of measuring points. σ_ρ^2 can be written as

$$\sigma_\rho^2 = \sigma_{\rho\,stat}^2 + \sigma_{\rho\,syst}^2 \qquad (7)$$

with

$$\sigma_{\rho\,stat}^2 = (NM)^{-1} \sum\sum [\rho_{reconstructed} - \langle\rho_{reconstructed}\rangle]^2 \qquad (8)$$

and

$$\sigma_{\rho\,syst}^2 = N^{-1} \sum [\langle\rho_{reconstructed}\rangle - \rho_{input}]^2 \qquad (9)$$

Here < > denotes an average over many runs. Hence σ_ρ is the quadratic sum of the average statistic error of each point of the profile and the systematic error in the reconstruction.

In Fig.1a and 1b the results are presented for two cases: a) a uniform ρ-profile, b) a ρ-profile which exhibits a local minimum (which could represent a large magnetic island). The noise level is 2.5% of T(0) in these cases.The profile of the power density corresponds to an experimental situation where half of the input power is lost through radiation in the edge. Input data are based on expected values of the new Dutch tokamak RTP : T(0) = 1 KeV, P_{total} = 200 KW, R = 0.72 m, a = 0.16 m.

The plots on the left show the normalized input profiles of p, ρ, and the corresponding profile of T. The plots on the right show the input ρ-profiles together with $<\rho_{reconstructed}>\pm$ standard deviation. The hatched areas correspond to the new method; the broken lines (----) to the direct numerical solver. Clearly the new method gives in both cases a better result than the direct numerical solver. Both the systematic and the statistic error are significantly smaller.

It should be noted that the program automatically truncated the Fourier-series of T and q at the proper harmonic, i.e. where the spectrum sinks in the noise. For the T-profiles used in Fig.1a and 1b this happens after the 2nd and 4th harmonic, respectively.

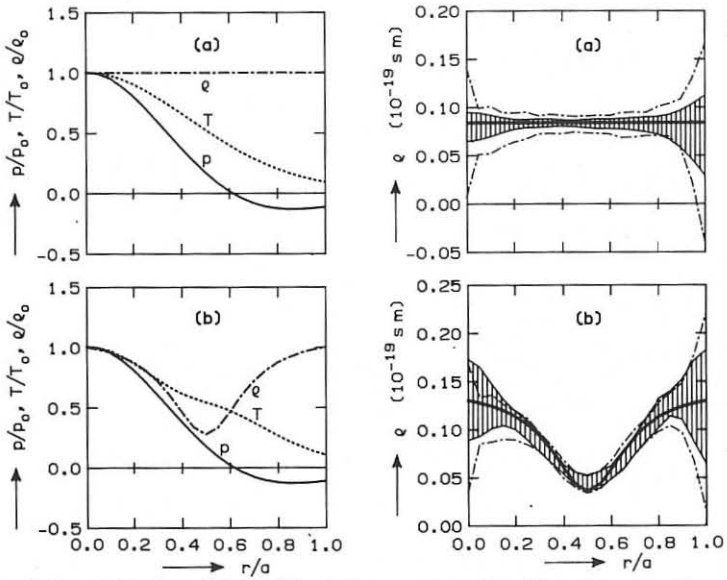

Fig. 1. Reconstruction of the profile of ρ from measured profiles of T and p using a direct solver (----) and the new method (——)

To further illustrate this, in Fig.2a and 2b the values of σ_ρ^2, $\sigma_{\rho\,stat}^2$ and $\sigma_{\rho\,syst}^2$ are plotted as a function of the number of harmonics that are retained in the spectra of T and q for the profiles shown in fig. 1a and 1b respectively. The position of the minimum is a function of σ_T and of the profile shapes. In case a, the profiles are smooth, hence the systematic error is small even when the spectra are truncated at a very low harmonic. In case b, the profiles do have significant higher harmonics; hence truncating the spectra at too low harmonics leads to a large systematic error. Clearly in this case an optimal reconstruction is obtained when using 4 harmonics.

Since estimates of errors in the Fourier coefficients of T and q are known, the statistic errors in the Fourier coefficients of ρ can be computed straightforwardly. From this error spectrum the errors on the points of the reconstructed ρ-profile are obtained. The following simple expression gives a reasonable estimate for σ_ρ at a point x in [0,1] :

$$\sigma_{\rho(x)\,stat} \approx \rho_0 \, | \, T_0'(x)^{-1} \, | \frac{\pi}{\lambda} \sigma_T \sqrt{N_t^3/3N} \qquad (10)$$

where N_t is the number of terms taken in the Fourier series of T.

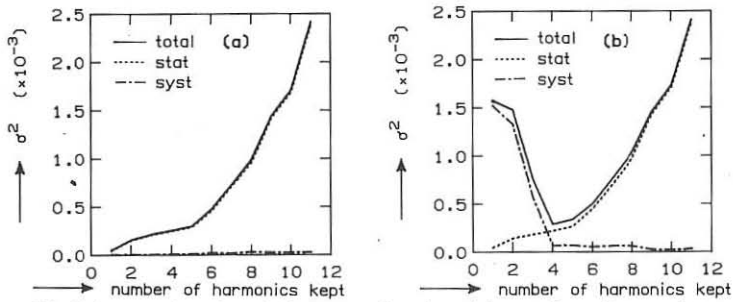

Fig. 2.Systematic and statistic error as function of the number of harmonics

In Fig.3 the errors for case b) according to Eq.(10) are plotted as a function of radius, and compared to the errors that are computed by making many runs with random variation of the input. Clearly the new formalism provides us with a means to assess the statistical error in the reconstructed ρ-profile in an analytic way.

Conclusion

A formalism is constructed to calculate ρ from the heat diffusion equation ρ=-gradT / q. By expanding the profiles around an educated guess, we were able to express ρ as a linear combination of the Fourier coefficjents of the profiles of T and q. This linear form allows the analytic calculation of the propagation of errors.An optimal reconstruction is obtained when the quadratic sum of the statistic and systematic errors is minimized. The error bars on the result can be computed directly from the errors on the T- and q-profiles. For these reasons, the proposed formalism is superior to a straightforward numerical solver.

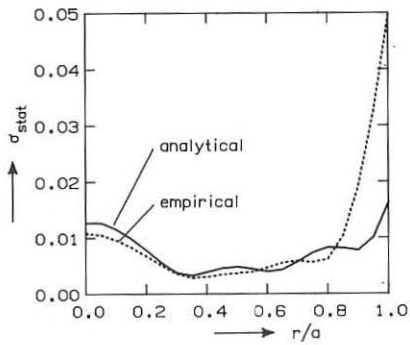

Fig. 3. Calculated (Eq.10) and empirical error bars on the reconstructed ρ

Acknowledgement

This work was performed under the Euratom-FOM association agreement with financial support from NWO and Euratom. One of the authors (G.H.) gratefully acknowledges the hospitality of the FOM Instituut voor Plasmafysica 'Rijnhuizen' and the financial support from the IAEA.

References

[1] Christiansen J. et al, Proc. 15th Europ. Conf. on Controlled Fusion and Plasma Heating, Dubrovnik, May 16-20 1988, Vol 12BI,115
[2] Goldston R. et al, Proc. 15th Europ. Conf. on Controlled Fusion and Plasma Heating, Dubrovnik, May 16-20 1988, Vol 12BI,99
[3] Hogeweij G.M.D., Hordósy G., Lopes Cardozo N.J., submitted for publication in Comp.Phys.Comm.
[4] Soler M., Callen J.D., Nucl.Fusion 19 (1979) 703
[5] Tubbing B.J.D., Lopes Cardozo N.J., van der Wiel M.J., Nucl.Fusion 27 (1987) 1843

Expansions of the flux and the current density in toroidal systems

B.Ph. van Milligen
FOM Institute for Plasma Physics 'Rijnhuizen', Association EURATOM-FOM,
P.O.Box 1207, 3430 BE Nieuwegein, The Netherlands

Introduction

An important topic in tokamak fusion research is the determination of the magnetic equilibrium, determined by the Grad-Shafranov (GS) equation, inside the plasma, using magnetic probes that are located outside the plasma. This problem is ill-posed: small variations in the boundary data may cause large changes in the solution some distance away. The ill-posedness may be overcome by expanding the flux function in a set of solutions to the homogeneous GS equation, and taking only a finite number of terms into account. In order to find a solution inside the plasma, the current distribution must generally be restricted to some physically relevant class.

If, in the vacuum region outside the plasma, the flux function is expanded in a complete set of solutions to the homogeneous GS equation, obtained by separation in toroidal coordinates, the expansion coefficients are called multipolar moments. Such moments have been shown to provide a good description of the flux outside the plasma [1]. The moments method can also be applied to the problem of computing external fields and fluxes from a specified equilibrium. A drawback of the method is the absence of simple relationships between these moments and physically more meaningful global plasma parameters.

Current moments, on the other hand, are widely used to obtain such global plasma parameters as the total current, position of the current centre, etc. [2]. Because these moments can easily be computed from the magnetic signals, they are often used as plasma control parameters.

Method for obtaining relationships between multipolar and current moments

The poloidal flux function ψ obeys the GS equation:

$$\begin{aligned} \Delta^*\psi &= -2\pi\mu_0 R j_\phi && \text{inside the plasma} \\ \Delta^*\psi &= 0 && \text{outside the plasma} \end{aligned} \qquad (1)$$

where $\Delta^*\psi \equiv R^2\nabla(R^{-2}\nabla\psi)$, and j_ϕ is the toroidal current density.

Toroidal coordinates are defined by means of the following relationships with the usual cylindrical coordinates (R,Z,ϕ) [1, 5]:

$$R = \frac{R_0 \sinh\theta}{\cosh\theta - \cos\omega}, \qquad Z = \frac{R_0 \sin\omega}{\cosh\theta - \cos\omega} \qquad (2)$$

Here R_0 is the pole of the coordinate system. A complete set of solutions to the homogeneous GS equation $\Delta^*\psi = 0$ is found upon separating equation (1) in these coordinates. The solutions, called toroidal harmonics, are generally expressed in terms of the half integer Legendre functions [4, 5, 6]. It is now possible to expand the flux function ψ at any position in space in the toroidal harmonics. The expansion coefficients are called the internal and external multipolar moments, respectively.

A method has been found by which *any* current moment, as given by eq. (3), can be written in terms of the multipolar moments.

$$q_\chi \equiv \int_\Omega \chi j_\phi \, dS, \qquad \text{where } \Delta^*\chi = 0 \tag{3}$$

It is possible to choose χ such that the resulting current moments correspond to the usual polynomial current moments introduced in [2] and often used in tokamak research. Some families of solutions χ to the homogeneous GS equation are given in [3]. The following set of polynomials χ_n generates a useful set of current moments:

$$\chi_0 = 1, \qquad \chi_1 = Z,$$

$$\chi_n = R^n \sum_{k=0}^{\lfloor \frac{n}{2} \rfloor - 1} (-4)^{-k} \frac{(n-2)!}{k!(k+1)!(n-2k-2)!} \left[\frac{Z}{R}\right]^{n-2k-2} \qquad (n \geq 2) \tag{4}$$

where $\lfloor . \rfloor$ denotes rounding to the nearest smaller integer. These polynomials satisfy $\Delta^*\chi_n = 0$. The concrete relationships between the current moments corresponding to eq. (4) and the multipolar moments have been derived for $n \leq 6$. Results for $n \leq 2$ are shown in Table 1 (following the notation of [1]).

Table 1: Expression of current moments in terms of the multipolar moments

$\chi = \chi_0 = 1$:	$q_\chi^0 = I_p \equiv \int_\Omega (j_\phi) \, dS = -\frac{\sqrt{2}}{2\pi\mu_0 R_0} \sum_{m=0}^{\infty} M_m^{i,c}$	(total current)
$\chi = \chi_1 = Z$:	$q_\chi^1 = Z_{cur} I_p \equiv \int_\Omega (Z j_\phi) \, dS = \frac{\sqrt{2}}{\pi\mu_0} \sum_{m=0}^{\infty} m \, M_m^{i,s}$	(Z-coordinate of current centre)
$\chi = \chi_2 = R^2$:	$q_\chi^2 = R_{cur}^2 I_p \equiv \int_\Omega (R^2 j_\phi) \, dS = \frac{2\sqrt{2}R_0}{\pi\mu_0} \sum_{m=0}^{\infty} (m^2 - \frac{1}{4}) M_m^{i,c}$	(R-coordinate of current centre)

Expansion of the toroidal current density

It is possible to orthonormalize the functions given by eq. (4) by introducing an inner product $(\chi_i,\chi_j)_w$ defined by $(\chi_i,\chi_j)_w \equiv \int w\chi_i\chi_j \, dS$, where $w = w(R,Z)$ is a weight function. The integration is over the R-Z plane. One can now apply the Gram-Schmidt procedure [5] to orthonormalize the functions χ_i with respect to the inner product $(,)_w$. This yields a set of functions ξ_i satisfying $\Delta^*\xi_i = 0$ and $(\xi_i,\xi_j)_w = \delta_{ij}$.

In analogy with (3), current moments $q_\xi^i = \int \xi_i \, j_\phi \, dS = (\xi_i, w^{-1} j_\phi)_w$ are defined. Then

$$j'_\phi = \sum_{i=0}^{\infty} q_\xi^i \, \xi_i \, w \tag{5}$$

is the best approximation to j_ϕ in the space spanned by $\{\xi_i w\}$. Even so, this expansion is not necessarily a solution to the GS equation.

The expansion (5) should converge quickly, so the zeroth-order approximation to j_ϕ, j^0_ϕ, should in some sense be close to a realistic current profile. Note that from (5) follows $j^0_\phi = q^0_\xi w$, so that this demand is in fact a restriction on the shape of w. Also, w must be such that it produces a well-behaved inner product, or, in other words, w must be a function of rapid decay (i.e. fall off more rapidly than the inverse of any polynomial in R and Z), such that $(\chi_i,\chi_j)_w$ is integrable for all $\{\chi_i,\chi_j\}$.

These two considerations lead to the choice of a Gaussian for w:

$$w = \frac{1}{2\pi\sigma_w^2}\exp\left[-\frac{(R-R_w)^2}{2\sigma_w^2}\right] \qquad (6)$$

The normalization of w is such that $\|1\|_w = 1$. R_w and σ_w can still be chosen. R_w will typically correspond to the centre of a current distribution, while σ_w will correspond to its width.

It is very important to observe that the χ_i do not form a complete set. Nevertheless the total current, current weight centre etc. can still be produced accurately. When applying this method in practice, the approximation (5) can be optimized by choosing an optimal R_w and σ_w to fit a particular measurement. This is achieved by setting $R_w = [q^2_\chi/q^0_\chi]^{1/2}$. A good choice for σ_w can be provided by some scaling law. We have tried the method with a simple numerical model and found that it actually does provide a good approximation to the current profile, that can be obtained in a fast way. The expansion functions are displayed in the accompanying figure.

Error analysis

An error analysis on the methods for obtaining the multipolar and current moments was performed. Using a simple wire model of the plasma, we computed the various moments both directly and by using simulated measurements of fluxes and fields outside the plasma. These measurements were perturbed with random noise to simulate measurement errors. The current moments were found to be more stable with respect to this noise than the multipolar moments. To illustrate this, we compare the results for the first multipolar moment (m=1) and the corresponding current moment (i=2). At a measurement error level of 3%, $M^{i,c}_1$ could be recovered with 3% accuracy, $M^{e,c}_1$ with 12%, while the current moment, q^2_χ, could be recovered with 0.7% accuracy.

Acknowledgements

The author would like to express his gratitude to Dr. N.J. Lopes Cardozo for many inspiring discussions. Also, the criticism by Dr. B.J. Braams has been invaluable. This work was performed under the EURATOM-FOM Association agreement with financial support from NWO and EURATOM.

References

[1] ALLADIO, F., CRISANTI, F., Nucl. Fusion **9** (1986) 1143
[2] ZAKHAROV, L.E., SHAFRANOV, V.D., Sov. Phys. Tech. Phys., **18** (1973) 151
[3] BRAAMS, B.J., *Computational studies in tokamak equilibrium and transport*, Thesis, Utrecht (1986)
[4] FOCK, V.A., Fiz. Zh. Soviet Union **1** (1932) 215
[5] MORSE, P.M., FESHBACH, H., *Methods of Theoretical Physics*, McGraw-Hill, New York (1953)
[6] ABRAMOWITZ, M., STEGUN, I.A., *Handbook of mathematical functions*, National Bureau of Standards, Washington, D.C., 4th printing (1965)

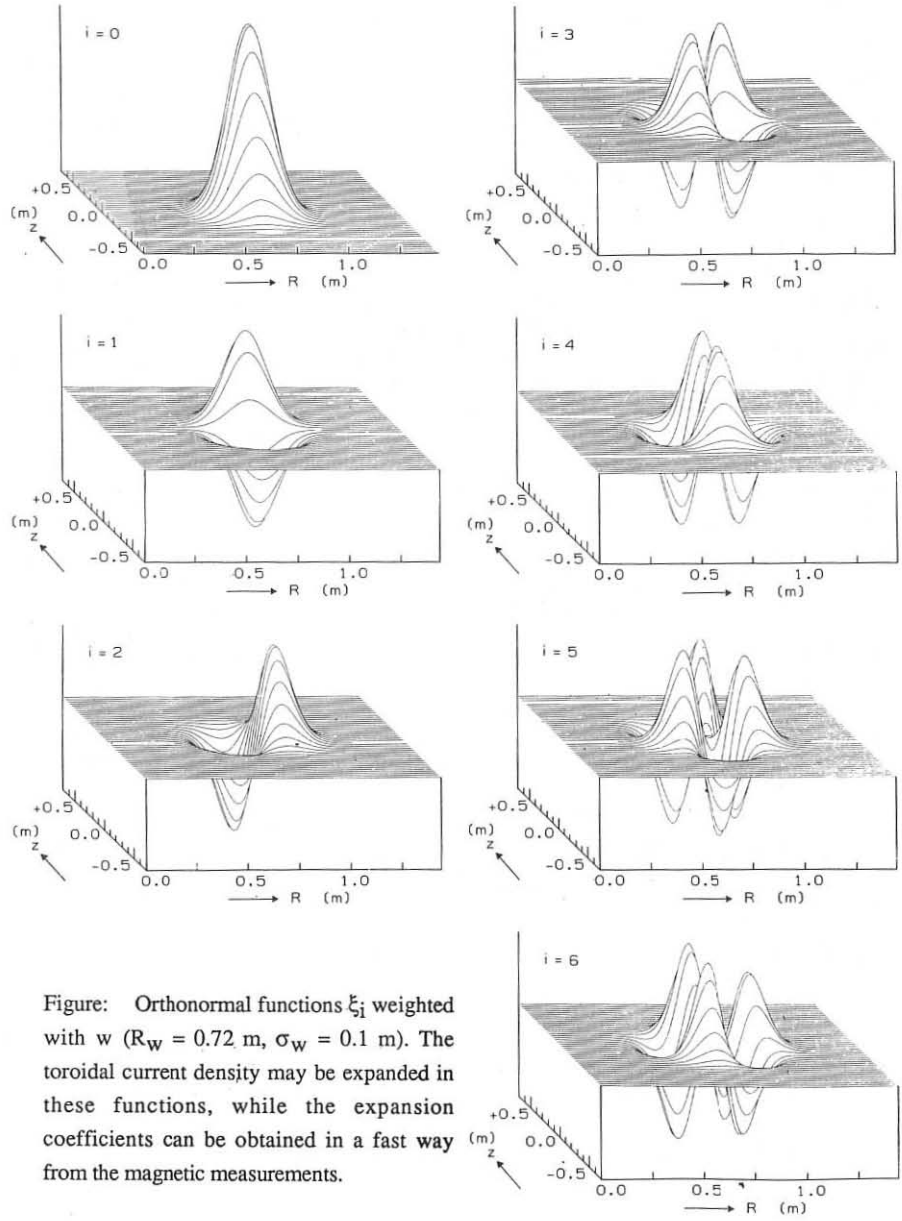

Figure: Orthonormal functions ξ_i weighted with w (R_w = 0.72 m, σ_w = 0.1 m). The toroidal current density may be expanded in these functions, while the expansion coefficients can be obtained in a fast way from the magnetic measurements.

RESPONSIBLE AUTHOR

INDEX *

* (First author is listed when responsible author was not indicated)